國立中央大學天文研究所
鹿林天文台年報

2012

No.10

國立中央大學天文研究所 編

目錄

研究報告

工作報告

相關報導

研究報告

Astronomy & Astrophysics manuscript no. pap1633˙final
July 18, 2012

Variability of the blazar 4C 38.41 (B3 1633+382) from GHz frequencies to GeV energies⋆

C. M. Raiteri[1], M. Villata[1], P. S. Smith[2], V. M. Larionov[3,4,5], J. A. Acosta-Pulido[6,7], M. F. Aller[8], F. D'Ammando[9], M. A. Gurwell[10], S. G. Jorstad[11,3], M. Joshi[11], O. M. Kurtanidze[12,13,14,15], A. Lähteenmäki[16], D. O. Mirzaqulov[17], I. Agudo[18,11], H. D. Aller[8], M. J. Arévalo[6,7], A. A. Arkharov[4], U. Bach[19], E. Benítez[20], A. Berdyugin[21], D. A. Blinov[3], K. Blumenthal[11], C. S. Buemi[22], A. Bueno[6,7], T. M. Carleton[2], M. I. Carnerero[6,7,1], D. Carosati[23,24], C. Casadio[18], W. P. Chen[25], A. Di Paola[26], M. Dolci[27], N. V. Efimova[3,4], Sh. A. Ehgamberdiev[17], J. L. Gómez[18], A. I. González[7], V. A. Hagen-Thorn[3,5], J. Heidt[14], D. Hiriart[28], Sh. Holikov[17], T. S. Konstantinova[3], E. N. Kopatskaya[3], E. Koptelova[25,29], S. O. Kurtanidze[12], E. G. Larionova[3], L. V. Larionova[3], J. León-Tavares[16], P. Leto[22], H. C. Lin[25], E. Lindfors[21], A. P. Marscher[11], I. M. McHardy[30], S. N. Molina[18], D. A. Morozova[3], R. Mujica[31], M. G. Nikolashvili[12], K. Nilsson[32], E. P. Ovcharov[33], N. Panwar[25], M. Pasanen[21], I. Puerto-Gimenez[6,34], R. Reinthal[21], G. M. Richter[13], J. A. Ros[35], T. Sakamoto[36,37], R. D. Schwartz[38], A. Sillanpää[21], N. Smith[39], L. O. Takalo[21], J. Tammi[16], B. Taylor[11,40], C. Thum[41], M. Tornikoski[16], C. Trigilio[22], I. S. Troitsky[3], G. Umana[22], A. T. Valcheva[33], and A. E. Wehrle[42]

(Affiliations can be found after the references)

ABSTRACT

Context. After years of modest optical activity, the quasar-type blazar 4C 38.41 (B3 1633+382) experienced a large outburst in 2011, which was detected throughout the entire electromagnetic spectrum, renewing interest in this source.

Aims. We present the results of low-energy multifrequency monitoring by the GASP project of the WEBT consortium and collaborators, as well as those of spectropolarimetric/spectrophotometric monitoring at the Steward Observatory. We also analyse high-energy observations of the *Swift* and *Fermi* satellites. This combined study aims to provide insights into the source broad-band emission and variability properties.

Methods. We assemble optical, near-infrared, millimetre, and radio light curves and investigate their features and correlations. In the optical, we also analyse the spectroscopic and polarimetric properties of the source. We then compare the low-energy emission behaviour with that at high energies.

Results. In the optical–UV band, several results indicate that there is a contribution from a quasi-stellar-object (QSO) like emission component, in addition to both variable and polarised jet emission. In the optical, the source is redder-when-brighter, at least for $R \gtrsim 16$. The optical spectra display broad emission lines, whose flux is constant in time. The observed degree of polarisation increases with flux and is higher in the red than the blue. The spectral energy distribution reveals a bump peaking around the U band. The unpolarised emission component is likely thermal radiation from the accretion disc that dilutes the jet polarisation. We estimate its brightness to be $R_{\rm QSO} \sim 17.85$–18 and derive the intrinsic jet polarisation degree. We find no clear correlation between the optical and radio light curves, while the correlation between the optical and γ-ray flux apparently fades in time, likely because of an increasing optical to γ-ray flux ratio.

Conclusions. As suggested for other blazars, the long-term variability of 4C 38.41 can be interpreted in terms of an inhomogeneous bent jet, where different emitting regions can change their alignment with respect to the line of sight, leading to variations in the Doppler factor δ. Under the hypothesis that in the period 2008–2011 all the γ-ray and optical variability on a one-week timescale were due to changes in δ, this would range between ~ 7 and ~ 21. If the variability were caused by changes in the viewing angle θ only, then θ would go from $\sim 2.6^\circ$ to $\sim 5^\circ$. Variations in the viewing angle would also account for the dependence of the polarisation degree on the source brightness in the framework of a shock-in-jet model.

Key words. galaxies: active – galaxies: quasars: general – galaxies: quasars: individual: 4C 38.41 – galaxies: jets

1. Introduction

The Compton Gamma Ray Observatory (CGRO) launched in 1991 revealed 271 γ-ray sources, one fourth of which were identified as blazars (Hartman et al., 1999), i.e. active galactic nuclei (AGNs) showing the most extreme properties. They are indeed characterised by violent activity at almost all frequencies on different timescales, from long-term flux changes to intraday variability (IDV), by high radio to optical polarisation, and by the superluminal motions of radio knots. The observations can be explained by assuming that their emission is relativistically beamed, which occurs if the emitting plasma jet, produced by a supermassive black hole fed by an accretion disc, is directed toward us. The polarised, low-energy emission (from the radio to the optical–X-ray band) is likely synchrotron radiation produced by relativistic electrons in the jet, while the high-energy emission (from the X-ray to the γ-ray frequencies) is usually interpreted as the result of inverse-Compton scattering of low-energy photons off the same relativistic electrons. Whether these low-energy photons come from the jet itself (synchrotron self-Compton, or SSC, models) or from the AGN environment (external Compton, or EC, models), and in the latter case whether they come from the accretion disc, the broad line region, or the dusty torus, is still a matter of debate.

⋆ The radio-to-optical data collected by the GASP-WEBT collaboration are stored in the GASP-WEBT archive; for questions regarding their availability, please contact the WEBT President Massimo Villata (villata@oato.inaf.it).

Blazars include flat spectrum radio quasars (FSRQs) and BL Lacertae objects. Frequently FSRQs exhibit quasi-stellar-object (QSO) like broad emission lines, as well as a blue and unpolarized continuum that is presumed to be the signature of the thermal emission from the accretion disc, the so-called "big blue bump" (e.g. Wills et al., 1992; Pian et al., 1999; Raiteri et al., 2007; D'Ammando et al., 2009). In contrast, BL Lacertae objects may have by definition at most weak lines, even if sometimes these sources challenge their classification (e.g. Vermeulen et al., 1995).

Researchers are trying to understand the structure of blazars and the mechanisms behind their emission and variability by analysing the multifrequency behaviour of these objects extended over the broadest possible energy range with data sampling and quality that is as high as possible (see e.g. Marscher et al., 2010; Jorstad et al., 2010; Agudo et al., 2011a,b). The international collaboration known as the Whole Earth Blazar Telescope (WEBT)[1] was created in 1997 for this purpose, and involves tens of optical, radio, and near-infrared observatories. The WEBT campaigns have produced low-frequency light curves of extraordinary sampling, and these results have often been analysed in conjunction with high-frequency data from satellites (see e.g. Villata et al., 2006; Raiteri et al., 2008b,c; Larionov et al., 2008; Böttcher et al., 2009; Villata et al., 2009b; Raiteri et al., 2009, and references therein).

Renewed interest in blazars occurred with the launch of the new-generation γ-ray satellites Astrorivelatore Gamma a Immagini Leggero (AGILE) in 2007, and particularly with that of *Fermi* (formerly GLAST) in 2008, which operates in survey mode. To acquire low-energy data to compare with the high-energy observations of AGILE and *Fermi*, in 2007 the WEBT started the GLAST-AGILE Support Program (GASP; see e.g. Villata et al., 2008, 2009a; D'Ammando et al., 2009; Raiteri et al., 2010, 2011a; D'Ammando et al., 2011). Since 2008, a ground-based monitoring programme has been running at the Steward Observatory (Smith et al., 2009), providing support for the *Fermi* gamma-ray telescope. It uses the 2.3 m Bok and 1.54 m Kuiper telescopes with the SPOL spectropolarimeter (Schmidt et al., 1992) and provides publicly available spectropolarimetry, spectrophotometry, and calibrated broad-band flux measurements for about 40 blazars[2].

In this paper, we study the multifrequency behaviour of one blazar, namely the optically violent variable (OVV) FSRQ 4C 38.41 (1633+382) at redshift $z = 1.814$, which belongs to the target list of both the GASP and the Steward Observatory monitoring programmes. The period of observations presented here includes a big optical outburst in 2011 (Raiteri et al., 2011b) that was also detected at γ-ray energies by *Fermi* (Szostek, 2011), and in the X-ray and UV bands by the *Swift* satellite, providing an excellent opportunity to study the source variability over most of the electromagnetic spectrum.

4C 38.41 had already been observed in γ-rays by the Energetic Gamma Ray Experiment Telescope (EGRET) instrument onboard CGRO several times, and from these data its emission was found to vary significantly on a day timescale (Mattox et al., 1993). The maximum flux detected by EGRET above 100 MeV was $(107.5 \pm 9.6) \times 10^{-8}$ ph cm^{-2} s^{-1} in mid September 1991[3]. AGILE observed 4C 38.41 several times. In particular, a preliminary analysis of the AGILE Gamma Ray Imaging Detector (GRID) data between 2009 December 1 and 2010 November 30 yielded a γ-ray flux $F_{\rm E>100\,MeV} = (28 \pm 5) \times 10^{-8}$ ph cm^{-2} s^{-1}. This flux is consistent with the value reported in the Second *Fermi* Large Area Telescope (LAT) Catalog (Nolan et al., 2012). A refined analysis of the AGILE/GRID data, along with a search for possible short-term variability, will be presented in Vercellone et al. (2012, in preparation). Multifrequency observations of 4C 38.41 during the γ-ray flares observed by *Fermi* in 2009–2010, including Very Long Baseline Array (VLBA) images, was presented by Jorstad et al. (2011). They conclude that high states at γ-ray energies are due to interaction between a disturbance travelling down the jet and the 43 GHz VLBI core.

2. Optical and near-infrared photometry

As mentioned in the introduction, the GASP was started in 2007 to perform long-term optical-to-radio monitoring of selected γ-loud blazars during the observations of the AGILE and *Fermi* γ-ray satellites. In the optical, GASP data are collected in the *R* band only. However, for this paper we also added data taken by the GASP-WEBT observers in the *B*, *V*, and *I* bands. Calibration of 4C 38.41 was achieved by performing differential photometry with respect to stars A and B in the source field, whose standard magnitudes in the *B*, *V*, and *R* bands were derived by Villata et al. (1997). We obtained standard magnitudes in the *I* band from the Sloan Digital Sky Survey's *r* and *i* photometry, after applying the transformations of Chonis & Gaskell (2008). In this way, we derived $I = 15.20 \pm 0.05$ for star A and $I = 15.06 \pm 0.06$ for star B. The GASP near-infrared (near-IR) data are collected in the *J*, *H*, and *K* bands, where calibration is performed according to the photometric sequences obtained with the AZT-24 telescope at Campo Imperatore[4].

The optical and near-IR light curves of 4C 38.41 in the period 2008–2011 are shown in Fig. 1. The GASP-WEBT observations were performed by the following observatories: Abastumani, Calar Alto[5], Campo Imperatore, Crimean, Galaxy View, Goddard (GRT), Lowell (Perkins), Lulin, Mount (Mt.) Maidanak, Roque (KVA and Liverpool), Rozhen, Sabadell, San Pedro Martir, St. Petersburg, Teide (IAC80 and TCS), Tijarafe, and Torino. The *V* and *R*-band light curves are complemented by data taken at the Steward Observatory in the framework of the monitoring programme in support of the *Fermi* observations (see Sect. 3). The figure also displays optical data acquired by the UVOT instrument onboard the *Swift* satellite (see Sect. 5.1).

Light curves were carefully checked and cleaned by reducing the data scattering through binning data close in time from the same telescope, when possible, and by removing clear outliers as well as data with errors greater than 0.2 mag.

Substantial variability characterises the source behaviour, especially in 2009 and 2011. The near-IR light curves were more coarsely sampled than the optical ones, but show the same trend. In particular, they confirm the sharp brightness fall following the peak of the 2011 outburst. The range of magnitude spanned over the whole period is 2.1–3.0 mag, depending on the band, and in general appears to be larger at lower frequencies. This is a well-known feature of FSRQs, which is ascribed to a mixture of variable emission from a jet and almost constant emission from an accretion disc.

[1] http://www.oato.inaf.it/blazars/webt/
[2] http://james.as.arizona.edu/~psmith/Fermi/
[3] http://cossc.gsfc.nasa.gov/cossc/egret/
[4] http://www.astro.spbu.ru/staff/vlar/NIRlist.html
[5] Calar Alto data were acquired as part of the MAPCAT project http://www.iaa.es/~iagudo/research/MAPCAT

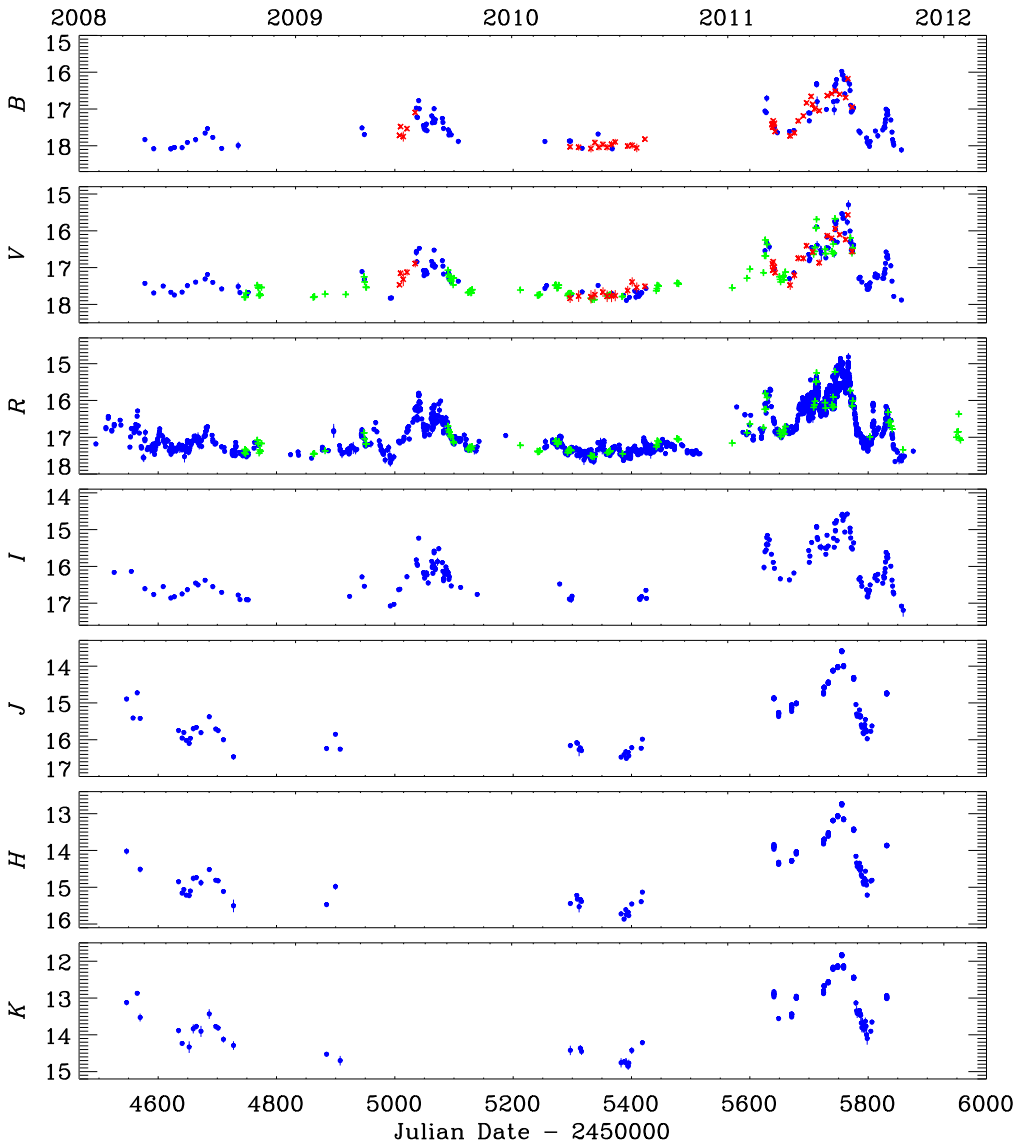

Fig. 1. Optical and near-infrared light curves of 4C 38.41 in 2008–2011 built with GASP-WEBT data (blue dots), *Swift*-UVOT data (red crosses), and data from the Steward Observatory (green plus signs). The UVOT *v*-band points have been shifted by −0.1 mag to match the ground-based data.

2.1. Colour analysis

The contribution of thermal radiation from the accretion disc is expected to lead to a redder-when-brighter spectral behaviour in the optical band. We verified this by performing a colour analysis. Figure 2 shows the source *R*-band light curve and the $B - R$ colour behaviour since 1995. Pre-GASP data were provided from the Abastumani, Calar Alto, Crimean, Mt. Maidanak, Torino[6], and St. Petersburg observatories. The historical light curve in the top panel shows that the source was very active in 1995–1998 and subsequently faded to $R > 16$ until 2007, when it reached $R \sim 15.5$. Other flares peaking at $R \sim 15.5$–16 occurred in 2009 and at the beginning of 2011, while during the big outburst of mid 2011 the source returned to its previous brightness levels of 1995 and 1997 ($R \lesssim 15$).

We derived $B - R$ colour indices by coupling the highest-quality *R* and *B* data (with errors smaller than 0.05 and 0.1 mag, respectively) acquired by the same telescope within 20 minutes. We obtained 372 indices, with a mean time separation between *B* and *R* exposures of about 6 minutes. The lack of a *B*-band light curve with sampling equivalent to the *R*-band one makes the $B - R$ versus time plot rather discontinuous. In particular, most of the colour indices were derived during faint states of the source, as illustrated by the difference between the average magnitude of the whole dataset ($R = 16.42$) and that of the data used to get the colour indices ($R = 16.98$). The minimum and maximum values of the colour index are 0.39 and 1.04, respectively, and its average value is $< B - R >= 0.64$, with a standard deviation $\sigma = 0.14$.

The dependence of the colour index on brightness appears complex, with a large dispersion in faint states. However, a general redder-when-brighter trend is recognisable for $R \gtrsim 16$; in brighter states, the colour index may even decrease. This is rem-

[6] Data taken at the Torino Observatory in 1995–1996 were published in Villata et al. (1997) and Raiteri et al. (1998), but for the present paper we reprocessed all the frames with both aperture photometry and Gaussian fitting of the PSF; in particular, we carefully re-analysed the observations of 1995 June 27–28 that led to the detection of the optical outburst announced by Bosio et al. (1995).

iniscent of the "saturation effect" first noticed by Villata et al. (2006) for another FSRQ: 3C 454.3. The shift from a redder-when-brighter to a bluer-when-brighter trend as the brightness increases would mark the transition from a quasar-like to a BL Lac-like spectral behaviour, the latter occurring when the synchrotron radiation dominates over the thermal emission. The dispersion in the data points during faint states is apparently caused by at a given magnitude the source appearing to be redder during active periods than in more quiescent phases, as the comparison between the upper and middle panel of Fig. 2 suggests. However, we cannot rule out that at least part of this effect is due to an unverifiable photometric offset between different datasets that do not overlap in time.

Furthermore, assuming as a first approximation that the source spectrum in the optical band follows a power-law ($F_\nu \propto \nu^{-\alpha}$), we can derive the energy index $\alpha = [(B-R) - 0.32]/0.41$, where we adopted Galactic extinction values of 0.048 and 0.030 mag in the B and R bands[7], respectively, and effective wavelengths as well as zero-mag fluxes by Bessell et al. (1998). The range of colour index values cited above then translates into a range of energy index values from 0.17 to 1.76. Thus, in the usual spectral energy distribution (SED) representation $\log(\nu F_\nu)$ versus $\log \nu$, the optical spectrum of 4C 38.41 is flat when $B-R$ is low, i.e. in general during faint states, while it becomes steep for $B-R > 0.73$, which usually corresponds to bright levels.

2.2. Rapid optical variability

We analysed the R-band light curve presented in Fig. 1 to search for the most noticeable intraday variability (IDV) episodes, involving changes of more than 0.3 mag in less than six hours. We found six nights where such rapidly occurring episodes were observed: on JD = 2455065, Tijarafe observations following St. Petersburg ones revealed a brightening of 0.32 mag in 2.82 hours (0.113 mag/hour); on JD = 2455699, a very dense monitoring at the Mt. Maidanak Observatory showed a fading of 0.31 mag in 4.15 hours (0.075 mag/hour); on JD = 2455702, observations at the KVA revealed a 0.39 mag brightening with respect to St. Petersburg observations about four hours before (0.099 mag/hour); on JD = 2455715, we derived a 0.34 mag change in 3.41 hours from the data of Goddard and Lowell (0.100 mag/hour); on JD = 2455756, intense monitoring at the Mt. Maidanak and Abastumani observatories revealed variations of 0.34 mag in 4.7 hours (0.072 mag/hour); finally, on JD = 2455759 a very rapid brightening of 0.31 mag in 0.74 hours was inferred by comparing Crimean with Mt. Maidanak data, which implies an impressive rate of 0.42 mag/hour. A careful check of the corresponding frames and photometry confirmed the results, so we conclude that this extreme variability episode is most likely genuine. A similarly rapid variability episode was reported by Raiteri et al. (2008c) for another quasar-type blazar, 3C 454.3, in January 2008 (0.40 mag/hour), and an even more extreme episode was discussed by Raiteri et al. (2008a) for the same object, which brightened by 1.1 mag in 1.5 hours and then dimmed by 1.2 mag in one hour in December 2007.

Moreover, 4C 38.41 exhibited extraordinary optical activity in 2011, with flux variations of several tenths of a magnitude on a day timescale, as shown by Fig. 3. The most noticeable one was a dimming of 0.77 mag in 13.81 hours observed on JD = 2455702–2455703, while variations $\gtrsim 1$ mag were detected in 52 hours on JD = 2455700–2455702 and in 72 hours on JD = 2455805–2455808.

[7] From the NASA/IPAC Extragalactic Database, http://ned.ipac.caltech.edu/

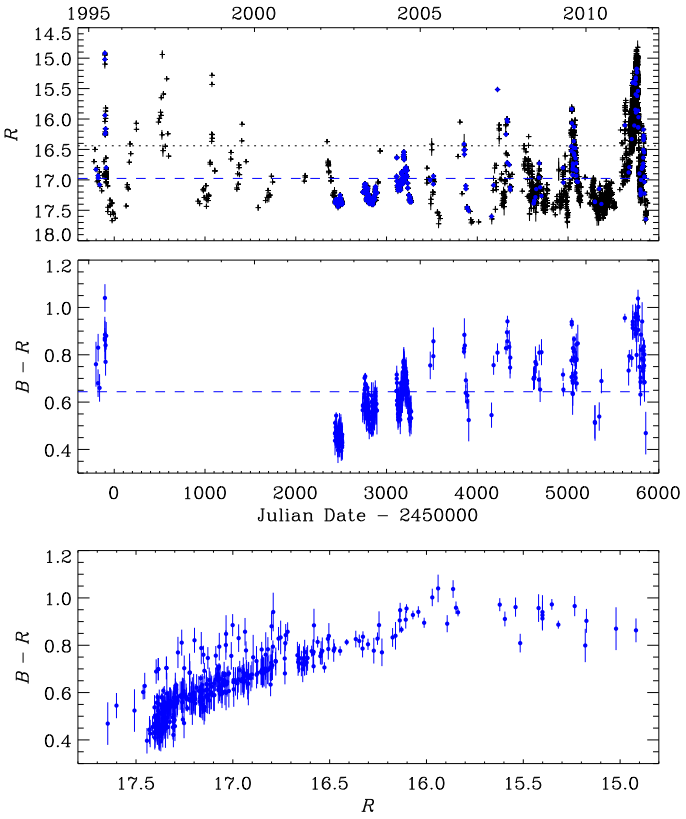

Fig. 2. The R-band light curve of 4C 38.41 in 1995–2011 (top panel). Blue dots indicate the data used to derive the $B-R$ colour indices shown both as a function of time (middle panel) and as a function of magnitude (bottom panel). The black dotted and blue dashed lines in the top panel indicate the average magnitude for the whole dataset and the data used for the colour indices, respectively. In the middle panel, the blue dashed line marks the average colour index.

3. Optical polarimetry, spectropolarimetry, and spectrophotometry

Polarimetric data for the present paper were provided by the Steward, Crimean, Lowell, Calar Alto, and St. Petersburg observatories. The Steward Observatory also supplied spectropolarimetry and spectrophotometry data.

Figure 4 shows the behaviour of the observed degree of optical polarisation P, as well as that of the position angle of the polarisation vector Θ as a function of time. To solve the $\pm 180°n$ ambiguity in Θ, we consider only data for which $P/\sigma_P > 5$ and then require that the change across contiguous epochs be $\leq 90°$. Visual inspection of the figure reveals that in general periods of high flux correspond to periods of high polarisation degree, so that there is some correlation between P and brightness, which is investigated further below. For the polarisation position angle, there appears to be a smooth rotation of about 200° in 0.6 years, from 2008.4 to 2009.0, followed by an ever increasing rotation of about 270° in 0.6 years, from 2009.2 to 2009.8. Thereafter, Θ shows only smaller fluctuations between $\sim -100°$ and 40°in 2010 and 2011. Hence, the 2009 outburst occurred during a phase of noticeable change in Θ, in contrast to the 2011 one.

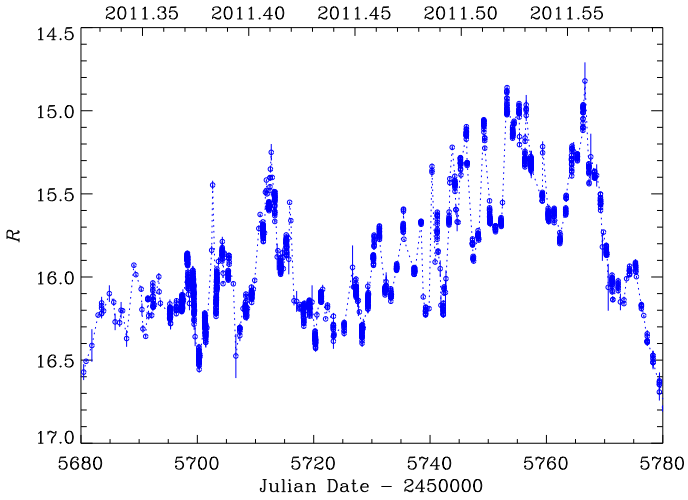

Fig. 3. The *R*-band light curve of 4C 38.41 in the most active period of 2011, showing noticeable intraday and interday variability episodes. The total number of data points is 2046, 1686 of which come from the Mt. Maidanak Observatory.

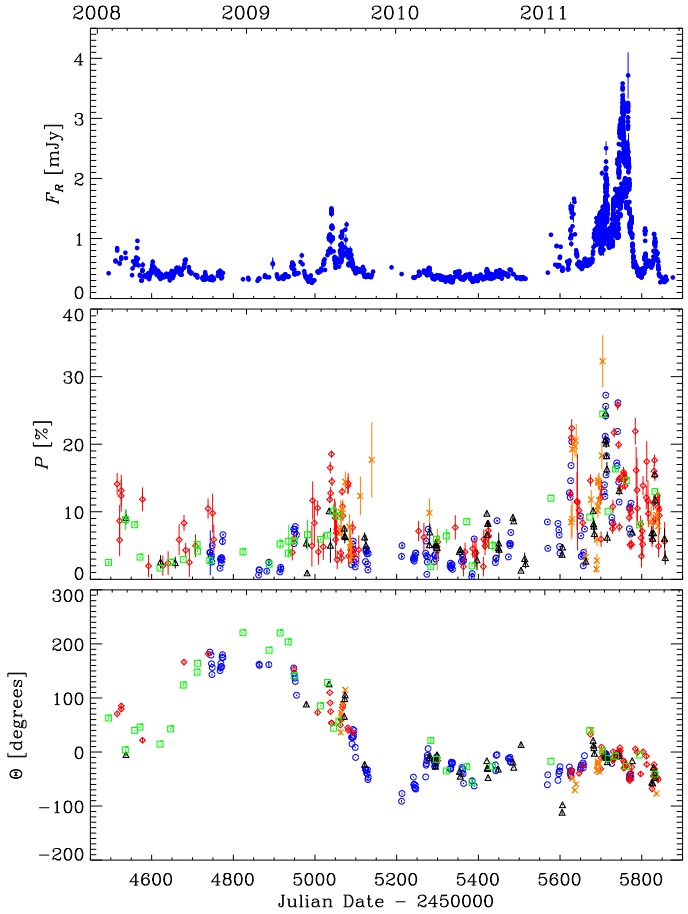

Fig. 4. Optical flux densities in the *R* band (top panel), percentage of polarised flux (middle panel), and polarisation position angle (bottom). Data are from the following observatories: Steward (blue circles), Crimean (red diamonds), Lowell (black triangles), Calar Alto (green squares), and St. Petersburg (orange crosses). The $\pm 180°n$ ambiguity in Θ is solved by using only data for which $P/\sigma_P > 5$ and then requiring that the change across contiguous epochs be $\leq 90°$.

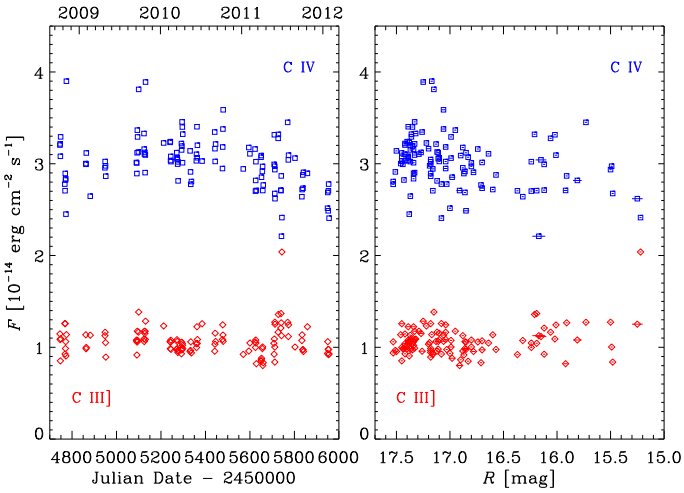

Fig. 5. The flux in the observed frame of the C IV (blue squares) and C III] (red diamonds) emission lines as a function of time (left panel) and source brightness (right panel). During the period of monitoring, there is little evidence of significant emission-line variability in 4C 38.41. Data are derived from the ongoing monitoring programme at Steward Observatory.

3.1. Emission lines

With a redshift of $z = 1.81$, two prominent broad emission-lines fall within the 4000–7550 Å spectral window that is sampled by the Steward Observatory spectrophotometry of 4C 38.41: C IVλ1550 and C III]λ1909. In Fig. 5, we plot the emission-line fluxes measured on 116 nights from 2008 October to 2012 January against both time and the optical brightness of 4C 38.41. The same trends for the line fluxes are observed as seen for the Balmer lines in PKS 1222+216 (Smith et al., 2011) and 3C 454.3 (Raiteri et al., 2008c). That is, the data are consistent with the line fluxes being constant, the scatter in the measurements seen within an observing campaign (about a week long) being roughly the same magnitude as during the entire monitoring period. Likewise, the substantial variations in the equivalent widths of the lines in 4C 38.41 (ranging from −83 to −11 Å for C IV) are consistent with only the continuum having varied since 2008 August. The size of the broad-line region in quasars (Kaspi et al., 2000) and the added delay in variability caused by the redshift of the object make significant line variability impossible on timescales as short as a week, so the scatter in the data is a reflection of the systematic uncertainties in the spectrophotometric measurements. The average C IV line flux is measured to be $(3.02\pm0.28)\times10^{-14}$ erg cm^{-2} s^{-1}. For C III], the average flux is $(1.07\pm0.15)\times10^{-14}$ erg cm^{-2} s^{-1}. The line fluxes were measured by fitting a single Gaussian to the line profiles. The Gaussian fits yield an average full width at half maximum (FWHM) of (4800 ± 300) km s^{-1} for C IV and (6500 ± 1200) km s^{-1} for C III]. The large uncertainty in the measured width of C III] is due to its relatively small equivalent width, especially when 4C 38.41 is bright, and its larger FWHM relative to C IV is likely caused by the inclusion of Al IIIλ1858 within the fitted line profile.

3.2. Continuum flux and colour

The Steward spectrophotometry can be used to examine how the optical continuum of 4C 38.41 varies with time and flux as shown in Fig. 2, but avoiding the non-variable emission features that fall within the standard photometric-filter bandpasses.

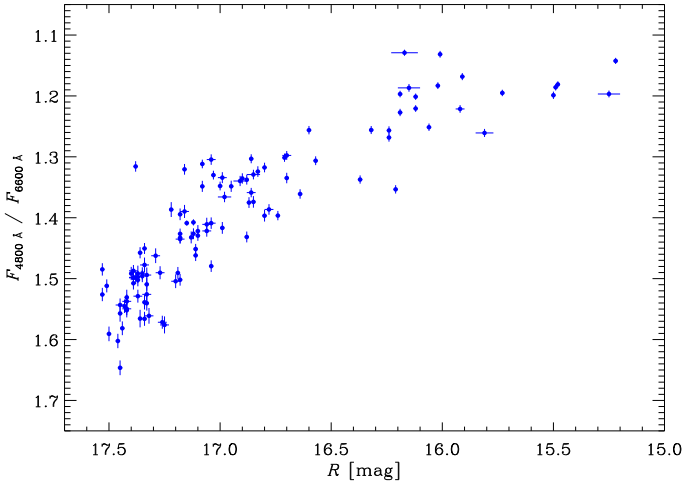

Fig. 6. The continuum colour of 4C 38.41 as a function of the source brightness. The continuum colour is approximated by the flux ratio of the two 400 Å-wide bins centred on 4800 Å and 6600 Å in the observed reference frame.

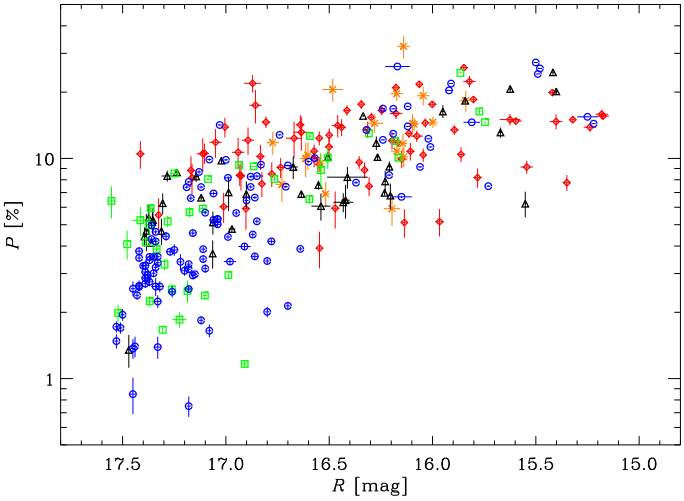

Fig. 7. The observed degree of optical polarisation plotted against the brightness of 4C 38.41 in the R band. Data are from the following observatories: Steward (blue circles), Crimean (red diamonds), Lowell (black triangles), Calar Alto (green squares), and St. Petersburg (orange crosses). Only data having $P/\sigma_P > 5$ are included for clarity.

Figure 6 shows the colour of 4C 38.41 as a function of brightness in the R band. The colour is determined by taking the ratio of the fluxes within two 400 Å-wide bins centred on 4800 Å ("blue") and 6600 Å ("red"). Although the spectra extend to 7550 Å, using a redder measurement would include uncorrected terrestrial oxygen and water absorption features and would corrupt the determination of the continuum flux ratio. The trend in Fig. 6 of the continuum becoming redder as the object brightens confirms the broad-band filter results shown in Fig. 2. Despite a range in wavelength of only 640 Å between the flux bins in the rest frame of the object, the correlation between colour and brightness is pronounced, and suggests that the dominant source of continuum light is different when 4C 38.41 is bright than when the blazar is faint.

3.3. Polarisation and flux

A strong correlation between the degree of optical linear polarisation, P, and the R-band optical brightness is evident from the data and shown in Fig. 7. Generally, 4C 38.41 is more highly polarised when bright than when faint. Given the correlation identified between optical continuum colour and brightness in Sect. 3.2, the trend observed between P and brightness translates into a strong correlation between optical colour and degree of polarisation. This correlation is shown in Fig. 8, with the continuum flux ratio of the 4800 Å to 6600 Å bins used as the measure of optical colour. High polarisation in 4C 38.41 is associated with a redder continuum. This result is further evidence that the dominant source of continuum flux is different when the object is bright than when it is faint, as suggested by the observed relationship between the flux and colour. When bright, 4C 38.41 is generally optically redder and more highly polarised.

In addition to the degree of polarisation, we searched for correlations between the polarisation position angle and optical flux, colour, and P. No apparent correlations were found.

Jorstad et al. (2011) found that at least from June to November 2009 there was good agreement between the position angle of optical polarisation and that of polarisation in the 43 GHz core, and between the general behaviour of P in the two bands, except for the time when, according to the VLBA images, a superluminal knot was passing through the core. At this time,

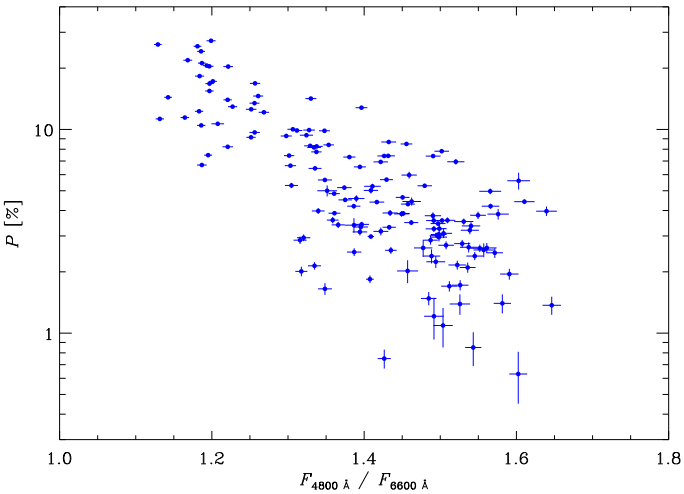

Fig. 8. The observed degree of polarisation plotted against the optical continuum colour (as defined in Fig. 6) of 4C 38.41. The polarisation and flux ratio measurements are simultaneous, with the polarisation data being derived from the median value within a 5000–7000 Å bin from the Steward Observatory spectropolarimetry.

the optical polarization peaked, while P in the core was minimal and the optical position angle and the position angle in the core differ by $\sim 90°$. This implies that the core was optically thick, most likely due to passage of the knot, which is consistent with the knot kinematics.

3.4. Wavelength dependence of the optical polarisation

The striking correlations observed in 4C 38.41 between the optical flux, colour, and polarisation have been noted in other strong emission-line blazars (see e.g. Sitko et al., 1985; Smith et al., 1986, 2011) and have been found to be in the same sense. That is, as objects fade, they become bluer and are generally not as highly polarised. During optical flares, a redder and more highly

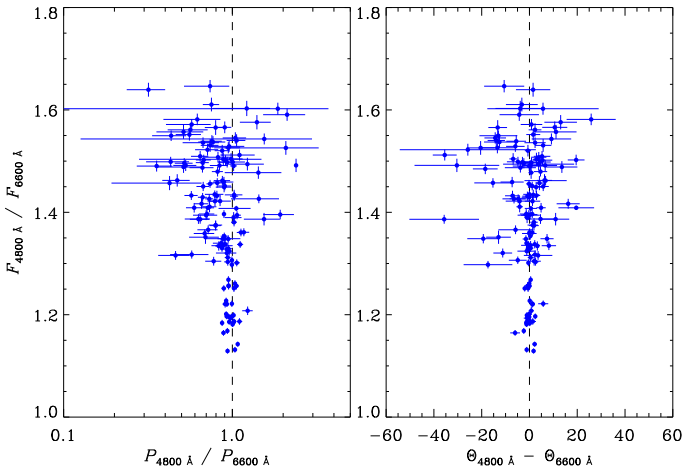

Fig. 9. Left panel: relationship between the ratio of observed polarisation in the blue to red bins and colour, defined as in Fig. 6. Right panel: relationship between the difference between the polarisation position angles in the blue and red bins, and colour.

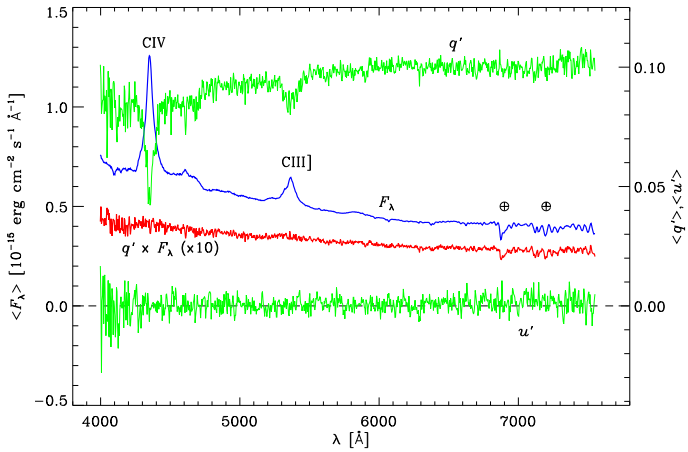

Fig. 10. The median flux (blue), polarised flux (red), and normalised q' and u' Stokes (green) spectra for 4C 38.41. These spectra were compiled from 144 spectropolarimetric observations of the blazar. The polarised flux spectrum is derived by multiplying the flux spectrum by q' and displays a featureless power-law as expected from a synchrotron source. The polarised flux spectrum is scaled by a factor of 10 for clarity. See the text for a full description of the q' and u' spectra. Telluric absorption features are identified with ⊕ symbols.

polarised source of continuum flux appears to dominate the optical continuum. The short (daily) variability timescales and the power-law spectrum at optical wavelengths of the variable component indicate that this is the beamed synchrotron continuum from the relativistic jet in these sources. As a flaring object fades, one can wonder whether the trends seen between flux, colour, and polarisation are simply a reflection of the evolution of the jet, or if fainter emission contributions, not directly associated with the beamed continuum, are becoming more dominant. A key to understanding these trends has been investigations of how the linear polarisation varies with wavelength. We used 144 available spectropolarimetric observations of 4C 38.41 obtained between 2008 October and the end of 2012 January to examine the optical spectra of P, Θ, and the polarised flux.

Figure 9 shows the ratio of the fluxes in the blue to red bins (defined in Sect. 3.2) plotted against the ratio of the observed polarisation in the same bins. As the blazar becomes bluer (fainter), the polarisation in the blue tends to be less than P measured in the red bin. The strength of this wavelength dependence in P generally increases as the object becomes bluer (fainter), although the low levels of polarisation and flux encountered result in relatively large uncertainties in $P_{4800Å}/P_{6600Å}$. Figure 9 also shows the difference between the polarisation position angles determined in the two continuum bins. Most observations are consistent with no wavelength dependence in Θ. This general trend of Θ being constant in wavelength suggests that there is only a single source of polarised flux from the jet that dominates at any given time. If a second non-thermal source of polarised flux that has a significantly different spectral index and polarisation position angle becomes bright enough to compete with the original source, then a strong wavelength dependence in Θ can occur (see e.g. Holmes et al., 1984; Sitko et al., 1984), although this does not seem to happen often (Sitko et al., 1985; Smith et al., 1987; Mead et al., 1990). Much of the wavelength dependence may of course be hidden if the sources of polarised flux have similar spectral indices and/or polarisation position angles within the spectral region being observed.

To more clearly illustrate the spectral dependence of P for an object as faint as 4C 38.41, we took a median of the 144 available polarisation spectra obtained throughout the monitoring period. This was done by rotating each polarisation spectrum so that all of the polarised flux is in the q Stokes parameter. That is, the observed q and u spectra were transformed (rotated) to q' and u', where u' averages to 0 over the entire spectrum. The resulting q' spectra were then scaled to $q' = 0.1$ (10% polarisation) within the 6400–6800 Å bin and then median Stokes spectra were obtained. An important advantage of using q' instead of P is that the Stokes parameters have normal error distributions, while P is biased since it is a positive, definite quantity (e.g. Wardle & Kronberg, 1974).

The median q' and u' spectra for 4C 38.41 are displayed in Fig. 10 and identify the likely cause of the general decrease in the polarisation toward the blue end of the spectrum. In addition to a decrease in q' for the continuum at $\lambda \lesssim 6000$ Å, there are marked decreases in the polarisation at C IV and C III]. This indicates that the broad emission lines are not highly polarised, if at all. Indeed, the q' spectrum appears to be very similar to an inverted spectrum of a QSO down to the blended He II+O III] emission feature close to the red wing of C IV and suggests that the observed wavelength dependence is caused by the dilution of the polarised flux by an unpolarised spectrum that is similar to that of an optically selected QSO. The flat, featureless spectrum of u' supports the assertion that was made from Fig. 9 that any wavelength dependence in the optical polarisation position angle is transitory and typically not strong.

Figure 10 also displays the median flux (F_λ) and polarised flux ($q' \times F_\lambda$) spectra of 4C 38.41. Here, the nature of the source of polarised flux becomes evident. The median polarised spectrum is featureless and well fit by a power-law with a spectral index −1.25, which is generally redder than the continuum of the median total flux spectrum. The spectral index of the polarised continuum is identical to that of the synchrotron continuum under the assumption that the intrinsic jet polarisation (P_0) is independent of wavelength over this spectral region. Since the synchrotron power-law is redder than the QSO-like emission components (broad emission lines + blue continuum), P decreases into the blue. The amount of dilution and the strength of the wavelength dependence of the polarisation are both a function of the relative brightness between the unpolarised, non-

varying (at least on timescales measured in months to years) emission from the QSO component and the highly variable non-thermal emission from the relativistic jet and its spectral index. This model not only successfully explains the wavelength dependence of the observed polarisation, but also explains the correlations seen in 4C 38.41 between continuum flux, colour, and level of polarisation because the bluer QSO component contributes more strongly to the optical spectrum when the object is faint. The same general model has also been shown to apply to lower-redshift blazars with strong emission lines, such as 3C 345 (Smith et al., 1986), PKS 1546+027 (Smith et al., 1994), and PKS 1222+216 (Smith et al., 2011). The results for 4C 38.41 extend the evidence of the two-component nature of these types of blazars into the ultraviolet down to C IVλ1550.

With the polarisation and flux information in hand, it is impossible to distinguish the optical spectrum of the object into polarised power-law synchrotron and unpolarised components since it is impossible to break the degeneracy between the intrinsic polarisation (P_0; assumed to be constant with wavelength) and its brightness unless the SED of unpolarised component is assumed. The problem, however, is reasonably constrained as the unpolarised component cannot be so bright that P_0 is driven to excessively high values. The intrinsic polarisation certainly must be $< 100\%$, but $P_0 < 40$–45%, which is the observed maximum for blazars (see e.g. Impey et al., 1982; Mead et al., 1990), is likely to be the upper limit. In addition, given the longer timescales observed for variations in AGNs that are not blazars, the unpolarised component cannot be brighter than the optical photometric minimum observed in the light curves shown in Fig. 1 and Fig. 2 (roughly $R \sim 17.8$).

Two methods have been used to break the P_0-brightness degeneracy to estimate the true polarisation of the optical synchrotron continuum throughout the monitoring period of 4C 38.41. First, the brightness of the unpolarised QSO component can be estimated from the strengths of the C IV and C III] emission lines based on the line-to-continuum flux ratios of a standard template spectrum for radio-quiet QSOs (e.g. Francis et al., 1991). For C IV, this yields an R-band magnitude for the QSO component of 17.3, and for C III], $R \sim 18.0$. The discrepancy is caused by the C IV/C III] line ratio in 4C 38.41 differing significantly from the chosen template QSO, which cannot be explained by reddening. Alternatively, if each spectropolarimetric observation of 4C 38.41 is fit with a combination of the QSO template and polarised power-law, ignoring the line fluxes and leaving the non-thermal spectral index, QSO brightness, and P_0 as free parameters, we find an average R magnitude of 17.85 for the QSO. The median spectral index of the polarised power-law from these 106 fits is -1.6, as compared to -1.25 found from the median spectrum of q'.

The estimate of the QSO brightness based on the strength of C IV can be ruled out, as it would make the overall R-band light curve difficult to explain because 4C 38.41 often becomes fainter. The estimates based on C III] and the model fits are consistent with the observed light curve. The intrinsic polarisation of the synchrotron continuum is given by $P_0 = P_{\rm obs} \times F_{\rm obs}/(F_{\rm obs} - F_{\rm QSO})$, where $P_{\rm obs}$ and $F_{\rm obs}$ are the observed polarisation and flux within the R filter bandpass. In Fig. 11, the intrinsic polarisation is plotted against the brightness of the blazar, assuming $R = 17.85$ for the unpolarised QSO component. Similar results are obtained if $R = 18$ is assumed, but with smaller corrections being required between the observed and intrinsic polarisations. The correction of P for the non-beamed nuclear emission greatly lessens the correlation between P and optical brightness displayed in Fig. 7. The correlation is not completely destroyed as there are no cases of $P \lesssim 5\%$ being observed when 4C 38.41 is in a major optical outburst, but P_0 approaching 20–30% can occur when the object is near its faintest flux levels during the monitoring period.

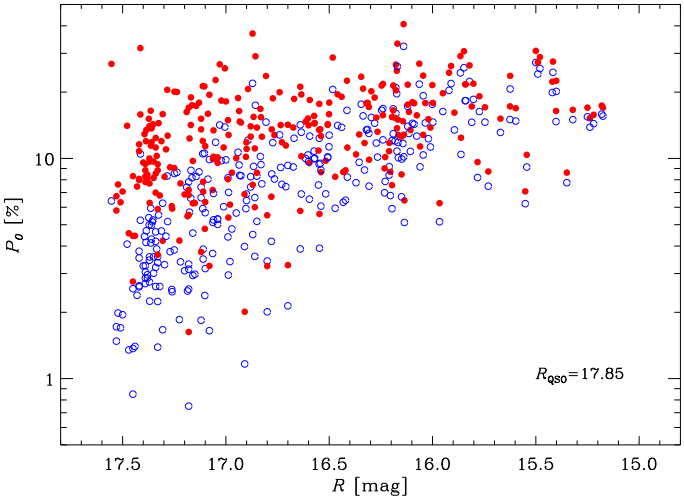

Fig. 11. The intrinsic polarisation of the optical synchrotron emission P_0 (red filled symbols) as a function of the brightness of 4C 38.41. For comparison, the observed polarisation measurements (Fig. 7) are also shown (blue empty symbols). Correcting P for unpolarised emission from a QSO-like component with $R = 17.85$ yields P_0 (see text).

4. Long-term observations at radio and millimetre wavelengths

We analysed radio data provided to the GASP project by the Submillimeter Array (SMA, 230, 275, and 345 GHz[8]) and by the radio telescopes of Medicina (5, 8, and 22 GHz), Metsähovi (37 GHz), Noto (38 and 43 GHz), and UMRAO (4.8, 8.0, and 14.5 GHz). Additional data at 86 and 230 GHz were supplied for this paper by the IRAM 30 m telescope[9]. We also collected archival data, which were supplied by the SMA (230 GHz), Medicina (5, 8, and 22 GHz), Metsähovi (37 GHz), Noto (5, 8, 22 and 43 GHz), and UMRAO (4.8, 8.0, and 14.5 GHz) telescopes, as well as 22, 37, and 87 GHz data acquired with the Metsähovi and Crimean radio antennas and published in Salonen et al. (1987) and Teräsranta et al. (1992, 1998, 2004, 2005). The long-term radio light curves of 4C 38.41 at the best-sampled wavelengths are displayed in Fig. 12, starting from JD = 2449500. The radio flux densities are compared with the optical R-band ones.

The variability maximum amplitude ($F_{\rm max}/F_{\rm min}$) decreases with decreasing frequency (with the exception of the 230 GHz light curve, which lacks data before 2002), suggesting that the corresponding jet emitting regions become larger. The shape of the major event in 2001–2003, clearly visible at 37, 22, and 14.5 GHz, changes with wavelength: it shows two peaks of similar intensity at 22 GHz, while at 37 (14.5) GHz the first (sec-

[8] These data were obtained as part of the normal monitoring programme initiated by the SMA (see Gurwell et al., 2007) as well as part of a dedicated programme by Ann Wehrle.

[9] IRAM 30 m data were acquired as part of the POLAMI (Polarimetric AGN Monitoring with the IRAM-30 m-Telescope) and MAPI (Monitoring AGN with Polarimetry at the IRAM-30 m-Telescope) programmes. Data reduction was performed following the procedures described in Agudo et al. (2006, 2010).

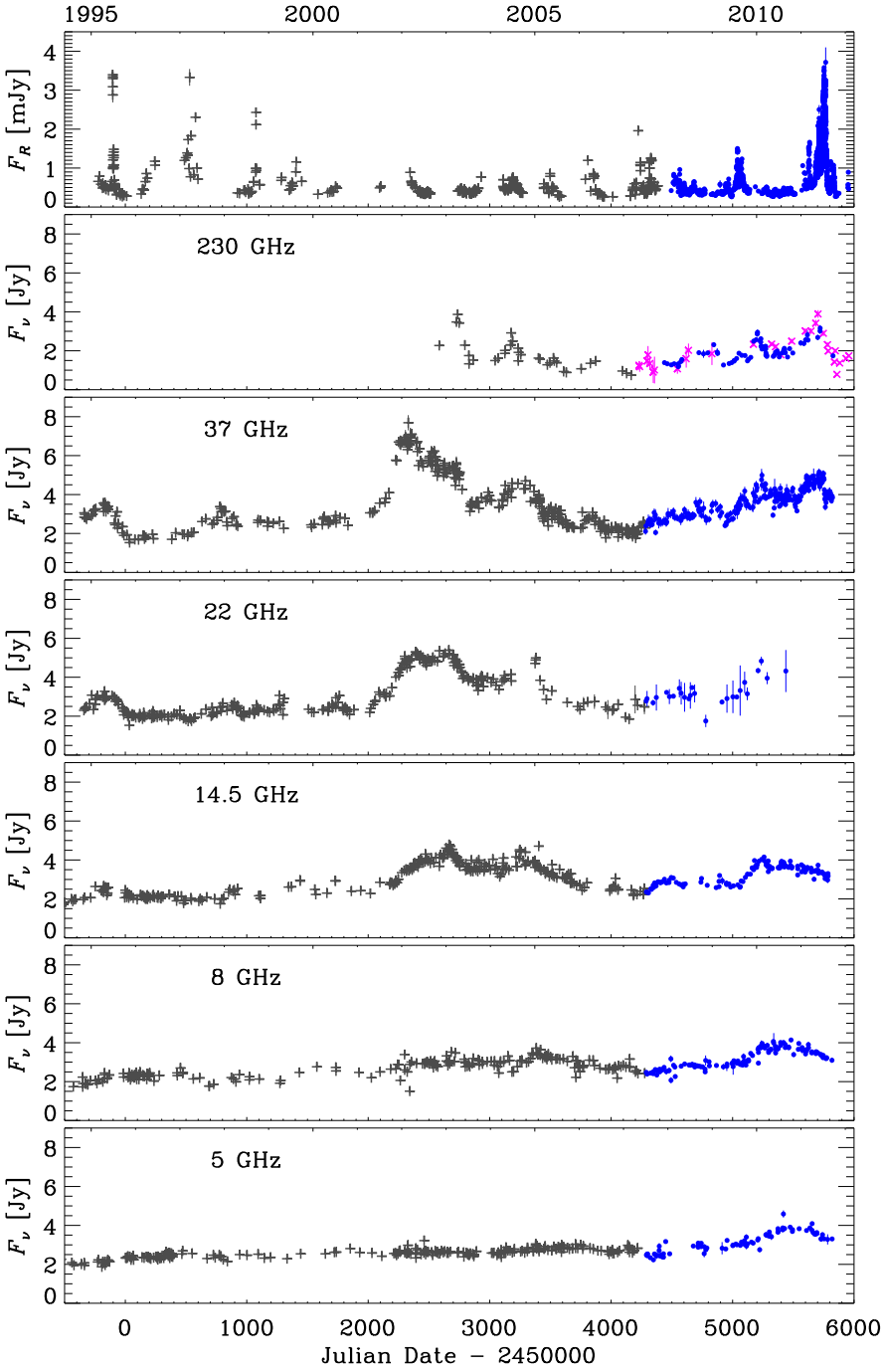

Fig. 12. *R*-band optical flux densities (top) compared to the radio light curves at different frequencies in 1994–2011. Blue dots refer to data collected in the ambit of the GASP project, complemented by 230 GHz data from the IRAM 30 m telescope (purple crosses). Black plus sign symbols are historical data taken from the participating observatories' archives and from the literature (see text for details).

ond) peak prevails. It is hard to say whether we are seeing here the evolution of a single event, or rather the effect of two overlapping events. Cross-correlation of the 37 and 14.5 GHz light curves by means of the discrete correlation function (DCF; Edelson & Krolik, 1988; Hufnagel & Bregman, 1992; Peterson, 2001) shows a first peak at a time lag of 120 days, and another peak at 360 days (see Fig. 13), indicating a time delay of several months of longer-wavelength flux variations. This is a common feature in blazars and suggests that lower-frequency photons are produced downstream in the jet from the higher-frequency ones.

The comparison between the optical and radio-mm light curves (Fig. 12) reveals a lack of general correlation: the big outbursts that occurred at high radio frequencies in 2001–2003 show no optical counterpart. Moreover, the big optical outbursts of 1995 and 1997 do not seem to have been followed by major radio events on a few-month timescale. The possibility remains that we either missed some important optical flare or that the radio-optical correlation occurs on much longer timescales than expected for this kind of objects. While we need to wait to see whether a big radio outburst will follow the 2011 optical event, we note that the systematically higher radio flux in 2009–2011,

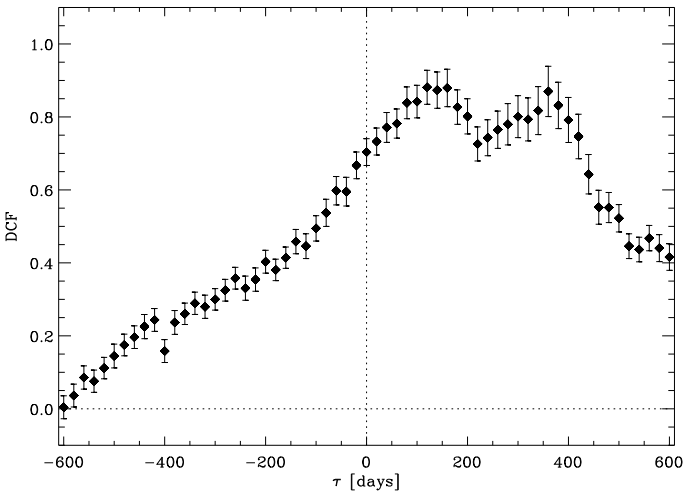

Fig. 13. Discrete correlation function between the 37 GHz and 14.5 GHz light curves shown in Fig. 12.

unusually at all wavelengths, may be related to the renewed optical activity of the past years.

In the framework of a geometrical interpretation of blazar variability previously proposed for other objects (see e.g. Villata & Raiteri, 1999; Villata et al., 2007, 2009b; Raiteri et al., 2009, 2010, 2011a), one could assume an inhomogeneous curved jet, where the optical and radio emitting regions were more misaligned in the past. In particular, a closer alignment of the optical region with the line of sight in 1995–1998 would have made the optical radiation more relativistically beamed toward us, while in 2001–2005 the radio-emitting region would have been better aligned, with the consequent greater Doppler enhancement of the radio flux. The increased activity of the past few years at both radio and optical frequencies would then indicate that the radio-optical misalignment has decreased and that both emitting regions are seen at small viewing angles. An analysis of the variations in the viewing angle of the parsec-scale jet will be performed in Jorstad et al. (2012, in preparation).

5. *Swift* observations

The *Swift* spacecraft (Gehrels et al., 2004) carries three instruments: the Burst Alert Telescope (BAT; Barthelmy et al. 2005), observing between 15 keV and 150 keV; the X-ray Telescope (XRT; Burrows et al. 2005), observing between 0.3 and 10 keV; and the Ultraviolet/Optical Telescope (UVOT; Roming et al. 2005), acquiring data in the 170–600 nm range. Up to 2011 September 30, *Swift* targeted 69 times 4C 38.41.

5.1. UVOT observations

The UVOT observations were performed in the optical *v*, *b*, and *u* bands, as well as in the UV filters *uvw*1, *uvm*2, and *uvw*2 (Poole et al., 2008). We reduced the data with the HEAsoft package version 6.10, with the 20101130 release of the *Swift*/UVOTA CALDB. Multiple exposures in the same filter at the same epoch were summed with `uvotimsum`, and aperture photometry was then performed with the task `uvotsource`. Source counts were extracted from a circular region with a 5 arcsec radius, while background counts were estimated in a neighbouring source-free circular region with a 10 arcsec radius. The results are shown in Fig. 14 (and in Fig. 1, where the *v*-band points have been shifted by −0.1 mag to match the Johnson's *V*-band data). The ranges of

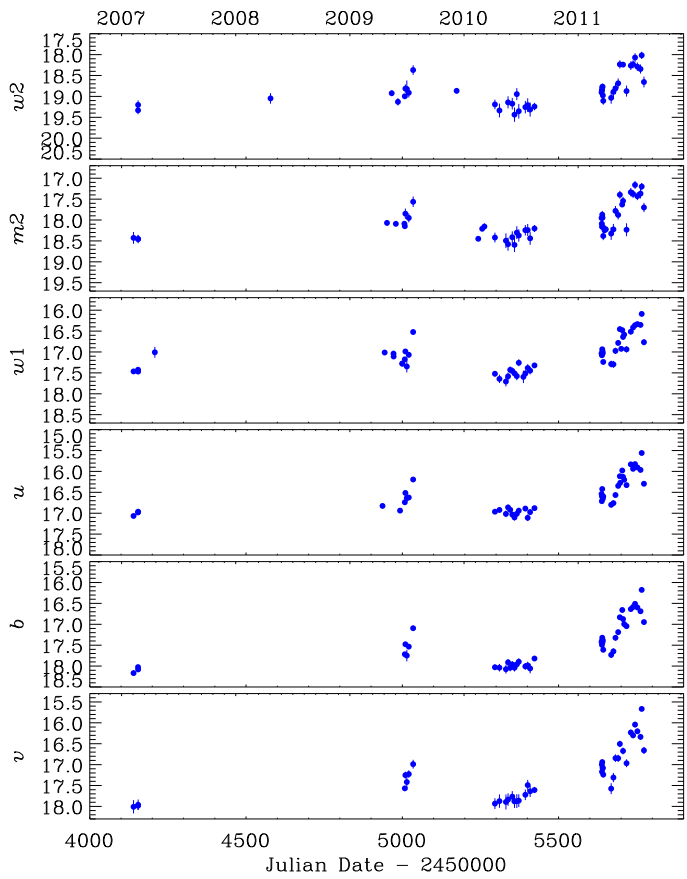

Fig. 14. Optical and UV light curves of 4C 38.41 built with *Swift*-UVOT data.

magnitude spanned in the various bands are about 2.3, 2.0, 1.6, 1.6, 1.4, and 1.4 mag going from the *v* to the *uvw*2 filter. Hence, the source variability decreases as the frequency increases, extending the trend already observed in the near-IR–optical band in Sect. 2.

To clarify whether there are any emission contributions in the UVOT energy range, we compiled SEDs for all the 36 epochs where good observations in all the six UVOT filters were available. We took into account the calibration updates introduced by Breeveld et al. (2011), including in particular new $\lambda_{\rm eff}$, count-rate-to-flux conversion factors, and effective areas for the UV filters. We calculated the (small) Galactic extinction in the various bands by convolving the Cardelli et al. (1989) laws (setting $R_v = 3.1$ and $A_v = 0.037$[10]) with the new effective areas, and used the results to obtain de-reddened flux densities. The source SEDs are shown in Fig. 15.

5.2. XRT observations

Although a few SEDs have a wavy shape, likely because of the data imprecision, most SEDs have a common pattern, with a bump peaking in the *u* band in the faintest states turning progressively into a steeper and steeper curved spectrum as the source brightness increases. Correction for the small flux contribution of the C IV emission line (see Sect. 3.1) to the *b* band would not change the SED shape appreciably. This again suggests that there is a thermal contribution from the accretion disc,

[10] From the NASA/IPAC Extragalactic Database, `http://ned.ipac.caltech.edu/`

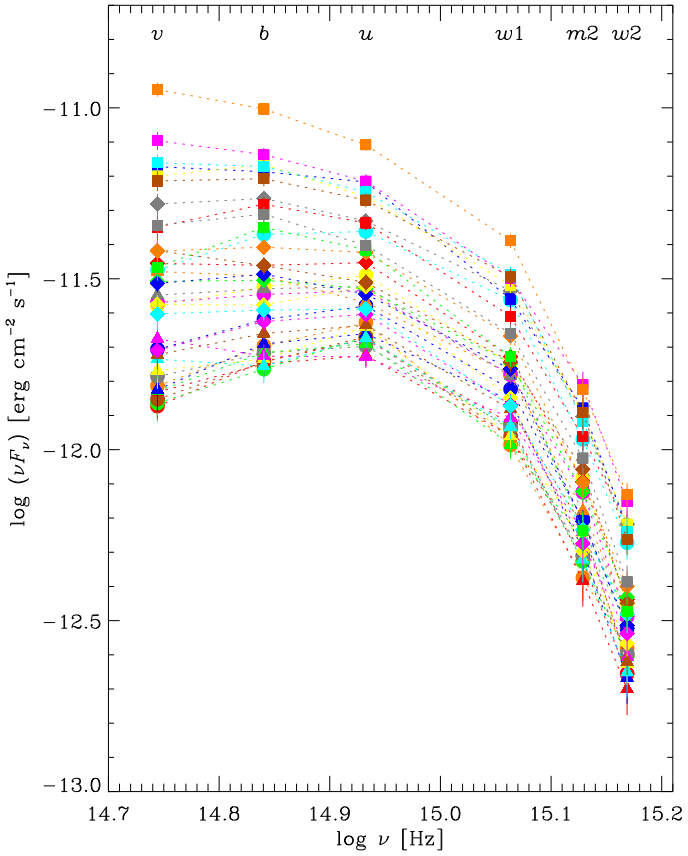

Fig. 15. Spectral energy distributions of 4C 38.41 in the optical–UV frequency range compiled with UVOT data. As the jet synchrotron emission becomes fainter, the contribution of the thermal radiation from the accretion disc emerges, peaking around the *u* band.

which peaks around the *u* band (as expected because of the high source redshift) and emerges when the jet synchrotron contribution weakens.

We processed the XRT event files acquired in pointing mode, using the HEASoft package version 6.11 with the calibration files 20110915[11]. We considered the observations with exposure times longer than 5 minutes, including 65 observations in photon-counting (PC) mode. The task `xrtpipeline` was run with standard filtering and screening criteria, in particular selecting event grades 0–12. Source counts were extracted from a 25 pixel circular region (∼ 60 arcsec) centred on the source, and background counts were derived from a surrounding annular region with radii of 100 and 150 pixels. The count rate was always lower than 0.5 counts/s, so no correction for pile-up was needed. The `xrtmkarf` task was used to generate ancillary response files (ARF), which account for different extraction regions, vignetting, and PSF corrections. The X-ray light curve (net count rate and de-absorbed 1 keV flux density) is shown in Fig. 16 and is discussed in the next section.

We performed spectral analysis with the `xspec` package. After "grouping" the data with the task `grppha` in order to have a minimum of 20 counts per energy channel to apply the χ^2 statistics, only ∼ 20% of the spectra resulted in more than 10 channels. We therefore used the Cash statistics, which extends the χ^2 statistics to the case of a low number of counts (Cash, 1979; Nousek & Shue, 1989). We applied an absorbed

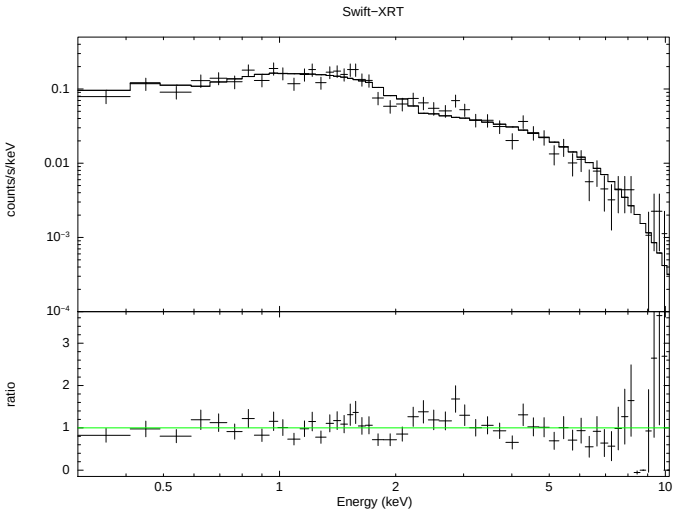

Fig. 17. The *Swift*-XRT spectrum of 4C 38.41 on 2011 May 15. Data are fitted with a power-law with fixed Galactic absorption. The lower panel shows the ratio of the data to the folded model.

power-law model, where absorption is modelled according to Wilms et al. (2000) and the hydrogen column is fixed to the LAB[12] Galactic value $N_{\rm H} = 0.111 \times 10^{21}$ cm^{-2}. We tested the results of the Cash statistics with the `goodness` command, which performs Monte Carlo spectral simulations based on the model and gives the percentage of them that have fit statistics smaller in value than that of the data. Moreover, we compared the results of the Cash method with those of the χ^2 statistics, when the latter was applicable. We obtained robust spectral fits (excluding the cases in the tails of the goodness distribution) in about 70% of cases. These cases indicate a hard spectrum, with the photon index Γ ranging from 1.31 to 1.87, with a mean value of 1.62. The lowest values correspond to the highest fluxes, in agreement with the "harder-when-brighter" trend often observed in blazars (e.g. D'Ammando et al., 2011, and references therein).

In particular, the data acquired on 2011 May 15 (JD = 2455697), corresponding to the X-ray peak visible in Fig. 16, are best-fitted by a power-law with $\Gamma = 1.31 \pm 0.07$, 1 keV de-absorbed flux density $F_{1\,\rm keV} = (1.46 \pm 0.09)\,\mu$Jy, and observed[13] flux between 0.3 keV and 10 keV of $(2.24 \pm 0.14) \times 10^{-11}$ erg cm^{-2} s^{-1}. The result of the goodness test is 54%, which assures us that the observed spectrum is well-reproduced by the model. The corresponding spectrum and the folded model is shown in Fig. 17.

6. Cross-correlations from radio to γ-ray frequencies

Figure 16 compares 4C 38.41 light curves at different frequencies in the period 2008–2011, i.e. from the beginning of the *Fermi* γ-ray observations. From top to bottom, one can see: 1) the daily photon flux in the 100 MeV – 300 GeV energy range; 2) the corresponding weekly γ-ray light curve[14]; 3) the X-ray light

[11] `http://heasarc.gsfc.nasa.gov/docs/heasarc/caldb/Swift/`

[12] Kalberla et al. (2005); `http://www.astro.uni-bonn.de`

[13] The unabsorbed flux is only 1% higher.

[14] The daily and weekly γ-ray light curves were downloaded from the *Fermi*-LAT monitored source site (`http://Fermi.gsfc.nasa.gov/ssc/data/access/lat`), but their preliminary nature does not affect the results of our analysis. The comparison with an independent analysis available at the ISDC

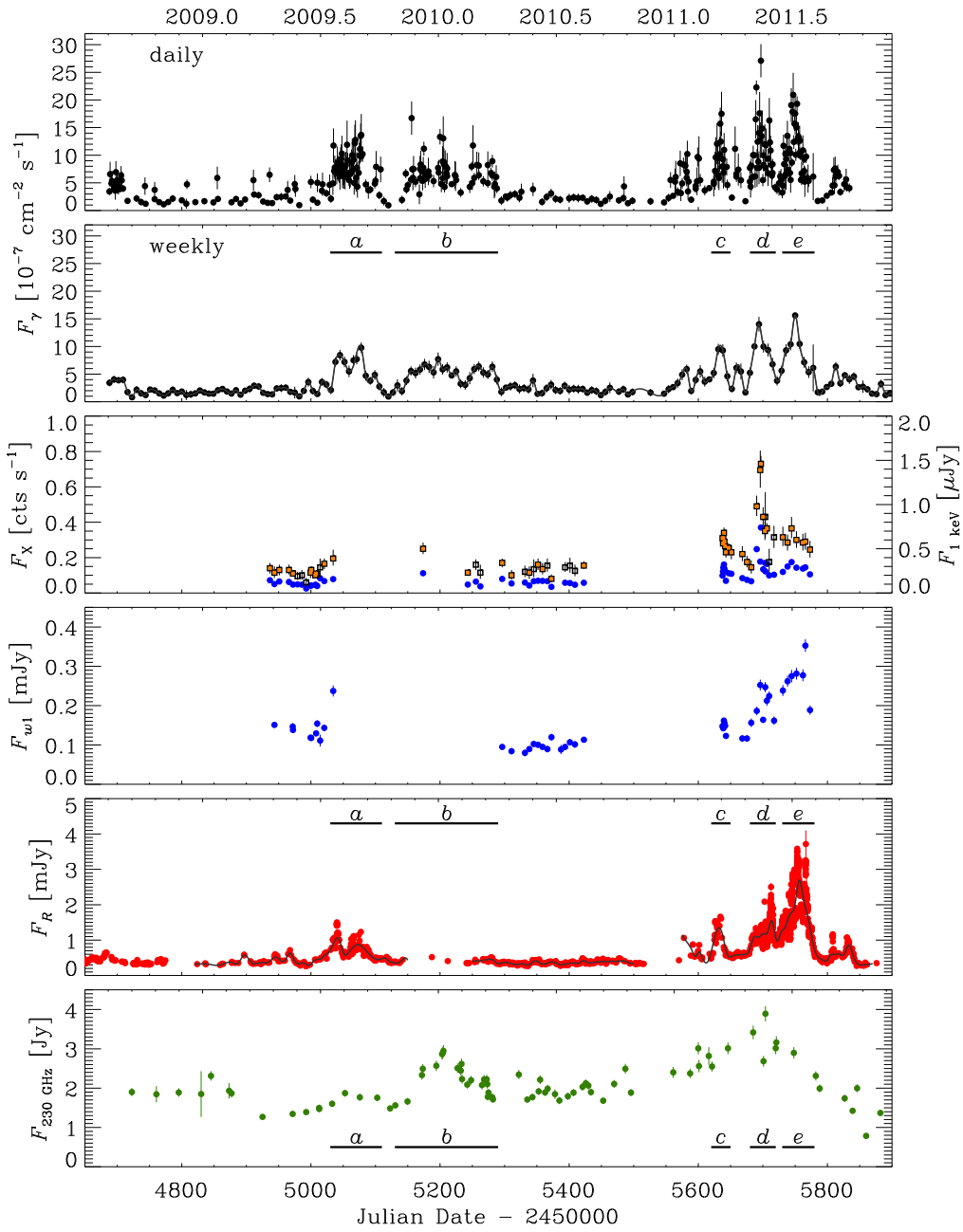

Fig. 16. Light curves of 4C 38.41 at different frequencies in 2008–2011. From top to bottom: 1) the daily γ-ray light curve from *Fermi*-LAT in the 100 MeV – 300 GeV range (10^{-7} ph cm^{-2} s^{-1}); 2) the corresponding weekly γ-ray light curve with its cubic spline interpolation; 3) the X-ray light curve from *Swift*-XRT, derived as explained in Sect. 5.2; blue dots are counts s^{-1} , while black squares represent 1 keV de-absorbed fluxes (μJy), which are filled in orange when resulting from robust spectral fits; 4) the de-absorbed *Swift*-UVOT flux density light curve in the *uvw*1 band (mJy); 5) the de-absorbed GASP *R*-band flux-density light curve (mJy) with the cubic spline interpolation through the 7-day binned data; 6) the millimetre radio light curve at 230 GHz (Jy).

curve from *Swift*-XRT (net count rate, as well as de-absorbed 1 keV flux densities derived as explained in Sect. 5.2); 4) the de-absorbed UV flux densities in the *uvw*1 band (mJy); 5) the *R*-band de-absorbed flux densities (mJy); 6) the millimetre radio light-curve at 230 GHz (Jy).

A zoomed image of the most interesting periods in 2009–2010 and 2011 is displayed in Figs. 18 and 19, respectively.

To make the comparison among bands easier, we highlighted five periods, corresponding to flaring states in γ-rays. Moreover, we also plotted cubic spline interpolations through the weekly binned γ-ray and optical data, in the latter case to emphasize the smoothed trend of the flux, beyond the fast variability. We note the following features:

- In γ-rays and in the optical band, where the sampling is dense enough, all events appear as a succession of several short-term flares.
- All events (more precisely: the envelope over the substructure) show a similar duration in γ-rays and in the optical band (apart from event *b* that does not have enough optical coverage).

`http://www.isdc.unige.ch/heavens/` indeed reveals a fair agreement.

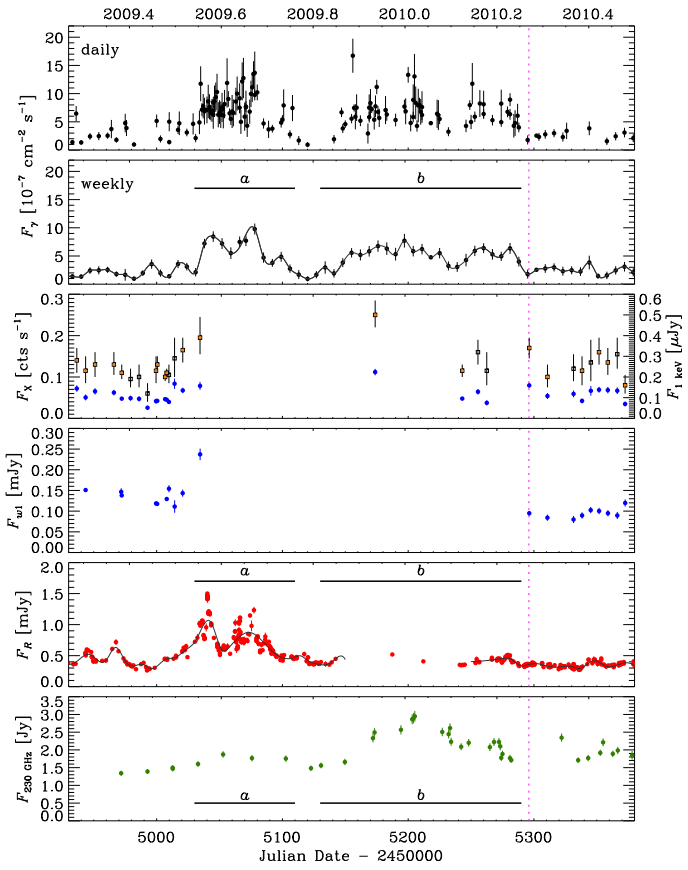

Fig. 18. An enlargement of Fig. 16 in 2009–2010. The pink vertical line marks the epoch of one of the SEDs shown in Fig. 22.

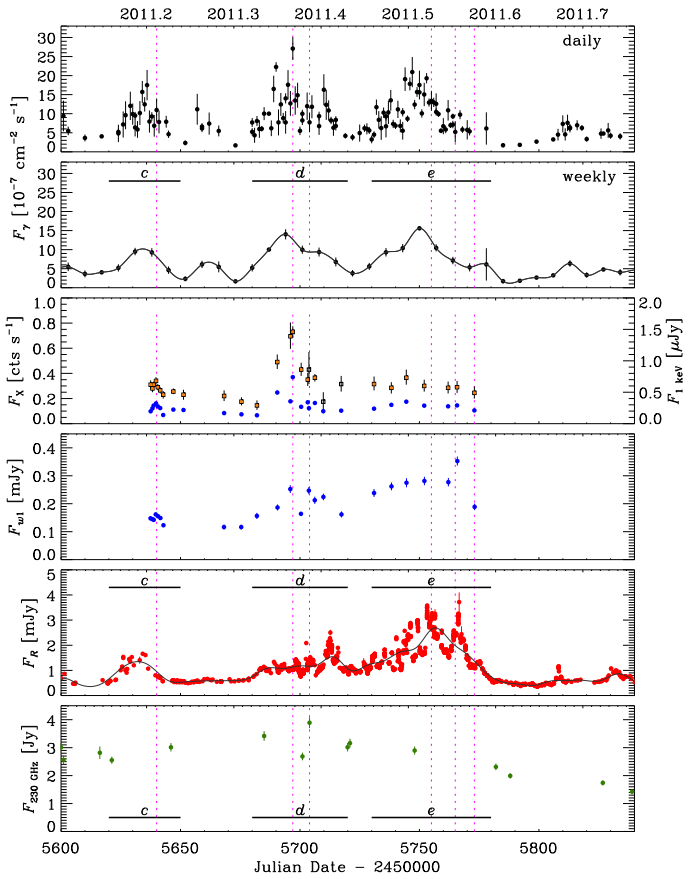

Fig. 19. An enlargement of Fig. 16 in 2011. The pink vertical lines mark the epochs of six of the SEDs shown in Fig. 22.

– At all frequencies, the maximum flux during the 2011 flare is greater than the maximum flux during the 2009 and 2010 flares.
– Flare *a* is double-peaked in both γ-rays and the optical. However, the second γ peak is higher than the first one, while in the optical the reverse is true. A little bump is also visible at 230 GHz.
– Flare *b* occurred during solar conjunction so that the optical coverage is almost null. However, the few contemporaneous data do not reveal an increase in the optical flux. Interestingly, the millimetre light curve shows a bump simultaneous with the γ event.
– The shape of flare *c* is similar at γ-ray and optical frequencies.
– In flare *d*, the most active phase in γ-rays and X-rays precedes that in the optical band and the mm flux reaches its maximum value.
– A shift between the γ-ray and optical smoothed-trend flux maxima also occurs in flare *e*, where furthermore the last optical spike has no relevant counterpart at γ-ray energies.

In conclusion, the correlation between the source emission in γ-rays and optical (and maybe millimetre) frequencies is clear, because flares are observed to occur in the same periods and their strength increases from 2009–2010 to 2011 at both frequencies. This would suggest that the jet regions where photons at these frequencies are produced either coincide or are very close. The more coarsely sampled X-ray and UV light curves indicate some correlation with the γ-ray and optical ones, so that the X-ray and (the non-thermal part of) the UV radiation may also come from the same jet zone.

However, the γ-optical correlation is complex. The shape and relative brightness of the flares differ indeed considerably. Cross-correlation of the γ-ray daily flux with the *R*-band flux by means of the DCF yields a strong bump (DCF_{peak} = 0.93, see Fig. 20) peaking at zero time lag, but the centroid of the bump, which provides a more robust estimate of the time lag (Peterson, 2001), appears shifted toward positive time-lags. Hence, the correlation between the γ-ray and optical fluxes is strong, and there is possibly a delay in the optical variations after those in the γ-rays, but the broadness of the DCF bump would suggest that this delay may be variable. Moreover, this result appears in contrast to the findings of Jorstad et al. (2011), who found a strong correlation between the optical and γ flux variations in 2009–2010, with the γ variations lagging by 5 ± 3 days. To investigate in greater detail the matter, we thus restrict the calculation of the DCF to the period investigated by Jorstad et al. (2011), and essentially confirm their result. As shown in Fig. 21, we find a peak at zero time-lag, indicating that there is a strong correlation (DCF_{peak} = 0.95) with simultaneous flux variations. However, the centroid of the distribution, which provides a higher time resolution, is $\tau_{cen} = -2.5$ days, which means that the γ-ray variations would follow the optical ones by 2.5 days. We determine the uncertainty in this result by performing Monte Carlo simulations according to the "flux redistribution/random subset selection" method (FR/RSS; Peterson et al., 1998; Raiteri et al., 2003), which tests the importance of sampling and data errors. Among the 1000 simulations, about 74% ($\gtrsim 1\,\sigma$) of them yield centroids between −3 and −2 days, so we can conservatively conclude that the delay of the γ flux variations after the optical ones is 2.5 ± 0.5 days. If we then run the DCF for the follow-

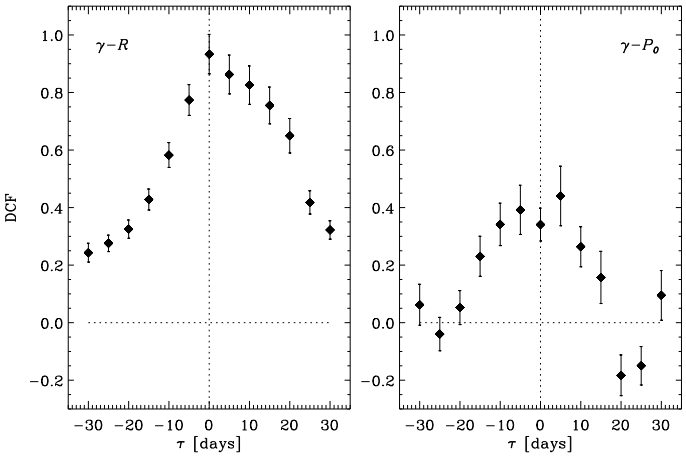

Fig. 20. Discrete correlation function between the daily γ-ray flux and R-band flux density light curves shown in Fig. 16 (left) and between the daily γ-ray flux and the QSO-corrected polarisation P_0 (right, see Sect. 3).

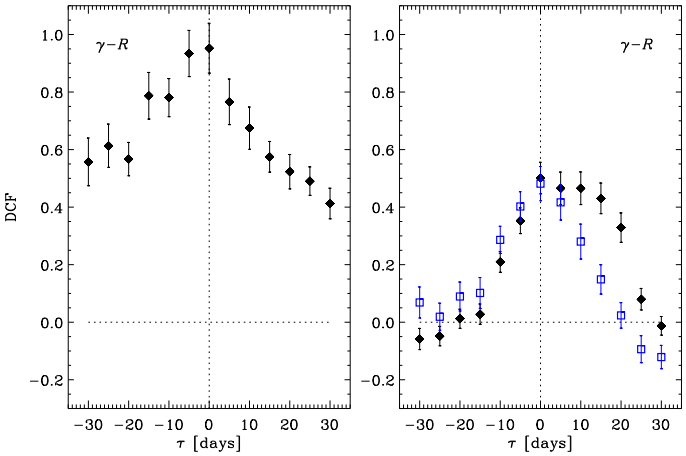

Fig. 21. Discrete correlation function between the daily γ-ray flux and R-band flux density light curves shown in Fig. 16 before (left) and after (right) JD = 2455450 for a comparison with the Jorstad et al. (2011) results (see the text). The blue squares represent the case where the light curves are stopped at JD = 2455763 to avoid the influence of the optical flare without any significant γ-ray counterpart at JD ∼ 2455767.

ing period, including the 2011 outburst, the result changes completely (see Fig. 21). The peak is still at $\tau = 0$ days, but the correlation weakens ($DCF_{peak} = 0.50$), and the centroid indicates that the optical variations follow the γ ones by about 7 days. This result is strongly affected by the presence of the optical flare without γ-ray counterpart at JD ∼ 2455767. If we indeed stop the light curves at JD = 2455763, the resulting DCF still shows a weak correlation, but now the peak and the centroid coincide at $\tau = 0$ days. The reason for the lack of a strong γ-optical correlation in 2011 has probably to be ascribed to the increase in the optical to γ-ray flux ratio starting from JD ∼ 2455700 and culminating with the last "sterile" optical flare.

We also investigate the possible correlation between the γ-ray flux and the QSO-corrected optical polarisation P_0 derived in Sect. 3. The corresponding DCF, which is shown in the right panel of Fig. 20, does not provide evidence of any significant correlation.

7. Pair-production optical depth

In the emitting plasma jet, γ-ray photons should be absorbed because of collisions with lower-energy photons, mostly X-rays, which lead to pair production. Relativistic beaming of the emitted radiation can explain why we actually observe a γ-ray flux. The minimum value of the Doppler factor[15] δ to avoid pair production, i.e. to have an optical depth $\tau_{\gamma\gamma} = 1$, was derived by Mattox et al. (1993), and corrected by Madejski et al. (1996), under the hypothesis that the X-ray and γ-ray emissions are cospatial and that the emission region is spherical in the comoving frame

$$\delta_{\rm low} = [5\times10^{-4}\,(1+z)^{-2\alpha}\,(1+z-\sqrt{1+z})^{-2}\,h_{75}^2\,T_5\times (F_{\rm keV}/\mu{\rm Jy})^{-1}\,(E_\gamma/{\rm GeV})^{-\alpha}]^{-1/(2\alpha)}\,, \quad (1)$$

where α is the X-ray energy spectral index $F(E) = F_{1\,\rm keV}(E/{\rm keV})^{-\alpha}$ whose relationship with the photon spectral index Γ is $\alpha = \Gamma - 1$, T_5 is the flux variability timescale in units of 10^5 s, and E_γ is the minimum energy of the observed γ-ray photons. By setting $h_{75} = H_0/(75\,{\rm km s^{-1} Mpc^{-1}}) = 0.95$, $\alpha = 0.31$, $F_{1\,\rm keV} = 1.46\,\mu$Jy (see Sect. 5.2), $E_\gamma = 0.1$ GeV, and by considering a variability timescale of 12–24 hours, we obtain $\delta_{\rm low} = 4.1$–3.7. This is the lower limit to the Doppler factor affecting the radiation emitted from the jet region where the γ and X-ray photons are produced.

8. Broad-band SED

Broad-band SEDs of 4C 38.41 are presented in Fig. 22 for seven epochs characterised by different brightness levels and good broad-band data coverage (see also Figs. 18 and 19). They are obtained with simultaneous data at near-IR, optical, and higher frequencies, where flux variations are faster, while in the radio band we searched for data within a few days. Near-IR, optical, UV, and X-ray flux densities are corrected for Galactic extinction as explained in the corresponding sections.

In the upper left inset, we show an enlargement of the near-IR to UV frequency range. We note that in the SEDs corresponding to JD = 2455296 and JD = 2455773, where ground and space optical data overlap, the space data points are lower than the ground-based data in the V band, especially in the fainter SED. This agrees with our need in Fig. 1 to shift the v-band UVOT data points by −0.1 mag to reconcile them with the ground ones and does not change the conclusion of Sect. 5.1 that the thermal-emission contribution likely peaks around the u band. The shape of the low-energy bump traced by the data shown in Fig. 22 suggests that the synchrotron peak lies in the far-IR–sub-mm frequency range.

The spectral analysis of the X-ray data acquired by *Swift* has been presented in Sect. 5.2. All the five X-ray spectra shown in Fig. 22 are the result of statistically valid spectral fits, whose spectral indices are indicated in the figure.

To obtain the γ-ray spectra, we reduced the publicly available *Fermi*-LAT data[16] corresponding to the epochs of interest. The data reduction is based on the unbinned likelihood analysis with python using the ScienceTools software package version v9r23p1[17]. We extracted the data from a circular region of

[15] $\delta = [\Gamma_{\rm b}(1-\beta\cos\theta)]^{-1}$, where $\Gamma_{\rm b}$ is the Lorentz factor of bulk motion $\Gamma_{\rm b} = (1-\beta^2)^{-1/2}$, β is the ratio of the plasma velocity to the speed of light, and θ is the viewing angle.

[16] `http://Fermi.gsfc.nasa.gov/`

[17] `http://fermi.gsfc.nasa.gov/ssc/data/analysis/scitools/python_tutorial.html`

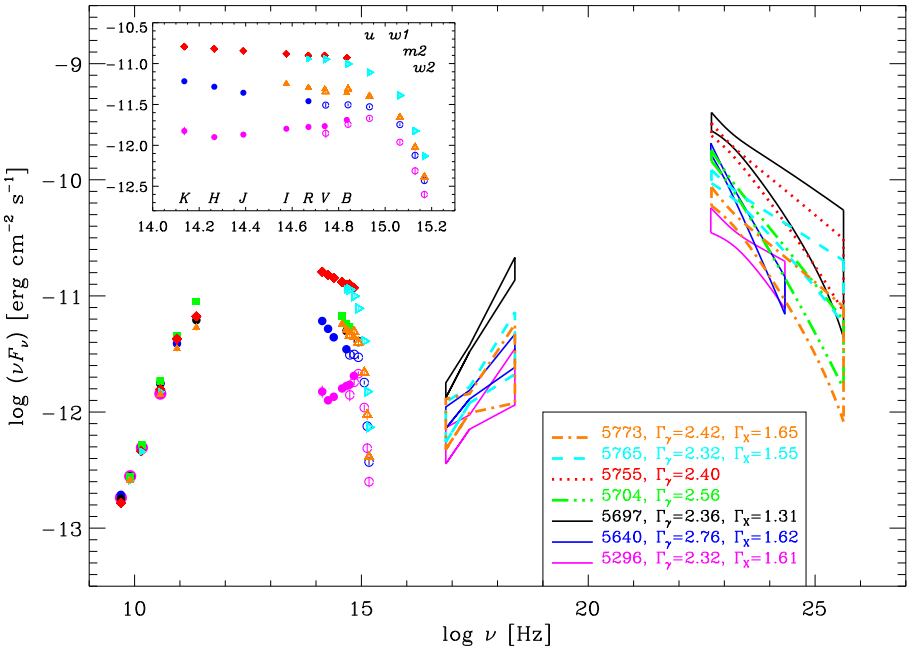

Fig. 22. Spectral energy distributions of 4C 38.41 from the radio to the γ-ray frequencies. Different colours correspond to different epochs, whose JD – 2450000 is indicated in the lower inset together with the γ and X-ray spectral indices. The near-IR to UV spectral band is enlarged in the upper inset. Filled (empty) circles display ground (space) data. Radio to optical ground data were collected in the framework of the GASP and collaborators; space optical, UV, and X-ray data are from *Swift*, γ-ray data from *Fermi*.

interest (RoI) of radius 10° centred around the location of 4C 38.41 and included events with high photon probability by keeping only the "source class" events (event class 2). The energy range used in data processing is from 200 MeV to 200 GeV. We also filtered the data by excluding photons observed at a zenith angle of > 100° to reduce contamination from the Earth limb γ-rays that result from cosmic rays interacting with the upper atmosphere.

The γ-ray flux and spectrum were calculated using the current public Galactic diffuse emission model (gal_2yearp7v6_v0.fits) and the recommended isotropic model[18] for the extragalactic diffuse emission (iso_p7v6source.txt), which includes the residual cosmic-ray background. The instrument response function (IRFs) valid for the isotropic spectrum (P7SOURCE_V6) were used for data sets with front and back events combined to carry out the spectral analyses.

For each of the seven epochs, we calculated the livetime cube, exposure map, and diffuse response of the instrument, and applied the algorithm as prescribed by the unbinned likelihood analysis with python. We used the user contributed tool (make2FGLxml.py) to correctly model the background by including all of the sources of interest within the RoI of 4C 38.41, and generated the corresponding XML model file. We carried out the first spectral fit by setting the spectral model corresponding to 4C 38.41 to "PowerLaw2" in the file and keeping the normalisation or integral factors and photon indices of all sources along with the normalisation factors of the Galactic diffuse and isotropic components as free parameters. The XML model also includes sources between 10 and 15 degrees from the target, which can contribute to the total counts observed in the RoI owing to the energy-dependent size of the point spread function of the instrument. For these additional sources, normalizations and index were kept fixed to the values of the Second *Fermi* LAT Catalog (Nolan et al., 2012). The first fit was then used to obtain the final spectral fit after fixing all the free parameters of this fit except for those of 4C 38.41.

[18] `http://fermi.gsfc.nasa.gov/ssc/data/access/lat/BackgroundModels.html`

We explored the significance of the γ-ray signal from the source using the test statistic (TS) based on the likelihood ratio test. To ensure a high TS value, we carried out binning using three different time intervals: (1) 14 days centred around JD = 2455296, 2455640, 2455704, 2455765, and 2455773; (2) 3 days centred around JD = 2455697, and (3) 5 days centred around JD = 2455755. The TS value for all seven time intervals are well in excess of 100 (> 10 σ).

We used the user contributed tool (likeSED.py) to obtain the spectral points and butterfly plots for each of the seven γ-ray states. We created nine customised energy bins to ensure more photons per bin. The tool creates an exposure map and an event file for each of the energy bins. We used the final fit from our likelihood analysis to fit individual bins and, as before, kept parameters of all sources fixed except for the integral factor and photon index of 4C 38.41. The source exhibits a slight spectral variation during the seven time intervals. The individual photon-index values for all seven epochs are displayed in Fig. 22, with errors indicated by their respective bow-tie patterns.

As displayed in Fig. 22, the results of the above analysis reveal that the γ-ray spectra are always very steep and that all epochs are characterised by a strong Compton dominance, as usually found for quasar-like blazars. This also seems to be true when the jet emission is faint and the thermal contribution prevails in the optical band, as shown by the JD = 2455296 SED. Moreover, by comparing the γ-ray spectra with the X-ray ones, we can see that higher γ-ray states correspond to higher X-ray ones. Finally, the data suggest that the peak of the high-energy bump is located in the 10^{21}–10^{22} Hz frequency interval, i.e. in the MeV range.

9. Discussion

As discussed in Sect. 6, in 2009 we found a strong γ-optical correlation, with a delay in the γ-ray flux variations after the optical ones of 2–3 days, in agreement with Jorstad et al. (2011). In contrast, in the 2011 outburst the correlation was weak, and the flux changes in the optical band apparently follow those at γ-rays by about one week. A similar time lag of the optical flux variations after the γ-ray ones was found by Hayashida et al. (2012) when

analysing the light curves of another FSRQ, 3C 279. These authors explain the time delay in terms of a decreasing ratio of the external radiation to the magnetic energy densities along the jet, which shifts the location where the optical luminosity reaches a maximum downstream from where the γ luminosity peaks. As we saw in Sect. 8, 4C 38.41 also has a strong Compton dominance, which is at the basis of the Hayashida et al. (2012) argument, so the same explanation might hold for this source too.

However, our analysis suggests that the apparent optical delay may be due to an increase in the optical flux relative to that in γ rays, even leading to an optical flare without a significant γ-ray counterpart. A similar situation was found by Raiteri et al. (2011a) for the 2008–2009 outbursts of 3C 454.3.

We obtained a lower limit to the Doppler factor $\delta_{\rm low} = 3.7$–4.1 to avoid self-absorption of the γ radiation. Savolainen et al. (2010) combined apparent jet speeds derived from high-resolution VLBA images from the MOJAVE project with flux densities at millimetre wavelengths derived from monitoring data acquired at the Metsähovi Radio Observatory to estimate the jet Doppler factors, Lorentz factors $\Gamma_{\rm b}$, and viewing angles for a sample of 62 blazars. For 4C 38.41 they derived $\beta_{\rm app} = 29.5$, $\delta = 21.3$, $\Gamma_{\rm b} = 31.1$, and $\theta = 2.6°$. Since according to Jorstad et al. (2011) the γ-ray emitting region is close to the millimetre one, we can investigate whether the Savolainen et al. (2010) findings agree with ours.

If the emission is isotropic in the jet rest-frame and the intrinsic spectrum follows a power-law with index α, then the observed flux density $F_\nu(\nu) = \delta^{n+\alpha} F'_{\nu'}(\nu)$, where $n = 3$ for a discrete, essentially point-like emission region, and $n = 2$ for a smooth, continuous jet (e.g. Urry & Padovani, 1995). Taking into account the uncertainty in both the emitting region structure and the value of α, we can assume a flux density dependence on δ^3. If the flux density variations that we observe are only due to variations in δ, then $\delta = \delta_{\rm max}(F_\nu/F_{\nu,{\rm max}})^{1/3}$.

Under the hypotheses that $\delta_{\rm max} = 21.3$ from Savolainen et al. (2010) and that all the variability shown by the γ-ray and optical lightcurves in Fig. 16 *on a one-week timescale* is due to variations in the Doppler factor, we find that δ should range between this maximum value and $\delta_{\rm min} = 8.0$ to explain the weekly γ-ray lightcurve. In the optical band, an uncertainty comes from the subtraction of the QSO contribution derived in Sect. 3 from the *R*-band flux densities. If we consider the weekly-binned *R*-band lightcurve, $\delta_{\rm min} = 6.7$ if $R_{\rm QSO} = 17.85$, while $\delta_{\rm min} = 7.5$ if $R_{\rm QSO} = 18.0$. Hence, both the γ-ray and optical $\delta_{\rm min}$ are consistent with, i.e. greater than, the lower limit $\delta_{\rm low}$ that we obtained.

Moreover, we can also estimate the corresponding variation in the viewing angle $\theta = \arccos\{[\Gamma_{\rm b}\,\delta - 1]/[\sqrt{\Gamma_{\rm b}^2 - 1}\,\delta]\}$ under the assumption that all the variability is of a geometrical nature. Adopting $\Gamma_{\rm b} = 31.1$ after Savolainen et al. (2010), we obtain $\theta_{\rm min} = 2.6°$ corresponding to $\delta_{\rm max} = 21.3$ for both the γ-ray and optical emitting regions, while we derive $\theta_{\rm max} = 4.8°$ for the γ radiation, and $\theta_{\rm max} = 5.0$ or $5.3°$ for the optical when $R_{\rm QSO} = 18.0$ or 17.85, respectively.

In conclusion, the hypothesis that all the flux variability on a weekly timescale is due to changes in the Doppler factor does not contradict the observations. Had we considered shorter variability timescales, we would have obtained lower $\delta_{\rm min}$ values, down to $\delta_{\rm min} = 4.3$ in the extreme case that we attributed *all* the *R*-band flux density variations to changes in δ and set $R_{\rm QSO} = 17.85$. Even this case is still compatible with the estimated $\delta_{\rm low}$. However, it is likely that the most rapid flux changes are due to intrinsic processes of an energetic nature, such as shocks propagating downstream in the jet. In contrast, had we considered variability timescales longer than a week, we would have obtained weaker constrains. Hence, we suggest that Doppler factor variations of a geometric nature provide the most likely explanation of the *long-term* flux variability of this source, as already proposed for other blazars (see e.g. Villata et al., 2009b; Larionov et al., 2010; Raiteri et al., 2011a, and references therein).

Furthermore, in Sect. 3 we saw that there is a clear dependence of polarisation on brightness (Fig. 7) that cannot be completely explained in terms of a simple dilution effect from an unpolarised QSO-like emission component (Fig. 11). The intrinsic polarisation variability can be interpreted by various available models. Here we investigate whether the changes in the viewing angle discussed above to explain the flux variations can also provide a plausible explanation of the variations in the polarisation degree. If we suppose that for a statistically significant part of time we see shock waves propagating downstream in the jet, because of relativistic aberration the angle between the line of sight and the direction of the normal to the shock-wave front can be expressed as

$$\psi = \arctan\left(\frac{\sin\theta}{\Gamma_{\rm b}\,(\cos\theta - \sqrt{1-\Gamma_{\rm b}^{-2}})}\right)$$

and the degree of polarisation

$$P_0 \approx \frac{\alpha+1}{\alpha+5/3}\,\frac{(1-\eta^{-2})\sin^2\psi}{2-(1-\eta^{-2})\sin^2\psi}$$

(e.g. Hughes et al., 1985). Here η is the degree of compression of the shock wave and α is the optical spectral index (see Sects. 2 and 3). The results of the model are shown in Fig. 23 for an optical spectral index $\alpha = 1.6$ (but they are weakly dependent on α) and different choices of η. They can closely reproduce the behaviour of the intrinsic degree of polarisation of the jet emission P_0 derived in Sect. 3 as a function of brightness (here, the intrinsic jet flux density in the *R* band, which is obtained after correcting the observed flux for the QSO-like contribution and Galactic extinction). Most of the data point dispersion can be accounted for by varying the compression parameter from $\eta = 1.15$ to 1.7. We note that choosing $R_{\rm QSO} = 18$, which was obtained as a possible alternative value for the unpolarised emission component in Sect. 3, would shift the points toward the bottom-right, worsening the agreement between data and model.

10. Conclusions

We have presented the results of a huge observing effort on the FSRQ 4C 38.41, carried out by the GASP-WEBT and collaborators from 2007.5 to 2011.9 and by the Steward Observatory from 2008.8 to 2012.1. Earlier data were also collected, so that the optical and radio light curves cover in total about 17 years. Moreover, we also analysed the UV and X-ray data acquired in 2007–2011 by the *Swift* satellite and the γ-ray data taken in 2008–2011 by *Fermi*. Light curves from the near-IR to the UV band, spanning a factor ~ 11 in frequency, show a quite impressive correlation, presumably because this whole range is in the upper part of the synchrotron bump. In the near-IR-to-UV spectral range, the presence of a QSO-like emission contribution in addition to the synchrotron emission from the jet, is revealed by several findings:

– the maximum flux-variation amplitude decreases with increasing frequency;

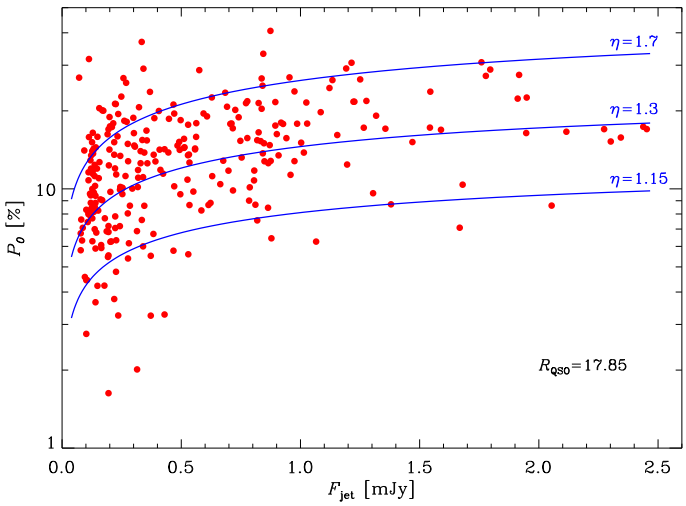

Fig. 23. The intrinsic polarisation of the jet emission P_0 derived in Sect. 3 versus the jet flux density in the R band. We have assumed an observed brightness $R_{QSO} = 17.85$ to correct for the QSO-like unpolarised emission contribution that affects both the flux and polarisation degree observed. The blue lines represent the results of a shock-in-jet model where the direction of the front wave, hence the polarisation degree, vary because of the variation in the viewing angle. We adopted an optical spectral index of 1.6, as found in Sect. 3. Values of the shock wave degree of compression η in the 1.15–1.7 range can account for most of the data dispersion.

– the optical colour shows a redder-when-brighter trend;
– the optical spectrum reveals unpolarised broad emission-lines with constant flux;
– the optical polarisation is higher in the red than in the blue;
– the SEDs display a bump peaking around the u band in faint states.

This unpolarised emission component is likely thermal emission from the accretion disc. Thermal AGN signatures have apparently been found in several blazars based on different information (see e.g. Perlman et al. 2008 for a review, and Ghisellini et al. 2009), but this is maybe the first time so much observational evidence has been collected for a single object. Furthermore, we have been able to estimate the brightness of the unpolarised component, $R_{QSO} \sim 17.85$–18, and to correct the observed degree of polarisation for its dilution effect to obtain the polarisation of the jet emission. This still shows a dependence on brightness, which is thus an intrinsic dependence.

The analysis of the radio light curves confirms a scenario where radiation of increasing wavelength is emitted in progressively larger and more external jet regions. Optical and radio light curves do not show a general correlation, at least on month–year timescales. One possible explanation, which has already been proposed for other blazars, is that the optical and radio emissions come from different jet zones that have variable orientations with respect to the line of sight. Optical and radio flares would thus result when the corresponding emitting regions are more closely aligned, with a consequent enhancement of the Doppler factor.

We found a general correlation between the flux variations in the optical band and at γ-ray energies, as the optical and γ-ray periods of increased activity coincide. However, the shape of the γ-ray outbursts differs from that of the optical ones, and the flux ratios as well as the time lags between variations at the two frequencies change with time. The correlation was strong during 2009, but became weaker in 2011, likely because of an increased activity in the optical band.

We analysed broad-band SEDs of 4C 38.41 built with contemporaneous data in different brightness states. A careful spectral analysis of both the X-ray data from *Swift* and γ-ray data from *Fermi* was also performed to obtain a reliable spectral shape in the high-energy part of the SED. All the selected epochs show a strong Compton dominance, even when the jet emission is weak and the unpolarised component clearly emerges in the optical band.

We finally discussed a geometrical interpretation of the flux and polarisation variability, which is able to fairly account for the observational data. In this view, at least the long-term flux variations can be ascribed to changes in the Doppler boosting factor produced by changes in the viewing angle. In particular, the weekly γ-ray and optical light curves would imply changes in δ and θ in the ranges of $\sim$ 7–21 and $\sim$ 2.6°–5°, respectively. When using these values in the framework of a shock-in-jet model, where the direction of the wave front, and hence the polarisation degree, changes according to the viewing angle, we could also account for the trend of polarisation with brightness.

Acknowledgements. We thank the referee, Robert Hartman, for his useful comments and suggestions. We are grateful to Stefano Vercellone for information about the AGILE detection of 4C 38.41. We acknowledge financial contribution from the agreement ASI-INAF I/009/10/0. Partly based on observations with the Medicina and Noto telescopes operated by INAF - Istituto di Radioastronomia. The work at U. Michigan was supported by NSF grant AST-0607523 and NASA/Fermi GI grants NNX09AU16G, NNX10AP16G and NNX11AO13G. The Submillimeter Array is a joint project between the Smithsonian Astrophysical Observatory and the Academia Sinica Institute of Astronomy and Astrophysics and is funded by the Smithsonian Institution and the Academia Sinica. This paper is partly based on observations carried out at the German-Spanish Calar Alto Observatory, which is jointly operated by the MPIA and the IAA-CSIC. This paper is partly based on observations carried out at the IRAM–30m Telescope, which is supported by INSU/CNRS (France), MPG (Germany), and IGN (Spain). Acquisition of the MAPCAT, POLAMI, and MAPI data is partly supported by CEIC (Andalucía) grant P09-FQM-4784 and by MINECO (Spain) grant and AYA2010-14844. This work is partly supported by the Georgian National Science foundation grant GNSF/ST09/4-521. This article is partly based on observations made with the telescopes IAC80 and TCS operated by the Instituto de Astrofisica de Canarias in the Spanish Observatorio del Teide on the island of Tenerife. Most of the observations were taken under the rutinary observation programme. The IAC team acknowledges the support from the group of support astronomers and telescope operators of the Observatorio del Teide. The Steward Observatory spectropolarimetric monitoring project is supported by the *Fermi* Guest Investigator grants NNX08AW56G and NNX09AU10G. Data at SPM observatory were obtained through the support given by PAPIIT grant IN116211. The Metsähovi team acknowledges the support from the Academy of Finland to our observing projects (numbers 212656, 210338, 121148, and others). The BU group acknowledges support by NASA grants NNX08AV61G, NNX10AU15G, and NNX11AQ03G. The PRISM camera at Lowell Observatory was developed by K. Janes et al. at BU and Lowell Observatory, with funding from the NSF, BU, and Lowell Observatory. The Liverpool Telescope is operated on the island of La Palma by Liverpool John Moores University in the Spanish Observatorio del Roque de los Muchachos of the Instituto de Astrofisica de Canarias, with funding from the UK Science and Technology Facilities Council. The St. Petersburg University team acknowledges support from Russian RFBR foundation via grant 12-02-00452. AZT-24 observations are made within an agreement between Pulkovo, Rome, and Teramo observatories. Data at NAO Rozhen were obtained through the support given by the BSF grant DO02 340/08. We acknowledge the use of public data from the *Swift* data archive. This research has made of the XRT Data Analysis Software (XRTDAS) developed under the responsibility of the ASI Science Data Center (ASDC), Italy. This research has made use of the SAO/NASA's Astrophysics Data System (ADS) and of the NASA/IPAC Extragalactic Database (NED), which is operated by the Jet Propulsion Laboratory, California Institute of Technology, under contract with the National Aeronautics and Space Administration. This research has made use of data obtained through the High Energy Astrophysics Science Archive Research Center Online Service, provided by the NASA/Goddard Space Flight Center.

References

Agudo, I., Jorstad, S. G., Marscher, A. P., et al. 2011a, ApJ, 726, L13
Agudo, I., Krichbaum, T. P., Ungerechts, H., et al. 2006, A&A, 456, 117
Agudo, I., Marscher, A. P., Jorstad, S. G., et al. 2011b, ApJ, 735, L10
Agudo, I., Thum, C., Wiesemeyer, H., & Krichbaum, T. P. 2010, ApJS, 189, 1
Barthelmy, S. D., Barbier, L. M., Cummings, J. R., et al. 2005, Space Sci. Rev., 120, 143
Bessell, M. S., Castelli, F., & Plez, B. 1998, A&A, 333, 231
Bosio, S., de Francesco, G., Ghisellini, G., et al. 1995, IAU Circ., 6183, 2
Böttcher, M., Fultz, K., Aller, H. D., et al. 2009, ApJ, 694, 174
Breeveld, A. A., Landsman, W., Holland, S. T., et al. 2011, in American Institute of Physics Conference Series, Vol. 1358, American Institute of Physics Conference Series, ed. J. E. McEnery, J. L. Racusin, & N. Gehrels, 373–376
Burrows, D. N., Hill, J. E., Nousek, J. A., et al. 2005, Space Science Reviews, 120, 165
Cardelli, J. A., Clayton, G. C., & Mathis, J. S. 1989, ApJ, 345, 245
Cash, W. 1979, ApJ, 228, 939
Chonis, T. S. & Gaskell, C. M. 2008, AJ, 135, 264
D'Ammando, F., Pucella, G., Raiteri, C. M., et al. 2009, A&A, 508, 181
D'Ammando, F., Raiteri, C. M., Villata, M., et al. 2011, A&A, 529, A145
Edelson, R. A. & Krolik, J. H. 1988, ApJ, 333, 646
Francis, P. J., Hewett, P. C., Foltz, C. B., et al. 1991, ApJ, 373, 465
Gehrels, N., Chincarini, G., Giommi, P., et al. 2004, ApJ, 611, 1005
Ghisellini, G., Tavecchio, F., & Ghirlanda, G. 2009, MNRAS, 399, 2041
Gurwell, M. A., Peck, A. B., Hostler, S. R., Darrah, M. R., & Katz, C. A. 2007, in Astronomical Society of the Pacific Conference Series, Vol. 375, From Z-Machines to ALMA: (Sub)Millimeter Spectroscopy of Galaxies, ed. A. J. Baker, J. Glenn, A. I. Harris, J. G. Mangum, & M. S. Yun, 234
Hartman, R. C., Bertsch, D. L., Bloom, S. D., et al. 1999, ApJS, 123, 79
Hayashida, M., Madejski, G. M., Nalewajko, K., et al. 2012, ApJ, submitted
Holmes, P. A., Brand, P. W. J. L., Impey, C. D., et al. 1984, MNRAS, 211, 497
Hufnagel, B. R. & Bregman, J. N. 1992, ApJ, 386, 473
Hughes, P. A., Aller, H. D., & Aller, M. F. 1985, ApJ, 298, 301
Impey, C. D., Brand, P. W. J. L., & Tapia, S. 1982, MNRAS, 198, 1
Jorstad, S. G., Marscher, A. P., Agudo, I., et al. 2011, Journal of Astrophysics and Astronomy, 32, 239
Jorstad, S. G., Marscher, A. P., Larionov, V. M., et al. 2010, ApJ, 715, 362
Kalberla, P. M. W., Burton, W. B., Hartmann, D., et al. 2005, A&A, 440, 775
Kaspi, S., Smith, P. S., Netzer, H., et al. 2000, ApJ, 533, 631
Larionov, V. M., Jorstad, S. G., Marscher, A. P., et al. 2008, A&A, 492, 389
Larionov, V. M., Villata, M., & Raiteri, C. M. 2010, A&A, 510, A93
Madejski, G., Takahashi, T., Tashiro, M., et al. 1996, ApJ, 459, 156
Marscher, A. P., Jorstad, S. G., Larionov, V. M., et al. 2010, ApJ, 710, L126
Mattox, J. R., Bertsch, D. L., Chiang, J., et al. 1993, ApJ, 410, 609
Mead, A. R. G., Ballard, K. R., Brand, P. W. J. L., et al. 1990, A&AS, 83, 183
Nolan, P. L., Abdo, A. A., Ackermann, M., et al. 2012, ApJS, 199, 31
Nousek, J. A. & Shue, D. R. 1989, ApJ, 342, 1207
Perlman, E., Addison, B., Georganopoulos, M., Wingert, B., & Graff, P. 2008, in Blazar Variability across the Electromagnetic Spectrum
Peterson, B. M. 2001, in Advanced Lectures on the Starburst-AGN Connection, ed. I. Aretxaga, D. Kunth, & R. Mújica (Singapore: World Scientific), 3
Peterson, B. M., Wanders, I., Horne, K., et al. 1998, PASP, 110, 660
Pian, E., Urry, C. M., Maraschi, L., et al. 1999, ApJ, 521, 112
Poole, T. S., Breeveld, A. A., Page, M. J., et al. 2008, MNRAS, 383, 627
Raiteri, C. M., Ghisellini, G., Villata, M., et al. 1998, A&AS, 127, 445
Raiteri, C. M., Villata, M., Aller, M. F., et al. 2011a, A&A, 534, A87
Raiteri, C. M., Villata, M., Bruschini, L., et al. 2010, A&A, 524, A43
Raiteri, C. M., Villata, M., Capetti, A., et al. 2009, A&A, 507, 769
Raiteri, C. M., Villata, M., Chen, W. P., et al. 2008a, A&A, 485, L17
Raiteri, C. M., Villata, M., Ehgamberdiev, S. A., Mirzaqulov, D. O., & Holikov, S. 2011b, The Astronomer's Telegram, 3483, 1
Raiteri, C. M., Villata, M., Larionov, V. M., et al. 2008b, A&A, 480, 339
Raiteri, C. M., Villata, M., Larionov, V. M., et al. 2008c, A&A, 491, 755
Raiteri, C. M., Villata, M., Larionov, V. M., et al. 2007, A&A, 473, 819
Raiteri, C. M., Villata, M., Tosti, G., et al. 2003, A&A, 402, 151
Roming, P. W. A., Kennedy, T. E., Mason, K. O., et al. 2005, Space Science Reviews, 120, 95
Salonen, E., Teräsranta, H., Urpo, S., et al. 1987, A&AS, 70, 409
Savolainen, T., Homan, D. C., Hovatta, T., et al. 2010, A&A, 512, A24
Schmidt, G. D., Stockman, H. S., & Smith, P. S. 1992, ApJ, 398, L57
Sitko, M. L., Schmidt, G. D., & Stein, W. A. 1985, ApJS, 59, 323
Sitko, M. L., Stein, W. A., & Schmidt, G. D. 1984, ApJ, 282, 29
Smith, P. S., Balonek, T. J., Elston, R., & Heckert, P. A. 1987, ApJS, 64, 459
Smith, P. S., Balonek, T. J., Heckert, P. A., & Elston, R. 1986, ApJ, 305, 484
Smith, P. S., Montiel, E., Rightley, S., et al. 2009, ArXiv e-prints
Smith, P. S., Schmidt, G. D., & Jannuzi, B. T. 2011, ArXiv e-prints
Smith, P. S., Schmidt, G. D., Jannuzi, B. T., & Elston, R. 1994, ApJ, 426, 535
Szostek, A. 2011, The Astronomer's Telegram, 3333, 1
Teräsranta, H., Achren, J., Hanski, M., et al. 2004, A&A, 427, 769
Teräsranta, H., Tornikoski, M., Mujunen, A., et al. 1998, A&AS, 132, 305
Teräsranta, H., Tornikoski, M., Valtaoja, E., et al. 1992, A&AS, 94, 121
Teräsranta, H., Wiren, S., Koivisto, P., Saarinen, V., & Hovatta, T. 2005, A&A, 440, 409
Urry, C. M. & Padovani, P. 1995, PASP, 107, 803
Vermeulen, R. C., Ogle, P. M., Tran, H. D., et al. 1995, ApJ, 452, L5
Villata, M. & Raiteri, C. M. 1999, A&A, 347, 30
Villata, M., Raiteri, C. M., Aller, M. F., et al. 2007, A&A, 464, L5
Villata, M., Raiteri, C. M., Balonek, T. J., et al. 2006, A&A, 453, 817
Villata, M., Raiteri, C. M., Ghisellini, G., et al. 1997, A&AS, 121, 119
Villata, M., Raiteri, C. M., Gurwell, M. A., et al. 2009a, A&A, 504, L9
Villata, M., Raiteri, C. M., Larionov, V. M., et al. 2008, A&A, 481, L79
Villata, M., Raiteri, C. M., Larionov, V. M., et al. 2009b, A&A, 501, 455
Wardle, J. F. C. & Kronberg, P. P. 1974, ApJ, 194, 249
Wills, B. J., Wills, D., Breger, M., Antonucci, R. R. J., & Barvainis, R. 1992, ApJ, 398, 454
Wilms, J., Allen, A., & McCray, R. 2000, ApJ, 542, 914

[1] INAF, Osservatorio Astronomico di Torino, Italy
[2] Steward Observatory, University of Arizona, Tucson, AZ, USA
[3] Astron. Inst., St.-Petersburg State Univ., Russia
[4] Pulkovo Observatory, St.-Petersburg, Russia
[5] Isaac Newton Institute of Chile, St.-Petersburg Branch
[6] Instituto de Astrofisica de Canarias (IAC), La Laguna, Tenerife, Spain
[7] Departamento de Astrofisica, Universidad de La Laguna, La Laguna, Tenerife, Spain
[8] Department of Astronomy, University of Michigan, MI, USA
[9] Dip. di Fisica, Università degli Studi di Perugia, Perugia, Italy
[10] Harvard-Smithsonian Center for Astrophysics, Cambridge, MA, USA
[11] Institute for Astrophysical Research, Boston University, MA, USA
[12] Abastumani Observatory, Mt. Kanobili, Abastumani, Georgia
[13] Astrophysikalisches Institut Potsdam, An der Sternwarte 16, Potsdam, Germany
[14] Landessternwarte Heidelberg-Königstuhl, Heidelberg, Germany
[15] Engelhardt Astronomical Observatory, Kazan Federal Univ., Tatarstan, Russia
[16] Aalto University Metsähovi Radio Observatory, Kylmälä, Finland
[17] Maidanak Observatory of the Ulugh Beg Astronomical Institute, Uzbekistan
[18] Instituto de Astrofísica de Andalucía, CSIC, Granada, Spain
[19] Max-Planck-Institut für Radioastronomie, Bonn, Germany
[20] Instituto de Astronomía, Universidad Nacional Autónoma de México, México DF, México
[21] Tuorla Observatory, Dept. of Physics and Astronomy, Univ. of Turku, Piikkiö, Finland
[22] INAF, Osservatorio Astrofisico di Catania, Italy
[23] EPT Observatories, Tijarafe, La Palma, Spain,
[24] INAF, TNG Fundación Galileo Galilei, La Palma, Spain
[25] Graduate Inst. of Astronomy, National Central Univ., Jhongli, Taiwan
[26] INAF, Osservatorio Astronomico di Roma, Italy
[27] INAF, Osservatorio Astronomico di Collurania Teramo, Italy
[28] Instituto de Astronoma, Universidad Nacional Autónoma de México, Ensenada, México
[29] Department of Physics, National Taiwan University, Taipei, Taiwan
[30] Dept. of Physics and Astronomy, Univ. of Southampton, Southampton, United Kingdom
[31] Instituto Nacional de Astrofisica, Óptica y Electrónica, Puebla, México
[32] Finnish Centre for Astronomy with ESO (FINCA), University of Turku, Piikkiö, Finland
[33] Department of Astronomy, University of Sofia, Sofia, Bulgaria
[34] European Space Astronomy Centre (INSA-ESAC), Villanueva de la Caada, Madrid, Spain
[35] Agrupació Astronòmica de Sabadell, Spain
[36] CRESST and Astroparticle Physics Laboratory NASA/GSFC, Greenbelt, MD, USA
[37] Dept. of Physics, Univ. of Maryland, Baltimore County, Baltimore, MD, USA
[38] Galaxy View Observatory, Sequim, Washington, USA
[39] Cork Institute of Technology, Cork, Ireland
[40] Lowell Observatory, Flagstaff, AZ, USA
[41] Institut de Radio Astronomie Millimétrique, St. Martin d'Hères, France
[42] Space Science Institute, Boulder, CO, USA

A&A 537, A101 (2012)
DOI: 10.1051/0004-6361/201116848

Astronomy & Astrophysics

Physical studies of 81P/Wild 2 from the last two apparitions⋆

Z.-Y. Lin[1,3], L. M. Lara[1], J. B. Vincent[2], and W.-H. Ip[3]

[1] Instituto de Astrofísica de Andalucía (CSIC), Glorieta de la Astronomía s/n, 18008 Granada, Spain
e-mail: zlin@iaa.csic.es
[2] Max-Planck-Institut für Sonnensystemforschung, Max-Planck-Strasse 2, 37191 Katlenburg-Lindau, Germany
[3] Institute of Astronomy, National Central University, Taiwan

Received 8 March 2011 / Accepted 2 November 2011

ABSTRACT

Context. We downloaded data for the comet 81P/Wild 2 for May and June 2004 from the ESO archive and monitored this comet from January to August 2010 during its 6th perihelion passage since its discovery in 1978. Photometric data were used to monitor the comet's gas and dust activity as a function of heliocentric distance. Non-photometric data were used for an analysis of the evolution of the dust coma morphology.

Aims. The goal of the analysis of the observational data was to characterize the evolution of the cometary activity as the nucleus approaches the Sun. We also aimed to assess the gas and dust production rates for the last two apparitions and investigated the evolution of the dust coma morphology during the last passage in 2010.

Methods. The long-slit spectra data were acquired with the EFOSC2 instrument mounted at the 3.6. m ESO telescope in Chile, while narrowband and broadband images were obtained using the 1-m telescope at the Lulin Observatory in Taiwan. Image enhancing techniques were used to investigate the evolution of the dust coma morphology in the R-broadband images, and we modeled the evolution of these dust jets. Where possible, we studied the dust and gas production rate, and the radial profiles of the dust brightness in the Sun-anti-sunward directions.

Results. The morphological analysis helped us to detect the jet structures in the dust coma by using the Larson-Sekanian filter. In May 2004, only one feature had been found on the sunward side. In 2010, one of the jet features had been switched-off after January, and at least four new jets were found from April to May. The physical properties show an average reddening between 4420 Å and 6840 Å of 8.4% per 1000 Å and the average resulting log of the C_2-to-CN production rate ratio is –0.454 ± 0.13, which would place Wild 2 in the "depleted" category according to the taxonomic classification. The slope of the radial dependence of the gas production rates for CN and C_2 is very consistent with observations of many other Jupiter-family comets. The slopes of the surface brightness lie between 0.98 and 1.38 in the images taken at the Lulin observatory, whose the range interval from 2000 km to 30 000 km is roughly consistent with the ρ^{-1} law. However, the gradient of the radial profile in the sunward direction in the outer region ($4.0 \leq \log \rho(\mathrm{km}) \leq 4.5$) is slightly steeper than that in the inner region ($3.3 \leq \log \rho(\mathrm{km}) \leq 4.0$).

Key words. comets: individual: 81P/Wild 2

1. Introduction

Comet 81P/Wild 2 (hereafter Wild 2) is a Jupiter-family comet (JCF) discovered by Paul Wild in early January, 1978. Owing to a close encounter with Jupiter in 1974 at a distance of 0.006 AU from the planet, the orbital parameters changed such that the perihelion distance decreased by 3.5 AU, from 4.9 AU to 1.4 AU, allowing the cometary surface to receive a higher amount of radiation from the Sun. The orbital period of comet Wild 2 also changed from 57 years to 6.4 years (Sekanina 2003). This relatively young photometric age of 13 cy, a parameter related to cometary activity, was estimated by using the secular light curves obtained in the 1990, 1997, and 2003 apparitions (Ferrin 2007). As a consequence of this young age, comet Wild 2 has probably encountered fewer intense heating episodes than other JFCs, therefore we can expect to detect new and pristine material in future apparitions.

Comet Wild 2 was the target of NASA's Stardust mission, with a close encounter on 2 January 2004. The Stardust project was primarily a dust sample return mission whose primary goal was to collect sub-millimeter particles for laboratory analysis (Brownlee et al. 2004). During its flyby, Stardust also obtained many high-resolution images. These images revealed large numbers of jets projecting around almost the entire perimeter of the nucleus. The highly collimated jets indicate that the source regions on the cometary surface or subsurface were small. This phenomenon was also seen in the comet 19P/Borrelly (Yelle et al. 2004; Soderblom et al. 2004). Unfortunately, the observing conditions of ground-based telescopes during the 2003 perihelion and flyby time were extremely poor, because the comet was in conjunction with the Sun. Under these poor conditions, very little data were obtained at very high airmass (Farnham et al. 2005). In addition, most of the quality data were taken in May and June of 2004.

In 2010, comet Wild 2 was only 0.67 AU distant from Earth. This represented a good chance to obtain relatively good spatial resolution and was an opportunity to study the dust and gas properties in the cometary coma. In addition, we also downloaded Wild 2 data from the ESO archive for May 1 and June 16, 2004, which we compared with the comet's at long heliocentric distance. In this paper, we present the photometric and spectrophotometric results from our analysis of the data acquired during the last two apparitions.

⋆ Based on observations made with the European Southern Observatory telescopes obtained from the ESO/ST-ECF Science Archive Facility.

Table 1. Log of Observations performed at the ESO and Lulin observatories.

Date	r_H (AU)	Δ (AU)	PsAng (deg)	α (deg)	Pixel scale (km)	Observatory
2004						
May 1	2.53	2.04	259.3	22.3	464.6	ESO
June 16	2.81	1.85	255.3	8.4	421.3	ESO
2010						
January 14	1.64	1.10	292.7	35.5	410.8	Lulin
January 15	1.64	1.09	292.6	35.4	407.1	Lulin
January 16	1.64	1.08	292.5	35.4	404.0	Lulin
January 17	1.64	1.07	292.5	35.4	399.7	Lulin
January 18	1.64	1.06	292.4	35.3	384.7	Lulin
February 26	1.60	0.78	286.8	28.7	291.3	Lulin
April 7	1.66	0.67	264.8	10.3	250.3	Lulin
April 24	1.71	0.70	180.5	4.8	264.2	Lulin
May 4	1.74	0.75	139.2	8.7	281.0	Lulin
May 20	1.81	0.86	122.2	16.1	322.0	Lulin
May 31	1.86	0.96	117.8	20.1	358.9	Lulin
August 1	2.19	1.80	106.6	27.3	672.7	Lulin

Notes. r_h and Δ are the geocentric and heliocentric distances in AU. PsAng is the position of the extended Sun-comet vector, measured from north toward east. α is the phase angle Sun-comet-observer.

2. Observations and data reduction

2.1. Instrumentation

The first set of observations from 2004 are available worldwide from the European Southern Observatory (ESO) Archive, obtained with the 3.6 m telescope of the ESO, in La Silla, Chile, using the EFOSC2 instrument (1030 × 1030 pixels, binned pixel size: 0.314″, FOV 5.39′ × 5.39′). A spectrograph covering the wavelength ranges from 319 nm to 1095 nm at a dispersion of 6.6 Å/pixel was used for this relatively faint comet on May 1 and June 16. The maximum magnitude measured in 2004 was a hundred times less than that in 2010, because of the difference between the heliocentric and geocentric distances. The slit width was 2.0 arcsec and the slit length was 4.1 arcmin with a spatial scale of 0.157″/pixel. The spatial scale used in this study is 0.314″/pixel, because of the pixel binning. Notice that the slit used here was oriented along the north-south line, which was nearly perpendicular to the Sun-comet direction.

The second observational program, using the one-meter telescope at Lulin Observatory in Taiwan, was planned from January 14 to August 1, 2010. During this observational period, the comet passed through its perihelion (1.598 AU) on February 22 and made its closest approach to Earth (0.673 AU) on April 5, 2010. The observations were carried out using an Asahi *R*-broadband filter and the narrowband filters of the Rosetta filter set. The specifications of these narrowband filters are described as follows: CN (387/6 nm), C_2 (514/12 nm), blue continuum (445/4 nm), and red continuum (687.4/6 nm). The camera (PI 1300B) had a pixel scale of 0.516″ and a field of view of 11.2′ × 11.6′. Details of our observations of comet Wild 2 are given in Table 1.

2.2. CCD images and reduction

The data reduction followed standard procedures. In the outline, the procedure began with bias subtraction in the ESO images and dark-current subtraction in the Lulin images. Then we flat-field corrected of all frames followed by the subtraction of the night sky contribution. For the observations obtained at the ESO in 2004 and the Lulin observatory in 2010, the night sky levels were determined from parts of the cometary images that do not contain contributions from the cometary coma. The extinction coefficients of the narrowband and broadband R-filters were determined for all nights based on the photometric sky conditions, using photometric stars, like Feige 67, observed at various airmasses during the night. These data were used to convert the measured counting rates into physical units; for details see Lin et al. (2007).

2.3. Spectra and reduction

The spectrum taken on May 1, 2004, at ESO is shown in Fig. 1 (left-panel). The spectroscopic data were reduced following the standard procedure, including bias and flat-field corrections and cosmic-ray removal. Owing to the relatively faint brightness of comet Wild 2 in 2004, the sky background can be determined by averaging directly at both sides of the spatial directions (Fig. 1, middle-panel). Using this averaged image, the sky-background of the spectrum of comet Wild 2 can be subtracted. Wavelength calibration was performed based on helium-argon lamps exposed at both the beginning and the end of the observations every night, after which the atmospheric extinction effect (using the standard extinction curve for La Silla) was corrected. Finally, flux calibration of each spectrum was conducted based on observations of the spectro-phometric flux standard star LTT7987 (Hamuy et al. 1992) as a flux calibrator in the range of 330 nm ~1000 nm.

3. Data analysis and results

3.1. Gas production rate

In order to determine the gas production rates from cometary frames in 2010, the mean radial emission profiles of CN and C_2 were derived from the images with the continuum subtracted (Lin et al. 2009). We fitted the mean radial brightness profiles of CN and C_2 using the Haser model (Haser 1957), which describes the isotropic emission of cometary neutral molecules and their daughter molecules and radicals. The parameter used for the parent velocity is $v_p = 0.85\ r^{-0.5}$ km s^{-1} (Fray et al. 2005) and for the daughter velocity it is 1 km s^{-1}. The fluorescence

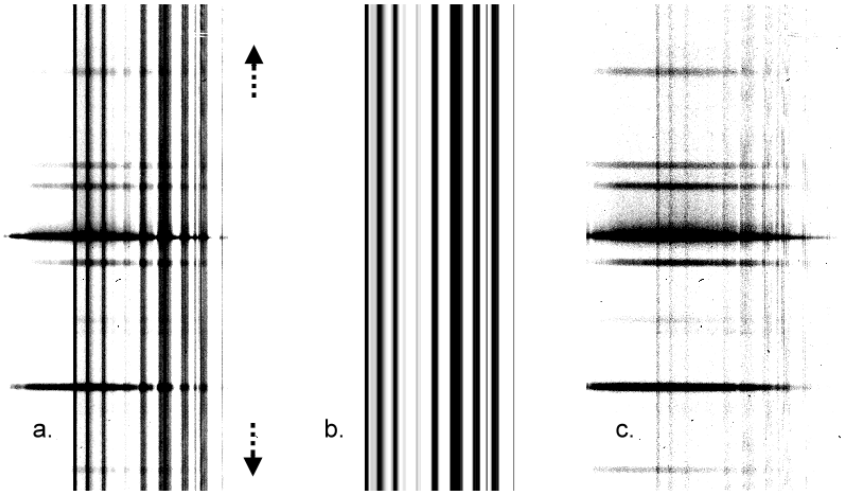

Fig. 1. Spectrum of comet 81P/Wild 2 with sky-background reduction and subtraction: **a)** the spectrum reduced for bias and flat. The region of the sky-background can be measured directly at both sides (arrows) of the spectrum. **b)** The average sky-background spectrum. **c)** The cometary spectrum with the sky-background subtraction.

Table 2. Emission and continuum bands extracted from the spectra.

Spectral region (Å)	Species	Blue-side continuum (Å)	Red-side continuum (Å)
3830–3950	CN	3700–3815	3910–3970
4860–5185	C_2	4780–4850	5195–5295

efficiency factors (g-factors) of CN are 3.1×10^{-13} in January and 4.2×10^{-13} in May (Schleicher et al. 2010) and C_2 in January and May are 4.5×10^{-13} (A'Hearn et al. 1995). The scale-lengths used here for r_H at 1 AU, l_p and l_d, are 1.3×10^4 km, 2.1×10^5 km for CN and 2.2×10^4 km, 6.6×10^4 km for C_2, respectively (A'Hearn et al. 1995). The results indicated in Fig. 2 with open-circle symbols.

From the spectra obtained in 2004, the spectral range of CN, C_2 and the continuum at both sides of the gas emission are specified and listed in Table 2 (Lara et al. 2001). Here, we used the red- and blue-side continuum for linear fitting, and based on the fitting results subtracted the underlying continuum in the gas emission bands. After subtraction, we integrated the spectral regions for Haser profile fitting. The g-factor used in the spectra of CN is 4.1×10^{-13} (Schleicher 2010) and for C_2 it is 4.5×10^{-13} (A'Hearn et al. 1995). The results of the production rate in these two apparitions are also indicated by the open triangles in Fig. 2.

In Fig. 2 we plot the logarithm of the production rates for CN and C_2 as a function of the heliocentric distance (r_H). The data points including those obtained by Farnham et al. (2005) for pre-perihelion and post-perihelion observations and the ESO and Lulin results are presented here. There are three implicit assumptions made in Fig. 2 with multiple apparitions: there are no secular variations from one apparition to another, the Haser scale lengths are nearly the same, and the rotational variations in the production rates are small. We used the linear fitting to estimate the slope of the radial dependence of the gas production rate, $Q \sim r^{\alpha}$ (Fig. 2, dashed line), and the slopes (α) of CN and C_2 are –3.68 and –4.39, respectively. The measurements of gas and dust production rate in 1978 were significantly higher than for the other apparitions because of the evolution effect. This effect was associated with Wild 2's first approach to the Sun after its orbit was changed in 1974. (Farnham et al. 2005). We therefore discarded the data taken by Farnham in 1978 (opened squares in Fig. 2). The slopes of CN and C_2 would consequently change from –3.68 to –2.58 and from –4.39 to –2.60, respectively (Fig. 2, solid-line). This result is completely consistent with the observations of many other Jupiter-family comets, i.e. $Q(\mathrm{gas}) \sim {r_H}^{-2.7}$ (A'Hearn et al. 1995).

3.2. Composition

The mean value in the log $[Q(C_2)/Q(CN)]$ for typical comets is approximately +0.13 and for depleted comets approximately –0.11 in A'Hearn et al. (1995). The average value in this work (Table 3) is -0.45 ± 0.13, which would place Wild 2 in the "depleted" category according to this taxonomic classification. However, the value is about four times lower than the mean value for depleted comets but is similar to the average value (-0.58 ± 0.15) estimated by Fink et al. (1999), which was measured to be (-0.34 ± 0.17) by Farnham et al. (2005). The data of log $[Q(C_2)/Q(CN)]$ for the interval from 1978 to 2010 is plotted in Fig. 3.

3.3. Dust coma properties

We used the Afρ parameter (A'Hearn et al. 1984) to characterize the dust activity of Wild 2. The derived values for January to August 2010 at several cometocentric distances are presented in Table 4. The derived Afρ values for the narrowband filter can be taken to estimate the color of the cometary dust (Jewitt & Meech 1986) as the normalized gradient of the Afρ product between the blue (BC, λ_0 = 4430 Å) and red (RC, λ_0 = 6840 Å) continuum filters. The dust colors can be converted to percentage of reddening per 1000 Å, allowing for the different locations of the band passes between the two filters sets, and is defined by the following relation:

$$\mathrm{color} = \frac{RC_{\mathrm{Af}\rho} - BC_{\mathrm{Af}\rho}}{6840-4430}\,\frac{2000}{RC_{\mathrm{Af}\rho} + BC_{\mathrm{Af}\rho}}. \quad (1)$$

The color examined between the blue- and red-continuum filters on January 15 and May 4 is 8.2% and 8.6%, respectively. These values agree with those presented by Schulz et al. (2003)

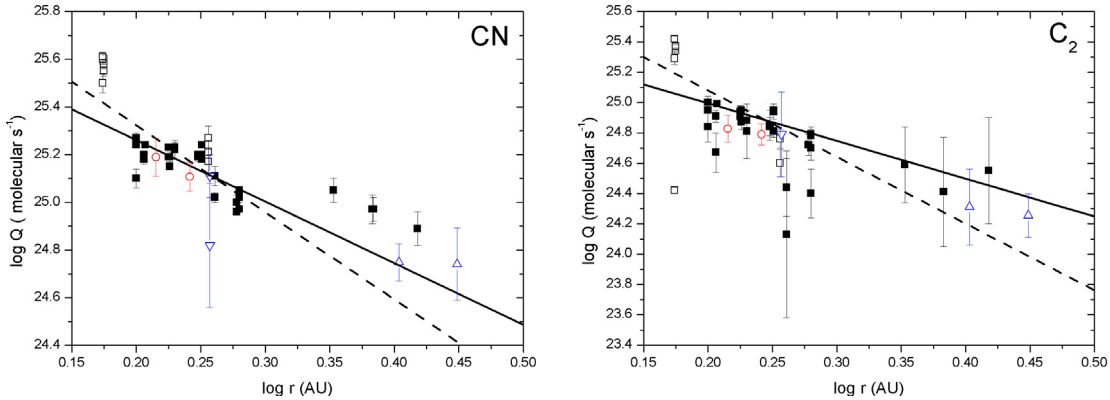

Fig. 2. Log of production rates for CN (*left*) and C_2 (*right*) plotted as a function of the log of the heliocentric distance. Different symbols come from different data sets; opened square, filled symbols and opened inverse-triangle are the data from four apparitions (1978 ~ 2003) taken by Farnham et al. (2005). The open circle and triangle symbols are the data taken from the Lulin observatory in 2010 and from La Silla in 2004, respectively. Notice that the data from 2003 ~ 2004 are all represented by triangle symbols. Two different results of the linear fitting are present. The dash line is representative of all data obtained from 1978 to 2010 and the solid line is for all data obtained from 1983 to 2010.

Table 3. The results and ratio of gas production rates.

Date	CN $Q(10^{24}$ molecules/s)	C_2 $Q(10^{24}$ molecules/s)	Log[$Q(C_2)/Q$(CN)]
2004 May 1	5.6 ± 1.1	2.0 ± 1.6	–0.447
2004 June 16	5.5 ± 2.3	1.8 ± 0.7	–0.482
2010 Jan. 15	15.5 ± 2.1	3.8 ± 0.5	–0.607
2010 May 4	5.9 ± 1.0	3.1 ± 0.5	–0.280

Table 4. Dust coma properties.

Date	r_H (AU)	α (deg)	Afρ^a (cm)	Afρ^b (cm)	Slope(-m) $(3.3 \le \log \rho \le 4.5)$	$(3.3 \le \log \rho \le 4.0)$	$(4.0 \le \log \rho \le 4.5)$
2004 (ESO)							
May 1	2.53	22.3			1.71^c, 1.31^d	1.62^c, 1.40^d	1.47^c, 0.98^d
June 16	3.81	1.85			1.74^c, 1.07^d	1.71^c, 1.22^d	1.99^c, 1.01^d
2010 (Lulin)							
January 14	1.64	35.5	868.4	782.8	2.08^c; 1.02^d	1.27^c; 1.08^d	3.38^c; 0.99^d
January 15	1.64	35.4	566.3	538.1	1.38^c; 0.99^d	1.29^c; 1.05^d	1.55^c; 0.97^d
January 16	1.64	35.4	566.2	534.8	1.34^c; 0.99^d	1.26^c; 1.03^d	1.51^c; 0.95^d
January 17	1.64	35.4	613.3	573.1	1.37^c; 0.98^d	1.34^c; 1.04^d	1.46^c; 0.96^d
January 18	1.64	35.3	608.3	570.9	1.38^c; 1.04^d	1.21^c; 1.10^d	1.63^c; 0.97^d
February 26	1.60	28.7			1.21^c; 1.04^d	1.13^c; 1.13^d	1.46^c; 0.99^d
April 7	1.66	10.3			1.13^c; 1.17^d	1.20^c; 1.14^d	1.24^c; 1.22^d
April 24	1.71	4.8	604.2	531.6	1.23^c; 1.23^d	1.27^c; 1.19^d	1.13^c; 1.27^d
May 4	1.74	8.7	569.9	532.0	1.06^c; 1.19^d	1.10^c; 1.13^d	1.01^c; 1.27^d
May 20	1.81	16.1			1.12^c; 1.16^d	1.17^c; 1.09^d	1.02^c; 1.28^d
May 31	1.86	20.1			1.09^c; 1.17^d	1.17^c; 1.10^d	1.03^c; 1.30^d
August 1	2.19	27.3	192.3	195.0	1.09^c; 1.18^d	1.23^c; 1.10^d	1.01^c; 1.42^d

Notes. Afρ values are derived for a photometric circular aperture. $^{(a)}$ The radius in aperture is 10 000 km; $^{(b)}$ the radius in aperture is 20 000 km; $^{(c)}$ is measured from the sunward direction; $^{(d)}$ is refers to tailward direction. Errors estimated here are 5% for the Afρ and 4% in slopes, respectively.

from broadband BVR images and those found by Farnham et al. (2005) from narrowband filters with intervals [4450 Å–5260 Å].

3.4. Dust brightness profiles

To analyze the overall brightness distribution of the coma, one-dimensional profiles were obtained directly from the Sun-tail direction. In the double logarithmic representation, the radial coma profiles should be straight lines with a slope of $m = -1$ (Jewitt & Meech 1987) under a steady-state situation. Our measurements, based on the ESO 2004 and Lulin 2010 observations, are listed in Table 4. The slopes lie between 0.98 and 1.38 with a range interval from 2000 km to 30 000 km and are roughly consistent with the ρ^{-1} law (ρ is the projected radial distance from the nucleus in the plane of the sky). The slopes in the sunward direction for January 14, 2010, are also drived.

The slope on January 14, 2010, shows an interesting knee-like feature in the sunward direction (Fig. 4), with a slope of 1.27 in the inner region [2000 km ~ 10 000 km] and 3.38 in the outer region [10 000 km ~ 30 000 km]. These steeper slopes may be caused by non-steady state dust emission or possibly by dust grain fading or destruction (Baum et al. 1992). If this is the case, the dust grains associated with high Afρ (Table 4) could have come from an earlier outburst or other event. Unfortunately, no observations are available before January 14, which prevents a conclusion about whether we witnessed an outburst or if there

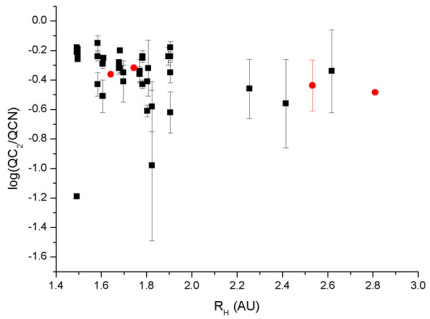

Fig. 3. Log $Q(C_2)$ to Q(CN) ratio plotted as a function of the heliocentric distance. The filled circles represent the estimates of the present work and the filled squares indicate the results obtained by Farnham et al. (2005).

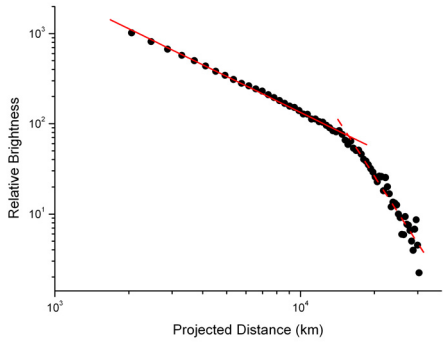

Fig. 4. Radial brightness profile, log B, vs. projected distance, log ρ on January 14, 2010. The slope of the sunward direction shows a very different knee-like phenomenon, wiht a slope 1.27 (solid line) in the inner region [2000 km ~ 10 000 km] and 3.38 (dashed line) in the outer region [10 000 km ~ 30 000 km].

was some earlier event. However, if we obtain the profile in the tailward direction, the results in the inner and outer tailward region and in the inner region are consistent with the ρ^{-1} law.

Apart from this interesting feature on January 14, we find that the gradient on January and February 2010 in the outer sunward region is also steeper than that in the inner sunward region. These steep profiles could be influenced by one or more factors: radiation pressure acting on the dust, or temporal changes in the optical properties of the grains, i.e. the sublimation of the ice grains (Jewitt & Meech 1987), changing either their size or albedo.

4. Morphology of coma structures

4.1. Morphology

We describe the morphology and evolution of coma structures acquired during the last two apparitions. During the period in 2004, the nucleus showed less activity because of the long heliocentric distance. In contrast, the nucleus displayed a lot of activity in the last apparition between January 14 and August 1, 2010, characterized by the presence of dust jets in the coma. These structures can be treated with routine procedures. Here we applied two independent methods: (1) Adaptive Laplace filter (Böhnhardt & Birkle 1994); and (2) Larson-Sekanina algorithm (Larson & Sekanina 1984). The first filter applies a Laplacian kernel to a logarithmized image, which can remove all gradual variations in linear and second order gradients. Adaptive filtering means to look for the spatial frequency band containing the relevant signal, especially to enhance particularly the structure in this band. Here we applied the MIDAS procedure FILTER/ADAPTIVE with the Laplace filter with the parameters chosen after extensive tests. The second technique is a direct subtraction between the rotated/shifted frame and the original frame. The results of the Larson-Sekanina filtered (angle = 10 degree) can be found in Fig. 5.

In case of doubt, we used additional techniques, such as mean-median profile subtraction or unsharp masking to clearly separate morphological features from artifacts. We also made a comparison with the processed images and isophotes of the original images (Fig. 6). Since the contribution of light from gas and ion emissions is small in the R-band, we interpret the observed structures as dust reflecting sunlight. We can therefore clearly identify the dust tail and coma fan structures produced by active dust-emitting sources on the rotating nucleus, as described by Sekanina (1987).

In addition to the dust tail (labeled T in Fig. 5) we identified up to seven different dust structures including two sub-structures in our images, as summarized in Table 5. Notice that the position of the coma structures in Table 5 does not correspond to the values that we found in the active regions located at the nucleus. From 14 to 18 January, 2010, a broad northeast jet, which can be divided into two substructures and a narrow southeast jet (labeled A, B, and C in Fig. 5) were detected in the solar direction. The difference between substructure A and B is the curvature feature. Substructure A extends first toward the Sun before bending in the tail direction. The apparent broadening away from the nucleus could be caused by the size-sorting of grains through radiation pressure. Substructure B and structure C do not display the same curvature, although this is very likely a projection effect. Notice that substructure B is very close to substructure A in the images and as the jet broadens when particles move away from the nucleus, the bent part of structure B cannot be distinguished from structure A. In the image taken on 26 February, only substructures A and B (northeast jet) are detected. Because we have a very good signal-to-noise ratio in these images, the disappearance of structure C is not a bias in our observations but rather indicates a change in activity, probably the switching-off of one active region. Notice that the Earth-comet observing geometry in January and February remained relatively constant. From early April to late May 2010, at least four new jets appear in addition to substructures A and B (labeled D, E, F, G in Fig. 5). There were three new identifiable jets in April and one new additional jet was found at PA 8 degrees in May. The last image in May suffers from the low signal/noise ratio so the structures can barely be noticed, although they might still be present. In August, only one jet can be found in the inner coma, which might have been present all the time from May to August, because their morphology and the orbital configuration did not change during these months.

Images obtained in 2004 are not included in Fig. 5 and Table 5. There were only a few usable images from that period because of the poor tracking. However, we were lucky to find the feature in the images we have. In Fig. 7 we can see the features processed in the dust tail, extending to the southwest, and the jet feature, bending to the south. Unfortunately, the image does not reveal how many features there were in the sunward direction owing to the low signal/noise ratio.

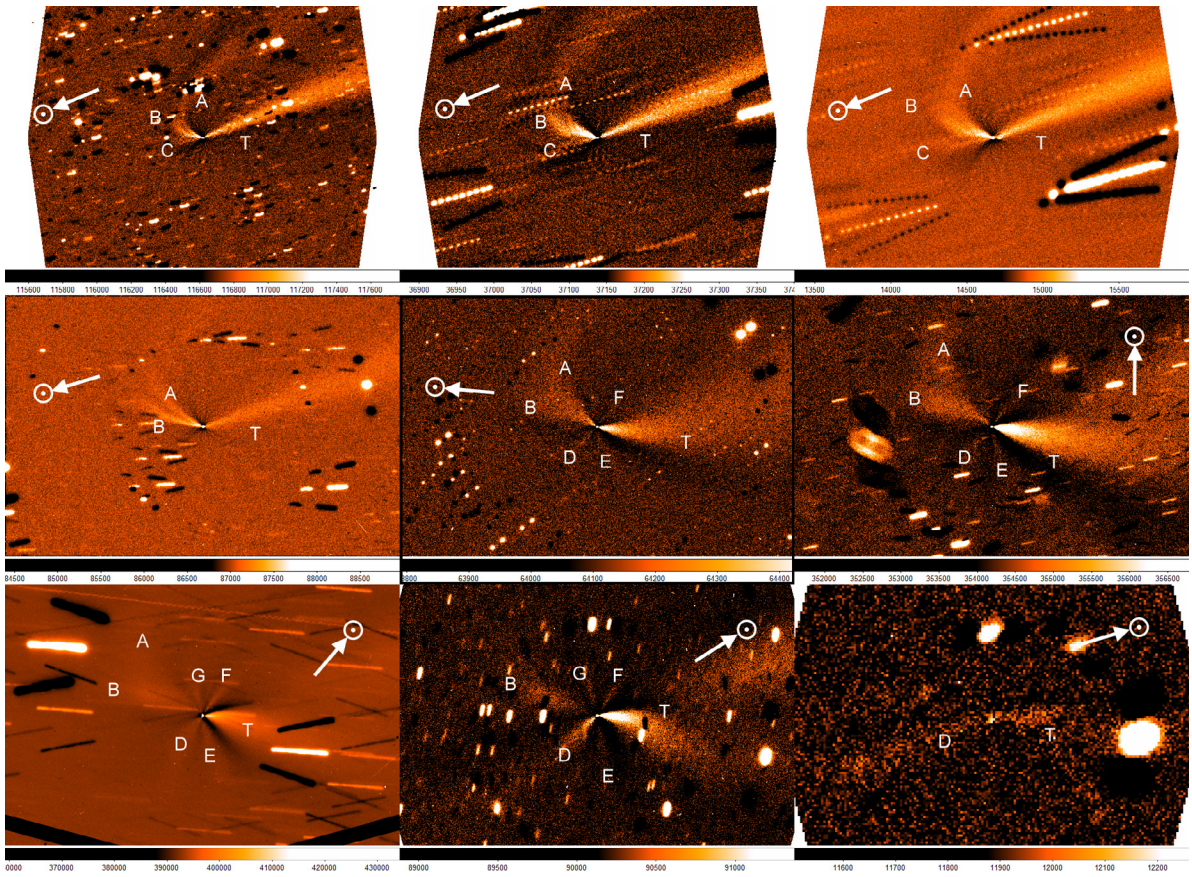

Fig. 5. Images after processing by the Larson-Sekanina algorithm taken on January 14, 17 and 18, (*top*, *from left to right*) February 26, April 7, 24 (*middle*, *from left to right*) May 4, May 20, August 1 (*bottom*, *from left to right*). In all images, north is up, east is to the left. The field of view is $5.85' \times 3.87'$. The arrow points in the solar projection direction. Structures are identified with capital letters, and T marks the position of the dust tail. All images were obtained with a broadband *R*-filter.

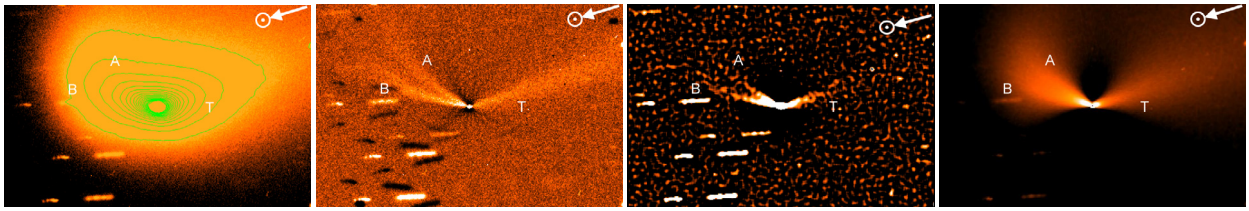

Fig. 6. Isophote of the original image, Larson-Sekanina filtered, adaptive-laplace filtered and divided by mean radial profile (*from left to right*) images of comet 81P/Wild2 displaying several coma structures on February 26, 2010. Structures are identified with capital letters, T marks the position of the dust tail. North is up, East is to the left., the field of view is $2.92' \times 1.94'$

Table 5. Position of structures in the dust coma in 2010.

Date	r_H (AU)	Δ (AU)	PsAng(°)	A(°)	B(°)	C(°)	D(°)	E(°)	F(°)	G(°)
Jan.-14	1.64	1.10	292.7	55	80	105	–	–	–	–
Jan.-15	1.64	1.09	292.6	55	80	105	–	–	–	–
Jan.-16	1.64	1.08	292.5	55	80	105	–	–	–	–
Jan.-17	1.63	1.07	292.5	55	80	105	–	–	–	–
Jan.-18	1.63	1.06	292.4	55	80	105	–	–	–	–
Feb.-26	1.59	0.78	286.8	55	80	–	–	–	–	–
Apr.-07	1.65	0.67	264.8	40	67	–	140	200	320	–
Apr.-24	1.70	0.70	180.5	40	67	–	140	200	328	–
May-04	1.74	0.74	139.2	43	69	–	140	200	320	8
May-20	1.80	0.85	122.2	–	65	–	130	200	328	8
May-31	1.85	0.95	117.8	–	–	–	130	–	–	–
Aug.-01	2.19	1.80	106.6	–	–	–	120	–	–	–

Notes. Identification of the coma structures as shown in Fig. 5. The given position angles refer to the center lines of the structures and may have a maximuma uncertainty of ±10°. North = 0°, East = +90°. PsAng is the position of the extended Sun-comet vector. The dash indicates that the structure was not detected.

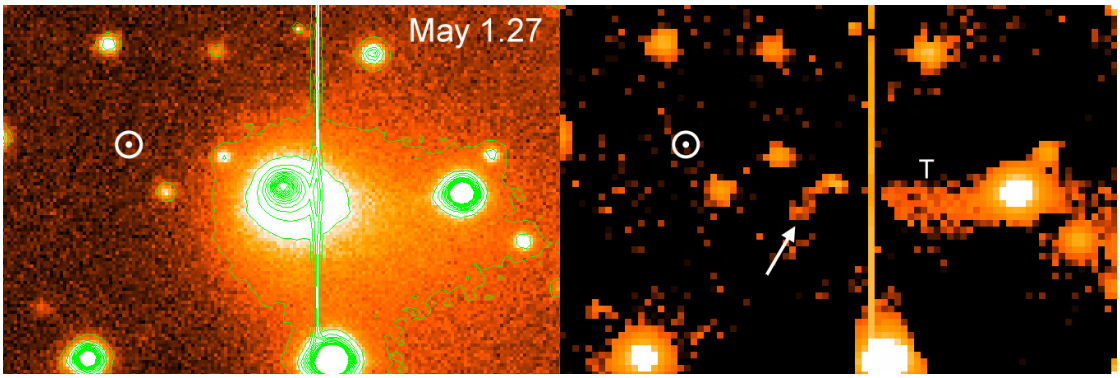

Fig. 7. *Left panel*: the isophote of the original image taken on May 1, 2004; *right panel*: same image after image processing by the Larson-Sekanina algorithm. To increase the signal-to-noise ratio, we used a binnned image in *the right panel*. Besides the dust tail, the jet feature was also detected. North is up, east is to the left. The field of view is $53'' \times 35''$.

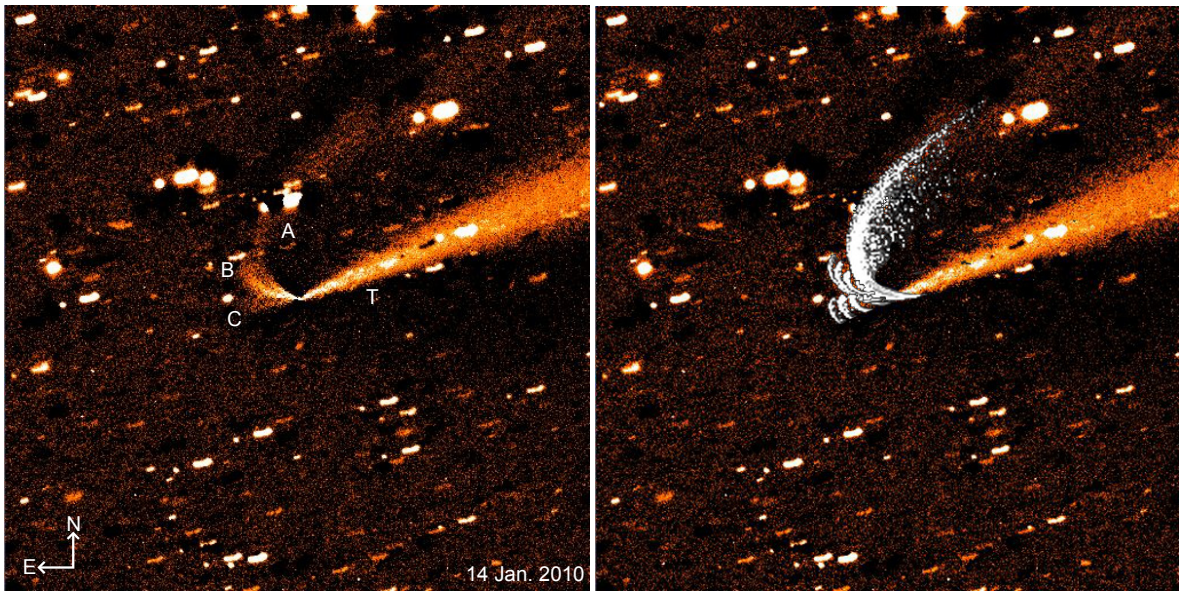

Fig. 8. *Left panel*: filtered image of comet 81P/Wild 2 showing the presence of dust coma structures on January 14, 2010; *right panel*: same image with simulated structures as a white overlay.

4.2. Modeling and interpretation

The fact that we detected several dust coma structures in 2010 does not come as a surprise; comet 81P/Wild 2 is known to be very active with many jets and active regions that were observed during its encounter with the spacecraft Stardust in January 2004 (Sekanina 2004). We aimed to investigate whether we were able to use our observations to localize the sources of activity at the surface of the nucleus, and determine whether there had been any changes with respect to what was observed in situ by Stardust six years ago. The analysis was made with the simulation code presented in Vincent et al. (2010), which creates images of dust jets emitted from discreet active regions at the surface of a three dimensional shape model of a cometary nucleus. We first used an ellipsoid to represent the nucleus, and then we refined the analysis by using a more complex model (Farnham et al. 2005). We did not infer the orientation of the spin axis from our images, but instead used the latest value of RA: 110±3° and Dec: −13±3° published by Duxbury et al. (2004).

Figure 8 shows an example of a simulation for an image acquired on January 14, 2010. In order to reproduce the coma structures, we needed three different active regions at latitudes of −30°, −10°, and +30°, emitting particles ranging in size from μm to a few tenths of μm. The activity is restrained to the equatorial region of the nucleus, and this result agrees with the localization of sources by Sekanina (2004) from the images obtained by Stardust. These three regions are active only during the day, any night-time activity during this epoch would produce different patterns than the observed ones. The switch-off of jet C after January 2010 is not connected to a change in illumination conditions at the surface, but could be explained for instance by the depletion in sublimating material in the associated active region. From April to the end of May 2010, many more dust structures were detected, and can be explained by the presence of new active regions in the same equatorial region.

5. Summary

The jet features of comet 81P/Wild 2 have been detected during the last two apparitions. The large Δ (~2 AU) and long perihelion distance (~2.5 AU) in 2004 might be the reason why we cannot detect any more jet features for this active comet. In addition, we observed the switch-off of jet C after January 2010. This phenomenon can be explained by the depletion of the sublimating material in the associated active region. Unfortunately, we did not have the Afρ variations in between these two months

because of the bad weather conditions in February. From April to the end of May 2010, many more dust structures were detected, and can be explained by the presence of new active regions in the same equatorial region.

We find that the dust brightness radial profile and dust production rate (Table 4) for January 14 are very distinct, with Afρ being higher in a factor of 1.5 compared to other days. Unfortunately, no observations are available before January 14, so we are unable to draw a conclusion about whether we witnessed an outburst or if there was some other earlier event. Aside from this date, as can be seen in the images taken at the Lulin observatory, the slopes lie between 0.98 and 1.38, with a range interval from 2000 km to 30 000 km, and are roughly consistent with a ρ^{-1} law. However, the gradient of the radial profile for the sunward direction in the outer region ($4.0 \leq \log \rho(\mathrm{km}) \leq 4.5$) is slightly steeper than that in the inner region ($3.3 \leq \log \rho(\mathrm{km}) \leq 4.0$). These steeper profiles could be caused by the effect of the radiation pressure, which acts on the dust when considering the longer cometocentric distance ρ.

The average color estimated from the imaging is very consistent with the results from former apparitions. In addition, the resulting log of the C_2-to-CN production rate ratio is -0.454 ± 0.13, from which is inferred Wild 2 belongs to the depleted class. The slope of the radial dependence of the gas production rates for CN (–2.58) and C_2 (–2.60) is very consistent with those from observations of many other Jupiter-family comets ($Q(\mathrm{gas}) \sim r_{\mathrm{H}}{}^{-2.7}$) if we ignore the 1978 data.

Acknowledgements. This work was based on observations obtained at Taiwan's Lulin Observatory. We thank the staff members and Lijing Huang for their assistances with the observations. A part of work is based on observations made with the European Southern Observatory telescopes obtained from the ESO/ST-ECF Science Archive Facility. The research was supported by project AyA2009-08011 of the Ministerio de Ciencia e Innovacin. Zhong Yi Lin acknowledges a post-doctoral grant awarded by the Junta de Andaluca through project number P07-TIC-274. This work was also supported by grant number NSC 99-2923-M-008-002-MY3 of the Formosa Program.

References

A'Hearn, M. F., Schleicher, D. G., Millis, R. L., Feldman, P. D., & Thompson, D. T. 1984, AJ, 89, 579
A'Hearn, M. F., Millis, R. L., Schleicher, D. G., Osip, D. J., & Birch, P. V. 1995, Icarus, 118, 223
Baum, W. A., Kreidl, T. J., & Schleicher, D. G. 1992, AJ, 104, 1216
Böhnhardt, H., & Birkle, K. 1994, A&A, 107, 101
Brownlee, D. E., Horz, F., Newburn, R. L., et al. 2004, Science, 304, 1764
Duxbury, T. C., Newburn, R. L., & Brownlee, D. E. 2004, JGR, 109
Farnham, T. L., & Schleicher, D. G. 2005, Icarus, 173, 533
Ferrin, I. 2007, Icarus, 191, 22
Fink, U., Hicks, M. P., & Fevig, R. A. 1999, Icarus, 141, 331
Fray, N., Bnilan, Y., Cottin, H., Gazeau, M.-C., & Crovisier, J. 2005, P&SS, 53, 1243
Jewitt, D. C., & Meech, K. J. 1987, ApJ, 317, 992
Hamuy, M., Walker, A. R., Suntzeff, N. B., et al. 1992, PASP, 104, 533
Haser, L. 1957, Bull. Soc. Roy. des Sci. Leige, 43, 740
Kurucz, R. L., Furenlid, I., Brault, J., & Testerman, L. 1984, N. S. O. Atlas No. 1
Lara, L. M., Schulz, R., Stüwe, J. A., & Tozzi, G. P. 2001, Icarus, 150, 124
Larson, S. M., & Sekanina, Z. 1984, AJ, 89, 571
Lin, Z. Y., Weiler, M., Rauer, H., & Ip, W. H. 2007, A&A, 469, 771
Lin, Z. Y., Lin, C. H., Ip, W. H., & Lara, L. M. 2009, AJ, 138, 625
Sekanina, Z. 1987, ESA SP-278, 315
Sekanina, Z. 2003, 108, SRD 2-1
Sekanina, Z., Brownlee, D. E., Economou, T. E., Tuzzolino, A. J., & Green, S. F. 2004, Science, 304, 1769
Schleicher, D. G. 2010, AJ, 140, 973
Schulz, R., Stüwe, J. A., Böhnhardt, H., Gaessler, W., & Tozzi, G. P. 2003, A&A, 398, 345
Soderblom, L. A., Boice, D. C., Britt, D. T., et al. 2004, Icarus, 167, 4
Yelle, R. V., Soderblom, L. A., & Jokipii, J. R. 2004, Icarus, 167, 30
Vincent, J.-B., Böhnhardt, H., & Lara, L.-M. 2010, A&A, 512, A60

Lightcurves of two Jupiter Trojan asteroids with long period M.D:Melita[1], F. dos Reis[1], F. Yoshida[2], S. Abe[3] and R.. Duffard[4], [1]IAFE (CONICET-UBA). Argentina, [2] NAOJ, Japan,[3]Lulin Observatory, Taiwan, [4]OSN and AA, Spain.

Introduction: We determined the light curves of two Jupiter Trojan asteroids, (16070) 1999 RB101 and (1867) Deiphobus. We synchronized over 9 nights of observations in total, made in telescopes of the Observatory of Sierra Nevada (Spain), Lulin (Taiwan) and Maidanak (Uzbekistan), to try to determine a curve that contains most of the phase of these objects. The reduction was performed using photometric Landolt standard stars. In cases where the standard reduction was not possible standard, we used field stars with values in the R filter contained in the catalog NOMAD1. For (16070) 1999 RB101 we found periods of 52.80hs or 26.40hs and for (1867) a value of 51.70hs, which does not exactly match the value given in the appearance 1994 (Mottola et al 2011). The amplitudes found were 0.3 and 0.4 mag respectively.

Methods: To calibrate the images we used the "Image Reduction and Analysis Facility" (IRAF). Usual calibration was performed with bias, dark (when present) and flat images. The photometry was performed using the tasks PHOT and DAOFIND from the DAOPHOT package, with a circular aperture that was set analyzing the profiles of objects for each night of observation. When standard photometry was not possible we used the average instrumental magnitude of 8 stars in the field and adding the average magnitude of the same catalog NOMAD(Naval Observatory Astrometric Dataset Mergered (see Table 2).

Once the time series was obtained, it was analyzed with methods for detecting periodicity in a series with data not equally spaced in time. We used a method that minimizes a givenentropy function, such as the Phase ispersion Minimization (Stelingwerf 1978) and method based on Fourier analysis such as the modified periodogram of Lomb - Scargle (Lomb 1976). Since our data have a significant dispersion, is the "smoothed" using a median filter with sliding window, thus high spurious periods were removed.

Results: The following section discusses the results for both objects. The figures below show our results with a sin plot with the corresponding period and amplitude.

(1867) Deiphobus: At the 1994, Mottolla et al. (2011) determined a period of 58.66hs and amplitude of 0.27 mag. We find that the period that best fits the data of each night is 51.7 hours with an amplitude of 0.4mag. Furthermore, this value of period corresponds approximately to twice the peak power of Lomb-Scargle periodogram and a minimum coefficient PDM, although this ratio appears to be very degenerate for values over 48 hours.

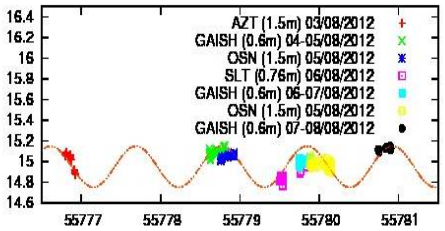

(16070) RB101: This is the first determination period for this object. The curve has peaks which are not symmetrical or amplitude or time. We found that the peak of the Lomb-Scargle periodogram suggests a period of two peaks of different heights of just over 26hs. If this proves a double peak structure of 1 single maximum, the period would then 52.80hs. 28hs a period of approximately corresponds to an overall minimum and has a coefficient PDM local mínimo around 52.80hs. In the light curve can be seen as the peak corresponding to the observations of AZT (1.5m) of 04/08/201 not be synchronized exactly with a period of 26.4hs, suggesting that the period is actually twice that value.

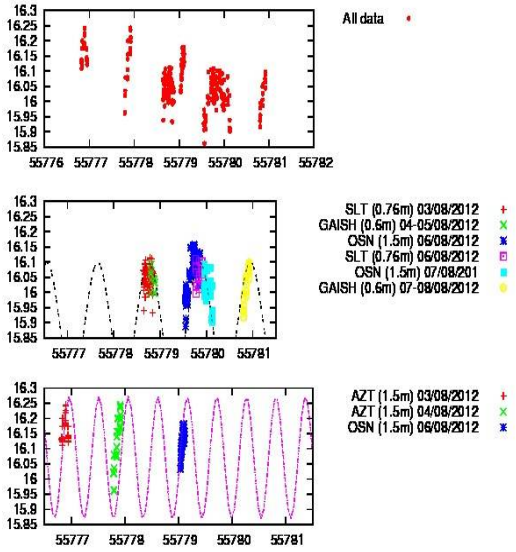

References:
Lomb, N.R., 1976 Ap&SS, 39, 447.
Mottola, S. et al. 2011 The Astronomical Journal. 141, 170.

The Astronomical Journal, 143:104 (16pp), 2012 May doi:10.1088/0004-6256/143/5/104

OBSERVATIONAL AND DYNAMICAL CHARACTERIZATION OF MAIN-BELT COMET P/2010 R2 (La Sagra)*

Henry H. Hsieh[1,19], Bin Yang[1], Nader Haghighipour[1], Bojan Novaković[2], Robert Jedicke[1], Richard J. Wainscoat[1], Larry Denneau[1], Shinsuke Abe[3], Wen-Ping Chen[3], Alan Fitzsimmons[4], Mikael Granvik[5], Tommy Grav[6], Wing Ip[3], Heather M. Kaluna[1], Daisuke Kinoshita[3], Jan Kleyna[1], Matthew M. Knight[7], Pedro Lacerda[4,20], Carey M. Lisse[8], Eric Maclennan[9], Karen J. Meech[1], Marco Micheli[1], Andrea Milani[10], Jana Pittichová[1], Eva Schunova[1,11], David J. Tholen[1], Lawrence H. Wasserman[7], William S. Burgett[1], K. C. Chambers[1], Jim N. Heasley[1], Nick Kaiser[1], Eugene A. Magnier[1], Jeffrey S. Morgan[1], Paul A. Price[12], Uffe G. Jørgensen[13,14], Martin Dominik[15,21], Tobias Hinse[16], Kailash Sahu[17], and Colin Snodgrass[18]

[1] Institute for Astronomy, University of Hawaii, 2680 Woodlawn Drive, Honolulu HI 96822, USA; hsieh@ifa.hawaii.edu
[2] Department of Astronomy, Faculty of Mathematics, University of Belgrade, Studentski trg 16, 11000 Belgrade, Serbia
[3] Institute of Astronomy, National Central University, 300 Jhongda Rd, Jhongli 32001, Taiwan
[4] Astronomy Research Centre, Queens University Belfast, Belfast BT7 1NN, United Kingdom
[5] Department of Physics, P.O. Box 64, 00014 University of Helsinki, Finland
[6] Department of Physics and Astronomy, Johns Hopkins University, 3400 North Charles Street, Baltimore, MD 21218, USA
[7] Lowell Observatory, 1400 West Mars Hill Road, Flagstaff, AZ 86001, USA
[8] Planetary Exploration Group, Space Department, Johns Hopkins University Applied Physics Laboratory, Laurel, MD 20723, USA
[9] Department of Physics and Astronomy, Northern Arizona University, 602 South Humphreys Street, Flagstaff, AZ 86011, USA
[10] Dipartimento di Matematica, Università di Pisa, Largo Pontecorvo 5, 56127 Pisa, Italy
[11] Department of Astronomy, Physics of the Earth and Meteorology, Comenius University, Mlynska dolina, 842 48 Bratislava, Slovakia
[12] Department of Astrophysical Sciences, Princeton University, Princeton, NJ 08544, USA
[13] Niels Bohr Institute, University of Copenhagen, Juliane Maries Vej 30, 2100 Copenhagen, Denmark
[14] Centre for Star and Planet Formation, Geological Museum, Øster Voldgade 5, 1350 Copenhagen, Denmark
[15] SUPA, University of St Andrews, School of Physics & Astronomy, North Haugh, St Andrews, KY16 9SS, United Kingdom
[16] Korea Astronomy & Space Science Institute (KASI), 776 Daedukdae-ro, Yuseong-gu, Daejeon, Republic of Korea
[17] Space Telescope Science Institute, 3700 San Martin Drive, Baltimore, MD 21218, USA
[18] Max-Planck-Institut für Sonnensystemforschung, 37191 Katlenburg-Lindau, Germany
Received 2011 September 26; accepted 2012 February 14; published 2012 March 20

ABSTRACT

We present observations of the recently discovered comet-like main-belt object P/2010 R2 (La Sagra) obtained by Pan-STARRS1 and the Faulkes Telescope-North on Haleakala in Hawaii, the University of Hawaii 2.2 m, Gemini-North, and Keck I telescopes on Mauna Kea, the Danish 1.54 m telescope (operated by the MiNDSTEp consortium) at La Silla, and the Isaac Newton Telescope on La Palma. An antisolar dust tail is observed to be present from 2010 August through 2011 February, while a dust trail aligned with the object's orbit plane is also observed from 2010 December through 2011 August. Assuming typical phase darkening behavior, P/La Sagra is seen to increase in brightness by >1 mag between 2010 August and December, suggesting that dust production is ongoing over this period. These results strongly suggest that the observed activity is cometary in nature (i.e., driven by the sublimation of volatile material), and that P/La Sagra is therefore the most recent main-belt comet to be discovered. We find an approximate absolute magnitude for the nucleus of $H_R = 17.9 \pm 0.2$ mag, corresponding to a nucleus radius of ~0.7 km, assuming an albedo of $p = 0.05$. Comparing the observed scattering surface areas of the dust coma to that of the nucleus when P/La Sagra was active, we find dust-to-nucleus area ratios of $A_d/A_N = 30$–60, comparable to those computed for fellow main-belt comets 238P/Read and P/2008 R1 (Garradd), and one to two orders of magnitude larger than for two other main-belt comets (133P/Elst-Pizarro and 176P/LINEAR). Using optical spectroscopy to search for CN emission, we do not detect any conclusive evidence of sublimation products (i.e., gas emission), finding an upper limit CN production rate of $Q_{\rm CN} < 6 \times 10^{23}$ mol s^{-1}, from which we infer an H_2O production rate of $Q_{\rm H_2O} < 10^{26}$ mol s^{-1}. Numerical simulations indicate that P/La Sagra is dynamically stable for >100 Myr, suggesting that it is likely native to its current location and that its composition is likely representative of other objects in the same region of the main belt, though the relatively close proximity of the 13:6 mean-motion resonance with Jupiter and the (3,−2,−1) three-body mean-motion resonance with Jupiter and Saturn mean that dynamical instability on larger timescales cannot be ruled out.

Key words: comets: general – comets: individual (P/2010 R2 (La Sagra)) – minor planets, asteroids: general

Online-only material: color figures

1. INTRODUCTION

Comet P/2010 R2 (La Sagra), hereafter P/La Sagra, was discovered by J. Nomen in images obtained on 2010 September 14.9 (UT) using the 0.45 m La Sagra Observatory in southern

* Some data presented herein were obtained at the Isaac Newton Group of telescopes on La Palma as part of Program I/2010B/P14, at the Gemini Observatory under program GN-2011B-Q-17, with the Danish 1.54 m telescope at the ESO La Silla Observatory, and at the W. M. Keck Observatory. The Keck Observatory is operated as a scientific partnership among the California Institute of Technology, the University of California, and the National Aeronautics and Space Administration, and was made possible by the generous financial support of the W. M. Keck Foundation.

[19] Hubble Fellow.
[20] Michael West Fellow.
[21] Royal Society University Research Fellow.

Table 1
Comet-like Main-belt Asteroids

Name	Type[a]	a[b]	e[c]	i[d]	T_J[e]	P[f]	H_R[g,h]	r_n[i]	$(A_d/A_N)_{max}$[j,h]	Discovery Date[k]
133P/Elst-Pizarro	MBC	3.160	0.162	1.386	3.184	5.62	15.49 ± 0.05 [1]	1.9	0.7 [8]	1996 Aug 7 [12]
238P/Read	MBC	3.165	0.253	1.266	3.153	5.63	19.05 ± 0.05 [2]	0.4	21 [2]	2005 Oct 24 [13]
176P/LINEAR	MBC	3.194	0.194	0.238	3.166	5.71	15.10 ± 0.05 [1]	2.0	0.3 [9]	2005 Nov 26 [14]
P/2008 R1 (Garradd)	MBC	2.726	0.342	15.903	3.217	4.50	20.3 ± 0.1 [3]	0.2	28 [3]	2008 Sep 2 [15]
P/2010 A2 (LINEAR)	DA	2.291	0.124	5.255	3.583	3.47	21.9 ± 0.1 [4]	0.06	...	2010 Jan 6 [16]
P/2010 R2 (La Sagra)	MBC	3.099	0.154	21.395	3.099	5.46	17.9 ± 0.2 [5]	0.7	60 [5]	2010 Sep 14 [17]
(596) Scheila	DA	2.928	0.165	14.661	3.209	5.01	8.54 [6]	56.67	2.2 [10]	2010 Dec 10 [18]
P/2006 VW_{139}	MBC	3.052	0.201	2.438	3.203	5.33	15.9 [7]	1.7	1.1 [11]	2011 Nov 05 [19]

Notes.
[a] Object classification as main-belt comet (MBC) or disrupted asteroid (DA).
[b] Osculating semimajor axis, in AU.
[c] Osculating eccentricity.
[d] Osculating inclination, in degrees.
[e] Tisserand parameter.
[f] Orbital period, in years.
[g] Absolute R-band magnitude of nucleus, assuming solar colors, in the IAU H, G system.
[h] **References.** [1] Hsieh et al. 2009a; [2] Hsieh et al. 2011c; [3] Maclennan & Hsieh 2012; [4] Jewitt et al. 2010; [5] This work; [6] Tedesco et al. 2004; [7] JPL Small Body Database (http://ssd.jpl.nasa.gov/sbdb.cgi); [8] Hsieh et al. 2010b; [9] Hsieh et al. 2011b; [10] Jewitt et al. 2011; [11] Hsieh et al. 2012b; [12] Elst et al. 1996; [13] Read et al. 2005; [14] Hsieh et al. 2006; [15] Garradd et al. 2008; [16] Birtwhistle et al. 2010; [17] Nomen et al. 2010; [18] Larson 2010; [19] Hsieh et al. 2011a.
[i] Estimated effective radius of nucleus, from same works referenced for H_R, in km.
[j] Peak observed dust-to-nucleus scattering surface area ratio.
[k] Discovery date of comet-like activity.

Spain (Nomen et al. 2010). With a semimajor axis of $a = 3.099$ AU, an eccentricity of $e = 0.154$, an inclination of $i = 21.^{\circ}39$, and a Tisserand parameter (with respect to Jupiter) of $T_J = 3.099$, it was immediately suspected to be a member of the recently identified class of main-belt comets (MBCs; Hsieh & Jewitt 2006), which are objects that exhibit cometary activity likely due to the sublimation of volatile ice, yet are dynamically indistinguishable from main-belt asteroids. Prior to the discovery of P/La Sagra, four MBCs – 133P/Elst-Pizarro, 176P/LINEAR, 238P/Read, and P/2008 R1 (Garradd) – were recognized, while a sixth possible MBC (P/2006 VW_{139}) has just recently been identified (Hsieh et al. 2011a). Two other comet-like main-belt objects—P/2010 A2 (LINEAR) and (596) Scheila—have also been observed, but as their comet-like morphologies are believed to be due to impact-generated ejecta clouds (Jewitt et al. 2010, 2011; Snodgrass et al. 2010; Bodewits et al. 2011; Yang & Hsieh 2011; Hainaut et al. 2012), and not cometary (i.e., sublimation-driven) dust emission, they are better characterized as disrupted asteroids. Orbital elements for the currently known MBCs and disrupted asteroids are listed in Table 1, and also plotted in Figure 1.

Observationally distinguishing MBCs and disrupted asteroids is not straightforward as both types of objects exhibit visible dust emission in the form of comet-like features like comae and tails. Distinctive morphological features helped betray the true natures of P/2010 A2 and Scheila, however (Hsieh et al. 2012a and references within). In the case of P/2010 A2, a gap between what appeared to be the nucleus of the "comet" and the dust tail indicated that the observed dust emission was possibly an impulsively generated ejecta cloud that was produced by an impact onto P/2010 A2's surface and was then drifting away. This hypothesis was later corroborated by numerical dust modeling and other physical arguments (Jewitt et al. 2010; Snodgrass et al. 2010). In the case of Scheila, no gap was seen between the nucleus and its emitted dust, but instead of forming a single tail, the dust emitted from Scheila appeared to form multiple plumes. Hsieh et al. (2012a) considered various scenarios that could produce multiple dust plumes, finding scenarios for sublimation-driven dust emission to be physically implausible as they required multiple active sites, which were argued to be unlikely on Scheila. Instead, a simpler scenario in which a single oblique impact caused dust emission in the form of a hollow cone which was then pushed back in the antisolar direction by radiation pressure was favored (Ishiguro et al. 2011a, 2011b). In this scenario, what appeared to be multiple plumes of dust were proposed to simply be optical projection effects (i.e., limb brightening of the hollow dust structure).

Early observation reports for P/La Sagra indicated that it exhibited a largely classical cometary morphology, with a visible coma and tail (Nomen et al. 2010), suggesting that it could be a true comet (Hsieh et al. 2012a), and was therefore likely to be just the fifth MBC to be discovered at that time. Numerical modeling by Moreno et al. (2011) furthermore showed that the evolution of P/La Sagra's dust tail was consistent with sublimation-driven dust emission, though they did not explicitly test impulsive impact-driven emission scenarios. In this paper, we seek to further assess whether P/La Sagra's dust emission is likely to be cometary (sublimation-driven) in nature, or if the object could instead be a disrupted asteroid. We also conduct observational and dynamical characterization analyses of the object to place it in the context of the small but growing known population of comet-like objects in the main asteroid belt.

2. OBSERVATIONS

Imaging observations of P/La Sagra were made in photometric conditions on multiple occasions in 2010 and 2011 (Table 2; Figure 2) by the 2.0 m Faulkes Telescope North (FTN) on Haleakala in Hawaii, the University of Hawaii (UH) 2.2 m telescope, the 8 m Gemini-North Observatory, and the 10 m Keck I telescope, all on Mauna Kea in Hawaii, the 1.54 m Danish telescope at La Silla Observatory in Chile, and the 2.5 m Isaac Newton Telescope (INT) at the Roque de los

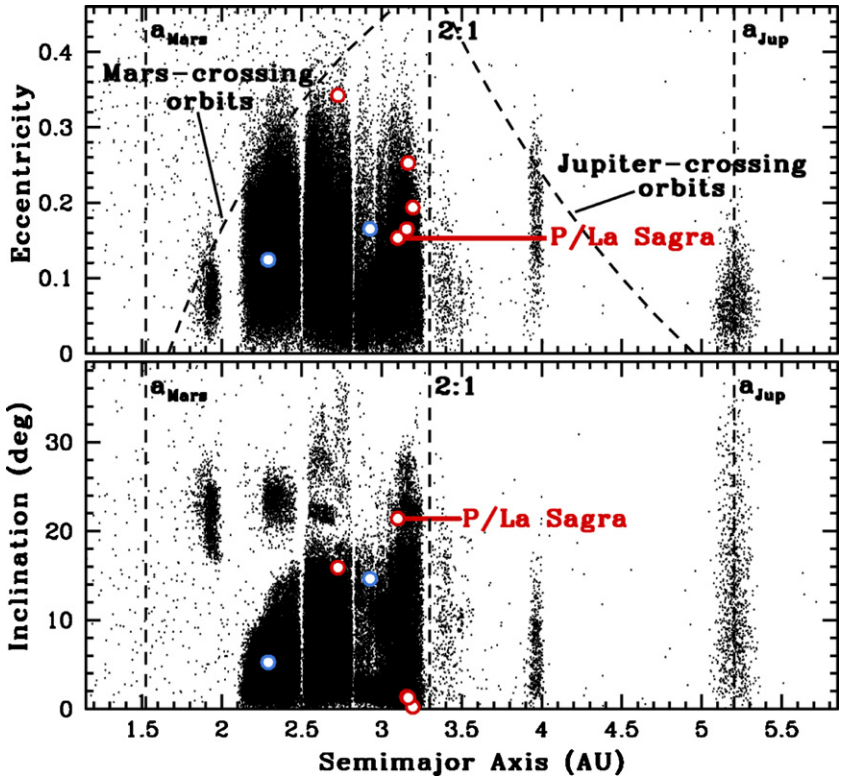

Figure 1. Plots of eccentricity (upper panel) and inclination (lower panel) vs. semimajor axis showing the distributions in orbital element space of main-belt asteroids (black dots), MBCs (red circles), and likely disrupted asteroids (blue circles). Also marked with dotted lines are the semimajor axes of Mars ($a_{\rm Mars}$) and Jupiter ($a_{\rm Jup}$), the semimajor axis of the 2:1 mean-motion resonance with Jupiter, and the loci of Mars-crossing orbits and Jupiter-crossing orbits.

(A color version of this figure is available in the online journal.)

Muchachos Observatory on La Palma in the Canary Islands (Spain). In addition, precovery observations of P/La Sagra were also obtained with the 1.8 m Pan-STARRS1 (PS1) survey telescope on Haleakala. To ensure proper calibration of PS1 data, we also obtained calibration observations using the Lowell Observatory 31″ telescope in Flagstaff, Arizona.

PS1 is a wide-field synoptic survey telescope that employs a 1.4 gigapixel camera consisting of a mosaic of 60 orthogonal transfer arrays (OTAs), each consisting of 64 590 × 598 pixel CCDs, giving a total field of view 3.2 deg in diameter (image scale of 0.″26 pixel^{-1}). PS1 observations were made using a Sloan Digital Sky Survey (SDSS) r'-band-like filter designated $r_{\rm P1}$ (Stubbs et al. 2010). Gemini observations (obtained as part of program GN-2011B-Q-17) were made using the Gemini Multi-Object Spectrograph (GMOS; Hook et al. 2004) in imaging mode. GMOS employs three 2048 × 2048 EEV CCDs behind a SDSS-like r'-band filter, and has an image scale of 0.″1456 pixel^{-1} when using 2 × 2 binning as we did for our observations of P/La Sagra. Keck observations were made using the Low Resolution Imaging Spectrometer (LRIS; Oke et al. 1995) in both imaging and spectroscopic mode. LRIS employs a Tektronix 2048 × 2048 CCD with an image scale of 0.″135 pixel^{-1} and standard Kron–Cousins B-band and R-band filters. The Danish 1.54 m telescope is currently exclusively used by the Microlensing Network for the Detection of Small Terrestrial Exoplanets (MiNDSTEp) consortium. Observations on the Danish 1.54 m were made using the Danish Faint Object Spectrograph and Camera (DFOSC) focal-reducing imager behind a standard Kron–Cousins R-band filter. The DFOSC imager has pixel dimensions of 2102 × 2102 and a pixel scale of 0.″39 pixel^{-1}. FTN observations were made using a 1024 × 1024 e2v CCD with an image scale of 0.″2785 pixel^{-1} behind a Bessell R-band filter.

Except for observations with PS1, FTN, and the INT, all other observations were conducted using non-sidereal tracking at the apparent rate and direction of motion of P/La Sagra on the sky. Sidereal tracking was used by PS1 because this was the standard mode of operation for survey operations. FTN observations were obtained using its web-based remote control interface, through which non-sidereal tracking is not possible. The INT is normally capable of tracking solar system objects non-sidereally, but was unable to do so during our observing run due to mechanical problems.

We performed standard image preparation (bias subtraction and flat-field reduction) for UH 2.2 m, Gemini, Keck, Danish 1.54 m, and INT data using Image Reduction and Analysis Facility (IRAF) software. For Keck data, flat fields were constructed from images of the illuminated interior of the Keck I dome, while for the other telescopes, dithered images of the twilight sky were used to construct flat fields. PS1 data were reduced using the system's Image Processing Pipeline (IPP; Magnier 2006) and then calibrated using field stars imaged later by the Lowell 31″ telescope. Calibration of Gemini data was performed using field star magnitudes provided by the SDSS (York et al. 2000). Photometry of Landolt (1992) standard stars and field stars was performed for all data using IRAF and obtained by measuring net fluxes within circular apertures, with background sampled from surrounding circular annuli. Conversion of magnitudes measured from PS1 and Gemini data obtained using SDSS-like r'-band filters to their Kron–Cousins R-band equivalents was accomplished using the transformation equations derived by R. Lupton and made available on the SDSS Web site

Table 2
Observation Log

UT Date	Telescope[a]	Moon[b]	Seeing[c]	N[d]	t[e]	Filter	R[f]	Δ[g]	α[h]	ν[i]	P.A.$_{-\odot}$[j]	P.A.$_{-v}$[k]	α_{pl}[l]
2010 Jun 26	*Perihelion*	...	...	...	...	...	2.623	2.228	22.3	0.0	241.2	242.8	−0.5
2010 Aug 16	PS1	N+6	1.0	2	80	r'	2.631	1.793	15.0	12.9	203.3	243.7	−9.4
2010 Sep 8	PS1	N	0.9	1	40	r'	2.641	1.739	12.0	18.5	162.1	241.1	−11.7
2010 Sep 19 (1)	Dk1.54	N+11	1.4	20	2400	R	2.649	1.756	12.3	21.3	138.8	239.7	−12.0
2010 Sep 19 (2)	UH2.2	N+11	1.6	5	1500	R	2.649	1.756	12.3	21.3	138.0	239.7	−12.0
2010 Sep 29	FTN	N−9	1.5	3	450	R	2.652	1.790	13.4	23.7	119.9	238.7	−11.7
2010 Oct 5	Keck	N−2	0.9	2	240	BR	2.659	1.824	14.4	25.2	110.7	238.2	−11.3
2010 Oct 5	Keck	N−2	0.9	4	3600	Spec.	2.659	1.824	14.4	25.2	110.7	238.2	−11.3
2010 Oct 19	UH2.2	N+11	1.1	3	900	R	2.666	1.922	16.8	28.5	94.5	237.7	−9.8
2010 Nov 26	UH2.2	N−9	1.8	6	1800	R	2.698	2.343	21.1	37.8	71.3	239.6	−4.0
2010 Dec 12	UH2.2	N+6	0.8	21	6300	R	2.713	2.535	21.3	41.3	65.7	241.4	−1.5
2011 Dec 31	INT	N−3	1.1	4	1200	R	2.733	2.793	20.5	45.9	60.5	243.9	1.2
2011 Feb 3	Keck	N	0.8	2	360	BR	2.772	3.210	17.0	53.5	53.4	248.7	4.4
2011 Aug 26	Keck	N−3	1.0	4	1200	BR	3.066	3.289	17.9	95.1	270.9	291.6	−5.7
2011 Aug 31	Gemini	N+2	0.8	6	1800	r'	3.073	3.231	18.2	96.0	270.8	292.5	−6.0
2013 Mar 13	*Aphelion*	...	...	...	...	...	3.570	2.758	10.5	180.0	76.6	302.8	7.5
2015 Nov 30	*Perihelion*	...	...	...	...	...	2.620	2.946	19.3	0.0	67.0	238.0	−2.8

Notes.
[a] Telescope used (PS1: 1.8 m Pan-STARRS1 telescope; Dk1.54: Danish 1.54 m telescope; FTN: 2.0 m Faulkes Telescope North; Gemini: 8 m Gemini-North telescope; Keck: Keck I 10 m telescope; UH2.2: University of Hawaii 2.2 m telescope; INT: 2.5 m Isaac Newton Telescope)
[b] Phase of moon expressed in offset from new moon ("N") in days.
[c] Approximate average seeing (FWHM) in arcsec.
[d] Number of images.
[e] Total effective exposure time in seconds.
[f] Heliocentric distance in AU.
[g] Geocentric distance in AU.
[h] Solar phase angle (Sun–P/La Sagra–Earth) in degrees.
[i] True anomaly in degrees.
[j] Position angle of the antisolar vector, as projected in the plane of the sky, in degrees east of north.
[k] Position angle of the negative velocity vector, as projected in the plane of the sky, in degrees east of north.
[l] Orbit-plane angle (between observer and object orbit plane as seen from object) in degrees.

(http://www.sdss.org/). Comet photometry was performed using both rectangular and circular apertures as described below, where to avoid dust contamination from the comet itself, background sky statistics are measured manually in regions of blank sky near, but not adjacent, to the object. Several (5–10) field stars in the comet images were also measured to correct for any extinction variation (typically negligible) during each night.

In addition to imaging observations, we also secured optical spectra of P/La Sagra on 2010 October 5 with LRIS on Keck. We adopted LRIS's 1.″0-wide long-slit mask, the 400/3400 grism, and the 460 dichroic on the blue side, giving a dispersion of 1.08 Å pixel^{-1} and a spectral resolution of approximately 7 Å. A total of 3600 s of data were obtained from four integrations on the comet while it was at an air mass of ∼1.1. Unfortunately, when taking calibration images, our observations were interrupted due to fog and we were forced to close the dome for over three hours. As such, we were only able to record a spectrum of a flux standard star and failed to obtain any spectra of nearby G-type standard stars, complicating our reduction and analysis (Section 3.3.1). Data reduction was accomplished using IRAF.

3. RESULTS AND ANALYSIS

3.1. Morphological Analysis

For each night during which observations were obtained, we construct composite images by aligning each night's set of images on the object's photocenter and adding them together. We see that P/La Sagra is clearly morphologically cometary between 2010 August and 2011 February (Figure 2), with a dust tail extending up to ∼30″ (∼4 × 10^4 km at the geocentric distance of the object at the time) from the nucleus's photocenter. The projected orientation of this dust tail on the plane of the sky is seen to rotate counterclockwise throughout this period, lagging slightly behind the similarly rotating antisolar vector (as projected on the sky). From 2010 August through 2010 November, we observe a single dust tail aligned with the projection of the antisolar vector in the sky, while between 2010 December and 2011 February, an apparent dust trail aligned with the projection of the heliocentric velocity vector (i.e., the plane of the object's orbit) appears in addition to the antisolar dust tail. By 2011 August (Figure 3), active dust emission appears to have ceased, though a residual dust trail (presumably consisting of large dust particles ejected during earlier activity) aligned with the projection of the object's heliocentric velocity vector in the sky is observed extending at least ∼1 arcmin (∼1.5 × 10^5 km at the geocentric distance of the object at the time) from the nucleus. This dust trail peaks in brightness well away (∼20″) from the nucleus.

In the formulation of dust dynamics outlined by Finson & Probstein (1968), the trajectory of an emitted dust particle depends on the orbit of the emitting comet, the particle's ejection time, its ejection velocity, and the ratio, β, of solar radiation pressure, F_{rad}, to solar gravity, F_{grav}, on the particle. In cases where β is small (i.e., for massive particles), radiation pressure is negligible, causing particles to follow orbits very close to that of the comet. Over time, these large grains will spread out along the comet's orbit to form a potentially observable trail.

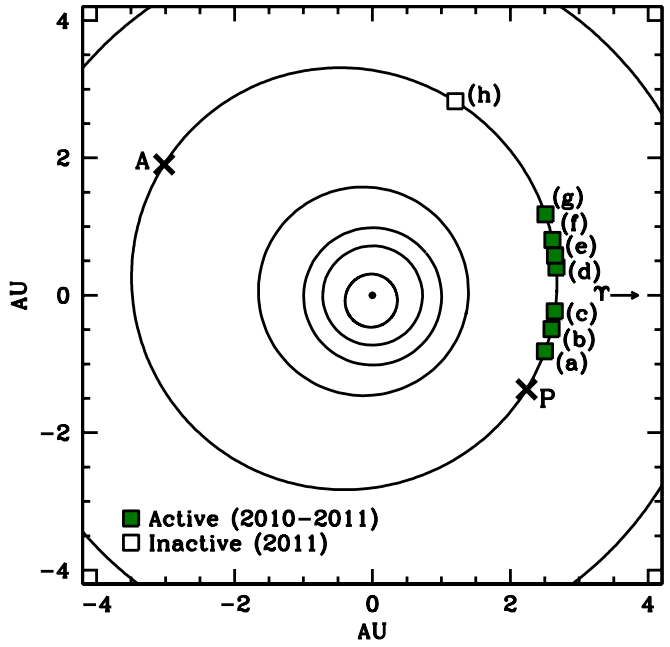

Figure 2. Orbital position plot of P/La Sagra observations detailed in Table 2. The Sun is shown at the center as a solid dot, with the orbits of Mercury, Venus, Earth, Mars, P/La Sagra, and Jupiter (from the center of the plot outward) shown as black lines. Solid squares mark positions where P/La Sagra was observed to be active in 2010 and early 2011, while an open square marks the position where P/La Sagra was observed to be inactive in 2011 August. Perihelion (P) and aphelion (A) positions are marked with crosses. Observations plotted were obtained on (a) 2010 August 16, (b) 2010 September 8–19, (c) 2010 October 5, (d) 2010 November 25–28, (e) 2010 December 12, (f) 2010 December 31, (g) 2011 February 3, and (h) 2011 August 26–31.

(A color version of this figure is available in the online journal.)

In cases where β is large (i.e., for small particles), radiation pressure is dominant over solar gravity, giving particles nearly directly antisolar motion in the rest frame of the comet. In the case of P/La Sagra, we observe both limiting cases: a tail consistently oriented in the antisolar direction (likely composed of small, high-β particles) from 2010 August through 2011 February (Figure 2), and a trail confined to the orbit plane (likely composed of large, low-β particles) from 2010 December through 2011 August (Figures 2 and 3). This assessment is in agreement with the modeling results obtained by Moreno et al. (2011) who found dust grain sizes ranging from $\sim$5 μm to $\sim$1 cm. Similar dust structures comprising widely varying particle sizes have also been observed for comets 2P/Encke (Reach et al. 2000; Lisse et al. 2004) and C/Austin 1990 V (Lisse et al. 1998).

Due to the ease by which they are accelerated by radiation pressure, the small particles comprising an antisolar tail are expected to dissipate quickly (on timescales of several weeks at the distance of the main belt; see Hsieh et al. 2004) unless they are continually replenished. No such separation of the antisolar tail from the nucleus is observed at any time from 2010 August through 2011 February, a span of 5.5 months, strongly suggesting that continuous dust production was ongoing over this time period, consistent with cometary activity. We note that the persistence of the orbit-aligned dust trail until 2011 August does not mean that dust production continued up until this time as well. In this latter case, the longevity of the dust trail is instead likely due to the large sizes, and therefore slow dissipation rates, of the particles in the trail (see P/2010 A2; Jewitt et al. 2010; Snodgrass et al. 2010), not continuous replenishment.

Qualitatively, we find that P/La Sagra's morphological appearance and evolution strongly suggest that its dust emission is cometary in nature. We caution however that more detailed dust modeling (similar that performed by Moreno et al. 2011, but also considering impulsive emission scenarios) will be required for quantitative confirmation of the conclusions reached here.

3.2. Photometric Analysis

3.2.1. Nucleus Size, Shape, and Color

Vigorous activity, such as that exhibited by P/La Sagra during the majority of our 2010 and 2011 observations, normally interferes with the measurement of physical properties for cometary nuclei (e.g., size, rotation period, and phase darkening behavior) due to obscuration caused by coma when such activity is present. As such, in order to accurately measure the physical properties of comet nuclei, it is typically necessary to observe them once activity has mostly or entirely ceased, as we did with P/La Sagra in 2011 August using the Keck I and Gemini telescopes (Table 2). We measure a mean apparent R-band magnitude (averaged in flux space and weighted by nominal uncertainties) of $m = 23.9 \pm 0.1$ mag, with a magnitude variation between the two nights of $\Delta m = 0.7 \pm 0.1$ mag ($m_{\rm avg} = 24.1 \pm 0.1$ mag on 2011 August 26, and $m_{\rm avg} = 23.4 \pm 0.1$ mag on 2011 August 31). Provided that the photometric variation between these two nights is real (intranight variations are on the order of $\sim$0.2 mag, with observations on each night only spanning 30 min or less) and due to rotation, the minimum ratio of the axes of the body as projected in the plane of the sky is then given by

$$a_N/b_N = 10^{0.4\Delta m} \quad (1)$$

giving us a lower limit (due to unknown projection effects) to the axis ratio for P/La Sagra of $a_N/b_N = 1.9 \pm 0.3$. Given the extremely limited data set on which this calculation is based, this axis ratio should of course be considered as a preliminary result only. Better constraints on the shape and structure of the nucleus of P/La Sagra will require additional observational sampling of the object's light curve (likely requiring large telescopes, given the small size of the object), ideally at multiple observing geometries.

Using the range of slope parameter (G) values in the IAU H, G photometric system computed for fellow MBCs 133P, 176P, 238P, and P/Garradd ($-0.03 < G_R < 0.26$; Hsieh et al. 2009a, 2011c; Maclennan & Hsieh 2012), we find an estimated absolute magnitude of $H_R = 17.9 \pm 0.2$ mag, consistent with the size estimate made by Bauer et al. (2012). Adopting a R-band albedo of $p_R = 0.05$ (as measured for 133P and 176P; Hsieh et al. 2009a), we then find an approximate effective nucleus radius of $r_N = 0.7 \pm 0.1$ km, making it comparable in size to 238P, about three times larger than P/Garradd, and about three times smaller than 133P and 176P (Table 1). Using the approximate axis ratio derived above and assuming a triaxial ellipsoidal shape, we find semimajor and semiminor axes for the nucleus of $a_N = 1.0$ km and $b_N = 0.5$ km, respectively.

We note that photometric variations on the scale of $\Delta m = 0.7$ mag were not seen at any time while P/La Sagra was active (2010 August through 2011 February) for any observations that were comparably closely spaced in time as the 2011 August observations analyzed above. For example, observations on four separate occasions between 2010 September 8 and 29 exhibited a maximum variation of just $\sim$0.1 mag (Table 3). This lack of corroborating detections of significant photometric variation during that period does not invalidate our detection

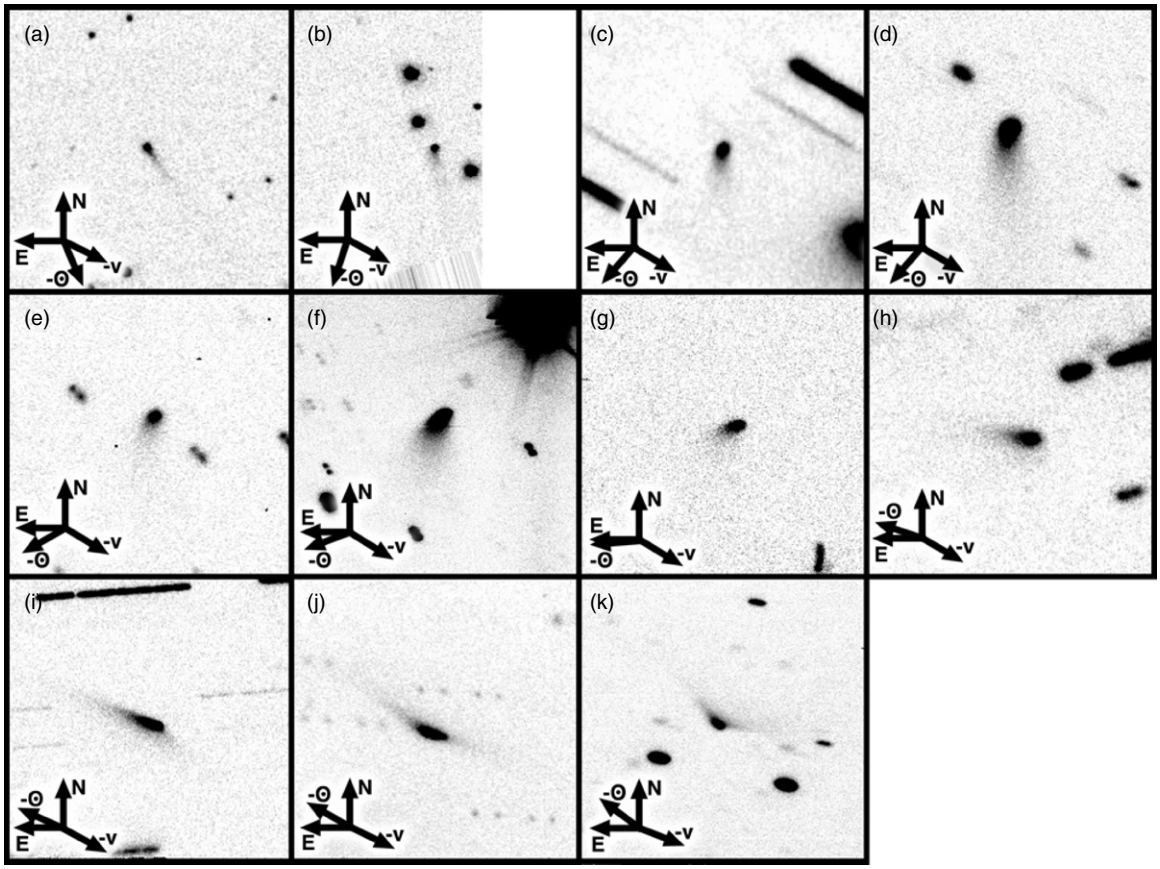

Figure 3. Composite images of P/La Sagra (at the center of each panel) constructed from data obtained on (a) 2010 August 16 (80 s of effective exposure time on PS1 in r'-band), (b) 2010 September 8 (40 s on PS1 in r'-band), (c) 2010 September 19 (2400 s on the Danish 1.54 m in R-band), (d) 2010 September 19 (1500 s on the UH 2.2 m in R-band), (e) 2010 September 29 (450 s on FTN in R-band), (f) 2010 October 5 (240 s on Keck I in R-band), (g) 2010 October 19 (900 s on the UH 2.2 m in R-band), (h) 2010 November 26 (1800 s on the UH 2.2 m in R-band), (i) 2010 December 12 (5400 s on the UH 2.2 m in R-band), (j) 2010 December 31 (1200 s on the INT in R-band), and (k) 2011 February 3 (360 s on Keck I in R-band). All panels are $60'' \times 60''$ in size with north (N), east (E), the antisolar direction ($-\odot$), and the negative heliocentric velocity vector ($-v$), as projected on the sky, marked.

Table 3
Photometry Results

UT Date	$m_{\rm avg}$[a]	$m_{\rm avg}(1,1,0)$[b]	$m_{\rm tot}$[c]	$m_{\rm tot}(1,1,0)$[d]	A_d/A_N[e]	A_d[f]	M_d[g]	$Af\rho$[h]
2010 Aug 16	18.49 ± 0.05	14.25 ± 0.15	18.3 ± 0.1	14.0 ± 0.2	30 ± 10	40 ± 15	7 ± 2	42 ± 6
2010 Sep 8	18.26 ± 0.05	14.20 ± 0.15	18.0 ± 0.1	13.9 ± 0.2	30 ± 10	45 ± 15	7 ± 2	45 ± 6
2010 Sep 19 (1)	18.28 ± 0.02	14.15 ± 0.15	17.9 ± 0.1	13.8 ± 0.2	30 ± 10	45 ± 15	8 ± 2	46 ± 6
2010 Sep 19 (2)	18.23 ± 0.02	14.10 ± 0.15	17.8 ± 0.1	13.7 ± 0.2	30 ± 10	45 ± 15	8 ± 2	48 ± 6
2010 Sep 29	18.39 ± 0.02	14.19 ± 0.15	18.0 ± 0.1	13.8 ± 0.2	30 ± 10	45 ± 15	8 ± 2	44 ± 6
2010 Oct 5	18.34 ± 0.03	14.05 ± 0.20	18.0 ± 0.1	13.7 ± 0.2	35 ± 10	50 ± 20	8 ± 3	49 ± 7
2010 Oct 19	18.47 ± 0.03	13.97 ± 0.20	18.1 ± 0.1	13.6 ± 0.2	35 ± 10	55 ± 20	9 ± 3	50 ± 8
2010 Nov 26	18.89 ± 0.03	13.80 ± 0.20	18.4 ± 0.1	13.3 ± 0.2	45 ± 15	65 ± 20	11 ± 4	49 ± 9
2010 Dec 12	18.78 ± 0.02	13.50 ± 0.20	18.4 ± 0.1	13.1 ± 0.2	60 ± 20	85 ± 30	14 ± 5	60 ± 11
2010 Dec 31	18.93 ± 0.04	13.45 ± 0.20	18.2 ± 0.2	12.7 ± 0.2	60 ± 20	85 ± 30	15 ± 5	57 ± 10[i]
2011 Feb 3	19.53 ± 0.08	13.85 ± 0.20	19.1 ± 0.1	13.4 ± 0.2	40 ± 10	60 ± 20	10 ± 3	34 ± 6
2011 Aug 26	24.1 ± 0.1	18.1 ± 0.3	...	...	...	...	...	0.7 ± 0.1
2011 Aug 31	23.4 ± 0.1	17.4 ± 0.3	...	...	...	...	...	1.2 ± 0.2

Notes.
[a] Mean apparent magnitude inside a $5''.0$ photometry aperture.
[b] Mean magnitude, normalized to $R = \Delta = 1$ AU and $\alpha = 0°$, assuming $-0.03 < G_R < 0.26$.
[c] Total apparent magnitude inside rectangular aperture enclosing entire comet (nucleus and dust tail).
[d] Total magnitude, normalized to $R = \Delta = 1$ AU and $\alpha = 0°$, assuming $-0.03 < G_R < 0.26$.
[e] Inferred ratio of scattering surface area of dust to nucleus scattering surface area.
[f] Inferred scattering surface area of dust, in 10^6 m^2, using $r_N = 0.6$ km.
[g] Estimated dust mass, in 10^5 kg, assuming 10 μm radius grains and $\rho = 1300$ kg m^{-3}.
[h] Dust contribution (computed using a $5''.0$ photometry aperture), as parameterized by A'Hearn et al. (1984), in cm.
[i] Computed from data in which comet was trailed by $4''.1$, and as such, represents a lower limit.

of a $\Delta m = 0.7$ mag variation in 2011 August, however, since rotational variations for a nucleus obscured by a steady-state coma (assumed to be optically thin) will be effectively damped by that coma. The extent of this damping can be determined using

$$\Delta m_{\rm obs} = 2.5 \log \frac{F_{\rm obs,\,max}}{F_{\rm obs,\,min}} = 2.5 \log \left(\frac{F_{N,\,\rm max} + F_d}{F_{N,\,\rm min} + F_d} \right), \quad (2)$$

where $\Delta m_{\rm obs}$ is the observed photometric range, $F_{\rm obs,\,max}$ and $F_{\rm obs,\,min}$ are the maximum and minimum fluxes observed for the active comet, $F_{N,\,\rm max}$ and $F_{N,\,\rm min}$ are the maximum and minimum fluxes for which the nucleus is responsible, and the flux due to dust, F_d, is assumed to be constant (Hsieh et al. 2011b).

Assuming that the nucleus and dust grains have similar albedos, flux terms in Equation (2) can be considered equivalent to the corresponding scattering surface areas of the comet components being considered. We find in the following section (Section 3.2.2) that the ratio of scattering surface areas of dust and the nucleus during the four September observations discussed above was $A_d/A_N \sim 30$ (Table 3). Thus, using $A_{N,\,\rm max} = \pi a_N r_N$, $A_{N,\,\rm min} = \pi b_N r_N$, and $A_d = \pi r_N^2$, we find $\Delta m_{\rm obs} = 0.025$ mag. In other words, during this period, even the minor ~0.1 mag photometric variation we observed for the object is unlikely to be due to the rotation of the nucleus. Instead, we surmise that the observed variation is more likely due to fluctuations in the seeing conditions between the different nights, causing fluctuations in the amount of coma contained within the fixed 5″.0 photometry apertures we used to measure the near-nucleus flux of the comet in all of our images. We also conclude that our non-detection of significant photometric variations in data obtained when P/La Sagra was active is not inconsistent with our apparent detection of a significant photometric variation while the object was inactive.

Multi-filter observations using LRIS on Keck I also permitted us to measure a $B - R = 0.9 \pm 0.1$ mag color for P/La Sagra's inactive nucleus, which within our uncertainties, is consistent with the color of the Sun ($B - R = 1.03$ mag; Hartmann et al. 1982, 1990). The colors we measure for P/La Sagra's dust coma while it was active are also approximately solar ($B - R = 1.02 \pm 0.05$ mag on 2010 October 5 and $B - R = 0.94 \pm 0.05$ mag on 2011 February 3), in good agreement with colors measured for the other MBCs (Jewitt et al. 2009; Hsieh et al. 2009b, 2010b, 2011b).

3.2.2. Activity Strength

Using the nucleus size computed above in Section 3.2.1, the expected apparent nucleus magnitude for P/La Sagra at the time of our first observations in 2010 August is $m_R = 22.2$ mag, not $m_R = 18.49$ mag as measured (Table 3). This discrepancy indicates that there was significant near-nucleus dust contamination even during our earliest observations of P/La Sagra. Assuming that the phase behavior of P/La Sagra's dust coma is similar to that of the nuclei of other MBCs whose phase functions have been measured (see Section 3.2.1; since we lack other meaningful constraints), we calculate the comet's corresponding absolute magnitudes, $m_{\rm tot}(1, 1, 0)$, at heliocentric and geocentric distances of $R = \Delta = 1$ AU and phase angles of $\alpha = 0°$ for each set of photometric measurements (using photometry apertures with radii of 5″.0) of the nucleus (Table 3). By comparing these absolute magnitudes to our estimated absolute magnitude for the nucleus, we then compute the ratio of the scattering surface area of dust in the coma, A_d, to that of the nucleus, A_N, using

$$\frac{A_d}{A_N} = \frac{1 - 10^{0.4(m_{\rm tot}(1,1,0) - H_R)}}{10^{0.4(m_{\rm tot}(1,1,0) - H_R)}}. \quad (3)$$

Then, assuming $A_N \sim \pi r_N^2$ and $a = 10$ μm radius grains with bulk densities of $\rho = 1300$ kg m^{-3} (see Hsieh et al. 2004; Jutzi et al. 2008), we estimate the total dust mass, M_d, in the coma using

$$M_d = \frac{4}{3} \rho a \cdot A_N \left(\frac{A_d}{A_N} \right). \quad (4)$$

We list the values we compute for A_d/A_N and M_d using the above procedures in Table 3. Comparing the minimum and maximum values of M_d during our observations, we find that P/La Sagra's coma increases in mass at an average net rate of $\dot{M}_d \sim 0.1$ kg s^{-1} (likely precise to an order of magnitude, at best) between 2010 August and December. This net increase in total dust mass represents the sum of the positive contribution of new dust production from the nucleus and the negative contribution of dust dissipation as individual grains disperse beyond the photometry aperture. As such, it represents a lower limit to the true dust production rate of the nucleus.

In addition to performing nucleus photometry, we also measure the total flux from the comet in our composite images from each night. We do so by using rectangular photometry apertures enclosing the entire visible dust cloud and oriented to avoid field star contamination. Background sky levels were then measured from nearby areas of blank sky and subtracted to obtain net fluxes, which were then calibrated using standard stars to obtain absolute photometry ($m_{\rm tot}$). Unfortunately, the faintness of the residual dust trail observed on 2011 August 26 and 31, and extensive contamination by nearby bright field stars means that we are unable to perform these measurements for data obtained on those dates. Repeating the mass production rate analysis described above, we find that P/La Sagra's coma and tail increase in mass at about twice the rate measured for the near-nucleus coma, or an average net rate of $\dot{M}_d \sim 0.2$ kg s^{-1}.

Since this analysis does not rely on a fixed aperture size, this net mass loss rate is closer to the true dust production rate of the nucleus than that computed above, though it still represents a lower limit due to the unknown dissipation rate of the dust as individual grains disperse from the coma and tail and become undetectable above the sky background. Comparing with other MBCs, we nonetheless find that P/La Sagra has a dust production rate comparable to or larger than that of 238P (Hsieh et al. 2009b), and at least an order of magnitude larger than those of 133P and 176P (Hsieh et al. 2004, 2011b).

For reference, we also use our measurements of the near-nucleus flux of the comet (using 5″.0 photometry apertures) in each set of observations to estimate the dust contribution as parameterized by $Af\rho$ (A'Hearn et al. 1984). These results are also shown in Table 3, and again indicate significantly stronger activity for P/La Sagra as compared to 133P, for which $Af\rho$ was also systematically tabulated (Hsieh et al. 2010b).

We also attempt to reproduce our observed photometry using a sublimation model similar to that used by (Hsieh et al. 2011c) to analyze the activity of 238P. This effort was hampered, however, by our lack of observational constraints on the start time of activity and the rate of its eventual decline. We do find that steadily increasing activity during the post-perihelion portion of P/La Sagra's orbit cannot be modeled by surface ice sublimation, indicating that the ice must instead reside at some depth below the surface of the nucleus, similar to what

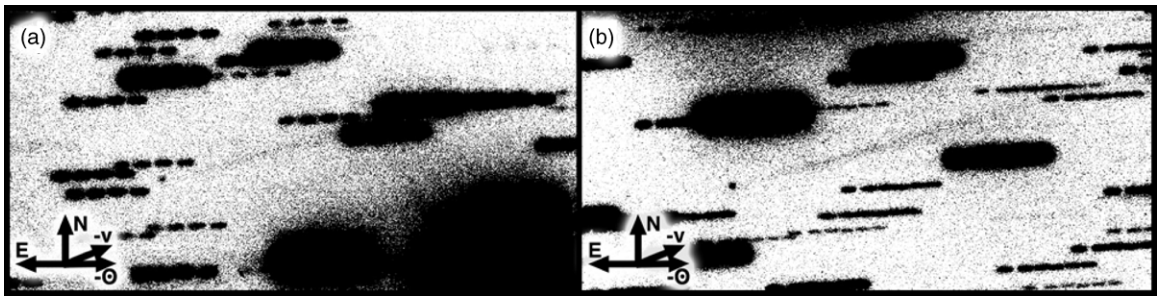

Figure 4. Composite images of P/La Sagra (point-like object in the lower left of each panel) constructed from data obtained on (a) 2011 August 26 (1200 s on Keck I in *R*-band) and (b) 2011 August 31 (1800 s on Gemini in r'-band). Panels are $120'' \times 60''$, with north (N), east (E), the antisolar direction ($-\odot$), and the negative heliocentric velocity vector ($-v$), as projected on the sky, marked.

was found for 238P (Hsieh et al. 2011c). Unfortunately, the numerous free parameters that can be modified in our model mean that this finding is the only meaningful result that can be derived at this time. Better sampling of the activity over a longer time baseline will be required to gain additional insight into the nature of P/La Sagra's activity via this method, and as such, should be considered an observational priority during its next expected period of activity (likely beginning in mid-2015).

We note that if P/La Sagra exhibits activity over a period of ∼1 year during each of its perihelion passages (similar to 133P; Hsieh et al. 2004), assuming an average mass loss rate of $\dot{M}_d = 0.2\,\mathrm{kg\ s^{-1}}$, a total mass loss of $\sim 10^7$ kg per orbit would be expected. Assuming a nucleus size of $r_N = 0.7$ km (Section 3.2.1) and $\rho = 1300\,\mathrm{kg\ m^{-3}}$, such a mass loss rate should consume the entire nucleus over the next $\sim 10^5$ orbits, or $< 10^6$ yr. However, activity in MBCs (even over just a portion of their orbits) is expected to be transient (see Hsieh et al. 2004), perhaps amounting to just 1% of an object's total lifetime (Hsieh 2009). As such, we expect a timescale for nucleus disintegration due to cometary activity closer to $\sim 10^8$ yr (Hsieh 2009), or approximately comparable to the $\sim 10^8$–10^9 yr collisional lifetime expected for a main-belt asteroid the size of P/La Sagra's nucleus (Bottke et al. 2005).

3.2.3. Comparison to Other MBCs

To further understand P/La Sagra's place among the population of known MBCs, we plot A_d/A_N for the first five known MBCs as functions of true anomaly, ν (Figure 5(a)). We note a few interesting features of this plot. First, we find quantitative confirmation that for their nucleus sizes, 238P and P/Garradd exhibit far more dust when active than 133P and 176P (also see Table 1). This fact has of course always been qualitatively apparent. The observed morphologies of 238P and P/Garradd, when active, resemble those of highly active comets (Hsieh et al. 2009b, 2011c; Jewitt et al. 2010), whereas the nuclei of 133P and 176P dominate the surface brightness profiles of those objects, even at the peaks of their active periods. Only comparatively faint dust tails and small amounts of photometrically detected unresolved near-nucleus dust have attested to the cometary natures of these latter MBCs (Hsieh et al. 2004, 2010b, 2011b). As for P/La Sagra, we find that it exceeds even 238P and P/Garradd in the amount of dust it produces for the size of its nucleus, producing ∼3 times as much dust relative to its nucleus size at its peak as 238P and P/Garradd produced at their peaks, which in turn were ∼50 times as productive relative to their nucleus sizes as 133P and 176P.

We caution that given the different geocentric distances at which the observations in question were made, the near-nucleus photometry performed for each MBC measures dust contained within different physical distances from the nucleus. As such, considering that other physical characteristics of the dust emission (e.g., grain sizes, bulk grain densities, and ejection velocities) for each MBC are unknown and likely also vary from object to object, these comparisons are best interpreted in terms of orders of magnitude. We therefore find 238P, P/Garradd, and

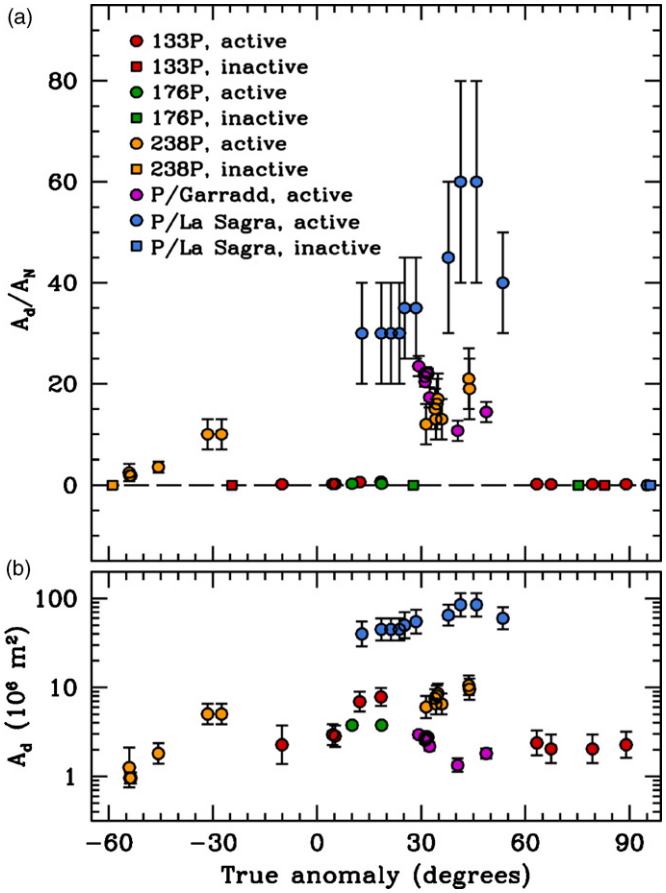

Figure 5. Comparisons of (a) dust-to-nucleus ratios (by scattering cross-section) and (b) total dust scattering cross-sections, in 10^6 km^2, as functions of true anomaly measured for the five known MBCs: 133P (red symbols; Hsieh et al. 2010b), 176P (green symbols; Hsieh et al. 2011b), 238P (orange symbols; Hsieh et al. 2011c), P/Garradd (purple symbols; Jewitt et al. 2009; Maclennan & Hsieh 2012), and P/La Sagra (blue symbols; This work). Observations where activity was detected either visually or from photometry are marked with circular symbols, while observations where no activity was detected are marked with squares. For points where no error bars are visible, the amount of uncertainty is equal to or less than the size of the plotted symbol.

(A color version of this figure is available in the online journal.)

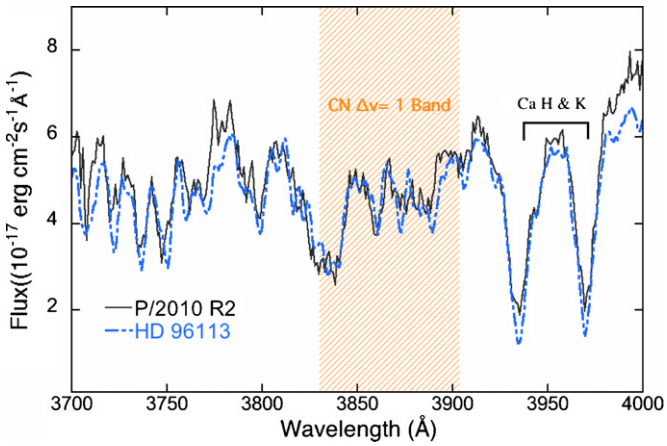

Figure 6. Plots of the sky-background-subtracted and flux-calibrated spectrum of P/La Sagra (solid black line), and the scaled spectrum of the solar analog, the G2V star HD 91163 (blue dashed line). The shaded region indicates the wavelength region where the CN emission band is expected. We note that the spectrum of P/La Sagra closely resembles that of HD 91163 and thus no emission features are observed within the uncertainties of our measurements.

(A color version of this figure is available in the online journal.)

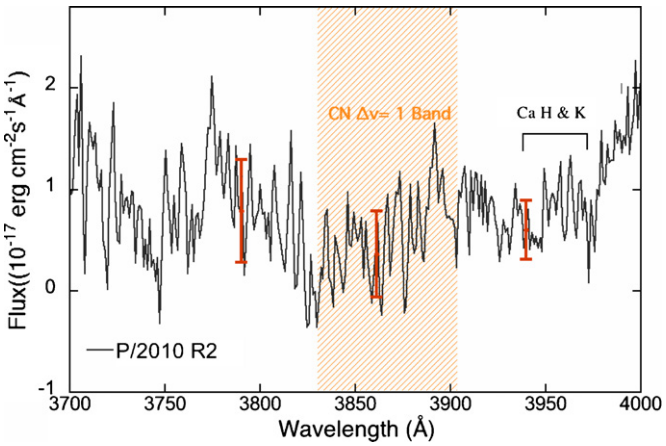

Figure 7. Spectrum of P/La Sagra with the underlying solar continuum removed. The three red error bars show the 1σ uncertainties in the three wavelength regions (3760–3830 Å, 3830–3900 Å, and 3900–3970 Å).

(A color version of this figure is available in the online journal.)

P/La Sagra to have similar levels of activity which are 1-2 orders of magnitude higher than those of 133P and 176P, implying similar ratios of fractional active surface areas for these objects.

To quantify the total amount of ejected dust exhibited by each comet, we also multiply the A_d/A_N values for each comet by estimates of A_N for each object (derived from nucleus radii listed in Table 1) to obtain absolute values for A_d. We plot the results as functions of true anomaly in Figure 5(b). Interestingly, we find that despite the high A_d/A_N values measured for 238P and P/Garradd, the total absolute amount of dust in those comets is approximately comparable to the amounts of dust present for 133P and 176P, which visually appear far less active in comparison. P/La Sagra is seen to produce roughly an order of magnitude more dust in absolute terms than any of the other MBCs (assuming similar particle size distributions).

We therefore find the interesting result that within an order of magnitude, all five MBCs considered here exhibit similar total amounts of visible dust in their comae and tails, despite the wide variation in their observed morphologies. Determining whether this finding is physically significant will require similar dust mass measurements for newly discovered MBCs to investigate whether this trend is maintained as the sample of known objects grows. We suggest that future research investigating the validity and implications of this possible trend may provide valuable insights into the origin and evolution of MBC activity.

3.3. Spectroscopic Analysis

3.3.1. Data Reduction

In the optical region of the electromagnetic spectrum, the emission band of the CN radical at 3880 Å is among the strongest among cometary gaseous species and therefore is considered to be the most sensitive probe for detecting gas resulting from sublimating ice. We search for evidence of the presence of the CN band in a one dimensional spectrum extracted from the spectral image using a $1\farcs0 \times 7\farcs5$ rectangular aperture centered on the continuum. We use a relatively wide extraction aperture to incorporate as much light as possible from the surrounding coma. The sky background is reconstructed and subtracted using flanking regions extending from 9″ to 15″ from the nucleus.

In Figure 6, we present the spectrum of P/La Sagra in the relevant spectral region from ∼3700 Å to ∼4000 Å. The continuum of the comet consists of scattered sunlight from dust particles in the inner coma and shows several absorption features in the Solar spectrum, such as the prominent Ca H and K absorption lines at 3933 Å and 3966 Å (Figure 6). The shaded spectral region from 3830 Å to 3905 Å indicates where we expect to detect CN emission if any is present (Cochran et al. 1992).

In order to correct for solar spectral features, the spectrum of a G2V solar analog star is needed. As discussed in Section 2, we were not able to observe a G2V star at the time of our P/La Sagra observations due to poor weather conditions. We instead adopt a flux-calibrated spectrum of G2V star HD 91163 which was obtained using the same instrument but was recorded a few months later on UT 2010 December 17 (Hsieh et al. 2012a). This spectrum was observed using the 600/4000 grism and thus has a higher spectral resolution than our P/La Sagra data, however, so the additional step of binning the HD 91163 spectrum to the same spectral resolution as our P/La Sagra spectrum is required. The scaled spectrum of HD 91163 is shown as the blue dashed line in Figure 6. We note that the spectra of P/La Sagra and HD 91163 are quite similar, particularly in the shaded region. However, minor discrepancies are observed at wavelengths $\lambda < 3800$ Å and $\lambda > 3980$ Å. These discrepancies may be due to the time and air-mass differences between the comet observations and standard star observations. We find no evidence of CN emission in the shaded wavelength region.

3.3.2. Upper Limits on Gas Production Rates

The continuum-removed spectrum of P/La Sagra is shown in Figure 7. In principle, this spectrum shows emission from atoms and molecules in the inner coma. We measure the standard errors in the residual spectrum in three wavelength regions 70 Å in width: 3760 Å–3830 Å, 3830 Å–3900 Å, and 3900 Å–3970 Å. The standard errors on either side of the expected CN band are 5.1×10^{-18} and 2.8×10^{-18} erg cm^{-2} s^{-1} Å^{-1}, respectively, shown as red error bars in Figure 7. The standard error in the region of the expected CN band is 4.2×10^{-18} erg cm^{-2} s^{-1} Å^{-1}. We choose the largest standard

error of 5.1×10^{-18} erg cm^{-2} s^{-1} Å^{-1} as a conservative estimate of our observational uncertainty in the region of the expected CN emission band. We therefore estimate a 3σ upper limit of 1.5×10^{-17} erg cm^{-2} s^{-1} Å^{-1}.

We calculate the integrated CN band flux by summing the estimated emission flux in the shaded N region, obtaining $f_{\rm CN} = 3.7 \times 10^{-16}$ erg cm^{-2} s^{-1}. We then convert the integrated flux to the total number of CN molecules using

$$L_{\rm CN} = 4\pi\Delta^2 f_{\rm CN} \quad (5)$$

$$N_{\rm CN} = \frac{L_{\rm CN}}{g(R)}, \quad (6)$$

where $N_{\rm CN}$ is the number of CN molecules, Δ and R are the geocentric and heliocentric distances, respectively, and $g(R)$ is the resonance fluorescence efficiency, which describes the number of photons scattered per second per radical for an optically thin coma, in erg s^{-1} molecule^{-1} at a heliocentric distance of R. At the time of our observations, P/La Sagra had a radial velocity of $\dot{R} = 1.1$ km s^{-1}, for which $g(R = 1\,{\rm AU}) = 2.86 \times 10^{-13}$ (Schleicher 2010). Substituting $f_{CN} = 3.7 \times 10^{-16}$ erg cm^{-2} s^{-1}, $R = 2.66$ AU, and $\Delta = 1.82$ AU, we find an upper limit of $N = 8.3 \times 10^{25}$ CN molecules in the extraction aperture.

A simple Haser model (Haser 1957) was used to derive the CN production rate based on the number of CN molecules. The details of the model are described in Hsieh et al. (2012a). We find an upper limit to the CN production rate of $Q_{\rm CN} < 6 \times 10^{23}$ mol s^{-1}. Taking average ratios measured for previously observed comets ($\log[Q_{\rm CN}/Q_{\rm OH}] = -2.5$; $Q_{\rm OH}/Q_{\rm H_2O} = 90\%$) (A'Hearn et al. 1995), we estimate an upper limit on the water production rate of $Q_{\rm H_2O} < 10^{26}$ mol s^{-1}. Incorporating the $Af\rho$ value calculated from data taken at the same time as these spectra (Section 3.2.2; Table 3), we find a lower-limit dust-to-gas ratio of $\log[Af\rho/Q_{\rm CN}] \gtrsim -22$, similar to values measured for other Jupiter-family comets (A'Hearn et al. 1995). As this result is only a lower limit, however, it is not possible to ascertain from these data the degree to which P/La Sagra is depleted in volatiles relative to other classical comets from its apparently long residence time in the inner solar system (Section 3.4.1).

3.3.3. Estimation of Effective Active Area

We can estimate the effective active area of the nucleus of P/La Sagra by comparing the observed mass loss rate with theoretical rates obtained from applying a simple thermal model. To calculate the sublimation rate of surface ice, we solve the energy balance equation for the equilibrium temperature on the object's surface:

$$\frac{S_\odot(1-p)}{r^2} J(\theta) = \epsilon\sigma T_e^4 + L\psi(T_e), \quad (7)$$

where $S_\odot = 1360$ W s^{-1} is the solar constant, $p = 0.05$ is the albedo, $R = 2.66$ AU, $J(\theta)$ is a function of the solar zenith angle θ which describes the ratio between the absorbing and radiating area, $\epsilon = 0.9$ is the emissivity, σ is the Stefan–Boltzmann constant, $L = 2.68 \times 10^6$ J kg^{-1} is the latent heat and T_e is the effective surface temperature. The specific sublimation rate, ψ (in kg m^{-2} s^{-1}), of water is given by

$$\psi = P(T_e)\sqrt{\frac{m}{2\pi k T_e}}, \quad (8)$$

where m is the mass of a water molecule, k is Boltzmann's constant, and $P(T_e)$ is the saturated vapor pressure (Fanale & Salvail 1984).

In the fast rotator approximation (which yields the coldest surface temperature), the nucleus is considered isothermal and $J = \langle\cos\theta\rangle = 1/4$. The hottest surface temperatures are derived in the sub-solar point (i.e., slow rotator) approximation, where the absorbing and radiating areas are identical and therefore $J = 1$. We obtain sublimation rates of 1.3×10^{-6} kg m^{-2} s^{-1} and 6.1×10^{-5} kg m^{-2} s^{-1} for the cold and hot scenarios, respectively. Assuming an average mass loss rate of $\dot{M}_d \sim 0.2$ kg s^{-1} (Section 3.2.2), we estimate active areas of 1.5×10^5 km^2 and 3.3×10^3 km^2, corresponding to total active surface fractions of ~3% and ~0.05% (likely precise to an order of magnitude, at best), for the cold and hot cases, assuming dust-to-gas mass ratios of unity. These derived active surface fractions are comparable to those of other Jupiter-family comets measured by A'Hearn et al. (1995). For comparison, both 133P and 176P are estimated to have active areas of $\sim 10^2$–10^3 m^2 (Hsieh et al. 2004; Hsieh 2009), corresponding to active surface fractions of 0.0002–0.002%, several orders of magnitude smaller than for P/La Sagra.

3.4. Dynamical Analysis

3.4.1. Stability Analysis

To better understand the likely origin of P/La Sagra, we also consider its dynamical properties. Jewitt et al. (2009) raised the possibility that MBC P/Garradd could have originated in a different part of the asteroid belt from where we see it today. As such, an important issue to consider is whether P/La Sagra is dynamically stable at its present location, or whether it is possible that it may have also originated elsewhere.

To assess P/La Sagra's dynamical stability, we randomly generate three sets of 100 test particles, each set with Gaussian distributions in orbital element space, centered on P/La Sagra's JPL-tabulated osculating orbital elements, where each set is characterized by a σ value equal to the JPL-tabulated uncertainties (as of 2011 January 1) for each orbital element. To investigate the stability of the region (in orbital element space) surrounding P/La Sagra, we also generate three additional sets of 100 Gaussian-distributed test particles each, where each set is again centered on P/La Sagra's osculating orbital elements but is characterized by a σ value equal to 100× the JPL-tabulated uncertainties. We then use the N-body integration package, Mercury (Chambers 1999), to integrate the orbits of each set of test particles forward in time for 100 Myr (limitations on available computing resources unfortunately prevent us from conducting these simulations over significantly longer time periods, e.g., 1–2 Gyr, in a reasonable amount of time), where we treat the eight major planets as massive particles and all test particles are considered to be massless.

Performing these integrations for all six sets of test particles, we find that 7% of the objects in the three 1σ test particle sets are ejected (i.e., reach a heliocentric distance of >50 AU) from the asteroid belt over the course of 100 Myr (Figure 8), and 11% of the objects in the three 100σ test particle sets are ejected (Figure 9). P/La Sagra itself is found to be stable over the 100 Myr test period, consistent with its Lyapunov time ($T_{\rm lyap}$), estimated by us to be ~200 kyr (computed using the procedure described in Tsiganis et al. 2003), where a body is generally considered to be stable for $T_{\rm lyap} > 100$ kyr. The 1σ test particles that are ejected are not localized to particular regions of orbital

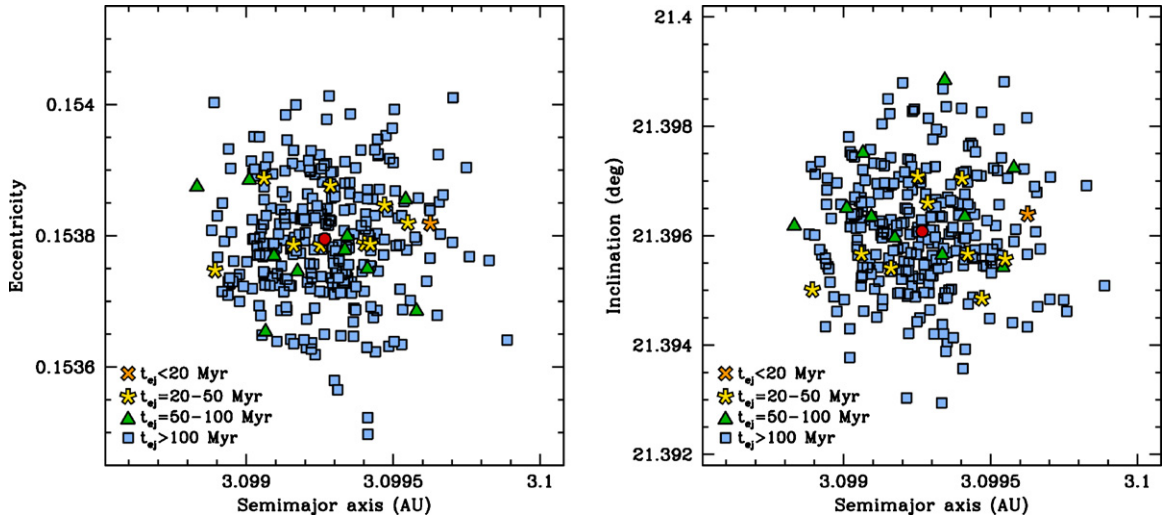

Figure 8. Plots of semimajor axis vs. eccentricity (left) and inclination (right) showing initial osculating elements of test particles in three sets of 100 Gaussian-distributed particles each of which are subjected to a 100 Myr dynamical integration (Section 3.4.1). Each set of test particles is centered on the current osculating orbital elements of P/La Sagra (red circle) and characterized by a σ value equal to the object's JPL-tabulated uncertainties. Particles ejected in less than 20 Myr, between 20 Myr and 50 Myr, and between 50 Myr and 100 Myr are plotted with orange X symbols, yellow asterisk symbols, and green triangles, respectively, while particles that are not ejected after the 100 Myr test period used in our simulations are marked with blue squares.

(A color version of this figure is available in the online journal.)

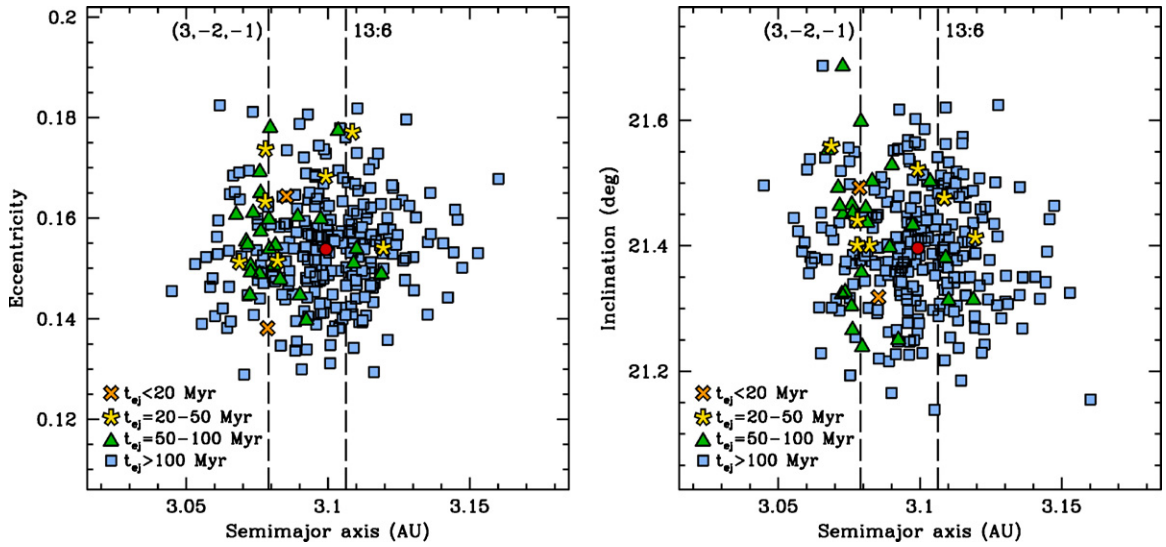

Figure 9. Same as Figure 8 for three sets of 100 Gaussian-distributed particles each, where each set is characterized by a σ value equal to 100× P/La Sagra's JPL-tabulated uncertainties. The locations of the (3, −2, −1) three-body mean-motion resonance (with Jupiter and Saturn) at $a = 3.0790$ AU and the 13:6 mean-motion resonance (with Jupiter) at $a = 3.1063$ AU are plotted with dashed lines.

(A color version of this figure is available in the online journal.)

element space near P/La Sagra, suggesting that their ejection may be a consequence of stochastic encounters with a weak mean-motion resonance (or multiple resonances), rather than the effect of a single dominant resonance. Nearby resonances include the "moderate-order" 13:6 mean-motion resonance with Jupiter at $a = 3.1063$ AU and the (3, −2, −1) three-body mean-motion resonance (with Jupiter and Saturn) at $a = 3.0790$ AU (Nesvorný & Morbidelli 1998). Both resonances are more than 1σ away in a, given the uncertainties for P/La Sagra's osculating elements, but could conceivably affect the object as its osculating elements fluctuate over time (Figure 10).

In our 100σ test particle simulations, the effect of the (3, −2, −1) three-body resonance is clear, with ∼70% of the ejected test particles in those simulations having initial semimajor axes within 0.01 AU of the resonance. The effect of the 13:6 resonance is comparatively less pronounced, with only ∼20% of the ejected particles in these simulations starting within 0.01 AU of the resonance, despite the fact that this resonance is closer to P/La Sagra than the (3, −2, −1) resonance and therefore lies in a more highly populated region of our initial test particle distribution. P/La Sagra itself has an initial osculating semimajor axis 0.06 AU of the 13:6 resonance, and even occasionally crosses the resonance during our simulations (Figure 10), yet is found to be stable over the 100 Myr test period considered here, suggesting that this resonance only weakly affects objects in this region of orbital element space.

We conclude from this analysis that the region in orbital element space occupied by P/La Sagra is largely stable, implying that the object is likely to be native to its present-day location. As such, its physical properties may be reflective of

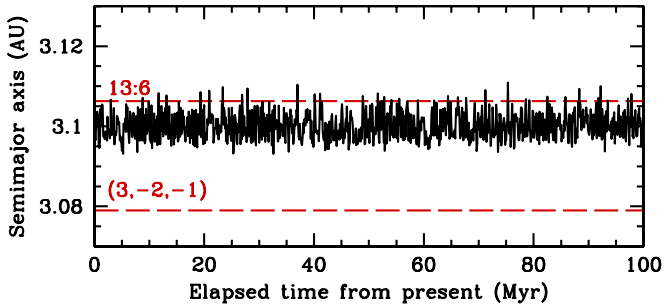

Figure 10. Plot of P/La Sagra's semimajor axis (AU) as a function of time (Myr), marked with a black solid line, as simulated in the numerical integrations described in Section 3.4.1, where the semimajor axes of the 13:6 mean-motion resonance with Jupiter and the (3, −2, −1) three-body mean-motion resonance with Jupiter and Saturn are marked with red dashed lines.

(A color version of this figure is available in the online journal.)

other objects in this region of the asteroid belt. However, between the nearby 13:6 mean-motion resonance with Jupiter and the (3, −2, −1) three-body mean-motion resonance with Jupiter and Saturn, enough dynamical instability is imparted to the region that a non-negligible fraction of simulated test particles escape in less than 100 Myr. Due to the non-negligible instability of this region, we therefore cannot definitively conclude that P/La Sagra formed in situ (and did not dynamically evolve onto its present-day orbit from elsewhere in the main belt, or even elsewhere in the solar system), particularly over timescales longer than the 100 Myr test period considered in this analysis. We further note that our analysis does not consider non-gravitational effects such as the Yarkovsky effect or the effects of asymmetric mass loss such as that associated with cometary jets. As such, in future investigations of this object, particularly those which pertain to the comparison of its physical properties to those of other MBCs, the possibility that P/La Sagra may not be native to its current location cannot be discounted.

3.4.2. Family Search

Having investigated the dynamical stability of P/La Sagra and its surroundings, we seek to further characterize the object's dynamical environment by searching for evidence of an associated asteroid family, i.e., a grouping of dynamically linked asteroids likely to be the result of either the catastrophic fragmentation of a larger parent asteroid (Hirayama 1918), or a significant cratering event on a still-existing asteroid (e.g., Vesta; Asphaug 1997). Such a search is particularly crucial for this object because of studies suggesting that MBCs may preferentially be found among families (Hsieh et al. 2004; Haghighipour 2009), and possibly specifically among extremely young families (Nesvorný et al. 2008; Hsieh 2009). The latter hypothesis is based on the facts that MBC 133P appears to be a member of the <10 Myr old Beagle family (Nesvorný et al. 2008), and collisional devolatilization of near-surface ice of km-scale MBCs (such as 133P and 176P) is expected to occur at rates incompatible with the existence of present-day activity, unless those MBCs are recently produced fragments of larger asteroids with significant interior ice reservoirs (Hsieh 2009).

Due to P/La Sagra's high inclination, we cannot search for an associated dynamical asteroid family using analytically determined proper orbital elements (Milani & Knežević 1994), as can be done for objects at lower inclinations. The complication stems from the fact that analytically computed proper elements are significantly less accurate for objects with high eccentricities or inclinations. The development of numerical methods for computing so-called synthetic proper elements for characterizing the long-term behavior of high-inclination and high-eccentricity objects resolved this problem (Knežević & Milani 2000), an advance that was employed by Gil-Hutton (2006) and Novaković et al. (2011) to conduct systematic searches for families among high-inclination asteroids.

Table 4
P/La Sagra Cluster Members

Object	a_p [a]	e_p [b]	$\sin(i_p)$ [c]	H_V [d]	$T_{\rm lyap}$ [e]
18901 (2000 MR_5)	3.0942	0.1223	0.3791	12.1	683
106020 (2000 SS_{294})	3.0928	0.1146	0.3812	14.4	480
106064 (2000 SA_{323})	3.0931	0.1215	0.3824	14.5	781
131501 (2001 SX_{272})	3.0889	0.1177	0.3831	14.2	999
(2002 RQ_{261})	3.0887	0.1150	0.3824	15.4	900
P/2010 R2 (La Sagra)	3.1001	0.1148	0.3817	18.3	270

Notes.
[a] Proper semimajor axis, in AU.
[b] Proper eccentricity.
[c] Sine of proper inclination.
[d] Absolute magnitude, in *V*-band.
[e] Lyapunov time, in kyr.

For our analysis of P/La Sagra, we first compute the object's own synthetic proper elements—proper semi-major axis (a_p), proper eccentricity (e_p), and proper inclination (i_p)—using the procedure described in Knežević & Milani (2000) and osculating orbital elements from the JPL Small-Body Database Browser. We list these results in Table 4. We then plot these newly computed synthetic proper elements in $a_p - e_p$ and $a_p - i_p$ space along with the synthetic elements of all of the families (as well as smaller or less-significant groupings designated as clumps or clusters) identified by Gil-Hutton (2006) and Novaković et al. (2011) to check for plausible close associations of P/La Sagra with any of these previously identified groupings (Figure 11). We find no such associations.

Finding no link between P/La Sagra and any currently known asteroid families, we turn to our own search for dynamically associated asteroids to determine whether a clustering specific to P/La Sagra may have missed simply because this newly discovered object was not considered in previous family searches. To do so, we add our computed proper elements for P/La Sagra to an updated list of synthetic proper elements for high-inclination asteroids (Novaković et al. 2011), and then employ the Hierarchical Clustering Method (HCM; Zappalà et al. 1990, 1994) to search for dynamically associated asteroids. Results from this analysis are plotted in Figure 12, where we show the number of asteroids associated with P/La Sagra as a function of cutoff "distance" (which, despite its name, has units of velocity).

We find just six objects in P/La Sagra's dynamical vicinity (including P/La Sagra itself) within a cutoff distance of 120 m s^{-1} (Table 4). Confirming our search (described above) for associations of P/La Sagra with previously identified groupings, none of these objects belong to any of the families, clumps, or clusters found by Gil-Hutton (2006) or Novaković et al. (2011). According to the criteria used by Novaković et al. for the outer belt region, this group of objects is neither compact nor large enough to be classified as a family or clump. At best, it can be classified as a cluster, defined by Novaković et al. (2011) as a compact group of objects that could share a common physical origin, but does not formally satisfy the criteria for being a family or clump, usually because the number of members that it contains is too small.

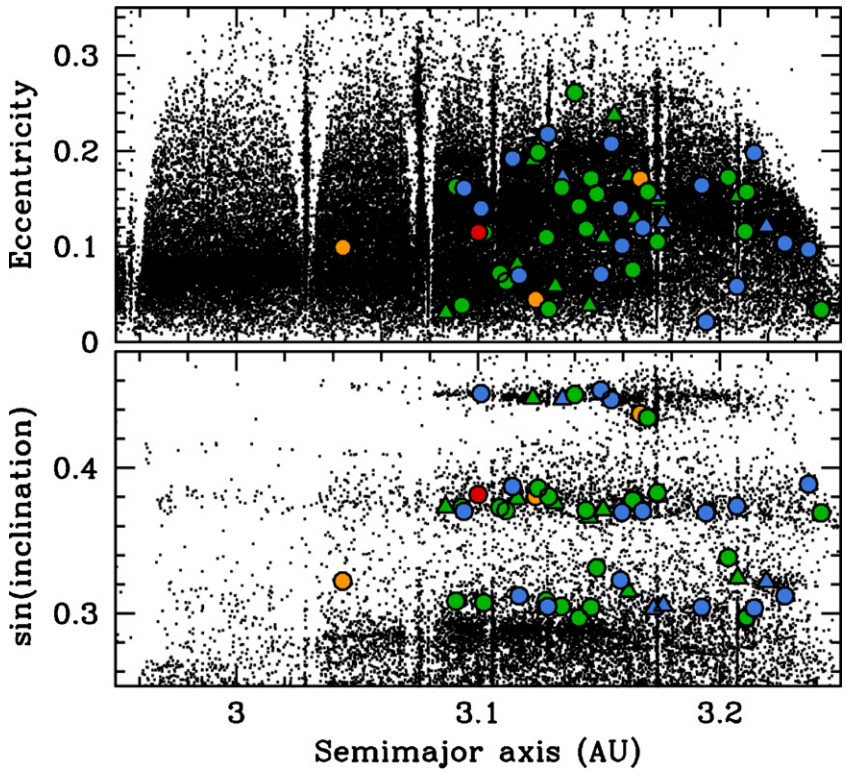

Figure 11. Synthetic orbital element plots of eccentricity (upper panel) and sine of inclination (lower panel) vs. semimajor axis of outer main-belt asteroids (small black dots), where the central bodies of families and clumps identified by Gil-Hutton (2006) are marked with blue and green triangles, respectively, and central bodies of families, clumps, and clusters identified by Novaković et al. (2011) are marked with blue, green, and orange circles, respectively. The location of P/La Sagra in synthetic proper element space is plotted with a red circle.

(A color version of this figure is available in the online journal.)

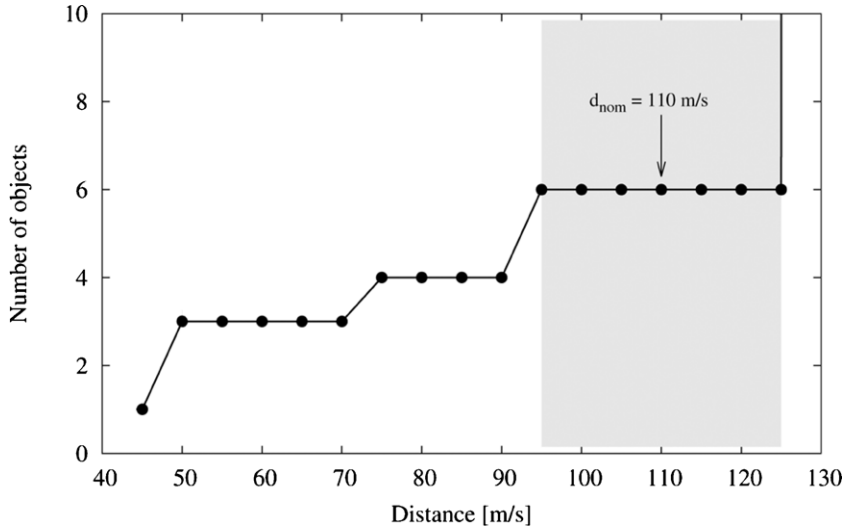

Figure 12. Number of objects associated with the P/La Sagra cluster. The six members determined to belong to this cluster are all linked within 95 m s^{-1}, with no more linkages found to other asteroids until 125 m s^{-1} when the group merges with the local background population. Our choice for the nominal cutoff distance for the cluster of 110 m s^{-1} is marked.

To obtain a quantitative assessment of the likelihood that members of the P/La Sagra group share a common physical origin, we use a method employed by Nesvorný & Vokrouhlický (2006) to estimate the probability that a certain cluster of objects is the result of random chance. Confining our analysis to the high-inclination region of the outer main belt ($2.825 < a_p < 3.278$ AU, $e_p < 0.4$, $0.3 < \sin(i_p) < 0.55$), we generate 10,000 random distributions of 9569 synthetic objects (the same number of objects currently known to populate this region) in proper orbital element space. We then perform HCM analysis on these synthetic populations to search for possible groupings with at least six objects within cutoff distances of 95 m s^{-1}. The results of this analysis show that there is a significant probability (~30%) that the P/La Sagra cluster could in fact be due to chance. While these results still leave a ~70% chance that this grouping is not random and

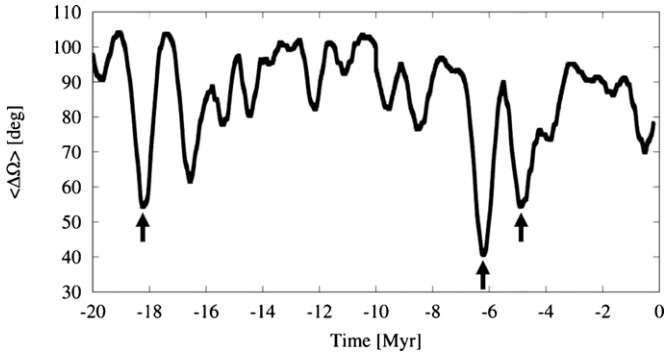

Figure 13. Average differences $\langle \Delta\Omega \rangle$ of the longitudes of the ascending nodes for members of the P/La Sagra cluster. Three significant clusterings at 4.9, 6.2, and 18.2 Myr in the past are marked with arrows.

therefore could have a physical origin, more information is certainly needed to establish whether or not this clustering can be considered real.

We compute Lyapunov times for members of the P/La Sagra group (Table 4), finding the orbits of all six bodies to be stable ($T_{\rm lyap}$ >100 kyr). This fact provides an opportunity to apply the backward integration method (BIM; Nesvorný et al. 2002) to this group. BIM is a means for estimating the age of a <20 Myr old family that is based on the premise that immediately after the disruption of a parent body, the orbits of the resulting fragments must have been nearly the same, and has been successfully applied to estimate the ages of the Karin cluster and Veritas family (Nesvorný et al. 2003).

In the case of the group of asteroids surrounding P/La Sagra, the purpose of the BIM analysis is twofold. If a suspicious clustering in the longitude of the ascending node (Ω) or the longitude of perihelion (ϖ) can be found, this analysis would not only allow us to estimate the age of the group, but would also provide support for the hypothesis that these objects share a physical origin in the first place. In the outer belt, however, application of this method is generally complicated by large gradients of secular frequencies with a_p, particularly when considering ϖ in the vicinity of the 2:1 resonance with Jupiter (Nesvorný et al. 2003). Although the P/La Sagra group is not particularly close to this resonance, the gradient dg/da_p, where g is the frequency of the longitude of perihelion, is still relatively large in this region (∼0.″1 yr^{-1} AU^{-1}). As such, for the purpose of our study we only consider Ω.

To investigate whether or not a clustering in Ω exists, we numerically integrate the orbits of all six known members of the P/La Sagra group for 20 Myr backward in time. We then calculate the average difference, $\langle \Delta\Omega \rangle$, calculated for all possible combinations of objects, where $\Delta\Omega = \Omega_i - \Omega_j$, and i and j denote two bodies under consideration. Plotting the results of this analysis (Figure 13), we find three clusterings within 60 deg. The clusterings at about 4.9 and 18.2 Myr ago are less significant than the one occurring about 6.2 Myr ago. This implies that the age of the cluster is likely close to 6.2 Myr, but due to the small number of asteroids involved, it is not possible to draw a definitive conclusion about the physical significance of this cluster.

The results shown in Figure 13 are obtained in a purely gravitational model. Including other forces (e.g., the Yarkovsky effect) could affect the positions and depths of various minima (see Novaković 2010). We believe, however, that such an analysis should be deferred pending the discovery of more members of the cluster so that more statistically meaningful results can be obtained than are currently achievable with just six possible cluster members. In the meantime, the determination of colors or acquisition of spectra of the currently suspected cluster members could provide some preliminary insights into the likelihood that these objects are physically related.

4. DISCUSSION

To date, the only published analysis of P/La Sagra prior to this work was presented by Moreno et al. (2011), who focused on numerical modeling of object's dust emission. They found that the activity can be plausibly modeled by an episode of continuous dust emission, consistent with a sublimation-driven dust ejection process and inconsistent with impulsive dust ejection as would be expected from an impact, beginning shortly before the object's perihelion passage and persisting over >7 months. Furthermore, they found that the dust cloud's morphology was best reproduced by anisotropic dust emission and indicated that their modeling suggests that P/La Sagra's activity could be seasonally modulated in a manner similar to that of other MBCs (e.g., Hsieh et al. 2004, 2011b). In our photometric analysis of the dust cloud (Section 3.2.2), we found steadily increasing dust mass between 2011 August and December, indicative of ongoing dust production, and consistent with the conclusion by Moreno et al. (2011) that P/La Sagra's dust emission appears to have persisted over an extended period of time, and therefore was likely to be cometary (i.e., sublimation-driven) in nature.

While the conclusion that P/La Sagra's dust emission is driven by the sublimation of volatile ices appears to be at odds with the results of our spectroscopic analysis (Section 3.3), we note that the extreme difficulty of detecting sublimation products in a cometary coma at the distance of the main belt means that the non-detection of gas emission in such observations cannot be considered conclusive evidence against the presence of gas (see Hsieh et al. 2012a). Rather, such non-detections should only be interpreted as evidence that the levels of gas emission for all MBCs for which spectroscopy has been obtained to date (133P, P/Garradd, and P/La Sagra; Licandro et al. 2011; Jewitt et al. 2009, and this work) have simply been below the sensitivity levels of those observations. However, the aforementioned observations were all obtained using large ground-based telescopes (the European Southern Observatory's 8 m Very Large Telescope in Chile, and the 10 m Keck I telescope in Hawaii), and so future attempts to detect gas in MBCs may need to focus on significantly more active MBCs (i.e., with higher gas emission levels) since significantly more powerful observing facilities are not currently available. It may also be possible that given the large distances and low activity levels (relative to other comets observed at much smaller heliocentric and geocentric distances) of the MBCs, conclusive evidence of gas emission may only ever be obtainable from a close-approaching spacecraft equipped to make such measurements.

Despite the lack of a successful gas detection (Section 3.3), we conclude from the numerical modeling of Moreno et al. (2011) and the morphological and photometric analyses presented in this work (Sections 3.1 and 3.2) that P/La Sagra's activity is likely to be sublimation-driven. As such, the object is likely to be a bona fide MBC such as 133P, 176P, 238P, and P/Garradd, where dust is ejected via gas drag from sublimating ice, and not as ejecta from a recent impact as is suspected in the cases of disrupted asteroids, P/2010 A2 and (596) Scheila (e.g., Jewitt et al. 2010, 2011; Snodgrass et al. 2010; Bodewits et al. 2011).

Definitive criteria for identifying the true nature of comet-like activity remain elusive, however (see Hsieh et al. 2012a). In the case of P/La Sagra, Moreno et al. (2011) show that comet-like dust emission can plausibly explain the appearance of P/La Sagra's dust tail, but by no means show that their solution is unique, a common weakness in virtually all dust modeling efforts where models are underconstrained by available observations. Given the case of P/2010 A2's long-lived dust tail (Jewitt et al. 2010; Snodgrass et al. 2010), the longevity of P/La Sagra's activity is likewise not incontrovertible evidence of sublimation-driven dust emission. Even the apparently steadily increasing dust mass in P/La Sagra's coma and tail (Section 3.2.2) could be considered inconclusive evidence of sublimation given the potential that fragmenting dust particles ejected in an impulsive event could mimic ongoing dust production as in the case of the 2007 outburst of comet 17P/Holmes (Hsieh et al. 2010a).

At this time, recurrent activity, separated by intervening periods of inactivity, appears to be the only reliably observable indicator of sublimation-driven dust emission that cannot also be plausibly explained by a scenario involving impact-driven dust ejection (Hsieh et al. 2011a). Repeated impacts on individual asteroids are unexpected from either theoretical calculations or empirical observations. The tendency of episodes of repeated activity to occur over similar arcs of each object's orbit makes such behavior even more difficult to explain as the action of random impacts rather than the effect of periodic cometary sublimation. Two of the six currently known MBCs have been observed to exhibit recurrent activity to date (133P and 238P; Hsieh et al. 2004, 2010b, 2011c), while 176P is expected to exhibit renewed activity shortly (Hsieh et al. 2011b). Confirmation of renewed activity in 176P will be crucial for supporting the hypothesis that its activity is cometary in nature. The remaining three MBCs (P/Garradd, P/La Sagra, and P/2006 VW_{139}), on the other hand, were actually discovered so recently that they have not yet completed full orbits since being discovered, but as they do (P/Garradd in early 2013, P/La Sagra in mid-2015, and P/2006 VW_{139} in mid-2016), observations to search for recurrent activity are highly encouraged.

5. SUMMARY AND CONCLUSIONS

We present a wide-ranging study of the recently discovered comet P/2010 R2 (La Sagra) including photometric and spectroscopic observations and dynamical analyses of the object. Key results are as follows.

1. A year-long observational monitoring campaign of P/La Sagra from 2010 August to 2011 August shows that the morphology of its dust cloud undergoes substantial evolution, exhibiting a strong coma and a single tail from 2010 August to November, and a coma and two tails from 2010 December to 2011 February, before diminishing to a faint, detached dust trail by 2011 August. A long-lived antisolar dust tail and the steadily increasing scattering surface area measured for the dust cloud over much of this period suggests that dust production was ongoing over a period of several months, exhibiting behavior consistent with dust ejection via the sublimation of volatile ice and inconsistent with dust ejection via the impulsive action of an impact on the surface of P/La Sagra.
2. We estimate that the nucleus of P/La Sagra has an absolute magnitude of $H_R = 17.9 \pm 0.3$ mag, corresponding to an approximate effective radius of $r_N = 0.7 \pm 0.1$ km. The $B - R$ color of the nucleus ($B - R = 0.9 \pm 0.1$ mag) is approximately solar, as are the $B - R$ colors of the active comet measured on two separate occasions in 2010.
3. Optical spectroscopic observations of the active P/La Sagra 20 days after it was discovered reveal no evidence of CN emission. Based on the sensitivity of our observations, we find upper-limit CN and H_2O production rates of $Q_{CN} < 6 \times 10^{23}$ mol s^{-1} and $Q_{H_2O} < 10^{26}$ mol s^{-1}, respectively.
4. Numerical integrations show that P/La Sagra is largely dynamically stable, indicating that it is likely native to its current location in the main belt. The surrounding region in orbital element space, however, is moderately unstable with two resonances, the 13:6 mean-motion resonance with Jupiter and the (3,−2,−1) three-body mean-motion resonance with Jupiter and Saturn, present nearby.
5. We find that P/La Sagra is not associated with any known asteroid families, though we do find a small cluster of asteroids in its dynamical vicinity. Due to the small number of objects in this cluster at the current time, however, we cannot confirm whether members of this cluster in fact resulted from the recent fragmentation of a larger parent asteroid, or if they are simply clustered in orbital element space by chance.

Despite our unsuccessful attempt to detect gas emission from P/La Sagra, we conclude from the long-lasting and steadily evolving morphology of the object's dust cloud that its activity is likely to be sublimation-driven, and unlikely to be the result of an impulsive impact. As such, it is likely to be a genuine comet, making it just the fifth MBC discovered (out of a total of six known to date). Numerical simulations indicating that P/La Sagra is likely to be native to its current location in the main belt mean that its physical composition is likely to be representative of other objects in the same region. A search for other MBCs in this region of orbital element space could prove fruitful. It has been hypothesized, however, that present-day MBC activity may require triggering by small impacts that excavate near-surface ice and expose it to the Sun (Hsieh et al. 2004; Hsieh 2009). As such, we caution that the lower rate of potential activity-triggering impacts at high inclinations (Farinella & Davis 1992) means that, overall, the rate of currently active MBCs in this region is likely to be lower than at lower inclinations.

In any event, the presence of P/La Sagra in a completely disparate region of orbital element space from the other MBCs underscores the caveat by Hsieh (2009) that the currently known population is far too small to make any conclusions about the abundance and distribution of such objects in the asteroid belt. Current and upcoming systematic searches of the entire asteroid belt for MBCs, now starting to see success in the case of PS1 (Hsieh et al. 2011a, 2012b), will be critical for ascertaining the true abundance and distribution of icy objects in the inner solar system.

We thank an anonymous referee for helpful comments that improved this manuscript. Support for this work was provided by NASA to H.H.H. through Hubble Fellowship grant HF-51274.01 awarded by the Space Telescope Science Institute, which is operated by the Association of Universities for Research in Astronomy, Inc., for NASA, under contract NAS 5-26555. B.Y. and N.H. acknowledge support through the NASA Astrobiology Institute under cooperative agreement no. NNA08DA77A issued through the Office of Space Science. B.N. is supported by the Ministry of Education and Science of Serbia, under Project 176011, while M.G. is funded

by the Academy of Finland grant 137853. C.S. additionally acknowledges funding from the European Union Seventh Framework Programme (FP7/2007-2013) under grant agreement no. 268421. We are grateful to John Dvorak and Richard Morriarty, Greg Wirth, Heather Hershley, Scott Dahm, Marc Kassis, Luca Rizzi, and Julie Renaud-Kim, and Jay Rhee, Jonathan Kemp, and Chad Trujillo for their assistance in obtaining observations on the UH 2.2 m, Keck, and Gemini telescopes, respectively, and Ilona Busenbender and Eduardo Solares for technical assistance at the INT. We also thank Alberto Cellino for valuable discussions about this work. Acquisition of some of the data presented was enabled using the PS1 System operated by the PS1 Science Consortium (PS1SC) and its member institutions. The PS1 Survey has been made possible through contributions of the Institute for Astronomy, the University of Hawaii, the Pan-STARRS Project Office, the Max-Planck Society and its participating institutes, the Max Planck Institute for Astronomy, Heidelberg and the Max Planck Institute for Extraterrestrial Physics, Garching, The Johns Hopkins University, Durham University, the University of Edinburgh, Queen's University Belfast, the Harvard-Smithsonian Center for Astrophysics, and the Las Cumbres Observatory Global Telescope Network, Incorporated, the National Central University of Taiwan, and the National Aeronautics and Space Administration under grant no. NNX08AR22G issued through the Planetary Science Division of the NASA Science Mission Directorate. The Gemini Observatory is operated by the Association of Universities for Research in Astronomy, Inc., under a cooperative agreement with the NSF on behalf of the Gemini partnership: the National Science Foundation (United States), the Science and Technology Facilities Council (United Kingdom), the National Research Council (Canada), CONICYT (Chile), the Australian Research Council (Australia), Ministério da Ciência e Tecnologia (Brazil), and Ministerio de Ciencia, Tecnología e Innovación Productiva (Argentina). Observations at the Danish 1.54 m telescope were supported by the Danish Natural Science Research Council (FNU). Funding for SDSS-III has been provided by the Alfred P. Sloan Foundation, the Participating Institutions, the National Science Foundation, and the U.S. Department of Energy Office of Science. The SDSS-III Web site is http://www.sdss3.org/. SDSS-III is managed by the Astrophysical Research Consortium for the Participating Institutions of the SDSS-III Collaboration.

REFERENCES

A'Hearn, M. F., Millis, R. L., Schleicher, D. G., Osip, D. J., & Birch, P. V. 1995, Icarus, 118, 223
A'Hearn, M. F., Schleicher, D. G., Millis, R. L., Feldman, P. D., & Thompson, D. T. 1984, AJ, 89, 579
Asphaug, E. 1997, Meteor. Planet. Sci., 32, 965
Bauer, J. M., Mainzer, A. K., Grav, T., et al. 2012, ApJ, 747, 49
Birtwhistle, P., Ryan, W. H., Sato, H., Beshore, E. C., & Kadota, K. 2010, IAU Circ., 9105, 1
Bodewits, D., Kelley, M. S., Li, J.-Y., et al. 2011, ApJ, 733, L3
Bottke, W. F., Durda, D. D., Nesvorný, D., et al. 2005, Icarus, 179, 63
Chambers, J. E. 1999, MNRAS, 304, 793
Cochran, A. L., Barker, E. S., Ramseyer, T. F., & Storrs, A. D. 1992, Icarus, 98, 151
Elst, E. W., Pizarro, O., Pollas, C., et al. 1996, IAU Circ., 6496, 1
Fanale, F. P., & Salvail, J. R. 1984, Icarus, 60, 476
Farinella, P., & Davis, D. R. 1992, Icarus, 97, 111
Finson, M. L., & Probstein, R. F. 1968, ApJ, 154, 327
Garradd, G. J., Sostero, G., Camilleri, P., et al. 2008, IAU Circ., 8969, 1
Gil-Hutton, R. 2006, Icarus, 183, 93
Haghighipour, N. 2009, Meteorit. Planet. Sci., 44, 1863
Hainaut, O. R., et al. 2012, A&A, arXiv:1112.2882
Hartmann, W., Cruikshank, D., & Degewij, J. 1982, Icarus, 52, 377
Hartmann, W., Tholen, D., Meech, K., & Cruikshank, D. 1990, Icarus, 83, 1
Haser, L. 1957, Bull. Soc. R. Sci. Liege, 43, 740
Hirayama, K. 1918, AJ, 31, 185
Hook, I. M., Jørgensen, I., Allington-Smith, J. R., et al. 2004, PASP, 116, 425
Hsieh, H. H. 2009, A&A, 505, 1297
Hsieh, H. H., Denneau, L., Wainscoat, R. J., et al. 2011a, CBET, 2920, 1
Hsieh, H. H., Fitzsimmons, A., Joshi, Y., Christian, D., & Pollacco, D. L. 2010a, MNRAS, 407, 1784
Hsieh, H. H., Ishiguro, M., Lacerda, P., & Jewitt, D. 2011b, AJ, 142, 29
Hsieh, H. H., & Jewitt, D. 2006, Science, 312, 561
Hsieh, H. H., Jewitt, D., & Fernández, Y. R. 2004, AJ, 127, 2997
Hsieh, H. H., Jewitt, D., & Fernández, Y. R. 2009a, ApJ, 694, L111
Hsieh, H. H., Jewitt, D., & Ishiguro, M. 2009b, AJ, 137, 157
Hsieh, H. H., Jewitt, D., Lacerda, P., Lowry, S. C., & Snodgrass, C. 2010b, MNRAS, 403, 363
Hsieh, H. H., Jewitt, D., & Pittichová, J. 2006, IAU Circ., 8704, 1
Hsieh, H. H., Meech, K. J., & Pittichová, J. 2011c, ApJ, 736, L18
Hsieh, H. H., Yang, B., & Haghighipour, N. 2012a, ApJ, 744, 9
Hsieh, H. H., et al. 2012b, ApJ, 748, L15
Ishiguro, M., Hanayama, H., Hasegawa, S., et al. 2011a, ApJ, 740, L11
Ishiguro, M., Hanayama, H., Hasegawa, S., et al. 2011b, ApJ, 741, L24
Jewitt, D., Weaver, H., Agarwal, J., Mutchler, M., & Drahus, M. 2010, Nature, 467, 817
Jewitt, D., Weaver, H., Mutchler, M., Larson, S., & Agarwal, J. 2011, ApJ, 733, L4
Jewitt, D., Yang, B., & Haghighipour, N. 2009, AJ, 137, 4313
Jutzi, M., Benz, W., & Michel, P. 2008, Icarus, 198, 242
Knežević, Z., & Milani, A. 2000, Celest. Mech., 78, 17
Landolt, A. U. 1992, AJ, 104, 340
Larson, S. M. 2010, IAU Circ., 9188, 1
Licandro, J., Campins, H., Tozzi, G. P., et al. 2011, A&A, 532, A65
Lisse, C. M., A'Hearn, M. F., Hauser, M. G., et al. 1998, ApJ, 496, 971
Lisse, C. M., Fernández, Y. R., A'Hearn, M. F., et al. 2004, Icarus, 171, 444
Maclennan, E. M., & Hsieh, H. H. 2011, ApJ, submitted
Magnier, E. 2006, in Proceedings of The Advanced Maui Optical and Space Surveillance Technologies Conference, ed. S. Ryan (Maui, Hawaii: The Maui Economic Development Board), E50
Milani, A., & Knežević, Z. 1994, Icarus, 107, 219
Moreno, F., Lara, L. M., Licandro, J., et al. 2011, ApJ, 738, L16
Nesvorný, D., Bottke, W. F., Jr., Dones, L., & Levison, H. F. 2002, Nature, 417, 720
Nesvorný, D., Bottke, W. F., Levison, H. F., & Dones, L. 2003, ApJ, 591, 486
Nesvorný, D., Bottke, W. F., Vokrouhlický, D., et al. 2008, ApJ, 679, L143
Nesvorný, D., & Morbidelli, A. 1998, AJ, 116, 3029
Nesvorný, D., & Vokrouhlický, D. 2006, AJ, 132, 1950
Nomen, J., Marsden, B. G., Birtwhistle, P., et al. 2010, IAU Circ., 9169, 1
Novaković, B. 2010, MNRAS, 407, 1477
Novaković, B., Cellino, A., & Knežević, Z. 2011, Icarus, 216, 69
Oke, J. B., Cohen, J. G., Carr, M., et al. 1995, PASP, 107, 375
Reach, W. T., Sykes, M. V., Lien, D., & Davies, J. K. 2000, Icarus, 148, 80
Read, M. T., Bressi, T. H., Gehrels, T., Scotti, J. V., & Christensen, E. J. 2005, IAU Circ., 8624, 1
Schleicher, D. G. 2010, AJ, 140, 973
Snodgrass, C., Tubiana, C., Vincent, J.-B., et al. 2010, Nature, 467, 814
Stubbs, C. W., Doherty, P., Cramer, C., et al. 2010, ApJS, 191, 376
Tedesco, E. F., Noah, P. V., Noah, M., & Price, S. D. 2004, IRAS Minor Planet Survey, IRAS-A-FPA-3-RDR-IMPS-V6.0. NASA Planetary Data System
Tsiganis, K., Varvoglis, H., & Morbidelli, A. 2003, Icarus, 166, 131
Yang, B., & Hsieh, H. H. 2011, ApJ, 737, L39
York, D. G., Adelman, J., Anderson, J. E., Jr., et al. 2000, AJ, 120, 1579
Zappalà, V., Celliono, A., Farinella, P., & Knežević, Z. 1990, AJ, 100, 2030
Zappalà, V., Cellino, A., Farinella, P., & Milani, A. 1994, AJ, 107, 772

The Astrophysical Journal Letters, 748:L15 (7pp), 2012 March 20 doi:10.1088/2041-8205/748/1/L15

DISCOVERY OF MAIN-BELT COMET P/2006 VW_{139} BY Pan-STARRS1

Henry H. Hsieh[1,16], Bin Yang[1], Nader Haghighipour[1], Heather M. Kaluna[1], Alan Fitzsimmons[2], Larry Denneau[1], Bojan Novaković[3], Robert Jedicke[1], Richard J. Wainscoat[1], James D. Armstrong[1,4], Samuel R. Duddy[5], Stephen C. Lowry[5], Chadwick A. Trujillo[6], Marco Micheli[1], Jacqueline V. Keane[1], Laurie Urban[1], Timm Riesen[1], Karen J. Meech[1], Shinsuke Abe[7], Yu-Chi Cheng[7], Wen-Ping Chen[7], Mikael Granvik[8], Tommy Grav[9], Wing-Huen Ip[7], Daisuke Kinoshita[7], Jan Kleyna[1], Pedro Lacerda[2,17], Tim Lister[4], Andrea Milani[10], David J. Tholen[1], Peter Vereš[1], Carey M. Lisse[11], Michael S. Kelley[12], Yanga R. Fernández[13], Bhuwan C. Bhatt[14], Devendra K. Sahu[14], Nick Kaiser[1], K. C. Chambers[1], Klaus W. Hodapp[1], Eugene A. Magnier[1], Paul A. Price[15], and John L. Tonry[1]

[1] Institute for Astronomy, University of Hawaii, 2680 Woodlawn Drive, Honolulu, HI 96822, USA; hsieh@ifa.hawaii.edu
[2] Astrophysics Research Centre, Queens University Belfast, Belfast BT7 1NN, UK
[3] Department of Astronomy, Faculty of Mathematics, University of Belgrade, Studentski trg 16, 11000 Belgrade, Serbia
[4] Las Cumbres Observatory Global Telescope Network, Inc., 6740 Cortona Dr. Suite 102, Santa Barbara, CA 93117, USA
[5] Centre for Astrophysics and Planetary Science, The University of Kent, Canterbury CT2 7NH, UK
[6] Gemini Observatory, Northern Operations Center, 670 N. Aohoku Place, Hilo, HI 96720, USA
[7] Institute of Astronomy, National Central University, 300 Jhongda Rd, Jhongli 32001, Taiwan
[8] Department of Physics, 00014 University of Helsinki, P.O. Box 64, Helsinki, Finland
[9] Planetary Science Institute, 1700 East Fort Lowell, Suite 106, Tucson, AZ 85719, USA
[10] Dipartimento di Matematica, Università di Pisa, Largo Pontecorvo 5, 56127 Pisa, Italy
[11] Planetary Exploration Group, Space Department, Johns Hopkins University Applied Physics Laboratory, Laurel, MD 20723, USA
[12] Department of Astronomy, University of Maryland, College Park, MD 20742, USA
[13] Department of Physics, University of Central Florida, 4000 Central Florida Blvd., Orlando, FL 32816, USA
[14] Indian Institute of Astrophysics, CREST Campus, Block-II, Koramangala, Sarjapur Road, Bangalore 560034, India
[15] Department of Astrophysical Sciences, Peyton Hall, Princeton University, Princeton, NJ 08544, USA
Received 2012 January 20; accepted 2012 February 8; published 2012 March 2

ABSTRACT

The main-belt asteroid (300163) 2006 VW_{139} (later designated P/2006 VW_{139}) was discovered to exhibit comet-like activity by the Pan-STARRS1 (PS1) survey telescope using automated point-spread-function analyses performed by PS1's Moving Object Processing System. Deep follow-up observations show both a short ($\sim 10''$) antisolar dust tail and a longer ($\sim 60''$) dust trail aligned with the object's orbit plane, similar to the morphology observed for another main-belt comet (MBC), P/2010 R2 (La Sagra), and other well-established comets, implying the action of a long-lived, sublimation-driven emission event. Photometry showing the brightness of the near-nucleus coma remaining constant over ~30 days provides further evidence for this object's cometary nature, suggesting it is in fact an MBC, and not a disrupted asteroid. A spectroscopic search for CN emission was unsuccessful, though we find an upper limit CN production rate of $Q_{\rm CN} < 1.3 \times 10^{24}$ mol s^{-1}, from which we infer a water production rate of $Q_{\rm H_2O} < 10^{26}$ mol s^{-1}. We also find an approximately linear optical spectral slope of 7.2%/1000 Å, similar to other cometary dust comae. Numerical simulations indicate that P/2006 VW_{139} is dynamically stable for >100 Myr, while a search for a potential asteroid family around the object reveals a cluster of 24 asteroids within a cutoff distance of 68 m s^{-1}. At 70 m s^{-1}, this cluster merges with the Themis family, suggesting that it could be similar to the Beagle family to which another MBC, 133P/Elst-Pizarro, belongs.

Key words: comets: general – minor planets, asteroids: general

Online-only material: color figures

1. INTRODUCTION

Main-belt comets (MBCs) exhibit cometary activity indicative of ice sublimation yet are dynamically indistinguishable from main-belt asteroids (Hsieh & Jewitt 2006). Much of the current interest in studying MBCs lies in the possible role of main-belt objects in the primordial delivery of terrestrial water (e.g., Morbidelli et al. 2000). Of the first five known MBCs, one (176P/LINEAR) was discovered via a targeted search (Hsieh 2009), while the other four were discovered serendipitously or by untargeted surveys (Elst et al. 1996; Read et al. 2005; Garradd et al. 2008; Nomen et al. 2010). Using MBCs as tracers of ice in the asteroid belt to ascertain its potential for water delivery will require a much larger sample of these objects, and as such, discovering more MBCs, ideally in untargeted surveys (e.g., Gilbert & Wiegert 2009; Sonnett et al. 2011), is a high priority.

Recently, main-belt objects P/2010 A2 (LINEAR) and (596) Scheila have exhibited comet-like dust emission, but these events are likely due to impact-generated ejecta clouds (Jewitt et al. 2010, 2011; Snodgrass et al. 2010; Bodewits et al. 2011; Yang & Hsieh 2011; Ishiguro et al. 2011; Hainaut et al. 2012). As such, these objects are better characterized as disrupted asteroids. Hsieh et al. (2012a) considered the problem of distinguishing MBCs and disrupted asteroids, and concluded that recurrent activity separated by periods of inactivity to be the strongest observable indicator that activity is sublimation-driven, particularly when the timing of active episodes corresponds closely to an object's orbital period (cf. 133P/Elst-Pizarro and 238P/Read; Hsieh et al. 2004, 2010, 2011c). Evaluating this criterion requires monitoring an object for many years, however. When observations of only one active episode for an object are available, Hsieh et al. (2012a) suggested that steady or

[16] Hubble Fellow.
[17] Michael West Fellow.

increasing activity and morphological indicators could be used as preliminary evidence of sublimation. Direct spectroscopic detection of sublimation products (i.e., gas) in an MBC would immediately confirm its cometary nature. Given the difficulty of obtaining sufficiently high-quality spectroscopy of such distant and weakly active comets and of timing observations to coincide with peak gas production though, the absence of gas detections to date (Jewitt et al. 2009; Hsieh et al. 2012b) should not be considered confirmation of the absence of sublimation.

2. OBSERVATIONS

Observations of activity in P/2006 VW_{139} were first obtained by the 1.8 m Pan-STARRS1 (PS1) wide-field synoptic survey telescope on Haleakala. PS1 employs a $3.^{\circ}2 \times 3.^{\circ}2$ 1.4 gigapixel camera, consisting of a mosaic of 60 orthogonal transfer arrays, each comprising 64 590 × 598 pixel CCDs, and Sloan Digital Sky Survey (SDSS) i'- and z'-band-like filters designated i_{P1} and z_{P1} (Tonry et al. 2012).

Follow-up imaging was performed using the 2.0 m Faulkes Telescope North (FTN) on Haleakala and Faulkes Telescope South (FTS) at Siding Spring, the University of Hawaii (UH) 2.2 m telescope on Mauna Kea, the 1.8 m Perkins Telescope (PT) at Lowell Observatory, the 2.0 m Himalayan Chandra Telescope (HCT) at the Indian Astronomical Observatory on Mt. Saraswati, the 4.2 m William Herschel Telescope (WHT; Program SW2011b20) at La Palma, the 3.54 m New Technology Telescope (NTT; Program 185.C-1033(K)) operated by the European Southern Observatory (ESO) at La Silla, and the Lulin One-meter Telescope (LOT) in Taiwan. We employed 4096 × 4096 pixel Fairchild CCDs and either SDSS or Bessell filters for Faulkes observations, a 2048 × 2048 pixel Textronix CCD and Kron-Cousins filters for UH observations, the Perkins ReImaging System and Kron–Cousins filters for Perkins observations, a 2048 × 2048 pixel E2V CCD and Bessell filters for HCT observations, the WHT's auxiliary-port camera (ACAM; Benn et al. 2008) and SDSS filters on the WHT, the ESO Faint Object Spectrograph and Camera (Buzzoni et al. 1984) and Bessell filters on the NTT, and a VersArray:1300B CCD (Kinoshita et al. 2005) and Bessell-like filters on the LOT.

We performed standard bias subtraction and flat-field reduction (using dithered twilight sky images) for all data, except those from PS1, using Image Reduction and Analysis Facility (IRAF) software. PS1 data were reduced using the system's image processing pipeline (IPP; Magnier 2006). Photometry of Landolt (1992) standard stars and field stars was performed by measuring net fluxes within circular apertures, with background sampled from surrounding circular annuli. For data obtained under non-photometric conditions, absolute calibration was accomplished using SDSS field star magnitudes (Aihara et al. 2011). Conversion of r'-band PS1, FTN, FTS, and WHT photometry to R-band was accomplished using transformations derived by Tonry et al. (2012) and by R. Lupton (http://www.sdss.org/). Comet photometry was performed using circular apertures with varying radii depending on the nightly seeing, where background statistics were measured in nearby, but non-adjacent, regions of blank sky to avoid dust contamination from the comet.

We also obtained long-slit spectroscopy with ACAM (3500–9400 Å) on the WHT, as well as with the Gemini Multi-Object Spectrographs (GMOS; 3600–9400 Å; Hook et al. 2004) on the 8 m Gemini North (GN; Program GN-2011B-Q-16) and Gemini South (GS; Program GS-2011B-Q-51) observatories. For ACAM observations, we employed a $2.''0$ wide slit, giving a spectral resolution of $R \sim 300$, aligned with the object's dust tail. For GMOS observations, we employed B600 dispersers, 2×2 binning, and $1.''0$ wide slits, giving $R \sim 850$, aligned with the dust trail. Reduction of GMOS data was performed using an IRAF package provided by Gemini.

3. RESULTS

3.1. Discovery of Cometary Activity

All PS1 moving object detections are screened for potential cometary activity by automated point-spread function (PSF) analyses executed nightly by PS1's Moving Object Processing System (MOPS). This screening process divides the measured second PSF moment of each transient source by the expected PSF width as determined from the median of all stellar PSFs in the field. This "`psfextent`" parameter is then plotted as a function of a detection quality parameter ("`psfquality`") ranging from 0 to 1, roughly corresponding to a normalized signal-to-noise ratio. Sources that show comet-like `psfextent` parameters and `psfquality` > 0.5 (to screen out faint sources for which measured PSF moments are unreliable) are flagged for human inspection and possible observational follow-up (Figure 1).

PS1 observations on 2011 November 5 showed that the PSF of the known main-belt asteroid, (300163) 2006 VW_{139} (semimajor axis, $a = 3.052$ AU; eccentricity, $e = 0.201$; and inclination, $i = 3.^{\circ}24$), had an FWHM of $1.''3$, while nearby stars had PSFs with FWHMs of $1.''0$ (Hsieh et al. 2011a). Precovery observations also obtained by PS1 showed that the object exhibited a similar PSF excess on 2011 August 30. At the time, however, the object was too faint (`psfquality` < 0.5) and was not flagged for inspection. In both the relatively shallow August and November PS1 data, no extended cometary features were seen. Deeper follow-up observations (Table 1), however, revealed the presence of both an antisolar dust tail and an orbit-aligned dust trail (Figure 2; Section 3.2), leading to the object's re-designation as P/2006 VW_{139}.

3.2. Morphological and Photometric Analysis

The morphology observed for P/2006 VW_{139} from mid-November 2011 through 2012 January (shortly after perihelion) remains approximately constant (Figure 2). We observe the presence of a short dust tail (∼10″) pointed in the antisolar direction, a longer dust trail (∼60″) aligned with the object's orbit plane, and a coma with an intrinsic FWHM of ∼0.″7 when deconvolved with the seeing. This morphology is similar to that observed for MBC P/2010 R2 (La Sagra) (Hsieh et al. 2012b), as well as other well-established comets (e.g., 2P/Encke, C/Austin 1990 V; Lisse et al. 1998; Reach et al. 2000). Detailed dust modeling will be required to confirm the nature of the observed dust features, but a simple syndyne plot (Figure 2; cf. Finson & Probstein 1968) indicates that the antisolar tail is likely composed of small particles with short dissipation times (requiring recent emission to still be present), while the orbit-aligned trail is composed of large particles with slow dissipation times (likely requiring months to traverse the observed distance from the nucleus). The contemporaneous observation of both recent and old dust emission implies the action of a prolonged event, consistent with sublimation and inconsistent with an impulsive impact. We furthermore compute that particles with radii of $a_d = 0.1\ \mu$m should move 10″ from the nucleus in just 22 days, creating an observable gap between the antisolar tail and the nucleus. No such gap is observed between November

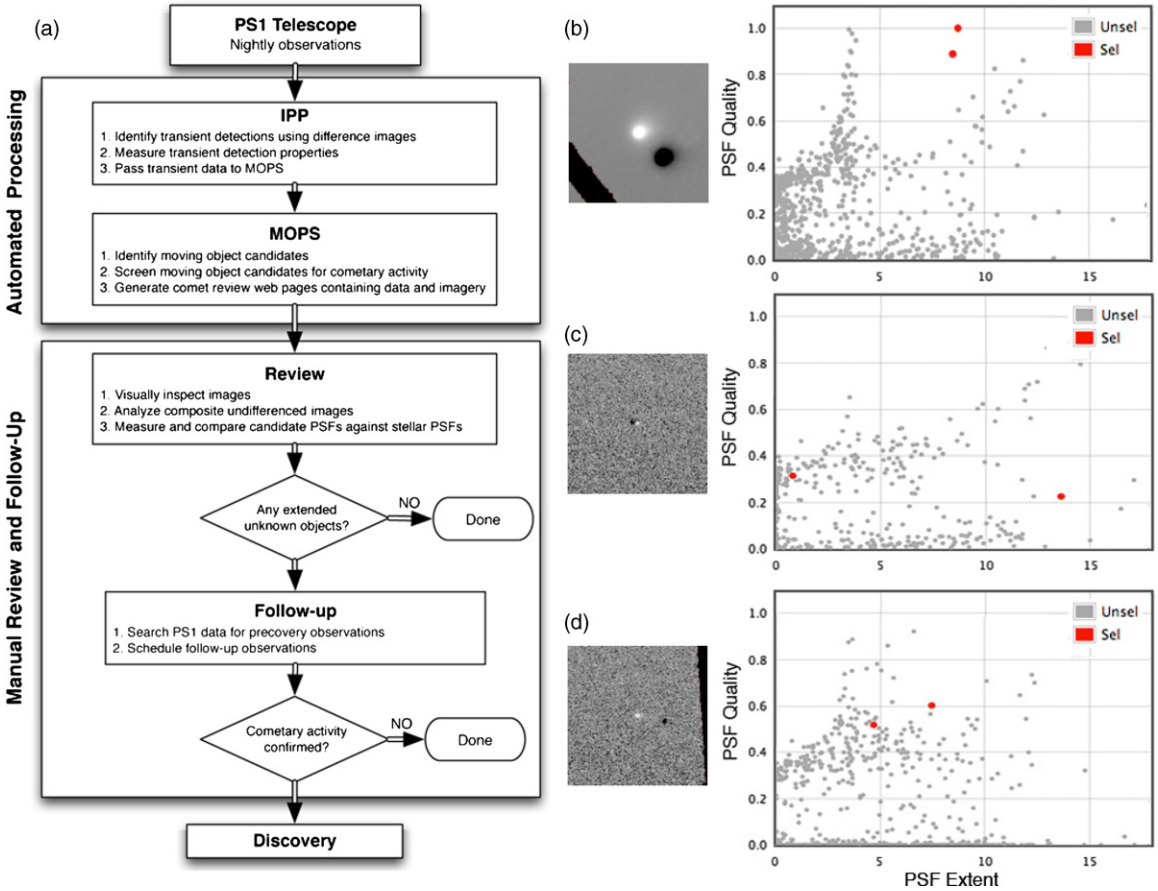

Figure 1. (a) Flowchart detailing PS1 comet screening procedures. (b) Difference image (left) and screening plot (right) for sample PS1 observations of 48P/Johnson where comet candidates ("selected") are plotted as red dots and "unselected" detections (generally consisting of inactive asteroids and false detections) are plotted as gray dots. (c) Image and screening plot for precovery observations of P/2006 VW_{139} on 2011 August 30. (d) Image and screening plot for discovery observations of P/2006 VW_{139} on 2011 November 5.

(A color version of this figure is available in the online journal.)

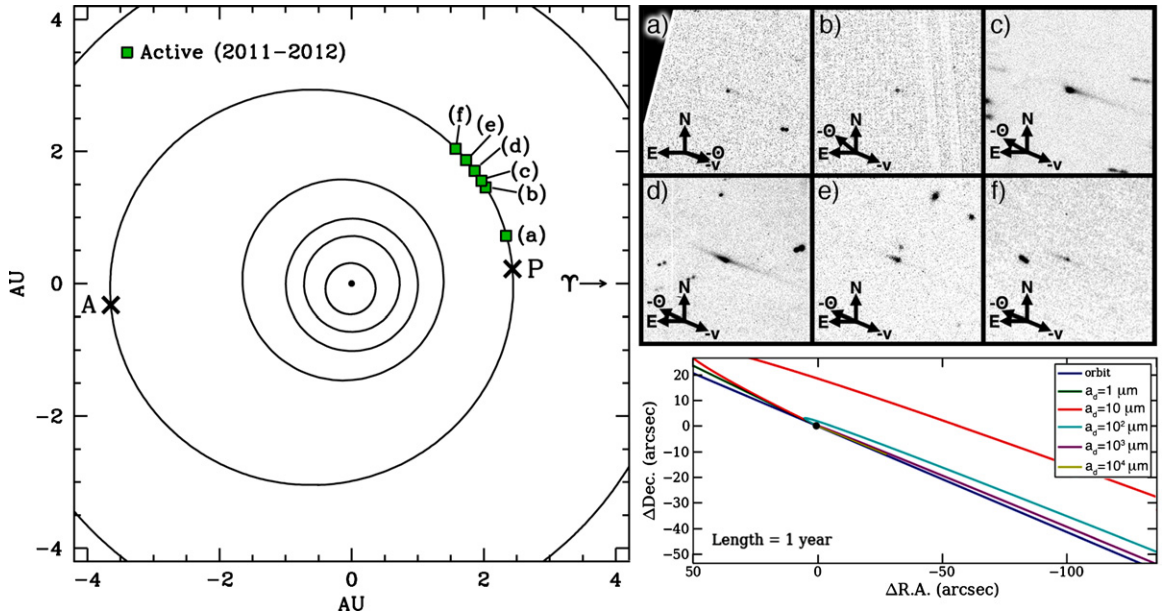

Figure 2. Orbital position plot (left) and composite images (upper right) constructed from observations detailed in Table 1, with the Sun (black dot) at the center, and the orbits of Mercury, Venus, Earth, Mars, P/2006 VW_{139}, and Jupiter shown as black lines. Perihelion (P) and aphelion (A) are marked with crosses. Plotted positions and images correspond to observations from (a) 2011 August 30, (b) 2011 November 5, (c) 2011 November 12–14 (November 14 UH composite image shown), (d) 2011 November 22–December 4 (December 4 NTT composite image shown), (e) 2011 December 16–19 (December 19 UH composite image shown), and (f) 2012 January 7. Each panel is 90″ × 90″ with the object at the center, and north (N), east (E), the antisolar vector ($-\odot$), and the negative heliocentric velocity vector ($-v$) marked with arrows. Also shown is a syndyne plot (lower right) for the 2011 November 22–December 4 period for a range of dust grain radii.

(A color version of this figure is available in the online journal.)

Table 1
Observations

UT Date	Tel.[a]	N[b]	t[c]	Filter	R[d]	Δ[e]	α[f]	ν[g]	PA$_{-\odot}$[h]	PA$_{-v}$[i]	α_{pl}[j]	$m(R, \Delta, \alpha)$[k]	$m_R(1, 1, 0)$[l]
2011 Jul 18	*Perihelion*.....				2.438	2.293	24.6	0.0	249.3	247.3	0.8	...	...
2011 Aug 30	PS1	2	60	z_{P1}	2.447	1.806	21.4	12.2	253.7	248.5	1.7	20.16 ± 0.14	15.6 ± 0.3
2011 Nov 05	PS1	2	90	i_{P1}	2.496	1.517	4.6	30.7	50.5	247.9	1.4	19.00 ± 0.09	15.1 ± 0.2
2011 Nov 12	FTN	11	660	r'	2.505	1.555	8.0	32.9	59.8	247.8	1.1	18.69 ± 0.09	15.1 ± 0.2
2011 Nov 14	UH	8	2400	R	2.506	1.561	8.4	33.2	60.4	247.7	1.1	18.62 ± 0.05	15.1 ± 0.2
2011 Nov 14	FTN	3	540	R	2.506	1.561	8.4	33.2	60.4	247.7	1.1	18.64 ± 0.05	15.1 ± 0.2
2011 Nov 18	PT	19	11100	R	2.510	1.586	10.0	34.3	62.2	247.7	0.9	18.60 ± 0.10	15.0 ± 0.2
2011 Nov 19	HCT	22	11400	R	2.512	1.596	10.6	34.6	62.8	247.6	0.9	18.64 ± 0.02	15.0 ± 0.2
2011 Nov 22	WHT	3	780	r'	2.516	1.621	11.9	35.5	63.8	247.6	0.8	18.89 ± 0.02	15.1 ± 0.2
2011 Nov 22	WHT	3	2700	spec.	2.516	1.621	11.9	35.5	63.8	247.6	0.8	...	...
2011 Nov 30	UH	5	3000	R	2.525	1.685	14.4	37.4	65.4	247.5	0.5	19.04 ± 0.02	15.1 ± 0.2
2011 Dec 02	GN	8	4800	spec.	2.527	1.704	15.0	38.0	65.7	247.5	0.4	...	...
2011 Dec 04	NTT	2	1200	R	2.530	1.724	15.6	38.5	66.0	247.4	0.4	19.12 ± 0.03	15.1 ± 0.2
2011 Dec 04	NTT	1	600	B	2.530	1.724	15.6	38.5	66.0	247.4	0.4	20.18 ± 0.03	...
2011 Dec 05	GS	6	3600	spec.	2.531	1.735	15.9	38.8	66.2	247.4	0.3	...	...
2011 Dec 16	FTS	12	720	r'	2.546	1.861	18.7	41.7	67.4	247.4	0.0	19.70 ± 0.09	15.3 ± 0.2
2011 Dec 19	UH	3	900	R	2.549	1.895	19.2	42.4	67.7	247.4	−0.1	19.68 ± 0.03	15.3 ± 0.2
2012 Jan 07	LOT	8	1440	R	2.577	2.152	21.7	47.4	69.2	247.6	−0.6	20.43 ± 0.10	15.7 ± 0.2
2014 Mar 13	*Aphelion*.....				3.660	2.697	4.5	180.0	278.6	294.1	−1.2	...	...
2016 Nov 08	*Perihelion*.....				2.436	1.823	21.3	0.0	65.1	248.2	1.1	...	...

Notes.
[a] Telescope.
[b] Number of exposures.
[c] Total integration time, in seconds.
[d] Heliocentric distance, in AU.
[e] Geocentric distance, in AU.
[f] Solar phase angle (Sun–object–Earth), in degrees.
[g] True anomaly, in degrees.
[h] Position angle of the antisolar vector, in degrees east of north.
[i] Position angle of the negative velocity vector, in degrees east of north.
[j] Orbit plane angle, in degrees.
[k] Mean apparent magnitude in specified filter.
[l] Absolute R-band magnitude (at $R = \Delta = 1$ AU and $\alpha = 0°$), assuming solar colors and IAU H, G phase-darkening where $G = 0.15$, where the listed uncertainty is dominated by the estimated uncertainty in G.

and January, implying continuous replenishment of the tail over this period, again consistent with cometary activity.

The disrupted asteroid (596) Scheila exhibited a 30% decline in coma brightness in 8 days (Jewitt et al. 2011). Meanwhile, other established MBCs exhibited steady or increasing coma brightness over longer periods of time (cf. Hsieh et al. 2012b). Photometry of P/2006 VW$_{139}$ (Table 1) shows no decline in near-nucleus brightness over 29 days between November and early December (though does show a 40% decline over 34 days between December and January). Coupled with our morphological analysis, the coma's photometric behavior over this period provides further support for the observed activity's sublimation-driven nature.

For reference, we compute the dust-to-nucleus scattering surface area ratio, A_d/A_N, determined for other MBCs (cf. Hsieh et al. 2012b). Lacking independent constraints at this time, we use the absolute R-band magnitude, $H_R = 16.4$ mag, computed by Spahr et al. (2009) only using observations obtained well before activity was discovered, and find $A_d/A_N \sim 2.5$ during the object's peak observed activity in November. This level of dust production relative to nucleus size is comparable to that of 133P and 176P, but an order of magnitude lower than for other MBCs, 238P, P/2008 R1 (Garradd), and P/La Sagra (Hsieh et al. 2012b). Multi-filter NTT observations (Table 1) indicate that the near-nucleus coma has an approximately Solar color of $B - R = 1.06 \pm 0.04$, similar to other MBCs (Jewitt et al. 2009; Hsieh et al. 2009b, 2010, 2011b, 2012b)

3.3. Spectroscopic Analysis

WHT spectroscopy was extracted using an aperture 10″ long along the slit centered on the target. A spectrophotometric standard, Feige 15, and a G2V solar analog star, HD 28099, were observed to allow removal of atmospheric absorption features and calculation of the relative reflectance spectrum. The resulting spectrum (Figure 3(a)) is approximately linear with a red slope of 7.2%/1000 Å, similar to that seen in other cometary dust comae (Kolokolova et al. 2004).

Gemini spectroscopy was extracted using an aperture 5.″1 long along the slit. A G5V solar analog star, HD 10097, was observed for approximate flux calibration and to calculate the relative reflectance spectra. The resulting GN and GS spectra (Figure 3(b)) are very similar. Given its slightly higher signal-to-noise ratio, however, we use the GN spectrum to compute gas production rates.

We measure the standard errors in three wavelength regions 70 Å in width and adopt the largest σ of 0.057 as the observational uncertainty of the violet CN emission band. We then employ a simple Haser (1957) model to derive the CN production rate (cf. Hsieh et al. 2012a; Jewitt & Guilbert-Lepoutre 2012), using a resonance fluorescence efficiency of $g[1\text{ AU}] = 3.63 \times 10^{-13}$ erg s^{-1} molecule^{-1} (Schleicher 2010). We find an upper limit to the CN production rate of $Q_{\rm CN} < 1.3 \times 10^{24}$ mol s^{-1}. No physical constraints on the CN to water production rate ratio in MBCs are currently available, but adopting the

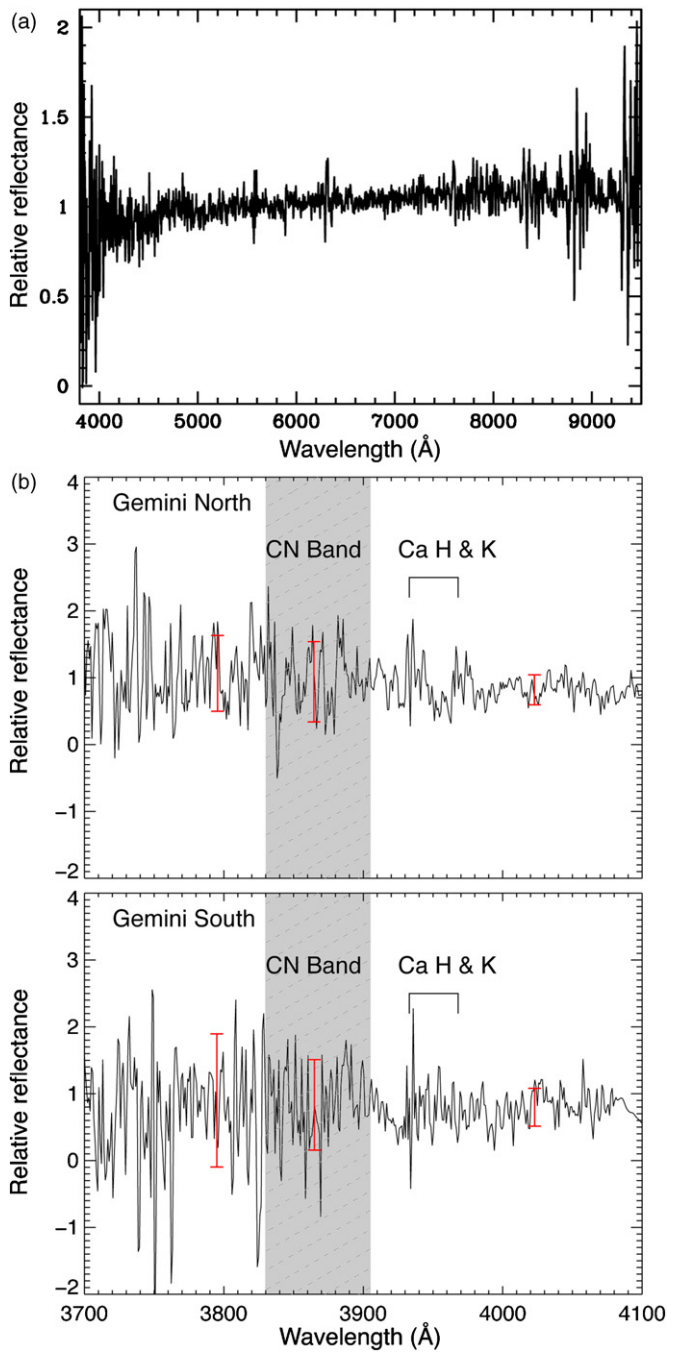

Figure 3. (a) Relative reflectance spectrum of P/2006 VW_{139} from the WHT. (b) Relative reflectance spectra of P/2006 VW_{139} from GN (upper panel) and GS (lower panel). Shaded regions indicate the wavelength region where the CN emission band is expected. Red error bars show 1σ uncertainties in the CN band region and in adjacent wavelength regions.

(A color version of this figure is available in the online journal.)

average ratio in other observed comets ($\log[Q_{CN}/Q_{OH}] = -2.5$; $Q_{OH}/Q_{H_2O} = 90\%$; cf. Hsieh et al. 2012a), we infer a water production rate of $Q_{H_2O} < 10^{26}$ mol s^{-1}.

3.4. Dynamical Analysis

To ascertain whether P/2006 VW_{139} is likely to be native to its current location, we analyze its dynamical stability (cf. Jewitt et al. 2009; Hsieh et al. 2012a, 2012b). We produce nine randomly generated sets of 100 Gaussian-distributed massless test particles in orbital element space, centered on the object's current osculating orbital elements, where three sets are characterized by σ values of $\sigma_a = 0.0001$ AU, $\sigma_e = 0.0001$, and $\sigma_i = 0.^{\circ}001$. These σ values are chosen to adequately explore the stability of the region. As a numbered asteroid, P/2006 VW_{139}'s true orbital element uncertainties are actually $\sim$100×–1000× smaller. Another three sets are characterized by σ values 10× as large, and the final three sets are characterized by σ values 100× as large. Treating the eight major planets as massive particles, we then use the *N*-body integration package, Mercury (Chambers 1999), to integrate the orbits of these test particles forward in time for 100 Myr. Limitations on computing resources unfortunately prevent us from conducting significantly longer integrations (e.g., $\geqslant$1 Gyr) in a reasonable amount of time.

We find that 5% of the 1σ test particles, 3% of the 10σ test particles, and 10% of the 100σ test particles exceed a heliocentric distance of 50 AU, and are effectively ejected from the asteroid belt, within 100 Myr (Figure 4). P/2006 VW_{139} itself is found to be stable over the 100 Myr test period (neglecting non-gravitational forces), consistent with its Lyapunov time of $T_{lyap} > 1$ Myr, where a body is considered stable if $T_{lyap} > 100$ kyr (Tsiganis et al. 2003). No systematic distribution is evident for ejected 1σ or 10σ test particles, though 44% of 100σ test particles with $a < 3.04$ AU are ejected, perhaps due to the 9J:4A mean-motion resonance with Jupiter at 3.029 AU (Figure 4(b)). For reference, P/2006 VW_{139} fluctuates between $a = 3.047$ AU and $a = 3.069$ AU over the course of our simulations.

As two MBCs (133P and 176P) belong to the ~2.5 Gyr old (Nesvorný et al. 2003) Themis asteroid family, and 133P additionally belongs to the young < 10 Myr Beagle sub-family (Nesvorný et al. 2008), we perform a search for any family associations that P/2006 VW_{139} may have. Employing hierarchical clustering method (Zappalà et al. 1990) analysis and analytically determined proper orbital elements retrieved on 2011 December 1 from AstDyS (http://hamilton.dm.unipi.it/astdys/), we compute the number of asteroids dynamically linked to P/2006 VW_{139} as function of cutoff distance, d_c (in velocity space). At $d_c = 63\,m\,s^{-1}$, we find a statistically significant clustering of 24 asteroids, which then merges with the Themis family at $d_c = 70\,m\,s^{-1}$ (Figure 4(c)). This possible P/2006 VW_{139} sub-family is separated from the main Themis family by several two- and three-body mean-motion resonances (11J:5A, 3J-2S-1A, and 1J+3S-1A) with Jupiter and Saturn, though our dynamical simulations indicate these resonances may be only weakly destabilizing (Figure 4(b)). P/2006 VW_{139}'s association with the Themis family is interesting because of the family's aforementioned association with 133P, 176P, and possibly 238P (Haghighipour 2009), though more detailed study is needed to clarify the nature of this association, as well as the significance of the possible sub-family.

4. DISCUSSION

While spectroscopy did not reveal any evidence of gas emission (Section 3.3), morphological and photometric analyses (Section 3.2) strongly suggest that the activity of P/2006 VW_{139} is cometary in nature, and not impact-driven. We conclude that this object is likely an MBC, making it the sixth such object discovered to date. The discovery circumstances of the known MBCs suggest that many more must exist, particularly in the outer main belt (Hsieh 2009). Therefore, we expect that current and next-generation all-sky surveys like Pan-STARRS

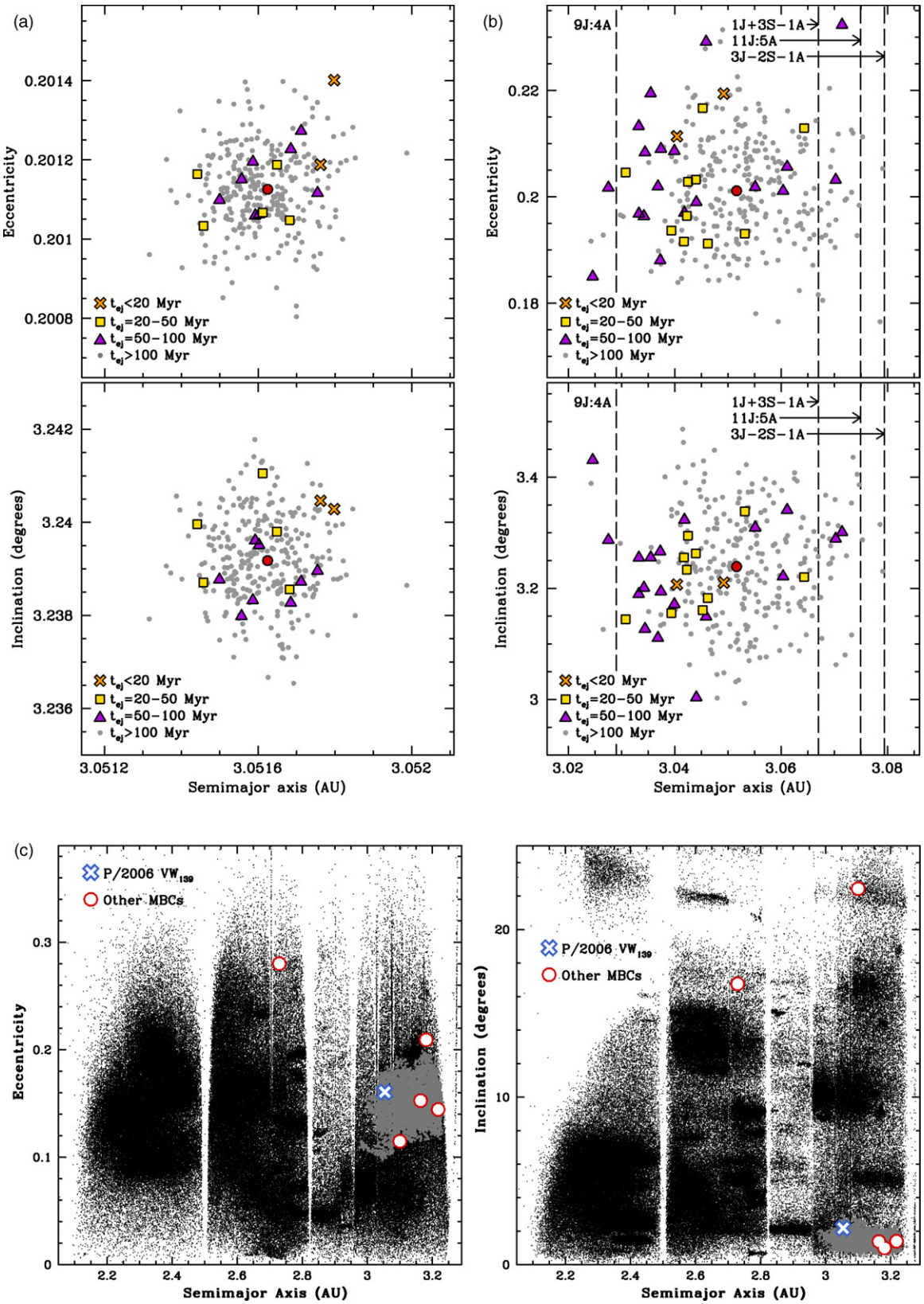

Figure 4. (a) Plots of semimajor axis versus eccentricity (top) and inclination (bottom) showing initial osculating elements of three 1σ sets of Gaussian-distributed test particles whose orbits are integrated for 100 Myr (Section 3.4), with the current osculating orbital elements of P/2006 VW_{139} shown as a red circle at the center of each panel. Particles ejected in <20 Myr, between 20 Myr and 50 Myr, and between 50 Myr and 100 Myr are plotted with orange X symbols, yellow squares, and purple triangles, respectively, while particles that are not ejected within 100 Myr are marked with gray dots. (b) Same as (a) but for 100σ test particle sets, where the positions of the 9J:4A, 1J+3S-1A, 11J:5A, and 3J-2S-1A mean-motion resonances are marked with dotted lines. (c) Plots of proper semimajor axis vs. proper eccentricity (left) and proper inclination (right) of main-belt asteroids (small black dots), Themis family members (small gray dots), P/2006 VW_{139} (blue X symbol), and other MBCs (red circles).

(A color version of this figure is available in the online journal.)

will reveal more of the true extent of the population in the coming years, provided that techniques can be deployed to efficiently screen for such objects amid the enormous amounts of data produced by these surveys. Thorough physical and dynamical investigations of each new discovered object will then be essential for first determining the most likely cause of the observed activity (cf. Hsieh et al. 2012a; Jewitt 2012), and then ascertaining the global properties of the population of objects confirmed as MBCs to better understand their implications for understanding terrestrial water delivery.

Additional observations of P/2006 VW_{139} itself are encouraged until the end (in 2012 March) of the 2011–2012 observing window to monitor the decline of activity for comparison to other MBCs (cf. Hsieh et al. 2011c, 2012b). Observations during the 2012–2013 observing window, when the object may be largely inactive, should be useful for determining its nucleus properties. By adding to our knowledge of the properties of inactive MBC nuclei (cf. Hsieh et al. 2009a; Licandro et al. 2011), the latter observations will help us better understand the relationship of active MBCs to the inactive main-belt population, perhaps facilitating the development of more powerful search methods, such as targeted monitoring of extremely likely MBC candidates. Furthermore, robust protocols for identifying icy objects, even in the absence of activity (which is transient even for known MBCs), will be crucial for ascertaining the true abundance and distribution of ice in the asteroid belt.

We appreciate comments from an anonymous referee that improved this manuscript. H.H.H. is supported by NASA through Hubble Fellowship Grant HF-51274.01 awarded by the Space Telescope Science Institute, which is operated by the Association of Universities for Research in Astronomy (AURA) for NASA, under contract NAS 5-26555. B.Y., N.H., H.M.K., and K.J.M. acknowledge support through the NASA Astrobiology Institute under Cooperative Agreement NNA08DA77A. B.N. is supported by the Ministry of Education and Science of Serbia (Project 176011). A.F. is supported by the Science and Technology Facilities Council (Grant ST/F002270/1). M.S.K. is supported by NASA Planetary Astronomy Grant NNX09AF10G. PS1 is operated by the PS1 Science Consortium and its member institutions, and also funded by NASA Grant NNX08AR22G issued through the NASA Science Mission Directorate's Planetary Science Division. Gemini is operated by AURA under a cooperative agreement with the National Science Foundation (NSF) on behalf of the Gemini partnership. The WHT is operated by the Isaac Newton Group in the Observatorio del Roque de los Muchachos of the Instituto de Astrofísica de Canarias. The Faulkes Telescopes are operated by Las Cumbres Observatory Global Telescope Network. SDSS-III (http://www.sdss3.org/) is funded by the Alfred P. Sloan Foundation, the Participating Institutions, NSF, and the U.S. Department of Energy Office of Science, and managed by the Astrophysical Research Consortium for the SDSS-III Collaboration.

REFERENCES

Aihara, H., Allende Prieto, C., An, D., et al. 2011, ApJS, 193, 29
Benn, C., Dee, K., & Agócs, T. 2008, Proc. SPIE, 7014, 229
Bodewits, D., Kelley, M. S., Li, J.-Y., et al. 2011, ApJ, 733, L3
Buzzoni, B., Delabre, B., Dekker, H., et al. 1984, ESO Messenger, 38, 9
Chambers, J. E. 1999, MNRAS, 304, 793
Elst, E. W., Pizarro, O., Pollas, C., et al. 1996, IAU Circ., 6456, 1
Finson, M. L., & Probstein, R. F. 1968, ApJ, 154, 327
Garradd, G. J., Sostero, G., Camilleri, P., et al. 2008, IAU Circ., 8969, 1
Gilbert, A. M., & Wiegert, P. A. 2009, Icarus, 201, 714
Haghighipour, N. 2009, Meteorit. Planet. Sci., 44, 1863
Hainaut, O. R., Kleyna, J., Sarid, G., et al. 2012, A&A, 537, A69
Haser, L. 1957, Bull. Soc. R. Sci. Liege, 43, 740
Hook, I. M., Jørgensen, I., Allington-Smith, J. R., et al. 2004, PASP, 116, 425
Hsieh, H. H. 2009, A&A, 505, 1297
Hsieh, H. H., Denneau, L., Wainscoat, R. J., et al. 2011a, CBET, 2920, 1
Hsieh, H. H., Ishiguro, M., Lacerda, P., & Jewitt, D. 2011b, AJ, 142, 29
Hsieh, H. H., & Jewitt, D. 2006, Science, 312, 561
Hsieh, H. H., Jewitt, D., & Fernández, Y. R. 2009a, ApJ, 694, L111
Hsieh, H. H., Jewitt, D. C., & Fernández, Y. R. 2004, AJ, 127, 2997
Hsieh, H. H., Jewitt, D., & Ishiguro, M. 2009b, AJ, 137, 157
Hsieh, H. H., Jewitt, D., Lacerda, P., Lowry, S. C., & Snodgrass, C. 2010, MNRAS, 403, 363
Hsieh, H. H., Meech, K. J., & Pittichová, J. 2011c, ApJ, 736, L18
Hsieh, H. H., Yang, B., & Haghighipour, N. 2012a, ApJ, 744, 9
Hsieh, H. H., et al. 2012b, AJ, in press
Ishiguro, M., Hanayama, H., Hasegawa, S., et al. 2011, ApJ, 741, L24
Jewitt, D. 2012, AJ, 143, 66
Jewitt, D., & Guilbert-Lepoutre, A. 2012, AJ, 143, 21
Jewitt, D., Weaver, H., Agarwal, J., Mutchler, M., & Drahus, M. 2010, Nature, 467, 817
Jewitt, D., Weaver, H., Mutchler, M., Larson, S., & Agarwal, J. 2011, ApJ, 733, L4
Jewitt, D., Yang, B., & Haghighipour, N. 2009, AJ, 137, 4313
Kinoshita, D., Chen, C.-W., Lin, H.-C., et al. 2005, Chin. J. Astron. Astrophys., 5, 315
Kolokolova, L., Hanner, M. S., Levasseur-Regourd, A.-C., & Gustafson, B. Å. S. 2004, in Comets II, ed. M. C. Festou, H. U. Keller, & H. A. Weaver (Tucson, AZ: Univ. Arizona Press), 577
Landolt, A. U. 1992, AJ, 104, 340
Licandro, J., Campins, H., Tozzi, G. P., et al. 2011, A&A, 532, A65
Lisse, C. M., A'Hearn, M. F., Hauser, M. G., et al. 1998, ApJ, 496, 971
Magnier, E. 2006, in Proc. Advanced Maui Optical and Space Surveillance Technologies Conference, ed. S. Ryan (Kihei: The Maui Economic Development Board), E50
Morbidelli, A., Chambers, J., Lunine, J. I., et al. 2000, Meteorit. Planet. Sci., 35, 1309
Nesvorný, D., Bottke, W. F., Levison, H. F., & Dones, L. 2003, ApJ, 591, 486
Nesvorný, D., Bottke, W. F., Vokrouhlický, D., et al. 2008, ApJ, 679, L143
Nomen, J., Marsden, B. G., Birtwhistle, P., et al. 2010, IAU Circ., 9169, 1
Reach, W. T., Sykes, M. V., Lien, D., & Davies, J. K. 2000, Icarus, 148, 80
Read, M. T., Bressi, T. H., Gehrels, T., Scotti, J. V., & Christensen, E. J. 2005, IAU Circ., 8624, 1
Schleicher, D. G. 2010, AJ, 140, 973
Snodgrass, C., Tubiana, C., Vincent, J.-B., et al. 2010, Nature, 467, 814
Sonnett, S., Kleyna, J., Jedicke, R., & Masiero, J. 2011, Icarus, 215, 534
Spahr, T. B., Williams, G. V., Marsden, B. G., Nakano, S., & Doppler, A. 2009, Minor Planets and Comets Orbit Supplement 157469, http://www.minorplanetcenter.net/iau/ECS/MPCarchive/2009/MPO_20090509.pdf
Tonry, J. L., et al. 2012, ApJ, submitted
Tsiganis, K., Varvoglis, H., & Morbidelli, A. 2003, Icarus, 166, 131
Yang, B., & Hsieh, H. H. 2011, ApJ, 737, L39
Zappalà, V., Cellino, A., Farinella, P., & Knežević, Z. 1990, AJ, 100, 2030

The Astrophysical Journal, 748:44 (7pp), 2012 March 20 doi:10.1088/0004-637X/748/1/44

GRB 071112C: A CASE STUDY OF DIFFERENT MECHANISMS IN X-RAY AND OPTICAL TEMPORAL EVOLUTION

K. Y. Huang[1], Y. Urata[2], Y. H. Tung[1,3], H. M. Lin[1,2], L. P. Xin[4], M. Yoshida[5,6], W. Zheng[7], C. Akerlof[7], S. Y. Wang[1], W. H. Ip[2], M. J. Lehner[1,8,9], F. B. Bianco[10,11], N. Kawai[12], D. Kuroda[6], S. L. Marshall[13], M. E. Schwamb[14], Y. Qiu[4], J. H. Wang[1], C. Y. Wen[1], J. Wei[4], K. Yanagisawa[6], and Z. W. Zhang[1]

[1] Institute of Astronomy and Astrophysics, Academia Sinica, P.O. Box 23-141, Taipei 106, Taiwan
[2] Institute of Astronomy, National Central University, Chung-Li 32054, Taiwan
[3] Institute of Astronomy and Department of Physics, National Tsing Hua University, Hsinchu 30013, Taiwan
[4] National Astronomical Observatories, Chinese Academy of Sciences, Beijing 100012, China
[5] Hiroshima Astrophysical Science Center, Hiroshima University, 1-3-1 Kagamiyama, Higashi-Hiroshima, Hiroshima 739-8526, Japan
[6] Okayama Astrophysical Observatory, National Astronomical Observatory of Japan, Kamogata, Asakuchi, Okayama 719-0232, Japan
[7] Department of Physics, University of Michigan, Ann Arbor, MI 48109, USA
[8] Department of Physics and Astronomy, University of Pennsylvania, 209 South 33rd Street, Philadelphia, PA 19104, USA
[9] Harvard-Smithsonian Center for Astrophysics, 60 Garden Street, Cambridge, MA 02138, USA
[10] Department of Physics, University of California Santa Barbara, Mail Code 9530, Santa Barbara, CA 93106-9530, USA
[11] Las Cumbres Observatory Global Telescope Network, Inc. 6740 Cortona Drive, Suite 102, Santa Barbara, CA 93117, USA
[12] Department of Physics, Tokyo Institute of Technology, 2-21-1 Ookayama, Meguro-ku, Tokyo 152-8551, Japan
[13] Kavli Institute for Particle Astrophysics and Cosmology, 2575 Sand Hill Road, MS 29, Menlo Park, CA 94025, USA
[14] Department of Physics, Yale University, P.O. Box 208121, New Haven, CT 06520-8121, USA
Received 2011 June 15; accepted 2012 January 12; published 2012 March 5

ABSTRACT

We present a study on GRB 071112C X-ray and optical light curves. In these two wavelength ranges, we have found different temporal properties. The *R*-band light curve showed an initial rise followed by a single power-law decay, while the X-ray light curve was described by a single power-law decay plus a flare-like feature. Our analysis shows that the observed temporal evolution cannot be described by the external shock model in which the X-ray and optical emission are produced by the same emission mechanism. No significant color changes in multi-band light curves and a reasonable value of the initial Lorentz factor ($\Gamma_0 = 275 \pm 20$) in a uniform interstellar medium support the afterglow onset scenario as the correct interpretation for the early *R* band rise. The result suggests that the optical flux is dominated by afterglow. Our further investigations show that the X-ray flux could be created by an additional feature related to energy injection and X-ray afterglow. Different theoretical interpretations indicate the additional feature in X-ray can be explained by either late internal dissipation or local inverse-Compton scattering in the external shock.

Key word: gamma-ray burst: individual (GRB 071112C)

1. INTRODUCTION

The *Swift* Gamma-Ray Explorer, launched in late 2004, has provided accurate positions for many gamma-ray bursts (GRBs), enabling a number of early X-ray and optical observations. The onboard X-Ray Telescope (XRT) data revealed that many GRBs have complicated evolutions (e.g., flare and shallow decay) and that their X-ray temporal evolution could be described by a three-component generic broken power law with an initial steep power-law decay ($F(\nu, t) \propto t^{-3\sim-5}$), followed by a very shallow decay ($F(\nu, t) \propto t^{-0.5}$) or a flare, finally changing to a steep decay ($F(\nu, t) \propto t^{-0.9\sim-1.3}$; Nousek et al. 2006; Zhang et al. 2006). These properties could be characterized by prompt emission from GRBs or a mixture of different emission components contributing to the observed X-ray emission (Willingale et al. 2007; Zhang 2007; Liang et al. 2009; Nardini et al. 2010). Early optical afterglow behaviors also show more diverse properties compared to the simpler late time evolutions. Panaitescu & Vestrand (2008) presented early afterglow behaviors of 28 known-redshift GRBs and grouped those GRBs as (1) fast-rising with peaks at about 100 s, (2) slow-rising with peaks after 100 s, (3) fast decay, and (4) plateau. They proposed that the angular asymmetry of the GRB ejecta viewed along different lines of sight generates the diversity of early optical afterglow light curves. A similar study with more samples was carried out by Kann et al. (2010) as well. They concluded that about 60% of early optical detections are the forward-shock-dominated afterglows.

Comparisons of X-ray and optical light curve have clearly shown that the evolutions for the two wavelengths are generally different (Panaitescu et al. 2006; Huang et al. 2007b). Significantly, there are GRBs whose decay indices during late-time evolution could not be explained by the external shock model in which X-ray and optical emission must be produced by the same emission mechanism (Urata et al. 2007). These studies suggest that the X-ray and optical emission are generated by different outflows. To explain possible emission mechanisms and provide reasonable interpretations, Ghisellini et al. (2007) proposed a late prompt emission scenario. They suggested that the late internal shocks with lower power could be created and superposed on the real afterglow emission of prompt GRB emission. However, it is still unclear how the early temporal evolution is affected by prompt emission and how long the prompt emission can sustain the overall temporal evolution. More extensive coverage of X-ray and optical observations are essential to solve this problem.

Recently, Liang et al. (2010) analyzed 32 GRBs with early smooth bumps in their early optical or X-ray light curves and investigated a possible relation with the initial Lorentz factor. They found that early bright X-ray emissions are usually dominated by non-forward shock components, but sometimes the forward shock emissions are observable in the X-ray

wavelength, and an achromatic feature in X-ray and optical is observed. In the study, they also discovered a good correlation between the initial Lorentz factor and the GRB apparent isotropic energy. Here, we examine our optical measurements of GRB 071112C as well as the corresponding simultaneous X-ray observations to explore their possible emission mechanisms.

On 2007 November 12, the *Swift* Burst Alert Telescope (BAT) detected GRB 071112C at 18:32:57 UT. This burst showed a single fast rise exponential decay peak and the measured T_{90} (15–350 keV) was 15 ± 12 s. The 80% total fluence in the 15–150 keV band was $(3.0 \pm 0.4) \times 10^{-6}$ erg cm^{-2}, which corresponded to a lower limit of isotropic energy $E_{\rm iso} = 5.3 \times 10^{51}$ erg at a redshift $z = 0.823$ (assume $H_0 = 70$ km s^{-1} Mpc^{-1}, $\Omega_{\rm M} = 0.3$, and $\Omega_\Lambda = 0.7$). The XRT started to observe this burst from 84 s after the BAT triggered. The XRT observations showed a smooth re-brightening around $t = 500$ s after the burst and followed a simple decay (Stratta et al. 2007). Two robotic optical telescopes, the ROTSE-IIIc and the TAOS, responded to this burst at 65 s and 93 s after the burst, respectively (Yuan et al. 2007; Huang et al. 2007a). In addition, the optical afterglow was observed by a number of ground telescopes in the *V*, *R*, *I*, *J*, and *K* bands (Uemura et al. 2007a; Wang et al. 2007; Klotz et al. 2007; Burenini et al. 2007; Chen et al. 2007; Nugent et al. 2007; Dintinjana et al. 2007; Ishimura et al. 2007; Greco et al. 2007; Stefano et al. 2007; Yoshida et al. 2007; Uemura et al. 2007b; Minezaki et al. 2007). The spectral measurements of the optical afterglow by the Very Large Telescope and the Gemini North telescope indicated that the redshift of this burst was 0.823 (Jakobsson et al. 2007; Cucchiara et al. 2007).

2. OPTICAL AND X-RAY TEMPORAL ANALYSIS

The ROTSE-IIIc and TAOS optical observations started around $t = 60$ s. The ROTSE-IIIc telescope (Akerlof et al. 2003) detected the GRB 071112C optical afterglow with brightness $R = 17.1 \pm 0.2$ at $t = 90.9$ s. At the same time, the optical afterglow was also detected by TAOS-A and TAOS-B telescopes (Lehner et al. 2009) with sequences of 1 s and 5 s exposures, respectively. Subsequently, a series of optical multi-band follow-up observations were also carried out by Xinglong 0.8 m and 1.0 m telescope in China (Zheng et al. 2008), the Lulin One-meter telescope (LOT) in Taiwan (Huang et al. 2005; Urata et al. 2005), and the 0.5 m MITSuME telescope in Japan (Kotani 2005). About one year after the burst, the host galaxy of GRB 071112C was clearly detected with the 3.8 m Canada–France–Hawaii Telescope (CFHT). The log of our optical observations is summarized in Table 1.

The optical images were processed by a standard procedure including bias and dark subtraction and flat-fielding using IRAF. The DAOPHOT package was used to perform point-spread function (PSF) photometry. Seven bright stars in the images were used to create the PSF model. The absolute photometric calibration for GRB field was determined using Landolt (Landolt et al. 1992) field SA 92, SA 95, and PG 0231+051 with a range of airmass. For calibration, we use 17 reference stars with colors similar to the afterglow ($V - R \sim 0.4$). Both photometric and systematic errors were included in the magnitude error. Besides our own observations, we re-calibrated the reported afterglow measurements by using the reference stars in the GRB 071112C field. Several measurements in GCN reports were calibrated by USNOB stars; the USNOB stars are on average 0.05 brighter than the stars of our calibration. Since the reference stars were provided by Burenini

Table 1
Observation Log of the GRB 071112C Optical Afterglow

$T_{\rm mid}$(s)	Filter	Exposure (s)	Mag	Telescope
738.7	*V*	300 s × 1	18.45 ± 0.10	Xinglong-1m
948.9	*V*	300 s × 1	18.60 ± 0.10	Xinglong-1m
1252.8	*V*	300 s × 1	19.13 ± 0.12	Xinglong-1m
1578.5	*V*	300 s × 1	19.74 ± 0.15	Xinglong-1m
1887.8	*V*	300 s × 1	19.77 ± 0.15	Xinglong-1m
2204.9	*V*	300 s × 1	19.67 ± 0.15	Xinglong-1m
2522.0	*V*	300 s × 1	19.67 ± 0.15	Xinglong-1m
2839.1	*V*	300 s × 1	20.15 ± 0.15	Xinglong-1m
3157.1	*V*	300 s × 1	20.35 ± 0.25	Xinglong-1m
3474.1	*V*	300 s × 1	20.18 ± 0.25	Xinglong-1m
3791.2	*V*	300 s × 1	20.05 ± 0.25	Xinglong-1m
4425.4	*V*	300 s × 3	20.67 ± 0.20	Xinglong-1m
5377.5	*V*	300 s × 3	20.31 ± 0.20	Xinglong-1m
7454.6	*V*	600 s × 5	20.89 ± 0.30	Xinglong-1m
90.9	*CR*	5 s × 5	17.10 ± 0.20	ROTSE-IIIc
147.0	*CR*	5 s × 5	17.40 ± 0.30	ROTSE-IIIc
273.3	*CR*	20 s × 5	17.10 ± 0.10	ROTSE-IIIc
96.2	*R*	5 s × 1	16.79 ± 0.15	TAOSB
104.4	*R*	5 s × 1	17.01 ± 0.17	TAOSB
112.6	*R*	5 s × 1	16.83 ± 0.14	TAOSB
120.8	*R*	5 s × 1	17.05 ± 0.15	TAOSB
129.0	*R*	5 s × 1	17.00 ± 0.16	TAOSB
137.2	*R*	5 s × 1	16.86 ± 0.17	TAOSB
145.4	*R*	5 s × 1	16.96 ± 0.16	TAOSB
157.7	*R*	5 s × 2	17.17 ± 0.12	TAOSB
174.1	*R*	5 s × 2	17.17 ± 0.18	TAOSB
190.5	*R*	5 s × 2	16.96 ± 0.14	TAOSB
206.9	*R*	5 s × 2	17.11 ± 0.15	TAOSB
223.3	*R*	5 s × 2	17.14 ± 0.12	TAOSB
231.7	*R*	5 s × 2	17.16 ± 0.12	TAOSB
256.1	*R*	5 s × 2	17.11 ± 0.14	TAOSB
272.5	*R*	5 s × 2	17.42 ± 0.18	TAOSB
288.9	*R*	5 s × 2	17.14 ± 0.16	TAOSB
309.5	*R*	5 s × 3	17.52 ± 0.22	TAOSB
330.3	*R*	5 s × 3	17.28 ± 0.13	TAOSB
359.7	*R*	5 s × 3	17.63 ± 0.15	TAOSB
384.6	*R*	5 s × 3	17.48 ± 0.17	TAOSB
409.2	*R*	5 s × 3	17.45 ± 0.22	TAOSB
437.9	*R*	5 s × 4	17.75 ± 0.18	TAOSB
470.7	*R*	5 s × 4	17.57 ± 0.15	TAOSB
520.3	*R*	5 s × 4	18.42 ± 0.31	TAOSB
573.2	*R*	5 s × 7	17.81 ± 0.19	TAOSB
630.7	*R*	5 s × 7	18.14 ± 0.24	TAOSB
701.1	*R*	5 s × 7	18.15 ± 0.22	TAOSB
824.7	*R*	5 s × 20	18.36 ± 0.22	TAOSB
1112.4	*R*	5 s × 50	19.01 ± 0.29	TAOSB
1894.6	*R*	5 s × 140	19.23 ± 0.26	TAOSB
124.4	*CR*	20 s × 1	17.13 ± 0.12	TNT-0.8m
160.7	*CR*	20 s × 1	16.82 ± 0.10	TNT-0.8m
184.0	*CR*	20 s × 1	17.30 ± 0.12	TNT-0.8m
206.5	*CR*	20 s × 1	17.04 ± 0.12	TNT-0.8m
228.9	*CR*	20 s × 1	17.37 ± 0.15	TNT-0.8m
252.3	*CR*	20 s × 1	17.31 ± 0.15	TNT-0.8m
274.8	*CR*	20 s × 1	17.26 ± 0.15	TNT-0.8m
297.2	*CR*	20 s × 1	17.43 ± 0.15	TNT-0.8m
343.0	*CR*	20 s × 1	17.42 ± 0.15	TNT-0.8m
366.3	*CR*	20 s × 1	17.48 ± 0.15	TNT-0.8m
388.8	*CR*	20 s × 1	17.62 ± 0.15	TNT-0.8m
412.1	*CR*	20 s × 1	17.35 ± 0.15	TNT-0.8m
434.6	*CR*	20 s × 1	17.68 ± 0.15	TNT-0.8m
457.0	*CR*	20 s × 1	17.87 ± 0.20	TNT-0.8m
480.4	*CR*	20 s × 1	17.80 ± 0.20	TNT-0.8m
502.8	*CR*	20 s × 1	17.87 ± 0.20	TNT-0.8m
525.3	*CR*	20 s × 1	17.66 ± 0.25	TNT-0.8m
548.6	*CR*	20 s × 1	18.44 ± 0.30	TNT-0.8m
571.1	*CR*	20 s × 1	18.12 ± 0.25	TNT-0.8m

Table 1
(Continued)

T_{mid}(s)	Filter	Exposure (s)	Mag	Telescope
632.4	*R*	60 s × 1	18.00 ± 0.15	TNT-0.8m
711.1	*R*	60 s × 1	18.28 ± 0.20	TNT-0.8m
789.7	*R*	60 s × 1	18.34 ± 0.20	TNT-0.8m
867.5	*R*	60 s × 1	18.46 ± 0.20	TNT-0.8m
946.2	*R*	60 s × 1	18.40 ± 0.20	TNT-0.8m
1063.6	*R*	60 s × 2	18.72 ± 0.15	TNT-0.8m
1262.3	*R*	60 s × 3	19.13 ± 0.20	TNT-0.8m
1740.1	*R*	300 s × 2	19.11 ± 0.10	TNT-0.8m
2376.0	*R*	300 s × 2	19.67 ± 0.15	TNT-0.8m
3170.0	*R*	300 s × 3	19.51 ± 0.15	TNT-0.8m
4123.0	*R*	300 s × 3	20.03 ± 0.20	TNT-0.8m
5243.6	*R*	300 s × 4	20.03 ± 0.20	TNT-0.8m
186.0	*Rc*	60 s × 1	17.11 ± 0.11	MITSuMe
280.5	*Rc*	60 s × 2	17.46 ± 0.11	MITSuMe
536.5	*Rc*	60 s × 5	18.03 ± 0.15	MITSuMe
911.5	*Rc*	60 s × 5	18.49 ± 0.23	MITSuMe
1934.5	*Rc*	60 s × 19	19.21 ± 0.25	MITSuMe
6372.0	*Rc*	300 s × 6	20.3 ± 0.3	LOT
69620.3	*Rc*	300 s × 12	22.7 ± 0.2	LOT
3.3×10^7	r'	300 s × 4	24.27 ± 0.19	CFHT
187.0	*Ic*	60 s × 1	16.57 ± 0.12	MITSuMe
289.0	*Ic*	60 s × 1	16.81 ± 0.15	MITSuMe
331.0	*Ic*	60 s × 1	16.73 ± 0.14	MITSuMe
514.5	*Ic*	60 s × 2	17.22 ± 0.14	MITSuMe
816.0	*Ic*	60 s × 6	17.87 ± 0.17	MITSuMe
1707.5	*Ic*	60 s × 6	19.03 ± 0.32	MITSuMe

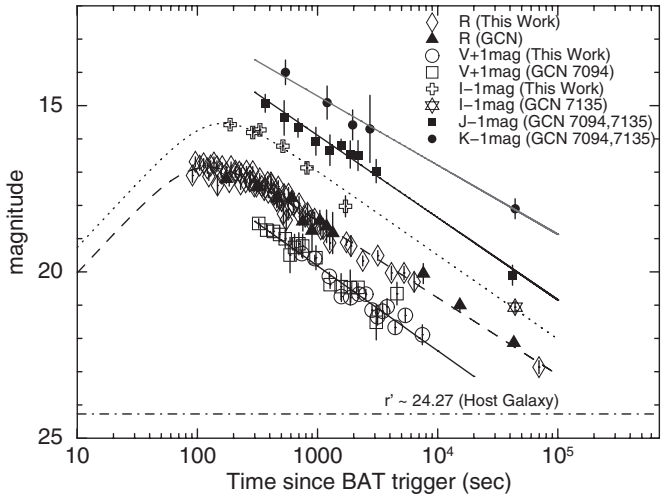

Figure 1. Optical light curves of GRB 071112C: the solid line presents the best fit by the single power-law model [$F \propto t^{-\alpha}$] for the *V* band ($\alpha_V = 1.02 \pm 0.05$), *J* band ($\alpha_V = 0.99 \pm 0.04$), and the *K* band ($\alpha_V = 0.83 \pm 0.04$). The dashed and dotted lines indicate the best fit by the broken power law [$F(\nu, t) = F^*_\nu/[(t/t_b)^{\alpha_1} + (t/t_b)^{\alpha_2}]$] with the *R* band ($\alpha_{R1} = -1.54 \pm 0.62$, $\alpha_{R2} = 0.92 \pm 0.02$, and $t_{Rb} = 99.4 \pm 7.3$ s) and with the *I* band ($\alpha_{I1} = -1.54$ (fix), $\alpha_{I2} = 1.01 \pm 0.04$, and $t_{Ib} = 138.3 \pm 32.7$ s), respectively. The dot-dashed line shows r'-band brightness of GRB 071112C host galaxy.

et al. (2007) and Uemura et al. (2007a, 2007b), we measured these stars from our LOT *R*-band and Xinglong *V*-band images and obtained their averaged magnitude and rms errors. The results were then used to re-calibrated the reported afterglow magnitude. The uncertainties with 1σ level confidence were adopted in this paper.

As shown in Figure 1, the *V*-, *R*-, and *I*-band light curves of GRB 071112C can be expressed in terms of a power law with $F(t) \propto t^{-\alpha_{opt}}$. Here, each α_{opt} is the power-law index in

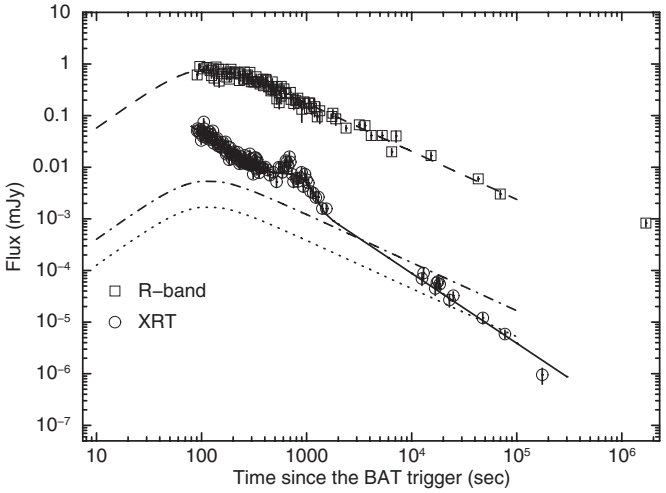

Figure 2. Observed X-ray and the *R*-band light curves and the expected X-ray flux from external shock model: the dashed line shows the best *R*-band fit presented in the Figure 1. The solid line presents the best fit with X-ray by a single power-law decay plus a Gaussian function. The dot-dashed line presents the maximum expected X-ray flux from external shock model($F_{x,exp} \propto F_{opt}(\nu_x/\nu_o)^{-0.61}$). The dotted line shows the expected X-ray flux in the region of $\nu_o < \nu_c < \nu_x$ ($F_{x,exp} \propto F_{opt}\ (\nu_c/\nu_o)^{-0.61}(\nu_x/\nu_c)^{-1.12}$); here the value $\nu_c = 10^7$ Hz is from Uehara et al. (2010).

each optical band. We find $\alpha_V = 1.02 \pm 0.05$ ($\chi^2/\nu = 1.51$ for $\nu = 28$) from *V*-band data, $\alpha_R = 0.85 \pm 0.02$ ($\chi^2/\nu = 2.16$ for $\nu = 76$) from *R*-band data, and $\alpha_I = 0.96 \pm 0.05$ ($\chi^2/\nu = 1.79$ for $\nu = 5$) from *I*-band data. Besides our optical data, we also analyzed the calibrated NIR measurements by Uemura et al. (2007b) and Minezaki et al. (2007). The *J*- and *K*-band light curves could be expressed by a single power law with index $\alpha_J = 0.99 \pm 0.04$ ($\chi^2/\nu = 0.38$ for $\nu = 8$) and $\alpha_K = 0.83 \pm 0.04$ ($\chi^2/\nu = 0.18$ for $\nu = 3$), respectively.

Note that the *R*-band light curve demonstrates a plateau in the early evolution. We next fit the *R*-band measurements with a broken power-law function, $F(\nu, t) = F^*_\nu/[(t/t_{Rb})^{\alpha_{R1}} + (t/t_{Rb})^{\alpha_{R2}}]$, where t_{Rb} is the break time in *R*-band light curve, α_{R1} and α_{R2} are the power-law indices before and after the *R*-band break time t_{Rb}, and F^*_ν is the flux at t_{Rb}. We obtain $\alpha_{R1} = -1.54 \pm 0.62$, $\alpha_{R2} = 0.92 \pm 0.02$, and $t_{Rb} = 99.4 \pm 7.3$ s ($\chi^2/\nu = 1.25$ for $\nu = 74$). The smaller chi-square value indicates that the broken power-law function is a reasonable fitting function to explain the *R*-band evolution in GRB 071112C and implies a rising behavior in early *R*-band light curve.

Figure 2 shows the *R*-band and XRT light curves of GRB 071112C. The XRT 0.3–10 keV light curve was downloaded from the *Swift*/XRT GRB light curve repository (Evans et al. 2007). To plot the *R*-band and X-ray light curves on a consistent scale, we converted the afterglow brightness to units of mJy. It is clear that a Gaussian-shaped flare appeared in the XRT light curve around $t = 500$ s after the burst. The XRT light curve can be fit with a single power law plus a Gaussian function ($F(t) = A_0 \times t^{-\alpha_x} + A_1 \times e^{-(t-A_2)^2/2A_3^2}$), where A_0 is a constant value, α_x is the single power-law index, A_1 is peak intensity at peak position A_2, and A_3 is the width of the Gaussian feature. The best-fit parameters are $\alpha_x = 1.36 \pm 0.02$, $A_0 = 23.51 \pm 2.12$, $A_1 = 4.23 \pm 0.5\ \mu$Jy, $A_2 = 763.13 \pm 35.05$ s, and $A_3 = 274.91 \pm 33.44$ s ($\chi^2/\nu = 1.27$ for $\nu = 117$). If we exclude the flare component, the overall XRT light curve could be well fit by a single power law with an index $\alpha_x = 1.36 \pm 0.02$. The afterglow decayed with an index of -1.36, consistent

with the analysis of Uehara et al. (2010). A flare occurred around $t = 500$ s following the burst and approached the original maximum brightness of 4.23 μJy. After the flare emission became weak, the afterglow emission again dominated the X-ray light curve and continued to decay with the same index ($\alpha_x = 1.36$) to the end of the XRT observations. The X-ray flare seems superposed on the X-ray decelerated temporal evolution and did not change the overall X-ray afterglow evolution significantly.

This analysis of X-ray and *R*-band light curve of GRB 071112C shows that the X-ray light curve was composed of a single power-law ($\alpha_x \sim 1.36$) decay plus a small flare while the *R*-band light curve exhibits a bump followed by a shallower single power-law decay ($\alpha_o \sim 0.92$).

3. DISCUSSION

3.1. Early Bump in Optical Light Curve

In the *Swift* era, many early optical afterglows show localized peaks, plateaus, or simple power-law decay behavior. A simple power-law decay is usually associated with a relativistic blast wave decelerated by its interaction with the ambient medium. Unfortunately, the nature of localized peaks and plateaus are unclear. Panaitescu & Vestrand (2008) proposed that the peak and plateau features could be caused by a structured outflow seen at different directions from the GRB ejecta. The different off-axis viewing angles produce different features in early optical light curves. The afterglows with plateaus have larger viewing angles than those with sharper peaks.

Alternatively, the afterglows with plateaus could be simply produced by long-lived GRBs which display shallow decay in the light curves and continue for up to 10^4 s after the GRB onset (Panaitescu & Vestrand 2011; Kann et al. 2010). Besides the interpretations we mentioned above, the optical afterglow peaks could also be produced by the onset of a normal afterglow or the passage of the synchrotron typical peak frequency.

Our analysis shows that the GRB 071112C *R*-band light curve peaked around 99 s after the burst and then decayed with an index of 0.92 until 6.9×10^4 s. The observed temporal evolution is not consistent with observers located off-axis of the GRB jet (Granot et al. 2002), which should peak thousands of seconds after the initial occurrence. For the scenario of long-lived GRBs, energy from the GRB ejecta could continue to supply and power the ambient medium surrounding the burst. The afterglow emission from the ambient medium could continuously be supplied and display plateaus or shallow decays in afterglow light curves. Similar features should be found in both the X-ray and optical light curves. Although the rising part in the *R* band was not visible in our measurements, the short duration peak in GRB 071112C implies that it is unlikely an example of the long-lasting plateau feature of long-lived GRBs (Zhang et al. 2006; Panaitescu & Vestrand 2008). In addition, in Figure 2, a comparison of X-ray and *R*-band light curves of GRB 071112C shows very different temporal evolutions for the two wavelengths. This indicates that the mechanism of long-lasting shallow decay produced by long-lived GRB ejecta cannot explain the observed X-ray and optical temporal evolution.

For the case of synchrotron frequency passage, the external shock model (Sari et al. 1998) predicts that the optical temporal light curve ($F_{t,\nu_{opt}} \sim t^{-\alpha}\nu^{-\beta}$) will show an initial increase with $t^{0.5}$, until the synchrotron peak (t_m) after which a power-law decay $t^{3(p-1)/4}$ will follow. Here, p is the electron spectral index and the ambient medium is assumed uniform. This model predicts that the passing times at different wavelengths should follow $t_1/t_2 \propto (\nu_1/\nu_2)^{(-2/3)}$. Chromatic breaks and color change are two significant clues in multi-band light curves to verify the passage of the synchrotron peak frequency.

Our *R*-band light curve is composed of a possible power law rising with index $\alpha_{R1} = -1.54 \pm 0.62$, a peak of brightness at $t_{Rb} = 99.4 \pm 7.3$ s followed by a decay with index $\alpha_{R2} = 0.92 \pm 0.02$. The *I*-band measurements could not be well fitted with a single power-law decay, which implies it has similar temporal property to that observed in the *R* band. To model the *I*-band measurements with more complicated formulae, we first fixed the rising power-law index, $\alpha_{I1} = -1.54$, to be the same as the *R* band and then fit the *I*-band light curve with a broken power-law formula. We found that the break time in the *I* band is $t_{Ib} = 138.3 \pm 32.7$ s after which follows a power-law decay $\alpha_{I2} = 1.01 \pm 0.04$ ($\chi^2/\nu = 1.04$ for $\nu = 4$). This fit is better than the single power-law fit. If the *R*-band peak was produced by the passage of the synchrotron peak frequency, the estimated *I*-band break time from external model will be at $t_I = 115.5 \pm 8.5$ s. The result is consistent with the break time from a broken power-law fit. However, few *I*-band measurements yielded large error of *I*-band break time and given the uncertainties to confirm the synchrotron peak frequency at *I* band. Fortunately, there is no significant color change between our *R*- and *I*-band measurements. An achromatic NIR evolution was also reported by Uehara et al. (2010), and which supports our optical results and indicates achromatic evolution in the *R*- and *I*-band light curves. The peak in the *R* band is thus unlikely due to the passage of the synchrotron peak.

In the scenario of afterglow onset, achromatic evolution is predicted in the multi-band light curves. Such GRBs are generated from high relativistic injection fireballs (Meśzaŕos 2002; Zhang & Meśzaŕos 2004; Piran 2004). The fireball maintains constant velocity until it sweeps up a significant amount of ambient medium and then is decelerated by the ambient medium to produce a smooth local peak in the afterglow light curve. During this process, the Lorentz factor, Γ, decreases. The peak time of the bump, from theoretical prediction, demonstrates that roughly half of the fireball energy is transferred to the medium and is detectable in the early afterglow light curve. For some bursts, in which the reverse shock component would not show up in the optical band, the smooth local peak signals the deceleration feature of the fireball and can be used to constrain the initial Lorentz factor and the deceleration radius (Sari & Piran 1999; Zhang et al. 2003; Kobayashi & Zhang 2007; Liang et al. 2010). In addition, this theory predicts that the peak should be sensitive to the initial Lorentz factor Γ_0 but is insensitive to other parameters.

Molinari et al. (2007) studied the NIR early peaks of GRB 060418 and GRB 060607A and concluded that such features could be explained by the onset of afterglows. Their estimated values of initial Lorentz factor (Γ_0) are consistent with predictions ($50 \lesssim \Gamma_0 \lesssim 1000$) from the standard fireball model (Piran 2000; Soderberg & Ramirez-Ruiz 2002; Meśzaŕos 2006). With the formula in Molinari et al. (2007), we calculated the expected time for the *R*-band light curve to reach its maximal brightness for GRB 071112C. The peak time $t_{peak} = t_b(-\alpha_{R1}/\alpha_{R2})^{1/(\alpha_{R2}-\alpha_{R1})}$ is 123 ± 8 s. The initial Lorentz factor Γ_0 is $\approx 257 \pm 20$ for a constant density medium and $\approx 69 \pm 6$ for a wind environment. In the wind environment, the interstellar medium (ISM) density distribution around a massive star can be defined as $n(r) = A \times (r)^{-2}\,\mathrm{cm}^{-3}$, where A is a constant. The estimated initial Lorentz factor is consistent

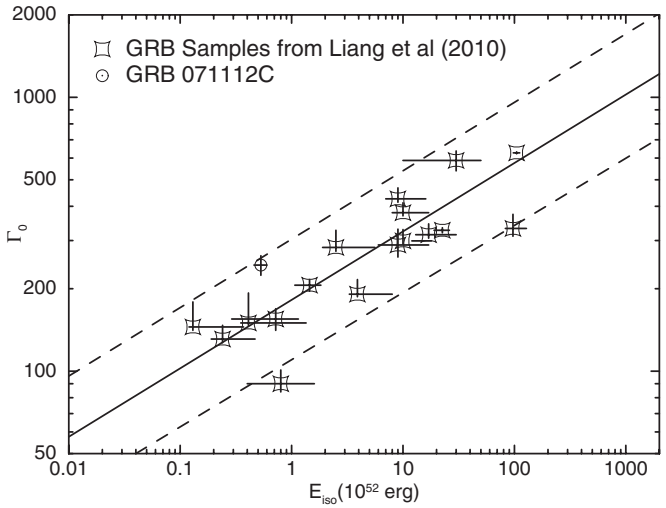

Figure 3. Correlation between Γ_0 and E_{iso}. The open stars shows optical selected samples from Liang et al. (2009) and the open circle presents the value of GRB 071112C derived from our *R*-band measurements. The solid and dashed lines are $\Gamma_0 \simeq 182 E_{\gamma,iso,52}^{0.25\pm0.03}$ and 2σ, respectively (Liang et al. 2009). This diagram shows that the derived initial Lorentz factor (Γ_0) and isotropic energy are fit in with other GRBs with bump-like feature in early optical light curves.

with the theoretical prediction at the lower end. On the other hand, Liang et al. (2010) found that when GRBs show onset feature in their early optical or X-ray light curves, their initial Lorentz factor, Γ_0, and GRB isotropic energy, E_{iso}, follow an empirical relation $\Gamma_0 \simeq 182 E_{iso,52}^{0.25\pm0.03}$. Here $E_{iso,52}$ is the GRB isotropic energy in units of 10^{52} erg and a uniform GRB ambient medium is assumed. Our estimation shows the initial Lorentz factor of GRB 071112C is $\Gamma_0 \sim 260$. Figure 3 depicts the empirical correlation between Γ_0 and $E_{iso,52}$. With the isotropic energy at $z = 0.823$, isotropic energy ($E_{iso,52} \sim 0.53$ erg) of GRB 071112C follows the empirical relation within the 2σ range. This analysis thus further supports the conclusion that the bump in GRB 071112C is most likely the onset afterglow at optical wavelengths.

3.2. Different Origin of X-ray and Optical Emission

As we have discussed, optical and X-ray light curves in GRB 071112C have different evolutions and the rising part of the *R*-band light curve is likely related to the onset of afterglow. In fact, several observations and studies show that the X-ray and optical light curves are often different and inconsistent with the external shock model in which X-ray and optical emission are produced by the same emission mechanisms (Panaitescu et al. 2006; Urata et al. 2007; Liang et al. 2009). Those GRBs usually have complicated and diverse temporal evolutions.

Urata et al. (2007) investigated the late temporal properties of 14 GRBs and found that a fraction of the events are outliers of the external shock model at normal decay phase in which neither the delayed energy injection nor time dependency of shock microphysics were considered. Uehara et al. (2010) studied the NIR to X-ray spectral energy distribution of GRB 071112C and concluded that the observed NIR to X-ray SEDs is consistent with the expectation from the normal afterglow component and that the cooling break (ν_c) is between the optical and X-ray bands. In other words, spectral evolution of the observed GRB 071112C should be in the region of $\nu_m < \nu_o < \nu_c < \nu_x$ and follow the relationships predicted by external shock models, $\alpha_o - \alpha_x > -1/4$ for uniform ambient median or $\alpha_o - \alpha_x < 1/4$ for stellar wind with a density variation $\rho \propto r^{-2}$ (Urata et al. 2007). The X-ray temporal power-law decay index, excluding the flare component, is $\alpha_x \sim 1.36$, and the optical decay index (after the bump feature) is $\alpha_o \sim 0.92$. The observed difference of power-law indices, $\alpha_o - \alpha_x = -0.44 \pm 0.03$ for GRB 071112C, is an outlier of the external shock model and suggests different origins or radiation processes for X-ray and optical emissions.

Nearly half of all *Swift* bursts have distinct X-ray flares and they are most likely due to late prompt emission caused by late central engine activity (Zhang et al. 2006; Falcone et al. 2007). Chincarini et al. (2010) and Bernardini et al. (2011) investigated early- and late-time X-ray flares and concluded that the internal shock origin is the most promising explanation for X-ray flares. Those studies give strongly indications that X-ray flares have a common origin with gamma-ray pulses. Besides, the presence of an underlying continuum with same slope before and after the flaring activity excluded the possibility that flares are related to the afterglow emission by forward external shocks. These investigations implies that additional energy is needed to produce the chromatic temporal properties in X-ray and optical wavelengths.

To explain the origin of both X-ray and optical evolutions constantly, Ghisellini et al. (2007) proposed that the observed X-ray and optical fluxes could be modified by two emission components. One is the afterglow emission produced by forward shocks. Another is late prompt emission, which has same origin as prompt emission, but is created at late times with smaller power and smaller Γ. In this interpretation, if the X-ray flux is dominated by late prompt emission and the optical flux is dominated by afterglow emission, the light curves in the two wavelengths will evolve independently and show no simultaneous break. A faint X-ray flare found around $t = 500$ s following the GRB 071112C burst could provide a clue that late prompt emission plays a role in the X-ray emission.

To further explore late internal dissipation in X-ray emission, we assume that the observed optical emission in GRB 071112C is the real afterglow predicted by the external shock model. In this model ($\nu_m < \nu_o < \nu_c < \nu_x$), the optical emission would follow $F_{t,\nu_{opt}} \sim t^{-\alpha}\nu^{-\beta} \sim t^{3(p-1)/4}\nu^{-(1-p)/2}$ leading to a relation, $\alpha_o = 1.5 \times \beta_o$. With the observed *R*-band power-law index, $\alpha_R = 0.92$, we estimate spectral index is $\beta_o = 0.61$ for the optical band and calculate the electron spectral index $p = 2.24$. Next we assume p is constant in the afterglow phase and calculate the X-ray spectral index produced by the external shock model, $\beta x = 1.12$. In Figure 2, the dotted line shows the expected X-ray emission from external shock model in the region of $\nu_m < \nu_o < \nu_c$ ($F_{x,exp} \propto F_{opt}(\nu_x/\nu_o)^{-0.61}$). Here, we adopt the value $\nu_c = 10^7$ Hz from Uehara et al. (2010). In addition, we also plot the maximum value of expected X-ray flux (the dot-dashed line in the Figure 2). It is clear that the observed X-ray flux is brighter than the expected flux from external shock. This supports the conclusion that the observed X-ray and optical emissions from GRB 071112C are caused by different emission mechanisms. The X-ray flux is created by late internal dissipation and X-ray afterglow emission while the optical flux is dominated by afterglow. In addition, the expected X-ray flux in the Figure 2 implies that the late prompt emission could last until 3000 s after the burst or even longer ($\sim 10^4$ s). This is consistent with late flares or shallow decay in some bursts, which are generally believed to be related to the late activity of the central engine (Burrows et al. 2005; Nousek et al. 2006; Zhang et al. 2006; Falcone et al. 2006).

Recently, Panaitescu & Vestrand (2011) proposed another interpretation. They proposed that the X-ray and optical

evolution could be decoupled by additional energy added to external shock in a wind-like medium. They suggested that the optical emission is from synchrotron and the X-ray emission is from local inverse-Compton scattering. In the internal–external model, the fireball ejecta collides with the ambient ISM and produce synchrotron afterglow emission in X-ray and optical wavelengths. At this moment, if additional energy is supplied into the ejecta, the low energy photons from synchrotron processes will obtain energy from relativistic electrons through inverse-Compton scattering and enhance the X-ray flux. In this scenario, the X-ray flux is predicted to have faster decay than the optical flux and no achromatic breaks will be found in the two wavelengths.

Panaitescu & Vestrand (2011) assumed that an energy injection ($E \sim t^{e}$) and a power-law distribution of electrons with energy $dN/d\gamma \sim \gamma^{-p}$ for the synchrotron self-Compton model. With the conditions, they derived the predicted optical (from synchrotron) and X-ray (from inverse-Compton) power-law decay indices. For a wind-like medium, the expected synchrotron decay index is $\alpha_{o} = 1/4 \times [3p - 1 - (p+1)e]$ at $\nu_{m}^{sy} < \nu_{o} < \nu_{c}^{sy}$ and the inverse-Compton decay index is $\alpha_{x} = p - 1 - (pe/2)$ at $\nu_{c}^{ic} < \nu_{x}$. Using our results on GRB 071112C ($\alpha_{o} = 0.92$ and $\alpha_{x} = 1.36$), we derived a relation between energy injection and electron spectral index $p = e - 0.04$. Applying the electron spectral index $p = 2.24$ from optical observation, we obtain $e = 2.2$ for the GRB 071112C. This result is consistent with other afterglows in which their decoupled X-ray and optical light curves can be explained by synchrotron self-Compton model (GRB 080129 with $e \simeq 2.0$, GRB 090424 with $e \simeq 1.0$, and GRB 090510 with $e \simeq 2.4$).

We investigated the X-ray and optical temporal evolution of the GRB 071112C. Our analysis shows that different emission mechanisms produce the decoupled X-ray and optical evolution. The optical flux is dominated by afterglow, which is produced by synchrotron emission. However, the X-ray flux is created by an additional feature related to energy injection and X-ray afterglow emission. Different theoretical interpretations indicate that the additional feature in X-ray can be explained by either late internal dissipation or inverse-Compton scattering in external shocks.

4. CONCLUSION

We analyzed X-ray and optical light curves of GRB 071112C and found that the X-ray light curve was described by a single power-law plus a flare-like feature, while the *R*-band light curve showed an initial rise followed by a power-law decay. No significant color changes and a value of $\Gamma_{0} = 257 \pm 20$ for initial Lorentz factor indicates that the afterglow onset scenario is likely the correct interpretation for the early *R* band rise. Based on the result, we conclude that the optical flux of the GRB 071112C is dominated by afterglow. Furthermore, compared with X-ray temporal evolution, we found that the observed temporal properties in the two wavelengths cannot be described by the external shock in which the X-ray and optical emission are produced by the same emission mechanism. An additional energy contribution in X-rays is thus necessary. The X-ray flux could be created by a additional feature related to energy injection and X-ray afterglow emission. The faint X-ray flare supports the scenario of energy injection and our analysis indicates either late internal dissipation or inverse-Compton scattering in external shocks is the possible interpretation for the additional feature by energy injection. More such samples with adequately sampled X-ray and optical light curves are important to investigate and understand the detailed emission mechanism for the two wavelengths.

This work is supported by grants NSC-99-2112-M-001-002-MY3 (K.Y.H.) and NSC-99-2112-M-008-003-MY3 (Y.U.). The TAOS project is supported in part by the thematic research program AS-88-TP-A02 at Academia Sinica and the ROTSE project is supported by NASA Grant NNX08AV63G and NSF Grant PHY-0801007. Access to the CFHT was made possible by the Ministry of Education and the National Science Council of Taiwan as part of the Cosmology and Particle Astrophysics (CosPA) initiative. This work made use of data supplied by the UK Swift Science Data Center at the University of Leicester.

Facilities: Swift (XRT), CFHT

REFERENCES

Akerlof, C., Kehoe, R. L., McKay, T. A., et al. 2003, PASP, 115, 132
Bernardini, M. G., Margutti, R., Chincarini, G., Guidorzi, C., & Mao, J. 2011, A&A, 526, 27
Burenini, R., Khamitov, I., Pavlinsky, M., et al. 2007, GCN Circ., 7066, 1
Burrows, D. N., Romano, P., Falcone, A., et al. 2005, Science, 309, 1833
Chen, I. C., Huang, K. Y., & Urata, Y. 2007, GCN Circ., 7067, 1
Chincarini, G., Mao, J., Margutti, R., et al. 2010, MNRAS, 406, 2113
Cucchiara, A., Fox, D. B., Berger, E., & Perri, M. 2007, GCN Circ., 7086, 1
Dintinjana, B., Maticic, S., Nikuz, H., & Skvarc, J. 2007, GCN Circ., 7078, 1
Evans, P. A., Beardmore, A. P., Page, K. L., et al. 2007, A&A, 469, 279
Falcone, A. D., Burrows, D. N., Lazzati, D., et al. 2006, ApJ, 641, 1010
Falcone, A. D., Morris, D., Racusin, J., et al. 2007, ApJ, 671, 1921
Ghisellini, G., Ghirlanda, G., Navy, L., & Firmani, C. 2007, ApJ, 658, L75
Granot, J., Panaitescu, A., Kumar, P., & Wooseley, S. E. 2002, ApJ, 570, L61
Greco, G., Terra, F., Bartolini, C., et al. 2007, GCN Circ., 7089, 1
Huang, K. Y., Urata, Y., Filippenko, A. V., et al. 2005, ApJ, 628, L93
Huang, K. Y., Schwamb, M. E., Wang, J. H., & Wen, C. Y. 2007a, GCN Circ., 7334, 1
Huang, K. Y., Urata, Y., Kuo, P. H., et al. 2007b, ApJ, 654, 25
Ishimura, T., Shimokawabe, T., Mori, Y., et al. 2007, GCN Circ., 7087, 1
Jalobsson, P., Fynbo, J. P. U., Vreeswijk, P. M., Malesani, D., & Sollerman, J. 2007, GCN Circ., 7076, 1
Kann, D. A., Klose, S., Zhang, B., et al. 2010, ApJ, 720, 1513
Klotz, A., Boer, M., & Atteia, J. L. 2007, GCN Circ., 7065, 1
Kobayashi, S., & Zhang, B. 2007, ApJ, 655, 973
Kotani, T., Kawai, N., Yanagisawa, K., et al. 2005, Nuovo Cimento C, 28, 755
Landolt, A. U. 1992, AJ, 104, 336
Lehner, M., Wen, C.-Y., Wang, J.-H., et al. 2009, PASP, 121, 138
Liang, E.-W., Lu, H.-J., Hou, S.-J., Zhang, B.-B., & Zhang, B. 2009, ApJ, 707, 328
Liang, E.-W., Yi, S.-X., Zhang, J., et al. 2010, ApJ, 725, 2209
Meśzaŕos, P. 2002, ARA&A, 40, 137
Meśzaŕos, P. 2006, Rep. Prog. Phys., 69, 2259
Minezaki, T., Price, P. A., Yoshii, Y., & Cowie, C. C. 2007, GCN Circ., 7135, 1
Molinari, E., Vergani, S. D., Malesani, D., et al. 2007, A&A, 469, L13
Nardini, M., Ghisellini, G., Ghirlanda, G., & Celotti, A. 2010, MNRAS, 403, 1131
Nousek, J. A., Kouveliotou, C., Grupe, D., et al. 2006, ApJ, 642, 389
Nugent, P., & Bloom, J. S. 2007, GCN Circ., 7069, 1
Panaitescu, A., Meśzaŕos, P., Burrows, J., et al. 2006, MNRAS, 369, 2059
Panaitescu, A., & Vestrand, W. T. 2008, MNRAS, 387, 497
Panaitescu, A., & Vestrand, W. T. 2011, MNRAS, 414, 353
Piran, T. 2000, Phys. Rep., 333, 529
Prian, T. 2004, Rev. Mod. Phys., 76, 114
Sari, R., & Prian, T. 1999, ApJ, 520, 641
Sari, R., Prian, T., & Narayan, R. 1998, ApJ, 497, L17
Soderberg, A. M., & Ramirez-Ruiz, E. 2002, MNRAS, 330, L24
Stefano, S. 2007, GCN Circ., 7090
Stratta, G., Perri, M., Krimm, H., et al. 2007, GCN Rep., 104.2
Uehara, T., Uemura, M., Kawabata, K. S., et al. 2010, A&A, 519, 56
Uemura, M., Sasada, M., Arai, A., & Uehara, T. 2007a, GCN Circ., 7062, 1
Uemura, M., Sasada, M., Arai, A., & Uehara, T. 2007b, GCN Circ., 7094, 1
Urata, Y., Huang, K. Y., Ip, W. H., et al. 2005, Nuovo Cimento C, 28, 775
Urata, Y., Yamazaki, R., Sakamoto, T., et al. 2007, ApJ, 668, L95

Wang, X. F., Xin, L. P., Zhai, M., et al. 2007, GCN Circ., 7063, 1
Willingale, R., O'Brien, P. T., Osborne, J. P., et al. 2007, ApJ, 663, 1093
Yoshida, M., Yanagisawa, K., Shimizu, Y., et al. 2007, GCN Circ., 7091, 1
Yuan, F., Rykoff, E. S., Rujopakarn, W., & Swan, H. 2007, GCN Circ., 7061, 1
Zhang, B. 2007, Adv. Space Res., 40, 1186
Zhang, B., Fan, Y. Z., Dyks, J., et al. 2006, ApJ, 642, 354
Zhang, B., Kobayashi, S., & Meśzaŕos, P. 2003, ApJ, 595, 950
Zhang, B., & Meśzaŕos, P. 2004, Int. J. Mod. Phys. A, 19, 2385
Zheng, W., Deng, J.-S., Zhai, M., et al. 2008, Chin. J. Astron. Astrophys., 8, 693

The Astrophysical Journal, 751:90 (21pp), 2012 June 1 doi:10.1088/0004-637X/751/2/90

PANCHROMATIC OBSERVATIONS OF THE TEXTBOOK GRB 110205A: CONSTRAINING PHYSICAL MECHANISMS OF PROMPT EMISSION AND AFTERGLOW

W. Zheng[1], R. F. Shen[2], T. Sakamoto[3,4,5], A. P. Beardmore[6], M. De Pasquale[7], X. F. Wu[8,9], J. Gorosabel[10], Y. Urata[11], S. Sugita[12], B. Zhang[8], A. Pozanenko[13], M. Nissinen[14], D. K. Sahu[15], M. Im[16], T. N. Ukwatta[17], M. Andreev[18,19], E. Klunko[20], A. Volnova[21], C. W. Akerlof[1], P. Anto[15], S. D. Barthelmy[5], A. Breeveld[7], U. Carsenty[22], S. Castillo-Carrión[23], A. J. Castro-Tirado[10], M. M. Chester[24], C. J. Chuang[11], R. Cunniffe[10], A. De Ugarte Postigo[25], R. Duffard[10], H. Flewelling[26], N. Gehrels[5], T. Güver[27], S. Guziy[10], V. P. Hentunen[14], K. Y. Huang[28], M. Jelínek[10], T. S. Koch[24], P. Kubánek[10], P. Kuin[7], T. A. McKay[1], S. Mottola[22], S. R. Oates[7], P. O'Brien[6], M. Ohno[29], M. J. Page[7], S. B. Pandey[30], C. Pérez del Pulgar[23], W. Rujopakarn[31], E. Rykoff[32], T. Salmi[14], R. Sánchez-Ramírez[10], B. E. Schaefer[33], A. Sergeev[18,19], E. Sonbas[5,34,35], A. Sota[10], J. C. Tello[10], K. Yamaoka[36], S. A. Yost[37], and F. Yuan[38,39]
[1] Department of Physics, University of Michigan, 450 Church Street, Ann Arbor, MI 48109, USA; zwk@umich.edu
[2] Department of Astronomy and Astrophysics, University of Toronto, Toronto, Ontario M5S 3H4, Canada; rfshen@astro.utoronto.ca
[3] Center for Research and Exploration in Space Science and Technology (CRESST), NASA Goddard Space Flight Center, Greenbelt, MD 20771, USA
[4] Joint Center for Astrophysics, University of Maryland, Baltimore County, 1000 Hilltop Circle, Baltimore, MD 21250, USA
[5] NASA Goddard Space Flight Center, Greenbelt, MD 20771, USA
[6] Department of Physics and Astronomy, University of Leicester, Leicester LE1 7RH, UK
[7] Mullard Space Science Laboratory, University College London, Holmbury Road, Holmbury St. Mary, Dorking RH5 6NT, UK
[8] Department of Physics and Astronomy, University of Nevada Las Vegas, Las Vegas, NV 89154, USA; zhang@physics.unlv.edu
[9] Purple Mountain Observatory, Chinese Academy of Sciences, Nanjing 210008, China
[10] Instituto de Astrofísica de Andalucía (IAA-CSIC), 18008 Granada, Spain
[11] Institute of Astronomy, National Central University, Chung-Li 32054, Taiwan
[12] EcoTopia Science Institute, Nagoya University, Furo-cho, chikusa, Nagoya 464-8603, Japan
[13] Space Research Institute (IKI), 84/32 Profsoyuznaya St., Moscow 117997, Russia
[14] Taurus Hill Observatory, Härkämäentie 88, 79480 Kangaslampi, Finland
[15] CREST, Indian Institute of Astrophysics, Koramangala, Bangalore 560034, India
[16] Center for the Exploration of the Origin of the Universe, Department of Physics and Astronomy, FPRD, Seoul National University, Shillim-dong, San 56-1, Kwanak-gu, Seoul, Republic of Korea
[17] Department of Physics and Astronomy, Michigan State University, East Lansing, MI 48824, USA
[18] Terskol Branch of Institute of Astronomy of RAS, Kabardino-Balkaria Republic 361605, Russian Federation
[19] International Centre of Astronomical and Medico-Ecological Research of NASU, 27 Akademika Zabolotnoho St., 03680 Kyiv, Ukraine
[20] Institute of Solar-Terrestrial Physics, Lermontov St., 126a, Irkutsk 664033, Russia
[21] Sternberg Astronomical Institute, Moscow State University, Universitetsky pr., 13, Moscow 119992, Russia
[22] Institute of Planetary Research, DLR, 12489 Berlin, Germany
[23] Department of EVLT, Universidad de Málaga, Campus de Teatinos, Málaga, Spain
[24] Department of Astronomy and Astrophysics, Penn State University, 525 Davey Laboratory, University Park, PA 16802, USA
[25] Dark Cosmology Centre, Niels Bohr Institute, University of Copenhagen, Juliane Maries Vej 30, DK-2100 Copenhagen O, Denmark
[26] Institute for Astronomy, 2680 Woodlawn Avenue, Honolulu, HI 96822, USA
[27] Department of Astronomy, University of Arizona, 933 North Cherry Avenue, Tucson, AZ 85721, USA
[28] Academia Sinica Institute of Astronomy and Astrophysics, Taipei 106, Taiwan
[29] Japan Aerospace Exploration Agency, Institute of Space and Astronautical Science, 3-1-1 Yoshinodai, Chuo-ku, Sagamihara, Kanagawa 252-5210, Japan
[30] Aryabhatta Research Institute of Observational Sciences (ARIES), Manora Peak, Nainital 263129, India
[31] Steward Observatory, The University of Arizona, Tucson, AZ 85721, USA
[32] E. O. Lawrence Berkeley National Laboratoy, 1 Cyclotron Road, Berkeley, CA 94720, USA
[33] Department of Physics and Astronomy, Louisiana State University, Baton Rouge, LA 70803, USA
[34] Department of Physics, University of Adıyaman, 02040 Adıyaman, Turkey
[35] Universities Space Research Association, 10211 Wincopin Circle, Suite 500, Columbia, MD 21044-3432, USA
[36] Department of Physics and Mathematics, Aoyama Gakuin University, 5-10-1 Fuchinobe, Chuo-ku, Sagamihara, Kanagawa 252-5258, Japan
[37] Department of Physics, College of St. Benedict, Collegeville, MN 56321, USA
[38] Research School of Astronomy and Astrophysics, The Australian National University, Weston Creek, ACT 2611, Australia
[39] ARC Centre of Excellence for All-sky Astrophysics (CAASTRO)
Received 2011 November 1; accepted 2012 March 22; published 2012 May 9

ABSTRACT

We present a comprehensive analysis of a bright, long-duration ($T_{90} \sim 257$ s) GRB 110205A at redshift $z = 2.22$. The optical prompt emission was detected by *Swift*/UVOT, ROTSE-IIIb, and BOOTES telescopes when the gamma-ray burst (GRB) was still radiating in the γ-ray band, with optical light curve showing correlation with γ-ray data. Nearly 200 s of observations were obtained simultaneously from optical, X-ray, to γ-ray (1 eV to 5 MeV), which makes it one of the exceptional cases to study the broadband spectral energy distribution during the prompt emission phase. In particular, we clearly identify, for the first time, an interesting two-break energy spectrum, roughly consistent with the standard synchrotron emission model in the fast cooling regime. Shortly after prompt emission ($\sim$1100 s), a bright ($R = 14.0$) optical emission hump with very steep rise ($\alpha \sim 5.5$) was observed, which we interpret as the reverse shock (RS) emission. It is the first time that the rising phase of an RS component has been closely observed. The full optical and X-ray afterglow light curves can be interpreted within the standard reverse shock (RS) + forward shock (FS) model. In general, the high-quality prompt and afterglow data allow us to apply the standard fireball model to extract valuable information, including the radiation mechanism (synchrotron),

radius of prompt emission ($R_{\rm GRB} \sim 3 \times 10^{13}$ cm), initial Lorentz factor of the outflow ($\Gamma_0 \sim 250$), the composition of the ejecta (mildly magnetized), the collimation angle, and the total energy budget.

Key word: gamma-ray burst: individual (GRB 110205A)

Online-only material: color figures

1. INTRODUCTION

Gamma-ray bursts (GRBs) are extremely luminous explosions in the universe. A standard fireball model (e.g., Rees & Mészáros 1992, 1994; Mészáros & Rees 1997; Wijers et al. 1997; Sari et al. 1998; see, e.g., Zhang & Mészáros 2004; Mészáros 2006 for reviews) has been developed following their discovery in 1973 (Klebesadel et al. 1973) to explain their observational nature. Generally, the prompt emission can be modeled as originating from internal shocks or the photosphere of the fireball ejecta or magnetic dissipation from a magnetically dominated jet, while the afterglow emission originates from external shocks that may include both forward shock (FS) and reverse shock (RS) components (Mészáros & Rees 1997, 1999; Sari & Piran 1999).

The leading radiation mechanisms of the GRB prompt emission are synchrotron radiation, synchrotron self-Compton (SSC), and Compton upscattering of a thermal seed photon source (e.g., Zhang 2011 for a review). All these mechanisms give a "non-thermal" nature to the GRB prompt spectrum. Observationally, the prompt spectrum in the γ-ray band can be fit with a smoothly broken power law called the Band function (Band et al. 1993). Since this function is characterized by a single break energy, it cannot adequately fit the spectrum if the spectral distribution is too complex. For example, the synchrotron mechanism predicts an overall power-law spectrum characterized by several break frequencies: ν_a (self-absorption frequency), ν_m (the frequency of minimum electron injection energy), and ν_c (cooling frequency) (Sari & Esin 2001). However, due to instrumental and observational constraints, it is almost impossible to cover the entire energy range and re-construct the prompt spectrum with all three predicted break points. Thus, despite its limited number of degrees of freedom, the Band function is an empirically good description for most GRBs.

The *Swift* mission (Gehrels et al. 2004), thanks to its rapid and precise localization capability, performs simultaneous observations in the optical to γ-ray bands, allowing broadband observations of the prompt phase much more frequently than previous GRB probes. This energy range may also span up to six orders of magnitude (e.g., GRB 090510, Abdo et al. 2009; De Pasquale et al. 2010) if a GRB is observed by both the *Swift* and *Fermi* satellites (Atwood et al. 2009; Meegan et al. 2009). Some prompt observations have shown signatures of a synchrotron spectrum from the break energies (ν_m,ν_c) (e.g., GRB 080928, Rossi et al. 2011). Prompt optical observations can also be used to constrain the self-absorption frequency ν_a (Shen & Zhang 2009), but, so far, no GRB has been observed clearly with more than two break energies in the prompt spectrum. Meanwhile, early-time observations in the optical band provide a greater chance to detect RS emission, which has only been observed for a few bursts since the first detection in GRB 990123 (Akerlof et al. 1999).

Here we report on the analysis of the long-duration GRB 110205A triggered by the *Swift*/BAT (Barthelmy et al. 2005). Both prompt and afterglow emissions are detected with good data sampling. Broadband energy coverage over six orders of magnitude (1 eV to 5 MeV) during prompt emission makes this GRB a rare case from which we can study the prompt spectrum in great detail. Its bright optical ($R = 14.0$ mag) and X-ray afterglows allow us to test the different external shock models and to constrain the physical parameters of the fireball model.

Throughout this paper, we adopt a standard cosmology model with $H_0 = 71$ km s^{-1} Mpc^{-1}, $\Omega_M = 0.27$, and $\Omega_\Lambda = 0.73$. We use the usual power-law representation of flux density $F(\nu) \propto t^\alpha \nu^{-\beta}$ for the further analysis. All errors are given at the 1σ confidence level unless otherwise stated.

2. OBSERVATIONS AND DATA REDUCTIONS

2.1. Observations

At 02:02:41 UT on 2011 February 5 (T_0), the *Swift*/BAT triggered and located GRB 110205A (trigger=444643; Beardmore et al. 2011). The BAT light curve shows many overlapping peaks with a general slow rise starting at T_0-120 s, with the highest peak at T_0+210 s, and ending at T_0+1500 s. T_{90} (15–350 keV) is 257 ± 25 s (estimated error including systematics). GRB 110205A was also detected by WAM (Sugita et al. 2011, also included in our analysis) on board *Suzaku* (Yamaoka et al. 2009) and Konus-*Wind* (Golenetskii et al. 2011; Pal'shin 2011) in the γ-ray band. A bright, uncataloged X-ray afterglow was promptly identified by the X-Ray Telescope (Burrows et al. 2005a) 155.4 s after the burst (Beardmore et al. 2011). The UVOT (Roming et al. 2005) revealed an optical afterglow 164 s after the burst at location R.A. (J2000) = $10^{\rm h}58^{\rm m}31\overset{\rm s}{.}12$, decl. (J2000) = $+67^\circ31'31\overset{''}{.}2$ with a 90% confidence error radius of about 0.63 arcsec (Beardmore et al. 2011), which was later seen to re-brighten (Chester & Beardmore 2011).

ROTSE-IIIb, located at the McDonald Observatory, Texas, responded to GRB 110205A promptly and confirmed the optical afterglow (Schaefer et al. 2011). The first image started at 02:04:03.4 UT, 82.0 s after the burst (8.4 s after the GCN notice time). The optical afterglow was observed to re-brighten dramatically to 14.0 mag ~1100 s after the burst, as was also reported by other groups (e.g., Klotz et al. 2011a, 2011b; Andreev et al. 2011). ROTSE-IIIb continued monitoring the afterglow until it was no longer detectable, 1.5 hr after the trigger.

Ground-based optical follow-up observations were also performed by different groups with various instruments, some of which are presented by Cucchiara et al. (2011) and Gendre et al. (2011). In this paper, the optical data include Global Rent-a-Scope 005 telescope at New Mexico (Hentunen et al. 2011); 1 m telescope at Mt. Lemmon Optical Astronomy Observatory (Im & Urata 2011; Lee et al. 2010); Lulin One-meter Telescope (LOT; Huang et al. 2005; Urata et al. 2011); 0.61 m Lightbuckets rental telescope LB-0001 in Rodeo, NM (Ukwatta et al. 2011); 2 m Himalayan Chandra Telescope (HCT; Sahu & Anto 2011); Zeiss-600 telescope at Mt. Terskol observatory (Andreev et al. 2011); and 1.6 m AZT-33IK telescope at Sayan Solar observatory, Mondy

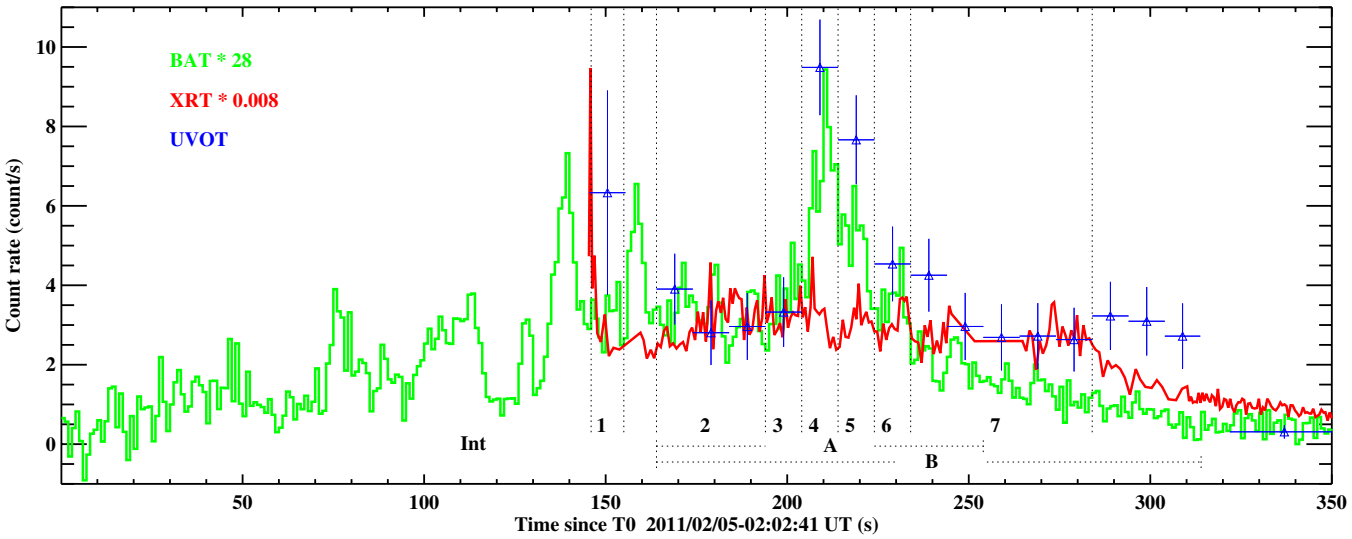

Figure 1. Prompt light curves of GRB 110205A from *Swift* BAT (green), XRT (red), and UVOT (blue). Arbitrary scale. For the UVOT data, the first data point is in v but has been normalized to *white* band, the rest of the data are in *white*. The vertical lines partition nine intervals for constructing the prompt spectra, where Int A and B are averaged ones.

(A color version of this figure is available in the online journal.)

(Volnova et al. 2011), as well as Burst Observer and Optical Transient Exploring System (BOOTES 1 and 2 telescopes), 1.23 m and 2.2 m telescope at Calar Alto Observatory, and 1.5 m OSN telescope, which are not reported in the GCNs.

The redshift measurement of GRB 110205A was reported by three independent groups with $z = 1.98$ (Silva et al. 2011), $z = 2.22$ (Cenko et al. 2011; Cucchiara et al. 2011), and $z = 2.22$ (Vreeswijk et al. 2011). Here we adopt $z = 2.22$, for which two observations are in very close agreement.

2.2. Data Reductions

The data from *Swift* and *Suzaku*, including UVOT, XRT, BAT, and WAM (50 keV to 5 MeV), were processed with the standard HEAsoft software (version 6.10). The BAT and XRT data were further automatically processed by the Burst Analyser pipeline[40] (Evans et al. 2007, 2009, 2010), with the light curves background subtracted. For the XRT data, Windowed Timing (WT) data and Photon Counting (PC) data were processed separately. Pile-up corrections were applied if necessary, especially at early times when the source was very bright. The UVOT data were also processed with the standard procedures. A count rate was extracted within a radius of 3 or 5 arcsec depending on the source brightness around the best UVOT coordinates. The data in each filter were binned with $\delta t/t = 0.2$ and then converted to flux density using a UVOT GRB spectral model (Poole et al. 2008; Breeveld et al. 2010, 2011). The UVOT photometry result is listed in Table 1.

For the ground-based optical data, different methods were used for each instrument. For the ROTSE data, the raw images were processed using the standard ROTSE software pipeline. Image co-adding was performed if necessary to obtain a reasonable signal-to-noise ratio. Photometry was then extracted using the method described in Quimby et al. (2006). Other optical data were processed using the standard procedures provided by the IRAF[41] software. A differential aperture photometry was applied with the DAOPHOT package in IRAF. Reference stars were calibrated using the photometry data from Sloan Digital Sky Survey (Smith et al. 2002). $Clear(C)$ band data were calibrated to R band. All ground-based photometry results are listed in Table 2.

The spectral fitting, including WAM, BAT, XRT, and optical data, was performed using Xspec (version 12.5). We constructed a set of prompt emission spectra over nine time intervals during which the optical data were available. Data from each instrument were re-binned to the same time intervals. In the afterglow phase, spectral energy distributions (SEDs) in four different epochs were constructed when we have the best coverage of multi-band data from optical to X-rays: 550 s, 1.1 ks, 5.9 ks, and 35 ks. All the spectral fittings were carried out under Xspec using χ^2 statistics, except the 1.1 ks SED of the afterglow, for which C-statistics was used.

3. MULTI-WAVELENGTH DATA ANALYSIS

3.1. Broadband Prompt Emission from Optical to γ-Rays

Thanks to its long duration ($T_{90} = 257 \pm 25$ s), GRB 110205A was also detected by XRT and UVOT during the prompt emission phase starting from 155.4 s and 164 s after the trigger, respectively. Both XRT and UVOT obtained nearly 200 s of high-quality and well-sampled data during the prompt phase. ROTSE-IIIb and BOOTES also detected the optical prompt emission 82.0 s and 102 s after the trigger, respectively. Together with the γ-ray data collected by BAT (15–150 keV) and *Suzaku*/WAM (50 keV to 5 MeV), these multi-band prompt emission data cover six orders of magnitude in energy, which allow us to study the temporal and spectral properties of prompt emission in great detail.

Figure 1 shows the prompt light curves from *Swift* BAT (green), XRT (red), and UVOT (blue). The BAT light curve shows multiple peaks until at least T_0 + 300 s with a peak count rate at T_0 + 210 s. The XRT data show a decay phase from a very bright peak at the start of XRT observations, followed by smaller peaks with complicated variability. The UVOT observations were performed mainly in the *white* band,

[40] http://www.swift.ac.uk/burst~analyser/

[41] IRAF is distributed by the National Optical Astronomy Observatory, which is operated by the Association of Universities for Research in Astronomy, Inc., under cooperative agreement with the National Science Foundation.

Table 1
Photomertric Observations for GRB 110205A from *Swift*/UVOT

$T - T_0$ (s)	Error (s)	Count	Error	Filter	$T - T_0$ (s)	Error (s)	Count	Error	Filter
169.0	5.0	3.905	0.890	*white*	24517.0	149.9	1.133	0.130	*white*
179.0	5.0	2.807	0.812	*white*	24734.3	63.5	1.037	0.198	*white*
189.0	5.0	2.963	0.840	*white*	35675.8	149.9	0.654	0.122	*white*
199.0	5.0	3.326	0.877	*white*	35979.3	149.9	0.653	0.123	*white*
209.0	5.0	9.487	1.203	*white*	36284.1	149.9	0.474	0.089	*white*
219.0	5.0	7.664	1.120	*white*	75564.8	149.9	0.234	0.080	*white*
229.0	5.0	4.538	0.939	*white*	75868.3	149.9	0.256	0.081	*white*
239.0	5.0	4.255	0.916	*white*	76171.9	149.9	0.316	0.083	*white*
249.0	5.0	2.964	0.845	*white*	87890.9	92.9	0.177	0.099	*white*
259.0	5.0	2.689	0.831	*white*	99845.1	88.9	0.085	0.100	*white*
269.0	5.0	2.722	0.829	*white*	110704.6	322.4	0.106	0.052	*white*
279.0	5.0	2.633	0.802	*white*	117007.3	147.4	0.008	0.075	*white*
289.0	5.0	3.229	0.858	*white*	122512.3	237.9	0.028	0.059	*white*
299.0	5.0	3.095	0.863	*white*	128037.7	322.4	0.097	0.052	*white*
308.9	4.9	2.720	0.826	*white*	133882.8	299.9	0.100	0.054	*white*
611.8	9.9	20.129	1.184	*white*	139643.2	305.9	0.034	0.052	*white*
784.5	9.9	63.173	2.257	*white*	145379.3	319.4	0.047	0.051	*white*
950.3	74.8	88.866	1.043	*white*	151192.4	308.4	0.167	0.055	*white*
1190.9	9.9	95.569	3.037	*white*	156929.3	321.9	0.038	0.051	*white*
1365.9	9.9	78.130	2.615	*white*	162706.6	321.4	0.041	0.051	*white*
1538.4	9.9	64.515	2.290	*white*	168487.5	320.9	0.042	0.051	*white*
1711.7	9.9	52.993	2.027	*white*	185834.0	315.4	0.006	0.051	*white*
5166.4	99.9	10.865	0.283	*white*	203156.9	319.9	0.088	0.052	*white*
6602.8	99.9	7.511	0.246	*white*	209526.6	120.9	0.019	0.083	*white*
11906.7	149.9	2.834	0.152	*white*	220477.0	322.9	0.022	0.050	*white*
12210.4	149.9	2.752	0.150	*white*	232055.5	315.9	0.042	0.052	*white*
12513.8	149.9	2.755	0.151	*white*	...	...	...	...	*white*
150.5	4.9	1.107	0.449	*v*	52773.8	149.9	0.077	0.039	*v*
661.9	9.9	6.853	0.643	*v*	53077.3	149.9	0.067	0.038	*v*
834.2	9.9	13.718	0.903	*v*	71192.4	18.0	0.069	0.121	*v*
1066.4	9.9	19.918	1.096	*v*	80344.4	149.9	0.004	0.035	*v*
1241.8	9.9	18.517	1.053	*v*	80648.3	149.9	0.047	0.037	*v*
1415.6	9.9	11.828	0.837	*v*	111203.5	169.5	0.063	0.036	*v*
1588.3	9.9	11.398	0.820	*v*	122914.8	158.1	0.038	0.035	*v*
1761.6	9.9	10.388	0.788	*v*	128677.6	310.6	0.049	0.026	*v*
5576.8	99.9	1.641	0.115	*v*	134477.4	288.0	0.013	0.026	*v*
7013.2	99.9	1.123	0.101	*v*	157567.5	309.5	0.018	0.025	*v*
16773.0	149.9	0.338	0.051	*v*	163345.1	309.6	0.015	0.024	*v*
17076.6	149.9	0.302	0.050	*v*	169123.9	308.7	0.018	0.025	*v*
17380.0	149.9	0.337	0.051	*v*	192030.6	102.3	0.039	0.045	*v*
41428.4	149.9	0.048	0.037	*v*	203748.6	264.3	0.050	0.028	*v*
41731.9	149.9	0.082	0.039	*v*	221119.4	312.7	0.016	0.024	*v*
42035.4	149.9	0.126	0.041	*v*	232682.9	304.9	0.013	0.025	*v*
52470.2	149.9	0.053	0.037	*v*	...	...	...	...	*v*
587.4	9.9	6.547	0.659	*b*	75259.9	149.9	0.114	0.050	*b*
760.2	9.9	20.774	1.144	*b*	87035.9	149.9	0.116	0.050	*b*
1164.5	9.9	33.987	1.501	*b*	87339.4	149.9	0.052	0.048	*b*
1341.7	9.9	28.043	1.347	*b*	87642.9	149.9	0.034	0.047	*b*
1514.1	9.9	21.021	1.154	*b*	99662.9	88.9	0.012	0.060	*b*
1686.7	9.9	18.354	1.076	*b*	110054.4	322.4	0.075	0.034	*b*
1860.6	9.9	15.713	1.035	*b*	116707.9	147.4	0.024	0.047	*b*
6397.2	99.9	2.714	0.148	*b*	122031.6	237.9	0.098	0.040	*b*
10993.9	149.9	0.958	0.093	*b*	127387.6	322.4	0.051	0.032	*b*
11297.6	149.9	1.020	0.094	*b*	133277.3	299.9	0.056	0.033	*b*
11601.7	149.9	1.102	0.095	*b*	139026.1	305.9	0.038	0.033	*b*
23604.9	149.9	0.332	0.059	*b*	144734.8	319.4	0.059	0.033	*b*
23908.6	149.9	0.405	0.061	*b*	150570.4	308.4	0.026	0.033	*b*
24212.1	149.9	0.359	0.060	*b*	156280.2	321.9	0.057	0.033	*b*
30146.5	149.9	0.265	0.056	*b*	162058.5	321.4	0.047	0.033	*b*
30449.9	149.9	0.308	0.058	*b*	167840.3	320.9	0.019	0.032	*b*
30676.6	73.1	0.192	0.085	*b*	190956.6	319.9	0.086	0.034	*b*
34763.7	149.9	0.194	0.054	*b*	196608.1	144.9	0.009	0.046	*b*
35067.2	149.9	0.063	0.049	*b*	202511.7	319.9	0.003	0.031	*b*
35370.8	149.9	0.167	0.053	*b*	209280.3	120.9	0.045	0.053	*b*

Table 1
(Continued)

$T - T_0$ (s)	Error (s)	Count	Error	Filter	$T - T_0$ (s)	Error (s)	Count	Error	Filter
59136.9	149.9	0.053	0.047	*b*	219825.9	322.9	0.006	0.032	*b*
59440.3	149.9	0.106	0.050	*b*	225640.3	315.9	0.040	0.032	*b*
74652.2	149.9	0.012	0.045	*b*	237196.2	315.9	0.008	0.032	*b*
336.9	15.0	0.311	0.170	*u*	65363.9	68.7	0.067	0.055	*u*
366.9	15.0	0.263	0.175	*u*	86123.4	149.9	0.047	0.032	*u*
396.9	15.0	0.453	0.187	*u*	86730.7	149.9	0.027	0.031	*u*
426.9	15.0	0.843	0.223	*u*	109403.9	322.4	0.029	0.021	*u*
456.9	15.0	0.618	0.199	*u*	114916.8	56.3	0.029	0.051	*u*
486.9	15.0	1.113	0.239	*u*	116407.8	147.4	0.031	0.031	*u*
516.9	15.0	1.753	0.288	*u*	126736.9	322.4	0.037	0.021	*u*
546.9	15.0	2.956	0.352	*u*	138408.5	305.9	0.002	0.020	*u*
566.8	4.9	3.160	0.632	*u*	144090.4	319.4	0.002	0.020	*u*
735.3	9.9	12.198	0.843	*u*	149947.9	308.4	0.030	0.022	*u*
1140.4	9.9	21.735	1.144	*u*	161409.7	321.4	0.028	0.021	*u*
1315.2	9.9	18.643	1.052	*u*	167193.0	320.9	0.003	0.020	*u*
1489.0	9.9	15.334	0.949	*u*	184561.2	315.4	0.047	0.022	*u*
1661.8	9.9	13.044	0.871	*u*	190310.9	319.9	0.029	0.022	*u*
1835.9	9.9	11.387	0.833	*u*	196145.9	311.4	0.003	0.020	*u*
6192.1	99.9	1.905	0.114	*u*	201865.8	319.9	0.009	0.020	*u*
7590.9	62.7	1.557	0.146	*u*	209033.6	120.9	0.008	0.033	*u*
22692.2	149.9	0.340	0.048	*u*	213551.4	300.9	0.009	0.021	*u*
22995.8	149.9	0.251	0.044	*u*	219174.3	322.9	0.033	0.021	*u*
23299.6	149.9	0.267	0.044	*u*	225002.7	315.9	0.004	0.020	*u*
29233.0	149.9	0.174	0.039	*u*	230780.7	315.9	0.029	0.021	*u*
29536.8	149.9	0.163	0.039	*u*	236558.5	315.9	0.017	0.021	*u*
29841.2	149.9	0.101	0.035	*u*	254513.9	859.1	0.005	0.012	*u*
47582.1	149.9	0.080	0.034	*u*	260333.6	859.3	0.018	0.012	*u*
47885.6	149.9	0.095	0.036	*u*	266093.7	859.3	0.012	0.012	*u*
48069.1	29.9	0.277	0.111	*u*	271853.7	859.2	0.030	0.013	*u*
58224.4	149.9	0.068	0.033	*u*	277673.7	859.3	0.022	0.013	*u*
58527.9	149.9	0.063	0.033	*u*	282893.6	319.2	0.002	0.020	*u*
58831.6	149.9	0.112	0.036	*u*	317849.0	104.0	0.027	0.037	*u*
710.9	9.9	0.481	0.174	*uvw1*	5987.1	99.9	0.110	0.030	*uvw1*
1115.9	9.9	1.735	0.309	*uvw1*	7423.1	99.9	0.107	0.031	*uvw1*
1290.9	9.9	0.869	0.226	*uvw1*	18825.6	383.8	0.024	0.011	*uvw1*
1464.7	9.9	0.452	0.173	*uvw1*	28626.8	449.9	0.013	0.008	*uvw1*
1637.4	9.9	0.918	0.235	*uvw1*	46975.9	449.9	0.007	0.008	*uvw1*
1811.6	9.9	0.525	0.183	*uvw1*	57618.1	449.9	0.010	0.008	*uvw1*

except for the first point that was observed in the *v* band but has been normalized to *white* using the late-time UVOT data. The UVOT light curve shows only two major peaks. The first small peak (146–180 s) shows weak correlation with the BAT. After ∼40 s, it re-brightens to its second and brightest peak at 209 s, coinciding with the brightest γ-ray peak in the BAT light curve. Overall, the optical data are smoother and trace the BAT data better than the XRT data.

Several vertical lines shown in Figure 1 partition the light curve into nine different intervals according to the UVOT significance criterion to obtain time-resolved joint-instrument spectral analysis using the XRT, the BAT, and the WAM data. Since the prompt emission of GRB 110205A is observed by multiple instruments, the systematic uncertainty among the instruments to perform the joint analysis must be carefully understood.

The energy response function of XRT has been examined by the observations of supernova remnants and active galactic nuclei with various X-ray missions such as *Suzaku* and *XMM-Newton*. According to the simultaneous observation of Cyg X-1 between XRT (WT mode) and *Suzaku*/XIS,[42] the photon index and the observed flux agree within ∼5% and ∼15%, respectively. The spectral calibration of BAT has been based on Crab Nebula observations at various boresight angles. The photon index and the flux are within ∼5% and ∼10% of the assumed Crab values based on Rothschild et al. (1998) and Jung (1989). Similarly, the WAM energy response has been investigated using the Crab spectrum collected by the Earth occultation technique (Sakamoto et al. 2011a). The spectral shape and its normalization are consistent within 10%–15% with the result of the *INTEGRAL* SPI instrument (Sizun et al. 2004). The cross-instrument calibration between BAT and WAM has been investigated deeply by Sakamoto et al. (2011b) using simultaneously observed bright GRBs. According to this work, the normalization of the BAT–WAM joint fit agrees within 10%–15% to the BAT data. The cross-instrument calibration between XRT (WT mode) and BAT has been investigated by the simultaneous observation of Cyg X-1. Both the spectral shape and the flux agree within the 5%–10% range between XRT and BAT.[43] In summary, based on the single instrument and the cross-instrument calibration effort, the systematic uncertainty among XRT, BAT,

[42] http://swift.gsfc.nasa.gov/docs/heasarc/caldb/swift/docs/xrt/SWIFT-XRT-CALDB-09_v16.pdf

[43] The presentation in the 2009 *Swift* conference: http://www.swift.psu.edu/swift-2009/.

Table 2
Photomertric Observations for GRB 110205A from Ground-based Telescopes

$T - T_0$ (s)	Exp (s)	Mag	Error	Filter	$T - T_0$ (s)	Exp (s)	Mag	Error	Filter
				ROTSE-IIIb					
135.5	107.0	17.79	0.42	C	1695.7	60.0	14.84	0.06	C
340.2	282.2	16.42	0.11	C	1765.0	60.0	14.89	0.08	C
520.5	60.0	16.33	0.20	C	1834.2	60.0	15.04	0.09	C
589.6	60.0	15.75	0.12	C	1903.0	60.0	15.01	0.07	C
658.4	60.0	15.25	0.09	C	1971.8	60.0	15.22	0.08	C
727.5	60.0	14.81	0.06	C	2040.7	60.0	15.28	0.08	C
796.6	60.0	14.50	0.06	C	2109.5	60.0	15.23	0.07	C
865.7	60.0	14.27	0.05	C	2178.4	60.0	15.44	0.11	C
935.1	60.0	14.19	0.04	C	2247.2	60.0	15.40	0.11	C
1004.3	60.0	14.08	0.03	C	2384.7	60.0	15.51	0.11	C
1073.5	60.0	14.06	0.03	C	2453.9	60.0	15.46	0.11	C
1142.7	60.0	14.14	0.05	C	2660.7	60.0	15.71	0.11	C
1211.9	60.0	14.18	0.04	C	2868.0	60.0	15.83	0.12	C
1281.0	60.0	14.31	0.06	C	2937.2	60.0	16.02	0.13	C
1350.3	60.0	14.40	0.06	C	3075.3	60.0	15.82	0.15	C
1419.5	60.0	14.53	0.05	C	3144.5	60.0	15.96	0.15	C
1489.1	60.0	14.53	0.05	C	3213.4	60.0	16.00	0.13	C
1558.0	60.0	14.55	0.06	C	3593.1	680.0	16.15	0.05	C
1626.6	60.0	14.67	0.06	C	...	...	...	...	–
				LOT (AB magnitude)					
39647.6	180.0	20.95	0.07	g'	43061.7	300.0	19.49	0.06	z'
42062.9	300.0	21.05	0.05	g'	39856.7	180.0	20.32	0.05	r'
45217.0	600.0	20.93	0.03	g'	42392.9	300.0	20.47	0.04	r'
48824.2	600.0	20.90	0.02	g'	45846.0	600.0	20.35	0.04	r'
52111.7	600.0	21.07	0.03	g'	49453.2	600.0	20.42	0.03	r'
55478.8	600.0	21.25	0.03	g'	52740.7	600.0	20.51	0.02	r'
58774.9	600.0	21.33	0.04	g'	56108.6	600.0	20.70	0.03	r'
62047.7	600.0	21.44	0.04	g'	59404.8	600.0	20.80	0.03	r'
65421.7	600.0	21.55	0.04	g'	62677.6	600.0	20.97	0.04	r'
40064.1	180.0	19.97	0.06	i'	66052.4	600.0	20.98	0.03	r'
42720.4	300.0	20.19	0.05	i'	68767.1	600.0	21.08	0.04	r'
46474.1	600.0	20.11	0.03	i'	69377.1	600.0	21.10	0.04	r'
50079.6	600.0	20.13	0.03	i'	69987.9	600.0	21.22	0.05	r'
53368.0	600.0	20.31	0.03	i'	129844.0	600.0	22.50	0.17	r'
56735.0	600.0	20.45	0.04	i'	130563.0	600.0	22.54	0.15	r'
60032.0	600.0	20.62	0.04	i'	131174.0	600.0	22.36	0.11	r'
63304.9	600.0	20.69	0.05	i'	133798.0	600.0	22.47	0.09	r'
66678.8	600.0	20.81	0.04	i'	134409.0	600.0	22.38	0.09	r'
40287.9	180.0	19.68	0.09	z'	135019.0	600.0	22.60	0.12	r'
				HCT					
67639.0	1080.0	21.00	0.04	R	72379.0	600.0	21.15	0.04	R
69019.0	540.0	21.00	0.05	R	...	...	...	...	–
				0.61 m Lightbuckets					
20747.0	300.0	18.67	0.02	C	27549.9	300.0	19.19	0.08	R
				GRAS 005					
3536.8	600.0	15.98	0.02	C	4248.7	600.0	16.44	0.02	R
5327.4	300.0	16.51	0.02	C	5857.5	600.0	16.89	0.03	R
6902.9	600.0	17.02	0.03	C	6378.8	300.0	17.10	0.04	R
8366.9	300.0	17.33	0.04	C	7992.8	300.0	17.62	0.08	R
				1.5 m OSN					
10152.2	300.0	18.93	0.03	B	12747.2	90.0	18.15	0.02	R
11527.2	300.0	19.07	0.03	B	13337.9	90.0	18.18	0.03	R
12426.7	150.0	19.17	0.03	B	14361.8	90.0	18.34	0.03	R
13091.5	150.0	19.21	0.03	B	14856.1	90.0	18.32	0.03	R
14115.7	150.0	19.32	0.03	B	85598.9	3300.0	20.89	0.05	R
14610.0	150.0	19.38	0.04	B	10489.4	300.0	18.67	0.06	U
76574.1	400.0	21.87	0.17	B	11871.4	500.0	18.96	0.06	U
9871.3	240.0	17.22	0.02	I	13592.3	500.0	19.22	0.06	U
11278.2	240.0	17.41	0.02	I	9644.8	180.0	18.04	0.02	V
12840.2	200.0	17.59	0.02	I	11094.4	180.0	18.35	0.02	V

Table 2
(Continued)

$T - T_0$ (s)	Exp (s)	Mag	Error	Filter	$T - T_0$ (s)	Exp (s)	Mag	Error	Filter
13430.8	120.0	17.65	0.03	*I*	12653.7	90.0	18.55	0.02	*V*
14454.7	120.0	17.77	0.03	*I*	13244.3	90.0	18.61	0.03	*V*
14949.0	120.0	17.78	0.03	*I*	14268.5	90.0	18.71	0.04	*V*
77630.9	300.0	20.56	0.19	*I*	14762.8	90.0	18.66	0.04	*V*
9409.4	180.0	17.59	0.02	*R*	76977.2	350.0	21.68	0.19	*V*
				1 m LOAO					
13101.0	720.0	19.32	0.16	*B*	12846.0	180.0	18.16	0.03	*R*
11974.0	180.0	18.14	0.03	*R*	13273.0	180.0	18.22	0.03	*R*
12416.0	180.0	18.11	0.03	*R*	...	...	...	...	–
				BOOTES-1					
219.4	117.0	17.43	0.38	*C*	2715.2	49.0	15.66	0.07	*C*
1603.5	48.0	14.61	0.05	*C*	2832.0	64.0	15.74	0.07	*C*
2118.2	48.0	15.18	0.05	*C*	3096.5	197.0	15.81	0.04	*C*
2218.1	48.5	15.29	0.05	*C*	3709.1	413.0	16.21	0.04	*C*
2317.5	48.0	15.45	0.06	*C*	4621.4	495.5	16.54	0.05	*C*
2417.5	48.5	15.44	0.06	*C*	5615.5	495.5	16.88	0.08	*C*
2516.8	48.0	15.35	0.05	*C*	6658.3	545.0	17.15	0.08	*C*
2615.8	48.0	15.51	0.07	*C*	8066.6	859.5	17.59	0.10	*C*
				BOOTES-2					
939.3	5.0	14.40	0.04	*R*	6300.8	363.5	17.19	0.04	*R*
994.7	5.0	14.24	0.04	*R*	7149.9	484.5	17.42	0.04	*R*
2015.1	72.5	15.26	0.05	*R*	8362.6	727.0	17.65	0.04	*R*
2375.1	63.0	15.63	0.08	*R*	9818.1	969.0	17.98	0.05	*R*
5120.9	189.5	16.67	0.04	*R*	11758.0	969.5	18.16	0.06	*R*
5373.4	187.0	16.83	0.04	*R*	13940.7	1212.0	18.52	0.08	*R*
5748.5	187.0	17.10	0.05	*R*	...	...	...	...	–
				1.23 m Calar Alto					
2467.0	60.0	15.59	0.06	*R*	9692.0	60.0	17.88	0.08	*R*
2582.0	60.0	15.64	0.06	*R*	10202.0	60.0	17.91	0.05	*R*
4198.0	60.0	16.48	0.05	*R*	10712.0	60.0	18.02	0.05	*R*
4661.0	60.0	16.60	0.04	*R*	11215.0	60.0	18.05	0.05	*R*
5107.0	60.0	16.73	0.05	*R*	11336.0	60.0	18.10	0.05	*R*
5559.0	60.0	16.85	0.05	*R*	11835.0	60.0	18.15	0.05	*R*
6008.0	60.0	16.99	0.05	*R*	12337.0	60.0	18.26	0.06	*R*
6461.0	60.0	17.05	0.05	*R*	12844.0	60.0	18.26	0.07	*R*
6909.0	60.0	17.23	0.04	*R*	13353.0	60.0	18.28	0.05	*R*
7358.0	60.0	17.41	0.05	*R*	13905.0	60.0	18.34	0.05	*R*
7804.0	60.0	17.49	0.05	*R*	14018.0	60.0	18.41	0.05	*R*
8670.0	60.0	17.73	0.05	*R*	14128.0	60.0	18.35	0.05	*R*
9182.0	60.0	17.75	0.05	*R*	14239.0	60.0	18.45	0.06	*R*
				2.2 m Calar Alto					
9475.0	100.0	17.67	0.03	*R*	12388.0	500.0	18.13	0.03	*R*
10064.0	500.0	17.76	0.03	*R*	12962.0	500.0	18.18	0.03	*R*
10639.0	500.0	17.88	0.03	*R*	13535.0	500.0	18.26	0.03	*R*
11214.0	500.0	17.97	0.03	*R*	14109.0	500.0	18.33	0.03	*R*
11787.0	500.0	18.04	0.03	*R*	14706.0	500.0	18.41	0.03	*R*
15281.0	500.0	18.49	0.03	*R*	...	...	...	...	–
				1.6 m AZT-33IK					
37988.0	3060.0	19.97	0.08	*R*	62132.0	6600.0	20.94	0.07	*R*
				Zeiss-600					
794.0	60.0	14.47	0.04	*R*	2006.2	60.0	15.26	0.06	*V*
853.6	60.0	14.18	0.03	*R*	2068.4	60.0	15.55	0.06	*V*
918.4	60.0	14.08	0.02	*R*	2128.0	60.0	15.52	0.06	*V*
1022.1	60.0	14.03	0.02	*R*	2230.0	2.0	15.27	0.05	*R*
1081.7	60.0	14.00	0.02	*R*	2350.9	2.0	15.46	0.05	*R*
1142.2	60.0	14.07	0.02	*R*	2742.3	2.0	15.54	0.06	*R*
1204.4	60.0	14.09	0.02	*R*	3133.7	2.0	15.92	0.09	*R*
1264.0	60.0	14.34	0.02	*R*	3284.9	2.0	16.06	0.08	*R*
1323.7	60.0	14.29	0.03	*R*	3436.1	2.0	16.08	0.04	*R*
1385.9	60.0	14.37	0.02	*R*	3557.9	2.0	16.11	0.04	*R*

Table 2
(Continued)

$T - T_0$ (s)	Exp (s)	Mag	Error	Filter	$T - T_0$ (s)	Exp (s)	Mag	Error	Filter
1446.3	60.0	14.48	0.03	*R*	3678.9	2.0	16.04	0.06	*R*
1506.0	60.0	14.52	0.03	*R*	3799.9	2.0	16.16	0.05	*R*
1568.2	60.0	14.59	0.03	*R*	3921.7	2.0	16.19	0.05	*R*
1627.8	60.0	14.58	0.03	*R*	4042.7	2.0	16.19	0.05	*R*
1688.3	60.0	14.74	0.03	*R*	4163.6	2.0	16.30	0.06	*R*
1814.4	60.0	14.84	0.03	*R*	4345.9	4.0	16.36	0.05	*R*
1886.1	60.0	15.16	0.09	*V*	4588.7	4.0	16.44	0.05	*R*
1945.7	60.0	15.38	0.04	*V*	4830.6	4.0	16.59	0.06	*R*

and WAM should be within 15% in both the spectral shape and its normalization of the spectrum. To accommodate systematic uncertainties, we include a multiplication factor in the range 0.85–1.15 for the flux normalization for each instrument.

We first applied the spectral analysis to the time-averaged interval B (intB; see Figure 1 for interval definition) and find that the photon index in a simple power-law model derived by the individual instrument differs significantly. The photon indices derived by the XRT, the BAT, and the WAM spectra are -1.12 ± 0.03, -1.71 ± 0.04, and $-2.27^{+0.22}_{-0.27}$, respectively (also listed in Table 3; spectral fitting errors in Table 3 and in this section are given in 90% confidence). Since these differences are significantly larger than the systematic uncertainty associated with the instrumental cross-calibration (the systematic error in the photon index is ± 0.3 for the worst case as discussed above), the apparent change of spectral slope is very likely intrinsic to the GRB. Thus, the observed broadband spectrum requires two breaks to connect the XRT, the BAT, and the WAM data.

According to the GRB synchrotron emission model, the overall spectrum should be a broken power law characterized by several break frequencies (e.g., the self-absorption frequency ν_a, the cooling frequency ν_c, and the frequency of minimum electron injection energy ν_m). However, the well-known Band function, which only includes one break energy, cannot represent the shape of the more complex spectrum of this particular event; therefore, we extended the analysis code, Xspec, to include two additional spectral functions. The first one is a double "Band" spectrum with two spectral breaks, which was labeled *bkn2band*:

$$f(E) = \begin{cases} AE^{\alpha}\exp(-E/E_0), & if\ E \leqslant \frac{E_0 E_1}{E_1 - E_0}(\alpha - \beta) \\ A\left[\frac{E_0 E_1}{E_1 - E_0}(\alpha - \beta)\right]^{\alpha-\beta}\exp(\beta - \alpha)E^{\beta}\exp(-E/E_1), & if\ \frac{E_0 E_1}{E_1 - E_0}(\alpha - \beta) < E \leqslant (\beta - \gamma)E_1 \\ A\left[\frac{E_0 E_1}{E_1 - E_0}(\alpha - \beta)\right]^{\alpha-\beta}\exp(\beta - \alpha)\cdot [(\beta - \gamma)E_1]^{\beta-\gamma}\exp(\gamma - \beta)E^{\gamma}, & if\ E > (\beta - \gamma)E_1 \end{cases} \quad (1)$$

where A is the normalization at 1 keV in units of photons $\mathrm{cm}^{-2}\ \mathrm{s}^{-1}\ \mathrm{keV}^{-1}$; α, β, and γ are the photon indices of the three power-law segments; and E_0 and E_1 are the two break energies. However, when fitting the spectrum using this new *bkn2band* model, the third power-law index, γ, is poorly constrained mainly due to the poor statistics in the high-energy WAM data above 400 keV. For this reason, the second new model, *bandcut*, replaces the third power-law component with an exponential cutoff:[44]

$$f(E) = \begin{cases} AE^{\alpha}\exp(-E/E_0), & if\ E \leqslant \frac{E_0 E_1}{E_1 - E_0}(\alpha - \beta) \\ A\left[\frac{E_0 E_1}{E_1 - E_0}(\alpha - \beta)\right]^{\alpha-\beta}\exp(\beta - \alpha)E^{\beta}\exp(-E/E_1), & if\ E > \frac{E_0 E_1}{E_1 - E_0}(\alpha - \beta). \end{cases} \quad (2)$$

Note that the exponential cutoff in the new *bandcut* model introduces a second break, E1, although different from the break in a doubly broken power-law model or *bkn2band* model. The new *bandcut* model can well characterize the prompt emission spectra of GRB 110205A. Hereafter, we use "two-break energy spectrum" to represent the *bandcut* model spectrum. Figure 2 shows the XRT, BAT, and WAM joint fit spectral analysis of intB based on the *bandcut* model and the Band function fit. The systematic residuals from the best-fit Band function are evident especially in the WAM data. The best-fit parameters based on the *bandcut* model are $\alpha = -0.50^{+0.09}_{-0.08}$, $E_0 = 5.0^{+1.1}_{-0.8}$ keV, $\beta = -1.54^{+0.10}_{-0.09}$, and $E_1 = 333^{+265}_{-118}$ keV ($\chi^2/\mathrm{dof} = 529.8/503$). On the other hand, the best-fit parameters based on the Band function are $\alpha = -0.59^{+0.06}_{-0.08}$, $\beta = -1.72^{+0.01}_{-0.03}$, and $E_{\mathrm{peak}} = 9.5^{+1.5}_{-0.9}$ keV ($\chi^2/\mathrm{dof} = 575.7/504$). Therefore, $\Delta\chi^2$ ($\equiv \chi^2_{\mathrm{Band}} - \chi^2_{\mathrm{bandcut}}$) between the Band function and the *bandcut* model is 45.9 for 1 dof. To quantify the significance of this improvement, we performed 10,000 spectral simulations assuming the best-fit Band function parameters by folding the energy response functions and the background data of XRT, BAT, and WAM. Then, we determine in how many cases the *bandcut* model fit gives χ^2 improvements equal to or greater than $\Delta\chi^2 = 45.9$ for 1 dof over the Band function fit. We found equal or higher improvements in none of the simulated spectra out of 10,000. Thus, the chance probability of having an equal or higher $\Delta\chi^2$ of 45.9 with the *bandcut* when the parent distribution is actually the Band function is <0.01%. A caveat for this simulation is that the statistical improvement of the joint fit may be not as high as this simulation indicates if the calibration uncertainties among the instruments are included.

The same method is then applied to perform the joint spectral fitting to the remaining time intervals. Table 3 shows the best-fit results from the *bandcut* model. This is the first time that two spectral breaks are clearly identified in the prompt GRB spectra. The two breaks are consistent with the expectation of the broken power-law synchrotron spectrum (see discussion in Section 4.1).

[44] Both *bkn2band* and *bandcut* new models can be downloaded from the following Web site: http://asd.gsfc.nasa.gov/Takanori.Sakamoto/personal/. They can be used to fit future GRBs with similar characteristics.

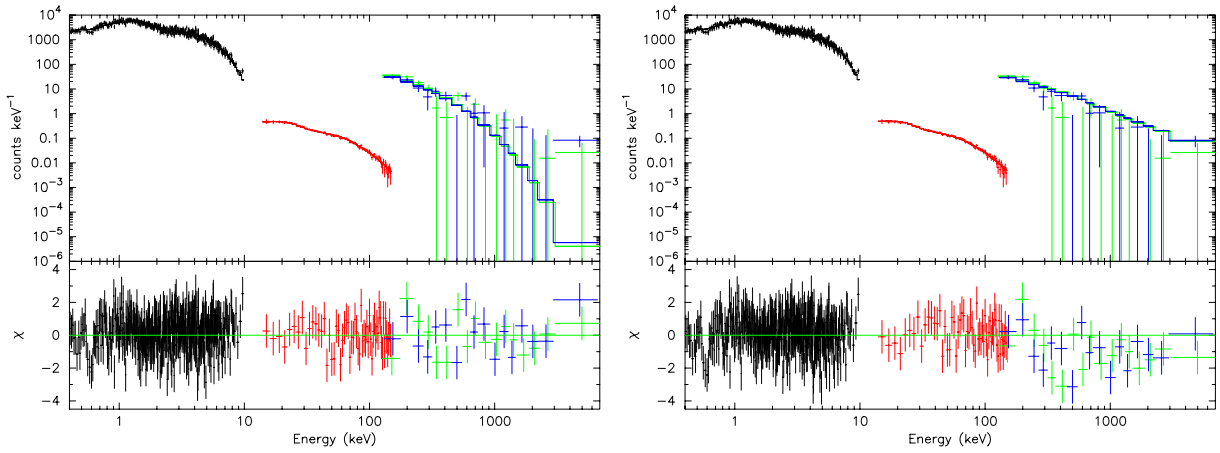

Figure 2. XRT (black), BAT (red), and WAM (green and blue) count spectra of intB with the *bandcut* model (left panel) and the standard Band function (right panel) fit. The improvement using the *bandcut* model can be easily seen in the residual panel at the bottom.

(A color version of this figure is available in the online journal.)

Table 3
Best Spectral Fit Result from XRT, BAT, and WAM Joint Fitting with the *bandcut* Model

Int	t_1	t_2	α	E_0	β	E_1	χ^2/dof	XRT	BAT	WAM
int1	146	155	$-0.40^{+0.43}_{-0.25}$	$4.9^{+4.7}_{-2.5}$	$-1.45^{+0.13}_{-0.21}$	207^{+468}_{-88}	$126.4/137 = 0.92$	$-1.05^{+0.11}_{-0.11}$	$-1.68^{+0.09}_{-0.09}$	$-2.24^{+0.48}_{-0.70}$
int2	164	194	$-0.22^{+0.15}_{-0.14}$	$4.4^{+1.4}_{-0.9}$	$-1.61^{+0.11}_{-0.19}$	258^{+615}_{-59}	$269.7/256 = 1.05$	$-0.94^{+0.05}_{-0.06}$	$-1.81^{+0.06}_{-0.06}$	$-2.72^{+0.63}_{-0.84}$
int3	194	204	$-0.41^{+0.31}_{-0.21}$	$5.5^{+4.5}_{-2.4}$	$-1.44^{+0.13}_{-0.14}$	264^{+336}_{-115}	$138.5/145 = 0.96$	$-0.99^{+0.10}_{-0.11}$	$-1.62^{+0.08}_{-0.08}$	$-2.14^{+0.57}_{-0.98}$
int4	204	214	$-0.26^{+0.37}_{-0.36}$	$4.1^{+8.2}_{-1.8}$	$-1.26^{+0.11}_{-0.08}$	299^{+175}_{-96}	$107.6/146 = 0.74$	$-0.91^{+0.09}_{-0.10}$	$-1.45^{+0.05}_{-0.06}$	$-2.22^{+0.20}_{-0.25}$
int5	214	224	$-0.37^{+0.31}_{-0.26}$	$5.8^{+7.6}_{-2.5}$	$-1.39^{+0.13}_{-0.11}$	273^{+189}_{-96}	$144.5/144 = 1.00$	$-0.87^{+0.09}_{-0.10}$	$-1.58^{+0.06}_{-0.06}$	$-2.42^{+0.43}_{-0.43}$
int6	224	234	$-0.34^{+0.25}_{-0.24}$	$4.4^{+3.1}_{-1.6}$	$-1.53^{+0.15}_{-0.11}$	289^{+750}_{-135}	$146.9/142 = 1.03$	$-1.00^{+0.09}_{-0.10}$	$-1.72^{+0.08}_{-0.08}$	$-1.98^{+0.38}_{-0.63}$
int7	234	284	$-0.61^{+0.16}_{-0.14}$	$4.7^{+2.3}_{-1.3}$	$-1.65^{+0.07}_{-0.13}$	342^{+958}_{-156}	$248.8/233 = 1.07$	$-1.24^{+0.06}_{-0.06}$	$-1.78^{+0.08}_{-0.08}$	$-2.00^{+0.55}_{-1.16}$
intA	164	254	$-0.32^{+0.10}_{-0.10}$	$4.7^{+1.1}_{-0.8}$	$-1.52^{+0.10}_{-0.07}$	346^{+229}_{-115}	$430.9/437 = 0.99$	$-1.00^{+0.03}_{-0.04}$	$-1.68^{+0.04}_{-0.04}$	$-2.28^{+0.19}_{-0.24}$
intB	164	314	$-0.50^{+0.09}_{-0.08}$	$5.0^{+1.1}_{-0.8}$	$-1.54^{+0.10}_{-0.09}$	333^{+265}_{-118}	$529.8/503 = 1.05$	$-1.12^{+0.03}_{-0.03}$	$-1.71^{+0.04}_{-0.04}$	$-2.27^{+0.22}_{-0.27}$

Note. The last three columns show the photon index from each single instrument fitting. Errors are given in 90% confidence.

Figure 3 shows the evolution of different parameters from the time-resolved spectral fitting between 146 s and 284 s. The two break energies, E_0 and E_1, remain almost constant during this time range, with $E_0 \sim 5$ keV and $E_1 \sim 300$ keV. However, the large errors for E_0 and E_1 prevent us from drawing a firmer conclusion regarding the temporal evolution of the two break energies. The low-energy photon index, α, also shows no statistically significant evolution. However, the high-energy photon index, β, does show a weak evolution: it becomes slightly harder during the brightest BAT peak around 210 s. Over all, the α value during the time range is around -0.35 and β is around -1.5. The peak energy derived from interval B (intB) is $E_p = (2+\beta)E_1 = 153^{+121}_{-54}$ keV.

Although the UVOT optical data are not included in the spectral fitting, they are shown in the best-fit spectra in Figure 4. For all the intervals, the optical data are above the extrapolation of the best spectral fits for high energies. A speculation may be that the observed α is somehow harder than the expected value of the synchrotron model. However, even if we set α to the predicted value, $-2/3$, the optical data are still above the best-fit spectra in some intervals. This suggests that the optical emission may have a different origin from the high-energy emission (see Section 4 for more detailed discussion).

3.2. Afterglow Analysis

3.2.1. Light Curves

Shortly after the prompt emission, the optical light curve is characterized by a surprisingly steep rise and a bright peak around 1100 s. The early steep rise, starting around 350 s, is observed by both ROTSE and UVOT, and the peak, which is wide and smooth, reaches $R = 14.0$ mag at 1073 s after the burst. Such a bright peak around this time with such a steep rise is rare and unusual (Oates et al. 2009; Panaitescu & Vestrand 2011) and has only been reported in a few cases (e.g., Volnova et al. 2010; Nardini et al. 2011). A peak brightness of $R = 14.0$ mag at $\sim$1100 s after the burst ranks the optical afterglow as one of the brightest ever observed in this same time range (Akerlof & Swan 2007). Following the peak, the light curve decays monotonically, as shown in Figure 5, and displays a slight flattening around 3000 s. Around 5×10^4 s, there is a re-brightening feature observed in the g', r', i', z' bands by LOT (Figure 6), and a final steepening is observed after $\sim 10^5$ s. Overall, no substantial color evolution is observed in the optical band.

The X-ray data show a different temporal behavior (see also Figure 5). Shortly after the prompt emission, the light curve has a very steep decay, between 350 s and 700 s. This is followed by a small re-brightening bump around 1100 s, the peak time of the optical light curve, and a monotonic decay afterward. There might be a late X-ray flare around 5000 s, but the lack of X-ray data just before $\sim$5000 s prevents any robust conclusion from being drawn.

The light curves were fit with one or the superposition of two broken power-law functions. The broken power-law function has been widely adopted to fit afterglow light curves with both the rising and decay phases (e.g., Rykoff et al. 2009) and works

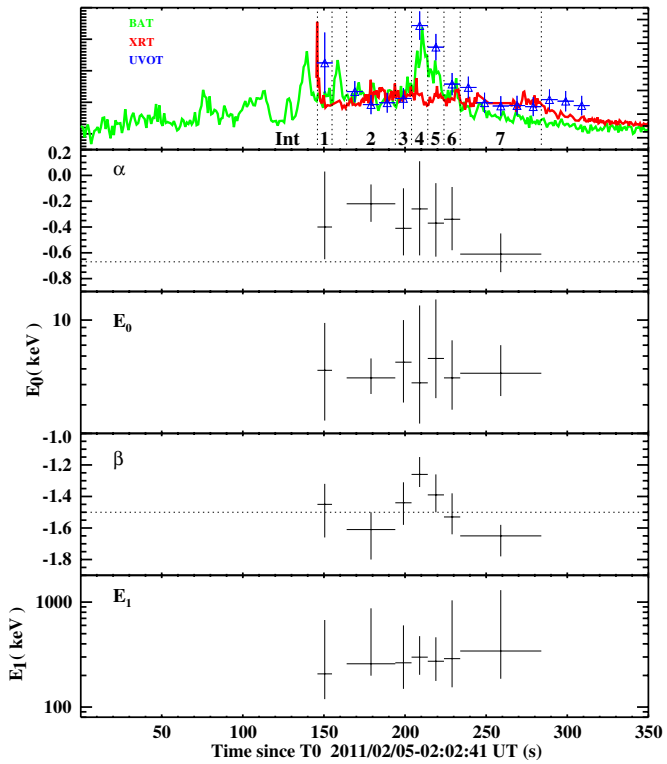

Figure 3. Time evolution of different parameters from the time-resolved spectral fitting of GRB 110205A. Top panel has the same key as Figure 1. The two horizontal dotted lines in α and β panels are the predicted synchrotron photon index value for fast cooling phase from the standard GRB fireball model. Errors are given at 90% confidence except the top panel.

(A color version of this figure is available in the online journal.)

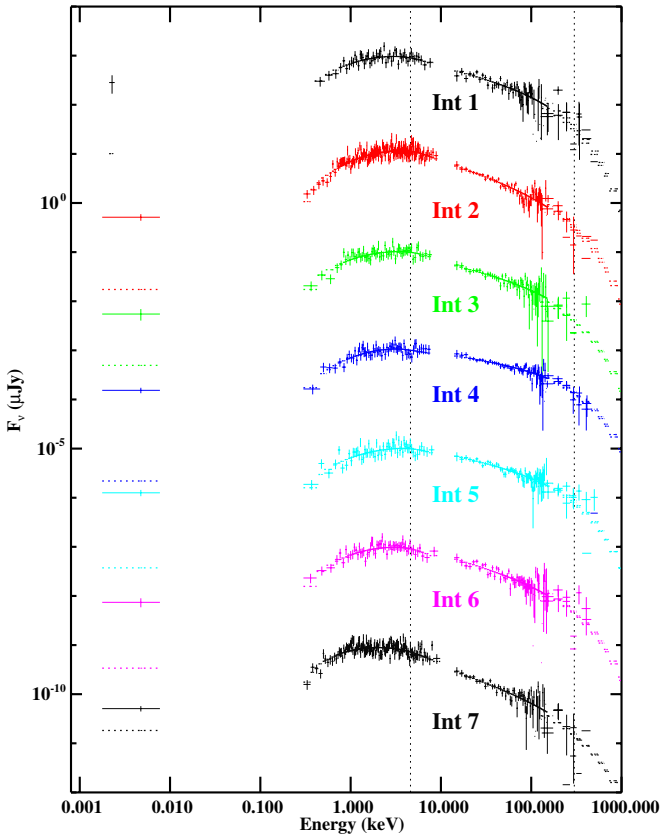

Figure 4. Best-fit prompt spectra of GRB 110205A, different colors present different intervals (see Figure 1 for interval definition). Note that WAM data above 400 keV are not shown in the figure due to large uncertainties when transforming counts to flux density in Xspec above this energy range. Intervals 2–7 are shifted by a factor of 10^{-2} accumulatively for the purpose of clarity. UVOT optical data are not included during the fitting, but they are shown in the best-fit spectrum. Solid lines present the observed data, while dashed lines present the prediction of the best-fit *bandcut* model. The two vertical lines show the mean value of E_0 and E_1 from the fitting.

(A color version of this figure is available in the online journal.)

well for most cases (e.g., Liang et al. 2010). The function can be represented as

$$f = \left(\frac{t}{t_b}\right)^{\alpha_1} \left[1 + \left(\frac{t}{t_b}\right)^{s(\alpha 1-\alpha 2)}\right]^{-1/s}, \quad (3)$$

where f is the flux, t_b is the break time, $\alpha 1$ and $\alpha 2$ are the two power-law indices before and after the break, and s is a smoothing parameter. According to this definition, the peak time t_p, where the flux reaches maximum, is

$$t_p = t_b \left(\frac{\alpha 1}{-\alpha 2}\right)^{1/s(\alpha 1-\alpha 2)}. \quad (4)$$

If a multiple broken power-law function is required to present more than one break time, Equation (2) in van Eerten & MacFadyen (2011) is adopted. We first tried one broken power-law component and found that it could not fully represent the feature near the optical peak, mainly because of its unusually late and steep rising feature, which was not observed in previous GRBs, and a slight flattening feature around 3000 s after the peak shown in R band. Noticing that there is a peak in both the optical and the X-ray light curves around 1100 s and that the optical light curve flattens around 3000 s, we speculate that there is a significant contribution of emission from the RS. An RS contribution to the X-ray band has not been well identified in the past. Theoretically, the RS synchrotron emission peaks around the optical band so that its synchrotron extension to the X-ray band is expected to be weak. In any case, under certain conditions, it is possible that the RS synchrotron (Fan & Wei 2005; Zou et al. 2005) or SSC (Kobayashi et al. 2007) emission would contribute significantly to the X-ray band to create a bump feature. In order to account for both the FS and the RS components, we fit both the optical and X-ray light curves with the superposition of two broken power-law functions. For the X-ray light curve, an additional single power-law component was applied for the steep decay phase, as usually seen in *Swift* afterglows (e.g., Tagliaferri et al. 2005).

Two light-curve models have been adopted. The standard afterglow model predicts that the blast wave enters the deceleration phase as the RS crosses the ejecta (Sari & Piran 1995; Zhang et al. 2003). If the FS ν_m is already below the optical band at the crossing time, both the FS and the RS would have the same peak time (t_p) in the optical band. This defines our first scenario, in which the optical peak is generated by both the RS and the FS. If, however, ν_m is initially above the optical band at the deceleration time, the FS optical light curve would display a rising feature ($\propto t^{1/2}$; Sari et al. 1998) initially, until reaching a peak at a later time when ν_m crosses the optical band. This is our second scenario. In this case, the early optical peak is mostly dominated by the RS component. This is the Type I light curve identified in Zhang et al. (2003) and Jin & Fan (2007). We now discuss the two scenarios in turn.

Scenario I. We performed a simultaneous fit to both optical R-band data and X-ray data by setting the same break time in the

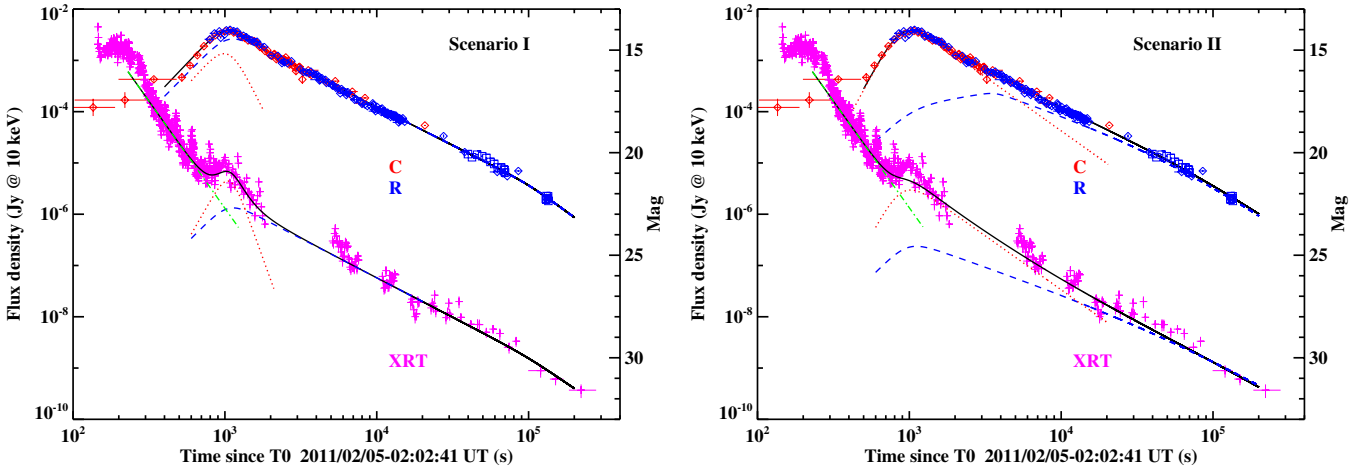

Figure 5. GRB 110205A light curves from XRT data (pink cross) and optical data, including *C* band (red diamond) and *R* band (blue square). Two scenarios are considered. Both scenarios consider superposition of FS (dashed line) and RS (dotted line) contribution. The main difference is that Scenario I (left panel) considers the optical peak as dominated by both FS and RS combination while Scenario II considers the optical peak as dominated by RS only. The dot-dashed line represents the steep decay phase for X-ray data. The solid line represents the combination of all components.

(A color version of this figure is available in the online journal.)

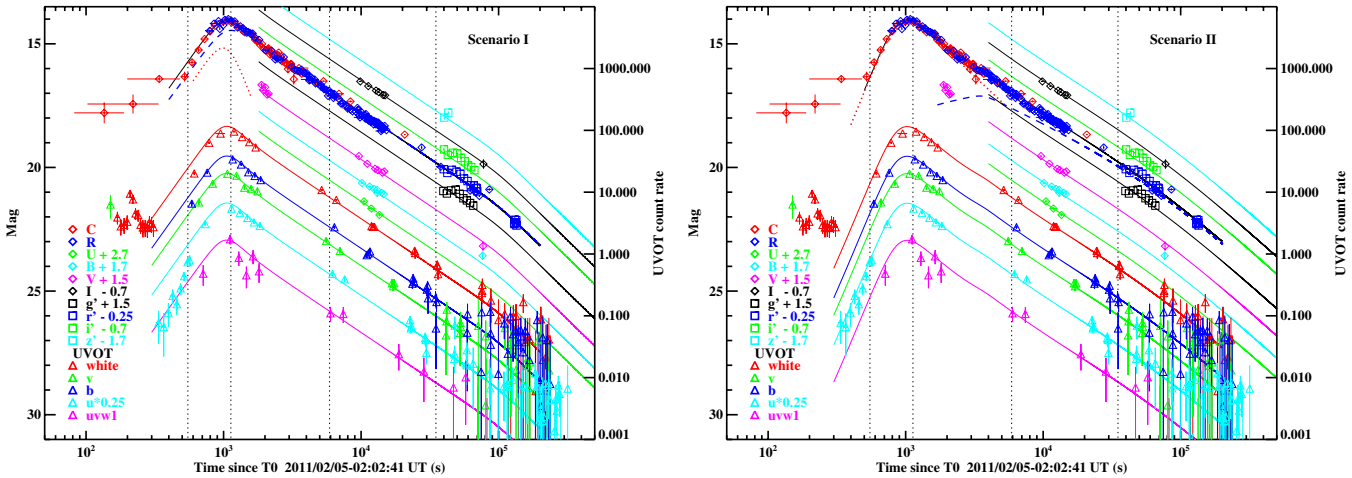

Figure 6. Optical light curves of GRB 110205A re-scaled from *R*-band best fit. The early fast rise behavior in optical band can be better explained by Scenario II (right panel) than Scenario I (left panel).

(A color version of this figure is available in the online journal.)

two bands. A late time break is invoked to fit both the *R*-band and X-ray light curves. However, we exclude the re-brightening feature around 5×10^4 s in the optical band and the steep decay phase of X-rays before 400 s, which is likely the tail of the prompt emission (Zhang et al. 2006). For the FS component, the rising temporal index is fixed to be 3 based on the slow cooling interstellar medium (ISM) model during the pre-deceleration phase[45] (e.g., Xue et al. 2009; Shen & Matzner 2012). The rising slope of the RS component is left as a free parameter to be constrained from the data. The best simultaneous fit results are summarized in Table 4 and shown in Figure 5 (left panel). The red dot and blue dashed lines represent the RS and FS components, respectively. The black solid line is the sum of all the components.

Next we apply the same best *R*-band fit parameters and re-scale to the optical data in other bands. The results are shown in Figure 6 (left panel). Light curves in different bands are properly shifted for clarity. As we can see, the model quite adequately describes most light curves. The only exception is the UVOT-*u* band, in which the model curve overpredicts the early-time flux between 300 s and 600 s.

Scenario II. In this scenario, the bright peak around 1100 s and the steep rise phase at early times in the optical band are contributed by the RS only. The FS component shows up later. According to the afterglow model, the FS component is characterized by a double broken power law with a rising index +3 before the deceleration time (t_p of the RS), +0.5 before the FS peak, and a normal decay (decay index to be fit from the data) after the FS peak (e.g., Sari et al. 1998; Zhang et al. 2003; Xue et al. 2009). For the RS component, the rising index is fixed to be 5.5, which is the mean value of a single power-law fit to the *R*-band data ($\alpha \sim 5$) and the UVOT-*u* band data ($\alpha \sim 6$) only. In the X-ray band, we still use a similar model as Scenario I with a superposition of an RS and an FS component. The model parameters are not well constrained, especially for the X-ray peak around 1100 s due to its narrow peak. We tried to fix several parameters in order to reach an acceptable fitting for this scenario. The best simultaneous fit results for both *R*-band

[45] In the coasting phase of a thin shell decelerated by a constant density medium, the forward shock has the scalings $\nu_m \propto t^0$, $\nu_c \propto t^{-2}$, and $F_{\nu,m} \propto t^3$. For $\nu_m < \nu_{\rm opt} < \nu_c$, one has $F_\nu \propto t^3$.

Table 4
Best-fit Result from *R*-band and X-Ray Light Curves

	Scenario I		Scenario II	
Par	Optical	X-ray	Optical	X-ray
FS			FS	
α_{f1}	3[a]	3[a]	3[a] $\rightarrow$0.5[a]	3[a]
t_p (s)	1064 ± 42	1064[b]	$3.64 \pm 1.0 \times 10^3$	1021 ± 26
F_p (Jy)	4.96×10^{-3}	1.32×10^{-6}	4.35×10^{-4}	1.42×10^{-7}
	14.48 mag		17.12 mag	
α_{f2}	-1.50 ± 0.04	-1.54 ± 0.10	-1.01 ± 0.01	-1.00[a]
t_{jb} (s)	$1.0 \pm 0.2 \times 10^5$	1.0×10^{5}[b]	$5.44 \pm 0.2 \times 10^4$	5.44×10^{4}[b]
α_{f3}	-2.18 ± 0.8	-2.05 ± 0.5	-2.05 ± 0.7	-1.75 ± 1.0
RS			RS	
α_{r1}	3.32 ± 1.2	5.19 ± 1.3	5.5[a]	5.5[a]
t_p(s)	1064[b]	1064[b]	1021[b]	1021[b]
F_p (Jy)	2.47×10^{-3}	4.40×10^{-6}	7.19×10^{-3}	3.59×10^{-6}
	15.24 mag		14.07 mag	
α_{r2}	-5.90 ± 1.0	-8.26 ± 1.3	-2.10[a]	-2.10[a]
		Steep decay		Steep decay
α_{sd}		-4.18 ± 0.2		-4.16 ± 0.2

Notes.
[a] This indicates that the parameter is fixed during the fitting.
[b] This indicates that the parameter is simultaneously fit for both optical and X-ray data.

and X-ray band data are also summarized in Table 4 and shown in Figure 5 (right panel). Similar to Scenario I, we then used the same model and parameters derived from the *R*-band fit re-scaled to other light curves. The results are shown in Figure 6 (right panel), again with shifting. This scenario can well explain the early fast rise behavior in all bands.

Comparing the two scenarios, we find that Scenario I can represent most optical data and can better account for the X-ray data than Scenario II. However, it cannot well match the early very steep rise in the UVOT-*u* band. On the other hand, Scenario II can represent the early fast rising behavior in the optical band (including UVOT-*u* band), but the fits to the X-ray data are not as good as Scenario I. We note that our Scenario II is similar to another variant of Scenario II recently proposed by Gao (2011), but we conclude that the optical data before $\sim$ 350 s are generated by the optical prompt emission.

3.2.2. Afterglow SED Analysis

In order to study the SED of the afterglow, we selected four epochs when we have the best multi-band data coverage: 550 s, 1.1 ks, 5.9 ks, and 35 ks. Since no significant color evolution is observed in the optical data, we interpolate (or extrapolate if necessary) the optical band light curve to these epochs when no direct observations are available at the epochs. The optical data used for constructing the SED are listed in Table 5. The X-ray data are re-binned using the data around the four epochs. The spectral fitting is then performed using Xspec software. During the fitting, the Galactic hydrogen column density, $N_{\rm H}$, is fixed to 1.6×10^{20} cm^{-2} (Kalberla et al. 2005), and the host galaxy hydrogen column density is fixed to 4.0×10^{21} cm^{-2}. These are derived from an average spectral fitting of the late-time XRT PC data. We tried both the broken power-law and the single power-law models for the afterglow SED. For the broken power-law model, we set $\Gamma_2 = \Gamma_1 - 0.5$, assuming a cooling break between the optical and X-ray bands. Meanwhile, we also investigated

Table 5
SED Data (in magnitude) at Four Different Epochs

Time	550 s	1.13 ks	5.9 ks	35 ks
uvw1	20.13 ± 0.50	16.91 ± 0.18	19.71 ± 0.30	22.50 ± 0.70
u	17.13 ± 0.20	14.98 ± 0.06	17.50 ± 0.10	20.47 ± 0.30
b	17.54 ± 0.16	15.23 ± 0.05	17.92 ± 0.07	20.97 ± 0.30
v	17.13 ± 0.30	14.68 ± 0.06	17.45 ± 0.14	20.63 ± 0.50
white	17.80 ± 0.12	15.25 ± 0.05	17.92 ± 0.05	20.74 ± 0.22
U	...	...	17.74 ± 0.1	20.69 ± 0.1
B	...	...	18.05 ± 0.1	20.86 ± 0.1
V	...	...	17.24 ± 0.1	20.20 ± 0.1
R	16.07 ± 0.20	14.10 ± 0.06	16.84 ± 0.1	19.73 ± 0.1
I	...	...	16.39 ± 0.1	19.21 ± 0.1
g	...	...	...	20.76 ± 0.07
r	...	...	...	20.12 ± 0.05
i	...	...	...	19.76 ± 0.06
z	...	...	...	19.46 ± 0.09

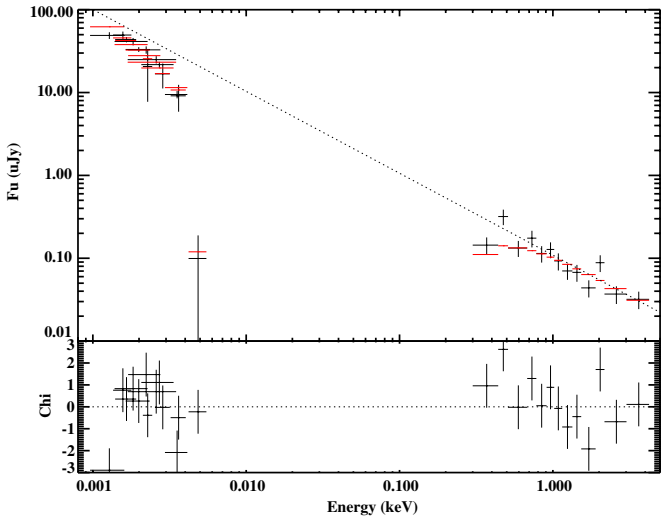

Figure 7. Afterglow SED of GRB 110205A at 35 ks. Black points are the observed data; red points are the predicted value from the model. Dotted line is the original power-law model without absorption or extinction.
(A color version of this figure is available in the online journal.)

the use of three different extinction laws, namely, the Milky Way (MW) and, Large and Small Magellanic Clouds (LMC and SMC), for the host galaxy extinction model. The $E(B-V)$ from the Galactic extinction is set to 0.01 (Schlegel et al. 1998) during the fitting. The best-fit results are listed in Table 6.

The 5.9 ks and 35 ks (see Figure 7) SEDs have the best data coverage, and they are ascribable to the FS component only. We therefore use these two SEDs to constrain the extinction properties of the afterglow. We find that the SMC and LMC dust models provide acceptable and better fits than the MW dust model. The data are equally well fit by the broken power-law and the single power-law model. For the broken power-law model, the break energy is found to be within the optical band (0.0025 ± 0.0006 keV). Within the 3σ error, one cannot separate the optical and X-ray data to two different spectral regimes. The lack of clear breaks in optical light curves between 5.9 and 35 ks also disfavors the possibility of the break energy passing through the optical band.

3.3. Host Galaxy Search

We have performed a deep search for the host galaxy of the GRB. Observations were performed with the 2.2 m Calar Alto

Table 6
SED Fitting at Different Epochs

Model	Time	$E(B-V)$	Γ_1	E_b (keV)	$\Gamma_2=\Gamma_1+0.5$	Norm	χ^2/dof
MW	Bknplaw						
	550 s	$0.11^{+0.02}_{-0.02}$	$1.36^{+0.033}_{-0.034}$	$0.41^{+0.074}_{-0.107}$	1.86	$0.23^{+0.039}_{-0.019}$	124.8/81 = 1.54
	1.13 ks	$0.19^{+0.009}_{-0.004}$	$2.10^{+0.021}_{-0.022}$	$4.94^{+4.93}_{-4.93}$	2.60	$0.038^{+4.39E-3}_{-4.0E-3}$	13.6/4 = 3.6
	5.9 ks	$0.16^{+0.02}_{-0.007}$	$1.59^{+0.0100}_{-0.027}$	$1.00\text{E-}03^{+1.5E-3}_{-1.0E-3}$	2.09	$0.086^{+4.34E-3}_{-0.022}$	20.2/23 = 0.88
	35 ks	$0.13^{+0.009}_{-0.008}$	$1.57^{+0.011}_{-0.012}$	$1.70\text{E-}03^{+3.66E-3}_{-1.57E-4}$	2.07	$4.03\text{E-}03^{+2.15E-4}_{-1.89E-3}$	38.9/22 = 1.77
MW	plaw						
	550 s	0.26	...	...	1.70	0.14	179.8/82 = 2.19
	1.13 ks	$0.19^{+0.009}_{-0.009}$	...	...	$2.10^{+0.022}_{-0.022}$	$0.038^{+0.004}_{-0.004}$	13.6/5 = 2.72
	5.9 ks	$0.16^{+0.020}_{-0.019}$	...	...	$2.09^{+0.027}_{-0.027}$	0.027^{+1E-4}_{-1E-4}	20.2/24 = 0.84
	35 ks	0.13	...	...	2.07	1.59E-04	55.6/23 = 2.42
LMC	Bknplaw						
	550 s	$0.10^{+0.021}_{-0.017}$	$1.39^{+0.033}_{-0.033}$	$0.36^{+0.0951}_{-0.151}$	1.89	$0.25^{+0.076}_{-0.027}$	116.1/81 = 1.43
	1.13 ks	$0.16^{+0.013}_{-0.004}$	$1.64^{+0.013}_{-0.030}$	$2.88^{+2.60E-3}_{3.34E-3}$	2.14	$0.72^{+0.035}_{-0.027}$	8.5/4 = 2.13
	5.9 ks	$0.13^{+0.018}_{-0.019}$	$1.61^{+0.099}_{-0.049}$	$2.87\text{E-}03^{+7.01E-4}_{-9.33E-4}$	2.11	$0.051^{+0.007}_{-0.020}$	16.1/23 = 0.70
	35 ks	$0.10^{+0.006}_{-0.007}$	$1.55^{+0.016}_{-0.014}$	$2.07\text{E-}03^{+5.14E-4}_{-3.48E-4}$	2.05	$3.70\text{E-}03^{+2.58E-4}_{-3.85E-4}$	26.4/22 = 1.20
LMC	plaw						
	550 s	$0.24^{+0.023}_{-0.021}$	...	...	$1.75^{+0.033}_{-0.031}$	$0.141^{+3.93E-3}_{-3.85E-3}$	162.5/82 = 1.98
	1.13 ks	$0.14^{+0.006}_{-0.006}$	...	...	$2.09^{+0.021}_{-0.021}$	$0.039^{+4.45E-3}_{-4.13E-3}$	13.9/5 = 2.78
	5.9 ks	$0.10^{+0.011}_{-0.011}$	...	...	$2.04^{+0.020}_{-0.020}$	$2.71\text{E-}03^{+0.001}_{-1.35E-4}$	19.4/24 = 0.81
	35 ks	$0.07^{+0.006}_{-0.009}$	...	...	$2.01^{+0.015}_{-0.015}$	$1.65\text{E-}04^{+1.04E-05}_{-1.05E-05}$	39.0/23 = 1.70
SMC	Bknplaw						
	550 s	$0.08^{+0.016}_{-0.014}$	$1.38^{+0.032}_{-0.032}$	$0.37^{+0.09}_{-0.14}$	1.88	$0.25^{+0.068}_{-0.026}$	114.3/81 = 1.41
	1.13 ks	$0.11^{+0.005}_{-0.005}$	$2.06^{+0.020}_{-0.021}$	$5.05^{+-4.93}_{-4.93}$	2.56	$0.039^{+4.56E-3}_{-2.24E-3}$	24.7/4 = 6.18
	5.9 ks	$0.09^{+0.005}_{-0.004}$	$1.56^{+0.024}_{-0.028}$	$2.74\text{E-}03^{+9.4E-4}_{-5.05E-4}$	2.06	$0.052^{+5.57E-3}_{-7.14E-3}$	17.3/23 = 0.75
	35 ks	$0.08^{+0.005}_{-0.006}$	$1.54^{+0.016}_{-0.013}$	$2.43\text{E-}03^{+4.53E-4}_{-3.7E-4}$	2.04	$3.42\text{E-}03^{+2.78E-4}_{-2.75E-4}$	24.3/22 = 1.1
SMC	plaw						
	550 s	0.19	...	...	1.75	0.136	189.5/82 = 2.31
	1.13 ks	$0.11^{+0.005}_{-0.005}$	...	...	$2.06^{+0.021}_{-0.020}$	$0.039^{+4.40E-3}_{-4.12E-3}$	24.7/5 = 4.14
	5.9 ks	$0.07^{+0.007}_{-0.007}$	...	...	$2.01^{+0.017}_{-0.017}$	$2.68\text{E-}03^{+1.3E-4}_{-1.3E-4}$	22.5/24 = 0.94
	35 ks	$0.05^{+0.005}_{-0.006}$	...	...	$1.98^{+0.014}_{-0.013}$	$1.65\text{E-}04^{+1.03E-05}_{-1.04E-05}$	36.7/23 = 1.60

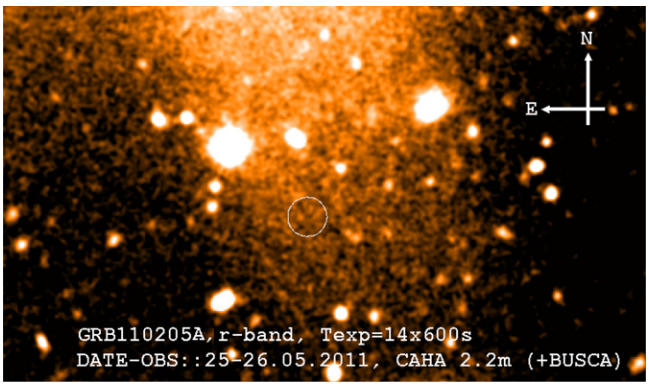

Figure 8. Host galaxy searching from 2.2 m Calar Alto telescope taken in r' band. The center of the circle indicates the afterglow location. No clear source is detected down to $r' \sim 24.8$ within 5″ of the afterglow location.

(A color version of this figure is available in the online journal.)

telescope 3.7 months after the burst. Images were taken with the BUSCA instrument in the u', g', r', and i' bands under good seeing condition, with image resolution of ∼0.″9. Co-adding was applied to a set of individual images in order to obtain a deeper limiting magnitude. Figure 8 shows one of the images taken in the r' band. The center of the circle indicates the afterglow location.

No clear source was detected near the afterglow location within a radius of 5″. The typical 3σ upper limits (AB magnitudes) are $u' \sim 24.1$, $g' \sim 24.4$, $r' \sim 24.8$, and $i' \sim 25.2$. A non-detection of the GRB host galaxy at $r' \sim 24.8$ is not surprising since a lot of GRB host galaxies are faint (e.g., Savaglio et al. 2009) or not detected at all (e.g., Ovaldsen et al. 2007). It is also superseded by the much deeper observation reported by Cucchiara et al. (2011) down to an upper limit of $r' \sim 27.21$ mag. At redshift $z = 2.22$, a magnitude of $r' \sim 27.2$ corresponds to an absolute magnitude $M_{r'} \sim -19.1$; the upper limit is fainter than 70% of the GRB host galaxies compared with large host galaxy samples searched systematically by some groups (see Figure 3 in Jakobsson & Fynbo 2010; Pozanenko et al. 2008).

4. THEORETICAL MODELING

The high-quality broadband data of GRB 110205A allow us to model both prompt emission and afterglow within the framework of the standard fireball shock model and derive a set of parameters that are often poorly constrained from other GRB

Table 7
Spectral Indices from Synchrotron Spectrum Prediction

Fast cooling				
	$\nu < \nu_a$	$\nu_a < \nu < \nu_c$	$\nu_c < \nu < \nu_m$	$\nu_m < \nu$
	2	1/3	$-1/2$	$-p/2$
Slow cooling				
	$\nu < \nu_a$	$\nu_a < \nu < \nu_m$	$\nu_m < \nu < \nu_c$	$\nu_c < \nu$
	2	1/3	$-(p-1)/2$	$-p/2$
Observed mean[a]		~0.6	~−0.5	

Note. [a]Spectral index = Γ + 1, i.e., α and β in *bandcut* model + 1.

observations. In the following, we discuss the prompt emission and afterglow modeling in turn.

4.1. Prompt Emission Modeling

4.1.1. General Consideration

The mechanism of GRB prompt emission is poorly known. It depends on the unknown composition of the jet, which affects the energy dissipation, particle acceleration, and radiation mechanisms (Zhang 2011). In general, GRB emission can be due to synchrotron, SSC in the regions where kinetic or magnetic energies are dissipated, or Compton scattering of thermal photons from the photosphere. Within the framework of the synchrotron-dominated model (e.g., the internal shock model; Rees & Mészáros 1994; Daigne & Mochkovitch 1998, or the internal magnetic dissipation model, e.g., Zhang & Yan 2011), one can have a broken power-law spectrum. Two cases may be considered according to the relative location of the cooling frequency ν_c and the synchrotron injection frequency ν_m: fast cooling ($\nu_c < \nu_m$) or slow cooling phase ($\nu_m < \nu_c$). The spectral indices are summarized in Table 7 (e.g., Sari et al. 1998).

For GRB 110205A, one may connect the two observed spectral breaks (E_0 and E_1) to ν_c and ν_m in the synchrotron model. Since the spectral index above E_1 is not well constrained from the data, we focus on the regime below E_1. The expected spectral density (F_ν) power-law index is -0.5 or $-(p-1)/2$, respectively, for the fast and slow cooling cases. The observed photon index $\beta \sim -1.5$ matches the fast cooling prediction closely. It is also consistent with slow cooling if the electron spectral index $p = 2$. For standard parameters, the prompt emission spectrum is expected to be in the fast cooling regime (Ghisellini et al. 2000). Slow cooling may be considered if downstream magnetic fields decay rapidly (Pe'er & Zhang 2006). The data are consistent with either possibility, with the fast cooling case favored by the close match between the predicted value and the data.

Below E_0 (which corresponds to ν_c for fast cooling or ν_m for slow cooling), the synchrotron emission model predicts a spectral index of 1/3. The observed mean value is ~0.60, which is harder than the predicted value. Considering the large errors of the spectral indices, this is not inconsistent with the synchrotron model. Furthermore, if the magnetic fields are highly tangled with small coherence lengths, the emission may be in the "jitter" regime. The expected spectral index can then be in the range of 0–1, consistent with the data (Medvedev 2006).

Overall, we conclude that the observed prompt spectrum is roughly consistent with the synchrotron emission model in the fast cooling regime. This is the first time that a clear two-break spectrum is identified in the prompt GRB spectrum that is roughly consistent with the prediction of the standard GRB synchrotron emission model.

The detection of bright prompt optical emission in GRB 110205A provides new clues to GRB prompt emission physics. The optical flux density of GRB 110205A is ~20 times above the extrapolation from the best-fit X/γ-ray spectra. On the other hand, the optical light curve roughly traces that of γ-rays. This suggests that the optical emission is related to high-energy emission but is powered by a different radiation mechanism or originates from a different emission location. The case is similar to that of GRB 080319B (Racusin et al. 2008) but differs from that of GRB 990123 (Akerlof et al. 1999), where the optical light curve peaks after the main episodes of γ-ray emission and is likely powered by the RS (Sari & Piran 1999; Mészáros & Rees 1999; Zhang et al. 2003; Corsi et al. 2005).

In the following, we discuss several possible interpretations of this behavior, i.e., the synchrotron + SSC model (Kumar & Panaitescu 2008; Racusin et al. 2008); the internal reverse + forward shock model (Yu et al. 2009); the two-zone models (Li & Waxman 2008; Fan et al. 2009); and the dissipative photosphere models (e.g., Pe'er & Waxman 2005; Pe'er et al. 2006; Giannios 2008; Lazzati et al. 2009, 2011; Lazzati & Begelman 2010; Toma et al. 2011; Beloborodov 2010; Vurm et al. 2011). We conclude that the synchrotron + SSC model and the photosphere model are disfavored by the data while the other two models are viable interpretations.

4.1.2. Synchrotron + SSC

Since the spectral shape of the SSC component is similar to the synchrotron component (Sari & Esin 2001), the observed two-break spectrum can be in principle due to SSC, while the optical emission is due to synchrotron. This scenario is, however, disfavored since it demands an unreasonably high energy budget. The arguments are the following:

We take interval 2 as an example since its flux varies relatively slowly. Let $h\nu_{\rm opt} \sim 10^{-2.3}$ keV and $h\nu_{\gamma,p} = E_0 \sim 10^{0.7}$ keV, the latter being the peak frequency of F_ν for the SSC component. Observations suggest that $F_{\nu_{\gamma,p}}/F_{\nu,\rm opt} \sim 20$ (see Figure 4 and Table 3). Define $\nu_{p,\rm syn}$ as the synchrotron F_ν peak frequency and $\beta_{\rm opt}$ as the spectral index around $\nu_{\rm opt}$ ($F_\nu \propto \nu^{\beta_{\rm opt}}$). Then, the Compton parameter can be written as

$$Y = \nu_{\gamma,p} F_{\nu_{\gamma,p}}/(\nu_{p,\rm syn} F_{\nu_{p,\rm syn}}) \approx 10^{4.3}(\nu_{p,\rm syn}/\nu_{\rm opt})^{-1-\beta_{\rm opt}}. \quad (5)$$

The inverse-Compton (IC) scattering optical depth is $\tau_e \sim F_{\nu_{\gamma,p}}/F_{\nu_{p,\rm syn}} \sim Y\nu_{p,\rm syn}/\nu_{\gamma,p} \sim 10^{1.3}(\nu_{p,\rm syn}/\nu_{\rm opt})^{-\beta_{\rm opt}}$.

One constraint ought to be imposed for the SSC scenario, that is, the high-energy spectrum of the synchrotron component at the lower bound of the X-ray band, i.e., $\nu_X = 0.3$ keV, must be below the observed flux density there. Since the spectral indices below and above $\nu_{\gamma,p}$ are consistent with 1/3 and $-1/2$, respectively, and the synchrotron spectral slope above its peak resembles that of its SSC component, one can express this constraint in terms of $F_{\nu_{p,\rm syn}}(\nu_X/\nu_{p,\rm syn})^{-1/2} < F_{\nu_{\gamma,p}}(\nu_X/\nu_{\gamma,p})^{1/3}$. With numbers plugged in, this translates to a lower limit on the Compton parameter:

$$Y > 10^{2.5}(\nu_{p,\rm syn}/\nu_{\rm opt})^{-1/2}. \quad (6)$$

The inferred high Y (Equation (5)) and τ_e values would inevitably lead to an additional spectral component due to the second-order IC scattering (Kobayashi et al. 2007; Piran et al. 2009). The second IC F_ν spectrum peaks at $h\nu_{\rm ic,2} \sim$

$h\nu_{\gamma,p}Y/\tau_e \sim 10^{0.7}(\nu_{p,\rm syn}/\nu_{\rm opt})^{-1}$ MeV, with a flux density $\sim\tau_e F_{\nu_{\gamma,p}} \sim 10^{1.3} F_{\nu_{\gamma,p}}(\nu_{p,\rm syn}/\nu_{\rm opt})^{-\beta_{\rm opt}}$. The nice fit of the *bandcut* model to the XRT–BAT–WAM spectrum rules out a second IC peak below 1 MeV (see Figure 4), which poses a constraint $\nu_{p,\rm syn}/\nu_{\rm opt} < 5$.

We then get a constraint $Y \gtrsim 10^4$ and $\tau_e \gtrsim 10$! This would lead to a serious energy crisis due to the second IC scattering. For $\nu_{p,\rm syn}/\nu_{\rm opt} \ll 1$, the second IC scattering might be in the Klein–Nishina regime and then be significantly suppressed, but the synchrotron peak flux density would be self-absorbed, causing the seed flux to be insufficient for the first IC scattering (Piran et al. 2009). In conclusion, the SSC scenario is ruled out due to the high Y value inferred.

4.1.3. Internal Reverse–Forward Shocks

Next we consider the internal shock model by calculating synchrotron emission from the RS and FS due to the collision of two discrete cold shells (e.g., Rees & Mészáros 1994; Daigne & Mochkovitch 1998; Yu et al. 2009). If the two shells have high density contrast, the synchrotron frequencies would peak around the γ-ray (reverse) and optical (forward) bands, respectively.

We first derive the frequency and flux ratio between the two shocks (Kumar & McMahon 2008). We define shell "1" as the fast-moving, trailing shell and shell "2" as the slower, leading shell. We use subscript "s" to represent the shocked region. The pressure balance at the contact discontinuity gives (e.g., Shen et al. 2010)

$$(\Gamma_{1s}^2 - 1)n_1 = (\Gamma_{2s}^2 - 1)n_2, \quad (7)$$

where Γ_{1s} and Γ_{2s} are the Lorentz factors (LFs) of the unshocked shells, respectively, measured in the shocked region rest frame, and n_1, n_2 are the unshocked shell densities measured in their own rest frames, respectively. This equation is exact and is valid for both relativistic and sub-relativistic shocks. Using Lorentz transformation of LFs, the above equation can give the shocked region LF Γ_s for given n_1/n_2, Γ_1, and Γ_2.

We assume that ϵ_e, ϵ_B, and p are the same for both RS and FS. In the shocked region, the magnetic field energy density is $U'_B = B'^2/8\pi = 4\bar{\Gamma}(\bar{\Gamma} - 1)\epsilon_B n$, where $\bar{\Gamma}$ is the relative LF between the downstream and upstream of the shock, which corresponds to Γ_{1s} and Γ_{2s} for RS and FS, respectively. Since the internal energy density is the same in the RS and FS regions (due to pressure balance at contact discontinuity), it is obvious that the two shocked regions have the same B', independent of the strengths of the two shocks. The injection energy and the cooling energy of the electrons are $\gamma_m \propto (\bar{\Gamma} - 1)$ and $\gamma_c \propto 1/(U'_B t')$, respectively. Since synchrotron frequency $\nu \propto \Gamma_s B' \gamma^2$, one finds the frequency ratios to be

$$\frac{\nu_{m,1}}{\nu_{m,2}} = \frac{(\Gamma_{1s} - 1)^2}{(\Gamma_{2s} - 1)^2}, \quad (8)$$

$$\frac{\nu_{c,1}}{\nu_{c,2}} = 1. \quad (9)$$

Thus, the injection frequency ratio can be determined for given Γ_1, Γ_2, and shell density ratio n_1/n_2. We numerically calculate $\nu_{m,1}/\nu_{m,2}$ as a function of n_1/n_2 and plot it in Figure 9, and we find that for different shell LF ratios $\nu_{m,1}/\nu_{m,2}$ lies between $(n_1/n_2)^{-1}$ and $(n_1/n_2)^{-2}$.

The maximum flux density is $F_{\nu,\rm max} \propto \Gamma_s N_e B'$, where N_e is the total number of the shocked electrons. So one has $F_{\nu,\rm max,1}/F_{\nu,\rm max,2} = m_1/m_2$, where m is the shock swept-up mass. We calculate the mass ratio in the rest frame of the shocked region. In this frame the density of the shocked fluid is $4\bar{\Gamma}n$; the rate of mass sweeping is proportional to the sum of the shock front speed and the unshocked fluid speed. We then get

$$\frac{m_1}{m_2} = \frac{\Gamma_{1s} n_1 (\beta_{rs,s} + \beta_{1s})}{\Gamma_{2s} n_2 (\beta_{sf,s} + \beta_{2s})}, \quad (10)$$

where the speeds β are all defined positive and are measured in the shocked fluid rest frame; the subscripts "rs" and "fs" refer to the RS and FS front, respectively. From the shock jump conditions (e.g., Blandford & McKee 1976), one gets

$$\beta_{rs,s} = \frac{(\hat{\gamma} - 1)\beta_{1s}}{1 + 1/\Gamma_{1s}}, \quad (11)$$

where $\hat{\gamma}$ is the adiabatic index for a relativistic fluid. Using an empirical relation $\hat{\gamma} = (4\bar{\Gamma} + 1)/(3\bar{\Gamma})$ to smoothly connect the sub-relativistic shock regime to the relativistic shock regime, we obtain $(\beta_{rs,s} + \beta_{1s}) = 4\beta_{1s}/3$. A similar result applies to the FS front. Thus, Equation (10) becomes

$$\frac{F_{\nu,\rm max,1}}{F_{\nu,\rm max,2}} = \frac{m_1}{m_2} = \frac{\Gamma_{1s}\beta_{1s} n_1}{\Gamma_{2s}\beta_{2s} n_2} = \left(\frac{n_1}{n_2}\right)^{1/2}, \quad (12)$$

where we have used Equation (7). This result is also numerically plotted in Figure 9.

According to Figure 9, in the internal RS–FS model, the optical emission shell must have a higher pre-shock density and a larger shock swept-up mass and hence should have a higher $F_{\nu,\rm max}$. The analysis of GRB 110205A prompt X/γ-ray spectrum suggests that the characteristic synchrotron frequencies are $h\nu_{c,\gamma} \sim 5$ keV and $h\nu_{m,\gamma} \sim 300$ keV (see Section 3.1); then we have $F_{\nu,\rm max,\gamma}/F_{\nu,\rm opt} \sim 20$ and $\nu_{m,\gamma}/\nu_{\rm opt} \sim 6\times 10^4$. Therefore, if the internal RS–FS model would work for this burst, the maximum flux density of the optical producing shell $F_{\nu,\rm max}$ must be $\gg F_{\nu,\rm opt}$; since the cooling frequencies of the two shells are equal (Equation (9)), the optical shell must be in the slow cooling ($\nu_m < \nu_c$) regime.

In order to have the observed $F_{\nu,\rm opt}$ much smaller than the optical shell $F_{\nu,\rm max}$, either $\nu_{\rm opt}$ has to be far below or far above ν_m, or the self-absorption frequency has to be $\nu_a > \nu_{\rm opt}$, or both. In the following, we use the observed $F_{\nu,\rm max,\gamma}/F_{\nu,\rm opt}$ and $\nu_{m,\gamma}/\nu_{\rm opt}$ as constraints and $\nu_a/\nu_{\rm opt}$ (for the optical shell) as a free parameter and derive the permitted relation between $\nu_{m,\gamma}/\nu_{m,\rm opt}$ and $n_\gamma/n_{\rm opt}$, where $n_\gamma/n_{\rm opt}$ is the density ratio of the γ-ray shell over the optical shell and is given by the maximum flux density ratio of the two shells (Equation (12)). We then overlay the permitted relations onto the internal RS–FS model predictions shown in Figure 9, right panel, in order to find the permitted model parameter values, i.e., shell LF ratio $\Gamma_{\rm fast}/\Gamma_{\rm slow}$, shell density ratio $n_\gamma/n_{\rm opt}$, and $\nu_a/\nu_{\rm opt}$.

For the optical shell, the relation between $F_{\nu,\rm opt}$ and $F_{\nu,\rm max}$ is determined according to the standard broken power-law synchrotron spectrum (e.g., Sari et al. 1998; Granot & Sari 2002), depending on the free parameter $\nu_a/\nu_{\rm opt}$, which varies from <1 to >1. In addition, we impose an additional constraint that the high-energy spectrum of the optical producing shell emission should not exceed the observed flux density at the lower bound of the X-ray band, i.e., at $\nu_X = 0.3$ keV, so that the spectral slope there would not be inconsistent with the observed one. The final results are shown in Figure 10.

From Figure 10, we conclude that the prompt SED data of GRB 110205A can be reproduced by the internal RS–FS synchrotron model under the following conditions: $\nu_{m,\gamma}/\nu_{m,\rm opt} \approx$

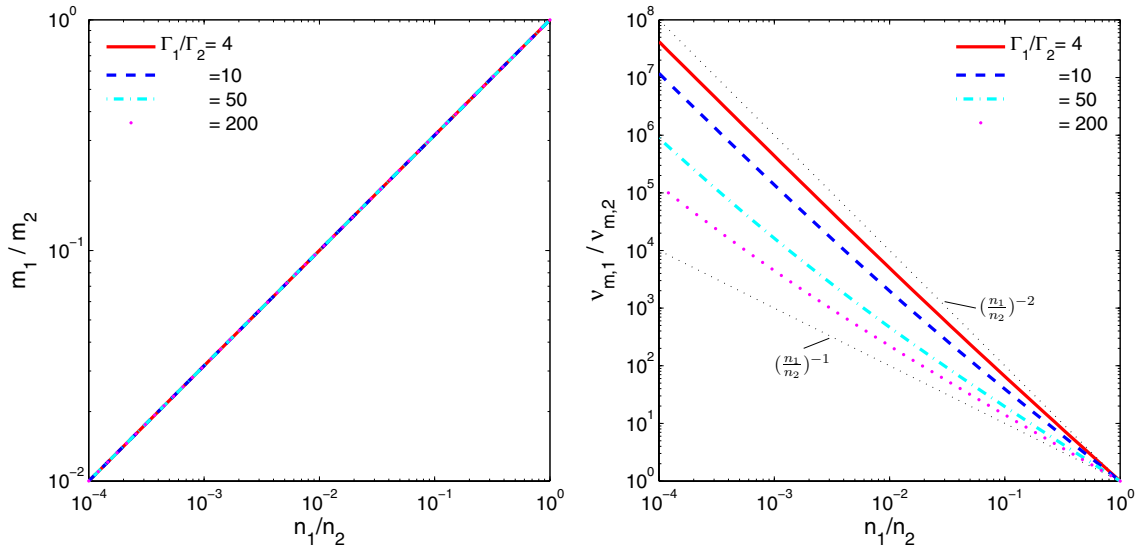

Figure 9. Ratios of the shock swept-up masses and synchrotron injection frequencies between the pair of shocks due to collision of two cold relativistic shells. The results are valid for both sub-relativistic and relativistic shocks and are insensitive to Γ_2 as long as $\Gamma_2 \gg 1$. Note that these results can be extrapolated to the region of $n_1 > n_2$, and each result is symmetric about the (1, 1) point.

(A color version of this figure is available in the online journal.)

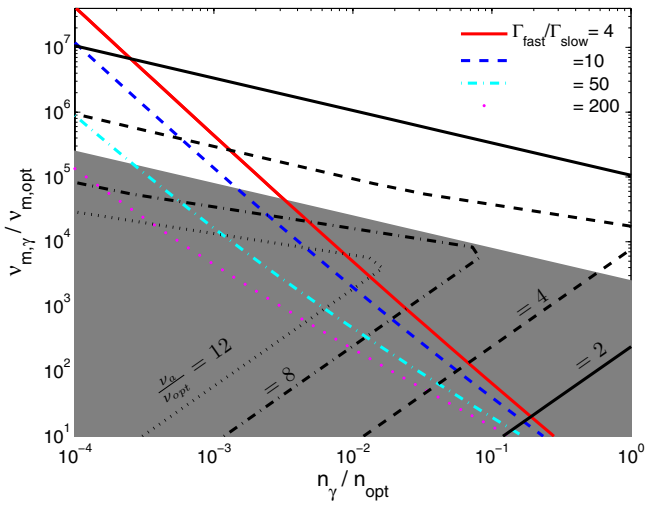

Figure 10. GRB 110205A-permitted $\nu_{m,\gamma}/\nu_{m,\rm opt}$ vs. $n_\gamma/n_{\rm opt}$ relations for varying $\nu_a/\nu_{\rm opt}$ values (black lines), superimposed on the internal RS–FS model predictions (colored lines, from the right panel of Figure 9). The locations where the data-permitted and the model-predicted relations intersect correspond to the specific model parameter values with which the model could work for GRB 110205A. Electron index $p = 3$ is assumed. The shaded region is forbidden because there the flux density at $\nu_X = 0.3$ keV in the emission spectrum of the optical producing shell will exceed the observed value of $F_{\nu,X}$, causing the spectral slope to be inconsistent with the observed one. Note that for $\nu_a < \nu_{\rm opt}$ the data-permitted $\nu_{m,\gamma}/\nu_{m,\rm opt}$ vs. $n_\gamma/n_{\rm opt}$ relations have no intersection with the internal RS–FS predictions unless $n_\gamma/n_{\rm opt}$ is unreasonably small.

(A color version of this figure is available in the online journal.)

10^6–10^7, $n_\gamma/n_{\rm opt} \approx 10^{-4}$–$10^{-3}$, and $\nu_a/\nu_{\rm opt} \approx$ 2–6 for the optical shell; and the LF ratio between the two shells falls into a wide range ~4–100. In Figure 10, the electron index $p = 3$ has been adopted. A smaller p value only increases the inferred $\nu_{m,\gamma}/\nu_{m,\rm opt}$ and decreases $n_\gamma/n_{\rm opt}$ both by a factor <10, without affecting the conclusion.

4.1.4. Emission Radius

The distance of the GRB emission region from the central engine ($R_{\rm GRB}$) has been poorly constrained. If prompt optical data are observed, one may apply the constraint on the synchrotron self-absorption frequency (ν_a) to constrain $R_{\rm GRB}$ (Shen & Zhang 2009). One needs to assume that the optical and γ-ray emissions are from essentially the same radius in order to pose such a constraint. This is the simplest scenario and is valid for some scenarios we have discussed, e.g., the internal RS–FS model as discussed in Section 4.1.3. In the following, we derive the emission radius based on the one-zone assumption, bearing in mind that optical and gamma-ray emissions can come from different zones.

For GRB 110205A, the synchrotron optical emission from the optical producing shell is self-absorbed and has the following frequency ordering: $\nu_m < \nu_{\rm opt} < \nu_a < \nu_c$ (Section 4.1.3). For such a frequency ordering, ν_a is determined by (Shen & Zhang 2009)

$$2\gamma_a m_e \nu_a^2 = F_{\nu_a}\left(\frac{D_L}{R}\right)^2 \frac{(1+z)^3}{\Gamma}, \quad (13)$$

where D_L is the luminosity distance, F_{ν_a} is the observed flux density at ν_a, and $\gamma_a = [16 m_e c(1+z)\nu_a/(3eB'\Gamma_s)]^{1/2}$ is the LF of electrons whose synchrotron frequency is ν_a. Expressing F_{ν_a} in terms of the self-absorbed optical flux density, $F_{\nu_a} = F_{\nu,\rm opt}(\nu_a/\nu_{\rm opt})^{5/2}$, we find that ν_a is canceled out in the above equation:

$$2m_e\left(\frac{16 m_e c}{3eB'}\right)^{1/2}\left(\frac{R}{D_L}\right)^2 \frac{(1+z)^{7/2}}{\Gamma_s^{3/2}} = F_{\nu,\rm opt}\nu_{\rm opt}^{-5/2}. \quad (14)$$

For an observed average $F_{\nu,\rm opt} \approx 10^{1.8}\mu$Jy, $h\nu_{\rm opt} \approx 10^{-2.3}$ keV, and other numbers for GRB 110205A, we obtain

$$R_{\rm GRB} \approx 2.8\times 10^{13}\left(\frac{\Gamma_s}{250}\right)^{3/4}\left(\frac{B'}{10^5\ {\rm G}}\right)^{1/4}\ {\rm cm}. \quad (15)$$

We have normalized Γ_s to 250 and B' to 10^5 G. The former normalization can be justified from the afterglow data (Section 4.2.1). The value of B' is loosely determined and may be estimated by $B' \sim 10^6\zeta L_{52}R_{13}\Gamma_2$ G, where $\zeta \leqslant 1$ is a constant parameter (Zhang & Mészáros 2002). This gives

$B' \sim 10^5$ G for the parameters of GRB 110205A. Interpreting E_1 as ν_m would also give rise to $B' \sim 10^5$ G if $\Gamma_{1s} \sim 3$ and $\epsilon_e \sim 0.1$. We note that $R_{\rm GRB}$ is a weak function of B', so that an estimate $R_{\rm GRB} \approx 3 \times 10^{13}$ cm is robust. This radius is consistent with the expectation of the internal shock model (e.g., Piran 2005).

Note that in the Shen & Zhang (2009) method one has to assume that both the optical and γ-rays belong to the same continuum component and partly rely on the γ-ray low-energy spectral slope to constrain the ν_a location. However, this assumption is discarded in the case of GRB 110205A: it is inferred that in the internal RS–FS model the optical shell has $\nu_{\rm opt} < \nu_a$ (Section 4.1.3), for which $R_{\rm GRB}$ is worked out without the aid of the γ-ray spectral information.

4.1.5. Two-zone Models

The GRB 110205A prompt observations might be also interpreted if the optical emission region is decoupled from the γ-ray/X-ray emission regions. There are models that envisage that the γ-rays are produced in internal shocks at small radii between shells with large LF contrasts, while the optical emission is generated in internal shocks at larger radii by shells with lower magnetic fields and smaller LF contrasts. This can happen in two scenarios. According to Li & Waxman (2008), even after collisions and mergers of shells with large LF contrasts, the outflow still comprises discrete shells with variations, though with reduced relative LFs, which could lead to the "residual" collisions at larger radii. Fan et al. (2009) considered a neutron-rich GRB outflow in which free neutrons are decoupled from the proton shells until decaying at large radii. Violent collisions among the proton shells occur at smaller radii, while some later-ejected, slower, proton shells catch up with the decayed neutron shells at large radii and give weaker collisions. Both scenarios might work for GRB 110205A, since in either case, the large-radii collisions would bear a similar temporal information as the small-radii collisions, rendering a coarse optical–γ-ray correlation. A defining property of these two-zone scenarios is that the optical pulses should display a larger variability timescale δt than the γ-ray pulses, and they should lag behind the γ-ray pulses by $\sim R_{\rm opt}/2\Gamma^2 c \sim 0.2\,{\rm s} R_{\rm opt,15}\Gamma_{2.5}^{-2}$ s. These predictions could be tested by future, high temporal resolution, prompt optical observations of similar bursts.

4.1.6. Dissipative Photosphere Emission Model

Recently, several independent groups (e.g., Giannios 2008; Toma et al. 2011; Beloborodov 2010; Lazzati & Begelman 2010; Vurm et al. 2011) have developed an improved version of the photosphere emission model of GRB prompt emission. This model invokes energy dissipation in the Thomson-thin layer of the photosphere, so that the photosphere spectrum deviates from the thermal form through IC upscattering. The same electrons also emit synchrotron photons, which may account for the optical excess. A difficulty of this scenario is that the low-energy spectral index below E_p is too hard (e.g., $\alpha = +0.4$; Beloborodov 2010) to account for the observations ($\alpha = -1.5$). The data of GRB 110205A (double breaks and spectral slopes) of the X/γ-ray component do not comply with the predictions of this model but are rather consistent with the standard synchrotron model (see Section 4.1.1). We conclude that the dissipative photosphere model does not apply at least to this burst.

4.2. Afterglow Modeling

4.2.1. Initial Lorentz Factor

For both Scenarios I and II, the optical peak time $t_p = 1045 \pm 63$ s corresponds to the deceleration time. Since this time is much longer than T_{90} ($\sim$257 s), it is pertinent to consider a "thin" shell regime (Sari & Piran 1995). The peak time can then be used to estimate the initial Lorentz factor of the ejecta (e.g., Mészáros 2006; Molinari et al. 2007): $\Gamma_0 \sim 560(E_{\gamma,{\rm iso},52}/\eta_{0.2} n_0 t_{p,z,1}^3)^{1/8}$, where $E_{\gamma,{\rm iso},52}$ is the isotropic equivalent energy in units of 10^{52} erg s^{-1}, $\eta_{0.2}$ is the radiative efficiency in units of 0.2, n_0 is local density in units of cm^{-3}, and $t_{p,z,1}$ is the peak time corrected for cosmological time dilation in units of 10 s. For GRB 110205A, with redshift $z = 2.22$ and fluence of $2.7^{+0.7}_{-0.4} \times 10^{-5}$ erg cm^{-2} (15–3000 keV; Sakamoto et al. 2011c), we derive the rest-frame 1 keV–10 MeV isotropic energy $E_{\gamma,{\rm iso}} = 46^{+4}_{-7} \times 10^{52}$ erg. With $t_{p,z,1} = 32.4 \pm 1.8$, we finally estimate

$$\Gamma_0 = 245^{+7}_{-10}(\eta_{0.2} n_0)^{-1/8}. \quad (16)$$

This value follows the empirical relation $\Gamma_0 \sim 182 {\rm E}_{\gamma,{\rm iso},52}^{0.25\pm0.03}$ recently found by Liang et al. (2010) within the 2σ range.

4.2.2. Light Curves

Scenario I

In this scenario, the optical bump around t_p is mostly contributed by the FS. Fitting the light curves, one can constrain the temporal slopes of the RS component. In the R band, the temporal indices are $\alpha_{r1} = 3.32 \pm 1.2$ (rising phase) and $\alpha_{r2} = -5.90 \pm 1.0$ (decaying phase), while in the X-ray band, they are $\alpha_{r1} = 5.19 \pm 1.3$ (rising) and $\alpha_{r2} = -8.26 \pm 1.3$ (decaying). The steep rising slope ($\sim$4) is consistent with the expectation in the thin shell ISM RS model (e.g., Kobayashi 2000; Zhang et al. 2003). The decaying slopes look too steep as compared with the theoretically expected values (e.g., roughly $-2-\beta$ for the so-called curvature effect; Kumar & Panaitescu 2000). However, strictly speaking, the expected decay index is valid when the time zero point is placed to t_p. The results are therefore not inconsistent with the theoretical expectations. Compared with other GRBs with the RS emission identified (which typically peaks around or shortly after the T_{90} duration), an RS emission peaking at $\sim$1100 s after the burst is rare and has not been seen before (though previously, the optical brightening in the ultra-long GRB 091024 was claimed by Gruber et al. 2011 to be caused by the rising RS, but its data coverage is very sparse and the RS origin was not exclusively determined, e.g., it could also be due to the FS peak in a wind medium).

For the FS component, the rising index is set to +3 during the fitting for both the optical and X-ray bands. The decay index after the peak is fitted to $\alpha_{of2} = -1.50 \pm 0.04$ in the optical band and $\alpha_{Xf2} = -1.54 \pm 0.1$ in the X-ray band. We also constructed two SEDs at the epochs 5.9 ks and 35 ks during the decay phase. We find that the only model that satisfies the closure relation (e.g., Sari et al. 1998; Granot & Sari 2002; Zhang & Mészáros 2004) is the ISM model in the $\nu_m < \nu_o < \nu_x < \nu_c$ spectral regime. For example, our SED at 5.9 ks gives a spectral slope $\beta \sim -1.01 \pm 0.02$ across the entire energy band. The optical temporal decay index $\alpha_o = -1.50 \pm 0.04$ matches the expected closure relation $\alpha = (3/2)\beta$ well. The X-ray decay slope $\alpha_{Xf2} = -1.54 \pm 0.1$ within 1σ error is consistent with the closure relation. The electron energy index, $p = -2\beta + 1 \sim 3.0$, is also consistent with its value derived from the temporal

index $p = (-4\alpha + 3)/3 = 3.0 \pm 0.08$ derived from α_o and $p = 3.05 \pm 0.14$ derived from α_x.

At late times around $\sim 10^5$ s, the decay index becomes steeper in both the optical and X-ray bands, which is probably caused by a jet break. The simultaneous fit suggests a $t_{jb} = 1.0 \pm 0.2 \times 10^5$ s from the two band light curves. The post-break temporal indices are consistent with a jet break without significant sideways expansion, which is predicted to be steeper by 3/4. But the conclusion is not conclusive due to large errors. The jet angle can be calculated using (Sari et al. 1999) $\theta = 1/6(t_{jb}/1+z)^{3/8}(n\eta_{0.2}/E_{\gamma,\rm iso,52})^{1/8}$. Taking $t_{jb} \simeq 1.0 \times 10^5$ s $=$ 1.2 days and $E_{\gamma,\rm iso,52} = 46.0$, we derive $\theta = (4.1^{+3.5}_{-1.0})^\circ$. With a beaming factor of $\theta^2/2$, the corresponding jet-angle-corrected energy is $E_\gamma = 1.2 \times 10^{51}$ erg.

Scenario II

In this scenario, the early steep rise and bright peak are dominated by the RS component only. It can also be well explained by an ISM model in the thin shell regime. Within this scenario, the FS component shows up and peaks later. The FS peak is defined by ν_m crossing the optical band. There should also be a break time in the FS light curve at the RS peak t_p, which is caused by the onset of the afterglow. After the FS peak, the afterglow analysis is similar to Scenario I. We find that the best afterglow model for this scenario is the ISM model assuming $\nu_m < \nu_c < \nu_o < \nu_x$. From the spectral index $\beta = -1.01$, one can derive $p = 2.02$. Since $\alpha \sim 1.0$ for both optical and X-ray, the closure relation $\alpha = (3\beta+1)/2$ is well satisfied.

The X-ray bump around 1000 s is also consistent with being the emission from the RS. Our SED fit (see Table 6) near the peak at 1.13 ks shows that the best fits are a single power-law (LMC and SMC model) or a broken power-law model (LMC model) with the break energy $\sim$2.9 keV. The result suggests that the optical and X-ray bands belong to the same emission component with $\nu_m < \nu_{\rm opt} < \nu_X < \nu_c$ (for single power law) or $\nu_m < \nu_{\rm opt} < \nu_c < \nu_X$ (for broken power law). In the case of a thin ejecta shell and ISM, the synchrotron cooling frequency at the time when the RS crosses the ejecta, t_p, can be estimated to be $\nu_c(t_p) = 2 \times 10^{26}\Gamma^{-4}\ (\epsilon_B n)^{-3/2}(1+z)t_p^{-2}$ Hz (also see Kobayashi 2000). Adopting $\Gamma \sim 250$, $z = 2.22$, and $t_p = 1.1$ ks, which are relevant for GRB 110205A, this would require $\epsilon_B n \sim 10^{-5}$ cm^{-3}. Such a value, although in the low end of the generally anticipated parameter distribution range, is not impossible.

The jet break time derived from this scenario is somewhat earlier than Scenario I, which is $\sim(5.44 \pm 0.2) \times 10^4$ s from the simultaneous fitting. Adopting this break time, we derived a jet angle for this scenario of $\theta = (3.2^{+2.6}_{-0.9})^\circ$, which corresponds to a jet-angle-corrected energy of $E_\gamma = 7.2 \times 10^{50}$ erg.

4.2.3. RS Magnetization

The composition of the GRB ejecta is still not well constrained. Zhang et al. (2003) suggested that bright optical flashes generally require that the RS is more magnetized than the FS, namely, the ejecta should carry a magnetic field flux along with the matter flux (see also Fan et al. 2002; Panaitescu & Kumar 2004 for case studies). Since GRB 110205A has a bright RS component, it is interesting to constrain the RS parameters to see whether it is also magnetized. For both Scenarios I and II, since the peak time and maximum flux of both FS and RS can be determined (also shown in Table 4), one can work out the constraints on the RS magnetization following the method delineated in Zhang et al. (2003). The same notations are adopted here as in Zhang et al. (2003).

For Scenario I, the FS peaks at $t_\times$, where $\nu_{m,f} < \nu_R < \nu_{c,f}$, and then decays as $F_{\nu,f} \propto t^{-3(p_f-1)/4}$. For Scenario II, in the FS, one has $\nu_R \leqslant \nu_{m,f} < \nu_{c,f}$ at $t_\times$. The FS light curve still rises as $t^{1/2}$, until reaching $t_{p,f}$, where $\nu_R = \nu_{m,f} < \nu_{c,f}$. We define $(t_{p,r}, F_{\nu,p,r})$ and $(t_{p,f}, F_{\nu,p,f})$ as the peak times and peak flux densities in optical for RS and FS, respectively. Similar to those presented in Zhang et al. (2003), it follows naturally from the above that

$$\Re_t \equiv \frac{t_{p,f}}{t_{p,r}} = \begin{cases} 1, & \text{for Scenario I} \\ \Gamma_\times^{4/3}\Re_B^{-2/3}\Re_\nu^{-2/3}, & \text{for Scenario II} \end{cases} \quad (17)$$

$$\Re_F \equiv \frac{F_{\nu,p,r}}{F_{\nu,p,f}} = \begin{cases} \Gamma_\times^{2-p_f}\Re_B^{\frac{p_f+1}{2}}\Re_\nu^{\frac{p_f-p_r}{2}}, & \text{for Scenario I} \\ \Gamma_\times \Re_B \Re_\nu^{-\frac{p_r-1}{2}}, & \text{for Scenario II.} \end{cases} \quad (18)$$

Note that Scenario I is actually a special case of $\Re_t = 1$ of the more general Scenario II. The results are identical to those in Zhang et al. (2003) except that we do not use the RS decay slope $\alpha_{r,2}$ after $t_\times$ as one of the parameters. This was to avoid the ambiguity of the blastwave dynamics after the shock crossing. Instead, we keep p_r in the formulae and determine p_r from the better-understood RS rising slope before $t_\times$: $\alpha_{r,1} = (6p_r - 3)/2$.

For Scenario I, one can derive $\Re_t \sim 1$, $p_r \approx 2$, $p_f \approx 3$, and $\Re_F \approx 0.5$. Note that the entire optical peak around $t_\times$ is contributed mainly from the FS, which means p_r is poorly constrained. So we take $p_r = p_f \approx 3$. Then from Equation (18) we get

$$\Re_B \sim 7\Gamma_{\times,2}^{1/2} \sim 7.7. \quad (19)$$

For Scenario II, $\Re_t \approx 3.6$, $\Re_F \approx 16.5$, and $p_r \approx 2.3$. Plugging in numbers and from Equation (17), we have $\Re_B\Re_\nu \sim \Gamma_\times^2/6.8$. Combining it with Equation (18) and canceling out $\Re_\nu$, we get

$$\Re_B \sim 7\Gamma_{\times,2}^{0.18} \sim 7.2. \quad (20)$$

The numerical values are obtained by taking $\Gamma_\times = \Gamma_0/2 \sim 120$.

In both scenarios, the magnetic field strength ratio $\Re_B \equiv B_r/B_f$ is $\sim$7. This suggests that the RS is more magnetized than the FS. Since the magnetic field in the FS is believed to be induced by plasma instabilities (Weibel 1959; Medvedev & Loeb 1999; Nishikawa et al. 2009), a stronger magnetic field in the RS region must have a primordial origin, i.e., from a magnetized central engine.

4.2.4. Discussion

Comparing with the other recent work on GRB 110205A (Cucchiara et al. 2011; Gao 2011; Gendre et al. 2011), our Scenario II analysis, which concludes that the bright optical peak around 1000 s is dominated by the RS emission, agrees with that by Gendre et al. (2011) and Gao (2011). Our Scenario I analysis, though close to the conclusion by Cucchiara that it is dominated by the FS emission, has slight difference, as we also consider the RS contribution in our Scenario I.

Both scenarios in our analysis can interpret the general properties of the broadband afterglow. However, each scenario has some caveats. For Scenario I, as explained above, the best-fit model light curve is not steep enough to account for the data in the UVOT-u band ($\alpha \sim 5$ for R and $\alpha \sim 6$ for UVOT-u if we apply a single broken power-law fitting). Since the inconsistency only occurs in the bluest band with adequate data to constrain

the rising slope, we speculate that the steeper rising slope may be caused by a decreasing extinction with time near the GRB. No clear evidence of the changing extinction has been observed in other GRBs. In any case, theoretical models have suggested that dust can be destructed by strong GRB X-ray and UV flashes along the line of sight, so that a time-variable extinction is not impossible (e.g., Waxman & Draine 2000; Fruchter et al. 2001; Lazzati et al. 2002a; De Pasquale et al. 2003). For Scenario II, the model cannot well fit the X-ray peak around 1100 s. The main reason is that the required RS component to fit the optical light curve is not as narrow as that invoked in Scenario I. It is possible that the X-ray feature is simply an X-ray flare due to late central engine activities, which have been observed in many GRBs (e.g., Burrows et al. 2005b; Liang et al. 2006; Chincarini et al. 2007).

In the late optical light curve around 5×10^4 s, there is a re-brightening bump observed by LOT in four bands. Such bumps have been seen in many GRBs (e.g., GRB 970508, Galama et al. 1998; GRB 021004, Lazzati et al. 2002b; GRB 050820, Cenko et al. 2006; GRB 071025, Updike et al. 2008; GRB 100219A, Mao et al. 2012), which are likely caused by the medium-density bumps (e.g., Lazzati et al. 2002b; Dai & Wu 2003; Nakar & Granot 2007; Kong et al. 2010). Microlensing is another possibility (e.g., Garnavich et al. 2000; Gaudi et al. 2001; Baltz & Hui 2005), although the event rate is expected to be rather low.

Interestingly, linear polarization at a level of $P \sim 1.4\%$ was measured by the 2.2 m telescope at Calar Alto Observatory (Gorosabel et al. 2011) 2.73–4.33 hr after the burst. During this time, the afterglow is totally dominated by the FS in Scenario I or mostly dominated by the FS (with a small contamination from the RS) in Scenario II. The measured linear polarization degree is similar to several other detections in the late afterglow phase (e.g., Covino et al. 1999, 2003; Greiner et al. 2003; Efimov et al. 2003), which is consistent with the theoretical expectation of synchrotron emission in external shocks (e.g., Gruzinov & Waxman 1999; Sari 1999; Ghisellini & Lazzati 1999).

5. SUMMARY

We have presented a detailed analysis of the bright GRB 110205A, which was detected by both *Swift* and *Suzaku*. Thanks to its long duration, *Swift* XRT, UVOT, ROTSE-IIIb, and BOOTES telescopes were able to observe when the burst was still in the prompt emission phase. Broadband simultaneous observations are available for nearly 200 s, which makes it one of the exceptional opportunities to study the SED during the prompt phase. The broadband time-resolved spectra are well studied. For the first time, an interesting two-break energy spectrum is identified throughout the observed energy range, which is roughly consistent with the synchrotron emission spectrum predicted by the standard GRB internal shock model. Shortly after the prompt emission phase, the optical light curve shows a bump feature around 1100 s with an unusual steep rise ($\alpha \sim 5.5$) and a bright peak ($R \sim 14.0$ mag). The X-ray band shows a bump feature around the same time. This is followed by a more normal decay behavior in both optical and X-ray bands. At late times, a further steepening break is visible in both bands.

The rich data in both the prompt emission and afterglow phase make GRB 110205A an ideal burst to study GRB physics, to allow the study of the emission mechanisms of GRB prompt emission and afterglow, and to constrain a set of parameters that are usually difficult to derive from the data. It turns out that the burst can be well interpreted within the standard fireball shock model, making it a "textbook" GRB. We summarize our conclusions as follows:

1. The two-break energy spectrum is highly consistent with the synchrotron emission model in the fast cooling regime. This is consistent with the internal shock model or the magnetic dissipation model that invokes first-order *Fermi* acceleration of electrons.
2. The prompt optical emission is ~20 times greater than the extrapolation from the X/γ-ray spectrum. Our analysis rules out the synchrotron + SSC model to interpret the optical + X/γ-ray emission. We find that the prompt emission can be explained by a pair of reverse/forward shocks naturally arising from the conventional internal shock model. In a two-shell collision, the synchrotron emission from the slower shock that enters the denser shell produces optical emission and is self-absorbed, while that from the faster shock entering the less dense shell produces the X/γ-ray emission. The required density ratio of two shells is $\sim 10^{-4}$ to 10^{-3}.
3. If the optical and gamma-ray emissions originate from the same radius, as is expected in the internal forward/reverse shock model, one can pinpoint the prompt emission radius to $R \sim 3 \times 10^{13}$ cm by requiring that the synchrotron optical photons are self-absorbed.
4. The data can be also interpreted within a two-zone model where X/γ-rays are from a near zone while the optical emission is from a far zone. The dissipative photosphere model is inconsistent with the prompt emission data.
5. The broadband afterglow can be interpreted within the standard RS + FS model. Two scenarios are possible: Scenario I invokes both FS and RS to peak at 1100 s, while Scenario II invokes RS only to peak at 1100 s, with the FS peak later when ν_m cross the optical band. In any case, this is the first time that a rising RS—*before* its passage of the GRB ejecta (not after, when the RS emission is fast decaying, like in GRB 990123 and a few other cases)—was observed in great detail.
6. In either scenario, the optical peak time can be used to estimate the initial Lorentz factor of GRB ejecta, which is found to be $\Gamma_0 \approx 250$.
7. From the RS/FS modeling, we infer that the magnetic field strength ratio in reverse and forward shocks is $\Re_B \equiv B_r/B_f \sim 7$. This suggests that the GRB ejecta carry a magnetic flux from the central engine.
8. Jet break modeling reveals that the GRB ejecta are collimated, with an opening angle $\sim 4.^\circ 1$ (Scenario I) or $\sim 3.^\circ 2$ (Scenario II). The jet-corrected γ-ray energy is $E_\gamma \sim 1.2 \times 10^{51}$ erg or $E_\gamma \sim 7.2 \times 10^{50}$ erg.

We thank the anonymous referee for helpful comments and suggestions to improve the manuscript. This research is supported by the NASA grant NNX08AV63G and the NSF grant PHY-0801007. R.F.S. is supported by an NSERC Discovery grant. A.P.B., A.A.B., N.P.K., M.J.P., and S.R.O. acknowledge the support from the UK Space Agency. B.Z. acknowledges NASA NNX10AD48G and NSF AST-0908362 for support. M.I. acknowledges support from the CRI grant 2009-0063616, funded by MEST of the Korean government. The Centre for All-sky Astrophysics is an Australian Research Council Centre of Excellence, funded by grant CE11E0090. This research made use of public data supplied by the High Energy Astrophysics Science Archive Research Center (HEASARC) at the NASA

Goddard Space Flight Center. This work has been supported by Spanish Junta de Andalucía through program FQM-02192 and from the Spanish Ministry of Science and Innovation through Projects (including FEDER funds) AYA 2009-14000-C03-01 and AYA2008-03467/ESP. We thank INTA and EELM-CSIC for hosting the BOOTES observatories. The work is based partly on data acquired at the Centro Astronómico Hispano Alemán (CAHA) de Calar Alto and Observatorio de Sierra Nevada (OSN). This research was also supported by the UK STFC.

REFERENCES

Abdo, A. A., Ackermann, M., Ajello, M., et al. 2009, Nature, 462, 331
Akerlof, C. W., Balsano, R., Barthelmy, S., et al. 1999, Nature, 398, 400
Akerlof, C. W., & Swan, H. F. 2007, ApJ, 671, 1868
Andreev, M., Sergeev, A., & Pozanenko, A. 2011, GCN Circ., 11641, 1
Atwood, W. B., Abdo, A. A., Ackermann, M., et al. 2009, ApJ, 697, 1071
Band, D., Matteson, J., Ford, L., et al. 1993, ApJ, 413, 281
Baltz, E. A., & Hui, L. 2005, ApJ, 618, 403
Barthelmy, S., Barbier, L. M., Cummings, J. R., et al. 2005, Space Sci. Rev., 120, 143
Beardmore, A. P., Baumgartner, W. H., Burrows, D. N., et al. 2011, GCN Circ., 11629, 1
Beloborodov, A. M. 2010, MNRAS, 407, 1033
Blandford, R. D., & McKee, C. F. 1976, Phys. Fluids, 19, 1130
Breeveld, A. A., Curran, P. A., Hoversten, E. A., et al. 2010, MNRAS, 406, 1687
Breeveld, A. A., Landsman, W., Holland, S. T., et al. 2011, in AIP Conf. Proc., 1358, Gamma Ray Bursts 2010 (Melville, NY: AIP), 373
Burrows, D. N., Hill, J. E., Nousek, J. A., et al. 2005a, Space Sci. Rev., 120, 165
Burrows, D. N., Romano, P., Falcone, A., et al. 2005b, Science, 309, 1833
Cenko, S. B., Hora, J., & Bloom, S. 2011, GCN Circ., 11638, 1
Cenko, S. B., Kasliwal, M., Harrison, F. A., et al. 2006, ApJ, 652, 490
Chester, M. M., & Beardmore, A. P. 2011, GCN Circ., 11634, 1
Chincarini, G., Moretti, A., Romano, P., et al. 2007, ApJ, 671, 1903
Cucchiara, A., Cenko, S. B., Bloom, J. S., et al. 2011, ApJ, 743, 154
Corsi, A., Piro, L., Kuulkers, E., et al. 2005, A&A, 438, 829
Covino, S., Lazzati, D., Ghisellini, G., et al. 1999, A&A, 348, L1
Covino, S., Malesani, D., Ghisellini, G., et al. 2003, A&A, 400, L9
Dai, Z. G., & Wu, X. F. 2003, ApJ, 591, L21
Daigne, F., & Mochkovitch, R. 1998, MNRAS, 296, 275
De Pasquale, M., Piro, L., Perna, R., et al. 2003, ApJ, 592, 1018
De Pasquale, M., Schady, P., Kuin, N. P. M., et al. 2010, ApJ, 709, 146
Efimov, Y., Antoniuk, K., Rumyantsev, V., & Pozanenko, A. 2003, GCN Circ., 2144, 1
Evans, P. A., Beardmore, A. P., Page, K. L., et al. 2007, A&A, 469, 379
Evans, P. A., Beardmore, A. P., Page, K. L., et al. 2009, MNRAS, 397, 1177
Evans, P. A., Willingale, R., Osborne, J. P., et al. 2010, A&A, 519, 102
Fan, Y.-Z., Dai, Z.-G., Huang, Y.-F., & Lu, T. 2002, Chin. J. Astron. Astrophys, 2, 449
Fan, Y. Z., & Wei, D. 2005, MNRAS, 364, L42
Fan, Y. Z., Zhang, B., & Wei, D. M. 2009, Phys. Rev. D, 79, 021301
Fruchter, A., Krolik, J. H., & Rhoads, J. E. 2001, ApJ, 563, 597
Galama, T. J., Groot, P. J., van Paradijs, J., et al. 1998, ApJ, 497, L13
Gao, W. 2011, Res. Astron. Astrophys., 11, 1317
Garnavich, P. M., Loeb, A., & Stanek, K. Z. 2000, ApJ, 544, L11
Gaudi, B. S., Granot, J., & Loeb, A. 2001, ApJ, 561, 178
Gehrels, N., Chincarini, G., Giommi, P., et al. 2004, ApJ, 611, 1005
Gendre, B., Atteia, J. L., Boër, M., et al. 2011, ApJ, 748, 59
Giannios, D. 2008, A&A, 480, 305
Ghisellini, G., Celotti, A., & Lazzati, D. 2000, MNRAS, 313, L1
Ghisellini, G., & Lazzati, D. 1999, ApJ, 309, 7
Golenetskii, S., Aptekar, R., Mazets, E., et al. 2011, GCN Circ., 11659, 1
Gorosabel, J., Duffard, R., Kubanek, P., & Guijarro, A. 2011, GCN Circ., 11696, 1
Granot, J., & Sari, R. 2002, ApJ, 568, 820
Greiner, J., Klose, S., Reinsch, K., et al. 2003, Nature, 426, 157
Gruber, D., Krühler, T., Foley, S., et al. 2011, A&A, 528, 15
Gruzinov, A., & Waxman, E. 1999, ApJ, 511, 852
Hentunen, V. P., Nissinen, M., & Salmi, T. 2011, GCN Circ., 11637, 1
Huang, K. Y., Urata, Y., Filippenko, A. V., et al. 2005, ApJ, 628, L93
Im, M., & Urata, Y. 2011, GCN Circ., 11643, 1
Jacobson, P., & Fynbo, J. 2010, in AIP Conf. Proc. 1279, Deciphering the Ancient Universe with Gamma-ray Bursts, ed. N. Kawai & S. Nagataki (Terrsa, Kyoto, Japan: AIP), 167
Jin, Z., & Fan, Y. 2007, MNRAS, 378, 1043
Jung, G. V. 1989, ApJ, 338, 972
Kalberla, P. M., Burton, W. B., Hartmann, D., et al. 2005, A&A, 440, 775
Klebesadel, R., Strong, I., & Olson, R. 1973, ApJ, 182, L85
Klotz, A., Gendre, B., Lass, M., Boer, M., & Atteia, J. L. 2011a, GCN Circ., 11630, 1
Klotz, A., Gendre, B., Lass, M., Boer, M., & Atteia, J. L. 2011b, GCN Circ., 11632, 1
Kobayashi, S. 2000, ApJ, 545, 807
Kobayashi, S., Zhang, B., Mészáros, P., & Burrows, D. N. 2007, ApJ, 655, 391
Kong, S. W., Wong, A. Y. L., Huang, Y. F., & Cheng, K. S. 2010, MNRAS, 402, 409
Kumar, P., & McMahon, R. 2008, MNRAS, 384, 33
Kumar, P., & Panaitescu, A. 2000, ApJ, 541, L51
Kumar, P., & Panaitescu, A. 2008, MNRAS, 391, L19
Lazzati, D., & Begelman, M. C. 2010, ApJ, 725, 1137
Lazzati, D., Covino, S., & Ghisellini, G. 2002a, MNRAS, 330, 583
Lazzati, D., Morsony, B. J., & Begelman, M. C. 2009, ApJ, 700, 47
Lazzati, D., Morsony, B. J., & Begelman, M. C. 2011, ApJ, 732, 34
Lazzati, D., Rossi, E., Covino, S., Ghisellini, G., & Malesani, D. 2002b, A&A, 396, L5
Lee, I., Im, M., & Urata, Y. 2010, J. Korean Astron. Soc., 43, 95
Li, Z., & Waxman, E. 2008, ApJ, 674, L65
Liang, E., Yi, S., Zhang, J., et al. 2010, ApJ, 725, 2209
Liang, E., Zhang, B., O'Brien, P. T., et al. 2006, ApJ, 646, 351
Mao, J., Malesani, D., D'Avanzo, P., et al. 2012, A&A, 538, A1
Medvedev, M. V. 2006, ApJ, 637, 869
Medvedev, M. V., & Loeb, A. 1999, ApJ, 526, 697
Meegan, C., Lichti, G., Bhat, P. N., et al. 2009, ApJ, 702, 791
Mészáros, P. 2006, Rep. Prog. Phys., 69, 2259
Mészáros, P., & Rees, M. J. 1997, ApJ, 476, 232
Mészáros, P., & Rees, M. J. 1999, MNRAS, 306, L39
Molinari, E., Vergani, S. D., Malesani, D., et al. 2007, A&A, 469, 13
Nakar, E., & Granot, J. 2007, MNRAS, 380, 1744
Nardini, M., Greiner, J., Krühler, T., et al. 2011, A&A, 531, 39
Nishikawa, K.-I., Niemiec, J., Hardee, P. E., et al. 2009, ApJ, 698, L10
Oates, S. R., Page, M. J., Schady, P., et al. 2009, MNRAS, 395, 490
Ovaldsen, J.-E., Jaunsen, A. O., Fynbo, J. P. U., et al. 2007, ApJ, 662, 294
Pal'shin, V. 2011, GCN Circ., 11697, 1
Panaitescu, A., & Kumar, P. 2004, MNRAS, 353, 511
Panaitescu, A., & Vestrand, W. T. 2011, MNRAS, 414, 3537
Pe'er, A., Mészáros, P., & Rees, M. J. 2006, ApJ, 642, 995
Pe'er, A., & Waxman, E. 2005, ApJ, 633, 1018
Pe'er, A., & Zhang, B. 2006, ApJ, 653, 454
Piran, T. 2005, in AIP Conf. Proc. 784, Magnetic Fields in the Universe, (Melville, NY: AIP), 164
Piran, T., Sari, R., & Zou, Y. C. 2009, MNRAS, 393, 1107
Poole, G., Breeveld, A. A., Page, M. J., et al. 2008, MNRAS, 383, 627
Pozanenko, A. S., Rumyantsev, V. V., Loznikov, V. M., Volnova, A. A., & Shulga, A. P. 2008, Astron. Lett., 34, 141
Quimby, R. M., Rykoff, E. S., Yost, S. A., et al. 2006, ApJ, 640, 402
Racusin, J. L., Karpov, S. V., Sokolowski, M., et al. 2008, Nature, 455, 183
Rees, M. J., & Mészáros, P. 1992, MNRAS, 258, 41P
Rees, M. J., & Mészáros, P. 1994, ApJ, 430, L93
Roming, P. W. A., Kennedy, T. E., Mason, K. O., et al. 2005, Space Sci. Rev., 120, 95
Rossi, A., Schulze, S., Klose, S., et al. 2011, A&A, 529, 142
Rothschild, R. E., Blanco, P. R., Gruber, D. E., et al. 1998, ApJ, 496, 538
Rykoff, E. S., Aharonian, F., Akerlof, C. W., et al. 2009, ApJ, 702, 489
Sahu, D. K., & Anto, P. 2011, GCN Circ., 11670, 1
Sakamoto, T., Barthelmy, S. D., Baumgartner, W. H., et al. 2011a, ApJS, 195, 2
Sakamoto, T., Barthelmy, S. D., Baumgartner, W. H., et al. 2011b, GCN Circ., 11692, 1
Sakamoto, T., Pal'Shin, V., Yamaoka, K., et al. 2011c, PASJ, 63, 215
Sari, R. 1999, ApJ, 524, 43
Sari, R., & Esin, A. A. 2001, ApJ, 548, 787
Sari, R., & Piran, T. 1995, ApJ, 455, L143
Sari, R., & Piran, T. 1999, ApJ, 517, L109
Sari, R., Piran, T., & Halpern, J. 1999, ApJ, 519, L17
Sari, R., Piran, T., & Narayan, R. 1998, ApJ, 497, L17
Savaglio, S., Glazebrook, K., & LeBorgne, D. 2009, ApJ, 691, 182
Schaefer, B. E., Flewelling, H., Rujopakarn, W., & Guver, T. 2011, GCN Circ., 11631, 1
Schlegel, D. J., Finkbeiner, D. P., & Davis, M. 1998, ApJ, 500, 525
Shen, R., Kumar, P., & Piran, T. 2010, MNRAS, 403, 229
Shen, R., & Matzner, C. 2012, ApJ, 744, 36
Shen, R., & Zhang, B. 2009, MNRAS, 398, 1936

Silva, R., Fumagalli, M., Worseck, G., & Prochaska, X. 2011, GCN Circ., 11635, 1
Sizun, P., Shrader, C. R., Attiéé, D., et al. 2004, in Proc. 5th INTEGRAL Workshop on the INTEGRAL Universe, ed. V. Schönfelder, G. Lichti, & C. Winkler (ESA SP-552; Noordwijk: ESA), 815
Smith, J. A., Tucker, D. L., Kent, S., et al. 2002, AJ, 123, 2121
Sugita, S., Yamaoka, K., Vasquez, N., et al. 2011, GCN Circ., 11682, 1
Tagliaferri, G., Goad, M., Chincarini, G., et al. 2005, Nature, 436, 985
Toma, K., Wu, X.-F., & Mészáros, P. 2011, MNRAS, 415, 1663
Ukwatta, T., Sonbas, E., Gehrels, N., et al. 2011, GCN Circ., 11655, 1
Updike, A. C., Haislip, J. B., Nysewander, M. C., et al. 2008, ApJ, 685, 361
Urata, Y., Chuang, C., & Huang, K. 2011, GCN Circ., 11648, 1
van Eerten, H. J., & MacFadyen, A. I. 2011, ApJ, 733, 37
Volnova, A., Klunko, E., & Pozanenko, A. 2011, GCN Circ., 11672, 1
Volnova, A., Pozanenko, A., Klunko, E., & Korobtsev, I. 2010, GCN Circ., 11270, 1
Vreeswijk, P., Groot, P., Carter, P., et al. 2011, GCN Circ., 11640, 1
Vurm, I., Beloborodov, A. M., & Poutanen, J. 2011, ApJ, 738, 77
Waxman, E., & Draine, B. T. 2000, ApJ, 537, 796
Weibel, E. S. 1959, Phys. Rev. Lett., 2, 83
Wijers, R., Rees, M., & Mészáros, P. 1997, MNRAS, 288, 51
Xue, R., Fan, Y., & Wei, D. 2009, A&A, 498, 671
Yamaoka, K., Endo, A., Enoto, T., et al. 2009, PASJ, 61, 35
Yu, Y. W., Wang, X. Y., & Dai, Z. G. 2009, ApJ, 692, 1662
Zhang, B. 2011, C. R. Phys., 12, 206
Zhang, B., Fan, Y. Z., Dyks, J., et al. 2006, ApJ, 642, 354
Zhang, B., Kobayashi, S., & Meśzaŕos, P. 2003, ApJ, 595, 950
Zhang, B., & Mészáros, P. 2002, ApJ, 581, 1236
Zhang, B., & Mészáros, P. 2004, Int. J. Mod. Phys. A, 19, 2385
Zhang, B., & Yan, H. 2011, ApJ, 726, 90
Zou, Y., Wu, X., & Dai, Z. 2005, MNRAS, 363, 93

The Astrophysical Journal, 751:118 (5pp), 2012 June 1 doi:10.1088/0004-637X/751/2/118

A POSSIBLE DETECTION OF OCCULTATION BY A PROTO-PLANETARY CLUMP IN GM Cephei

W. P. Chen[1], S. C.-L. Hu[1,2], R. Errmann[3], Ch. Adam[3], S. Baar[3], A. Berndt[3], L. Bukowiecki[4], D. P. Dimitrov[5], T. Eisenbeiß[3], S. Fiedler[3], Ch. Ginski[3], C. Gräfe[3,6], J. K. Guo[1], M. M. Hohle[3], H. Y. Hsiao[1], R. Janulis[7], M. Kitze[3], H. C. Lin[1], C. S. Lin[1], G. Maciejewski[3,4], C. Marka[3], L. Marschall[8], M. Moualla[3], M. Mugrauer[3], R. Neuhäuser[3], T. Pribulla[3,9], St. Raetz[3], T. Röll[3], E. Schmidt[3], J. Schmidt[3], T. O. B. Schmidt[3], M. Seeliger[3], L. Trepl[3], C. Briceño[10], R. Chini[11], E. L. N. Jensen[12], E. H. Nikogossian[13], A. K. Pandey[14], J. Sperauskas[7], H. Takahashi[15], F. M. Walter[16], Z.-Y. Wu[17], and X. Zhou[17]
[1] Graduate Institute of Astronomy, National Central University, 300 Jhongda Road, Jhongli 32001, Taiwan
[2] Taipei Astronomical Museum, 363 Jihe Rd., Shilin, Taipei 11160, Taiwan
[3] Astrophysikalisches Institut und Universitäts-Sternwarte, FSU Jena, Schillergäßchen 2-3, D-07745 Jena, Germany
[4] Toruń Centre for Astronomy, Nicolaus Copernicus University, Gagarina 11, PL87-100 Toruń, Poland
[5] Institute of Astronomy and NAO, Bulg. Acad. Sc., 72 Tsarigradsko Chaussee Blvd., 1784 Sofia, Bulgaria
[6] Christian-Albrechts-Universität Kiel, Leibnizstraße 15, D-24098 Kiel, Germany
[7] Moletai Observatory, Vilnius University, Lithuania
[8] Gettysburg College Observatory, Department of Physics, 300 North Washington St., Gettysburg, PA 17325, USA
[9] Astronomical Institute, Slovak Academy of Sciences, 059 60, Tatranská Lomnica, Slovakia
[10] Centro de Investigaciones de Astronomia, Apartado Postal 264, Merida 5101, Venezuela
[11] Instituto de Astronomía, Universidad Católica del Norte, Antofagasta, Chile
[12] Department of Physics and Astronomy, Swarthmore College, Swarthmore, PA 19081-1390, USA
[13] Byurakan Astrophysical Observatory, 378433 Byurakan, Armenia
[14] Aryabhatta Research Institute of Observational Science, Manora Peak, Nainital, 263 129, Uttarakhand, India
[15] Institute of Astronomy, The University of Tokyo, 2-21-1 Osawa, Mitaka, Tokyo, 181-0015, Japan
[16] Department of Physics and Astronomy, Stony Brook University, Stony Brook, NY 11794-3800, USA
[17] Key Laboratory of Optical Astronomy, NAO, Chinese Academy of Sciences, 20A Datun Road, Beijing 100012, China
Received 2011 December 12; accepted 2012 March 23; published 2012 May 14

ABSTRACT

GM Cephei (GM Cep), in the young (∼4 Myr) open cluster Trumpler 37, has been known to be an abrupt variable and to have a circumstellar disk with a very active accretion. Our monitoring observations in 2009–2011 revealed that the star showed sporadic flare events, each with a brightening of $\lesssim$0.5 mag lasting for days. These brightening events, associated with a color change toward blue, should originate from increased accretion activity. Moreover, the star also underwent a brightness drop of ∼1 mag lasting for about a month, during which time the star became bluer when fainter. Such brightness drops seem to have a recurrence timescale of a year, as evidenced in our data and the photometric behavior of GM Cep over a century. Between consecutive drops, the star brightened gradually by about 1 mag and became blue at peak luminosity. We propose that the drop is caused by the obscuration of the central star by an orbiting dust concentration. The UX Orionis type of activity in GM Cep therefore exemplifies the disk inhomogeneity process in transition between the grain coagulation and the planetesimal formation in a young circumstellar disk.

Key words: occultations – planets and satellites: formation – protoplanetary disks – stars: individual (GM Cephei) – stars: pre-main sequence – stars: variables: T Tauri, Herbig Ae/Be

Online-only material: color figures

1. INTRODUCTION

The current paradigm suggests that stars are formed in dense molecular cores, and planets are formed, almost contemporaneously with the star, in circumstellar disks. The grain growth process already initiated in the parental molecular cloud continues to produce progressively larger solid bodies. Details are still lacking on how grain coagulation proceeds to eventual planet formation in a turbulent disk. Competing theories include gravitational instability (Safronov 1972; Goldreich & Ward 1973; Johansen et al. 2007) and planetesimal accretion (Weidenschilling 2000). In any case, density inhomogeneities in the young stellar disk mark the critical first step in the process. Measurements of the fraction of stars with infrared excess—arising from thermal emission by circumstellar dust—indicate a clearing timescale of optically thick disks in less than ∼10 Myr (Mamajek et al. 2004; Briceño et al. 2007; Hillenbrand 2008). Observationally, this epoch corresponds to the pre-main sequence (PMS) stellar evolution from disk-bearing classical T Tauri stars (CTTSs) to weak-lined T Tauri stars with no optically thick disks.

The open cluster Trumpler 37 (Tr 37), at a heliocentric distance of 870 pc (Contreras et al. 2002), is associated with the prominent H II region IC 1396 and is a part of the Cepheus OB2 association. With a disk frequency of ∼39% (Mercer et al. 2009) and an age of 1–4 Myr (Marschall et al. 1990; Patel et al. 1995; Sicilia-Aguilar et al. 2005), Tr 37 serves as a good target to search for and to characterize exoplanets in formation and early evolutionary stages (see Neuhäuser et al. 2011 and references therein on Tr 37).

GM Cephei (GM Cep; R.A. = 21:38:17.3, Decl. = +57:31:23, J2000) is a solar-type variable in Tr 37. The star has a spectral type of G7 to K0, an estimated mass of 2.1 $M_{\odot}$, and a radius of 3–6 $R_{\odot}$ (Sicilia-Aguilar et al. 2008). The youth of GM Cep is exemplified by its emission-line spectrum, prominent infrared excess (Sicilia-Aguilar et al. 2008), and X-ray emission (Mercer et al. 2009), all characteristics of a CTTS. The star has a circumstellar disk (Mercer et al. 2009) with an accretion rate

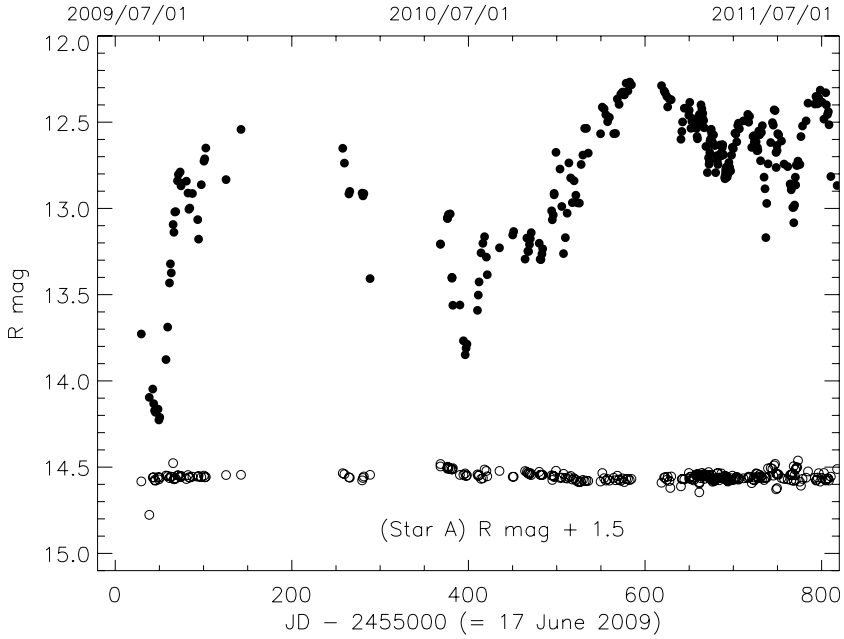

Figure 1. *R*-band light curves of GM Cep (top) and of a comparison star (bottom, offset by 1.5 mag for display clarity) from mid-2009 to mid-2011. Typical photometric errors (0.005 mag) are smaller than the sizes of the symbols and are not shown.

up to $10^{-6}\,M_{\odot}$ yr^{-1}, which is two to three orders higher than the median value of the CTTSs in Tr 37 (Sicilia-Aguilar et al. 2006). It is also one of the fastest rotators in the cluster, with $v \sin i \sim 43.2$ km s^{-1} (Sicilia-Aguilar et al. 2008).

Most PMS objects are variables. Herbst et al. (1994) classified such variability into three categories. One class of variation is caused by the rotational modulation of cool star spots. Another class of variation arises because of the unsteady accretion onto a hot spot on the stellar surface; stars of this type are called EXors, with EX Lupi being the most extreme case. Stars with the third kind of variation, called UX Orionis-type variables or UXors, are those that experience variable obscuration by circumstellar dust clumps. About a dozen UXors have been identified so far, with some showing cyclic variability with periods ranging from 8.2 days (Bouvier et al. 2003) to 11.2 years (Grinin et al. 1998).

GM Cep is known to be an abrupt variable, but interpretations about its variability have been controversial. Sicilia-Aguilar et al. (2008) collected photometry of the star from 1952 to 2007 in the literature, supplementing with their own intensive multi-wavelength observations, and suggested GM Cep to be an EXor-type variable, i.e., with outbursts and accretion flares. Xiao et al. (2010) measured archival plates taken between 1895 and 1993, and concluded otherwise—that the variability in the century-long light curve is dominated by dips (possibly from extinction) superposed on quiescent states. If this is the case, GM Cep should be a UXor-type variable, as also claimed by Semkov & Peneva (2011).

GM Cep has been observed by the Young Exoplanet Transit Initiative (YETI) collaboration, a network of small telescopes in different longitude zones (Neuhäuser et al. 2011). In addition to the YETI data, the observations reported here also included those collected during non-YETI campaign time, by the SLT 40 cm telescope at Lulin in Taiwan, the Tenagra II 81 cm telescope in Arizona, USA, the Jena University Observatory 25 cm and 90/60 cm telescopes in Germany (Mugrauer & Berhold 2010), and the 1.5 m telescope of Moleitai Observatory in Lithuania. For the list of the YETI telescope and instrument parameters, please refer to Neuhäuser et al. (2011). While the primary goal of the YETI campaigns, each with uninterrupted monitoring of a target cluster for 7–10 days, is to search for exoplanet transit events in young open clusters—hence possibly finding the youngest exoplanets—the continuous and high-cadence observations produce data sets also valuable for a young stellar variability study that is very relevant to planet formation (Bouvier et al. 2003). Here we present the light curve of GM Cep from 2009 to 2011 which reveals T-Tauri-type flares and UXor-type variability, with the possible detection of cyclic occultation events by a dust clump in the circumstellar disk.

2. LIGHT CURVES AND COLOR VARIATIONS

All the CCD images were processed by the standard procedure of bias, dark, and flat-field correction. The photometry of GM Cep was calibrated by a linear regression with the seven comparison stars listed by Xiao et al. (2010). Images taken under inferior sky conditions were excluded in the analysis. Figure 1 shows the light curves of GM Cep and one of the comparison stars observed from mid-2009 to mid-2011. The variability of GM Cep is obvious. The star experienced a sharp brightening soon after our observations started in mid-2009, prompting us to follow this star closely beyond the YETI campaigns. Our intense monitoring started in 2010. A brightness dip with a depth of $\Delta R \sim 0.82$ mag lasting for 39 days occurred, followed by a gradual brightening (by ~1 mag) and fading. The falling and rising parts of the dip are roughly symmetric. In 2011, a dip also happened, but with rapid fluctuations. The star fluctuated some $\Delta R \sim 1.7$ mag in 2010 and also in 2009. We conclude that the sharp brightening in 2009 corresponded to the rising part of the dip seen in 2010. If so, the recurrent timescale of the dip would be 346 days, and the minimum of the dip brightened from 2009 ($R \sim 14.2$ mag), to 2010 ($R \sim 13.9$ mag), to 2011 ($R \sim 13.2$ mag). When this trend is taken out, the gradual brightening and fading is more or less symmetric in time with the peak luminosity happening between two consecutive dips, much like the round-topped light curves seen in contact binaries. Such repeated dips plus a slow brightening and fading can be

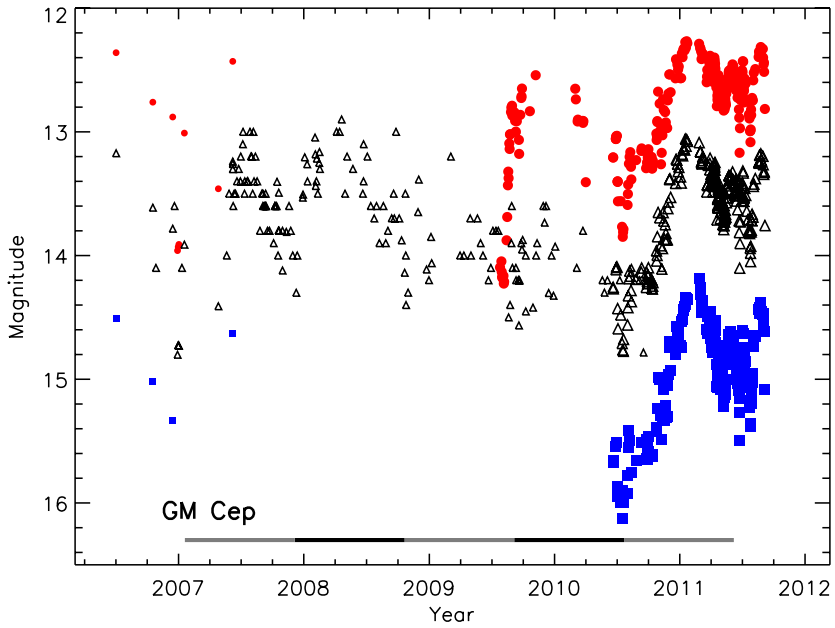

Figure 2. Light curves of GM Cep in the *B* (red circles), *V* (black triangles), and *R* (blue squares) bands between late 2006 and 2011. The symbols with larger sizes, i.e., those after 2009, represent our observations. Each segment of the horizontal black and gray line is shown for the duration of 320 days to coincide roughly with the brightness dips.

(A color version of this figure is available in the online journal.)

seen in the long-term light curve reported by Xiao et al. (2010), who claimed no periodicity in the data perhaps because of the sparse sampling.

Figure 2 shows the light curves of GM Cep in the B, V, and R bands since late 2006, with additional data taken from Sicilia-Aguilar et al. (2008) and AAVSO. Analysis by the NStED (NASA/IPAC/NExScI Star and Exoplanet Database) Periodogram Service, based on the Lomb–Scargle algorithm, shows the first-ranked period to be 311 days with a broad peak in the power spectrum suggesting a quasi-periodicity as shown in Figure 3. Such a recurrence timescale of 310–320 days indeed seems to coincide with the minima in the light curve (see Figure 2), at least for the last five cycles for which sampling has been sufficiently dense (Hu et al. 2012). In addition, superimposed on the above light variations, there are sporadic flaring-like episodes with an amplitude less than 0.5 mag, each lasting for about 10 days, characteristic of T Tauri activity.

While the YETI campaigns are carried out in the R band, our intensified observations of GM Cep since 2010 also included those taken in the V band. The color changes during the dip, as well as during the brightening and fading episodes, are particularly revealing. Figure 4 shows the R-band light curve and $V - R$ color variations in 2010/2011. The dip in the beginning has a depth of about $\Delta V \sim 0.68$ mag, so while the star became fainter (depth in R was 0.82 mag), the $V - R$ value decreased, i.e., its color turned bluer. During the general brightening, the star also became bluer.

To summarize, the light curve of GM Cep is characterized by (1) a brightness dip of about 1 mag lasting for a month, with a recurrence timescale of about a year, (2) in between the dips, a gradual brightening of about 1 mag, followed by a roughly symmetric fading, and, superimposed on both (1) and (2), (3) intermittent flares $\lesssim$0.5 mag, each lasting for several days.

3. DISCUSSION

The abrupt behavior in GM Cep's light curve is not uncommon among Herbig Ae/Be stars with modulations of various timescales, i.e., "cyclic, but not exactly periodic" (Herbst & Shevchenko 1999, p. 7), superimposed on the deep minima. A flare with a blue color can be accounted for by the enhanced accretion of clumpy material. Semkov & Peneva (2011) published the B, V, R, and I light curves of GM Cep from mid-2008, i.e., one year earlier but in lower cadence than our data. Their data showed $R \sim 12$ mag in 2008 with no obvious dips, an obscuration event in 2009, and another one in 2010. These authors proposed that GM Cep is a UXor variable. At the end of their observations, in early 2011, the star again reached $R \sim 12$ mag, also shown in our data.

The most striking feature of the light curve of GM Cep is the month-long dips. There are various possible mechanisms for producing such a phenomenon, e.g., by star spots or a rotating accretion column, which has a typical timescale of a few hours to days. A notable case, the T Tauri star AA Tau, is known to show deep fading ($\sim$1.4 mag) lasting for about a week and believed to be caused by occultation by a warp in the magnetospheric accretion disk (Bouvier et al. 1999) with a quasi-cyclic timescale of 8.2 days (Bouvier et al. 2003, 2007). The dip phenomenon appears to be common among young stars with inner dusty disks (Herbst & Shevchenko 1999). In a study by the *CoRoT* satellite of the young star cluster NGC 2264, Alencar et al. (2010) found a fraction of 30%–40% young stars exhibiting obscuration variations.

We propose that the month-long dip seen in GM Cep is a manifestation of obscuration by an orbiting dust concentration in the circumstellar disk, i.e., GM Cep is a UXor-type variable, as reported by Xiao et al. (2010) and by Semkov & Peneva (2011). If so, the orbital period of the dip gives information on the distance of the clump from the star, whereas the duration of the obscuration and amount of starlight extinction give, respectively, the size and the column density of the clump. The mass of the star is uncertain for this PMS star, but assuming 2.1 $M_{\odot}$ (Sicilia-Aguilar et al. 2008), a Keplerian motion, and a period of $P = 320$ days, the orbital distance of the clump would be $r \sim 1.2$ AU. The duration of the obscuration, $t \sim 39$ days, is

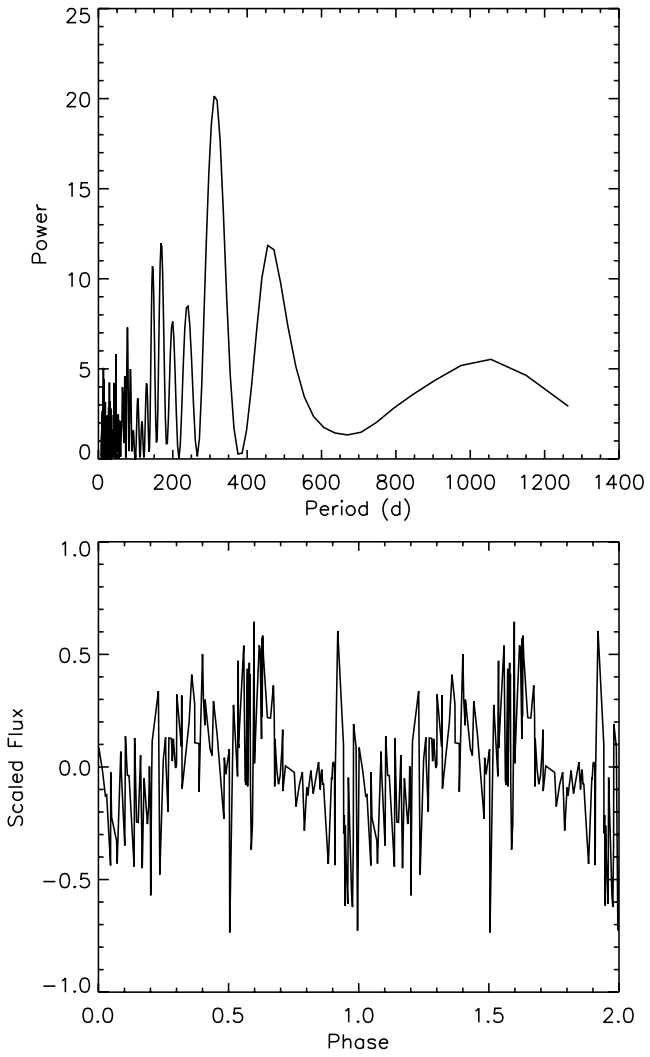

Figure 3. (Top) Power spectrum of the light curve in Figure 2 analyzed by the Lomb–Scargle algorithm, peaking at 311 days. (Bottom) The phased light curve with the 311 day period.

related to the half-size of the clump R_c by $t/P = (2R_c)/(2\pi r)$; hence $R_c \sim 0.4$ AU, or about 15–30 stellar radii (Sicilia-Aguilar et al. 2008).

The extinction A_λ at wavelength λ is related to the amount of obscuring dust along the line of sight, i.e., $A_\lambda = 1.086\, N_d\, \sigma_d\, Q_{\rm ext}$, where N_d is the column density of the dust grains, $\sigma_d = \pi a^2$ is the geometric cross-section of a grain of a radius of a, and $Q_{\rm ext}$ is the dimensionless extinction efficiency factor. Stars as young as GM Cep should have large grains settled into the midplane, but because the disk is inclined (Sicilia-Aguilar et al. 2008), we assume that the obscuration is caused mostly by small dust grains with an average radius of $a \sim 0.1\,\mu$m. Thus $Q_{\rm ext} \sim 1$, and we cautiously note the possibility of abnormal dust sizes in the disk (Sicilia-Aguilar et al. 2008, or along the line of sight, Clayton & Fitzpatrick 1987). It follows from the observed obscuration of 0.68 mag in the V band that $N_d = 2.0 \times 10^9\,{\rm cm}^{-2}$. This amount of intervening dust is hardly excessive. The flux drop during the dip phase, ~1 mag, is comparable to the extinction of the star $A_V \sim 1.5$ (Contreras et al. 2002; Sicilia-Aguilar et al. 2004), a value commonly seen among CTTSs. The moderate extinction also indicates a line of sight out of the disk plane. What is intriguing in GM Cep, of course, is the distinct on–off behavior of the obscuration. The column mass density is, given the same amount of extinction, proportional to the dust size a and in this case is $\Sigma \sim 2.9 \times 10^{-5}\,{\rm g\,cm}^{-2}$. Even for $a = 10\,\mu$m grains, the column mass density would still be several orders less than the minimum solar nebula, for which Σ is a few thousands g cm^{-2} at 1 AU (Weidenschilling 1977).

It is not clear whether the clump has a line-of-sight (radial) dimension comparable to its transverse size ($2R_c$) or is merely a ringlet. Even if it is spherical, thus yielding the maximum mass, the mean volume density would be $n_d = N_d/2R_c = 1.7 \times 10^{-4}\,{\rm cm}^{-3}$ at the clump's center. Given the proximity of the clump to the star ($r = 1.2$ AU), we assume the dust composition to be mostly silicates, having an average density of $\rho = 3.5$ g cm^{-3}. This leads to an estimated mass of $M_d = 2.3 \times 10^{21}$ g for the clump, which is about that of an asteroid, if the mass is uniformly spread. For a clump this substantial in size, our line of sight does not need to line up to the orbital plane in order to detect the occultation. From the fast rotation, the infrared spectral energy distribution, and the Hα profile, an intermediate inclination angle was inferred (Sicilia-Aguilar et al. 2008). A clump extending in a radial direction would have been tidally unstable. The clump is thus extended along the orbit, but short radially.

The blueing phenomenon during the obscuration is most puzzling. It has been seen in UX Ori itself (Herbst & Shevchenko 1999) and other UXors (Grinin et al. 2001). Semkov & Peneva (2011) also reported the "color reversal" or the blueing effect in GM Cep, and attributed it to possible anomalous dust properties, or disk geometry such as self-shadowing or a piled up wall in the inner disk (Dullemond et al. 2003). One appealing proposal by Grinin et al. (1994) is that blueing happens when dust along the line of sight completely dims the star, and dust particles near the line of sight scatter preferentially blue light into view, a mechanism supported by increased polarization during maximum extinction. In GM Cep when the clump blocks out the star, either the hot boundary layer—a region between the star and the active accretion disk—or the magnetospheric accretion column must have contributed much to the emission during the dip phase.

It is interesting to note that, except for the flare events, the light curve of GM Cep, namely the repeated occultation modulated by gradual, symmetric brightening and fading, bears resemblance to that of an eclipsing binary or an exoplanet transit with phase variations (Borucki et al. 2009), though the time and flux change scales are vastly different. In GM Cep the flares are caused by enhanced accretion activity and the dip, as we propose here, by the occultation of the central star by a patch of dust in the circumstellar disk. The gradual brightening and fading, then, is the result of the orbital modulation of reflected starlight, as witnessed in high-precision light curves of eclipsing binaries or transiting exoplanets (Borucki et al. 2009). Without the shape information of the clump, it is difficult to quantify this effect, but the amount of reflected light allows us to estimate the height of the clump. If the yearly brightening trend in 2009–2011 is removed, the gradual brightening in 2010 amounted to ~0.7 mag, meaning approximately an equal contribution between the reflected light and the direct starlight. Without knowledge of the density distribution and optical properties of dust, we made a simple analogy of dust grains as a translucent mirror, made up of a total number of $N_{\rm tot}$ particles. Assuming the Bond albedo a_B, the reflected light is $(L_*/4\pi r^2)\ \pi a^2 a_B N_{\rm tot}$, and an ensemble of dust on the back side of, and 1.2 AU away from, the star would yield

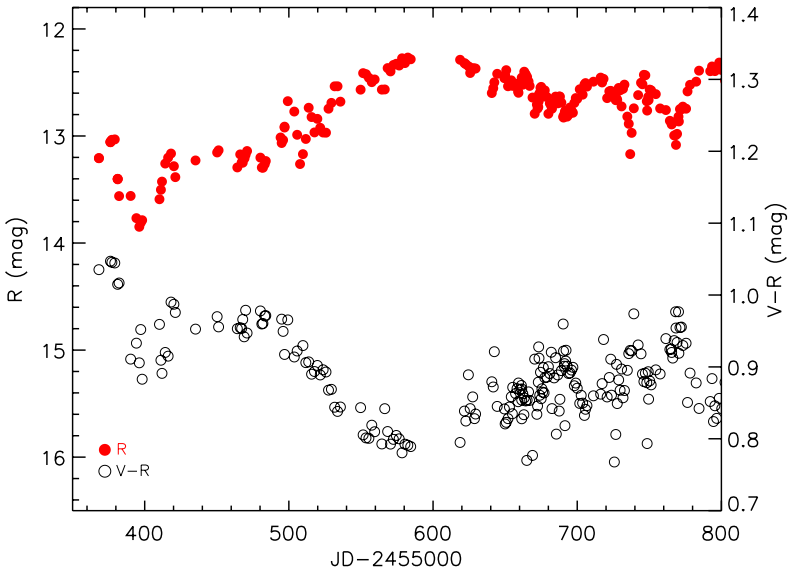

Figure 4. *R*-band light curve (left *y*-axis) and the $V - R$ color variations (right *y*-axis, redder to the top) of GM Cep from mid-2010 to mid-2011. Note that the star became blue when faintest and brightest.

(A color version of this figure is available in the online journal.)

$N_{\rm tot} \sim 3\times10^{36}/a_B$. A rudimentary estimate, assuming an albedo of 4% (cometary nuclei), thus gives a height not much less than the perimetric dimension.

If our hypothesis that the same clump has been responsible for the yearly dip holds, the clump must be dynamically stable. The mass we derived is only for the dust, and there is no evidence, even with a sufficient amount of associated gas, that the clump is on the verge of gravitational instability (Chang & Oishi 2010). In any case, the density of the clump is not likely to have a high contrast relative to the rest of the disk. In other words, it may be just a density inhomogeneity, such as a local dust concentration in a warped, spiral-armed disk or density enhancement by a companion star (Grinin et al. 1998), that gives rise to the characteristic light curve seen in GM Cep.

In conclusion, our photometric monitoring of GM Cep confirms its UXor nature. Moreover, the light curves and color variations suggest a density inhomogeneity of dust in the young stellar disk. Such enhanced density contrast may be a signpost of the transition phase from grain growth to the onset of planetesimal formation. GM Cep may not be an isolated example, and intense monitoring should be carried out for young stars known to exhibit abrupt light variations. Further characterization of the clumpy disk of GM Cep, e.g., by polarization, infrared spectroscopy, and high angular resolution submillimeter imaging, at epochs in and out of the occultation, should shed light on our hypothesis of this interesting young star.

We thank the anonymous referee for very constructive suggestions on an earlier version of the paper. The work at NCU is financially supported in part by the grant NSC99-2119-M-008-021. Lulin Observatory is operated by the National Central University of Taiwan and is funded partially by the National Science Council and Ministry of Education of Taiwan. The Jena co-authors thank DFG, the Thuringian government, and the EU (MTKD-CT-2006-042514) for support. The Jena and Toruń co-authors thank DAAD PPP-MNiSW (50724260-2010/2011) for support. Part of the observations reported here have been obtained with telescopes at the University Observatory Jena, which is operated by the Astrophysical Institute of the Friedrich-Schiller-University.

REFERENCES

Alencar, S. H. P., Teixeira, P. S., Guimarães, M. M., et al. 2010, A&A, 519, 88
Borucki, W. J., Koch, D., Jenkins, J., et al. 2009, Science, 325, 709
Bouvier, J., Alencar, S. H. P., Boutelier, T., et al. 2007, A&A, 463, 1017
Bouvier, J., Chelli, A., Allain, S., et al. 1999, A&A, 349, 619
Bouvier, J., Grankin, K. N., Alencar, S. H. P., et al. 2003, A&A, 409, 169
Briceño, C., Hartmann, L., Hernández, J., et al. 2007, ApJ, 661, 1119
Chang, P., & Oishi, J. S. 2010, ApJ, 721, 1593
Clayton, G. C., & Fitzpatrick, E. L. 1987, AJ, 93, 157
Contreras, M. E., Sicilia-Aguilar, A., Muzerolle, J., et al. 2002, AJ, 124, 1585
Dullemond, C. P., van den Ancker, M. E., Acke, B., & van Boekel, R. 2003, ApJ, 594, L47
Goldreich, P., & Ward, W. 1973, ApJ, 183, 1051
Grinin, V. P., Kozlova, O. V., Natta, A., et al. 2001, A&A, 379, 482
Grinin, V. P., Rostopchina, A. N., & Shakhovskoi, D. N. 1998, Astron. Lett., 24, 802
Grinin, V. P., The, P. S., de Winter, D., et al. 1994, A&A, 292, 165
Herbst, W., Herbst, D. K., Grossman, E. J., & Weinstein, D. 1994, AJ, 108, 1906
Herbst, W., & Shevchenko, V. S. 1999, AJ, 118, 1043
Hillenbrand, L. A. 2008, Phys. Scr., 130, 4024
Hu, S. C.-L., Chen, W. P., & the Young Exoplanet Transit Initiative 2012, in ASP Conf. Ser. 451, The 9th Pacific Rim Conf. on Stellar Astrophysics, ed. S. B. Qian et al. (San Francisco, CA: ASP), 345
Johansen, A., Oishi, J. S., Mac Low, M.-M., et al. 2007, Nature, 448, 1022
Mamajek, E. E., Meyer, M. R., Hinz, P. M., et al. 2004, ApJ, 612, 496
Marschall, L. A., Karshner, G. B., & Comins, N. F. 1990, AJ, 99, 1536
Mercer, E. P., Miller, J. M., Calvet, N., et al. 2009, AJ, 138, 7
Mugrauer, M., & Berhold, T. 2010, Astron. Nachr., 331, 449
Neuhäuser, H., Errmann, R., Berndt, A., et al. 2011, Astron. Nachr., 332, 547
Patel, N., Goldsmith, P. F., Snell, R. L., Hezel, T., & Xie, T. 1995, ApJ, 447, 721
Safronov, V. S. 1972, in Evolution of the Protoplanetary Cloud and Formation of the Earth and Planets (Jerusalem: Keter)
Semkov, E. H., & Peneva, S. P. 2011, Ap&SS, 338, 95
Sicilia-Aguilar, A., Hartmann, L. W., Briceño, C., Muzerolle, J., & Calvet, N. 2004, AJ, 128, 805
Sicilia-Aguilar, A., Hartmann, L. W., Fürész, G., et al. 2006, AJ, 132, 2135
Sicilia-Aguilar, A., Hartmann, L. W., Hernández, J., Briceño, C., & Calvet, N. 2005, AJ, 130, 188
Sicilia-Aguilar, A., Merín, B., Hormuth, F., et al. 2008, ApJ, 673, 382
Weidenschilling, S. J. 1977, Ap&SS, 51, 153
Weidenschilling, S. 2000, Space. Sci. Rev., 92, 295
Xiao, L., Kroll, P., & Henden, A. 2010, AJ, 139, 1527

The Astrophysical Journal, 754:114 (22pp), 2012 August 1 doi:10.1088/0004-637X/754/2/114

THE STRUCTURE AND EMISSION MODEL OF THE RELATIVISTIC JET IN THE QUASAR 3C 279 INFERRED FROM RADIO TO HIGH-ENERGY γ-RAY OBSERVATIONS IN 2008–2010

M. Hayashida[1,2], G. M. Madejski[1], K. Nalewajko[3,4], M. Sikora[4], A. E. Wehrle[5], P. Ogle[6], W. Collmar[7], S. Larsson[8,9,10], Y. Fukazawa[11], R. Itoh[11], J. Chiang[1], Ł. Stawarz[12,13], R. D. Blandford[1], J. L. Richards[14], W. Max-Moerbeck[14], A. Readhead[14], R. Buehler[1], E. Cavazzuti[15], S. Ciprini[15,16], N. Gehrels[17], A. Reimer[1,18], A. Szostek[1,13], T. Tanaka[1], G. Tosti[16,19], Y. Uchiyama[1], K. S. Kawabata[20], M. Kino[21], K. Sakimoto[11], M. Sasada[11], S. Sato[21], M. Uemura[20], M. Yamanaka[11], J. Greiner[7], T. Kruehler[22], A. Rossi[23], J. P. Macquart[24], D. C.-J. Bock[25], M. Villata[26], C. M. Raiteri[26], I. Agudo[27,28], H. D. Aller[29], M. F. Aller[29], A. A. Arkharov[30], U. Bach[31], E. Benítez[32], A. Berdyugin[33], D. A. Blinov[34], K. Blumenthal[28], M. Böttcher[35], C. S. Buemi[36], D. Carosati[37,38], W. P. Chen[39], A. Di Paola[40], M. Dolci[41], N. V. Efimova[30,34], E. Forné[42], J. L. Gómez[27], M. A. Gurwell[43], J. Heidt[44], D. Hiriart[45], B. Jordan[46], S. G. Jorstad[28,34], M. Joshi[28], G. Kimeridze[47], T. S. Konstantinova[34], E. N. Kopatskaya[34], E. Koptelova[39,48], O. M. Kurtanidze[47], A. Lähteenmäki[49], A. Lamerato[35], V. M. Larionov[30,34,50], E. G. Larionova[34], L. V. Larionova[34], P. Leto[36], E. Lindfors[33], A. P. Marscher[28], I. M. McHardy[51], S. N. Molina[27], D. A. Morozova[34], M. G. Nikolashvili[47], K. Nilsson[52], R. Reinthal[33], P. Roustazadeh[35], T. Sakamoto[17], L. A. Sigua[47], A. Sillanpää[33], L. Takalo[33], J. Tammi[49], B. Taylor[28,53], M. Tornikoski[49], C. Trigilio[36], I. S. Troitsky[34], and G. Umana[36]

[1] Kavli Institute for Particle Astrophysics and Cosmology, SLAC National Accelerator Laboratory, Stanford University, 2575 Sand Hill Road M/S 29, Menlo Park, CA 94025, USA; mahaya@slac.stanford.edu, madejski@slac.stanford.edu
[2] Department of Astronomy, Graduate School of Science, Kyoto University, Sakyo-ku, Kyoto 606-8502, Japan
[3] University of Colorado, UCB 440, Boulder, CO 80309, USA; knalew@Colorado.edu
[4] Nicolaus Copernicus Astronomical Center, 00-716 Warsaw, Poland; sikora@camk.edu.pl
[5] Space Science Institute, Boulder, CO 80301, USA
[6] Infrared Processing and Analysis Center, California Institute of Technology Pasadena, CA 91125, USA
[7] Max-Planck Institut für Extraterrestrische Physik, 85748 Garching, Germany
[8] Department of Physics, Stockholm University, AlbaNova, SE-106 91 Stockholm, Sweden
[9] The Oskar Klein Centre for Cosmoparticle Physics, AlbaNova, SE-106 91 Stockholm, Sweden
[10] Department of Astronomy, Stockholm University, SE-106 91 Stockholm, Sweden
[11] Department of Physical Sciences, Hiroshima University, Higashi-Hiroshima, Hiroshima 739-8526, Japan
[12] Institute of Space and Astronautical Science, JAXA, 3-1-1 Yoshinodai, Chuo-ku, Sagamihara, Kanagawa 252-5210, Japan
[13] Astronomical Observatory, Jagiellonian University, 30-244 Kraków, Poland
[14] Cahill Center for Astronomy and Astrophysics, California Institute of Technology, Pasadena, CA 91125, USA
[15] Agenzia Spaziale Italiana (ASI) Science Data Center, I-00044 Frascati (Roma), Italy
[16] Dipartimento di Fisica, Università degli Studi di Perugia, I-06123 Perugia, Italy
[17] NASA Goddard Space Flight Center, Greenbelt, MD 20771, USA
[18] Institut für Astro- und Teilchenphysik and Institut für Theoretische Physik, Leopold-Franzens-Universität Innsbruck, A-6020 Innsbruck, Austria
[19] Istituto Nazionale di Fisica Nucleare, Sezione di Perugia, I-06123 Perugia, Italy
[20] Hiroshima Astrophysical Science Center, Hiroshima University, Higashi-Hiroshima, Hiroshima 739-8526, Japan
[21] Department of Physics and Astrophysics, Nagoya University, Chikusa-ku, Nagoya 464-8602, Japan
[22] Dark Cosmology Centre, Niels Bohr Institute, University of Copenhagen, 2100 Copenhagen, Denmark
[23] Thuringer Landessternwarte Tautenburg, D-07778 Tautenburg, Germany
[24] International Centre for Radio Astronomy Research and Curtin University of Technology, Bentley, WA 6845, Australia
[25] CSIRO Astronomy and Space Science P.O. Box 76, Epping, NSW 1710, Australia
[26] INAF, Osservatorio Astronomico di Torino, I-10025 Pino Torinese (TO), Italy
[27] Instituto de Astrofísica de Andalucía, CSIC, E-18080 Granada, Spain
[28] Institute for Astrophysical Research, Boston University, Boston, MA 02215, USA
[29] Department of Astronomy, University of Michigan, Ann Arbor, MI 48109-1090, USA
[30] Pulkovo Observatory, 196140 St. Petersburg, Russia
[31] Max-Planck-Institut für Radioastronomie, Auf dem Hügel 69, 53121 Bonn, Germany
[32] Instituto de Astronomía, Universidad Nacional Autónoma de México, México, D. F., Mexico
[33] Tuorla Observatory, Department of Physics and Astronomy, University of Turku, FI-21500 Piikkiö, Finland
[34] Astronomical Institute, St. Petersburg State University, St. Petersburg, Russia
[35] Astrophysical Institute Department of Physics and Astronomy, Ohio University, Athens, OH 45701, USA
[36] INAF, Osservatorio Astrofisico di Catania, 95123 Catania, Italy
[37] EPT Observatories, Tijarafe, La Palma, Spain
[38] INAF, TNG Fundacioń Galileo Galilei, La Palma, Spain
[39] Graduate Institute of Astronomy, National Central University, Jhongli 32001, Taiwan
[40] INAF, Osservatorio Astronomico di Roma, I-00040 Monte Porzio Catone (Roma), Italy
[41] INAF, Osservatorio Astronomico di Collurania "Vincenzo Cerruli," 64100 Teramo, Italy
[42] Agrupació Astronòmica de Sabadell, 08206 Sabadell, Spain
[43] Harvard-Smithsonian Center for Astrophysics, Cambridge, MA 02138, USA
[44] ZAH, Landessternwarte, Universität Heidelberg, Königstuhl, D 69117 Heidelberg, Germany
[45] Instituto de Astronomía, Universidad Nacional Autónoma de México, Ensenada, B. C., Mexico
[46] School of Cosmic Physics, Dublin Institute for Advanced Studies, Dublin 2, Ireland
[47] Abastumani Observatory, Mount Kanobili, 0301 Abastumani, Georgia
[48] Department of Physics, National Taiwan University, 106 Taipei, Taiwan
[49] Aalto University Metsähovi Radio Observatory, FIN-02540 Kylmälä, Finland
[50] Isaac Newton Institute of Chile, St. Petersburg Branch, St. Petersburg, Russia
[51] School of Physics and Astronomy, University of Southampton, Highfield, Southampton, SO17 1BJ, UK
[52] Finnish Centre for Astronomy with ESO (FINCA), University of Turku, FI-21500 Piikiiö, Finland
[53] Lowell Observatory, Flagstaff, AZ 86001, USA

Received 2012 February 3; accepted 2012 May 30; published 2012 July 16

ABSTRACT

We present time-resolved broadband observations of the quasar 3C 279 obtained from multi-wavelength campaigns conducted during the first two years of the *Fermi Gamma-ray Space Telescope* mission. While investigating the previously reported γ-ray/optical flare accompanied by a change in optical polarization, we found that the optical emission appears to be delayed with respect to the γ-ray emission by about 10 days. X-ray observations reveal a pair of "isolated" flares separated by ∼90 days, with only weak γ-ray/optical counterparts. The spectral structure measured by *Spitzer* reveals a synchrotron component peaking in the mid-infrared band with a sharp break at the far-infrared band during the γ-ray flare, while the peak appears in the millimeter (mm)/submillimeter (sub-mm) band in the low state. Selected spectral energy distributions are fitted with leptonic models including Comptonization of external radiation produced in a dusty torus or the broad-line region. Adopting the interpretation of the polarization swing involving propagation of the emitting region along a curved trajectory, we can explain the evolution of the broadband spectra during the γ-ray flaring event by a shift of its location from ∼1 pc to ∼4 pc from the central black hole. On the other hand, if the γ-ray flare is generated instead at sub-pc distance from the central black hole, the far-infrared break can be explained by synchrotron self-absorption. We also model the low spectral state, dominated by the mm/sub-mm peaking synchrotron component, and suggest that the corresponding inverse-Compton component explains the steady X-ray emission.

Key words: galaxies: active – galaxies: jets – gamma rays: galaxies – quasars: individual (3C 279) – radiation mechanisms: non-thermal – X-rays: galaxies

Online-only material: color figures

1. INTRODUCTION

Blazars are active galactic nuclei characterized by highly luminous and rapidly variable continuum emission at all observed bands. The most commonly accepted scenario has their broadband emission Doppler-boosted by a relativistic jet pointing close to our line of sight (e.g., Ulrich et al. 1997). While the jet emission usually dominates the observed broadband spectrum, the optical/ultraviolet (UV) and infrared (IR) spectra often also reveal signatures of the central engine: broad emission lines, and in some cases, quasi-thermal optical/UV emission and IR dust emission, indicating the presence of an accreting supermassive black hole. Most viable current models for the origin of such jets involve conversion of the gravitational energy of matter flowing onto the black hole to the kinetic energy of the relativistic outflow or tapping the rotation energy of a spinning black hole. However, the conversion process itself is not well understood, and many additional questions regarding the dissipation region of the jet's energy into radiation and, in particular, its location remain unanswered.

Major advances in understanding blazars came as a result of the discovery by the EGRET instrument on board the *Compton Gamma-Ray Observatory* (*CGRO*) that they are strong γ-ray emitters, with γ-rays dominating radiative output (Hartman et al. 1999). With this, multi-band observations, including the γ-ray band, hold the promise of answering many outstanding questions regarding the structure of the relativistic jets of blazars.

3C 279 ($z = 0.536$; Lynds et al. 1965) is in fact one of the first γ-ray blazars discovered by EGRET in 1991 (Hartman et al. 1992). The γ-ray signal had been significantly detected in each observation by EGRET since its discovery (see, e.g., Hartman et al. 2001a), with the flux having ranged over roughly two orders of magnitude, from $\sim 10^{-7}$ up to $\sim 10^{-5}$ photons cm^{-2} s^{-1} above 100 MeV (Maraschi et al. 1994; Wehrle et al. 1998), and a factor of two variation on timescales as short as 8 hr. The photon index in the EGRET γ-ray band ranged from 1.8 to 2.3 (Nandikotkur et al. 2007). On a few occasions, 3C 279 was also detected at lower energies by *CGRO*'s OSSE (50 keV–1 MeV; McNaron-Brown et al. 1995) and COMPTEL (0.75–30 MeV; Hermsen et al. 1993; Collmar et al. 2001) instruments, indicating that the γ-ray emission forms a broad peak in the νF_ν representation. In 2008 July, the *AGILE* satellite observed a γ-ray flare associated with the source with 11.1σ significance (Giuliani et al. 2009), with an average flux above 100 MeV of $(21.0 \pm 3.8) \times 10^{-7}$ photons cm^{-2} s^{-1} and the photon index of 2.22 ± 0.23 between 100 and 1000 MeV. In the very high energy (VHE) γ-ray regime above 100 GeV, the imaging atmospheric Cherenkov telescope MAGIC detected flares twice in 2006 February (Albert et al. 2008) and in 2007 January (Aleksić et al. 2011), which made this source the most distant currently known VHE γ-ray emitter.

Optical and UV observations of the source in relatively low states—when the jet emission was relatively faint—allowed a study of the accreting black hole and the associated accretion disk. The luminosity of the accretion disk was estimated to be $L_D \sim 2 \times 10^{45}$ erg s^{-1} (Pian et al. 1999). The mass of central supermassive black hole was estimated to be in the range of $(3\text{–}8) \times 10^8\, M_\odot$ using the luminosity of optical broad line (Woo & Urry 2002) or the H_β line width (Gu et al. 2001). Those values are similar to the estimates based on the luminosity of the host galaxy (Nilsson et al. 2009).

3C 279 contains a compact radio core, associated with time-variable jet-like structure. Radio observations at 43 GHz by Very Long Baseline Array (VLBA) between 1998 March and 2001 April revealed superluminal motion of the jet with apparent speeds that range from $5c$ to $17c$ (Jorstad et al. 2004, 2005). Those observations also allowed an estimate of the Lorentz factor of the jet flow of $\Gamma_j = 15.5 \pm 2.5$ and of the viewing angle of the jet $\Theta_0 = 2\overset{\circ}{.}1 \pm 1\overset{\circ}{.}1$, corresponding to a Doppler beaming factor of $\delta = 24.1 \pm 6.5$. A change of the trajectory of a jet component has also been reported in radio observations with VLBA (Homan et al. 2003). Those authors estimated the jet component to be moving with a Lorentz factor $\Gamma_j \gtrsim 15$ at an initial viewing angle of $\lesssim 1^\circ$.

The broadband spectral energy distribution (SED) of the source is characterized by a two-bump structure, similar to many other γ-ray blazars. In the context of widely accepted

leptonic models, the lower-frequency bump, peaking at the far-IR and extending to the extreme UV band, is commonly ascribed to synchrotron radiation from relativistic electrons in the jet. The second bump, spanning from the X-ray to the γ-ray band with a peak in the MeV–GeV range, is believed to be generated via inverse-Compton scattering, presumably by the same population of particles that radiate at lower energies via the synchrotron process. The seed photons for the Compton scattering can be synchrotron photons (synchrotron self-Compton: SSC; Maraschi et al. 1992; Bloom & Marscher 1996), accretion disk photons (external Compton scattering of direct disk radiation: ECD; Dermer et al. 1992; Dermer & Schlickeiser 1993) and accretion disk photons re-scattered by the broad-line region clouds/intercloud medium (ECC; Sikora et al. 1994; Blandford & Levinson 1995), or infrared radiation from a torus located beyond the broad-line region (ERC-IR; Sikora et al. 1994). Specific to 3C 279, multi-wavelength snapshot observations for several epochs including γ-rays were presented in Hartman et al. (2001a). Those authors explained the overall spectra using the leptonic model, where the X-ray photons are mainly produced by SSC, and both ECD and ECC contribute to the γ-ray emission. Spectral variability was explained by variations of the bulk Lorentz factor of the jet, accompanied by changes in the spectral shape of the electron distribution.

The optical variability of 3C 279 is extreme: in 1937, it showed optical (B) magnitude of 11.27 (Eachus & Liller 1975), making it one of the most luminous active galaxies ever recorded. The strong variability recorded in all bands provides an opportunity to establish the relationship between emission in those bands, and thus can be used to constrain theoretical models of physical regions of the jet responsible for such emission. Many such multi-wavelength campaigns have been conducted (see, e.g., Maraschi et al. 1994; Wehrle et al. 1998; Larionov et al. 2008; Collmar et al. 2010), but they have not revealed a simple relationship between the variability in various bands: radiation in different spectral regimes does not always rise and fall simultaneously, although the periods of increased rapid activity in all bands seem to last for several months, and take place when the source is relatively bright. A recent paper by Chatterjee et al. (2008) presents the results of the monitoring of 3C 279 for 11 years in radio, optical, and X-rays, and discusses the details of the jet structure based on multi-band correlation studies. However, due to the lack of deployed instruments, long-term monitoring observations could not include the γ-ray regime, where the source often shows stronger variability than in other bands.

The launch of the *Fermi Gamma-ray Space Telescope* on 2008 June 11 has rejuvenated multi-band studies of blazars. The Large Area Telescope (LAT; Atwood et al. 2009) instrument on board *Fermi* can monitor all γ-ray sources on the sky with its a wide field of view and a much larger effective area compared to earlier γ-ray missions. Taking advantage of this new instrument for γ-ray observations, we have organized intensive multi-wavelength campaigns for 3C 279 from radio to the high-energy γ-ray energy ranges. Many ground-based telescopes (cm, mm, near-IR, and optical) and various satellites (IR, UV, X-ray, hard X-ray, and high-energy γ-ray) participated in this campaign. We reported the first results of the campaign in Abdo et al. (2010b, hereafter Paper I), where we discovered the dramatic change of the optical polarization coincident with the γ-ray flare. Here, we provide details of the multi-band observations and the interpretation of those data for the two-year interval between 2008 August and 2010 August. In Section 2, we present and briefly discuss the features of the LAT γ-ray data; in Section 3, we present the data in lower energy bands. Section 4 highlights the features of time series measured in various bands including their cross-correlations, and the general properties of the broadband SED. In Section 5, we provide viable emission models for the source in the context of leptonic scenarios.

2. *FERMI*-LAT DATA AND RESULTS

Fermi-LAT is a pair-production telescope with large effective area (8000 cm^2 on axis at 1 GeV for the event class considered here), and large field of view (2.4 sr at 1 GeV), sensitive to γ-rays in the energy range from 20 MeV to >300 GeV. Information regarding on-orbit calibration procedures is given in Abdo et al. (2009a). *Fermi*-LAT normally operates in a scanning "sky-survey" mode, which provides a full-sky coverage every two orbits (3 hr). For operational reasons, the standard rocking angle (defined as the angle between the zenith and the center of the LAT field of view) for survey mode was increased from 35° to 50° on 2009 September 3.

2.1. Observation and Data Reductions

The data used here comprise two-year observations obtained between 2008 August 4 and 2010 August 6 (MJD 54682–55414). We used the standard LAT analysis software, *ScienceTools v9r21*. The events were selected using so-called diffuse class events. In addition, we excluded the events with zenith angles greater than 100° to avoid the contamination of the Earth-limb secondary γ radiation. The events were extracted in the range between 200 MeV and 300 GeV within a 15° acceptance cone of the region of interest (ROI) centered on the location of 3C 279 (R.A. = 195.°047, decl. = −5.°789, J2000). Below 200 MeV, the effective collection area of LAT for the diffuse class events drops very quickly and thus larger systematic errors are expected. The γ-ray flux and spectrum were calculated using the instrument response function (IRF) of "P6_V11_DIFFUSE" by an unbinned maximum likelihood fit of model parameters. We examined the significance of the γ-ray signal from the sources by means of the test statistic (TS) based on the likelihood ratio test.[54] The background models included a component for the Galactic diffuse emission along the plane of the Milky Way, which was modeled by the map cube file "*gll_iem_v02_P6_V11_DIFFUSE.fits*." An isotropic component (*isotropic_iem_v02_P6_V11_DIFFUSE.txt*) was also included to represent the extragalactic diffuse emission and residual instrumental background. Besides those components, the model in our analysis also included the emission from all nearby point sources inside the ROI from the first *Fermi*-LAT catalog (1FGL: Abdo et al. 2010c). The spectra of those sources were modeled by power-law functions except for a pulsar 1FGL J1231.1–1410 (=PSR J1231–1411), for which we included an additional exponential cutoff in its spectral modeling. During the spectral fitting, the normalization factors of the Galactic diffuse and isotropic components and the nearby sources were left as free parameters, and the photon indices of the nearby sources were fixed to the values from the 1FGL catalog except for 3C 273, whose photon index was allowed to vary freely. In the light curve analysis, we considered only two bright sources in the background model as nearby point sources, namely, 3C 273

[54] TS = 25 with two degrees of freedom corresponds to an estimated ∼4.6σ pre-trials statistical significance assuming that the null-hypothesis TS distribution follows a χ^2 distribution (see Mattox et al. 1996).

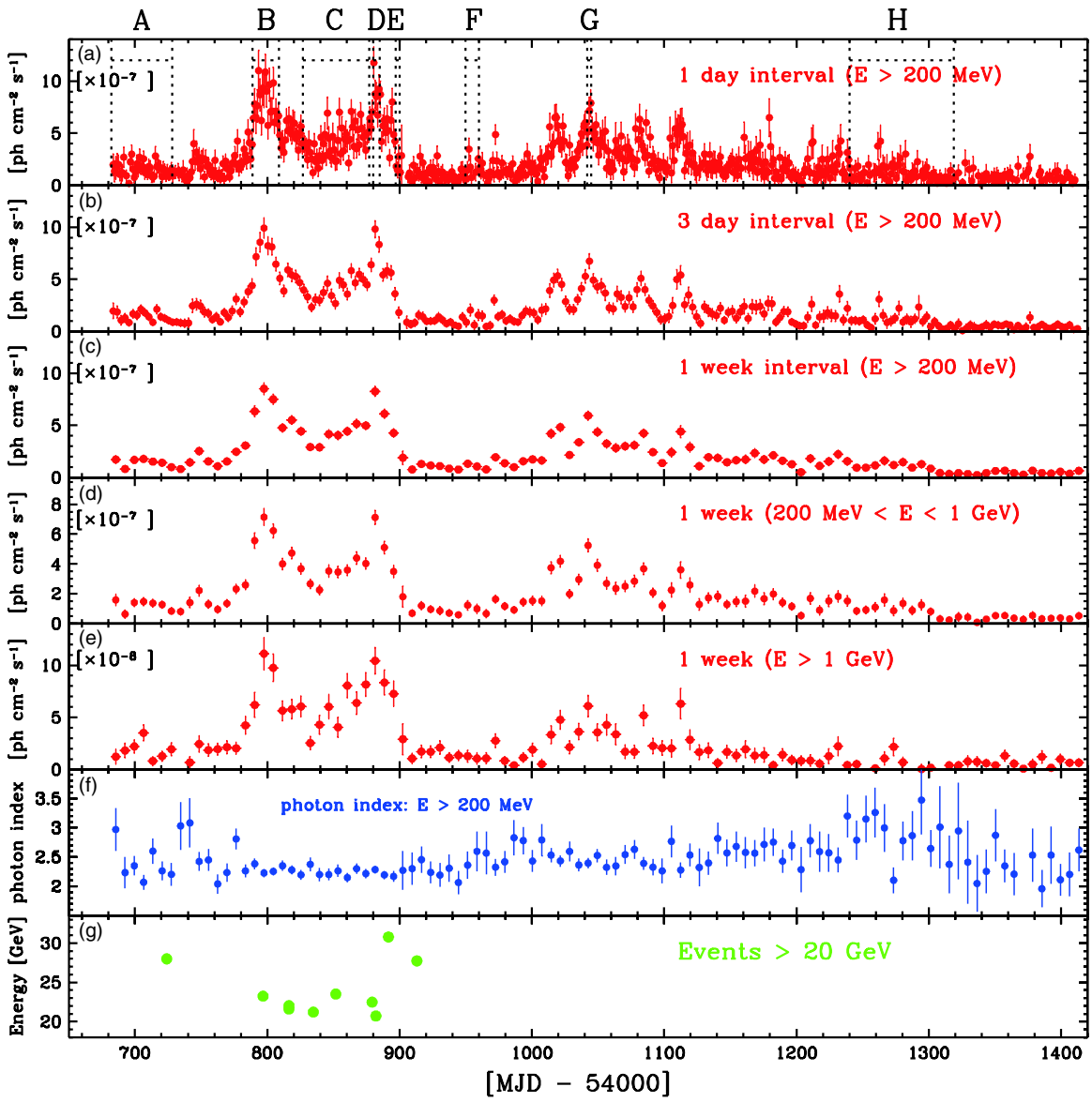

Figure 1. Gamma-ray light curves of 3C 279 during the first two years of the *Fermi*-LAT observations from 2008 August to 2010 August, plotted in (a) one day intervals at energies above 200 MeV, (b) three day intervals at energies above 200 MeV, (c) one week intervals at energies above 200 MeV, (d) one week intervals at energies between 200 MeV and 1 GeV, (e) one week intervals at energies above 1 GeV. The panel (f) shows the history of the photon index at energies above 200 MeV in one week intervals, while the panel (g) shows arrival time distribution of >20 GeV events associated with 3C 279. The vertical axis of the panel (g) represents the estimated energy of events. The highest energy photon corresponds to 30.8 GeV at MJD 54891. The dotted lines and capital letters represent time intervals where γ-ray spectra are extracted (see also Table 1).

(A color version of this figure is available in the online journal.)

and 1FGL J1231.1–1410, because other nearby sources had a negligible contribution to γ-ray signal, especially in such relatively short timescales (shorter than a week) for the light curves considered here. The fluxes used for the light curve were calculated by a simple power-law model fit using data in the given energy ranges.

2.2. Temporal Behavior

The γ-ray light curve measured by *Fermi*-LAT can be seen in Figure 1. The figure shows the flux history above 200 MeV averaged over (a) one day intervals, (b) three day intervals, and (c) one week intervals. It also includes one week light curves of (d) the flux between 200 MeV and 1 GeV, (e) the flux above 1 GeV, and (f) the photon index in the range above 200 MeV.

The γ-ray flux clearly shows variability. The source showed high-flux states between MJD 54700 and 54900, in which two prominent flares can be seen: one of the flares at ∼MJD 54800 and the other at ∼MJD 54880. During the second flare, a change in the optical polarization associated with a γ-ray flare was discovered (Paper I). We detected some flux variability between MJD 55000 and 55120, but after that, the source remained in a relatively low activity state until the end of the period considered in this paper. During this two-year period, the highest integral flux above 200 MeV occurred on MJD 54880 in the one day interval light curve with flux of $F_{E>200\,\mathrm{MeV}} = (11.8 \pm 1.5) \times 10^{-7}$ photons cm^{-2} s^{-1} and TS = 306. By extrapolating the spectrum down to 100 MeV, an integral flux above 100 MeV on that day yields $F_{E>100\,\mathrm{MeV}} = (31.0 \pm 6.0) \times 10^{-7}$ photons cm^{-2} s^{-1}, which is still a factor of 3–4 times lower

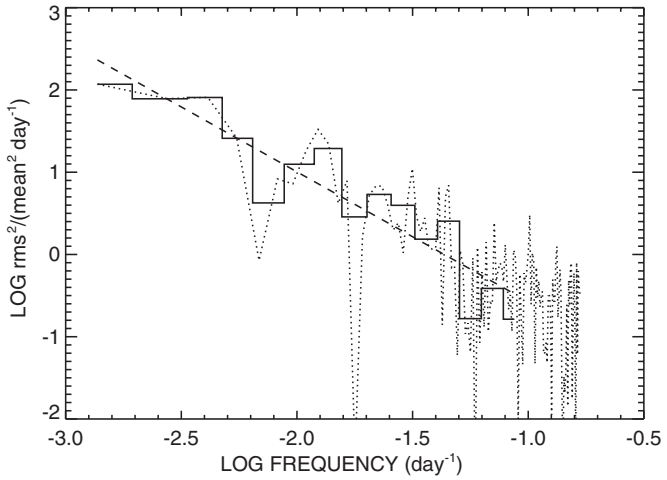

Figure 2. Power density spectrum of 3C 279 for the three day binned γ-ray light curve. The white noise level has been subtracted. The solid line histogram describes the PDS averaged in logarithmic frequency bins while the dotted curve describes the raw PDS before binning. The dashed line represents a linear fit to the binned PDS.

than the flux of the brightest flare ($\sim 1 \times 10^{-5}$ photons cm^{-2} s^{-1}) detected during the EGRET observations of the source (Wehrle et al. 1998; Hartman et al. 2001b).

We quantified the flux variability using one week interval data for energies above 200 MeV (full band), between 200 MeV and 1 GeV (soft band), and above 1 GeV (hard band). This is based on the "excess variance" method (Nandra et al. 1997; Edelson et al. 2002) after subtracting the contribution expected from measurement errors ($\sigma_{\mathrm{err},i}$). Using the mean square error $\langle \sigma_{\mathrm{err},i} \rangle$, the excess variance F_{var} can be described as (Vaughan et al. 2003)

$$F_{\mathrm{var}} = \sqrt{\frac{S^2 - \langle \sigma_{\mathrm{err},i} \rangle^2}{\langle F \rangle^2}}, \quad (1)$$

where S is the variance of the flux, and $\langle F \rangle$ is the mean value of the flux. The definition of associated error can be found in Vaughan et al. (2003). In the calculation, we excluded bins of 8, 82, 87, and 90 because the fit in the hard band failed due to poor statistics of the data samples. Resulting F_{var} values are 0.695 ± 0.015, 0.648 ± 0.017, and 0.839 ± 0.030 for the full, soft, and hard bands, respectively. The resulting values indicate that the flux of the hard band showed significantly stronger variability than that of the soft band. For comparison, $F_{\mathrm{var}} = 0.79 \pm 0.02$ for $E > 300$ MeV has been reported during the first 11 months of the *Fermi* scientific mission (Abdo et al. 2010f), when the source has clearly been more active.

A power density spectrum (PDS) for the three day binned light curve was calculated using a Fourier transform and is shown in Figure 2. The power density was normalized to fractional variance per frequency unit (rms^2 I^{-2} day^{-1}) and the PDS points were averaged in logarithmic frequency bins. The white noise level was estimated from the rms of the flux errors and was subtracted from the PDS. A slope of 1.6 ± 0.2 was obtained from a linear fit to the binned PDS for frequencies up to 0.1 day^{-1}. The main uncertainty in the estimated PDS slope is due to the stochastic nature of the variability which leads to variations in the determined slope between different time-limited observations. An additional effect which can cause a systematic bias in the observed PDS slope is the red noise leakage (e.g., Chatterjee et al. 2008). In the present analysis this effect is not taken into account.

Figure 3 shows plots of flux versus photon index (Γ) based on the weekly light curve results above 200 MeV (full band), between 200 MeV and 1 GeV (soft band), and above 1 GeV (hard band). The data that have TS > 10 were selected for the plots and are shown in gray points. An average photon index was calculated by fitting a constant value in each plot, corresponding to $\Gamma_{>200\,\mathrm{MeV}} = 2.334 \pm 0.015$, $\Gamma_{200\,\mathrm{MeV}-1\,\mathrm{GeV}} = 2.20 \pm 0.03$, and $\Gamma_{>1\,\mathrm{GeV}} = 2.48 \pm 0.04$ for the full, soft, and hard bands, respectively. The average photon index in the soft band shows a significantly harder spectrum than that in the hard band.

We also derived photon indices resulting from an analysis where the data were sorted in five bins using week-long fluxes for each energy band, and plotted the results as red points. Those photon indices of each flux bin are also shown in the insets in Figure 3. For the full band, although the change of the photon index is rather small ($\Delta\Gamma \sim 0.2$) compared to the flux variation (spanning about an order of magnitude), a weak "harder when brighter" effect can be seen. Such an effect was also measured in other LAT blazars (Abdo et al. 2010e). The soft band also shows the weak "harder when brighter" effect with a slightly larger change of the photon index ($\Delta\Gamma \sim 0.4$). On the other hand, the photon index of the hard band changes only sightly ($\Delta\Gamma \sim 0.1$) and is statistically consistent with a constant value.

2.3. Highest Energy Photons

During the two year observations, the highest energy photon associated with 3C 279 was detected at MJD 54891.60745 with an estimated energy of 30.8 GeV. The event was converted in the front-thin layers (so-called front event) of the LAT detector and still remains even when we apply the cleanest event selection (so-called data clean event), which was developed for studying extragalactic γ-ray background (Abdo et al. 2010g). The reconstructed arrival direction of the event is $5\farcm7$ ($= 0\fdg095$) away from 3C 279, and is within the 68% containment radius of the LAT point-spread function (PSF; $0\fdg114$ in the IRF of "P6_V11_DIFFUSE") for front events at 30.8 GeV. Based on our model fit of the epoch which contains that highest energy photon, we find the probability that the photon was associated with 3C 279 (as opposed to all other sources in the model including the diffuse emission and nearby point sources) is 88.6%.

In total, we found 10 events with estimated energies higher than 20 GeV within an $0\fdg25$ radius centered at 3C 279. All events lie within a 95% containment radius of the LAT PSF from 3C 279 and remain even after the "data clean selection" applied. The number of expected background events above 20 GeV within the $0\fdg25$ radius at the location of 3C 279 for the two year observations is only 0.16 events. The bottom panel of Figure 1 plots the arrival time distribution of those 10 events. All events except for two were detected between MJD 54780 and 54900 during the high-activity states. No photon above 20 GeV associated with 3C 279 has been detected after MJD 54914 during the two year observations.

2.4. Gamma-Ray Spectra

We extracted the γ-ray spectra using data for the entire two-year period and following eight sub-periods (see also Table 1): (A) the initial quiescent state in the γ-ray band (MJD 54682–54728), (B) the first γ-ray flaring state (MJD 54789–54809), (C) an intermediate state (MJD 54827–54877),

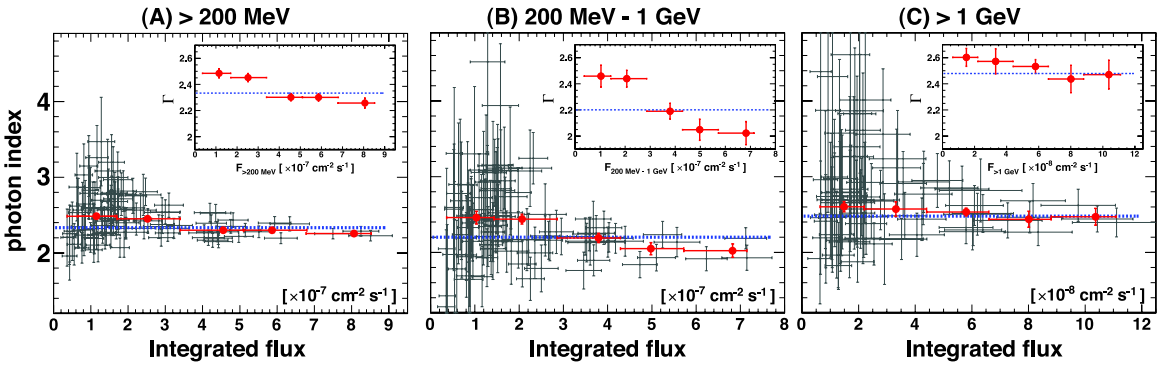

Figure 3. Plots of the integrated γ-ray flux vs. photon index of 3C 279 measured in week-long bins for energies above 200 MeV (A), between 200 MeV and 1 GeV (B), and above 1 GeV (C). Only points with TS $>$ 10 are plotted (gray points). The blue dotted horizontal lines indicate average photon indices of those data for each energy band. Red points show the photon indices resulting from an analysis where the data were sorted in five bins using week-long fluxes for each energy band. For the red points, the horizontal bars indicate the ranges of the week-long flux bins while the vertical bars indicate 1σ statistical errors. The insets show enlarged views of the red points as well as the average photon index of each energy band.

(A color version of this figure is available in the online journal.)

Table 1
Results of Spectral Fitting in the γ-Ray Band Measured by *Fermi*-LAT

Period	Gamma-Ray Spectrum (*Fermi*-LAT)						Flux ($>$100 MeV)
(MJD)	Fitting Model[a]	$\Gamma/\alpha/\Gamma_1$	β/Γ_2	$E_{\rm brk}$ (GeV)	TS	$-2\Delta L$[b]	(10^{-7} photons cm^{-2} s^{-1})
2 years	PL	2.38 ± 0.02	...	...	20272	...	6.10 ± 0.13
2008 Aug 4–2010 Aug 6	LogP	2.18 ± 0.03	0.08 ± 0.01	...	20267	46.5	5.18 ± 0.16
(54682–55414)	BPL	2.31 ± 0.02	2.95 ± 0.12	3.5 ± 0.3	20286	43.0	5.76 ± 0.15
Period A	PL	2.30 ± 0.07	...	...	797	...	3.7 ± 0.4
2008 Aug 4–2008 Sep 19	LogP	2.19 ± 0.15	0.04 ± 0.05	...	797	0.7	3.3 ± 0.5
(54682–54728)	BPL	2.21 ± 0.09	2.82 ± 0.40	3.4 ± 0.8	798	2.5	3.4 ± 0.4
Period B	PL	2.28 ± 0.04	...	...	3209	...	19.0 ± 1.1
2008 Nov 19–2008 Dec 9	LogP	1.95 ± 0.10	0.13 ± 0.04	...	3214	13.6	15.0 ± 1.3
(54789–54809)	BPL	2.00 ± 0.10	2.61 ± 0.11	1.0 ± 0.2	3215	13.7	15.8 ± 1.3
Period C	PL	2.25 ± 0.04	...	...	4107	...	10.0 ± 0.5
2008 Dec 27–2009 Feb 15	LogP	2.05 ± 0.08	0.08 ± 0.03	...	4110	8.2	8.6 ± 0.6
(54827–54877)	BPL	2.07 ± 0.08	2.43 ± 0.08	1.0 ± 0.2	4109	8.2	8.9 ± 0.6
Period D	PL	2.36 ± 0.08	...	...	1236	...	23.6 ± 2.3
2009 Feb 18–2009 Feb 23	LogP	2.16 ± 0.16	0.09 ± 0.06	...	1234	2.0	20.2 ± 2.8
(54880–54885)	BPL	2.25 ± 0.12	2.91 ± 0.61	2.3 ± 2.1	1235	2.9	21.8 ± 2.6
Period E	PL	2.64 ± 0.32	...	...	61	...	6.3 ± 2.5
2009 Mar 7–2009 Mar 10	LogP	2.64 ± 0.32	0.00 ± 0.00	...	61	0.0	6.3 ± 2.5
(54897–54900)							
Period F	PL	2.54 ± 0.24	...	...	85	...	3.5 ± 1.2
2009 Apr 29–2009 May 9	LogP	2.54 ± 0.24	0.00 ± 0.00	...	85	0.0	3.5 ± 1.2
(54950–54960)							
Period G	PL	2.44 ± 0.13	...	...	460	...	18.8 ± 2.9
2009 Jul 30–2009 Aug 2	LogP	2.37 ± 0.25	0.03 ± 0.10	...	460	0.1	17.7 ± 4.0
(55042–55045)							
Period H	PL	2.83 ± 0.11	...	...	398	...	3.7 ± 0.5
2010 Feb 13–2010 May 3	LogP	2.56 ± 0.23	0.16 ± 0.13	...	399	1.9	2.9 ± 0.6
(55240–55319)	BPL	2.72 ± 0.43	3.47 ± 0.57	1.6 ± 0.5	399	1.6	3.4 ± 1.7

Notes.
[a] PL: power-law model; LogP: log parabola model; BPL: broken power-law model. See definitions in the text.
[b] ΔL represents the difference of the logarithm of the likelihood of the fit with respect to a single power-law fit.

(D) the first five days of the second γ-ray flaring event (MJD 54880–54885), (E) the last three days of the second γ-ray flaring event (MJD 54897–54900), (F) during the isolated (first) X-ray flaring event (MJD 54950–54960; see Section 4), (G) during the second X-ray flaring event (MJD 55042–55045; see Section 4), and (H) a quiescent state (MJD 55240–55319). Those sub-periods were also selected taking into account observations in other energy bands. SEDs in the γ-ray band for each sub-period are presented in Figure 4. Each γ-ray spectrum was modeled using a simple power-law (PL; $dN/dE \propto E^{-\Gamma}$), a broken power-law (BPL; $dN/dE \propto E^{-\Gamma_1}$ for $E < E_{\rm brk}$ and $dN/dE \propto E^{-\Gamma_2}$ otherwise), and a log parabola (LogP; $dN/dE \propto (E/E_0)^{-\alpha-\beta\log(E/E_0)}$) model. In the case of LogP model, the parameter β represents the curvature around the

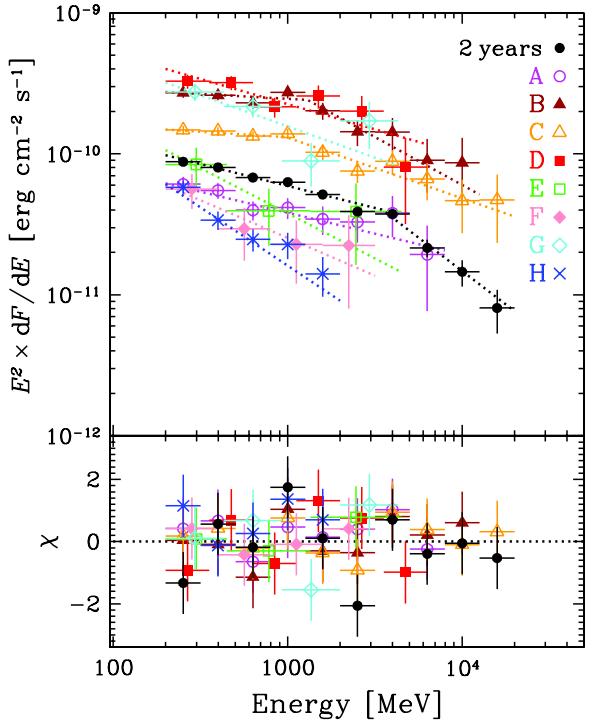

Figure 4. Gamma-ray spectral energy distributions of 3C 279 of each period as defined in the text or Table 1. Two-year averaged (black filled circles), Period A (magenta open circles), Period B (brown filled triangles), Period C (orange open triangles), Period D (red filled squares), Period E (green open squares), Period F (pink filled diamonds), Period G (cyan open diamonds), and Period H (blue crosses). The vertical bars indicate 1σ statistical errors while the horizontal bars indicate energy ranges of each bin. The best-fit spectral models are plotted as dotted lines for each period and their parameters are summarized in Table 1. We use the broken power-law model for the spectra of two years, Period B, and Period C because significant improvements in the spectral fits can be seen compared to the simple power-law model (see Table 1) while the simple power-law model is used for other periods. The lower panel shows the residuals, plotted as χ ($\equiv$ (data − model)/data error) from the best-fit models. A "dip" feature at ∼1–2 GeV in the spectrum of Period G (the third point in cyan) is a $\leqslant 2\sigma$ effect from the best-fit model, thus not statistically significant.

(A color version of this figure is available in the online journal.)

peak. We note that the choice of the reference energy E_0 in the LogP model does not affect the determination of the other two model parameters, and hence we fixed it at 300 MeV.

The best-fit parameters calculated by the fitting procedure are summarized in Table 1. The integral fluxes above 100 MeV[55] derived using each spectral model are also included. The averaged γ-ray spectral shape for the two year observation significantly deviates from a single power law. A LogP model is favored to describe the γ-ray spectral shape over the simple PL model with the difference of the logarithm of the likelihood fits[56] $-2\Delta L = 46.5$ (corresponding to a significance level of $\sim 7\sigma$),[57] and a BPL fit yields $-2\Delta L = 43.0$. Even in some individual periods as defined above, the spectra deviate from a single power law: for example, the spectrum in the Period B yields $-2\Delta L = 13.6$. This is consistent with our finding in Section 2.2 that the spectrum above 1 GeV is significantly softer than the spectrum below 1 GeV. We thus conclude that the γ-ray spectrum significantly deviates from a simple power law. The spectral break in 3C 279 is not as pronounced as that seen in the spectra, e.g., of 3C 454.3 (Ackermann et al. 2010). One the other hand, the BPL model returns break energies within a few GeV range regardless of the flux levels as observed in other bright FSRQs, such as 3C 454.3 and 4C+21.35 (Tanaka et al. 2011). Such a spectral feature could be due to γ–γ absorption to pair production by He II Lyman recombination continuum UV photons from the emission line region (see, e.g., Poutanen & Stern 2010), or a break in the electron distribution (Abdo et al. 2009b). We consider the γ-ray emission region to be located significantly beyond the broad emission region (see the Discussion in Section 5), and this implies that the break in the electron energy distribution is the more likely explanation.

[55] Although we use photon data from 200 MeV, the integral fluxes are extrapolated down to 100 MeV, which is convenient to compare with other γ-ray results.

[56] $-2\Delta L = -2\log(L0/L1)$, where $L0$ and $L1$ are the maximum likelihood estimated for the null and alternative hypothesis, respectively.

[57] Because the LogP model has one more free parameter than the PL model has, the $-2\Delta L$ distribution follows a χ^2 distribution with one degree of freedom.

3. MULTI-WAVELENGTH OBSERVATIONS AND DATA REDUCTION

3.1. X-Ray and Hard X-Ray: Suzaku

The *Suzaku* X-ray satellite (Mitsuda et al. 2007) observed 3C 279 as a part of multi-band studies of the object. The observations took place in two segments, with an interruption lasting roughly 1.5 days: (1) between 2009 January 19, 23:19:00 and 2009 January 22, 22:32:00 UTC (sequence number 703049010), and (2) between 2009 January 23, 20:45:00 and 2009 January 25, 03:00:00 UTC (sequence number 703049020). "Period C" (see Table 1) includes both *Suzaku* observations. The goals of the *Suzaku* observations were to monitor the soft-medium X-ray flux (0.3–12 keV) of the source with the X-ray Imaging Spectrometer (XIS; Koyama et al. 2007) and to take advantage of the data from the Hard X-ray Detector (HXD; Takahashi et al. 2007). The HXD consists of PIN silicon diodes for the lower energy band (10–70 keV) and GSO scintillators for the higher energy band (40–600 keV), to extend the spectral bandpass beyond the energies accessible with imaging instruments (>10 keV). The HXD nominal position was used for the observations to maximize its effective area. In the following analysis, the HXD/GSO data were not used because there was no significant detection of the source.

Although the observation conditions were nominal, the XIS1 data suffered from somewhat high and variable background, resulting in the total apparent counting rate ranging from one to three counts s^{-1} in source-free regions for the entire chip. Still, the background-subtracted spectrum determined from the XIS1 data below 8 keV was entirely consistent with that from XIS0 and XIS3 and thus we included the background-subtracted XIS1 data in the spectral fitting. The total duration of good data accumulated by the XIS instruments was 191 ks. We used the standard `ftools` data reduction package, provided by the *Suzaku* Science Operations Center, with the calibration files included in CALDB ver. 4.3.1. For the analysis of spectra and light curves, we extracted the counts from a region corresponding to a circle with 260″ radius, centered on the X-ray centroid; we used a region of a comparable size from the same chip to extract the background counts. The net count rates were 0.47, 0.63, and 0.56 count s^{-1} for XIS0, XIS1, and XIS3, respectively, with the typical count rate uncertainty in the entire observations of ∼3%. The data indicate no significant variability during the *Suzaku* observations.

The source was also detected in the HXD/PIN data, although the signal was relatively weak. We used the standard cleaned events, processed using the standard criteria applicable to

the rev. 2.13 of the *Suzaku* HXD data processing software. This yielded 95.4 ks of good data, with a total count rate of 0.3 counts s^{-1}. For the background subtraction, we used the standard background files provided by the *Suzaku* team through HEASARC. We applied the standard tool `hxdpinxbpi` which accounts for the particle background as well as for the contribution of the cosmic X-ray background as appropriate for the effective area and the solid angle of the HXD. The net counting rate was 0.02 counts s^{-1}, with the formal statistical uncertainty of ∼10%. We note that this formal uncertainty is probably lower than the standard systematic error due to the background subtraction of 3% of the average background (corresponding to 0.01 counts s^{-1}). Nonetheless, even if the additional uncertainty is included, the source was still detected by the HXD/PIN.

For the spectral analysis, we used the `XSPEC` spectral analysis software. For the spectral fitting of the XIS data, we used the standard redistribution files and mirror effective areas generated with *Suzaku*-specific tools `xisrmfgen` and `xissimarfgen`. In the spectral fits, we used the counts corresponding to the energy range of 0.5–10.0 keV for XIS0 and XIS3, and 0.5–8.0 keV for the XIS1. We used all three XIS detectors simultaneously, but allowed for a small (a few %) variation of normalization. For the HXD/PIN data, we considered the data in the range of 20–50 keV and used the response file `ae_hxd_pinhxnome5_20080716.rsp`.

The source spectrum was modeled as an absorbed power law, with the cross-sections and elemental abundances as given in Morrison & McCammon (1983); other absorption models give similar results. The best-fit absorbing column was $(3.1 \pm 0.5) \times 10^{20}$ cm^{-2}, and the photon index was 1.76 ± 0.01. Inclusion of the HXD/PIN data in the fit did not change the fit parameters perceptibly. The χ^2 for the fit including the three XIS detectors and the HXD/PIN was acceptable, with 5061 for 5023 channels. The absorption inferred from the simple absorbed power-law model is marginally greater than the value inferred from the radio measurements of the column density of the material in the Galaxy of 2.0×10^{20} cm^{-2} (with an estimated error of ∼10%; Kalberla et al. 2005). We deem the difference not significant, since at such small column densities, it can be accounted for by even small systematic uncertainty in the knowledge of the effective area of the XIS instruments at the lowest end of the XIS bandpass. Furthermore, a modest additional column density is expected in the host galaxy of 3C 279. The observed model 2–10 keV flux is 8.0×10^{-12} erg cm^{-2} s^{-1}, with the statistical error of <2%, which is probably smaller than the systematic error resulting form the calibration uncertainty of the *Suzaku* instruments. We plot the *Suzaku* 3C 279 spectra in Figure 5.

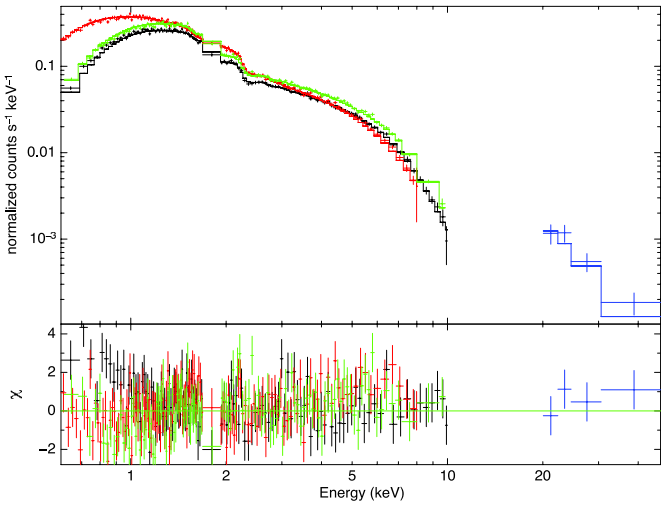

Figure 5. Count spectra of 3C 279 measured by *Suzaku* XIS0 (black), XIS1(red), XIS3 (green), and HXD/PIN (blue). The model plotted with the data is a broken power law obtained by fitting these three XISs and HXD/PIN data. The lower panel shows the residuals for this broken power-law model.

(A color version of this figure is available in the online journal.)

3.2. X-Ray: XMM-Newton

XMM-Newton observed 3C 279 once starting on 2009 January 21, 17:28 UT. The observation was largely devoid of flares (except for the period close to the end of the observation), and the total length of good data accumulated in the pointing was 16.8 ks. We used the standard Scientific Analysis System (SAS) data reduction package, provided by the *XMM-Newton* Science Operations Center. Since 3C 279 is a relatively bright source, we considered only the pn-CCD data. We note here that the spectra and light curves taken by MOS-CCDs were entirely consistent with the results inferred from the pn-CCD data.

For the analysis of spectra and light curves, we extracted the counts from within 40″ radius of the source; we used a region of the same size, from the same pn-CCD chip, to extract the background counts. The data indicate no significant variability during the *XMM-Newton* observation. The spectral analysis was performed using the `XSPEC` v.12 spectral analysis software with the standard redistribution files and mirror effective areas included in the SAS package. We used the counts corresponding to the energy range of 0.5–10.0 keV in our spectral fits.

The source spectrum was first modeled as an absorbed power law; the best-fit absorbing column was $(2.2 \pm 0.6) \times 10^{20}$ cm^{-2}, and the photon index was 1.77 ± 0.03, with χ^2 of 588 for 517 dof. The result is consistent with the spectral analysis results of the *Suzaku* observations as described in the previous section, which were performed during the same period as the *XMM-Newton* observation. We also considered a broken power-law model and found that the overall intrinsic source spectrum hardens with increasing energy. The absorbing column was $(3.4 \pm 0.7) \times 10^{20}$ cm^{-2}, and the low- and high-energy indices were, respectively, 1.83 ± 0.05 and 1.55 ± 0.2 with the break energy of 4.1 ± 0.8 keV. The resulting χ^2 was 563, for 515 dof. The broken power-law model is statistically only marginally superior to the simple power-law model, especially given that the absorption inferred form the simple power-law model is closer to the value inferred from Kalberla et al. (2005). For either model, the 2–10 keV flux is 7.7×10^{-11} erg cm^{-2} s^{-1}, with a statistical error of 5%, which is probably smaller than the systematic error resulting form the calibration uncertainty of the *XMM-Newton* pn-CCD.

3.3. X-Ray: RXTE-PCA

RXTE carried out 321 observations between 2008 July 3 (MJD 54650) and 2010 August 12 (MJD 55420). Those include 52 observations based on the Cycle 12 Guest observer (GO) program and 269 observations based on the Core program in Cycles 12–14. The fluxes resulting from the Cycle 12 GO observations have been already reported in Paper I. Most of the individual observations have exposure times in a range from 1.0 to 2.5 ks. We analyzed the data from the Proportional Counter Array (PCA) following standard procedures using the `rex` script in HEASOFT v.6.9. Only signals from the top layer (X1L and X1R) of PCU2 were extracted for data analysis. The

data were screened with the following data selection: source elevation above the horizon $>10^{\circ}$, pointing offset smaller than $0^{\circ}.02$, at least 30 minutes away from a South Atlantic Anomaly (SAA) passage and electron contamination smaller than 0.1. The background was estimated with standard procedures, and the detector response matrices were extracted with the RXTE tools (command PCARSO v.11.7.1). For the spectral analysis we re-binned the spectra into 11 channels. The spectra from the channels corresponding to nominal energies of 2.6–10.5 keV are adequately fitted by a single power-law model, absorbed by a fixed Galactic column density of 2.2×10^{20} cm^{-2} using the XSPEC v.12 software package. The value of the column density is based on our *XMM-Newton* results (in Section 3.2) and is also consistent with the value based on Kalberla et al. (2005).

3.4. X-Ray: Swift-XRT

In the HEASARC database,[58] there are 80 publicly available *Swift* X-Ray Telescope (XRT) observations between 2008 July 3 (MJD 54650) and 2010 August 12 (MJD 55420), which include 32 pointings based on an approved GI proposal in Cycle 4 (Proposal number: 5080069). The results of the flux history based on the data until 2009 May 31 have already reported in Paper I. Effective exposure times of these observations range between 1 and 3 ks, but some have longer exposure times, for example, 8.9 ks for ID:35019007 (MJD 54795), 22.5 ks for ID:35019009 (MJD 54797), 20.2 ks for ID:35019010 (MJD 54799), and 15.4 ks for ID:35019011 (MJD 54800). The XRT was used in the photon counting mode, and no evidence of pile-up was found. The XRT data were reduced with the standard software xrtpipeline v.0.12.6, applying the default filtering and screening criteria (HEADAS package, v.6.10). The source events were extracted from a circular region, 20 pixels in radius, centered on the source position. Exposure maps were used to account for PSF losses and the presence of dead pixels/columns. The background was determined using data extracted from a circular region, 40 pixels in radius, centered on (R.A., decl.: J2000) = ($12^{\rm h}56^{\rm m}26^{\rm s}$, $-05^{\circ}49'30''$), where no X-ray sources are found. Note that the background contamination is less than 1% of source flux even in the faint X-ray states of the source. The data were rebinned to have at least 25 counts per bin, and the spectral fitting was performed using the energy range between 0.3 keV and 10 keV using XSPEC v.12. The Galactic column density is fixed at 2.2×10^{20} cm^{-2} during the fittings as is the case in the *RXTE* data analysis.

Figure 6 shows a scatter plot between photon index and flux in the X-ray band as measured by *Swift*-XRT and *RXTE*-PCA. Generally, a "harder-when-brighter" trend can be seen. Only the highest flux point measured by *Swift*-XRT shows the photon index significantly harder (smaller) than 1.5.

3.5. Ultraviolet: Swift-UVOT

The *Swift* Ultra-Violet/Optical Telescope (UVOT; Roming et al. 2005) data used in this analysis included all of the observations performed during the time interval MJD 54650–55420. The UVOT telescope cycled through each of the six optical and ultraviolet filters (V, B, U, $W1$, $M2$, $W2$). The UVOT photometric system is described in Poole et al. (2008). Photometry was computed from a 5″ source region around 3C 279 using the publicly available UVOT FTOOLS data reduction suite. The background region was taken from an annulus with inner and outer radii of 27″.5 and 35″, respectively. Galactic absorption in the direction of 3C 279 was adapted as given in Larionov et al. (2008), namely, $A_V = 0.093$, $A_B = 0.123$, $A_U = 0.147$, $A_{W1} = 0.195$, $A_{M2} = 0.285$, and $A_{W2} = 0.271$. The measured magnitudes in each band during the two year observations are m_V = 15.6–18.7 (75 data points), m_B = 16.0–18.8 (80 data points), m_U = 15.1–18.0 (88 data points), m_{W1} = 15.3–18.0 (84 data points), m_{M2} = 15.4–18.2 (76 data points), and m_{W2} = 15.5–18.0 (81 data points). All observed data points are shown in Figure 7.

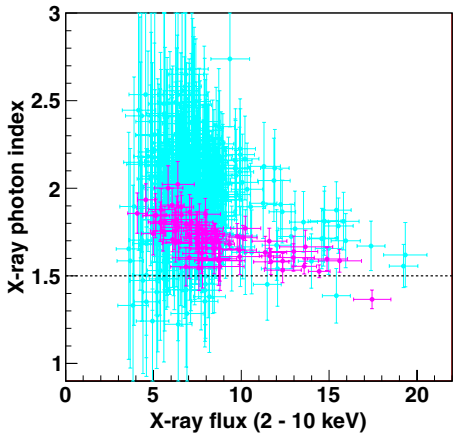

Figure 6. Scatter plot of flux vs. photon index of 3C 279 in the X-ray band with the data taken by *Swift*-XRT (magenta) and *RXTE*-PCA (cyan). The horizontal dotted line represents the photon index value of 1.5.

(A color version of this figure is available in the online journal.)

3.6. Optical, Near-infrared, and Radio Observations by GASP-WEBT

The GLAST-AGILE Support Program (GASP; Villata et al. 2008, 2009) is a project initially originating from the Whole Earth Blazar Telescope[59] (WEBT) in 2007. It is aimed to provide long-term monitoring in the optical (R band), near-IR, and mm–cm radio bands of 28 γ-ray-loud blazars during the lifetime of the *AGILE* and *Fermi* γ-ray satellites.

The observations of 3C 279 in the period considered in this paper were performed by the observatories listed in Table 2. The calibrated R-band magnitudes of the source were obtained through differential photometry with respect to the reference stars 1, 2, 3, and 5 by Raiteri et al. (1998). Near-IR data in the J, H, and K filters were acquired at Campo Imperatore and Roque de los Muchachos (Liverpool). When converting magnitudes into flux densities, optical, and near-IR data were corrected for Galactic reddening using $A_B = 0.123$ mag (Schlegel et al. 1998). We adapted the extinction laws by Cardelli et al. (1989), and the zero-mag fluxes by Bessell et al. (1998).

For the observations between 2008 August and 2010 August, the measured R-band magnitude ranged from 14.87 to 17.81 (673 data points). The R-band data have the best time coverage among the IR–optical–UV bands in our data thanks to the participation of a number of telescopes. The emission shows strong variability and the excess variance ($F_{\rm var}$; Equation (1)) of the source R-band flux (i.e., in linear scale) is 0.853 ± 0.001. The near-IR magnitudes in the J, H, and K bands were measured in ranges of m_J = 14.91–15.59 (20 data points), m_H = 12.04–14.90 (68 data points), and m_K = 11.19–13.45 (20 data

[58] http://heasarc.gsfc.nasa.gov/cgi-bin/W3Browse/swift.pl

[59] http://www.oato.inaf.it/blazars/webt

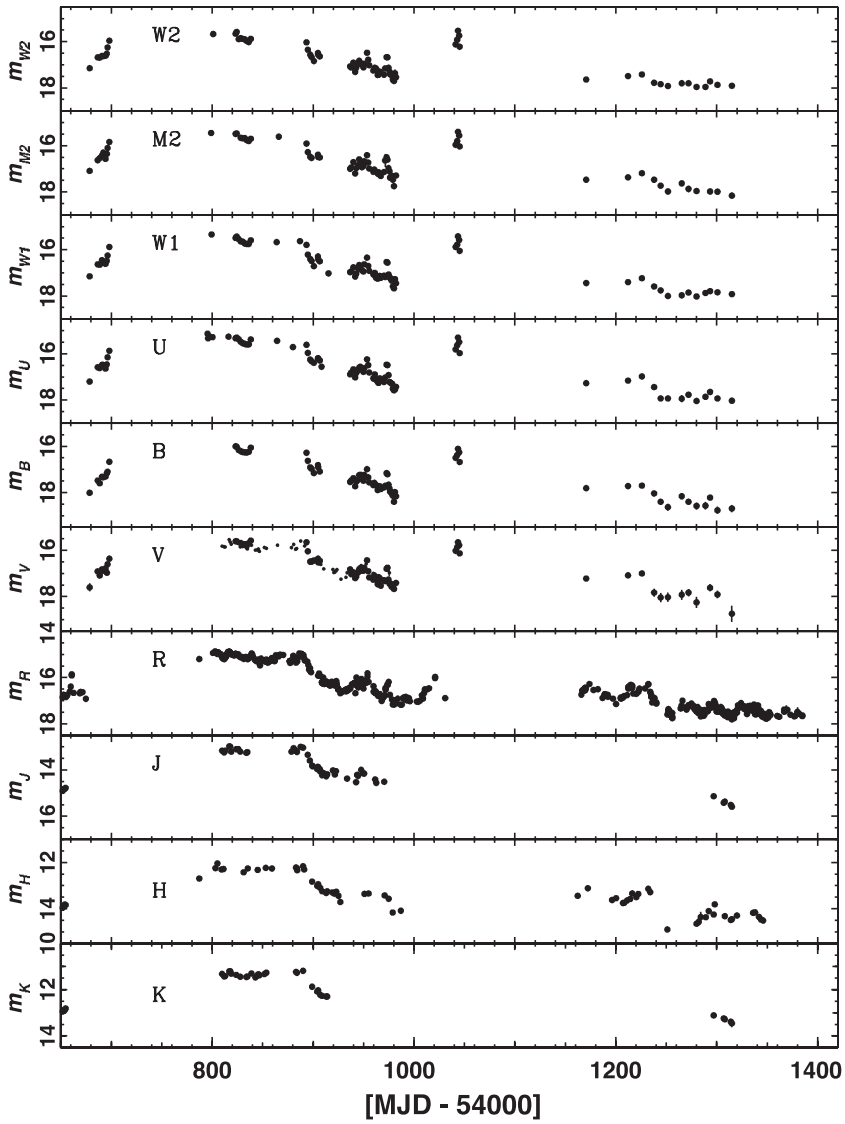

Figure 7. Light curves of all observed UV–optical–near-IR bands of 3C 279 in measured magnitude scale from 2008 August to 2010 August, including $W2$ (*Swift*-UVOT), $M2$ (*Swift*-UVOT), $W1$ (*Swift*-UVOT), U (*Swift*-UVOT), B (*Swift*-UVOT), V (Katana, *Swift*-UVOT), R (Abastumani, Calar Alto, ST-7, GRT, MDM, L'Ampolla, Perkins, SLT, KVA, LT, San Pedro, St. Petersburg, Tijarafe), J (AZT-24, Kanata), H (AZT-24, LT), and K (AZT-24, Kanata) bands.

points). Those data points are shown in Figure 7. The radio flux densities were measured in ranges of $F_{5\,\mathrm{GHz}} = 8.5$–$12.4$ Jy (109 data points), $F_{8\,\mathrm{GHz}} = 9.1$–$15.5$ Jy (124 data points), $F_{14.5\,\mathrm{GHz}} = 10.3$–$19.4$ Jy (118 data points), $F_{22\,\mathrm{GHz}} = 10$–$22$ Jy (16 data points), $F_{37\,\mathrm{GHz}} = 10$–$20$ Jy (168 data points), $F_{43\,\mathrm{GHz}} = 10$–$22$ Jy (20 data points), $F_{230\,\mathrm{GHz}} = 5.1$–$10.5$ Jy (62 data points), and $F_{345\,\mathrm{GHz}} = 6.0$–$6.8$ Jy (7 data points). The light curves of the radio flux densities in those bands are plotted in Figure 8.

3.7. Optical and Near-infrared: The Kanata Telescope

We performed the V-, J-, and Ks-band photometry and polarimetry of 3C 279 using TRISPEC installed to the 1.5 m Kanata telescope located in the Higashi–Hiroshima Observatory.

TRISPEC has a CCD and two InSb arrays, enabling photopolarimetric observations in an optical and two near-IR bands simultaneously (Watanabe et al. 2005). We obtained 64, 42 and 17 photometric measurements in the V, J, and Ks bands, respectively. A unit of the polarimetric observing sequence consisted of successive exposures at four position angles of a half-wave plates: $0°$, $45°$, $22.^{\circ}5$, $67.^{\circ}5$. The data were reduced according to the standard procedures of CCD photometry. We measured the magnitudes of objects with the aperture photometry technique. We performed differential photometry with a comparison star taken in the same frame of 3C 279. Its position is R.A. $= 12^{\mathrm{h}}56^{\mathrm{m}}16.^{\mathrm{s}}90$, decl. $= -05°50'43.''0$ (J2000) and its magnitudes are $V = 13.660$, $J = 12.377$, and $Ks = 11.974$ (Raiteri et al. 1998; Cutri et al. 2003). The photometric data have been corrected for the Galactic extinction with $A_V = 0.093$, $A_J = 0.026$, and $A_{Ks} = 0.010$. The measured optical and near-IR magnitudes by Kanata in the V, J, and Ks bands during the two year observations spanned $m_V = 15.54$–17.27 (56 data points), $m_J = 13.00$–14.58 (37 data points), and $m_{Ks} = 11.21$–11.47 (17 data points). Those data points are also shown in Figure 7.

We confirmed that the instrumental polarization was smaller than 0.1% in the V band using the observations of unpolarized standard stars. Hence, we did not apply any corrections for it. The zero point of the polarization angle is corrected as standard system (measured from north to east) by observing the polarized stars, HD19820 and HD25443 (Wolff et al. 1996). The polarization shows clear variability and the degree of

Table 2
List of Observatories that Contributed Data to the Campaign

Observatory	Detector/Telescope (diam.)	Band
	Gamma ray	
Fermi	LAT (survey mode)	>200 MeV
	X-ray	
Suzaku	XIS	0.5–10 keV
	HXD/PIN	15–50 keV
XMM-Newton	PN	0.5–10 keV
RXTE	PCA	3–10 keV
Swift	XRT	0.6–7 keV
	Ultraviolet, optical, infrared	
Swift	UVOT	$W2, M2, W1, U, B, V$
Spitzer	IRS	5–38 μm
	IRAC	3.6, 4.5, 5.8, 8.0 μm
	MIPS	24, 70, 160 μm
Abastumani, Georgia[a]	(70 cm)	R
Calar Alto[a,b]		R
Campo Imperatore, Italy[a]	AZT-24 (110 cm)	J, H, K
Crimean, Ukraine[a]	ST-7 (70 cm)	R
Goddard, USA[a]	GRT	R
Hiroshima, Japan	Kanata (150 cm)	V, J, Ks, polarization (V)
Kitt Peak, Arizona, USA[a]	MDM (130 cm)	R
La Silla, Chile	GROND (220 cm)	g, r, i, z, J, H, K
L'Ampolla[a]		R
Lowell (Perkins)[a]	Perkins	R
Lulin, Taiwan[a]	SLT (40 cm)	R
Roque, Canary Islands[a]	KVA (35 cm)	R, polarization (no filter)
Roque, Canary Islands[a]	LT (200 cm)	R, H
San Pedro Martir[a]	(84 cm)	R
St. Petersburg, Russia[a]	(40 cm)	R
Tijarafe[a]	(35 cm)	R
	Radio	
CARMA, USA	(array)	92.5, 227.5 GHz
Mauna Kea, USA[a]	SMA (8 × 6 m)	230, 345 GHz
Medicina, Italy[a]	(32 m)	5, 8, 22 GHz
Metsahovi, Finland[a]	(14 m)	37 GHz
Noto, Italy[a]	(32 m)	43 GHz
Owens Valley, USA	OVRO (40 m)	15 GHz
UMRAO, USA[a]	(26 m)	5, 8, 14.5 GHz

Notes.
[a] GASP-WEBT.
[b] Calar Alto data were acquired as part of the MAPCAT project: http://www.iaa.es/~iagudo/research/MAPCAT.

polarization was measured in the range of 3%–36% during our two year observational campaign. As we reported in Paper I, we found a rotation of the polarization angle by 208° together with a sharp drop of the degree of polarization from ~30% down to a few %. The event was coincident with a γ-ray flare (Periods D and E). In the second half of the two year observations, the source was generally in a quiet state in the optical band, and the degree of polarization was also relatively low.

3.8. Optical and Near-infrared: GROND

The Gamma-Ray burst Optical/Near-infrared Detector (GROND; Greiner et al. 2008) mounted at the MPI/ESO 2.2 m telescope at LaSilla observatory in Chile observed the field of 3C 279 in two nights of 2008 July (2008 July 30 and 2008 July 31) and four nights in 2009 January (2009 January 19 to 2009 January 22). In each observation, a total of 4 images in each $g'r'i'z'$ filter with integrations times of 35 s and 24 images of 10 s exposure in each JHK_s were obtained simultaneously.

GROND optical and near-IR data were reduced in standard manner using pyraf/IRAF (Tody 1993) similar to the procedure outlined in Krühler et al. (2008). The stacked images of each observation were flux calibrated against GROND observations of SDSS fields (Abazajian et al. 2009) taken immediately before or after the field of 3C 279 for the optical $g'r'i'z'$, and magnitudes of 2MASS field stars (Skrutskie et al. 2006) for the JHK_s filters. All data were corrected for the expected Galactic foreground reddening of $E_{(B-V)} = 0.029$ according to Schlegel et al. (1998). Results of GROND observations are summarized in Table 4.

Table 3
Results of GROND Observations

Filter	2008 Jul 31		2009 Jan 19–22		
	AB Magnitude	Flux (mJy)	AB Magnitude	Flux (mJy)	$A/A(V)$[a]
g'	17.62 ± 0.05	0.324 ± 0.015	16.06 ± 0.05	1.37 ± 0.06	1.23
r'	17.24 ± 0.05	0.462 ± 0.021	15.49 ± 0.05	2.31 ± 0.11	0.80
i'	16.83 ± 0.05	0.671 ± 0.031	15.05 ± 0.05	3.47 ± 0.16	0.62
z'	16.67 ± 0.05	0.776 ± 0.036	14.80 ± 0.05	4.37 ± 0.20	0.45
J	16.05 ± 0.06	1.387 ± 0.077	14.16 ± 0.06	7.86 ± 0.44	0.29
H	15.60 ± 0.07	2.098 ± 0.133	13.62 ± 0.07	12.90 ± 0.81	0.18
K	15.18 ± 0.09	3.062 ± 0.249	13.19 ± 0.09	19.18 ± 1.56	0.14

Notes. Results of both AB magnitude and flux are corrected for Galactic extinction. No significant daily variability was observed during the observations in 2009 January.
[a] Dereddening factors for correction of Galactic extinction.

Table 4
Spitzer Observation Log

Instrument	Start Time (UTC)	(MJD)	Duration (minute)	ObsID
MIPS	2008.7.31 11:09:06.3	54678.4647	9.19	27434240
	2009.2.15 07:08:08.6	54877.2973	14.61	27438592
	2009.2.16 23:12:32.0	54878.9670	14.61	27438080
	2009.2.17 20:42:36.5	54879.8629	14.61	27438848
	2009.2.18 19:39:30.8	54880.8191	14.60	27438336
	2009.2.19 14:19:04.4	54881.5966	14.60	27439360
	2009.2.20 09:23:37.4	54882.3914	14.60	27439104
IRS	2008.8.16 14:32:42.6	54694.6060	17.92	27425024
	2009.3.3 12:22:35.7	54893.5157	18.15	27435776
	2009.3.4 19:53:03.5	54894.8285	18.15	27437312
	2009.3.6 10:50:02.7	54896.4514	18.16	27436544
	2009.3.7 00:46:03.4	54897.0320	18.16	27435520
	2009.3.8 12:08:53.5	54898.5062	18.18	27437056
	2009.3.9 18:39:51.2	54899.7777	18.18	27436288
IRAC	2008.8.17 06:57:26.3	54695.2899	10.64	27429632
	2009.3.10 19:26:05.5	54900.8097	10.69	27433216
	2009.3.11 22:05:54.7	54901.9208	10.70	27432448
	2009.3.13 05:13:56.9	54903.2180	10.71	27433728
	2009.3.14 04:12:41.8	54904.1755	10.72	27432960
	2009.3.15 03:04:16.9	54905.1280	10.73	27433984
	2009.3.16 14:58:46.6	54906.6241	10.75	27433472

3.9. Infrared: Spitzer

We observed 3C 279 with *Spitzer* Infrared Spectrograph (IRS), Multiband Imaging Photometer for *Spitzer* (MIPS), and Infrared Array Camera (IRAC) at several epochs in 2008 and 2009 under the *Spitzer* program PID50231 (PI: A. Wehrle; see Table 3). The observations were conducted once with each instrument in 2008 July and August and approximately daily

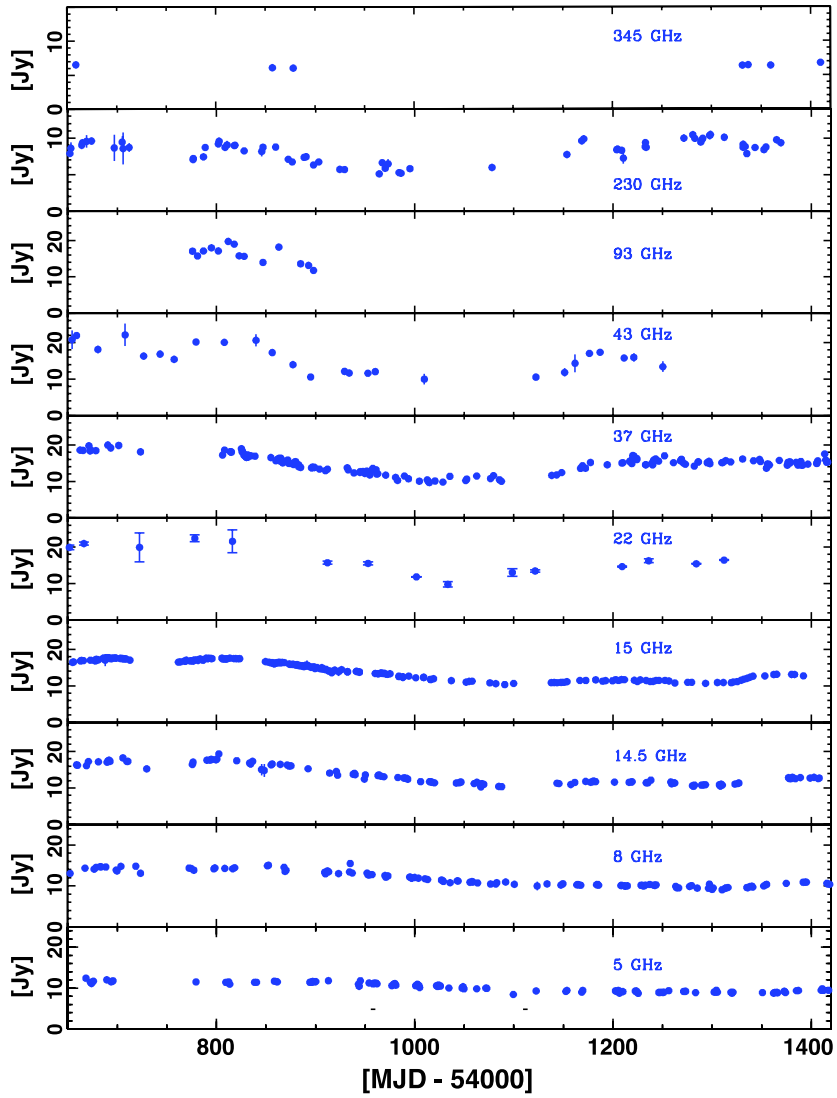

Figure 8. Radio light curves of 3C 279 from 2008 August to 2010 August measured at all observed radio frequencies: 345 GHz (SMA), 230 GHz (CARMA, SMA), 93 GHz (CARMA), 43 GHz (Noto), 37 GHz (Metsahovi), 22 GHz (Medicina), 15 GHz (OVRO), 14.5 GHz (UMRAO), 8 GHz (Medicina, UMRAO), and 5 GHz (Medicina, UMRAO).

(A color version of this figure is available in the online journal.)

during the instrument campaigns in the 2009 February–March visibility window.

For the IRS observations, high-accuracy blue peakup observations on a nearby star were used to center the spectrograph slit on the target. 3C 279 was observed with the low-resolution SL2, SL1, LL2, and LL1 modules, for three cycles of 14 s at each of two nod positions. *Spitzer*-IRS data reductions began with S18.7 *Spitzer* Science Center pipeline-processed, background-subtracted data. The background was removed by subtracting the alternate nod for each pointing. Additional processing steps were applied to clean bad data, remove fringes, and match and trim spectral orders. First, we cleaned bad, rogue pixels using the *Spitzer* Science Center procedure IRSCLEAN V2.0. One-dimensional spectra were then extracted using the standard point-source aperture and flux calibration in SPICE ver. 2.3. We used a custom spectral defringing tool to remove fringes introduced by the pointing-dependent instrumental flat field. This tool uses a predetermined flat-field fringing correction function, which is shifted to match and remove the observed fringes in the spectrum. Spectral orders were trimmed, and the SL2 and SL1 orders were scaled up by a factor of 1.06 to empirically correct for pointing-dependent point-source slit losses. Finally, the nod-spectra were averaged and combined into a single spectrum covering 5.2–35 μm rest wavelength. Figure 9 shows the reduced IRS spectra in the νF_ν representation.

We used the pipeline MIPS images (ver. 18) for aperture photometry using 13″, 35″, and 50″ radius for 24, 70, and 160 μm bands, respectively, with aperture corrections from Tables 3.13, 3.14, and 3.16 of the MIPS Data Handbook (ver. 3.2). No 160 μm data were obtained in 2008 August because the array was not cooled during that campaign. 3C 279 has very low ecliptic latitude (0.°2), hence the observed transients can be attributed to passing asteroids which appeared in various MIPS images. We used 6″ radius apertures for IRAC photometry on the pipeline data (ver. 18) with aperture corrections tabulated in Table 5.7 of the IRAC Data Handbook (ver. 3.0).

The *Spitzer*-MIPS photometric repeatability and absolute calibration uncertainties at 24 μm are, respectively, 0.4% and 4%; at 70 μm, 4.5% and 5%; and at 160 μm, 5% and 12% (Engelbracht et al. 2007; Gordon et al. 2007; Stansberry et al. 2007). We therefore adopt overall uncertainties of 10%, 10%, and 20% at 24, 70, and 160 μm, respectively. No color correction

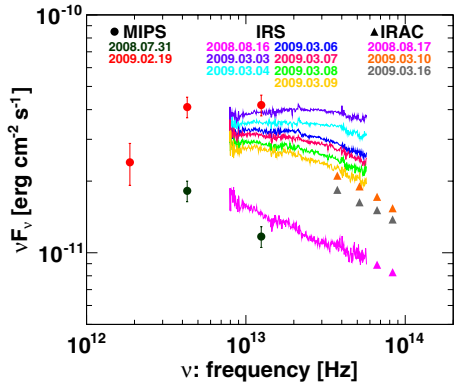

Figure 9. Spectral energy distribution of 3C 279 in the infrared band measured by *Spitzer*-IRS. IRS spectra from highest to lowest are on 2009 March 3, 2009 March 4, 2009 March 5, 2009 March 6, 2009 March 7, 2009 March 9, and 2008 August 16. Representative flux data points measured by *Spitzer*-MIPS (circles) and *Spitzer*-IRAC (triangles) are also included.

(A color version of this figure is available in the online journal.)

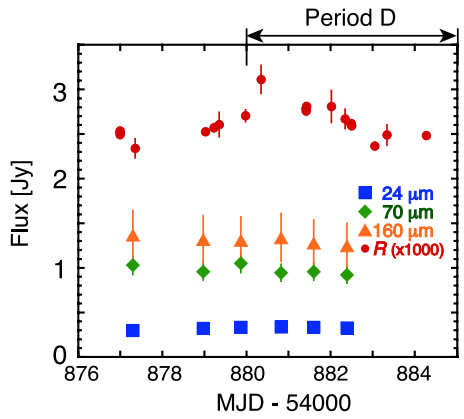

Figure 10. Light curve of 3C 279 at 24 μm, 70 μm, and 160 μm measured by *Spitzer*-MIPS. The error bars correspond to 10%, 10%, and 20%, respectively, for each band as mentioned in the text in Section 3.9. Optical *R*-band data taken by the ground-based telescopes are also plotted in red color for comparison.

(A color version of this figure is available in the online journal.)

has been applied to the data because the slope and smoothness of the spectrum over the bandpasses are not known. Figure 10 describes the MIPS flux history during the six epochs from 2009 February 15 to 20 together with *R*-band flux for comparison. No significant flux variation is found in all MIPS bands during those epochs, which include period D.

The *Spitzer*-IRAC calibration uncertainty is 3% overall and has photometric repeatability of 1.5% (Reach et al. 2005). We adopt the overall IRAC calibration uncertainty of 3%, but note the following characteristics of our images. In our IRAC frames, two standard comparison stars used in blazar monitoring were visible in the 3.6 μm images (Star 1 and Star 2).[60] One comparison star, Star 2, was visible in the 4.5, 5.8, and 8 μm images, located at the interstice of the chopping regions where the data are noisier than elsewhere. The spacecraft orientation, and hence the chopping orientation, was 180° different between 2008 July–August and 2009 March. The standard deviations in comparison Star 2's measurements in 2009 March at 3.6, 4.5, 5.8, and 8 μm are 0.68 mJy, 0.08 mJy, 0.08 mJy, and 0.09 mJy (5%, 1%, 2%, and 3%), respectively. The high 3.6 μm standard deviation was affected by a single high value on 2009 March 11, for which we found no obvious cause; excluding that value resulted in a standard deviation of 0.06 mJy (0.5%). In contrast, the flux of 3C 279 shows a steady decrease of 10%, 12%, 14%, and 13% at 3.6, 4.5, 5.8, and 8.0 μm, respectively, during the six epochs from 2009 March 10–16 as shown in Figure 11.

[60] See http://www.lsw.uni-heidelberg.de/projects/extragalactic/charts/1253-055.html (Raiteri et al. 1998; Villata et al. 1997).

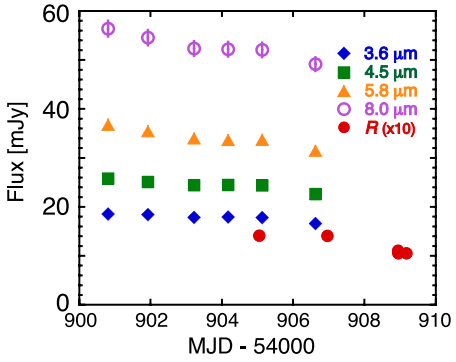

Figure 11. Light curve of 3C 279 at 3.6 μm, 4.5 μm, 5.8 μm, and 8.0 μm measured by *Spitzer*-IRAC. The error bars correspond to 3% for all IRAC bands as mentioned in the text in Section 3.9. Optical *R*-band data taken by the ground-based telescopes are also plotted in red color for comparison.

(A color version of this figure is available in the online journal.)

3.10. Radio: CARMA

Observations were obtained at mean frequencies of 92.5 and 227.5 GHz using the Combined Array for Research in Millimeter-wave Astronomy (CARMA; Bock et al. 2006). In all cases, the nominal signal to noise ratio exceeded 400 and calibration uncertainties dominated the errors. The source is bright enough to permit self-calibration on timescales of less than a minute and so atmospheric decorrelation was not expected to affect our results significantly even at the long baselines. However, observations in poor weather were not used due to the difficulty of reliably measuring pointing offsets in these conditions.

Data calibration and analysis was done with the MIRIAD software package (Sault et al. 1995). Flux densities were determined by first using phase self calibration with a short enough averaging interval to avoid any atmospheric phase decorrelation, then the flux density was determined from the vector average fringe amplitude at the position of 3C 279 over all baselines. For a strong point source such as 3C 279 this provides very robust and unbiased amplitude estimate independent of the weather or the interferometer baselines. We rely on regular system temperature measurements to provide flux calibration relative to the fixed system sensitivity. The absolute flux calibration of CARMA observations is usually quoted as 10%–15%. However, based on measurements made on the blazar 3C 454.3 we estimated the relative flux calibration at each frequency to be within 5% at 3 mm and 10% at 1 mm. The radio fluxes at 92.5 and 227.5 GHz measured by CARMA correspond to $F_{92.5\,\mathrm{GHz}} = 11.7$–$19.7$ Jy (14 data points) and $F_{227.5\,\mathrm{GHz}} = 6.3$–$9.2$ Jy (14 data points). Figure 8 includes the flux history of those radio data.

3.11. Radio: OVRO 40 m

The Owens Valley Radio Observatory (OVRO) 40 m radio data were collected as part of an ongoing long-term, fast-cadence γ-ray blazar monitoring campaign, described in detail in Richards et al. (2011). Flux densities were measured in a 3 GHz bandwidth centered on 15.0 GHz using dual, off-axis 2.′5 FWHM beams with 12.′95 separation. Dicke switching against a blank sky reference field to remove gain fluctuations

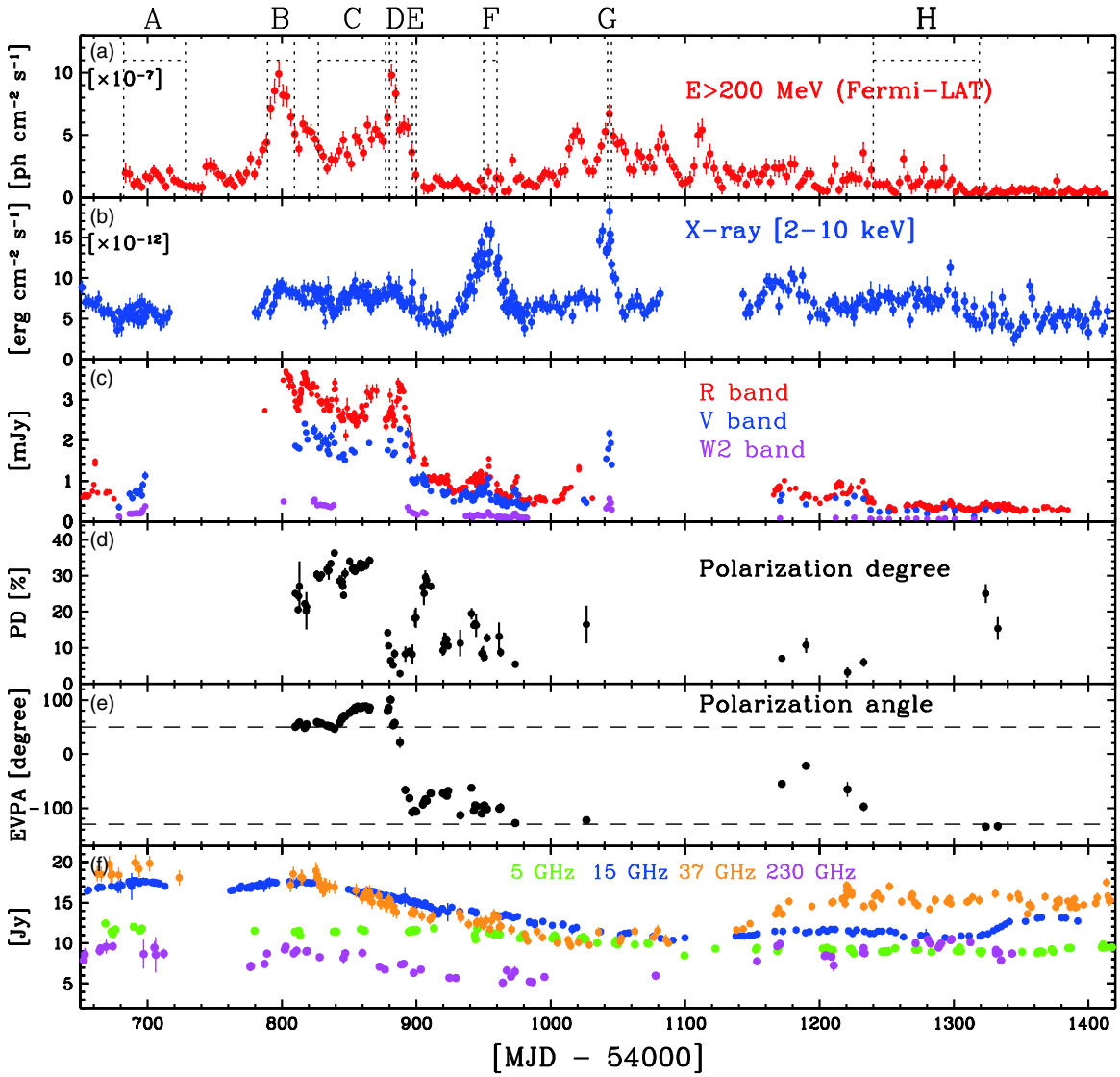

Figure 12. Multi-band light curves of 3C 279 for two years from 2008 August to 2010 August. (a) Gamma-ray flux above 200 MeV averaged over three days. (b) X-ray flux between 2 and 10 keV measured by *Swift*-XRT and *RXTE*-PCA. (c) UV–optical fluxes in *R* band (red), *V* band (blue), and *W*2 band (magenta). (d) Polarization degree in the optical band. (e) Polarization angle in the optical band. The horizontal dashed lines refer to the angle of 50° and −130°. (e) Radio fluxes in 230 GHz band (magenta), 37 GHz band (orange), 15 GHz band (blue), and 5 GHz band (green). All X-ray, UV, and optical data are corrected for the Galactic absorption.
(A color version of this figure is available in the online journal.)

and atmospheric and ground contamination were used. Flux densities from this program are found to have a minimum uncertainty of 4 mJy (mostly thermal) and a typical uncertainty of 3% for brighter sources. During the period included here, 3C 279 was observed as a pointing calibrator. The flux density scale was referred to the value for 3C 286 (3.44 Jy at 15 GHz; Baars et al. 1977) with a scale uncertainty of about 5%. The radio flux at 15 GHz measured by OVRO was ranging from 11.1 to 18.0 Jy among 124 data points during the two year observations. The light curve of the OVRO radio data is also plotted in Figure 8.

4. RESULTS OF THE MULTI-WAVELENGTH OBSERVATIONS

4.1. Correlations of Light Curves in Various Bands

The multi-band light curves of 3C 279 are presented in Figure 12. They include (a) γ-ray flux above 200 MeV (*Fermi*-LAT), (b) 2–10 keV X-ray flux measured by *Swift*-XRT and *RXTE*-PCA, (c) optical-UV fluxes in *R* band (GASP), *V* band (*Swift*-UVOT and Kanata), and *W*2 band (*Swift*-UVOT), (d,e) degree and angle of optical polarization (Kanata and KVA), and (f) radio fluxes in the 230, 37, 15, and 5 GHz bands (GASP, CARMA, and OVRO). We note that the X-ray fluxes determined by *Suzaku* and *XMM-Newton* are entirely consistent with those plotted in Figure 12. The extensive data set obtained in many bands for 3C 279 allows us to make general statements regarding the relative flux variability in various spectral bands, and the relationship of the time series to each other. The first such feature of the multi-band light curves is a general—although not exact—trend where the IR through optical emission seems to be correlated with the γ-ray flux. We calculated the discrete correlation function (DCF; Edelson & Krolik 1988) to quantify the correlation of the flux variations between the γ-ray and other bands, and to determine whether we can measure any clear lag between the bands.

For the DCF calculations, we use the γ-ray fluxes averaged over an interval of 1 day as shown in the top panel of Figure 1.

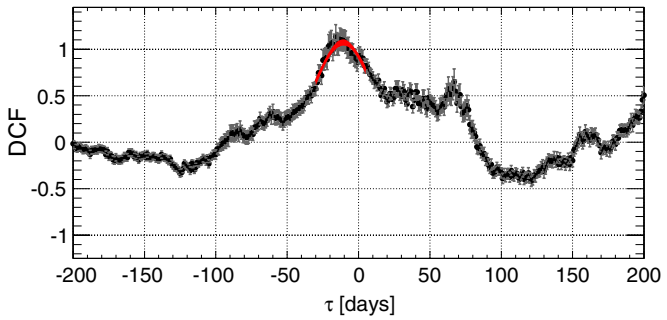

Figure 13. Discrete correlation function (DCF) derived for the γ-ray and optical R bands. Positive values of "τ" correspond to flux variations in the γ-ray band lagging flux variation in the optical band. The red curve represents a Gaussian fit to the data between -30 and 5 days. See the text for the fitting results.

(A color version of this figure is available in the online journal.)

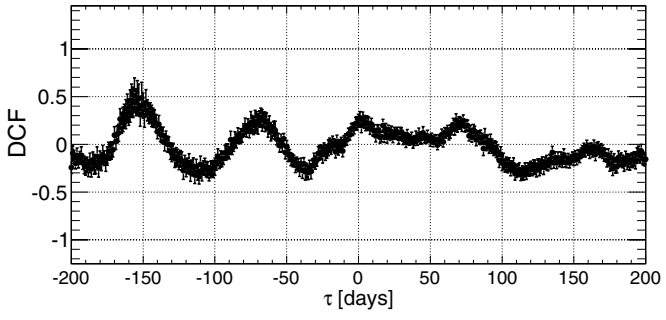

Figure 14. DCF between derived for the γ-ray and X-ray bands. Positive values of "τ" correspond to flux variations in the γ-ray band lagging flux variation in the X-ray band.

The resulting DCF between γ-ray and optical R-band fluxes is shown in Figure 13. Positive values of "τ" correspond to flux variations in the γ-ray band lagging flux variations in the other bands. In the DCF between γ-ray and optical R-band fluxes, a peak can be seen close to zero lag. We fit the DCF data points in the range between -30 and 5 days using a Gaussian function of the form $\mathrm{DCF}(\tau) = C_{\max} \times \exp[(\tau - \tau_0)^2/\sigma^2]$, where $C_{\max}$ is the peak value of the DCF, τ_0 is the time at which the DCF peaks, and σ is the Gaussian width of the DCF. The fit yields a position of the peak at $\tau_0 = -10.7 \pm 0.7$ days, corresponding to a value of $C_{\max} = 1.07 \pm 0.03$ with a dispersion of $\sigma = 19.4 \pm 1.4$ days. The result implies that the optical emission is possibly delayed with respect to the γ-ray emission by about 10 days.

In the framework of the one-zone synchrotron + external-radiation Compton (ERC) models, the same electron population, of roughly the same energies, is responsible for the radiation in both the optical and γ-ray bands. There, the observed lag can result from different profiles of the decreasing magnetic and radiation energy densities along the jet: we show that idea quantitatively in the Appendix. As is shown there, a very steep drop of the external radiation energy density is required to explain the lag in a conical jet with magnetic field $B' \propto 1/r$, where r is the distance along the jet. This condition can be relaxed in the scenario involving the re-confinement of a jet (e.g., Daly & Marscher 1988; Komissarov & Falle 1997; Nalewajko & Sikora 2009). In such a case, the magnetic field intensity can drop more slowly than $1/r$. If the lag of the optical emission is confirmed, the application of the results in the Appendix to the $\sim$10 day lag may imply the location of the active "blazar zone" at distances of a few pc in agreement with those postulated to explain the optical polarization swing (Periods D and E) in terms of a region containing an enhanced density of ultra-relativistic electrons propagating along a curved trajectory (Paper I). It is worth noting that similar γ-ray/optical lags have been reported during the outbursts of 3C 279 in early 1999 Hartman et al. (2001b), of PKS 1502+106 in 2008 (Abdo et al. 2010d), of PKS 1510−089 in early 2009 (Abdo et al. 2010a; D'Ammando et al. 2011), and of AO 0235+164 in late 2008 (Agudo et al. 2011b; Ackermann et al. 2012). On the other hand, no significant lags between γ-ray and optical signals have been detected in 3C 454.3 in late 2008 (Bonning et al. 2009; Jorstad et al. 2010), in 3C 66A in 2008 October (Abdo et al. 2011), and in OJ 287 in 2009 October (Agudo et al. 2011a). Based on investigations of long-term light curves of 3C 454.3 during 2008–2010, Raiteri et al. (2011) have shown that the optical and γ-ray flux variations are not always simultaneous and have proposed a geometrical scenario to explain the change in the γ/optical flux ratio during the outburst peaks in 3C 454.3. It is expected that the on-going multi-band monitoring of blazars will enable us to quantify such lags and find out how common they are.

Different behavior is apparent in the radio flux, where the energies of radio-emitting electrons are very different from the energies of the electrons involved in producing the observed optical and γ-ray emission. Variability appears to be much less rapid, and the excess variance (F_{var}; see definition in Equation (1)) in the radio regime is quite modest; for instance, 0.145 ± 0.004 at 37 GHz, 0.165 ± 0.001 at 15 GHz, and 0.104 ± 0.001 at 5 GHz. Those values are significantly less than ones in the γ-ray or optical bands. This suggests that the synchrotron emission from the γ-ray emitting region is self-absorbed at these wavelengths. The observed radiation is produced at much larger distances, where the light-travel effects smear out the sharp, rapid variability patterns observed in the optical and γ-ray bands.

Perhaps the most surprising behavior—and difficult to explain in the context of simple, one-component, single-zone models—is the relationship of the X-ray light curve to those in the IR–optical or γ-ray bands. In Paper I, we reported that the X-ray time series exhibits a relatively rapid, symmetrical flare at $\sim$ MJD 54950 (Period F) with a duration of $\sim$20 days, which is *not* accompanied with any prominent IR/optical or γ-ray flares. As we argued in Paper I, the hard (rising in νF_ν representation) X-ray spectrum is unlikely to be the "tail" of the synchrotron emission, but instead, it is more likely to be produced by the low-energy end of the electron distribution radiating via inverse-Compton process.

The continuing monitoring of the object in the X-ray band revealed another X-ray flare at $\sim$MJD 55040 (Period G), $\sim$90 days after the first X-ray flare. The separation of the two X-ray flares is remarkably close to the temporal separation of the two γ-ray flares, with the two pairs delayed with respect to each other by $\sim$155 days. Figure 14 presents the calculated DCF between γ-ray and X-ray fluxes, which shows a modest peak at ~ -155 days with a correlation coefficient of 0.6–0.7 and indicates no correlation between the γ-ray and the X-ray bands with zero lag. While confirming the physical connection of the two pairs would be very important, we cannot currently envision any situation where the two would be causally connected; the 155 day lag would imply the distance of the X-ray flare production $\sim 155\Gamma_{\mathrm{j}}^2$ lt-day $\sim 50(\Gamma_{\mathrm{j}}/20)^2$ pc and at such a distance should be accompanied by radio flares, which are not seen in our data. In such a scenario, the X-ray flares should be significantly broadened compared to the γ-ray flares; however, we observe a similar temporal structure in both bands.

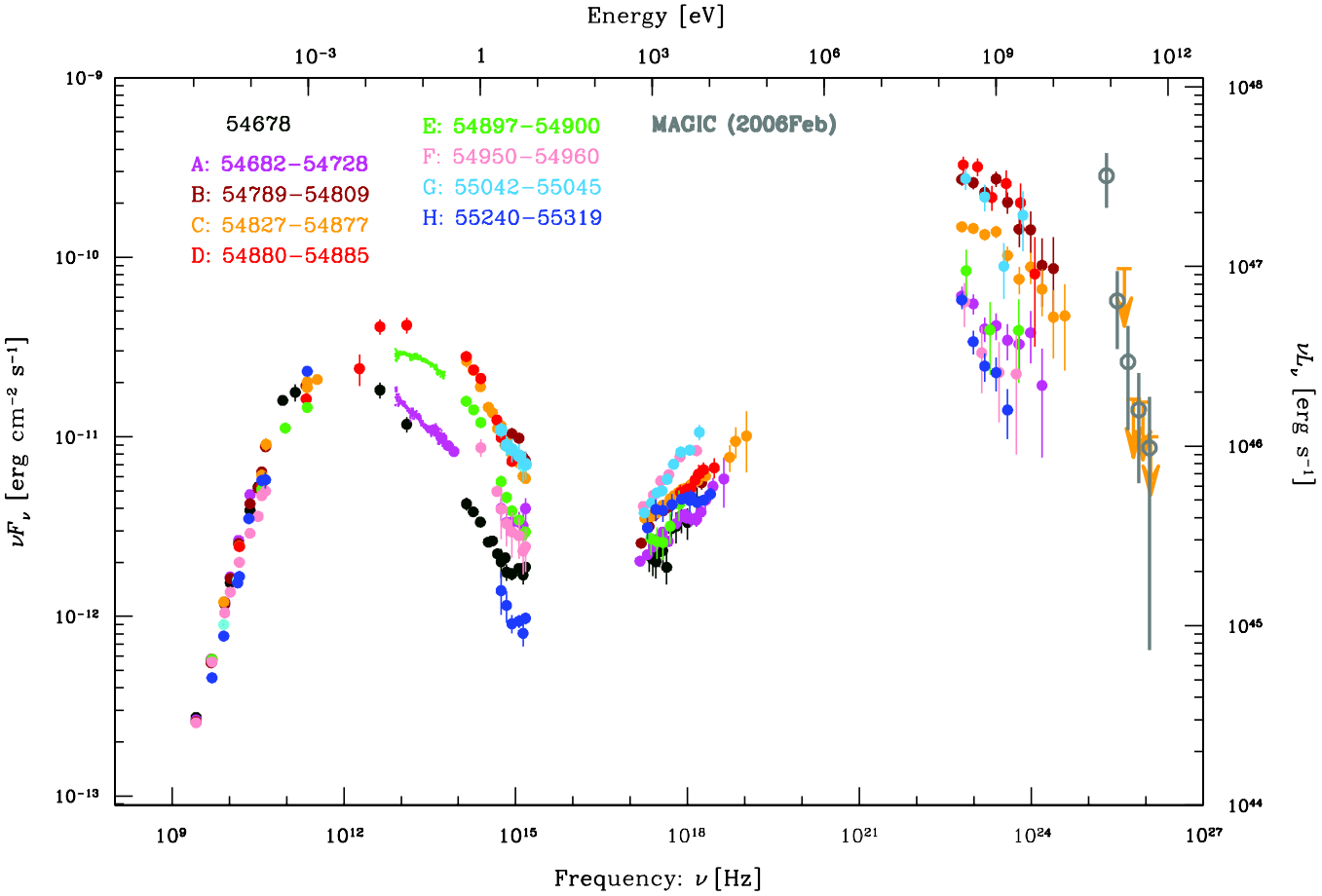

Figure 15. Time-resolved broadband spectral energy distributions of 3C 279 measured in Periods A–H (as defined in Table 1) and on 2008 July 31 (MJD 54678), covered by our observational campaigns in 2008–2010. X-ray, UV–optical–near-IR data are corrected for the Galactic absorption. Five-digit numbers in the panel indicate MJD of the periods. For comparison, the gray open circles in the very high energy γ-ray band represent measured spectral points by MAGIC in 2006 February (Albert et al. 2008).

Furthermore, we note that there are some optical and γ-ray peaks that might well be associated with the second X-ray flare. Hence, it is possible that the two prominent γ-ray/optical flares (Periods B and D), together with the subsequent two X-ray flares (Periods F and G), form a sequence of four events separated by a similar time intervals. Those intervals, in turn, can be possibly determined by instabilities in the jet launching region. Here, the different broadband spectra during these events may result from small changes of parameters, such as the jet direction, Lorentz factor, and/or location and geometry of the dissipation event.

A weak (and sporadically almost absent) correlation between X-rays and other spectral bands can also result from such processes that preferably contribute to radiation in the X-ray band. They can be related to the following three mechanisms/scenarios.

1. *Bulk-Compton process*. This involves Compton-scattering of ambient optical/UV light by the *cold* (non-relativistic) electrons in the jet. This mechanism is most efficient close to the accreting black hole where the processes responsible for the variability of X-rays may operate independently of those at larger distances and producing there variable non-thermal radiation (Begelman & Sikora 1987). A drawback of this scenario can be that the bulk-Compton spectrum is predicted to have a similar shape as the spectrum of the external radiation field (Ackermann et al. 2012), which significantly differs from what we observe in the X-ray band.
2. *Inefficient electron acceleration*. Acceleration of the relativistic electrons at proton-mediated shocks is likely to proceed in two steps: in the first one low-energy electrons may be pre-accelerated via, for example, some collective processes involving protons; in the second step, they may participate in the first-order Fermi acceleration process. If under some conditions the electron–proton coupling is inefficient, the fraction of electrons reaching the Fermi phase of acceleration will be small. In this case the X-rays, originating from lower energy electrons, are produced efficiently, while the γ-rays and optical radiation that involve more relativistic electrons are not.
3. The X-rays can be also contributed by hadronic processes, specifically by the pair cascades powered by protons losing their energy in the photo-mesonic process (Mannheim & Biermann 1992). For this process to be efficient, it requires extreme conditions (Sikora et al. 2009; Sikora 2011); however, operating in the very compact central region, at distances less than few hundred gravitational radii, it may occasionally dominate in the X-ray band.

4.2. Broadband Spectral Energy Distribution

Figures 15 and 16 show broadband SEDs of 3C 279 in all periods as defined in Table 1. In addition, we also extracted an SED using data taken on 2008 July 31 (MJD 54678), which has a good energy coverage of the synchrotron emission component

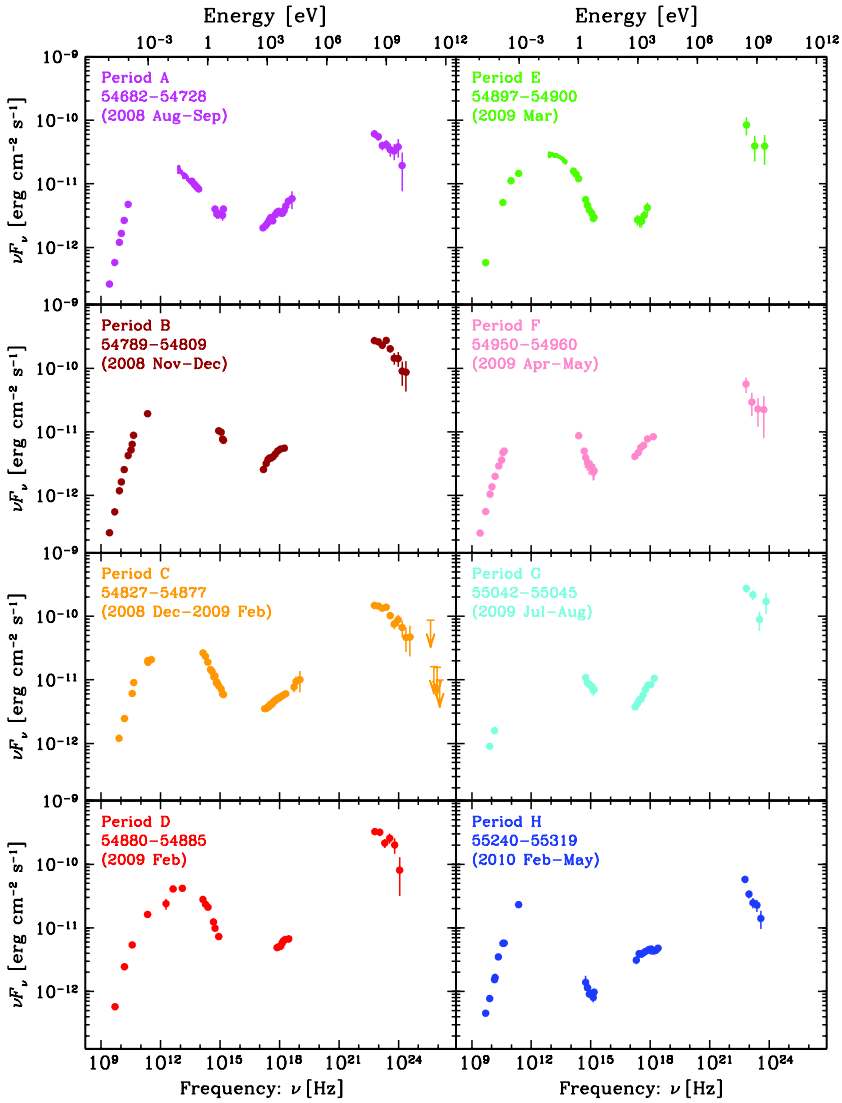

Figure 16. Time-resolved broadband spectral energy distributions of 3C 279 in each period (A–H), covered by the campaigns. The data points are the same as ones in Figure 15, but are plotted in a separate panel for each period. Five-digit numbers in each panel indicate MJD of the observing period of each broadband spectrum.
(A color version of this figure is available in the online journal.)

including *Spitzer* and GROND data, although the γ-ray data by *Fermi*-LAT are not available at that time because this was before the beginning of normal, all-sky science observations with *Fermi*-LAT. Both SEDs for Period D (2009 February; corresponding to the brightest γ-ray flare coincident with the optical polarization swing) and Period F (2009 April; corresponding to the first isolated X-ray flare) have already been partially reported in Figure 2 of Paper I. New *Spitzer*-MIPS data points are included in the SED for Period D in this paper. In Period C, there are observations by MAGIC, which provide upper limits above 100 GeV (Aleksić et al. 2011). For comparison, we also include VHE γ-ray fluxes detected with the MAGIC telescope in 2006 February as gray points (Albert et al. 2008) in Figure 15.

This is the richest set of time-resolved spectra ever collected for this source. The spectral coverage of the synchrotron bump is unprecedented, allowing us not only to constrain the parameters of the emission models, but also to study their time evolution. As we discussed in Section 2.4, the shape of the γ-ray spectrum deviates from a simple power law, in similarity to other FSRQ blazars. Strong variability, over one order of magnitude, is evident in near-IR/optical/UV and γ-ray bands. This contrasts with the moderate variability in the radio/mm and X-ray bands.

Particularly interesting is the behavior of this source in the mid-IR band, around $\sim 10^{13}$ Hz, where significant spectral variability is observed. In the low state in Period A, the mid-IR spectrum is relatively soft and can be extended with a power-law shape to the optical/UV band. In this case, the synchrotron component peaks in the mm/sub-mm band ($\sim 10^{11}$–10^{12} Hz). However, in the high state in Periods D and E, the mid-IR spectrum is much harder and shows a significant curvature. In Period D, there is a clear spectral break at $\sim 3 \times 10^{12}$ Hz ($\sim 100\,\mu$m). The spectral index between the 70 μm ($\sim 4.3 \times 10^{12}$ Hz) and 160 μm ($\sim 1.9 \times 10^{12}$ Hz) points is $\alpha_{70-160} = 0.35 \pm 0.23$, taking into account systematic errors described in Section 3.9. The synchrotron peak is located in the mid-IR band, at a frequency one order of magnitude higher than in the low state. This indicates that there are two independent synchrotron bumps, possibly produced at different locations. The mid-IR-peaking component, seen only in the IR/optical/UV flaring state, is characterized by a strong and rapid variability. The mm/sub-mm peaking component is more

persistent and dominates when the source is in the low state. The complex shape of the SED between the mm band and the 70 μm point in Period D requires a coexistence of these two components. A similar scenario of multiple synchrotron components was investigated in the case of 3C 454.3 by Ogle et al. (2011).

In the X-ray band, despite the smaller variability amplitude, we observe some spectral changes. In particular, in Periods F and G, which represent the two isolated X-ray flares, the spectrum is very similar and harder than on average. Figure 15 shows that these flares are not energetically important. If we extrapolate the X-ray spectra with power laws to the γ-ray band, we underpredict the observed γ-ray flux in Periods B, C, D, and H. Periods B, C, and D coincide with the high-activity γ-ray state. This indicates that the X-ray flux cannot originate from the same emission component as the γ-ray flux, at least in the flaring state. Because the γ-rays are correlated with the optical flux but not with the X-ray flux, the γ-rays can be related to the mid-IR-peaking synchrotron bump while the X-rays may correspond to the mm/sub-mm peaking synchrotron bump. We explore this possibility when modeling the SEDs at Periods A and D in Section 5.2.

5. MODELING THE BROADBAND EMISSION

We have fitted selected SEDs with one-zone leptonic models described in Moderski et al. (2003), including synchrotron emission and self-absorption, Comptonization of the local synchrotron radiation (SSC component) and external photons (ERC component), but also including the opacity due to internal pair-production. The external radiation includes broad emission lines (BEL) and infrared dust emission (IR). Their energy densities in the jet comoving frame as functions of the distance r along the jet are approximated by the formulae:

$$u'_{\rm BEL}(r) = \frac{\xi_{\rm BEL}\Gamma_{\rm j}^2 L_{\rm D}}{3\pi r_{\rm BEL}^2 c[1+(r/r_{\rm BEL})^{\beta_{\rm BEL}}]} \quad (2)$$

$$u'_{\rm IR}(r) = \frac{\xi_{\rm IR}\Gamma_{\rm j}^2 L_{\rm D}}{3\pi r_{\rm IR}^2 c[1+(r/r_{\rm IR})^{\beta_{\rm IR}}]}, \quad (3)$$

where $\xi_{\rm BEL} = 0.1$ and $\xi_{\rm IR} = 0.1$ are the fractions of the disk luminosity $L_{\rm D} \simeq 2\times10^{45}$ erg s^{-1} reprocessed into emission lines and into hot dust radiation, respectively, $r_{\rm BEL} = 0.1(L_{D,46})^{1/2}$ pc and $r_{\rm IR} = 2.5(L_{\rm D,46})^{1/2}$ pc [$L_{\rm D,46} \equiv L_{\rm D}/10^{46}$] are the characteristic distances where such reprocessing takes place, and $\Gamma_{\rm j}$ is the jet Lorentz factor. The external radiation fields are approximated in the jet comoving frame by Maxwellian spectra peaked at photon energies $E'_{\rm BEL} \sim 10$ eV $\times\,\Gamma_{\rm j}$ and $E'_{\rm IR} \sim 0.3$ eV $\times\,\Gamma_{\rm j}$. While the radiation density profile in the frame external to the jet should satisfy $\beta_{\rm BEL(IR)} \leqslant 2$, it is not applied to the profile in the jet comoving frame. This is because the transformation of radiation density depends on the angular distribution of external radiation, with radiation arriving at small incidence angles to the jet velocity vector being actually deboosted. This can result in a steeper profile of the radiation density in the jet comoving frame. Here, we adopt $\beta_{\rm BEL} = 3$ (Sikora et al. 2009) and $\beta_{\rm IR} = 4$ (see Section 5.1). We assume a conical jet geometry; the magnetic field, assumed to be dominated by the toroidal component, is taken to decline with distance r as $B' \propto 1/r$. Electrons are injected with a double-broken power-law distribution $Q(\gamma) \propto \gamma^{-p}$ with $p = p_1$ for $\gamma < \gamma_{\rm br1}$, $p = p_2$ for $\gamma_{\rm br1} < \gamma < \gamma_{\rm br2}$, and $p = p_3$ for $\gamma > \gamma_{\rm br2}$. Their evolution, including injection at a constant rate as well as radiative and adiabatic cooling, is followed over a distance $\Delta r = r/2$, where r is the position at which the injection ends. The emission is integrated over spherical thin shells within a conical region of opening angle $\theta_{\rm j} = 1/\Gamma_{\rm j}$. The observer is located within the jet opening cone, i.e., $\theta_{\rm obs} \lesssim \theta_{\rm j}$.

We begin by modeling the SED in Period D, which is the highest γ-ray state reached by the source during our observational campaigns. In Paper I, we showed that the flare event was accompanied by an optical polarization swing and proposed two interpretations of this event. The first one involved a cloud containing ultra-relativistic particles propagating along a curved trajectory. The duration of the polarization swing constrains the location of the cloud to be at a few parsecs from the central supermassive black hole, in the region where external radiation is dominated by the infrared dust emission. In Section 5.1, we present an ERC-IR model describing the SED in Period D and a physically related model of the SED in Period E. The second interpretation of the polarization swing involved the jet precession, which allowed arbitrary location of the emitting region, including the broad-line region. In Section 5.2, we present an ERC-BEL model of the SED in Period D. We show that in this scenario the far-IR break arises due to synchrotron self-absorption. We also show an ERC-IR model of the SED in Period A, which can explain the mm/far-IR and X-ray emission, as well as the low-state optical and γ-ray flux levels.

We assume the scenario where the X-ray emission is unrelated to the flaring component, since it showed little variability during the correlated γ-ray/optical flares. Our one-zone models of the flaring states are fitted only to the IR/optical/UV and γ-ray data, treating the simultaneous X-ray spectrum as only an upper limit to the SSC component and the ERC component from the low-energy electrons. The large γ-ray/X-ray luminosity ratio forces us to adopt a very hard electron energy distribution at low energies ($p = 1$), which can be alternatively obtained by imposing a minimum electron Lorentz factor $\gamma_{\rm min} \gg 1$.

5.1. Propagation Scenario for the Emitting Region

An intrinsically spherically symmetric emitting region is expected to produce the observed electric polarization vector aligned with the projected velocity of the emitting region. Nalewajko (2010) presented a simple model of its trajectory to explain the event of simultaneous smooth variations of the polarization degree and angle during the polarization swing which has been reported in Paper I. This model adopts a constant jet Lorentz factor $\Gamma_{\rm j} = 15$ and can be used to predict the viewing angles for a given observation time. For Period D we estimate $\theta_{\rm obs,D} \sim 1.^\circ5$, while for Period E: $\theta_{\rm obs,E} \sim 2.^\circ4$. Between Periods D and E ($\Delta t \sim 15$ days), the emitting region propagates over a distance $\Delta r \sim \Gamma_{\rm j}^2 c(\Delta t) \sim 2.8$ pc.

In Figure 17 we show Model D1 fitted to the SED in Period D at $r = r_{\rm IR}$ and Model E1 fitted to the SED in Period E at $r = r_{\rm IR} + \Delta r$. Model parameters are listed in Table 5. Both models use the magnetic field scaled to the same value at the distance of 1 pc. In order to explain the difference in the luminosity ratio of the ERC component and the synchrotron component, which decreased by factor ~4 between Model D1 and Model E1, we assume a distribution of the comoving IR radiation energy density dropping steeply with distance, adopting $\beta_{\rm IR} \sim 4$. This corresponds to a strongly stratified torus structure, with a significant concentration of hot dust very close to the sublimation radius (see, e.g., Mor & Netzer 2012). We should note that, although the relatively soft γ-ray spectrum was

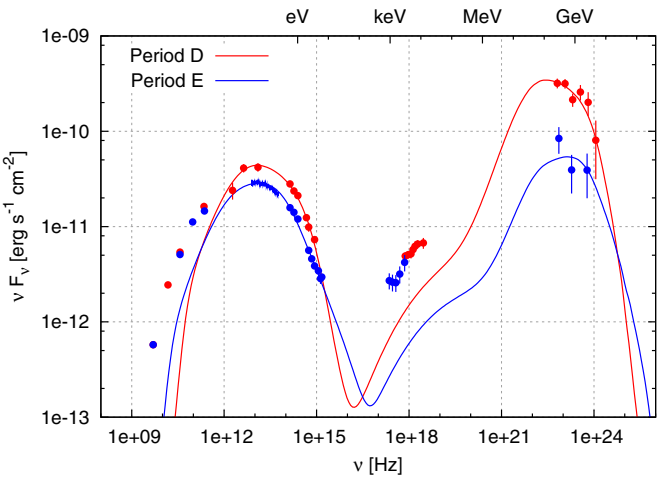

Figure 17. Emission models D1 (red line) and E1 (blue line) fitted to the spectral states at Periods D and E, respectively. Periods D and E correspond to the first five days and the last three days of the γ-ray flaring event accompanied by an optical polarization change, respectively. Those models adopt our "propagation scenario," where external radiation is dominated by infrared dust emission. We assume that the X-ray emission is not related to the flaring component, and consider the X-ray fluxes as only upper limits to the SSC and the ERC components during the flaring event. See the text in Sections 5 and 5.1 for details of the models and Table 5 for model parameters.

(A color version of this figure is available in the online journal.)

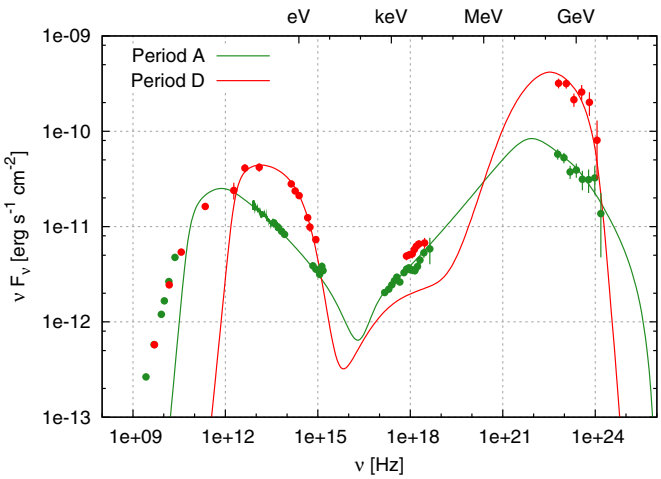

Figure 18. Emission Models A2 (green line) and D2 (red line) fitted to the spectral states at Periods A and D, respectively. Period A represents a quiescent state, and Period D corresponds to the γ-ray flaring event accompanied by an optical polarization change. Those models adopt our "jet precession scenario," which assumes the γ-ray flaring event (Period D) occurs within the broad-line region while the low-steady emission component (Period A) is generated outside the broad-line region. See the text in Sections 5 and 5.2 for details of the models and Table 5 for model parameters.

(A color version of this figure is available in the online journal.)

Table 5
Parameters of Emission Models

Model	D1	E1	D2	A2
Ext. rad.[a]	IR	IR	BEL	IR
r (pc)	1.1	3.9	0.045	3.9
R (pc)[b]	0.07	0.26	0.0023	0.19
Γ_j	15	15	20	20
θ_j [(°)]	3.8	3.8	2.9	2.9
θ_{obs} (°)	1.5	2.4	1.7	1.7
$B'_{1\,pc}$ (G)[c]	0.14	0.14	0.15	0.15
u'_{ext} (10^{-4} erg cm^{-3})[d]	78	0.97	8×10^4	1.8
γ_{br1}	800	800	170	440
γ_{br2}	6500	5000	1000	...
p_1	1	1	1	2.2
p_2	2.5	2.6	2.4	3.4
p_3	6	4.2	7	...

Notes.
[a] A dominant component of the external radiation. IR: infrared dust emission, BEL: broad emission lines.
[b] Radius of source emission region.
[c] Magnetic field intensity at the distance of 1 pc.
[d] Energy density of the dominant component of the external radiation in the jet comoving frame at the given distance r.

observed at Period E ($\Gamma = 2.64 \pm 0.32$, see Table 1), the peak of the ERC-IR component in the Model E1 falls at ~800 MeV, in the *Fermi*-LAT band.

The far-IR spectral break in Period D requires a sharp break in the electron distribution function at $\gamma_{br1} = 800$. As the cooling break is expected at $\gamma_c \sim 3m_e c^2/(2\sigma_T R u'_{ext}) \sim 660$ (where R is a radius of source emission region and u'_{ext} is the energy density of the external radiation in the jet comoving frame), γ_{br1} is located just within the fast-cooling regime. The electron distribution in the fast-cooling regime cannot be harder than $p = 2$, hence the resulting synchrotron spectral index $\alpha = (p-1)/2$ should be larger than 0.5. In fact, the mean value of the observed spectral index between 70 μm and 160 μm is smaller than 0.5 ($\alpha_{70-160} = 0.35 \pm 0.23$), which cannot be explained if the electron cooling is efficient. However, the uncertainty of the measurement does not allow us to reject this scenario.

5.2. The Jet Precession Scenario: Two Synchrotron Components

Alternatively, if the jet precession can cause the observed γ-ray flare event with the polarization swing, the γ-ray/optical emission can be generated much closer to the central black hole, even within the broad-line region (see also in Paper I). Therefore, we also attempted to model Period D placing the emitting region at r_{BEL}. For $\Gamma_j = 15$, with model parameters fitted using the synchrotron and ERC components, the X-ray flux is overproduced by the SSC process. To alleviate this problem, we increased the jet Lorentz factor to $\Gamma_j = 20$. In Figure 18, we show Model D2 with parameters listed in Table 5. The magnetic field strength scaled to the distance of 1 pc is almost the same as the value in Model D1. Because of a smaller size of emission region and higher energy density of the locally produced synchrotron radiation, the synchrotron self-absorption is able to produce a spectral cutoff at a higher frequency of $\sim 3 \times 10^{12}$ Hz (~100 μm), consistent with the far-IR break. This interpretation has an advantage that it also could explain the observed hard spectral index between 70 μm and 160 μm, even smaller than 0.5, independently of details of the electron energy distribution.

The low-energy synchrotron component, dominating the mm/sub-mm band, must be produced in a much larger region, placing it far outside the broad-line region. In Figure 18, we present Model A2, fitted to the SED at Period A. We kept the Lorentz factor and the magnetic field consistent with Model D2, but we set the source at the distance ~4 pc, the same as in Model E1. This low-state model of Period A can reproduce both observed X-ray and γ-ray spectra by a single broken power-law electron distribution. The γ-ray spectral index is consistent with the IR/optical/UV spectral index. The synchrotron

self-absorption is effective at $\sim 10^{11}$ Hz and the spectral peak is located in the mm/sub-mm band.

Those results suggest the existence of two synchrotron components: one peaking in the mm/sub-mm band and the other peaking in the mid-IR band. The component with the peak in the mid-IR band is more variable, and can be produced at shorter distances, within the broad-line region, where the far-IR break can be explained by the synchrotron self-absorption.

6. CONCLUSIONS

This paper reports details of the multi-band campaigns on the well-known blazar 3C 279 during the first two years of the *Fermi* mission between 2008 and 2010. Some key results were already presented in Paper I. Most important of them was the coincidence of a dramatic γ-ray/optical flare with a change in the optical polarization, which we interpreted as the result of a compact emitting region: either propagating along a curved relativistic jet or located at a constant distance in a precessing jet. In addition, we reported on an "isolated" X-ray flare, an event without a clear counterpart in other bands, and taking place a few months after the γ-ray/optical flare. Here, we extended the observation epoch until 2010 August yielding the best coverage of time-resolved SEDs ever collected for 3C 279 from radio through high-energy γ-ray bands. Based on those data, we arrived at several new conclusions about the structure and emission models of the relativistic jet in the quasar.

1. In the high-energy γ-ray band measured by *Fermi*-LAT, the source exhibited two prominent flares reaching as high as $\sim 3 \times 10^{-6}$ photons cm^{-2} s^{-1} above 100 MeV in the first year while it was in a relatively quiescent state in the second year. No significant correlation between flux and photon index has been measured in similarity to other LAT blazars. The two year averaged γ-ray spectral shape above 200 MeV clearly deviates from a single power law. The broken power-law model returns a break energy within a few GeV range, which does not appear to vary with the source flux. Such behavior is similar to that observed in other bright FSRQs.
2. The superb temporal coverage allowed us to measure in detail the cross-correlation of the γ-ray and optical fluxes. The optical signals appear to be delayed with respect to the γ-ray signals by $\sim$10 days. Such a lag can be explained in terms of the simple synchrotron and inverse-Compton model, in the scenario where a cloud containing ultra-relativistic electrons propagates down the jet through the regions where the ratio of the external radiation energy to the magnetic energy densities decrease with distance. We have verified this idea qualitatively (see the Appendix), but it still needs specific numerical modeling to be confirmed quantitatively.
3. X-ray observations reveal a pair of pronounced flares separated by $\sim$90 days. Those are not contemporaneous with a pair of bright γ-ray/optical flares—also separated by $\sim$90 days—but instead, are delayed with respect to the γ-ray/optical flares by about 155 days. Because of such a long delay, it seems implausible that these events are causally related. Instead, the possible scenarios of the X-ray flares may involve changes of the source parameters such as the jet direction, Lorentz factor, and/or location of the dissipation event, or may require more "exotic" solutions, for instance, bulk-Compton process, inefficient electron acceleration above a given energy, and hadronic processes. At this stage we cannot discriminate among any of those scenarios.
4. The spectral coverage of the infrared band with *Spitzer* enabled us to probe the detailed structure of the low-energy spectral bump, attributed to the synchrotron radiation. Significant spectral variability, with soft/power-law spectra in the low state and hard/curved spectra in the high state, as well as the detection of a sharp far-IR spectral break in the high state, strongly suggest the existence of two synchrotron components: one peaking in the mm/sub-mm band and the other peaking in the mid-IR band. The component with a peak at the mid-IR band can be responsible for emission during γ-ray flaring states.
5. We have applied our leptonic emission model for the SEDs during the γ-ray flaring state with a polarization change. Adopting the interpretation of the polarization swing involving the propagation of the emitting region—that suggested in Paper I—we can explain the evolution of the broadband SEDs from Periods D to E during the γ-ray flaring event by a shift of the position of the emitting region and a change of the viewing angle that are consistent with its trajectory. We used the same distribution of magnetic fields and only slightly changed electron spectra, but required a rather steep stratification of the external radiation density in the form of thermal emission from the dusty torus. In this case, the far-IR spectral break requires a break in the electron distribution. The observed *Spitzer*-MIPS spectral index $\alpha_{70-160} = 0.35 \pm 0.23$ is marginally consistent with the synchrotron emission in the fast-cooling regime.
6. We also discussed the model in which the γ-ray flare is generated within the broad emission line region at sub-pc scale from the central black hole according to the jet precession scenario. This model explains the mid-IR break during the flaring state of Period D by synchrotron self-absorption. Here, we also discussed the low-state SED in Period A where the mm/sub-mm band peaking synchrotron component can be dominant. The model shows the related ERC component can explain the steady X-ray emission.

The *Fermi*-LAT Collaboration acknowledges generous ongoing support from a number of agencies and institutes that have supported both the development and the operation of the LAT as well as scientific data analysis. These include the National Aeronautics and Space Administration and the Department of Energy in the United States, the Commissariat à l'Energie Atomique and the Centre National de la Recherche Scientifique/Institut National de Physique Nucléaire et de Physique des Particules in France, the Agenzia Spaziale Italiana and the Istituto Nazionale di Fisica Nucleare in Italy, the Ministry of Education, Culture, Sports, Science and Technology (MEXT), High Energy Accelerator Research Organization (KEK), and Japan Aerospace Exploration Agency (JAXA) in Japan, and the K. A. Wallenberg Foundation, the Swedish Research Council, and the Swedish National Space Board in Sweden. Additional support for science analysis during the operations phase is gratefully acknowledged from the Istituto Nazionale di Astrofisica in Italy and the Centre National d'Études Spatiales in France.

The Submillimeter Array is a joint project between the Smithsonian Astrophysical Observatory and the Academia Sinica Institute of Astronomy and Astrophysics and is funded by the Smithsonian Institution and the Academia Sinica. The St. Petersburg University team acknowledges support from the

Russian RFBR foundation via grant 09-02-00092. AZT-24 observations are made within an agreement between Pulkovo, Rome, and Teramo observatories. This paper is partly based on observations carried out at the German-Spanish Calar Alto Observatory, which is jointly operated by the MPIA and the IAA-CSIC. Acquisition of the MAPCAT data is supported in part by MICIIN (Spain) grant and AYA2010-14844, and by CEIC (Andalucía) grant P09-FQM-4784. The Metsähovi team acknowledges the support from the Academy of Finland to our observing projects (numbers 212656, 210338, 121148, and others). The Medicina and Noto telescopes are operated by INAF-Istituto di Radioastronomia. The research at Boston University was supported by NASA Fermi GI grants NNX08AV65G, NNX08AV61G, NNX09AT99G, and NNX09AU10G, and NSF grant AST-0907893. The PRISM camera at Lowell Observatory was developed by K. Janes et al. at BU and Lowell Observatory, with funding from the NSF, BU, and Lowell Observatory. The Liverpool Telescope is operated on the island of La Palma by Liverpool John Moores University in the Spanish Observatorio del Roque de los Muchachos of the Instituto de Astrofisica de Canarias, with funding from the UK Science and Technology Facilities Council. The Abastumani Observatory team acknowledges financial support by the Georgian National Science Foundation through grant GNSF/ST09/521 4-320. The research at the University of Michigan has been funded by a series of grants from NASA and from the NSF. Specific grant numbers are NASA grants NNX09AU16G, NNX10AP16G, NNX11AO13G, and NSF grant AST-0607523. Funding for the operation of UMRAO was provided by the University of Michigan.

M.H. is supported by the Research Fellowships of the Japan Society for the Promotion of Science for Young Scientists. This work was partially supported by the Polish MNiSW grants N N203 301635 and N N203 386337, the Polish ASTRONET grant 621/E-78/SN-0068/2007, and the Polish NCN grant DEC-2011/01/B/ST9/04845.

APPENDIX

POSSIBLE EXPLANATION OF A LAG BETWEEN THE γ-RAY AND OPTICAL FLARES

As we discussed in Section 4.1, the multi-band time series imply that during the flaring activity detected in 3C 279 the optical emission appears to be delayed with respect to the γ-ray emission. In the context of radiation models adopted here (Section 5), the same electron population produces optical synchrotron photons and also inverse-Compton γ-rays *in the fast-cooling regime*. A lag between the optical and γ-ray flares may therefore result from different profiles of decrease of the magnetic energy density $u'_{\rm B}(r)$ and the external (target) radiation energy density $u'_{\rm ext}(r)$ with the distance r along the jet, convolved with a non-monotonic profile of the electron injection rate within the outflow.

In the fast-cooling (FC) regime, the power injected into the relativistic particles $P_{\rm e,\,inj}$ is immediately radiated away and determines the total broadband luminosity produced by the cooled electrons $L_{\rm tot,\,FC}$. Assuming a strong inverse-Compton dominance, i.e., the observed inverse-Compton peak (γ-ray) luminosity $\simeq L_\gamma$ being much larger than the observed synchrotron peak (optical) luminosity $L_{\rm opt}$, one has

$$P_{\rm e,\,inj}(r) \propto L_{\rm tot,\,FC}(r) \simeq L_\gamma(r) + L_{\rm opt}(r) \sim L_\gamma(r), \qquad \text{(A1)}$$

while the optical luminosity is

$$L_{\rm opt}(r) \simeq \frac{u'_{\rm B}(r)}{u'_{\rm ext}(r)}\, L_\gamma(r) \propto \frac{u'_{\rm B}(r)}{u'_{\rm ext}(r)}\, P_{\rm e,\,inj}(r), \qquad \text{(A2)}$$

where we assumed $\delta = \Gamma_{\rm j}$ being independent on the position r along the jet. Hence, it is clear that while a maximum of $L_\gamma(r)$ is determined solely by the injection rate $P_{\rm e,\,inj}(r)$, a maximum of $L_{\rm opt}(r)$ may in general be quite different, depending on particular radial profiles of $P_{\rm e,\,inj}(r)$ and of the ratio $[u'_{\rm B}/u'_{\rm ext}]$ (r).

As a specific illustrative example, let us assume that the dissipation region propagating down the jet injects non-thermal energy into radiating particles at the rate being a broad Gaussian function of distance r with a maximum at r_0 and a width of $r_0/\sqrt{2}$,

$$P_{\rm e,\,inj} \propto \exp\big[-(r-r_0)^2/r_0^2\big], \qquad \text{(A3)}$$

and that magnetic field and external photon field energy densities scale with r as power laws with indices $\beta_{\rm B}$ and $\beta_{\rm ext}$,

$$u'_{\rm B}(r) \propto r^{-\beta_{\rm B}} \quad \text{and} \quad u'_{\rm ext}(r) \propto r^{-\beta_{\rm ext}}. \qquad \text{(A4)}$$

Then one can find that L_γ has a maximum at $r = r_0$, as expected, whereas $L_{\rm opt}$ attains a maximum at

$$r_{\rm cr} = \frac{r_0}{2} \times \left(1 + \sqrt{1 + 2\,(\beta_{\rm ext} - \beta_B)}\right), \qquad \text{(A5)}$$

which is larger than r_0 as long as $\beta_{\rm ext} > \beta_{\rm B}$ and thus results in the optical flare lagging the γ-ray flare. This is due to the fact that with the magnetic energy density decreasing less rapidly in the jet comoving frame than the external radiation energy density, the drop in the injection rate $P_{\rm e,\,inj}(r)$ between r_0 and $r_{\rm cr}$ is compensated by the *increase* in the ratio $[u'_{\rm B}/u'_{\rm ext}]$ (r).

Let us further consider the particular values of $\beta_{\rm B} = 2$ and $\beta_{\rm ext} = 4$ discussed in Section 5. With such, assuming again the electron injection rate being a broad Gaussian function of the distance r along the jet as in the example above, the observed time lag between the optical and γ-ray flares $\Delta t_{\rm obs}$ can be evaluated as roughly

$$\Delta t_{\rm obs} \simeq \frac{0.6\, r_0}{c\, \Gamma_{\rm j}^2} \simeq 3 \times \left(\frac{\Gamma_{\rm j}}{15}\right)^{-2} \left(\frac{r_0}{1\,{\rm pc}}\right) \text{ days}. \qquad \text{(A6)}$$

It is encouraging that a 10 day lag is expected for $\Gamma_{\rm j} \simeq 15$ and $r_0 \simeq 3$ pc, which are the bulk Lorentz factor and the location of the dissipation region comparable to that inferred from our ERC-IR modeling.

REFERENCES

Abazajian, K. N., Adelman-McCarthy, J. K., Agüeros, M. A., et al. 2009, ApJS, 182, 543
Abdo, A. A., Ackermann, M., Agudo, I., et al. (*Fermi*-LAT Collaboration) 2010a, ApJ, 721, 1425
Abdo, A. A., Ackermann, M., Ajello, M., et al. (*Fermi*-LAT Collaboration) 2009a, Astropart. Phys., 32, 193
Abdo, A. A., Ackermann, M., Ajello, M., et al. (*Fermi*-LAT Collaboration) 2009b, ApJ, 699, 817
Abdo, A. A., Ackermann, M., Ajello, M., et al. (*Fermi*-LAT Collaboration) 2010b, Nature, 463, 919
Abdo, A. A., Ackermann, M., Ajello, M., et al. (*Fermi*-LAT Collaboration) 2010c, ApJS, 188, 405
Abdo, A. A., Ackermann, M., Ajello, M., et al. (*Fermi*-LAT Collaboration) 2010d, ApJ, 710, 810
Abdo, A. A., Ackermann, M., Ajello, M., et al. (*Fermi*-LAT Collaboration) 2010e, ApJ, 710, 1271

Abdo, A. A., Ackermann, M., Ajello, M., et al. (*Fermi*-LAT Collaboration) 2010f, ApJ, 722, 520
Abdo, A. A., Ackermann, M., Ajello, M., et al. (*Fermi*-LAT Collaboration) 2010g, Phys. Rev. Lett., 104, 101101
Abdo, A. A., Ackermann, M., Ajello, M., et al. (*Fermi*-LAT Collaboration) 2011, ApJ, 726, 43
Ackermann, M., Ajello, M., Baldini, L., et al. (*Fermi*-LAT Collaboration) 2010, ApJ, 721, 1383
Ackermann, M., Ajello, M., Ballet, J., et al. (*Fermi*-LAT Collaboration) 2012, ApJ, 751, 159
Agudo, I., Jorstad, S. G., Marscher, A. P., et al. 2011a, ApJ, 726, L13
Agudo, I., Marscher, A. P., Jorstad, S. G., et al. 2011b, ApJ, 735, L10
Albert, J., Aliu, E., Anderhub, H., et al. (MAGIC Collaboration) 2008, Science, 320, 1752
Aleksić, J., Antonelli, L. A., Antoranz, P., et al. (MAGIC Collaboration) 2011, A&A, 530, A4
Atwood, W. B., Abdo, A. A., Ackermann, M., et al. (*Fermi*-LAT Collaboration) 2009, ApJ, 697, 1071
Baars, J. W. M., Genzel, R., Pauliny-Toth, I. I. K., & Witzel, A. 1977, A&A, 61, 99
Begelman, M. C., & Sikora, M. 1987, ApJ, 322, 650
Bessell, M. S., Castelli, F., & Plez, B. 1998, A&A, 333, 231
Blandford, R. D., & Levinson, A. 1995, ApJ, 441, 79
Bloom, S. D., & Marscher, A. P. 1996, ApJ, 461, 657
Bock, D. C.-J., Bolatto, A. D., Hawkins, D. W., et al. 2006, Proc. SPIE, 6267, 13
Bonning, E. W., Bailyn, C., Urry, C. M., et al. 2009, ApJ, 697, L81
Cardelli, J. A., Clayton, G. C., & Mathis, J. S. 1989, ApJ, 345, 245
Chatterjee, R., Jorstad, S. G., Marscher, A. P., et al. 2008, ApJ, 689, 79
Collmar, W., Böttcher, M., Krichbaum, T. P., et al. 2010, A&A, 522, A66
Collmar, W., Schönfelder, V., Zhang, S., et al. 2001, in AIP Conf. Proc. 587, Gamma 2001: Gamma-Ray Astrophysics, ed. S. Ritz, N. Gehrels, & C. R. Shroder (Melville, NY: AIP), 271
Cutri, R. M., Skrutskie, M. F., van Dyk, S., et al. 2003, VizieR Online Data Catalog, 2246, 0
Daly, R. A., & Marscher, A. P. 1988, ApJ, 334, 539
D'Ammando, F., Raiteri, C. M., Villata, M., et al. 2011, A&A, 529, A145
Dermer, C. D., & Schlickeiser, R. 1993, ApJ, 416, 458
Dermer, C. D., Schlickeiser, R., & Mastichiadis, A. 1992, A&A, 256, L27
Eachus, L. J., & Liller, W. 1975, ApJ, 200, L61
Edelson, R., Turner, T. J., Pounds, K., et al. 2002, ApJ, 568, 610
Edelson, R. A., & Krolik, J. H. 1988, ApJ, 333, 646
Engelbracht, C. W., Blaylock, M., Su, K. Y. L., et al. 2007, PASP, 119, 994
Giuliani, A., D'Ammando, F., Vercellone, S., et al. 2009, A&A, 494, 509
Gordon, C. W., Engelbracht, C. W., Fadda, D., et al. 2007, PASP, 119, 1019
Greiner, J., Bornemann, W., Clemens, C., et al. 2008, PASP, 120, 405
Gu, M., Cao, X., & Jiang, D. R. 2001, MNRAS, 327, 1111
Hartman, R. C., Bertsch, D. L., Bloom, S. D., et al. 1999, ApJS, 123, 79
Hartman, R. C., Bertsch, D. L., Fichtel, C. E., et al. 1992, ApJ, 385, L1
Hartman, R. C., Böttcher, M., Aldering, G., et al. 2001a, ApJ, 553, 683
Hartman, R. C., Villata, M., Balonek, T. J., et al. 2001b, ApJ, 558, 583
Hermsen, W., Aarts, H. J. M., Bennett, K., et al. 1993, A&AS, 97, 97
Homan, D. C., Lister, M. L., Kellermann, K. I., et al. 2003, ApJ, 589, L9
Jorstad, S. G., Marscher, A. P., Larionov, V. M., et al. 2010, ApJ, 715, 362
Jorstad, S. G., Marscher, A. P., Lister, M. L., et al. 2004, AJ, 127, 3115
Jorstad, S. G., Marscher, A. P., Lister, M. L., et al. 2005, AJ, 130, 1418
Kalberla, P. M. W., Burton, W. B., Hartmann, D., et al. 2005, A&A, 440, 775
Komissarov, S. S., & Falle, S. A. E. G. 1997, MNRAS, 288, 833
Koyama, K., Tsunemi, H., Dotani, T., et al. 2007, PASJ, 59, 23
Krühler, T., Küpcü Yoldaş, A., Greiner, J., et al. 2008, ApJ, 685, 376
Larionov, V. M., Jorstad, S. G., Marscher, A. P., et al. 2008, A&A, 492, 389
Lynds, C. R., Stockton, A. N., & Livingston, W. C. 1965, ApJ, 142, 1667
Mannheim, K., & Biermann, P. L. 1992, A&A, 253, L21
Maraschi, L., Ghisellini, G., & Celotti, A. 1992, ApJ, 397, L5
Maraschi, L., Grandi, P., Urry, C. M., et al. 1994, ApJ, 435, L91
Mattox, J. R., Bertsch, D. L., Chiang, J., et al. 1996, ApJ, 461, 396
McNaron-Brown, K., Johnson, W. N., Jung, G. V., et al. 1995, ApJ, 451, 575
Mitsuda, K., Bautz, M., Inoue, H., et al. 2007, PASJ, 59, 1
Moderski, R., Sikora, M., & Błażejowski, M. 2003, A&A, 406, 855
Mor, R., & Netzer, H. 2012, MNRAS, 420, 526
Morrison, R., & McCammon, D. 1983, ApJ, 270, 119
Nalewajko, K. 2010, Int. J. Mod. Phys. D, 19, 701
Nalewajko, K., & Sikora, M. 2009, MNRAS, 392, 1205
Nandikotkur, G., Jahoda, K. M., Hartman, R. C., et al. 2007, ApJ, 657, 706
Nandra, K., George, I. M., Mushotzky, R. F., Turner, T. J., & Yaqoob, T. 1997, ApJ, 476, 70
Nilsson, K., Pursimo, T., Villforth, C., Lindfors, E., & Takalo, L. O. 2009, A&A, 505, 601
Ogle, P. M., Wehrle, A. E., Balonek, T., & Gurwell, M. A. 2011, ApJS, 195, 19
Pian, E., Urry, C. M., Maraschi, L., et al. 1999, ApJ, 521, 112
Poole, T. S., Breeveld, A. A., Page, M. J., et al. 2008, MNRAS, 383, 627
Poutanen, J., & Stern, B. 2010, ApJ, 717, L118
Raiteri, C. M., Villata, M., Aller, M. F., et al. 2011, A&A, 534, A87
Raiteri, C. M., Villata, M., Lanteri, L., Cavallone, M., & Sobrito, G. 1998, A&AS, 130, 495
Reach, W. T., Megeath, S. T., Cohen, M., et al. 2005, PASP, 117, 978
Richards, J. L., Max-Moerbeck, W., Pavlidou, V., et al. 2011, ApJS, 194, 29
Roming, P. W. A., Kennedy, T. E., Mason, K. O., et al. 2005, Space Sci. Rev., 120, 95
Sault, R. J., Teuben, P. J., & Wright, M. C. H. 1995, in ASP Conf. Ser. 77, Astronomical Data Analysis Software and Systems IV, ed. R. A. Shaw, H. E. Payne, & J. J. E. Hayes (San Francisco, CA: ASP), 433
Schlegel, D. J., Finkbeiner, D. P., & Davis, M. 1998, ApJ, 500, 525
Sikora, M. 2011, in IAU Symp. 275, Jets at All Scales, ed. G. E. Romero, R. A. Sunyaev, & T. Belloni (Cambridge: Cambridge Univ. Press), 59
Sikora, M., Begelman, M. C., & Rees, M. J. 1994, ApJ, 421, 153
Sikora, M., Stawarz, Ł., Moderski, R., Nalewajko, K., & Madejski, G. M. 2009, ApJ, 704, 38
Skrutskie, M. F., Cutri, R. M., Stiening, R., et al. 2006, AJ, 131, 1163
Stansberry, J. A., Gordon, K. D., Bhattacharya, B., et al. 2007, PASP, 119, 1038
Takahashi, T., Abe, K., Endo, M., et al. 2007, PASJ, 59, 35
Tanaka, Y. T., Stawarz, Ł., Thompson, D. J., et al. 2011, ApJ, 733, 19
Tody, D. 1993, in ASP Conf. Ser. 52, Astronomical Data Analysis Software and Systems II, ed. R. J. Hanisch, R. J. V. Brissenden, & J. Barnes (San Francisco, CA: ASP), 173
Ulrich, M.-H., Maraschi, L., & Urry, C. M. 1997, ARA&A, 35, 445
Vaughan, S., Edelson, R., Warwick, R. S., & Uttley, P. 2003, MNRAS, 345, 1271
Villata, M., Raiteri, C. M., Ghisellini, G., et al. 1997, A&AS, 121, 119
Villata, M., Raiteri, C. M., Gurwell, M. A., et al. 2009, A&A, 504, L9
Villata, M., Raiteri, C. M., Larionov, V. M., et al. 2008, A&A, 481, L79
Watanabe, M., Nakaya, H., Yamamuro, T., et al. 2005, PASP, 117, 870
Wehrle, A. E., Pian, E., Urry, C. M., et al. 1998, ApJ, 497, 178
Wolff, M. J., Nordsieck, K. H., & Nook, M. A. 1996, AJ, 111, 856
Woo, J.-H., & Urry, C. M. 2002, ApJ, 579, 530

The Astrophysical Journal, 751:91 (19pp), 2012 June 1 doi:10.1088/0004-637X/751/2/91

EMPIRICAL DETERMINATION OF CONVECTION PARAMETERS IN WHITE DWARFS. I. WHOLE EARTH TELESCOPE OBSERVATIONS OF EC14012-1446*

J. L. Provencal[1,2], M. H. Montgomery[2,3], A. Kanaan[4], S. E. Thompson[1,2,5], J. Dalessio[1,2], H. L. Shipman[1,2], D. Childers[2,6], J. C. Clemens[7], R. Rosen[8], P. Henrique[4], A. Bischoff-Kim[9], W. Strickland[10], D. Chandler[10], B. Walter[10], T. K. Watson[11], B. Castanheira[12], S. Wang[3], G. Handler[12], M. Wood[13], S. Vennes[13], P. Nemeth[13], S. O. Kepler[14], M. Reed[15], A. Nitta[16], S. J. Kleinman[16], T. Brown[17], S.-L. Kim[18], D. Sullivan[19], W. P. Chen[20], M. Yang[20], C. Y. Shih[20], X. J. Jiang[21], A. V. Sergeev[22], A. Maksim[22], R. Janulis[23], K. S. Baliyan[24], H. O. Vats[24], S. Zola[25,26], A. Baran[25], M. Winiarski[25,26], W. Ogloza[25,26], M. Paparo[27], Z. Bognar[27], P. Papics[27], D. Kilkenny[28], R. Sefako[29], D. Buckley[29], N. Loaring[29], A. Kniazev[29], R. Silvotti[30], S. Galleti[30], T. Nagel[31], G. Vauclair[32], N. Dolez[33], J. R. Fremy[33], J. Perez[34], J. M. Almenara[34], and L. Fraga[14]

[1] Department of Physics and Astronomy, University of Delaware, Newark, DE 19716, USA; jlp@udel.edu
[2] Delaware Asteroseismic Research Center, Mt. Cuba Observatory, Greenville, DE 19807, USA
[3] Department of Astronomy, University of Texas, Austin, TX 78712, USA; mikemon@rocky.as.utexas.edu
[4] Departamento de Física, Universidade Federal de Santa Catarina, C.P. 476, 88040-900 Florianópolis, SC, Brazil; ankanaan@gmail.com
[5] SETI Institute, NASA Ames Research Center, Moffett Field, CA 94035, USA
[6] Department of Math and Science, Delaware County Community College, 901 South Media Road, Media, PA 19063, USA; dpc@udel.edu
[7] Department of Physics and Astronomy, University of North Carolina, 288 Phillips Hall, Chapel Hill, NC 27599, USA; clemens@physics.unc.edu
[8] NRAO, Green Bank, WV 24944, USA; rachel.rosen@gmail.com
[9] Department of Chemistry and Physics, Georgia College and State University, Milledgeville, GA 31061, USA; agnes.kim@gcsu.edu
[10] Meyer Observatory and Central Texas Astronomical Society, 209 Paintbrush, Waco, TX 76705, USA; chandler@vvm.com
[11] Institute for Astronomy, Southwestern University, Georgetown, TX, USA; tkw@sousthwestern.edu
[12] Institut für Astronomie Universität Wien, Türkenschanzstrasse 17, 1180 Vienna, Austria; gerald@camk.edu.pl
[13] Department of Physics & Space Sciences, Florida Institute of Technology, 150 West University Boulevard, Melbourne, FL 3290, USA; wood@fit.edu
[14] Instituto de Fíisica UFRGS, C.P. 10501, 91501-970 Porto Alegre, RS, Brazil; kepler@if.ufrgs.br
[15] Department of Physics, Astronomy and Material Science, Missouri State University and Baker Observatory, 901 S. National, Springfield, MO 65897, USA; MikeReed@missouristate.edu
[16] Gemini Observatory, Northern Operations Center, 670 North A'ohoku Place, Hilo, HI 96720, USA; atsuko.nittakleinman1@gmail.com
[17] Las Cumbres Observatory Global Telescope Network, Inc., 6740 Cortona Drive Suite 102, Santa Barbara, CA 93117, USA; tbrown@lcogt.com
[18] Korea Astronomy and Space Science Institute, Daejeon 305-348, Republic of Korea; slkim@kasi.re.kr
[19] School of Chemical & Physical Sciences, Victoria University of Wellington, P.O. Box 600, Wellington, New Zealand; denis.sullivan@vuw.ac.nz
[20] Lulin Observatory, National Central University, Jhongli City, Taoyuan County, Taiwan; wchen@astro.ncu.edu.tw
[21] National Astronomical Observatories, Academy of Sciences, Beijing 100012, PR China; xjjiang@bao.ac.cn
[22] Ukrainian National Academy of Sciences, Main Astronomical Observatory, Golosiiv, Kiev 022 252650, Ukraine; sergeev@terskol.com
[23] Institute of Theoretical Physics and Astronomy, Vilnius University, Vilnius, Lithuania; jr@itpa.lt
[24] Physical Research Laboratory, Ahmedabad 380009, India
[25] Mount Suhora Observatory, Cracow Pedagogical University, Ul. Podchorazych 2, 30-084 Krakow, Poland; zola@astro1.as.ap.krakow.pl
[26] Astronomical Observatory, Jagiellonian University, Ul. Orla 171, 30-244 Cracow, Poland
[27] Konkoly Observatory, P.O. Box 67, H-1525 Budapest XII, Hungary; paparo@konkoly.hu
[28] Department of Physics, University of the Western Cape, Private Bag X17, Belville 7535, South Africa
[29] South African Astronomical Observatory, P.O. Box 9, Observatory 7935, South Africa
[30] INAF-Osservatorio Astronomico di Capodimonte, via Moiariello 16, 80131 Napoli, Italy
[31] Institut für Astronomie und Astrophysik, Universiät Tübingen, Sand 1, 72076 Tübingen, Germany; nagel@astro.uni-tuebingen.de
[32] Laboratoire d'Astrophysique de Toulouse-Tarbes, Université de Toulouse, CNRS, 14 avenue Edouard Belin, F314000 Toulouse, France; gerardv@srvdec.obs-mip.fr
[33] Observatoire de Paris, LESIA, 92195 Meudon, France
[34] Instituto de Astrofisica de Canarias, 38200 La Laguna, Tenerife, Spain

Received 2012 January 23; accepted 2012 April 6; published 2012 May 9

ABSTRACT

We report on an analysis of 308.3 hr of high-speed photometry targeting the pulsating DA white dwarf EC14012-1446. The data were acquired with the Whole Earth Telescope during the 2008 international observing run XCOV26. The Fourier transform of the light curve contains 19 independent frequencies and numerous combination frequencies. The dominant peaks are 1633.907, 1887.404, and 2504.897 μHz. Our analysis of the combination amplitudes reveals that the parent frequencies are consistent with modes of spherical degree $l = 1$. The combination amplitudes also provide m identifications for the largest amplitude parent frequencies. Our seismology analysis, which includes 2004–2007 archival data, confirms these identifications, provides constraints on additional frequencies, and finds an average period spacing of 41 s. Building on this foundation, we present nonlinear fits to high signal-to-noise light curves from the SOAR 4.1 m, McDonald 2.1 m, and KPNO 2 m telescopes. The fits indicate a time-averaged convective response timescale of $\tau_0 = 99.4 \pm 17$ s, a temperature exponent $N = 85 \pm 6.2$, and an inclination angle of $\theta_i = 32\overset{\circ}{.}9 \pm 3\overset{\circ}{.}2$. We present our current empirical map of the convective response timescale across the DA instability strip.

Key words: asteroseismology – stars: evolution – stars: individual (EC14012-1446) – stars: oscillations – white dwarfs

Online-only material: color figures

1. INTRODUCTION

Stellar seismology, also known as *asteroseismology*, provides us with a unique tool for probing the interiors of stars, allowing us to study fundamental problems in stellar evolution such as energy transport, thermodynamics, and magnetism. White dwarfs, the evolutionary endpoint of most stars, are particularly important targets for asteroseismology. They are structurally simple: an electron degenerate carbon/oxygen core surrounded by thin non-degenerate layers of hydrogen and helium. DA white dwarfs represent ∼80% of all white dwarfs (Eisenstein et al. 2006), and they have a nearly pure layer of hydrogen on top of a layer of helium. DB white dwarfs lack this hydrogen layer, having a layer of nearly pure helium overlying a carbon/oxygen core. Lacking substantial nuclear reactions, white dwarfs simply cool as they age, passing through specific temperature ranges (the DBV and DAV instability strips) within which they pulsate. These pulsators are otherwise normal objects, so what we learn about their structure can be applied to the entire population of stellar remnants and further applied to our understanding of their main-sequence progenitors.

In this paper, we focus on combining asteroseismology of the DAV EC14012-1456 with nonlinear analysis of its light curve to provide an empirical description of its convection zone. Convection is one of the largest remaining sources of theoretical uncertainty in astrophysical modeling. Convection is traditionally treated through mixing length theory (MLT; Böhm-Vitense 1958). MLT is a simple, local, time-independent description first applied to stellar modeling by Biermann (1932). It describes the motions of "average" convective cells with a mean size $l = \alpha H_p$, where H_p is the local pressure scale height and α is an adjustable free parameter. MLT is clearly incomplete; we know turbulent flows are complex and there is no reason why α should remain constant throughout the convection zone of a single star, and certainly not for stars of different masses, chemical compositions, or evolutionary phases. As an example for white dwarfs, Bergeron et al. (1995) and Tremblay et al. (2010) show that model parameters such as flux, line profiles, energy distribution, color indices, and equivalent widths are extremely sensitive to the assumed MLT parameterization. Bergeron et al. (1995) find systematic uncertainties ranging from 25% for effective temperatures to 11% for mass and radius. The use of MLT to treat convective energy transport in white dwarf atmospheres thus represents a significant source of physical uncertainty in calculations of their atmospheric structure. We rely on these models to supply the information about white dwarf interiors, masses, and temperatures needed to calibrate white dwarf cooling sequences. This in turn produces detailed age estimates for white dwarfs (Ruiz & Bergeron 2001) and an estimate of the age of the Galactic disk (Winget et al. 1987; Harris et al. 2006). An observational test of MLT that leads to an improved description of convection is an important goal that will have implications beyond the study of white dwarfs.

Brickhill (1992) was the first to realize that a pulsating white dwarf's photospheric flux is modulated relative to the flux entering at the bottom of the convection zone by an amount that depends on the convection zone's thickness. The local convection zone depth is a function of the local effective temperature, and this varies during a pulsation cycle. The result is a distortion of the observed light curve, with narrow peaks and wider valleys (Figure 1). Convective light curve fitting exploits these nonlinearities to recover the thermal response timescale of the convection zone. Mathematical details of this technique can be found in Montgomery (2005c) and Montgomery et al. (2010b). For our purposes, applying convective light curve fitting to a target star requires three ingredients: (1) a pulsator with a nonlinear light curve, (2) precise knowledge of the star's pulsation frequencies and (l, m) values, and (3) high signal-to-noise light curves for use in the actual fitting process.

Asteroseismology provides the tools to identify white dwarf pulsation (l, m) values. White dwarfs are g-mode pulsators, and each pulsation mode can be described by a spherical harmonic of degree l, radial overtone k, and azimuthal number m, where m takes integer values between $-l$ and l. Given a sufficient sample of excited pulsation modes, we can match the observed frequencies with theoretical models. An important diagnostic for g-mode pulsators is the mean period spacing between modes of the same (l, m) but consecutive radial overtone k (e.g., the k and $k + 1$ modes). The mean period spacing depends mainly on stellar mass. Deviations of individual spacings from this mean value provide information on the thickness of the hydrogen and/or helium layers and on the chemical profile of the core (Montgomery 2009). We note here that the actual value of the radial overtone k cannot be determined observationally, but must be inferred from theoretical models.

A second diagnostic is given by the presence of multiplets. The multiplet components have the same (k, l) and are further described by the azimuthal index m, which takes integer values between $-l$ and l. To first order, the frequency difference relative to the $m = 0$ component of the multiplet is given by $\delta\nu_{klm} = -m\,\Omega\,(1 - C_{kl})$, where Ω is the rotation period and C_{kl} is a coefficient that depends on the pulsation eigenfunctions evaluated in the nonrotating case. In the high-k asymptotic limit for g-modes, $C_{kl} \sim 1/\ell(\ell + 1)$, although models predict it to vary by ≈10% over the range of observed periods in EC14012. Multiplet structure is a strong indication of a mode's l value. We expect a triplet for $l = 1$, a quintuplet for $l = 2$, and so on. The observed frequency differences (splittings) are a measure of the stellar rotation rate as sampled by a given mode. Deviations from equal frequency splitting within a single multiplet and changes in splittings from one multiplet to the next reveal information about differential rotation and magnetic field strength.

Applying convective light curve fitting to a wide sample of pulsating white dwarfs provides an empirical map of how the convective response timescale varies as a function of effective temperature, and this can be compared with theoretical models, both MLT and hydrodynamic. The Whole Earth Telescope (WET) is engaged in a long-term project to provide such a description of convection across the hydrogen atmosphere DAV ($T_{\rm eff} \approx$ 11,100–12,200 K) and the helium atmosphere DBV ($T_{\rm eff} \approx$ 22,000–29,000 K) instability strips. We present here our results for the DAV pulsator EC14012-1446. Our goals are three-fold: determine accurate frequency and (l, m) identifications, obtain several nights of high-quality light curves, and apply convective light curve fitting to obtain EC14012-1446's convective response timescale. In the following, we present the resulting data set and our analysis of the Fourier transforms (FTs), discuss the identified frequencies and (l, m) values, perform nonlinear light curve fits, and present the convective parameters for EC14012-1446.

* Based on observations obtained at the Southern Astrophysical Research (SOAR) telescope, which is a joint project of the Ministério da Ciência, Tecnologia, e Inovação (MCTI) da República Federativa do Brasil, the U.S. National Optical Astronomy Observatory (NOAO), the University of North Carolina at Chapel Hill (UNC), and Michigan State University (MSU).

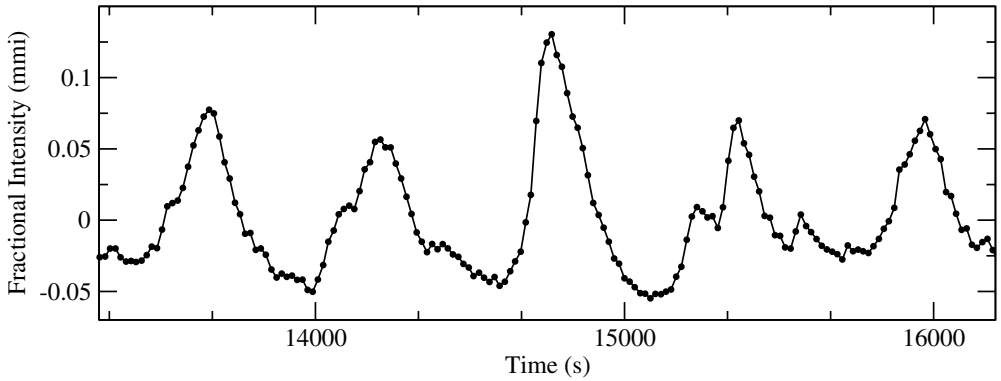

Figure 1. Portion of a high signal-to-noise SOAR light curve of EC14012-1446, showing the narrow peaks and broader valleys indicative of convective mixing. The error bars for each point are indicated by the size of the points. The dominant pulsation period is ≈600 s (1 mmi ≈1 mmag).

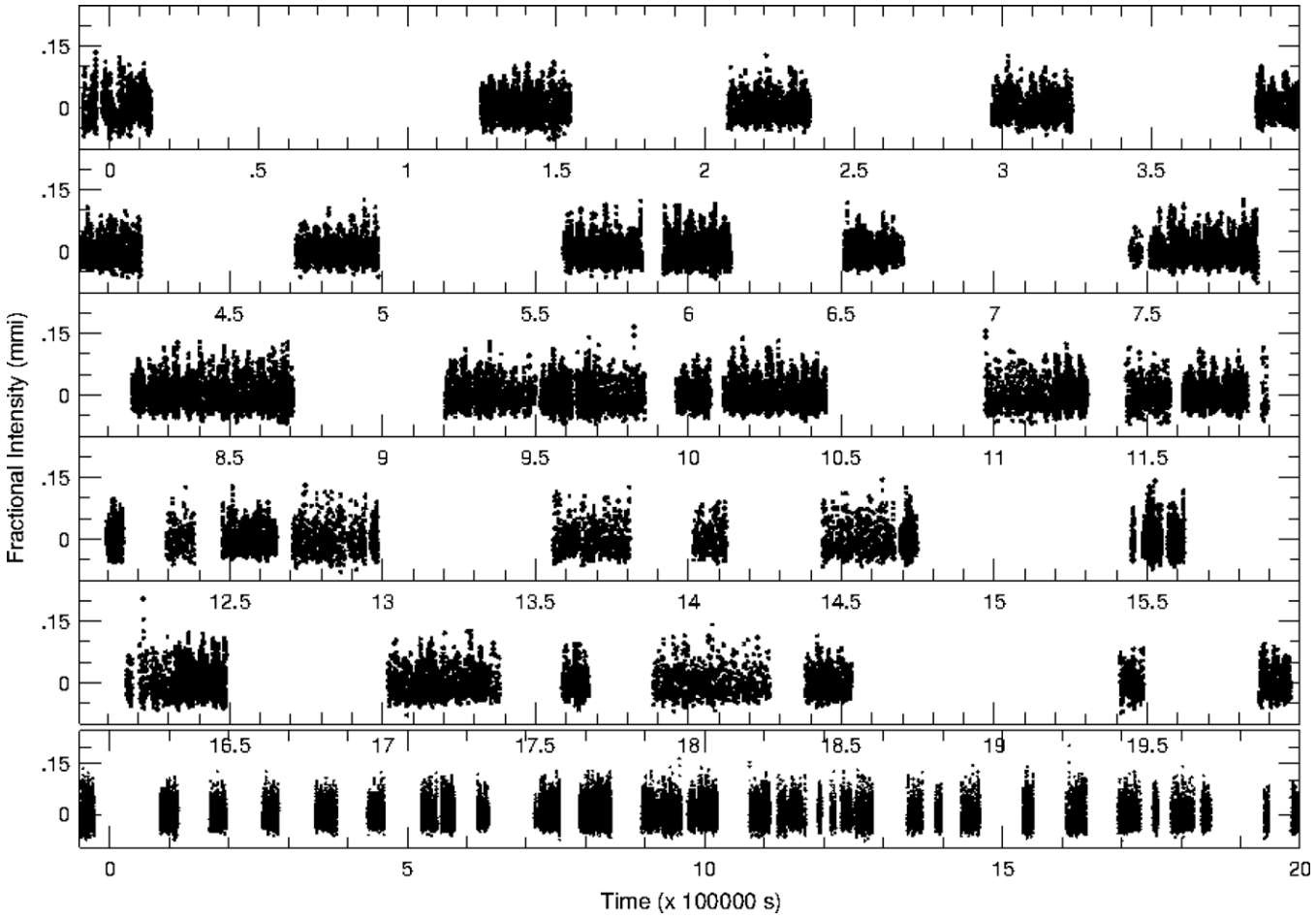

Figure 2. Final light curve of EC14012-1446 from XCOV26, representing the combination of all data listed in Table 1. The top five panels cover 400,000 s (4.63 days) each. The bottom panel displays the entire light curve, with time in days. The dominant pulsation period is ≈600 s.

2. OBSERVATIONS AND REDUCTIONS

EC14012-1446 (WD1401-147, $B = 15.67$) is a high-amplitude, multiperiodic DAV pulsator discovered by Stobie et al. (1995) and observed extensively by Handler et al. (2008). Our XCOV26 observations span 2008 March 25 to April 29, achieving 80% coverage during the central five days of the run (Figure 2). Twenty-seven telescopes distributed around the globe participated in XCOV26, 15 of which contributed a total of 71 runs (Table 1) on EC14012-1446. The observations were obtained with different CCD photometers, each with distinct effective bandpasses. We minimize the bandpass issues by using CCDs with similar detectors where possible and employing a red cutoff filter (BG40 or S8612) to normalize wavelength response and reduce extinction effects.

Standard procedure for a WET run calls for observers to transfer raw images and calibration files to WET headquarters for analysis at the end of each night. CCD data reduction follows the steps outlined in Provencal et al. (2009). We corrected each image for bias and thermal noise, and normalized by the flat field. Aperture photometry using the IRAF photometry pipeline described by Kanaan et al. (2002) was performed on each image, utilizing a range of aperture sizes for the target and selected comparison stars. We used the WQED pipeline (Thompson

Table 1
Journal of XCOV26 Observations EC14012-1446

Run Name	Telescope (m)	Detector	Date	Length (hr)
hawa20080325-09	Hawaii 2.2	E2V ccd47-10	2008 Mar 25	6.2
saao20080326-21	SAAO 1.0	UCT CCD	2008 Mar 26	5.9
tene20080327-20	Tenerife 0.8	TK1024	2008 Mar 27	3.0
saao20080327-20	SAAO 1.0	UCT CCD	2008 Mar 27	7.5
saao20080328-20	SAAO 1.0	UCT CCD	2008 Mar 28	7.3
saao20080329-20	SAAO 1.0	UCT CCD	2008 Mar 29	7.2
tene20080330-03	Tenerife 0.8	TK1024	2008 Mar 30	2.9
saao20080330-20	SAAO 1.0	UTC CCD	2008 Mar 30	7.5
saao20080331-20	SAAO 1.0	UTC CCD	2008 Mar 31	7.1
mcdo20080401-05	McDonald 2.1	E2V ccd57-10	2008 Apr 1	6.1*
saao20080401-20	SAAO 1.0	UTC CCD	2008 Apr 1	5.4
loia20080403-00	Loia 1.52	EEV 1300×1340B	2008 Apr 3	1.1
ctio20080403-01	CTIO 0.9	Tek2K$_3$	2008 Apr 3	7.5
soar20080403-02	SOAR 4.1	2K×4K MIT/Lincoln Lab CCD	2008 Apr 3	7.6*
sara20080403-05	SARA 1.0	CCD	2008 Apr 3	6.3
mcdo20080403-08	McDonald 2.1	E2V ccd57-10	2008 Apr 3	3.0
saao20080403-20	SAAO 1.0	UCT CCD	2008 Apr 3	6.8
salt20080403-21	SALT 10.0	CCD	2008 Apr 3	1.0
soar20080404-01	SOAR 4.1	CCD	2008 Apr 4	7.7*
salt20080404-02	SALT 10.0	E2V 44-82	2008 Apr 4	0.7
ctio20080404-02	CTIO 0.9	Tek2K$_3$	2008 Apr 4	7.0
mcdo20080404-05	McDonald 2.1	E2V ccd57-10	2008 Apr 4	5.4*
sara20080404-10	SARA 1.0	CCD	2008 Apr 4	0.6
saao20080404-21	SAAO 1.0	UTC CCD	2008 Apr 4	6.4
salt20080404-21	SALT 10.0	E2V 44-82	2008 Apr 4	1.0
soar20080405-01	SOAR 4.1	2K×4K MIT/Lincoln Lab CCD	2008 Apr 5	4.7*
salt20080405-02	SALT 10.0	E2V 44-82	2008 Apr 5	1.0
ctio20080405-03	CTIO 0.9	Tek2K$_3$	2008 Apr 5	6.3
mcdo20080405-09	McDonald 2.1	E2V ccd57-10	2008 Apr 5	1.7
mtjo20080405-11	Mt. John 1.0	E2V ccd57-10	2008 Apr 5	3.3
boao20080405-14	BOAO 1.8	SITe SI424AB CCD	2008 Apr 5	4.4
salt20080405-21	SALT 10.0	E2V 44-82	2008 Apr 5	1.0
saao20080405-22	SAAO 1.0	UTC CCD	2008 Apr 5	3.1
salt20080406-01	SALT 10.0	E2V 44-82	2008 Apr 6	1.0
soar20080406-02	SOAR 4.1	2K×4K MIT/Lincoln Lab CCD	2008 Apr 6	7.3*
mcdo20080406-09	McDonald 2.1	E2V ccd57-10	2008 Apr 6	2.0
ctio20080407-02	CTIO 0.9	Tek2K$_3$	2008 Apr 6	6.2
mcdo20080407-08	McDonald 2.1	E2V ccd57-10	2008 Apr 7	3.1
boao20080407-15	BOAO 1.8	SITe SI424AB CCD	2008 Apr 7	4.0
saao20080407-20	SAAO 1.0	UTC CCD	2008 Apr 7	5.9
salt20080407-20	SALT 10.0	E2V 44-82	2008 Apr 7	1.0
salt20080408-01	SALT 10.0	E2V 44-82	2008 Apr 8	1.0
ctio20080408-02	CTIO 0.9	Tek2K$_3$	2008 Apr 8	1.8
mcdo20080408-09	McDonald 2.1	E2V ccd57-10	2008 Apr 8	1.5
luli20080408-14	Lulin 1.0	E2V CCD36-40	2008 Apr 8	2.6
saao20080408-20	SAAO 1.0	UTC CCD	2008 Apr 8	4.9
ctio20080409-02	CTIO 0.9	Tek2K$_3$	2008 Apr 9	6.6
mcdo20080409-09	McDonald 2.1	E2V ccd57-10	2008 Apr 9	0.6
ctio20080410-02	CTIO 0.9	Tek2K$_3$	2008 Apr 10	6.9
boao20080410-14	BOAO 1.8	SITe SI424AB CCD	2008 Apr 10	3.0
ctio20080411-02	CTIO 0.9	Tek2K$_3$	2008 Apr 11	6.6
mcdo20080411-09	McDonald 2.1	E2V ccd57-10	2008 Apr 11	1.5
mcdo20080412-06	McDonald 2.1	E2V ccd57-10	2008 Apr 12	0.3
kpno20080412-07	KPNO 2.0	E2V ccd47-10	2008 Apr 12	3.7
ctio20080413-02	CTIO 0.9	Tek2K$_3$	2008 Apr 13	4.4
mcdo20080413-06	McDonald 2.1	E2V ccd57-10	2008 Apr 13	4.7
ctio20080414-02	CTIO 0.9	Tek2K$_3$	2008 Apr 14	7.1
kpno20080414-04	KPNO 2.0	E2V ccd47-10	2008 Apr 14	2.4
lash20080414-08	Las Cumbres 2.0	E2V CCD42-40	2008 Apr 14	3.4
mcdo20080414-09	McDonald 2.1	E2V ccd57-10	2008 Apr 14	1.7
luli20080414-17	Lulin 1.0	E2V CCD36-40	2008 Apr 14	2.4
ctio20080415-02	CTIO 0.9	Tek2K$_3$	2008 Apr 15	6.6
lash20080415-09	Las Cumbres 2.0	E2V CCD42-40	2008 Apr 15	3.8
luli20080415-16	Lulin 1.0	E2V ccd36-40	2008 Apr 15	4.3
mabu20080415-20	Mt. Abu 1.2	TEK CCD	2008 Apr 15	1.3

Table 1
(Continued)

Run Name	Telescope (m)	Detector	Date	Length (hr)
mabu20080416-20	Mt. Abu 1.2	TEK CCD	2008 Apr 16	2.2
kpno20080417-09	KPNO 2.0	E2V ccd47-10	2008 Apr 17	2.8
kpno20080418-07	KPNO 2.0	E2V ccd47-10	2008 Apr 18	3.9
braz20080426-04	LNA 1.6	WI106 CCD	2008 Apr 26	2.1
braz20080427-05	LNA 1.6	WI106 CCD	2008 Apr 27	1.9
braz20080428-04	LNA 1.6	WI106 CCD	2008 Apr 28	1.9
braz20080429-05	LNA 1.6	WI106 CCD	2008 Apr 29	1.2

Note. * High signal-to-noise light curves used for light curve fitting. All other observations were used to obtain accurate frequency information.

& Mullally 2009) to examine each nightly light curve for photometric quality, remove outlying points, divide by a suitable comparison star, and correct for differential extinction. Our observational technique is therefore not sensitive to oscillations longer than a few hours. The result is light curves with amplitude variations represented as fractional intensity (mmi). The unit is a linear representation of the fractional intensity of modulation (1 mmi ≈1 mmag). We present our FTs in units of modulation amplitude (1 mma = 1×10^{-3} ma = 0.1% = 1 ppt).

The final reduction step combines the individual light curves to produce the complete light curve for EC14012-1446. We assume EC14012-1446 oscillates about a mean light level. This assumption allows us to carefully assess overlapping segments from different telescopes and identify and correct any vertical offsets. As discussed in detail in Provencal et al. (2009), we find no significant differences between the noise levels of amplitude spectra using (1) the combination of all light curves including overlapping segments from different telescopes, (2) the combination of light curves where we retain only higher signal-to-noise observations in overlapping segments, and (3) combining all light curves using data weighted by telescope aperture.

The final XCOV26 light curve contains 308.3 hr of high-speed photometry. Our coverage is not complete, and this incompleteness produces spectral leakage in the amplitude spectrum. To quantify this, we sampled a single sinusoid using exactly the same times as the original data. The resulting amplitude spectrum, or "spectral window," is the pattern produced in the XCOV26 FT by a single frequency. The FT and spectral window of the complete light curve are given in Figure 3.

3. FREQUENCY IDENTIFICATION

3.1. Stability

Following Provencal et al. (2009), we begin by examining the stability of EC14012-1446's pulsation amplitudes and frequencies throughout the run. Amplitude and/or frequency variations produce artifacts in FTs, and greatly complicate the identification of intrinsic pulsation frequencies (Kepler et al. 2003). We divide the data set into three chunks, each spanning ≈185 hr (7.8 days). The FT of each chunk is given in Figure 4. Several of the dominant frequencies are consistent to within measurement error, but we do find evidence of amplitude variations in a number of frequencies.

We calculated spectrograms for the five largest amplitude frequencies to further explore the nature of these amplitude variations (Figure 5). A spectrogram quantifies the behavior of frequencies and amplitudes as a function of time. Our spectrograms are generated by dividing the total light curve into multiple 5 day segments, each of which overlap by 4.95 days. The FT of each segment is a measurement of frequencies and amplitudes centered on a specific time. Each panel in Figure 5 is an amalgam, where each segment FT corresponds to a vertical line. The *x*-axis is time, the *y*-axis is frequency, and amplitude is represented by color and is normalized to an amplitude of 1. The bottom panel in Figure 5 gives the pattern generated by a single sinusoid sampled with exactly the same times as the segment light curves (a time-dependent spectral window). The results show a slow 18σ increase in the amplitude of the dominant 1633.907 μHz (612 s) peak, from ≈22 to ≈31 mma, over the course of the run. We also find a similar increase in the 1548.146 μHz (645 s) peak. The 2308 μHz (433 s) peak shows a 25% decrease in amplitude during the middle of the run and a large apparent decrease at the end of the run. The amplitudes of the remaining two frequencies are consistent to within 3σ.

3.2. The XCOV26 Fourier Transform

Armed with amplitude stability information for the five largest peaks, we are ready to take a careful look at EC14012-1446's XCOV26 FT. We use *Period04* (Lenz & Breger 2005) for Fourier analysis and nonlinear least-squares fitting to select the statistically significant peaks in the XCOV26 FT. As detailed in Provencal et al. (2009), we adopt the criterion that a peak must have an amplitude at least four times greater than the mean noise level in the given frequency range. We define "noise" as the frequency-dependent mean amplitude after prewhitening by the dominant frequencies. This is a conservative estimate, as it is impossible to ensure that all of the "real" frequencies are removed when calculating the noise level. This is certainly true for EC14012-1446, where the peaks above ≈3000 μHz are mainly combination frequencies. Figure 6 displays the mean amplitude, specified as the square root of the simple mean power using a boxcar of 100 μHz, after prewhitening by 62 frequencies, as a function of frequency. Our noise is somewhat frequency dependent, but is near 0.2 mma.

To confirm our uncertainty estimates, we calculated Monte Carlo simulations using the routine provided in *Period04*. This routine generates a set of light curves using the original times, the fitted frequencies and amplitudes, and added Gaussian noise. A least-squares fit is performed on each simulated light curve, with the distribution of fit parameters giving the uncertainties. Our Monte Carlo results are consistent with our mean amplitude noise estimates of ≈0.2 mma.

Our frequency selection procedure involves identifying the largest amplitude resolved peak in the FT, fitting a sinusoid with that frequency to the data set, subtracting the fit from the light curve, recomputing the FT, examining the residuals, and repeating the process until no significant power remains.

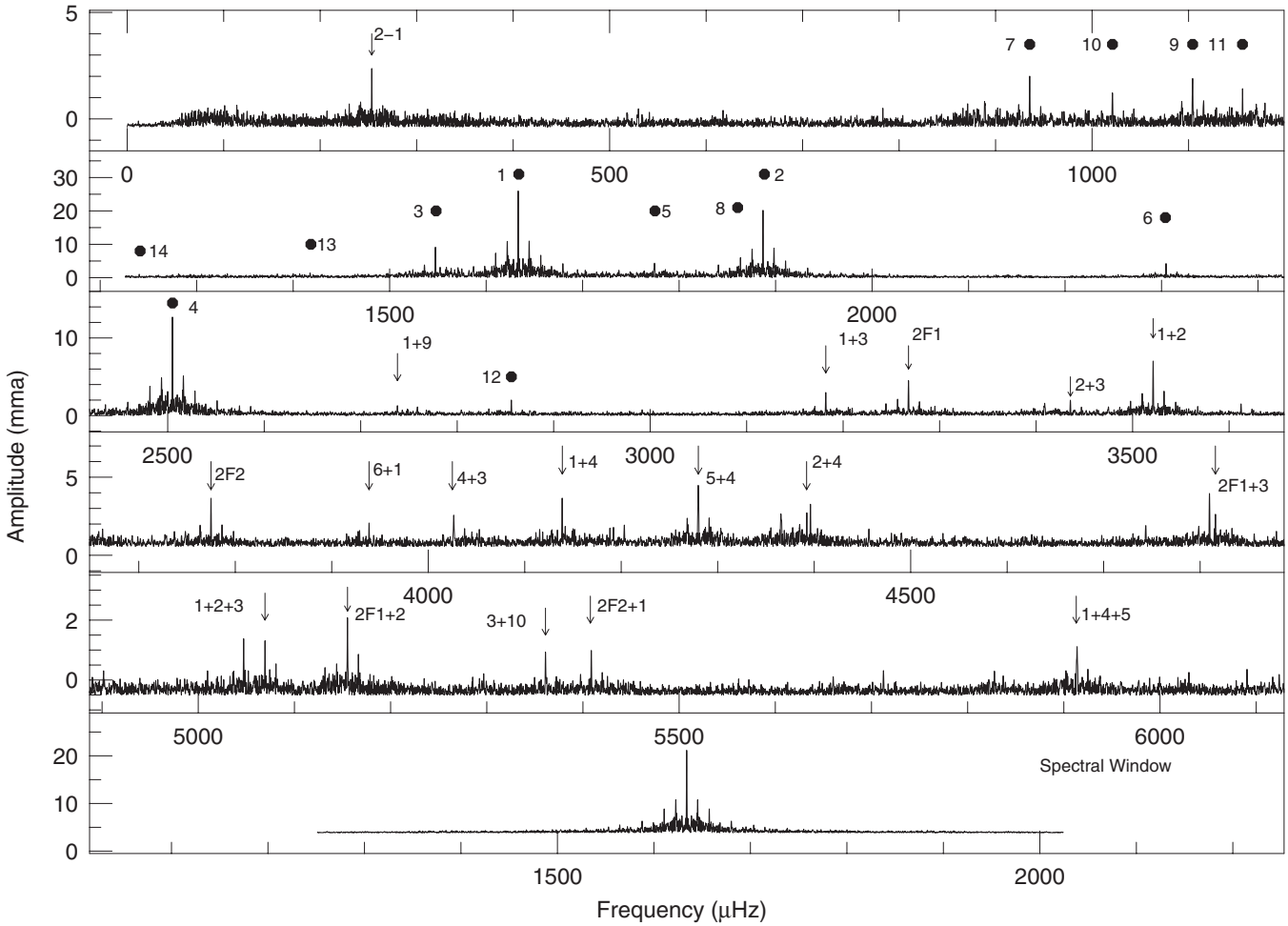

Figure 3. FT of the 2008 EC14012-1446 photometry observations (note vertical scale in each panel). Solid dots label 14 modes containing 19 independent frequencies. Arrows indicate a sample of combination frequencies (for example F1+F2). Unlabeled peaks are second-order (for example F1+F2) and third-order (for example F1+F2+F3) combinations. The spectral window is plotted in the last panel. Tables 2 and 3 list exact frequency identifications.

This technique, known as prewhitening, must be employed with an abundance of caution, especially since we are aware of amplitude and/or frequency modulation in our data set. The modulation will create artifacts that masquerade as additional frequencies. To illustrate, let us examine the region of dominant power at 1633.907 μHz (Figure 7). Comparison of the original FT (top panel) with the spectral window (bottom panel) demonstrates that most of the signal is concentrated at 1633.907 μHz. We fit a sinusoid to the data to determine frequency, amplitude, and phase, and subtract the result from the original light curve. The second panel of Figure 7 shows the prewhitened FT. Careful examination reveals two residual peaks (at 1633.450 and 1624.015 μHz identified with arrows) that are clearly not components of the spectral window. A third peak at 1622 μHz is part of a window pattern associated with 1633.450 μHz, but the alias pattern is asymmetric. Panel 3 shows the results of prewhitening by a simultaneous fit of 1633.907 and 1633.450 μHz. Both frequencies are removed, and 1622 μHz is diminished, leaving 1624.015 μHz. We next subtract a simultaneous fit of 1633.907, 1633.450, and 1624.015 μHz, with the results displayed in panel 4 of Figure 7. No significant power remains. However, a red flag is raised: the separation between 1633.907 and 1633.450 μHz is 0.457 μHz, the inverse of which is the run length. The 1633.450 μHz peak is a manifestation of the amplitude changes observed in Figure 5 and is not included in our final frequency list.

Similar analyses of several other frequencies turned out to be unexpectedly complex. The power at 1775 μHz (labeled "5" in Figure 3) is unresolved. Figure 8 establishes that prewhitening this peak requires four closely spaced frequencies, with frequency differences very similar to the inverse of the run length. This is a clear signature of amplitude and/or frequency instability. Figure 9 shows the spectrogram of this region using the same criteria as the spectrograms in Figure 5. Unlike the slow amplitude increase observed with the 1633 μHz peak, the 1775 μHz peak undergoes remarkably sudden variations, on timescales of a few days. We also find a decrease in its frequency of 1.2 μHz (5σ) over the course of the run. A second region of power at 1860 μHz displays similar behavior. Both peaks are labeled in Table 2.

Our final identifications result from a simultaneous nonlinear least-squares fit of 19 independent frequencies, amplitudes, and phases as well as 68 combination frequencies. Combination frequencies are fixed with respect to their parents but their amplitudes and phases are allowed to vary. Table 2 lists 19 identified independent frequencies, with consideration to those exhibiting amplitude and/or frequency modulation. The list includes a doublet with a splitting of 9.9 μHz associated with the

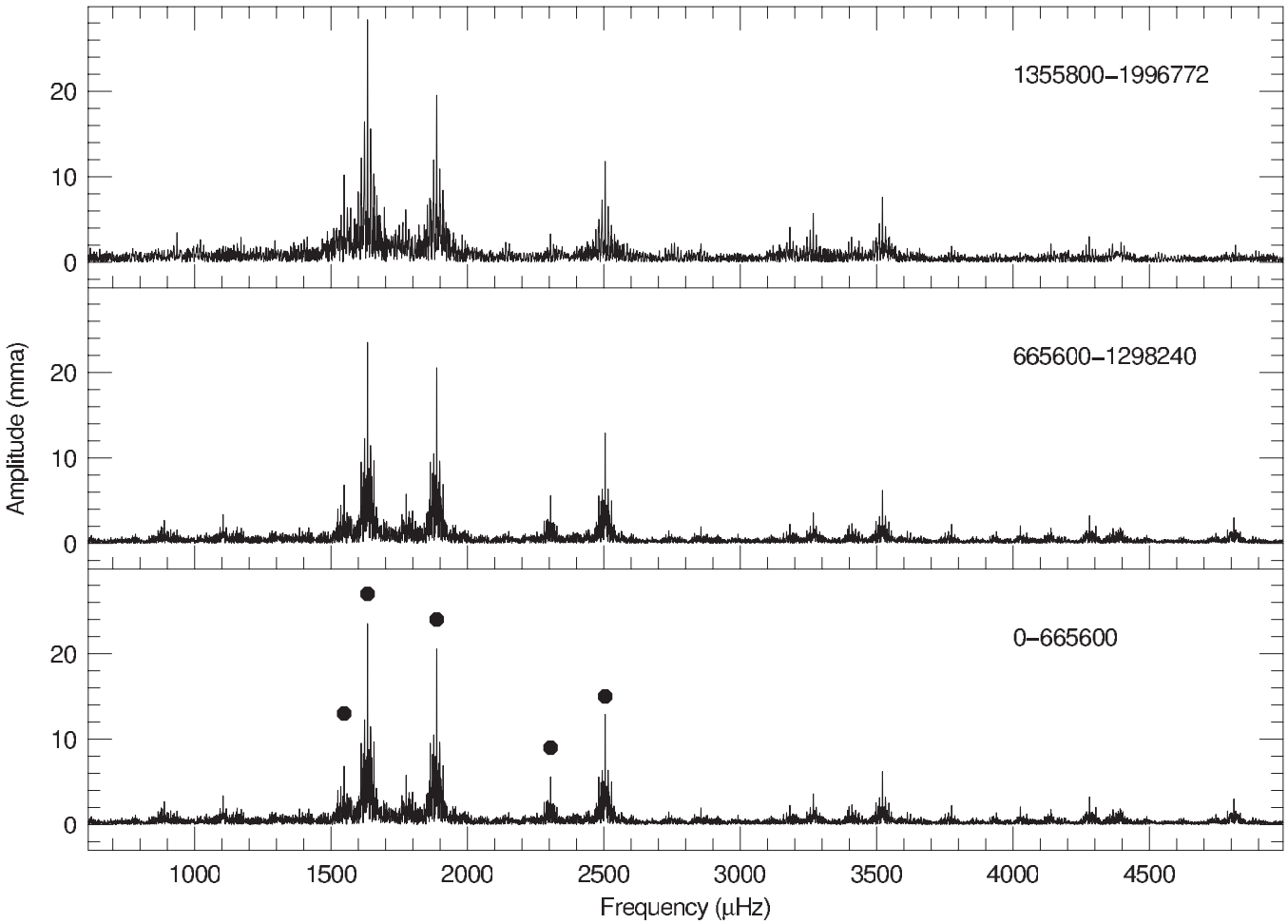

Figure 4. FTs of the EC14012-1446 data set subdivided into three chunks of ≈185 hr each. The labels in the right of each panel give the time segment covered by each chunk. The black points in the bottom panel identify the five largest amplitude modes. Some changes in each FT can be explained as differences in the window structure and effective resolution for each chunk. In particular, the final chunk has the least data coverage. We do find evidence of amplitude and/or frequency variations during the run. All peaks with frequencies higher than ≈3000 μHz are combination peaks.

1633.907 μHz peak (labeled 1 in Figure 3), a triplet at 1887 μHz with an average splitting of 3.8 μHz (labeled 2 in Figure 3), and a second doublet with a splitting of 3.1 μHz at 2504 μHz (labeled 4 in Figure 3). Table 3 presents the largest amplitude combination frequencies (see Section 4.1).

4. MODE IDENTIFICATION

Our ultimate goal is to use EC14012-1446's nonlinear light curve to extract the star's convective parameters. The requirements for convective light curve fitting include precise knowledge of the target star's frequencies and amplitudes, as well as a good idea of the (l, m) values for these frequencies. The parameter space to be explored to determine the best convective light curve fit is greatly constrained by knowledge of (l, m) indices for the excited pulsations. Montgomery's first application of this technique focused on the DA pulsators G29-38 and GD154 (Montgomery 2005a). In the data sets used, these objects were dominated by a single pulsation mode, so the number of potential (l, m) identifications was small enough that all possibilities could be explored. Montgomery et al. (2010b) recently expanded this work to the multiperiodic pulsator GD358, a well-studied object with detailed (l, m) identifications of its pulsation modes (Provencal et al. 2009; Metcalfe et al. 2000; Winget et al. 1994). While XCOV26 provided precise frequencies and amplitudes for the modes in EC14012-1446 (see Table 2), we lack prior (l, m) identifications. Even limiting ourselves to $l = 1$ and 2, as these are the spherical degrees most often observed in pulsating white dwarfs, yields a total number of possible combinations of order $(2l + 1)^{19}$, a very large number indeed. In this section, we will rely on analysis of the combination frequencies and the support of asteroseismology to constrain (l, m) identifications in EC14012-1446.

4.1. Combination Frequencies

Combination frequencies are typically observed in the FTs of moderate to large amplitude pulsators (e.g., Provencal et al. 2009; Dolez et al. 2006; Handler et al. 2002); they are identified by their relationships, which must be exact within measurement error. Combination frequencies can be integer multiples of a single parent (harmonics) or sums (or differences) of any two modes. These frequencies are not independent, but result from nonlinear effects most likely associated with the surface convection zone (Brickhill 1992; Brassard et al. 1995; Wu 2001; Ising & Koester 2001). Wu (2001) shows that the observed amplitudes of combination frequencies depend on geometric factors such as the (l, m) indices of the parent(s) and the inclination of the pulsation axis to the line of sight. EC14012-1446's FT contains a rich distribution of combinations that

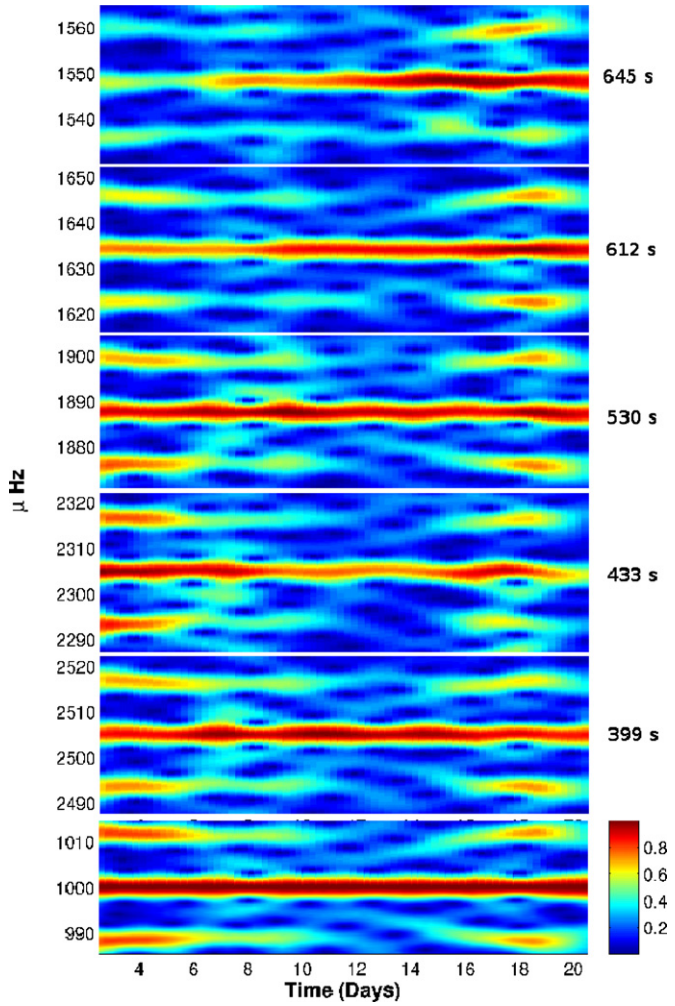

Figure 5. Spectrogram of the five largest amplitude modes in EC14012-1446's FT, arranged in order of decreasing period. The bottom panel gives the time-varying spectral window for a sample frequency at 1000 μHz (the pattern given by a single sinusoid sampled at exactly the same times as the data). Each panel is normalized to an amplitude of 1. We find a slow amplitude increase in the 1633.907 μHz (612 s) and 1548.146 μHz (645 s) peaks. In addition, the 2308 μHz (433 s) peak shows a decrease in amplitude during the middle of the run.

(A color version of this figure is available in the online journal.)

involve 13 of the 19 independent frequencies listed in Table 2. Our goal is to exploit the geometric sensitivities to provide (l, m) constraints for these frequencies.

Wu (2001) and Yeates et al. (2005) lay the foundations for our analysis by describing analytical expressions for the predicted amplitudes and phases of combination frequencies. These quantities depend on the inclination angle θ of the pulsation axis to the line of sight, the (l, m) indices of the parent mode(s), the amplitudes of the parent mode(s), and parameters describing the convection zone. To minimize the dependence on the convective parameters and focus on the geometric factors (l, m) and θ, our analysis follows Yeates et al. (2005) and considers only combination frequencies that are the sum of two parent frequencies. We combine a genetic algorithm (Charbonneau 1995) with Wu's (2001) formulae, and incorporate an improved treatment of limb darkening taken directly from the models of Koester (Montgomery et al. 2010b). For a single run of the code, the best simultaneous fit to the observed amplitudes of the parent and combination frequencies utilizes multiple generations and minimizes the root-mean-

Table 2
Table of XCOV27 Independent Frequencies

ID	Frequency (μHz)	Period (s)	Amplitude (mma)	S/N	Notes
7	935.3799 ± 0.002	1069.085	2.7 ± 0.1	9	
10	1021.139 ± 0.002	979.299	1.7 ± 0.1	8	
9	1104.252 ± 0.001	905.591	2.2 ± 0.2	10	
11	1155.925 ± 0.002	865.108	1.9 ± 0.2	8	
14	1241.403 ± 0.002	805.540	1.2 ± 0.2	5	
13	1418.369 ± 0.002	705.035	1.2 ± 0.2	5	
3a	1521.575 ± 0.002	657.214	2.2 ± 0.2	9	[a]
3	1548.146 ± 0.001	645.933	7.9 ± 0.1	32	
1a	1624.015 ± 0.003	615.758	3.1 ± 0.2	13	[a]
1	1633.907 ± 0.001	612.030	25.7 ± 0.1	104	
5	1774.989 ± 0.100	563.384	7.2 ± 0.3	9	[b]
8	1860.248 ± 0.400	537.563	6.4 ± 0.4	11	[b]
2a	1883.555 ± 0.003	530.911	1.5 ± 0.2	5	[a]
2	1887.404 ± 0.001	529.828	20.7 ± 0.1	79	
2b	1891.142 ± 0.002	528.781	3.8 ± 0.2	14	[a]
6	2304.745 ± 0.001	433.887	4.7 ± 0.1	23	[b]
4	2504.897 ± 0.001	399.218	12.7 ± 0.1	71	
4a	2508.060 ± 0.002	398.715	2.1 ± 0.2	12	[a]
12	2856.155 ± 0.002	350.121	2.0 ± 0.2	9	

Notes.
[a] Frequency IDs with small letters indicate components of the same multiplet.
[b] Frequencies displaying long timescale amplitude modulation.

Table 3
Table of Combination Frequencies

Frequency	Period (μHz)	Amplitude (s)	S/N (mma)	Parents
253.466 ± 0.002	3945.302	2.9 ± 0.2	9	2−1
2569.286 ± 0.002	350.121	0.6 ± 0.2	4	1+7
2738.153 ± 0.002	365.210	0.9 ± 0.2	4	1+9
3096.255 ± 0.002	322.971	0.6 ± 0.2	3	2f3
3182.045 ± 0.002	314.263	2.7 ± 0.2	12	1+3
3267.794 ± 0.002	306.015	4.3 ± 0.2	13	2f1
3408.939 ± 0.002[a]	293.346	1.6 ± 0.2	5	6+5
3409.912 ± 0.002[a]	293.263	1.7 ± 0.2	4	1+5
3435.538 ± 0.002	291.075	2.0 ± 0.2	6	2+3
3494.064 ± 0.002[a]	286.152	0.8 ± 0.2	4	1+8
3521.306 ± 0.002	283.986	7.0 ± 0.2	33	1+2
3525.050 ± 0.002	283.684	0.9 ± 0.2	5	1+2b
3774.810 ± 0.001	264.914	2.1 ± 0.2	12	2f2
3938.646 ± 0.002	253.894	0.9 ± 0.2	5	1+6
4026.445 ± 0.002	248.358	1.4 ± 0.2	7	4+3a
4053.043 ± 0.002	246.728	0.7 ± 0.2	4	3+4
4138.800 ± 0.002	241.616	2.0 ± 0.2	8	1+4
4192.150 ± 0.002	238.541	0.7 ± 0.2	4	2+6
4279.907 ± 0.002[a]	233.650	2.6 ± 0.2	10	4+5
4365.040 ± 0.002[a]	234.464	0.9 ± 0.2	4	4+8
4365.608 ± 0.002[a]	229.063	1.3 ± 0.2	5	4+8
4392.348 ± 0.002	227.669	1.5 ± 0.2	7	2+4
4396.055 ± 0.002	227.477	1.8 ± 0.2	8	2b+4
4743.561 ± 0.002	210.812	0.9 ± 0.2	5	2+12
4809.633 ± 0.002	207.916	2.2 ± 0.2	12	4+6
5009.696 ± 0.002	199.613	0.7 ± 0.2	4	2f4
5155.187 ± 0.002	193.979	2.2 ± 0.2	8	1+1+2
5361.052 ± 0.002	186.531	1.2 ± 0.2	6	3+10
5408.698 ± 0.002	184.887	1.3 ± 0.2	6	3+3+1
5913.800 ± 0.002	169.096	1.4 ± 0.2	7	1+4+5

Note. [a] Combination including parent with amplitude modulation.

squared residuals, $\mathrm{Res}_{\mathrm{rms}}$, between the predicted and observed amplitudes. In practice, we run the code 1000 times and select

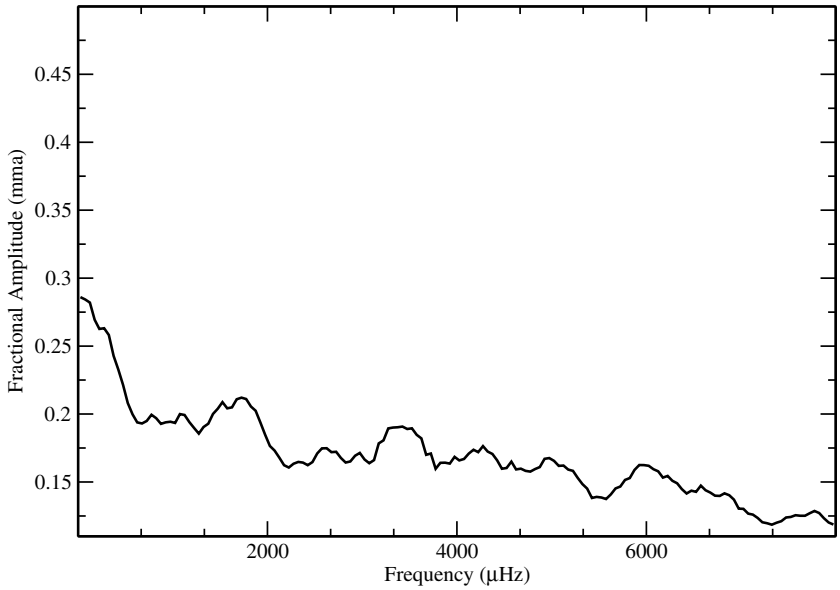

Figure 6. Mean noise as a function of frequency for XCOV26. The data set was prewhitened by the 62 largest amplitude frequencies. Our noise is frequency dependent, but is near 0.2 mma. This is a conservative estimate, as we have probably not prewhitened by all the combination frequencies.

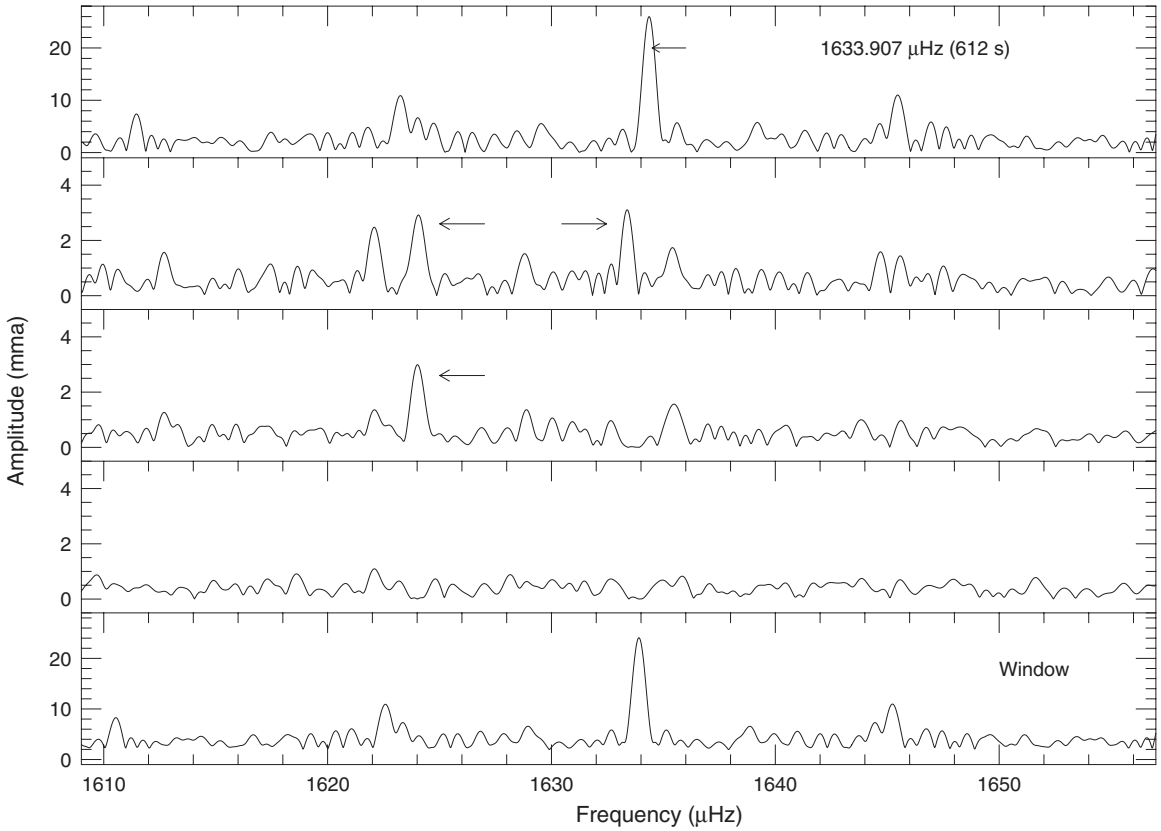

Figure 7. Prewhitening of the dominant 1633.907 μHz mode in the 2008 FT. We begin with the removal of the largest amplitude resolved peak (top panel), a careful comparison of the residuals in the next panel with the spectral window (last panel), and the subsequent removal of additional frequencies. The fourth panel shows the residuals after simultaneously removing 1633.907, 16233.450, and 1624.017 μHz. The 1633.450 μHz component (right arrow in the second panel) is the result of amplitude changes.

the solutions having $\mathrm{Res_{rms}}$ below a limiting value. This process produces a sample of best-fit solutions whose distribution provides information on the range of values allowed for these parameters.

To test that this approach recovers known input, we used the nonlinear light curve fitting code of Montgomery et al. (2010b) to generate a synthetic light curve based on EC14012-1446's parent frequencies. The nonlinear light curve fitting code is discussed in more detail in Section 5. For our purposes in this test, the importance of using synthetic light curves generated by this code rather than a simple simulation employing multiple sine functions is that the synthetic light curve will include

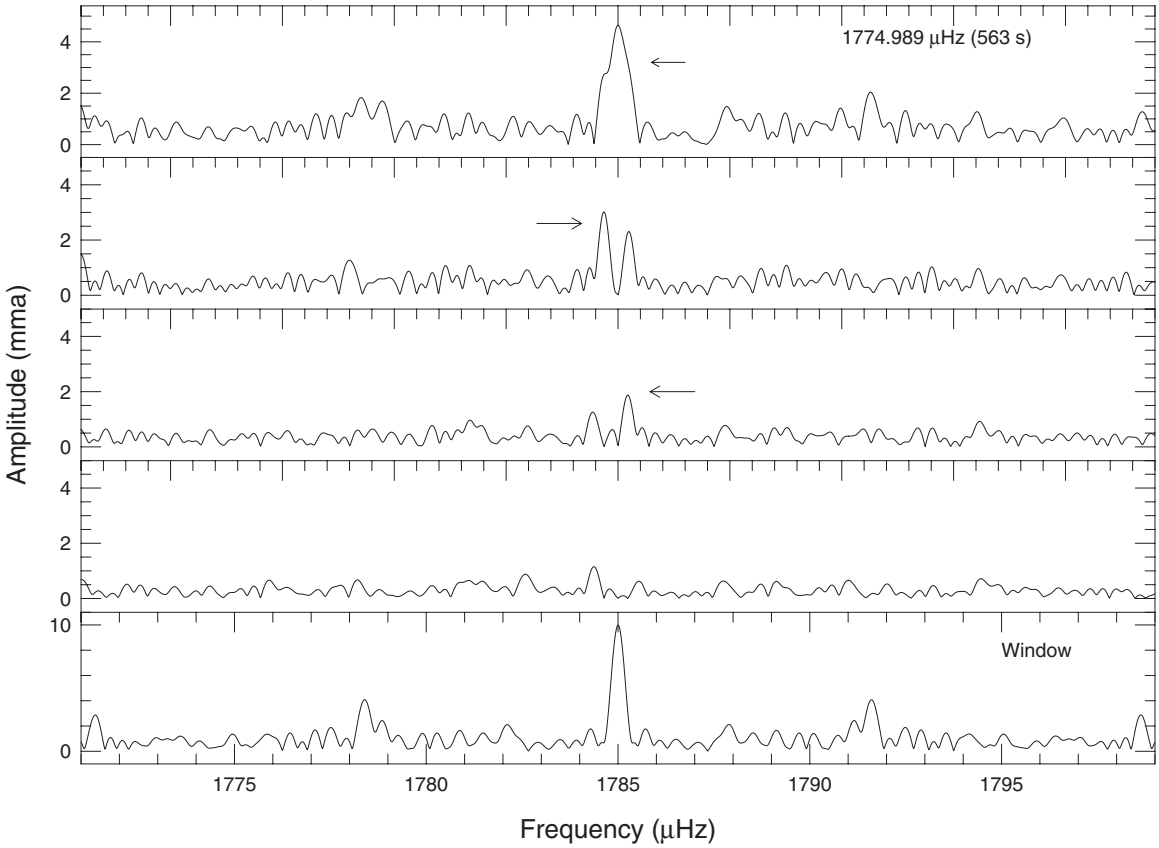

Figure 8. 1775 μHz (563 s) mode in the 2008 FT. This power is unresolved and requires at least four closely space frequencies for prewhitening, with frequency differences very similar to the inverse of the run length. This is a clear signature of amplitude and/or frequency instability.

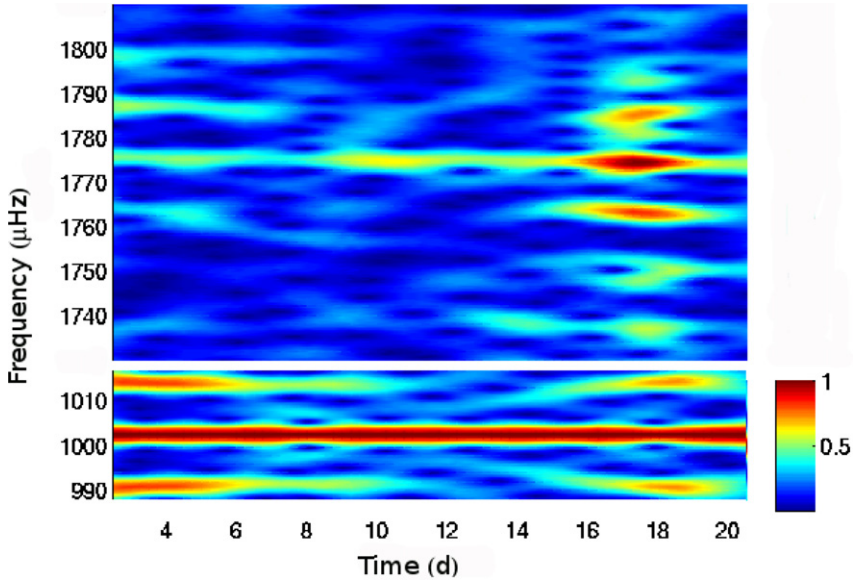

Figure 9. Spectrogram of the 1775 μHz region in the 2008 FT. This region of power exhibits remarkable amplitude changes on a timescale of days. The bottom panel gives the time-dependent window. The spectrogram amplitudes (colors) have been normalized to a value of 1.
(A color version of this figure is available in the online journal.)

combination frequencies produced via nonlinear effects due to convection (Montgomery et al. 2010b). Our purpose is to recover the input frequency identifications using these combination frequencies. We assigned reasonable (l, m) values to the input frequencies, chose values for θ, the time-averaged convective response time τ_0, and A_o, where A_o describes the response of the stellar material to the pulsations and includes a bolometric correction factor (Wu 2001), and added noise. Using the method outlined in the previous paragraph, we successfully recovered (l, m) for all large-amplitude input parent frequencies, while experiencing some disagreement with low-amplitude parents. This is because low-amplitude modes have even lower amplitude

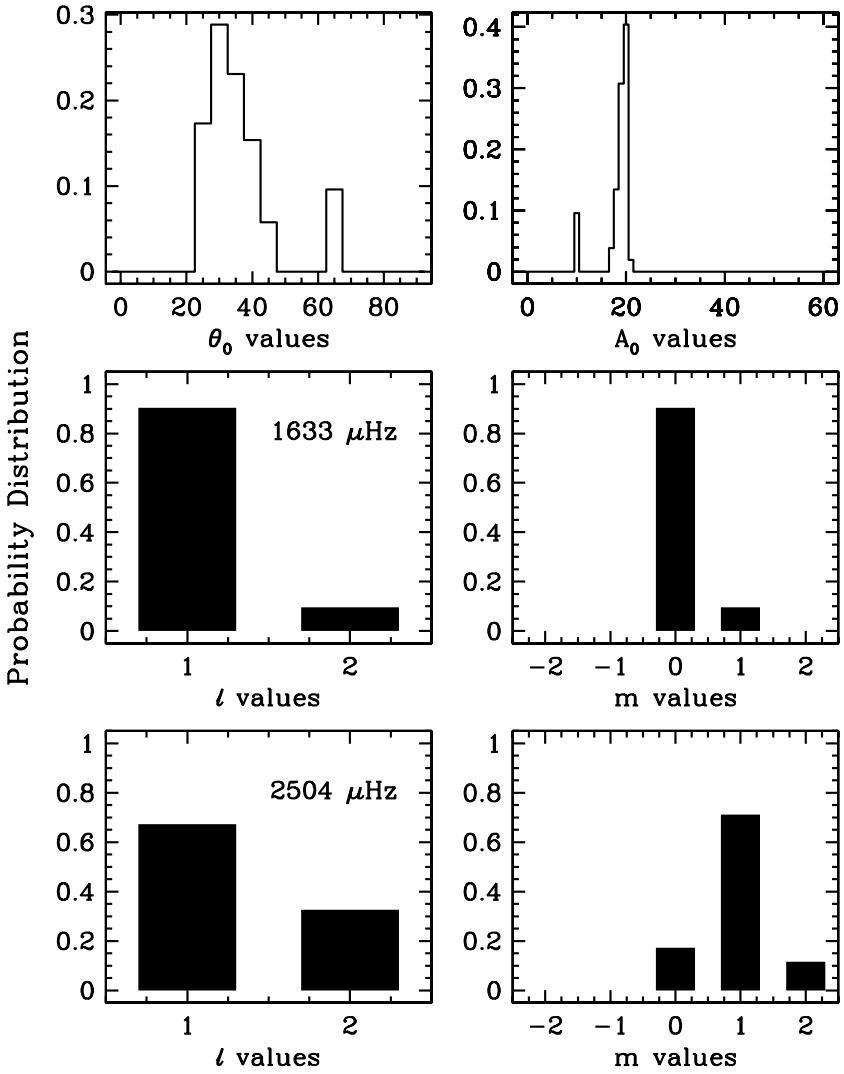

Figure 10. Probability distribution (from 0 to 1) of l, m, θ, and A_o for the 1633.907 μHz (612 s) and the 2504.897 μHz (399 s) variations. The solutions are from individual runs with $Res_{rms} < 0.38$ mmi. The top panel gives the probability distributions of θ and A_o found for all frequencies, with preferred values of $\theta \sim 32^\circ$ and $A_o \sim 20$, respectively. The middle and lower panels give the l and m identification distributions for the 1633.907 μHz (612 s) and 2504.897 μHz (399 s) modes. The amplitudes of EC14012-1446's observed combination frequencies argue that 1633.907 μHz is $l = 1$, $m = 0$, while 2504.897 μHz is $l = 1$, $m = 1$.

combination frequencies, which are difficult to detect and so are not as numerous. Since our method treats both the high-amplitude parent modes and the low-amplitude combination frequencies equally in the fits, this has the effect of de-emphasizing the importance of low-amplitude combination frequencies.

Figure 10 shows the resulting probability distribution of l, m, θ, and A_o values for fits having $Res_{rms} < 0.38$ mmi, for EC14012-1446's 1633.907 μHz (612 s) and 2504.897 μHz (399 s) variations. For 1633.907 μHz (612 s), the analysis of combination amplitudes strongly argues that the variations are best represented as spherical degree $l = 1$ and azimuthal index $m = 0$, with an inclination angle of $30^\circ \pm 10^\circ$, and a value of $A_o = 20 \pm 2$. We find nearly identical results for 1887.404 μHz (529 s) and 1548.146 μHz (646 s). For 2504.897 μHz (399 s), we find the same distributions for θ and A_o, but in this case $(l, m) = (1, 1)$ is strongly preferred. As we found previously, the statistical significance of (l, m) identifications determined by combination amplitudes is amplitude dependent and we do not find unambiguous identifications for the lower amplitude frequencies. The complete list of (l, m) identifications derived from the combination amplitudes are given in Table 4.

Our analysis of EC14012-1446's combination amplitudes indicates that nine of the dominant independent frequencies are consistent with spherical degree $l = 1$; in Table 4 we list the most likely (l, m) identifications for these modes. We would like to constrain the identifications of the remaining independent frequencies to improve our chances of success with nonlinear convective light curve fitting. Using the combination analysis as a basis, we now turn to asteroseismology to provide constraints on the identifications of the remaining frequencies.

4.2. Asteroseismology

4.2.1. Period Spacing

As mentioned in the introduction, we look for two clues to indicate (l, m) identifications of pulsations in white dwarfs. The first is the expectation that g-mode pulsations of a given l corresponding to successive radial overtones k will be approximately equally spaced in period, provided k is large enough (Unno et al. 1989). For the simple example of a homogeneous star, we find

$$P_{kl} = k\ \Delta\Pi\ [l(l+1)]^{-1/2} + C, \quad (1)$$

Table 4
Frequency (l, m) Identifications

Frequency (μHz)	Period (s)	Combination (l, m)	Asteroseismology (l, m)	Final Nonlinear Fit (l, m)
935.3799 ± 0.002	1069.085		(1, any)	(2, −1)
1021.139 ± 0.002	979.299		(1, any)	(2, 2)
1104.252 ± 0.001	905.591		(1, any)	(2, 1)
1155.925 ± 0.002	865.108		(1, any)	(2, 2)
1241.403 ± 0.002	805.540		(1, any)	(2, 2)
1418.369 ± 0.002	705.035		(2, any)	(2, 1)
1521.575 ± 0.002	657.214		(1, 1)	1, 1)
1548.146 ± 0.001	645.933	(1, 0)	(1, any)	(1, 0)
1624.015 ± 0.003	615.758	(1, 1)	(1, 1)	(1, 1)
1633.907 ± 0.001	612.030	(1, 0)	(1, 0/1)	(1, 1)
1774.989 ± 0.100	563.384	(1, −1)	(1, any)	(1, 1)
1860.248 ± 0.400	537.563		(2, any)	(2, 0)
1883.555 ± 0.003	530.911		(1, 1)	(1, 1)
1887.404 ± 0.001	529.828	(1, 0)	(1, 0)	(1, 0)
1891.142 ± 0.002	528.781	(1, −1)	(1, −1)	(1, −1)
2304.745 ± 0.001	433.887	(1, −1)	(2, any)	(1, 0)
2504.897 ± 0.001	399.218	(1, 1)	(1, 1)	(1, 0)
2508.060 ± 0.002	398.715	(1/2, 1/0)	(1, 0)	(1, −1)
2856.155 ± 0.002	350.121	(2, 0/1)	(2, any)	(2, 0)

where $\Delta\Pi$ is a uniform period spacing, P_{kl} is the period for a given mode (k, l), and C is a constant (Tassoul et al. 1990). The mean period spacing $\Delta\Pi$ for a series of modes of a given l and consecutive k is an important asteroseismic measure of stellar mass and effective temperature that is mostly independent of internal composition (Unno et al. 1989).

A white dwarf has a host of available pulsation frequencies. For reasons that are not understood, in most cases only a subset are observed at any given time (Córsico et al. 2002). This is true for EC14012-1446. The 19 independent frequencies detected during XCOV28 show no obvious evidence of equal period spacing so we are lacking consecutive radial overtones for any l value. A good strategy to identify the complete set of available modes is to combine results from multiple seasons of observations. Handler et al. (2008) present an analysis of EC14012-1446 observations spanning 2004–2007, during which the star exhibited different subsets of excited modes. Figure 11 shows a schematic representation of excited modes for the combined observations spanning 2004–2008. Figure 12 focuses on the obvious groupings between 800 and 500 s (1250 and 2000 μHz). Since we are searching for equal period spacings, we present these figures using period as the x-axis. The large groupings at 768 s (1302 μHz), 721 s (1387 μHz), 682 s (1466 μHz), and 612 s (1633 μHz) have a decreasing observed width with shorter period. This decrease translates into an equal width in frequency space of ≈24 μHz.

We calculated a simple average period for each group, which is given in Table 5. A statistical test for the presence of uniform period spacing is provided by the Kolmogorov–Smirnov (K-S) test (Winget et al. 1991). The K-S test calculates the probability that an input list is randomly distributed. Any statistically nonrandom period spacing will therefore appear as a minimum value in the output. In our case, we use the test to determine the probability that the list of average periods in Table 5 is from a uniform distribution for a given period spacing $\Delta\Pi$ (Kawaler 1988). Figure 13 shows the results, finding a period spacing of ≈41 s, consistent with the expectations for $l = 1$ (Bischoff-Kim & Metcalfe 2012). We find no significant period spacings at ≈23 s as predicted for $l = 2$ modes.

Table 5
Table of Average Frequencies (2004–2008)

Period (s)	Frequency (μHz)	No. of peaks	Radial Overtone
2856.164	350.120	1	
2738.076	365.220	1	$k_o - 6$
2505.405	399.137	6	$k_o - 5$
2304.854	433.865	2	
1887.505	529.800	10	$k_o - 2$
1860.431	537.510	2	
1774.954	563.395	2	$k_o - 1$
1633.597	612.146	16	k_o
1548.155	645.930	2	$k_o + 1$
1463.668	683.215	8	$k_o + 2$
1418.353	705.040	1	
1384.903	722.072	14	$k_o + 3$
1332.851	750.249	1	
1298.863	769.904	6	$k_o + 4$
1219.836	819.782	2	$k_o + 5$
1163.163	859.710	2	$k_o + 6$
1136.538	879.865	4	$k_o + 7$
1104.240	905.600	1	
1035.443	965.770	2	$k_o + 9$
964.748	1036.540	3	$k_o + 11$
935.375	1069.090	1	
821.254	1217.650	1	

Notes. This table gives the simple average frequencies for the groupings in Figures 11 and 12. The column "No. of peaks" gives the number of frequencies contained within each group. The radial overtone k is impossible to determine observationally, so we give values relative to 1633 μHz, defined to have k_o. The relative k values denote a series of nearly consecutive modes of spherical index $l = 1$ with a period spacing of ≈41 s.

Using 1633.907 μHz as our reference point, we assigned relative radial overtone values to the frequencies listed in Table 5. We plot the expected locations of consecutive radial overtones for $l = 1$ in Figures 11 and 12. These points in the bottom of both figures are given with bars representing the 24 μHz "grouping" width. For periods above 900 s, the grouping

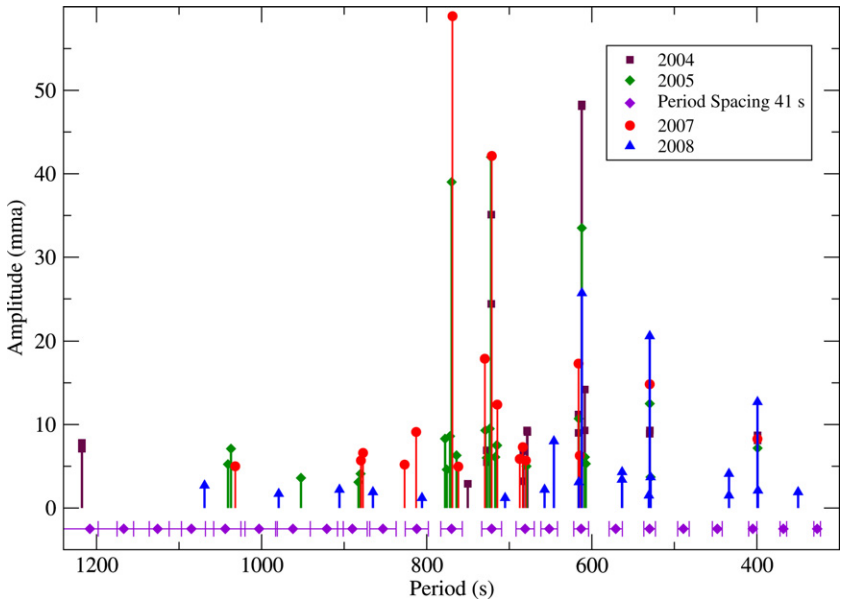

Figure 11. Schematic representation of EC14012-1446's independent frequencies for data from 2004 to 2008. The bottom points indicate the expected locations of consecutive $l = 1$ modes with a mean period spacing of 41 s. The associated bars illustrate the "grouping width" of $\pm 24\,\mu$Hz. Frequencies within this range should belong to the given k multiplet. Note that the x-axis is period, not frequency.

(A color version of this figure is available in the online journal.)

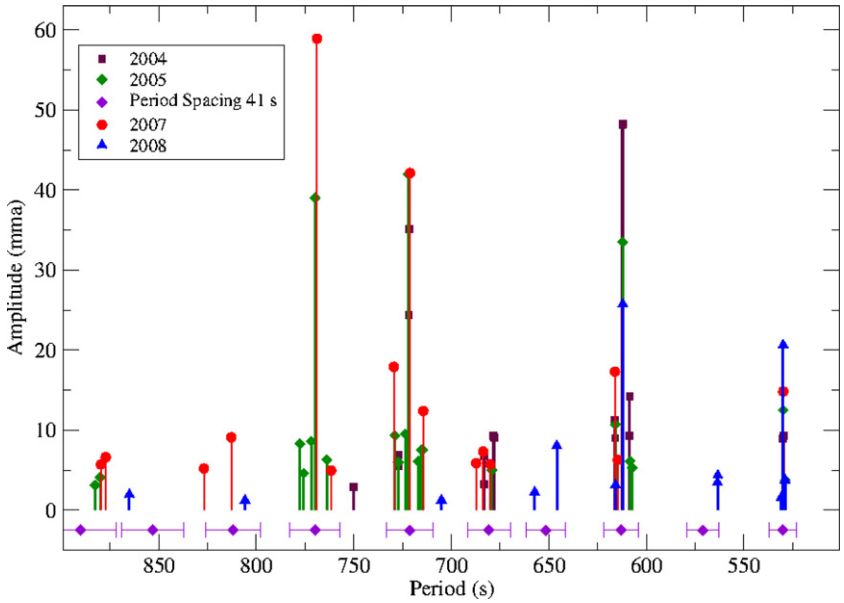

Figure 12. Zoom-in of Figure 11 to periods in the range 800–500 s. The bottom points give the expected locations of consecutive $l = 1$ modes with a mean period spacing of 41 s. The period width denoted by the bars represents the 24 μHz "grouping width" of the modes. Frequencies found within this range should belong to the given k multiplet. Please note that the x-axis is period, not frequency.

(A color version of this figure is available in the online journal.)

widths for consecutive radial overtones overlap, illustrating the difficulty of assigning relative k values to modes with periods longer than this value. Nonetheless, we find that most of EC14012-1446's pulsation frequencies can be identified as $l = 1$.

Unlike our simple example of a homogeneous star, white dwarfs are compositionally stratified, so the individual period spacings will not be uniform. We can retrieve detailed information about interior structure from the distribution of excited pulsation frequencies. A long-standing problem with the asteroseismology of DA pulsating white dwarfs is the lack of objects with rich pulsation spectra (Bischoff-Kim & Metcalfe 2012). In this respect, EC14012-1446 immediately reveals its potential. Using our calculated average periods from Table 5, we show how individual period spacings ΔP differ as a function of period (and relative k value) in Figure 14. We use "forward differencing," where ΔP is defined as $\Delta P = P_k - P_{k+1}$. The filled points represent the periods between ≈900 and 500 s that we are certain are consecutive radial overtones of $l = 1$. The open circles represent those periods above ≈900 s with ambiguous k identifications. The roughly cyclic behavior in Figure 14 is a sign of mode trapping. Mode trapping occurs in compositionally stratified stars when there is a resonance between a pulsation frequency and a surface layer. In theoretical models, a resonance occurs when a radial node coincides with a transition layer. In a DA white dwarf, transition zones occur at the

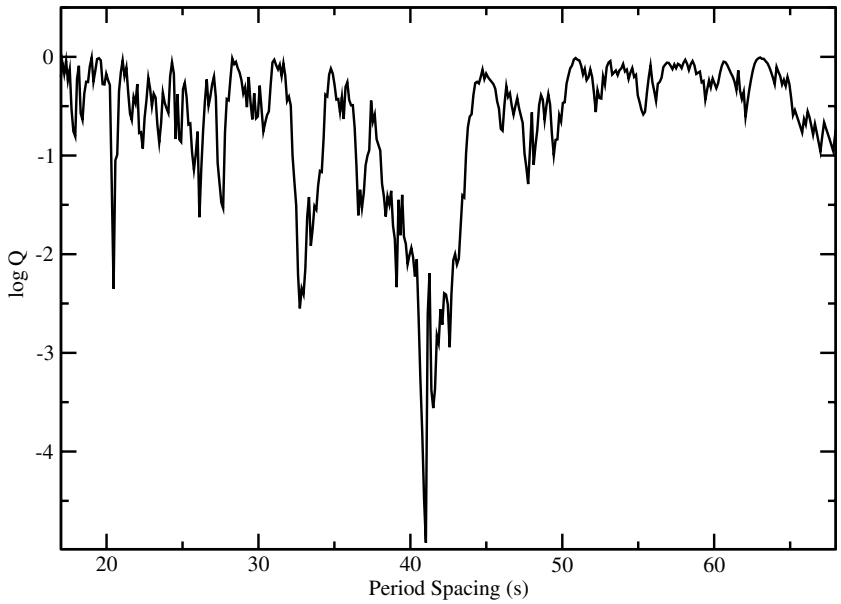

Figure 13. K-S test applied to the average periods in Table 5. A period spacing is defined as significant with a confidence level of $(1 - Q) \times 100\%$. The results reveal an average period spacing of ≈41 s with a confidence level of 99.99%.

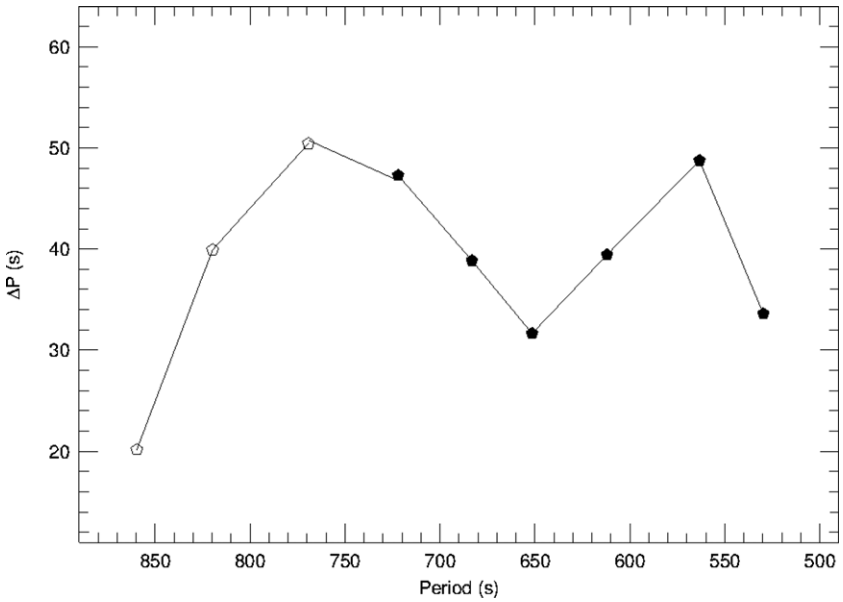

Figure 14. ΔP vs. P for EC14012-1446, using the average periods from Table 5. We use forward differencing ($\Delta P = P_k - P_{k+1}$), where the radial overtone k increases to the left. The solid points represent those frequencies with $l = 1$ identifications. The open points represent those where our identification is uncertain.

boundary of the hydrogen and helium layers, the helium layer and the carbon/oxygen core, and at points in a possibly chemically stratified core (Montgomery 2005b). The trapping cycle (the number of frequencies from minimum to minimum) is most sensitive to the location of the trapping layer, e.g., the base of the surface hydrogen layer. In addition, the trapping amplitude (the depth of the minima) is sensitive to the density gradient in the composition transition zone. In general, a larger gradient produces a larger trapping amplitude. Work is underway to determine EC14012-1446's detailed mass and internal structure (Bischoff-Kim & Metcalfe 2012).

4.2.2. Multiplet Structure

A second clue to constrain (l, m) identifications of pulsations in white dwarfs is the presence of rotationally split multiplets. The multiplet components have the same (k, l) and are further described by the azimuthal index m, which takes integer values between $-l$ and l. To first order, the frequency difference relative to the $m = 0$ component of the multiplet is given by $\delta\nu_{klm} = -m\,\Omega\,(1 - C_{kl})$, where Ω is the rotation period and C_{kl} is a coefficient that depends on the pulsation eigenfunctions evaluated in the nonrotating case. In the high-k asymptotic limit for g-modes, $C_{kl} \sim 1/\ell(\ell + 1)$, although models predict it to vary by ≈10% over the range of observed periods in EC14012. We adopt the convention that a positive value of m represents a prograde mode; retrograde modes are denoted by negative m values (Winget et al. 1994). An additional important diagnostic is given by the ratio of splittings for $l = 1$ and $l = 2$, where we expect $\delta\nu_{\ell=1}/\delta\nu_{\ell=2} \simeq 0.6$ for g-modes (Winget et al. 1991).

For EC14012-1446 during XCOV26, we find one triplet (1887 μHz) and two doublets (1633 and 2504 μHz) among our list of 19 frequencies (Table 2). We begin by assuming that the

1887 μHz triplet is a rotationally split multiplet. Our combination analysis argues that the central component (1887.404 μHz, 529.828 s) is (1, 0) and the 1891.142 μHz (528.781 s) component is (1, −1). The 1883.555 μHz (530.911 s) component is low amplitude and is not identified as a parent of any detected combination frequencies. We cannot constrain its (l, m) identification via that method. Given (l, m) identifications for the first two modes, the 1883.555 μHz component should be (1, 1). The average multiplet splitting of 3.8 μHz implies a rotation period as sampled by these modes of 1.53 ± 0.01 days. This is a perfectly reasonable result, as spectroscopic studies of white dwarfs reveal upper limits of $v \sin i = 10$ km s^{-2}, consistent with rotation periods of order days or longer (Berger et al. 2005).

In the limit of uniform slow rotation, we expect additional $l = 1$ multiplets to exhibit similar splittings and $l = 2$ modes to have splittings near 6.3 μHz (Winget et al. 1991). Recalling that every m component is not necessarily excited, we turn to the doublet at 1633 μHz (612 s). Period spacing argues that this doublet is $l = 1$, and our combination analysis indicates that the 1633.907 μHz (612.03 s) mode is (1, 0). The 1624.015 μHz (615.758 s) component is not found as a parent of any detected combination frequencies. If 1633.907 μHz is indeed the central component of an $l = 1$ triplet, then 1624.015 μHz is $m = 1$ and we do not detect the $m = -1$ component. However, the splitting of 9.89 μHz differs significantly from the expected value of $\approx$3.8 μHz found for the 1887 μHz triplet. A second possibility is that the combination analysis is incorrect and we are missing the multiplet's central component. In this case, the 1633.907 μHz mode is (1, −1) and the 1624.015 μHz is (1, 1), resulting in an average splitting of 4.95 μHz (9.89/2). Moving to the 2504 μHz (399 s) doublet, period spacing again argues that this multiplet is $l = 1$. Our combination analysis indicates that the 2504.987 μHz (399.204 s) component is (1, 1). Again, the 2508.060 μHz (398.715 s) component is not identified as a parent of any detected combination frequency. The frequency splitting between the two components is 3.16 μHz and by comparison with the splitting of the 1887 μHz triplet, we can argue that these modes have consecutive m values, identifying the 2508.060 μHz component as (1, 0).

Multiplet splittings may also be used to eliminate the possibility that EC14012-1446's frequencies represent a mixture of $l = 1$ and $l = 2$ modes. Assuming the 1887 μHz triplet is $l = 1$, we do not find evidence for $l = 2$ splittings of $\delta\nu_{l=2} = (3.8/0.6) = 6.3 \mu$Hz as predicted in the limit of slow, uniform rotation. Although both the period spacing and the combination analysis argue against it, to play devil's advocate we consider the possibility that the 1887 μHz triplet is actually an $l = 2$ quintuplet, since all m components are not necessarily excited to observable levels. In this case, then the expected $l = 1$ multiplet splitting is $\delta\nu_{l=1} = 3.8 \times 0.6 = 2.3$ μHz. We find no examples of multiplet splittings near this value. Finally, we must consider that $\delta\nu_{3.16}/\delta\nu_{4.95} = 0.64$. Based on multiplet structure alone, we could argue that the 1633.907 μHz frequency is $l = 2$, and 2504.897 μHz is $l = 1$, but this is not supported by either the period spacings or the combination analysis and leaves no clear explanation for the 1887 μHz triplet.

Clearly, the multiplets found in EC14012-1446's XCOV26 data set are not well explained based on the simple model of rotational splitting. Multiplet structure should be determined by the star's rotation rate and structure. We expect this to remain unchanged over time. The classical example is PG1159-035, which exhibits triplets and quintuplets corresponding to $l = 1$ and $l = 2$ (Winget et al. 1991). However, complex multiplets are not unusual for white dwarf pulsators. In some instances, the assumption of rigid rotation is clearly violated (Córsico et al. 2011). In cooler pulsators with moderate amplitudes and well-developed convection zones, observed multiplet structure can exhibit complicated behavior. For example, Provencal et al. (2009) show changes in the DBV GD358's multiplet structure that cannot be explained with simple rotational splitting. For this same star, Winget et al. (1994) show a dependence of multiplet splittings that is not explained by expected variations of C_{kl}. Processes that may play a role in multiplet structure of cooler pulsators include changing weak magnetic fields similar to the solar cycle, oblique pulsation, and differential rotation. Our XCOV26 data on EC14012-1446 provide us with a single snapshot of this star's multiplet structure. We need more observations to understand their behavior.

We turn again to the combined observations from 2004 to 2008. The four large groupings at 768 s (1302 μHz), 721 s (1387 μHz), 682 s (1466 μHz), and 612 s (1633 μHz) in Figure 12 all show indications of multiplet structure within their groups. We extracted an average multiplet for each of the four large groupings in Figure 12 by calculating a simple average frequency value for the $m = 1$, $m = 0$, and $m = +1$ components. The results are presented in Figure 15. In each case, the prograde ($m = +1$) mode splitting is larger than the $m = -1$ mode, and both the splittings and the asymmetries increase with increasing radial node k.

The qualitative behavior of the low-k and high-k modes can be explained in terms of a very general model. g-modes are standing waves of buoyancy in a spherical cavity and can be thought of as superpositions of traveling waves bouncing back and forth between an inner and outer turning point. In general, low-k (shorter period) modes have deeper outer turning points while high-k (longer period) modes have turning points closer to the stellar surface, meaning that these modes sample the outer regions of the star more than do low-k modes. Figure 15 shows that the unknown process affecting EC14012-1446's multiplet structure acts more dramatically on the high-k modes, arguing that the structural perturbation must be in the outer layers. A surface magnetic field and/or the convection zone are obvious candidates. In addition, we should consider both radial and latitudinal differential rotation. Work is underway to improve our understanding of multiplet structure in pulsating white dwarfs (J. Dalessio 2012, private communication).

Asteroseismology of EC14012-1446's distribution of excited frequencies shows that the observed pulsations are dominated by a series of $l = 1$ modes. If $l = 2$ modes are present, the modes are low amplitude and will not greatly affect the nonlinear light curve fitting process. For the 1887, 1663, and 2504 μHz multiplets, we are able to constrain the m identifications as well. The combination of these results with the combination amplitude analysis (Table 4) gives us a strong foundation on which to proceed to nonlinear light curve fitting.

5. NONLINEAR ANALYSIS

Montgomery (2005a) and Montgomery et al. (2010b) give a detailed description of fitting observed non-sinusoidal light curves of white dwarfs to extract the time-averaged thermal response timescale of the convection zone. To summarize, the aspect of the convection zone sampled by the pulsations is the thermal response timescale, τ_c, which is directly related to the convection zone's mass and depth, and therefore its

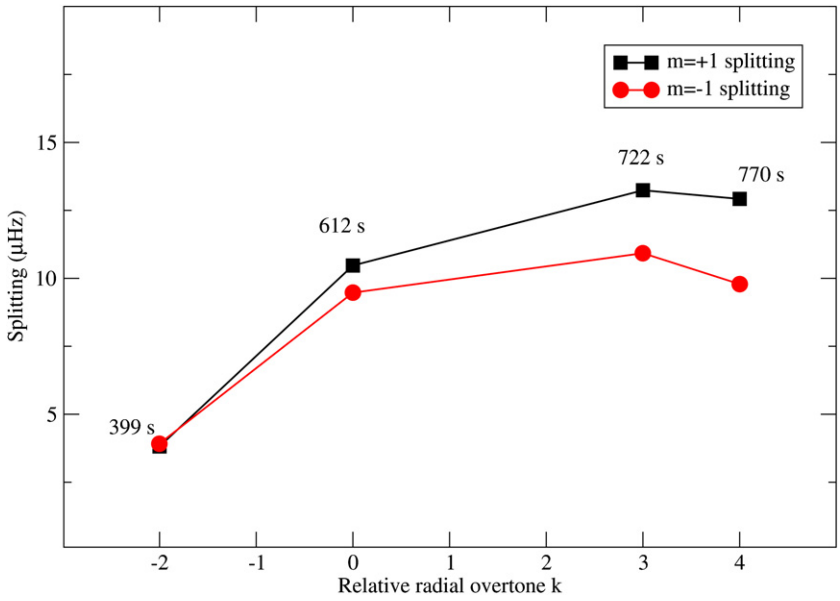

Figure 15. Average multiplet structure associated with the large groupings at 770 s (1302 μHz), 722 s (1387 μHz), 612 s (1633 μHz), and 399 s (1887 μHz). The $m = +1$ (prograde) splitting is always larger than the $m = -1$ splitting, and the asymmetry increases with increasing k.
(A color version of this figure is available in the online journal.)

heat capacity. A DAV such as EC14012-1446 will experience local temperature excursions of ±250 K. In response, the local mass and depth of the convection zone will vary throughout a pulsation cycle.

MLT predicts that τ_c should scale as

$$\tau_c \approx \tau_0 (T_{\rm eff}/T_{\rm eff,0})^{-N}, \quad (2)$$

where $T_{\rm eff}$ is the instantaneous effective temperature, $T_{\rm eff,0}$ is the equilibrium $T_{\rm eff}$, τ_0 is the time-averaged convective timescale, and N describes the sensitivity of τ_c to changes in $T_{\rm eff}$. For DAs, MLT predicts $N \approx 90$ (Montgomery 2005a; Wu 2001; Brickhill 1992). The convection zone's mass, depth, and heat capacity are therefore extraordinarily temperature sensitive, and can vary by a factor of ≈10 throughout a pulsation cycle. This modulation of depth and heat capacity is the source of the large nonlinearities in white dwarf light curves. We focus on these observed nonlinearities to determine the time-averaged convective timescale τ_0, the temperature sensitivity parameter N, and the inclination of the pulsation axis to the line of sight θ.

Our analysis follows the approach of Montgomery et al. (2010b). EC14012-1446 is a multiperiodic pulsator, and because of nonlinear effects, a pulse shape obtained by folding its light curve at a period of interest is not equivalent to a pulse shape obtained in the absence of additional frequencies (Montgomery 2007). Therefore, we use the accurate frequencies and (l, m) identifications obtained for the 2008 WET campaign to calculate point by point nonlinear light curve fits to light curves obtained during XCOV26. High signal-to-noise light curves (S/N ≈ 1000) are vital, since we are interested in the nonlinear portion of the data, which is smaller than the linear component. We chose the SOAR 4 m light curves and the two longest runs from the McDonald 2.1 m (selected runs are marked with "*" in Table 1). These six runs span 3 days, a timebase long enough to constrain the phases of the closely spaced frequencies, yet short enough to avoid possible implications of amplitude modulation found in our frequency analysis (see Section 3.1). The dominant frequencies can be considered to be stable over a 3 day timescale. Using model atmosphere tables provided by D. Koester, we calculate the conversion from bolometric to the observed bandpass as described in Montgomery et al. (2010b), assuming the following parameters for this star: $T_{\rm eff,0} = 11768 \pm 23$ K and $\log g = 8.08 \pm 0.008$ in cgs units (Koester et al. 2009).

We began the fitting process by including the frequencies in Table 4 with firm (l, m) identifications. We then included the additional frequencies with strong (l, m) constraints. It is prudent to point out that this fitting process is *nonlinear*. Adding additional frequencies based on criteria such as amplitude is not necessarily the best procedure. We experimented extensively by computing numerous fits encompassing a wide range of (l, m) identifications for the lower amplitude frequencies. The values of τ_0 for all fits range from 99 to 230 s, indicating that τ_0 is not strongly dependent on these identifications.

Our investigation does reveal that the temperature parameter N can be highly sensitive to the input m identification for large amplitude modes. Numerous attempts to fit EC14012-1446's light curve while assigning the 1633.907 μHz mode an (l, m) identification of (1,0) as derived from our combination analysis (see Section 4.1) yielded $\tau_0 = 171$ s, $\theta = 28°$, and $N = 39$. While the values of τ_0 and θ are reasonable values based on MLT, the value of N implies a temperature sensitivity that is far below the predictions of MLT (Montgomery et al. 2010b); this is not a physically relevant fit. We also experimented by assigning a spherical index $l = 2$ to this mode, resulting in the following fit parameters: $\tau_0 = 228$ s, $N = 26$, and $\theta = 15°$. Again, the value of N obtained remains too low. Ising & Koester (2001) warn that a perturbation analysis of combination amplitudes (Wu 2001) may have difficulties for photometric variations of high amplitude, and this mode has the largest amplitude in the data set. In addition, the asteroseismology analysis of the 1633 μHz multiplet structure cannot solidly constrain the m value for this mode (see Section 4.2). Following this reasoning, we experimented by assigning the 1633.907 μHz mode an (l, m)

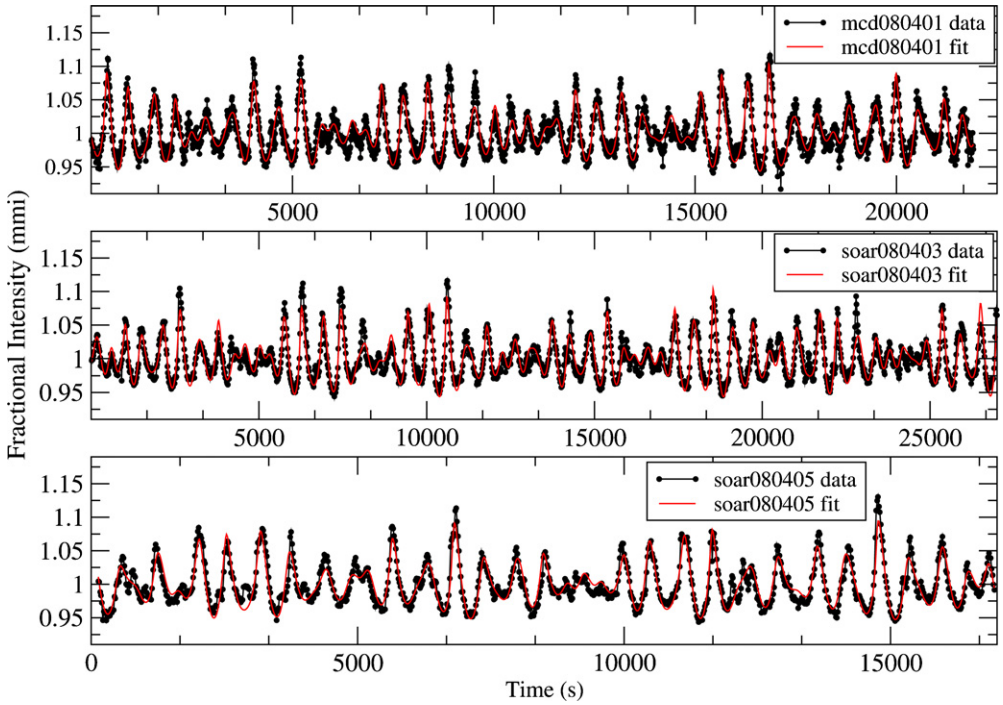

Figure 16. Simultaneous fit of the periods of 19 modes (solid line) to the light curves from mcdo080401, soar080403, and soar080405 (filled circles). Note the change in the *x*-axis for each plot.

(A color version of this figure is available in the online journal.)

value of (1, 1). The resulting fit finds $N = 85$, in much better agreement with MLT predictions (Wu 2001; Montgomery 2005a).

The final simultaneous nonlinear fit to the six high signal-to-noise light curves includes the frequencies and (l, m) identifications given in Table 4. This fit produced the following parameters: $\tau_0 = 99.4 \pm 12$ s, $N = 85 \pm 6$, and $\theta = 32.^{\circ}9 \pm 3.^{\circ}2$. Figure 16 shows the ability to reproduce the essential features of the light curves.

6. DISCUSSION

Convective energy transport in stellar environments is typically modeled using MLT. A particular version by Böhm & Cassinelli (1971), denoted as ML2, includes reduced horizontal energy loss relative to the formulation of Böhm-Vitense (ML1; 1958), increasing the overall convective efficiency. ML2 has been the standard convection model adopted for stellar atmosphere fits of white dwarfs for the past 20 years, with $\alpha = 0.6$ the preferred value for the mixing length (Bergeron et al. 1995). Tremblay et al. (2010) recently re-calibrated the assumed convective efficiency for white dwarf models, using model spectra incorporating an improved treatment of Stark broadening (Tremblay & Bergeron 2009). Tremblay et al. (2010) fit an improved set of *Hubble Space Telescope* and *International Ultraviolet Explorer* ultraviolet (UV) and near UV spectra, varying α until reaching agreement between the optical and UV temperatures. They find the best internal consistency between optical and UV effective temperatures and $\log g$ measurements using ML2 with $\alpha = 0.8$. This is a much more efficient version of MLT than found by Bergeron et al. (1995), but is in closer agreement with that required by nonadiabatic models to fit the observed blue edge of the DA instability strip (Fontaine & Brassard 2008). This convective parameterization is becoming the standard for DA model atmospheres (Freytag et al. 2012; Kilic et al. 2012).

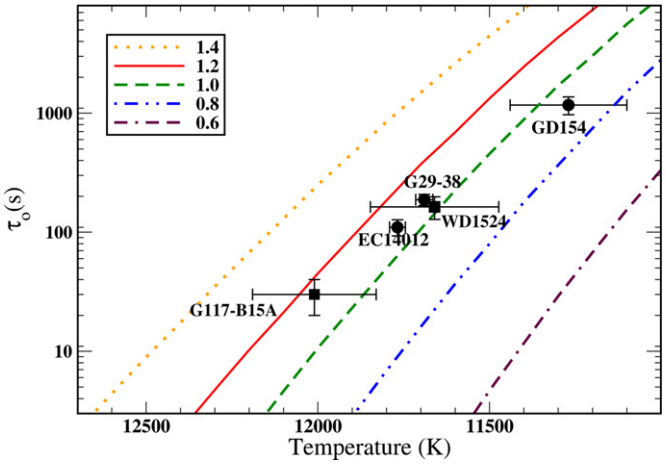

Figure 17. Comparison of EC14012-1446's derived convective parameters with values expected from ML2 convection. The additional labeled points are individual objects taken from Montgomery (2005a), Montgomery et al. (2010a), and Provencal et al. (2011). The curves represent ML2 theoretical calculations of the thermal response time τ_0 for various values of the mixing length α ($\log g = 8.0$).

(A color version of this figure is available in the online journal.)

One of our goals is to produce an empirical map of the time-averaged convective timescale τ_0 at the base of the convection zone as a function of $T_{\rm eff}$ and $\log g$ for a population spanning the DAV instability strip (≈11,100–12,200 K) and compare this with MLT predictions of τ_0. As an individual DA white dwarf cools through the instability strip, the base of its surface hydrogen convection zone will deepen, increasing its total mass and the value of τ_0. MLT makes specific predictions for the behavior of τ_0 given different choices of input parameters. For instance, Figure 17 shows that ML2 with $\alpha = 1.0$ predicts τ_0 values ranging from ∼1 s at the blue edge of the instability strip to ∼6000 s at the red edge.

Table 6
Stellar Parameters

Star	$T_{\rm eff}$ (K)	log g	Period (s)	τ_0 (s)	$P_{\rm max}$	θ	N
G117-B15A	12010 ± 180	8.33	215.2	30 ± 10	188 ± 63	–	–
EC14012-1446	11768 ± 23	8.11	612.3	99 ± 12	624 ± 75	33 ± 3	85 ± 6
G29-38	11690 ± 120	8.11	615.2	187 ± 20	1177 ± 126	66 ± 3	95 ± 8
WDJ1524-0030	11660 ± 180	8.06	697.3	163 ± 35	1024 ± 220	58 ± 10	95 ± 15
GD154	11270 ± 170	7.95	1185.9	1169 ± 200	7345 ± 1257	10 ± 10	127 ± 25

Notes. $T_{\rm eff}$ measurements are from Koester et al. (2009), Koester & Holberg (2001), and Koester & Allard (2000). Given pulsation periods are for the largest amplitude frequency. Entries marked with "–" did not have unique values determined by the fits.

In Figure 17 we also plot current determinations of τ_0 versus $T_{\rm eff}$ for five DAVs, including our solution for EC14012-1446; the derived stellar parameters are listed in Table 6. To ensure a uniform treatment of all the stars in our sample, we have used $T_{\rm eff}$ determinations that do not include the recent updates to the line profile calculations by Tremblay & Bergeron (2009); rather, the plotted effective temperatures and horizontal error bars are based on earlier spectroscopic fits employing ML2 (Koester et al. 2009; Koester & Holberg 2001; Koester & Allard 2000). Overlaid on this figure are the τ_0 predictions of ML2 convection for various values of the mixing length parameter α. Our current results do indicate an increase in τ_0 (and hence an increase in depth and mass of the convection zone) with decreasing temperature and are marginally consistent with $\alpha = 1.0$. Decreasing the $T_{\rm eff}$ error bars, either through higher signal-to-noise spectra and/or new model atmosphere fits, will provide more precise constraints on convection in these stars.

Finally, we point out that convective light curve fitting extracts the value of τ_0 at the base of the convection zone. There is no reason why the same value of α should describe both the photosphere and the deeper convective layers, so our results do not necessarily have to agree with the results of Tremblay et al. (2010) or Bergeron et al. (1995). For instance, Ludwig et al. (1994) use sophisticated two-dimensional hydrodynamic simulations to show that, while MLT is a reasonable approximation to predict the rough photospheric temperature structure of DA white dwarfs, the deeper layers have a higher convective efficiency than predicted by MLT.

Our treatment of the nonlinearities in white dwarf light curves is based on the larger picture of how a surface convection zone leads to driving in these stars. In particular, Brickhill (1991) and Goldreich & Wu (1999) demonstrate that excitation of g-mode pulsations should occur when the convective driving exceeds the radiative damping, and that this condition is given by $\omega\tau_0 \gtrsim 1$. In terms of period, this relation states that g-modes should be driven when $P \lesssim P_{\rm max}$, where $P_{\rm max} \equiv 2\pi\,\tau_0$ and P is the period of a given mode. In Figure 18 we compare the dominant oscillation period in each of the DAVs we have fit with their theoretical value of $P_{\rm max}$, as calculated from each star's value of τ_0. The agreement is good for $\tau_0 \lesssim 100$ s, but the values diverge for larger values of τ_0. Given that τ_0 is related to a star's $T_{\rm eff}$ (see Figure 17), this says that the agreement is good from the blue edge to near the middle of the instability strip, but that from this point to the red edge another effect is operating that prevents the dominant mode periods from increasing as rapidly as $P_{\rm max}$.

It is natural to assume that the cause of this behavior is related to whatever unknown phenomenon produces the red edge of the instability strip. Wu & Goldreich (2001) point out that a deepening convection zone attenuates the flux variations entering at its base, so that for deep enough convection zones the surface amplitudes will be below detection limits. However,

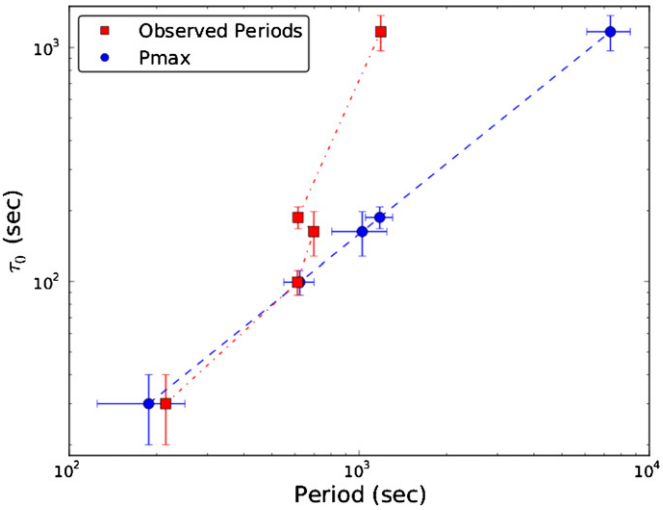

Figure 18. Comparison of the dominant observed pulsation period in a star (dot-dashed curve, red squares) with the theoretical value of $P_{\rm max}$ (dashed line, blue circles) for each DAV star with a measured value of τ_0. Cooler stars are to the left, hotter stars to the right. While simple theory predicts that these curves should be very similar, we find a significant departure for cooler stars.
(A color version of this figure is available in the online journal.)

this is an amplitude effect and does not predict that the dominant periods should be different from $P_{\rm max}$. Brickhill (1991), Goldreich & Wu (1999), and Wu & Goldreich (2001) also discuss the importance of turbulent damping in a narrow shear layer at the base of the convection zone; damping from this region may be more significant for cooler stars. Another possibility is that the maximum period for which complete surface reflection of g-modes can occur is much lower than expected; typical estimates place this number on the order of ~5000 s for $l = 1$ modes and ~3000 s for $l = 2$ modes (Hansen et al. 1985), although it is possible that improved treatment of the surface layers could alter these estimates. At any rate, this phenomenon is likely related to the deepening of the convection zone toward the red edge; we are exploring other phenomena that could lead to this behavior.

7. CONCLUSIONS

Until the advent of convective light curve fitting, our Sun was the only star with empirical constraints on its convection zone depth. Determinations of the time-averaged convective timescale τ_0 and the temperature sensitivity parameter N can now potentially be obtained for any white dwarf pulsator of moderate amplitude (Montgomery et al. 2010b); approximately two-thirds of all white dwarf pulsators show significant nonlinearities in their light curves. Our ultimate goal is to map τ_0 as a function of $T_{\rm eff,0}$ and log g for a population spanning the

instability strips of both the DAV and DBV white dwarfs. Such a map will provide important empirical constraints on convection for white dwarfs and eventually other types of pulsating stars.

We have taken the first steps in this direction with our investigation of EC14012-1446. XCOV26 produced 308.3 hr of data, and our analysis has identified 19 independent frequencies distributed in 14 multiplets. Combined with archival observations, we have identified a series of $l = 1$ modes with an average period spacing of 41 s. EC14012-1446 is now one of the few DAVs with over a dozen identified modes in its pulsation spectrum. The large number of modes means that asteroseismology can be used to provide constraints on its interior structure.

Future goals focus on the determination of τ_0 and N for additional white dwarf pulsators. An increased sample size will improve our empirical map of τ_0 as a function of $T_{\rm eff}$ and also allow us to further explore the observed behavior of P and $P_{\rm max}$ as a function of τ_0. Our goals also include the reduction of errors associated with spectroscopic temperatures. Convective light curve fitting demands uniform treatment of convection between the spectroscopic temperatures we choose and the temperatures we use to calculate the light curve fits. Since WD1524-0030 was not included in the new temperatures of Gianninas et al. (2011) that incorporate recent updates to line profile calculations, we use a consistent set of older published temperatures for the objects presented in this work. Incorporating the new temperatures will be a first step toward reducing the spectroscopic errors. We must recalculate our existing nonlinear light curve fits using these updated $T_{\rm eff}$ and $\log g$ determinations. On average, the temperatures of Gianninas et al. (2011) increase over older published values by ≈500 K. Preliminary work indicates that the empirical value of τ_0 will not change significantly with such an increase. However, the theoretical MLT predictions for τ_0 *will* change; larger values of α will be needed to keep τ_0 and the convection zone depth the same for these higher values of $T_{\rm eff}$.

The Delaware Asteroseismic Research Association (DARC) is grateful for the support of the Crystal Trust Foundation and Mt. Cuba Observatory. DARC also acknowledges the support of the University of Delaware, through their participation in the SMARTS consortium. M.H.M. gratefully acknowledges the support of the NSF under grant AST-0909107 and the Norman Hackerman Advanced Research Program under grant 003658-0252-2009. S.L.K. acknowledges partial support by the KASI (Korea Astronomy and Space Science Institute) grant 2012-1-410-02. This paper uses observations made at the South African Astronomical Observatory (SAAO). This work is further supported by the Austrian Fonds zur Förderung der wissenschaftlichen Forschung under grant P18339-N08. We thank the various Telescope Allocation Committees for the awards of telescope time.

Facilities: MCAO:0.6m, Struve, KPNO:2.1m, UH:0.6m, BOAO:1.8m, Lulin:1.8m, Beijing:2.16m, Maidanek:1.0m, Peak Terskol, SAAO:1.0m ( ), SALT, SOAR, CTIO:0.9m, LCOGT, BOAO:1.8m.

REFERENCES

Berger, L., Koester, D., Napiwotzki, R., Reid, I. N., & Zuckerman, B. 2005, A&A, 444, 565
Bergeron, P., Wesemael, F., Lamontagne, R., et al. 1995, ApJ, 449, 258
Biermann, L. 1932, Z. Astrophys., 5, 117
Bischoff-Kim, A., & Metcalfe, T. 2012, in ASP Conf. Ser., Progress in Solar and Stellar Physics with Asterseismology, ed. H. Shibahashi, in press
Böhm, K. H., & Cassinelli, J. 1971, A&A, 12, 21
Böhm-Vitense, E. 1958, Z. Astrophys., 46, 108
Brassard, P., Fontaine, G., & Wesemael, F. 1995, ApJS, 96, 545
Brickhill, A. J. 1991, MNRAS, 251, 673
Brickhill, A. J. 1992, MNRAS, 259, 519
Charbonneau, P. 1995, ApJS, 101, 309
Córsico, A. H., Althaus, L. G., Benvenuto, O. G., & Serenelli, A. M. 2002, A&A, 387, 531
Córsico, A. H., Althaus, L. G., Kawaler, S. D., et al. 2011, MNRAS, 418, 2519
Dolez, N., Vauclair, G., Kleinman, S. J., et al. 2006, A&A, 446, 237
Eisenstein, D. J., Liebert, J., Koester, D., et al. 2006, AJ, 132, 676
Fontaine, G., & Brassard, P. 2008, PASP, 120, 1043
Freytag, B., Steffen, M., Ludwig, H.-G., et al. 2012, J. Comput. Phys., 231, 919
Gianninas, A., Bergeron, P., & Ruiz, M. T. 2011, ApJ, 743, 138
Goldreich, P., & Wu, Y. 1999, ApJ, 511, 904
Handler, G., Romero-Colmenero, E., & Montgomery, M. H. 2002, MNRAS, 335, 399
Handler, G., Romero-Colmenero, E., Provencal, J. L., et al. 2008, MNRAS, 388, 1444
Hansen, C. J., Winget, D. E., & Kawaler, S. D. 1985, ApJ, 297, 544
Harris, H. C., Munn, J. A., Kilic, M., et al. 2006, AJ, 131, 571
Ising, J., & Koester, D. 2001, A&A, 374, 116
Kanaan, A., Kepler, S. O., & Winget, D. E. 2002, A&A, 398, 896
Kawaler, S. E. 1988, in IAU Symp. 123, Advances in Helio- and Asteroseismology, ed. J. Christensen-Dalsgaard & S. Frandsen (Dordrecht: Reidel), 329
Kepler, S. O., Nather, R. E., Winget, D. E., et al. 2003, A&A, 401, 639
Kilic, M., Patterson, A. J., Barber, S., Leggett, S. K., & Dufour, P. 2012, MNRAS, 419, L59
Koester, D., & Allard, N. 2000, Balt. Astron., 9, 119
Koester, D., & Holberg, J. 2001, in ASP Conf. Ser. 226, 12th European Conference on White Dwarfs, ed. J. L. Provencal, H. L. Shipman, J. MacDonald, & S. Goodchild (San Francisco, CA: ASP), 299
Koester, D., Voss, B., Napiwotzki, R., et al. 2009, A&A, 505, 441
Lenz, P., & Breger, M. 2005, Commun. Asteroseismol., 146, 53
Ludwig, H., Jordan, S., & Steffen, M. 1994, A&A, 284, 105
Metcalfe, T. S., Nather, R. E., & Winget, D. E. 2000, ApJ, 545, 974
Montgomery, M. H. 2005a, ApJ, 633, 1142
Montgomery, M. H. 2005b, in ASP Conf. Ser. 334, 14th European Workshop on White Dwarfs, ed. D. Koester & S. Moehler (San Francisco, CA: ASP), 553
Montgomery, M. H. 2005c, in ASP Conf. Ser. 334, 14th European Workshop on White Dwarfs, ed. D. Koester & S. Moehler (San Francisco, CA: ASP), 483
Montgomery, M. H. 2007, in ASP Conf. Ser. 372, 15th European Workshop on White Dwarfs, ed. R. Napiwotzki & M. R. Burleigh (San Francisco, CA: ASP), 635
Montgomery, M. H. 2009, in AIP Conf. Proc. 1170, Stellar Pulsation: Challenges for Theory and Observation, ed. J. A. Guzik & P. A. Bradley (Melville, NY: AIP), 605
Montgomery, M. H., Hermes, J. J., & Winget, D. E. 2010a, in AIP Conf. Proc. 1273, 17th European White Dwarf Workshop, ed. K. Werner (Melville, NY: AIP), 512
Montgomery, M. H., Provencal, J. L., Kanaan, A., et al. 2010b, ApJ, 716, 84
Provencal, J. L., Montgomery, M. H., Kanaan, A., et al. 2009, ApJ, 693, 564
Provencal, J. L., Montgomery, M. H., Mullaly, S., Dalessio, J., & Shipman, H. 2011, BAAS, 43, 21734105
Ruiz, M. T., & Bergeron, P. 2001, ApJ, 558, 761
Stobie, R. S., O'Donoghue, D. O., Ashley, R., et al. 1995, MNRAS, 272, L21
Tassoul, M., Fontaine, G., & Winget, D. E. 1990, ApJS, 72, 335
Thompson, S. E., & Mullally, F. 2009, J. Phys.: Conf. Ser., 172, 012081
Tremblay, P. E., & Bergeron, P. 2009, in AIP Conf. Proc. 1171, Recent Directions in Astrophysical Quantitative Spectroscopy and Radiation Hydrodynamics (Melville, NY: AIP), 101
Tremblay, P.-E., Bergeron, P., Kalirai, J. S., & Gianninas, A. 2010, ApJ, 712, 1345
Unno, W., Osaki, Y., Ando, H., Saio, H., & Shibahashi, H. 1989, Nonradial Oscillations of Stars (Tokyo: Univ. Tokyo Press)
Winget, D. E., Hansen, C. J., Liebert, J., et al. 1987, ApJ, 315, L77
Winget, D. E., Nather, R. E., Clemens, J. C., et al. 1991, ApJ, 378, 326
Winget, D. E., Nather, R. E., Clemens, J. C., et al. 1994, ApJ, 430, 839
Wu, Y. 2001, MNRAS, 323, 248
Wu, Y., & Goldreich, P. 2001, ApJ, 546, 469
Yeates, C. M., Clemens, J. C., Thompson, S. E., & Mullally, F. 2005, ApJ, 635, 1239

The Astrophysical Journal, 757:176 (9pp), 2012 October 1 doi:10.1088/0004-637X/757/2/176

TOWARD IDENTIFYING THE UNASSOCIATED GAMMA-RAY SOURCE 1FGL J1311.7-3429 WITH X-RAY AND OPTICAL OBSERVATIONS

J. Kataoka[1], Y. Yatsu[2], N. Kawai[2], Y. Urata[3], C. C. Cheung[4,7], Y. Takahashi[1], K. Maeda[1], T. Totani[5], R. Makiya[5], H. Hanayama[6], T. Miyaji[6], and A. Tsai[3]

[1] Research Institute for Science and Engineering, Waseda University, 3-4-1, Okubo, Shinjuku, Tokyo 169-8555, Japan; kataoka.jun@waseda.jp
[2] Tokyo Institute of Technology, 2-12-1, Ohokayama, Meguro, Tokyo 152-8551, Japan
[3] Institute of Astronomy, National Central University, Chung-Li 32054, Taiwan
[4] National Research Council Research Associate, National Academy of Sciences, Washington, DC 20001, USA
[5] Department of Astronomy, Kyoto University, Kitashirakawa, Sakyo-ku, Kyoto 606-8502, Japan
[6] Ishigakijima Astronomical Observatory, National Astronomical Observatory of Japan, 1024-1 Arakawa, Ishigaki, Okinawa, 907-0024, Japan
Received 2012 July 14; accepted 2012 August 9; published 2012 September 17

ABSTRACT

We present deep optical and X-ray follow-up observations of the bright unassociated *Fermi*-LAT gamma-ray source 1FGL J1311.7-3429. The source was already known as an unidentified EGRET source (3EG J1314-3431, EGR J1314-3417), hence its nature has remained uncertain for the past two decades. For the putative counterpart, we detected a quasi-sinusoidal optical modulation of $\Delta m \sim 2$ mag with a period of $\simeq$1.5 hr in the Rc, r', and g' bands. Moreover, we found that the amplitude of the modulation and peak intensity changed by $\gtrsim$1 mag and $\sim$0.5 mag, respectively, over our total six nights of observations from 2012 March to May. Combined with *Swift* UVOT data, the optical–UV spectrum is consistent with a blackbody temperature, $kT \simeq 1$ eV and the emission volume radius $R_{\rm bb} \simeq 1.5 \times 10^4\ d_{\rm kpc}$ km ($d_{\rm kpc}$ is the distance to the source in units of 1 kpc). In contrast, deep *Suzaku* observations conducted in 2009 and 2011 revealed strong X-ray flares with a light curve characterized with a power spectrum density of $P(f) \propto f^{-2.0\pm0.4}$, but the folded X-ray light curves suggest an orbital modulation also in X-rays. Together with the non-detection of a radio counterpart, and significant curved spectrum and non-detection of variability in gamma-rays, the source may be the second "radio-quiet" gamma-ray emitting millisecond pulsar candidate after 1FGL J2339.7-0531, although the origin of flaring X-ray and optical variability remains an open question.

Key words: gamma rays: stars – pulsars: general – X-rays: general

Online-only material: color figures

1. INTRODUCTION

The Large Area Telescope (LAT; Atwood et al. 2009) on board the *Fermi Gamma-Ray Space Telescope* is a successor to EGRET on board the *Compton Gamma-Ray Observatory* (Hartman et al. 1999), with much improved sensitivity, resolution, and energy range. The second *Fermi*-LAT catalog, based on the first 24 months of all-sky survey data (2FGL; Nolan et al. 2012), provides source location, flux, and spectral information, as well as light curves on month time bins for 1873 γ-ray sources detected and characterized in the 100 MeV–100 GeV range. Thanks to their small localization error circles (or ellipses) with typical 95% confidence radii, $r_{95} \simeq 0.^\circ1$–$0.^\circ2$, for relatively bright sources, 69% of the 2FGL sources are reliably associated or firmly identified with counterparts of known or likely γ-ray producing sources. In particular, more than 1000 sources are proposed to be associated with active galactic nuclei (AGNs; of mainly the blazar class) and 87 sources with pulsars (PSRs), including 21 millisecond pulsars (MSPs), which are a new category of γ-ray sources discovered with *Fermi*-LAT (Nolan et al. 2012; Abdo et al. 2009a). Other sources, albeit of a relative minority compared to AGNs and PSRs, also constitute important categories of new GeV sources like supernova remnants (SNRs; Abdo et al. 2009b, 2010a, 2010b, 2010c), low-mass/high-mass binaries (Abdo et al. 2009c, 2009d, 2009e), pulsar wind nebula (Abdo et al. 2010d, 2010e), one nova (Abdo et al. 2010f), normal and starburst galaxies (Abdo et al. 2010g, 2010h), and the giant lobes of a radio galaxy (Abdo et al. 2010i).

Despite such great advances in the identification of *Fermi*-LAT sources, 575 (31%) sources in the 2FGL catalog still remain unassociated. Note that a substantial fraction of the unassociated sources (51%) have at least one analysis flag due to various issues, while only 14% of the associated sources have been flagged (Nolan et al. 2012). This may suggest that some of unassociated sources are spurious due to complexity/difficulty of being situated in a crowded region near the Galactic plane. Nevertheless, many of them are bright enough to be listed in the one year *Fermi*-LAT catalog (1FGL; Abdo et al. 2010j) and some of them are even listed in the bright source list based on the first 3 months of data (0FGL; Abdo et al. 2009f). By comparing the distribution of associated and unassociated sources in the sky, a number of interesting features in the map were reported (Nolan et al. 2012). For example, (1) the number of unassociated sources decreases with increasing Galactic latitude, (2) the number of unassociated sources increases sharply below Galactic latitudes, $|b| < 10^\circ$, and (3) the fraction of sources with curved gamma-ray spectra among the unassociated sources is greater (28%) than the fraction of curved spectra sources among the associated sources (16%). Further extensive studies based on a statistical approach in an effort to correlate their gamma-ray properties with the AGN and PSR populations was presented for 1FGL unassociated sources (Ackermann et al. 2012).

In this context, 1FGL J1311.7-3429 (or 2FGL name, 2FGL J1311.7-3429) is a *classical* unassociated gamma-ray

[7] Resident at Naval Research Laboratory, Washington, DC 20375, USA.

source situated at high Galactic latitude ($l = 307.^{\circ}6859$, $b = 28.^{\circ}1951$), and was first discovered by EGRET about 20 years ago as 3EG J1314-3431 (Hartman et al. 1999) or EGR J1314-3417 (Casandjian & Grenier 2008). The source was also reported by *Fermi*-LAT in the 0FGL list with a gamma-ray flux $F_{0.1-20\,\mathrm{GeV}} = (11.7 \pm 1.1) \times 10^{-8}$ photons cm^{-2} s^{-1}, which is marginally consistent with the gamma-ray flux determined by EGRET, $F_{0.1-20\,\mathrm{GeV}} = (18.7 \pm 3.1) \times 10^{-8}$ photons cm^{-2} s^{-1}, within the 2σ level. In the 2FGL catalog, the detected significance of 1FGL J1311.7-3429 is 43.1σ, which is one of the brightest sources with an UNID flag. Based on the one-month binned >100 MeV gamma-ray light curve of 1FGL J1311.7-3429 over two years of data as published in the 2FGL catalog,[8] no statistically significant variability was observed (VARIABILITY_INDEX = 19.09; Nolan et al. 2012). The gamma-ray spectrum is significantly curved with curved significance SIGNIF_CURVE of 6.33 (Nolan et al. 2012).[9]

The first X-ray follow-up observation of 1FGL J1311.7-3429 was conducted as a part of *Suzaku* X-ray observations of 11 unidentified *Fermi*-LAT objects at high Galactic latitude, $|b| > 10^{\circ}$ (Maeda et al. 2011; Takahashi et al. 2012). The X-ray source associated with 1FGL J1311.7-3429 showed a very rapid X-ray flare with the count rate changing by a factor of 10. Subsequent *Chandra* ACIS-I (2010 March 21 for a 19.87 ks exposure, obsID 11790) and *Swift* XRT observations (2009 February 27 for a 3.34 ks exposure, obsID 31358; see also Table 1) confirmed that the brightest X-ray source within the *Fermi*-LAT error ellipse is the most credible counterpart and that the X-ray source is also variable on month-to-year timescales. The unabsorbed X-ray flux observed with *Chandra* was 1.03×10^{-13} erg cm^{-2} s^{-1} in the 0.5–8 keV band, with a differential photon spectral index, $\Gamma = 1.26^{+0.38}_{-0.37}$ (Cheung et al. 2012).

Motivated by the initial X-ray results, we conducted further deep observations of 1FGL J1311.7-3429 with *Suzaku*, together with deep optical observations using a 105 cm Ritchey–Chrétien telescope (g', Rc, and Ic bands) at the Ishigakijima Astronomical Observatory (IAO) in Japan, as well as the 1 m telescope (r' band) at Lulin Observatory in Taiwan. In Section 2, we describe the details of the *Suzaku* observations and optical observations and data reduction procedures. Very recently, Romani (2012) reported quasi-sinusoidal optical modulation of this source with a 1.56 hr (5626 s) period, suggesting that the source is another black-widow-type MSP like that recently discovered for 1FGL J2339.7-0531 (Romani & Shaw 2011; Kong et al. 2012). Our paper confirms some of those optical findings for 1FGL J1311.7-3429, plus provides results from multiple epoch optical monitoring between 2012 March and May and completely new X-ray data based on a long *Suzaku* observation conducted in 2011 together with our previously published archival 2009 data. The results of these observations are given in Section 3. Based on our new observational data in optical and X-ray, and various observed gamma-ray parameters compiled in the 2FGL source catalog, we support that 1FGL J1311.7-3429 could be a "radio-quiet" gamma-ray emitting MSP candidate like 1FGL J2339.7-0531. The variable optical/X-ray source is posited as the counterpart to the gamma-ray source and throughout, we refer to it simply as 1FGL J1311.7-3429.

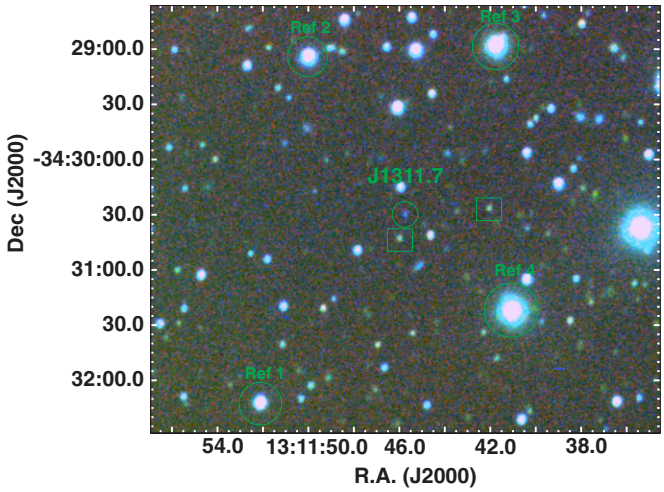

Figure 1. Tri-color optical image of 1FGL J1311.7-3429 constructed from data taken in the g', Rc, and Ic bands by the IAO 1.05 m telescope (Table 1). The four reference stars used in the analysis of the IAO data are denoted as Ref 1–4, while two reference stars used in the analysis of the LOT data are shown as boxes.

(A color version of this figure is available in the online journal.)

2. OBSERVATIONS AND DATA REDUCTION

2.1. Optical/UV

As discussed in Cheung et al. (2012), the brightest X-ray source within the *Fermi*-LAT error ellipse, CXOU J131145.71-343030.5, is the most credible counterpart and exactly the one detected in our previous (AO4; below) *Suzaku* observation (Maeda et al. 2011). The source was also detected with the *Swift* XRT (observation ID 31358). Within the *Chandra* error circle (0.″6 at 90% level), there is a $R = 17.9$ mag, $B = 20.5$ mag star in the USNO A-2.0 catalog (Muslimov & Harding 2003), that is 0.″56 apart from CXOU J131145.71-343030.5. The same star is also listed as $R = 18.8$ mag, $B = 21.0$ mag in USNO-B1.0 catalog, suggesting a hint of temporal variability (a typical uncertainty of these measurements is $\simeq$0.3 mag; Muslimov & Harding 2003). The same optical source is also seen in the DSS (Digital Sky Survey), but its optical magnitude is unclear. Moreover, *Swift* UVOT observations taken simultaneously with the XRT detected the source. Our analysis using archival *Swift* UVOT data indicate: $v > 19.51$ (upper limit only), $b = 20.10 \pm 0.30$, $u = 20.77 \pm 0.27$, $uvw1 = 21.70 \pm 0.31$, $uvm2 = 21.58 \pm 0.24$, and $uvw2 = 22.05 \pm 0.22$.

We made further deep follow-up observations of the field of CXOU J131145.71-343030.5, centered at (R.A., decl.) = ($197.^{\circ}940400$, $-34.^{\circ}508306$), with the 105 cm Ritchey–Chrétien telescope at the Ishigakijima Astronomical Observatory in Japan. These observations were obtained on 2012 May 25 and started at 12:31:11:13 and ended 15:41:11:63 (UT). The telescope in IAO is equipped with a tricolor camera that performs simultaneous imaging in the SDSS-g' (hereafter, g'), Rc and Ic bands. The total net exposure amounts to 8400 s (300 s × 28 frames; see Table 1 for the observation log). All images were flat field and bias corrected. The absolute magnitudes were calibrated against the four reference stars shown in Figure 1. In the Rc and Ic bands, the reference star

[8] http://heasarc.gsfc.nasa.gov/FTP/fermi/data/lat/catalogs/source/lightcurves/2FGL_J1311d7m3429_lc.png

[9] As detailed in Nolan et al. (2012), the VARIABILITY_INDEX is an indicator of the flux being constant across the full 2 year period. A value of VARIABILITY_INDEX > 41.6 is used to identify variable sources at a 99% confidence level. Similarly, the SIGNIF_CURVE parameter is an indicator of the spectrum being curved, by comparing the likelihood values calculated for a LogParabola and a single power-law function. SIGNIF_CURVE is distributed as χ^2 with 1 degree of freedom, and SIGNIF_CURVE > 16 corresponds to 4σ significance of curvature.

Table 1
Observation Log of 1FGL J1311.7-3429 Analyzed in This Paper

Obs Start (UT)	Obs End (UT)	Observatory	Band	Exposure
2009-08-04 04:56:35	2009-08-05 07:18:14	*Suzaku* XIS	X-ray	33.0 ks
2011-08-01 16:48:20	2011-08-03 17:40:15	*Suzaku* XIS	X-ray	65.2 ks
2009-02-27 18:41:59	2009-02-27 22:04:57	*Swift* UVOT	UV	276/276/276/552/742/1106[a]
2012-03-24 17:45:37	2012-03-24 19:38:35	LOT 1 m	r'	5 min × 21
2012-03-25 17:48:26	2012-03-25 19:26:33	LOT 1 m	r'	5 min × 12
2012-03-26 17:25:14	2012-03-26 18:29:59	LOT 1 m	r'	5 min × 12
2012-04-12 16:35:08	2012-04-12 18:24:30	LOT 1 m	r'	5 min × 21
2012-05-24 13:00:49	2012-05-24 15:34:44	LOT 1 m	r'	5 min × 29
2012-05-25 12:31:11	2012-05-25 15:41:11	IAO 105 cm	g', Rc, Ic	20 min × 7

Note. [a] *Swift* UVOT exposures for the $v/b/u/uvw1/uvm2/uvw2$ bands in seconds.

magnitudes were based on the NOMAD catalog (Monet et al. 2003). Because the target area was not covered by the SDSS, we employed a system conversion formula of USNO-B Bc and Rc magnitudes (Sesar et al. 2006) for the four reference stars to obtain g' magnitudes. Moreover, the observed magnitudes were corrected for Galactic extinction using $A_{g'} = 0.247$ mag, $A_{Rc} = 0.167$ mag, and $A_{Ic} = 0.120$ mag.

We also conducted optical SDSS-r' (hereafter r') band monitoring observations with the Lulin One-meter Telescope (LOT; Huang et al. 2005). Observations were conducted on five nights between 2012 March and May (see Table 1). Photometric images with 300 s exposure were obtained using the PI1300B CCD camera. We performed the dark-subtraction and flat-fielding correction using the appropriate calibration data. For these LOT data, the four reference stars used in the IAO photometry were saturated in the detector and therefore could not be used. Instead, the LOT photometric results are presented as differential magnitudes against two other fainter reference stars (boxed in Figure 1).

2.2. Suzaku XIS

As noted above, the first X-ray follow-up observation of 1FGL J1311.7-3429 was conducted in 2009 as a part of AO-4 *Suzaku* program (PI: J. Kataoka; OBS_ID 804018010) aimed at observing an initial four out of 11 unidentified *Fermi*-LAT objects at high Galactic latitude, $|b| > 10^\circ$ (Maeda et al. 2011; see also Takahashi et al. 2012). To further investigate the nature of the detected variable X-ray counterpart, we conducted the second *Suzaku* observation of 1FGL J1311.7-3429 in 2011 as a part of AO-6 program (PI: J. Kataoka, OBS_ID 706001010). The observation started at 2011 August 1 16:48:20 and ended at August 3 17:40:15. The total exposure amounted to 65.2 ks, and is almost twice as long as that obtained in AO-4 (see Table 1). For both the AO-4 and AO-6 data analysis, we excluded the data collected during the time and up to 60 s after the South Atlantic Anomaly (SAA), and excluded data corresponding to less than 5° of the angle between Earth's limb and the pointing direction. Moreover, we excluded time windows during which the spacecraft was passing through the low cutoff rigidity (COR) of below 6 GV. We set the same source region to within a $1'$ radii around the respective X-ray flux maximum and the selection criteria for the data analysis for the two data sets were completely the same. Although *Suzaku* also carries a hard X-ray detector (HXD), consisting of the PIN and GSO, hereafter, we do not use the data because the source is too faint to be detected with HXD/PIN or GSO.

3. RESULTS

3.1. Optical/UV

Figure 1 shows a multicolor image of 1FGL J1311.7-3429 constructed from the IAO g' (blue), Rc (green), and Ic (red) data from 2012 May 24. The optical counterpart of the X-ray source is clearly detected in the image, but apparently the source is rather "blue" compared with reference stars and nearby galaxies. Aperture photometry yielded average magnitudes of the source, $g' = 20.97 \pm 0.13$, $Rc = 21.17 \pm 0.16$, and $Ic < 18.38$ (3σ upper limit). We also checked the temporal profile of the optical emission for the IAO data (Figure 2). Relative photometry for the IAO images against the four field stars shows large amplitude ($\Delta m \sim 2$ mag) quasi-sinusoidal modulation in the g' and Rc bands with a timescale of 1.5 hr, as suggested by Romani (2012).

To search for possible long-term variability, Figure 3 (top) compares the r'-band light curve reconstructed only from LOT data between 2012 March and May. The differential magnitudes are derived by comparison with two reference stars in the field (see Figure 1). Note, the r'-band magnitude of the reference stars remain constant within $\Delta m = 0.068$ mag over the five nights of observations. Interestingly, the amplitude of modulation and the light-curve profile seems to have changed among the five nights of observations. Specifically, a clear modulation of $\Delta m \sim 2$ mag is visible in the May 24 data, while $\Delta m \sim 1$ mag in the March 24 data, and almost unseen ($\Delta m \lesssim 0.2$ mag) in the March 26 data. Moreover, the peak magnitude differs by $\Delta m \sim 0.5$ mag among the five nights, much larger than the fluctuations in the magnitudes of reference stars. Figure 3 (bottom) shows the folded light curves of differential r'-band magnitudes with a best-fit period of 1.56278 hr (5626 s) proposed by Romani (2012). Phase zero is defined here as MJD 56010.76808, so that the time of the observed minimum r'-band magnitude in the May 24 data is set at orbital phase $\phi = 1.0$. The peak r'-band magnitude is around $\simeq$20.5 for five nights of data from 2012 March to April. Note, this is exactly consistent with what has been observed with IAO on May 25 (Figure 2, right). To further investigate the temporal variability/flaring in the UV data, we also reanalyzed the archival *Swift* UVOT data. However, the UVOT exposures for each filter (b, u, $uvw1$, $uvm2$, $uvw2$) were too short to search for variability (see Table 1).

3.2. Suzaku XIS

During the AO-4 observation, significant X-ray variability was detected at the beginning of the observation, where the count rate changed by a factor of 10 (Maeda et al. 2011). Figure 4 compares the *Suzaku* XIS FI (XIS0+3) images in

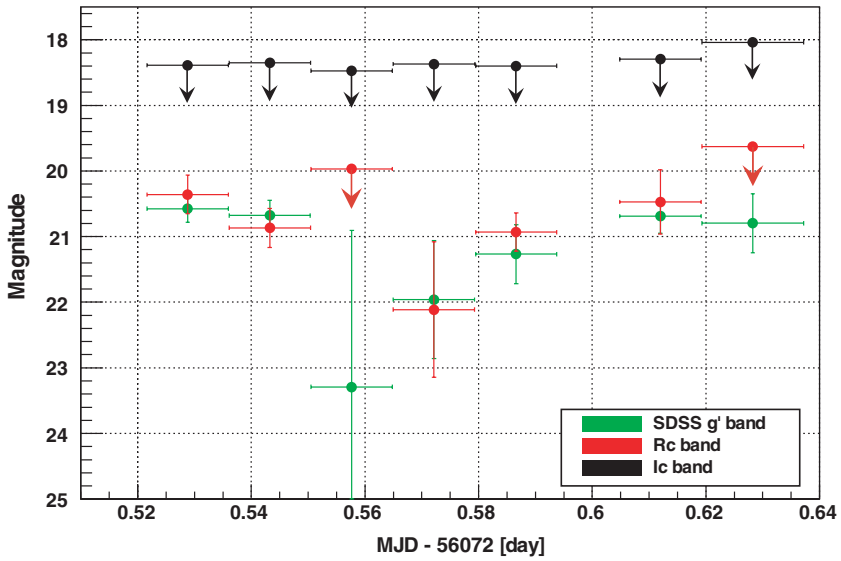

Figure 2. Multi-band optical light curves of 1FGL J1311.7-3429 observed with the IAO 1.05 m telescope on May 25 (g', Rc, and Ic bands). Data are binned by 1200 s (300 s × 4 frames) for the IAO data. The source is not detected in the Ic band and 3σ upper limits are provided.

(A color version of this figure is available in the online journal.)

the 0.5–10 keV range, reconstructed by using the data during the first 20 ks (top) and the last 74 ks (bottom). The images are corrected for exposure and vignetting, and are non-X-ray (detector) background subtracted. The images were also smoothed by a Gaussian function with $\sigma = 0.'17$, following the procedure given in Maeda et al. (2011). Note that the source is clearly detected in the first 20 ks, but almost unseen in the last 74 ks. Also Cheung et al. (2012) argues that the 0.3–10 keV *Swift* XRT count rate of $(6.1 \pm 1.8) \times 10^{-3}$ counts s^{-1} is equivalent to a 0.5–8 keV flux of $\simeq 3.1 \times 10^{-13}$ erg cm^{-2} s^{-1}, indicating a $\sim 3\times$ brighter source about one year prior to the *Chandra* observation, and providing further evidence of long-term X-ray variability in this source.

Figure 5 summarizes the X-ray light curve of 1FGL J1311.7-3429 thus obtained during the AO-6 observation and compares them with those obtained in the AO-4 observation. All the XIS0, 1, 3 count rates are summed in the various energy bands of 0.4–1 keV, 1–2 keV, 2–4 keV, and 4–8 keV (from top to bottom). Note that X-ray variability is clearly seen above 1 keV, but not in the 0.4–1 keV light curve. To see this more quantitatively, we calculated the normalized excess variance $\sigma^2_{\rm NXS}$ (Vaughan et al. 2003; see also Kataoka et al. 2007) for the AO4 and AO6 light curves and for the combined AO4+AO6 light curves. The $\sigma^2_{\rm NXS}$ parameter is an estimator of the intrinsic source variance after subtracting the contribution expected from measurement errors. As shown in Figure 6 (top), $\sigma^2_{\rm NXS}$ is consistent with zero for the 0.4–1 keV band, while almost constant (within error bars) and significantly positive above 1 keV.[10]

Figure 6 (bottom) presents the normalized power spectrum density (NPSD; Hayashida et al. 1998), which is a technique for calculating the PSD of unevenly sampled light curves. Note that data gaps are unavoidable for low Earth orbit X-ray satellites like *Suzaku*. Since the orbital period of *Suzaku* is ∼5760 s, Earth occultations create artificial periodic gaps every 5760 s in the data, even when the source is continuously monitored. To calculate the NPSD of our data sets, we made light curves of two different bin sizes of 256 s and 5760 s for each of the AO4 and AO6 light curves (Kataoka et al. 2001). The NPSD calculated for each light curves is well represented by a steep power law with $P(f) \propto f^{-2.00 \pm 0.32}$ (AO4) and $P(f) \propto f^{-2.04 \pm 0.44}$ (AO6). Note that the amplitude of the NPSD is larger for the AO4 (red) data than in the AO6 (blue) data. This is due to large flare observed in the first 20 ks of the AO4 observation (Figure 4) and is consistent with the larger value of $\sigma^2_{\rm NXS}$ compared with variability during AO6 observation (Figure 6, top).

Figure 7 shows the folded X-ray light curves from the *Suzaku* AO4 (top) and AO6 (bottom) data sets. The XIS0, 1, and 3 data are all summed in 0.4–10 keV band. The phase zero is defined as MJD 56010.76808 as in the optical folded light curves shown in Figure 3 (bottom). The vertical axis represents the source counts divided by the average source intensity in the frame. Although there is a regular exposure gap for phases $\phi = 0.3$–0.4 due to Earth occultations, there appears to be a clear excess at phases $\phi = 0.4$–0.6 in AO4 data (see also Romani (2012)). Moreover, we found similar structure in the AO6 data, but at different phases of $\phi = 0.6$–0.8 with much smaller amount of excess. To check that this excess is *not* due to artifacts caused by periodic gaps due to Earth occultation, we also made the folded light curves of the nearby X-ray source in the same field of view (src B in Maeda et al. 2011, or CXOU J131147.0-343205 in Cheung et al. 2012; see Figure 4), whose X-ray flux is comparable to the average X-ray flux of 1FGL J1311.7-3429. The results presented as dashed lines in Figure 7 show no clear excess for the nearby source. This suggests that the X-ray excesses in the folded light curves are most likely due to orbital motion of 1FGL J1311.7-3429 itself.

Finally, Figure 8 compares the unfolded X-ray spectrum for 1FGL J1311.7-3429 averaged over the AO4 (red) and AO6 (blue) observations. The best model fits for both observations consist of power-law continua with photon indices, $\Gamma \simeq 1.3$–1.7. Significant curvature (or deficit of photons below 2 keV) was observed only in the 2009 data, which was tentatively modeled by an excess value of Galactic column density $N_{\rm H}$; $N_{\rm H}$ is,

[10] The fractional root mean square variability amplitude, $F_{\rm var}$ is often chosen in preference to $\sigma^2_{\rm NXS}$, although the two convey exactly the same information. Here, we prefer $\sigma^2_{\rm NXS}$ simply because variability is not significant for the 0.4–1 keV light curve and negative values of $\sigma^2_{\rm NXS}$ are possible.

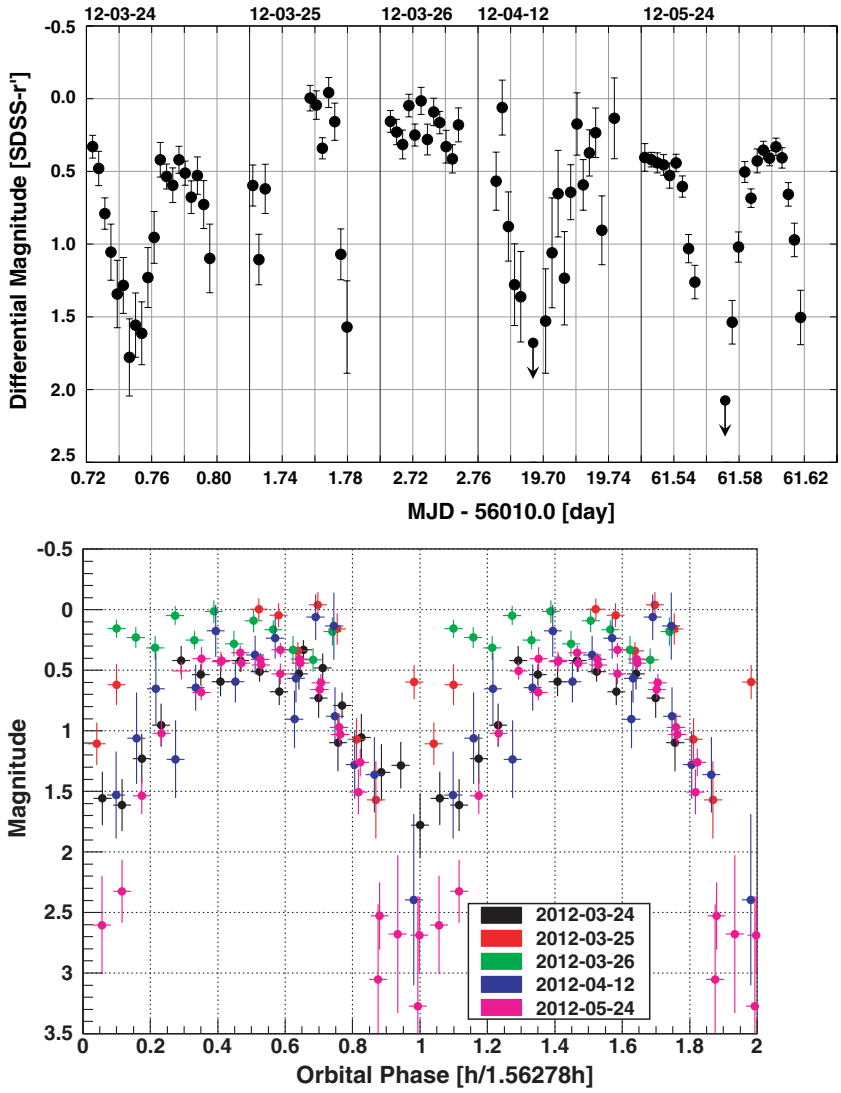

Figure 3. (Top) Temporal variations in the differential r'-band magnitudes derived by comparison with a reference star in the field, observed with the Lulin 1 m telescope from 2012 March to May. The r'-band magnitude of reference star remains constant within $\Delta m = 0.068$ mag. Note that the modulation profile differs largely among five nights of observations. (Bottom) Folded light curve of the differential r'-band magnitudes with a best-fit period of 1.56278 hr (5626 s) proposed by Romani (2012). The phase zero is defined as MJD 56010.76808. Note that both the amplitude of the modulation and the peak intensity changed by $\gtrsim$1 mag and $\sim$0.5 mag, respectively, over the five nights of observations.

(A color version of this figure is available in the online journal.)

Table 2
Fitting Parameters of *Suzaku* Data for the Power-law Model

Parameter	AO4 Value and Errors[a]	AO6 Value and Errors[a]
$N_{\rm H}$ (10^{20} cm^{-2})	$0.33^{+0.15}_{-0.13}$	<0.07
Γ	$1.71^{+0.18}_{-0.17}$	$1.26^{+0.08}_{-0.07}$
Flux (0.5–2 keV)[b]	$0.99^{+0.27}_{-0.19}$	$0.83^{+0.08}_{-0.06}$
Flux (2–10 keV)[b]	$1.78^{+0.16}_{-0.15}$	2.96 ± 0.15
χ^2 (dof)	17.4 (15)	17.6 (15)
$P(\chi^2)$	0.29	0.29

Notes.
[a] All errors are 1σ.
[b] In unit of 10^{-13} erg cm^{-2} s^{-1}.

however, consistent with zero for the 2011 data. The model fitting results are summarized in Table 2. Although the nearby X-ray source (src B in Maeda et al. 2011, or CXOU J131147.0-343205 in Cheung et al. 2012; see Figure 4) is located only 1.′6 apart to the south, contamination from this source and other nearby faint sources is estimated to be less than 5% for the applied region of interest of 1′.

4. DISCUSSION AND CONCLUSIONS

During the first (AO4; 2009) and second (AO6; 2011) *Suzaku* observations, we detected significant variability in 1FGL J1311.7-3429 characterized by repeated flaring activity, with a timescale of $\sim$10 ks. The variability is only clearly seen above 1 keV. The NPSD is well characterized by $P(f) \propto f^{-2}$, as is the case for the X-ray variability of various classes of AGNs including Seyferts and blazars (e.g., Hayashida et al. 1998; Vaughan et al. 2003). The latter class constitutes the majority of *Fermi*-LAT sources but the X-ray variability timescales of blazars are in general somewhat longer, typically $\simeq$1 day (e.g., Kataoka et al. 2001). Such "red-noise" PSD behavior is also observed in X-ray (Galactic black hole and neutron star) binary systems, but on much shorter time scales. For example, variability as short as $\sim$1–10 ms has been observed for the

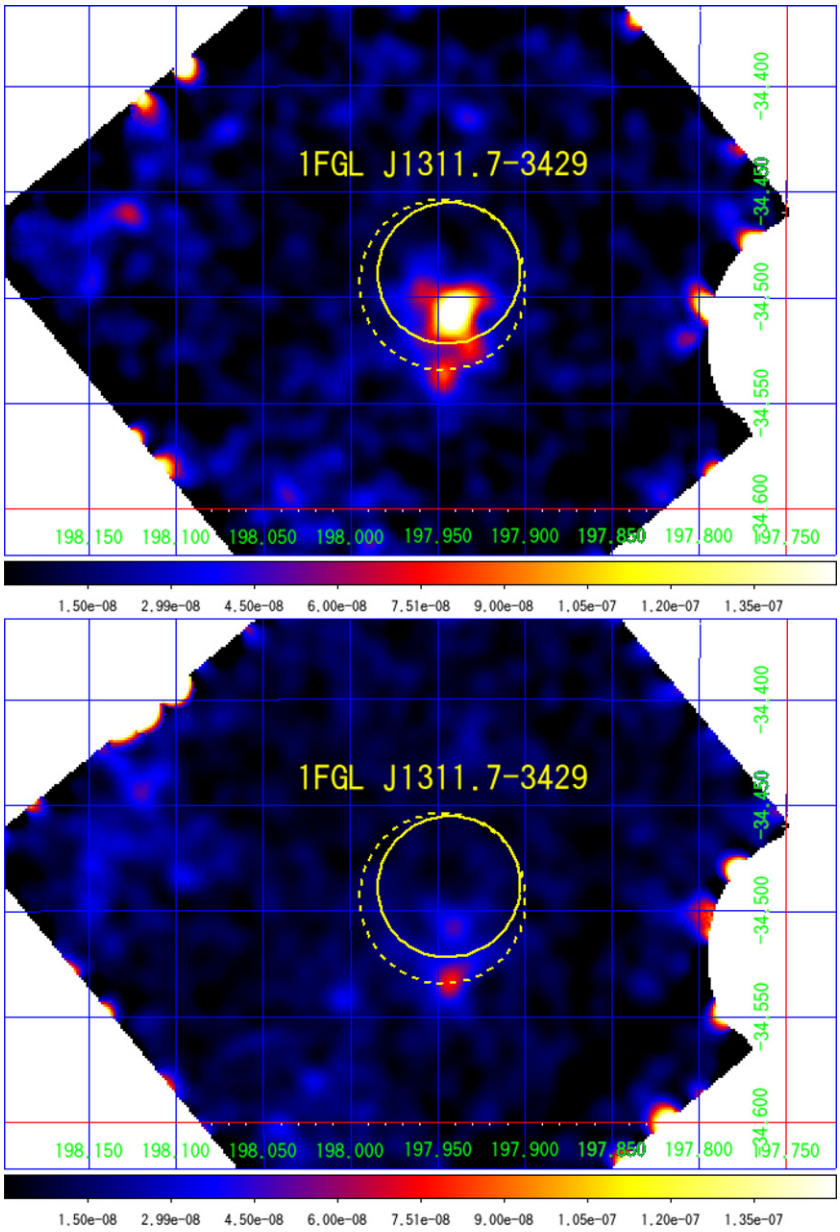

Figure 4. *Suzaku* XIS FI(XIS0+3) images of the 1FGL J1311.7-3429 region in the 0.5–10 keV photon energy range using the data during the first 20 ks (top; flare) and the last 74 ks (bottom; after the flare) in the 2009 observation obtained in AO4. The image shows the relative excess of smoothed photon counts (arbitrary units indicated in the color bar) and is displayed with linear scaling. The thick solid ellipse denotes the 95% position error of 1FGL J1311.7-3429 in the 2FGL catalog, while the dashed ellipse shows that reported in the 1FGL catalog. Note that the faint source to the south presented (and denoted as src B) in Maeda et al. (2011) is outside the 2FGL error circle.

(A color version of this figure is available in the online journal.)

famous Galactic black hole source Cyg X-1 (e.g., Meekins et al. 1984; Hayashida et al. 1998).

Significant variability has also been observed in the optical (g', Rc, r'), where it is rather a quasi-sinusoidal flux modulation with a 1.56 hr period, as recently reported by Romani (2012). Moreover, we also found that the modulation profile, including the amplitude of modulation and peak intensity, has changed largely among the six nights of observations. The apparent modulation of magnitude observed in both the IAO and LOT data is quite similar to those observed in 1FGL J2339.7-0531, which is characterized by a 4.63 hr orbital period in optical and X-ray data (Romani & Shaw 2011; Kong et al. 2012). Note that 1FGL J2339.7-0531 is now suggested to be a "radio-quiet" gamma-ray emitting black-widow MSP with a $\simeq$0.1 $M_{\odot}$ late-type companion star, viewed at inclination $i \simeq 57^{\circ}$. Moreover, this compact object companion in 1FGL J2339.7-0531 is strongly heated, with $T_{\rm eff}$ varying from $\sim$6900 K (superior conjunction) to $<$3000 K at minimum (Romani & Shaw 2011).

In this context, the spectral energy distribution (SED) of 1FGL J1311.7-3419 from radio to gamma-rays (Figure 9, top) may provide some hints on the nature of this mysterious source. 1FGL J1311.7-3419 has been the subject of both radio pulsar counterpart searches and blind searches for gamma-ray pulsations, but to date no pulsed emission has been detected (Ransom et al. 2011), and the situation is quite similar to the case for 1FGL J2339.7-0531. There are no NVSS radio sources catalogued within the 2FGL ellipse of 1FGL J1311.7-3429 down to 1.4 GHz flux completeness limit of $\simeq$2.5 mJy

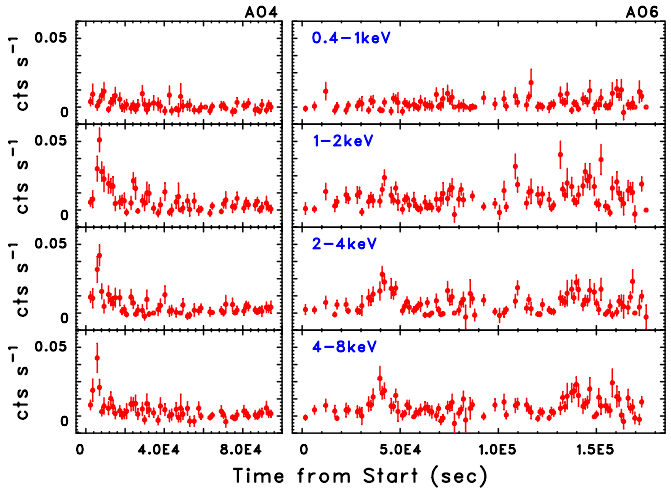

Figure 5. Multi-band *Suzaku* X-ray light curves of 1FGL J1311.7-3429 obtained during AO4 (2009) and AO6 (2011) observations: 0.4–1 keV, 1–2 keV, 2–4 keV, and 4–8 keV (from top to bottom). The XIS-0, 1, 3 data are summed.

(A color version of this figure is available in the online journal.)

(Condon et al. 1998), which is given as an arrow in Figure 9 (top). From the 0.1–100 GeV gamma-ray flux listed in the 2FGL catalog, $F_\gamma \equiv F_{0.1-100\,\mathrm{GeV}} \simeq 6.2 \times 10^{-11}$ erg cm^{-2} s^{-1}, we obtain $F_\gamma/F_X \simeq 300$, $F_\gamma/F_R \gtrsim 1.7 \times 10^6$ for 1FGL J1311.7-3429, where F_X and F_R are the X-ray and radio fluxes measured in 2–10 keV and at 1.4 GHz, respectively. Note, these values are almost comparable to those measured in 1FGL J2339.7-0531, with $F_\gamma \simeq 3.0 \times 10^{-11}$ erg cm^2 s^{-1}, $F_\gamma/F_X \simeq 150$ and $F_\gamma/F_R \gtrsim 8.7 \times 10^5$. Although its flat spectrum X-ray continua and relatively high γ-ray-to-X-ray energy flux ratio (of $\gtrsim$100) is typical of the subclass of blazars (FSRQ; Nolan et al. 2012), the non-detection in the radio as well as its curved gamma-ray spectrum seems to strongly disfavor an AGN association for 1FGL J1311.7-3429.

To further support the MSP association of 1FGL J1311.7-3429, Figure 9 (bottom) shows a close-up of the SED of 1FGL J1311.7-3429 in the optical/UV bands, reconstructed from IAO and *Swift* UVOT data. Observed magnitudes were converted to flux density based on Fukugita et al. (1995). Red dashed line indicates a tentative fit with a blackbody model of $T \simeq 1.2 \times 10^4$ K (or $kT \simeq 1$ eV) assuming an emission volume radius of $R_{\rm bb} \simeq 1.5 \times 10^4\ d_{\rm kpc}$ km, where $d_{\rm kpc}$ is the distance to the source in units of 1 kpc. Therefore, the optical/UV spectrum of 1FGL J1311.7-3429 seems compatible with what is expected from a companion star of a radio-quiet MSP like 1FGL J2339.7-0531. A slightly higher temperature than 1FGL J2339.7-0531 ($kT \simeq 0.3$–0.6 keV; Romani & Shaw 2011) may indicate $\times 2$ smaller orbital radius, $\sim 5 \times 10^5$ km, for the 1FGL J1311.7-3429 binary system, assuming that the mass of the companion star is 0.1 $M_\odot$ and the pulsar spin-down luminosity is $L \simeq 10^{34}$ erg s^{-1} (parameters suggested for 1FGL J2339.7-0531 binary system; Romani & Shaw 2011). A change of the modulation profile observed in the r' band may be accounted for by rapid changes in the companion star temperature, but this remains uncertain.

Since both the optical and X-ray light curves in the case of 1FGL J2339.7-0531 clearly exhibits a 4.63 hr orbital modulation (Romani & Shaw 2011; Kong et al. 2012), the detection of periodicity in the X-ray light curve of 1FGL J1311.7-3429 is also likely. In fact, the folded X-ray light curve exhibits an excess feature around $\phi = 0.5$. As indicated by Romani (2012), this is presumably a pulsar superior conjunction, although both the

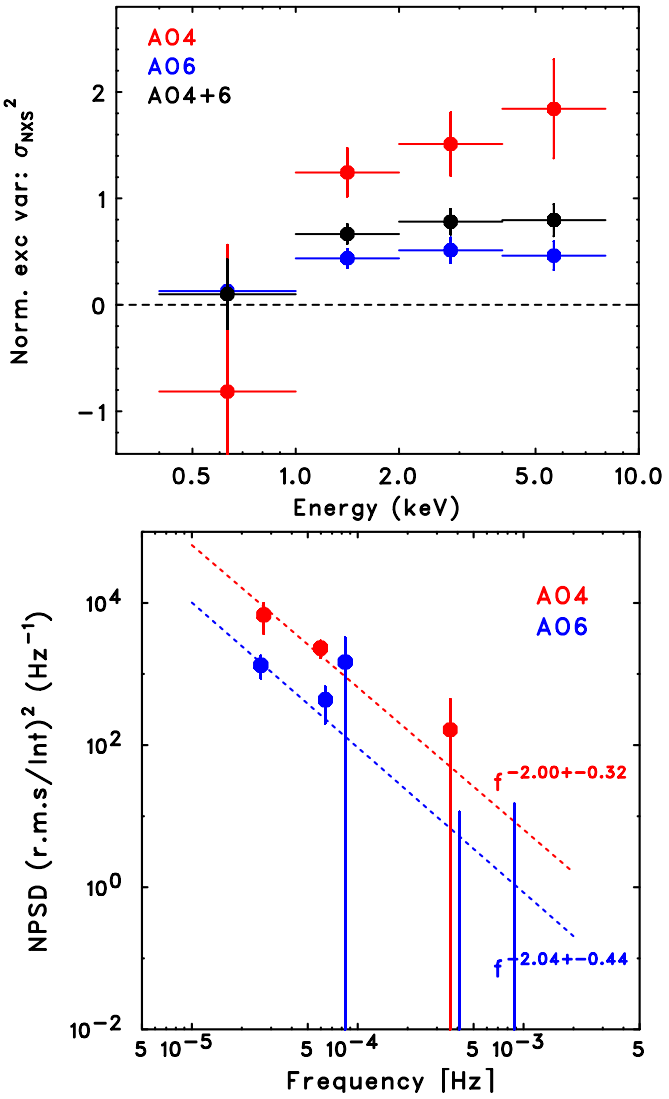

Figure 6. (Top) Energy dependence of X-ray variability of 1FGL J1311.7-3429. The variability parameter, excess variance was calculated for the total exposures in AO4 (2009; red) and AO6 (2011; blue) in four energy bands (see Figure 5). (Bottom) Normalized PSD (NPSD) calculated from the X-ray light curves of 1FGL J1311.7-3429. The dotted line shows the best-fitting power-law function of $\propto f^{-2.0}$.

(A color version of this figure is available in the online journal.)

normalized intensity as well as the phase peak appear to have changed substantially between the 2009 (AO4) and 2011 (AO6) observations. We therefore expect that X-ray variability consists of at least two different components—one associated with the binary motion as for the optical data, and the other a rather random fluctuation well represented by the NPSD of $P(f) \propto f^{-2}$, whose physical origin is still unknown but possibly related with perturbations associated with shock acceleration.

Such flaring X-ray variability has not yet been observed for 1FGL J2339.7-3429, but solely in 1FGL J1311.7-3429. In a review of X-ray emission from MSPs, Zavlin (2007) describes three primary sources of X-ray emission: (1) intrabinary shock, (2) the neutron star (NS) itself, and (3) pulsar wind nebula outside the binary system (see also Archibald et al. 2010). In fact, thermal emission of $kT \sim 0.1$–0.2 keV is often observed from MSPs, which is thought to arise from the surface of the NS and is steady with time (e.g., Marelli et al. 2011; Maeda et al. 2011). More recently, thermal emission of $kT \simeq 0.1$ keV was

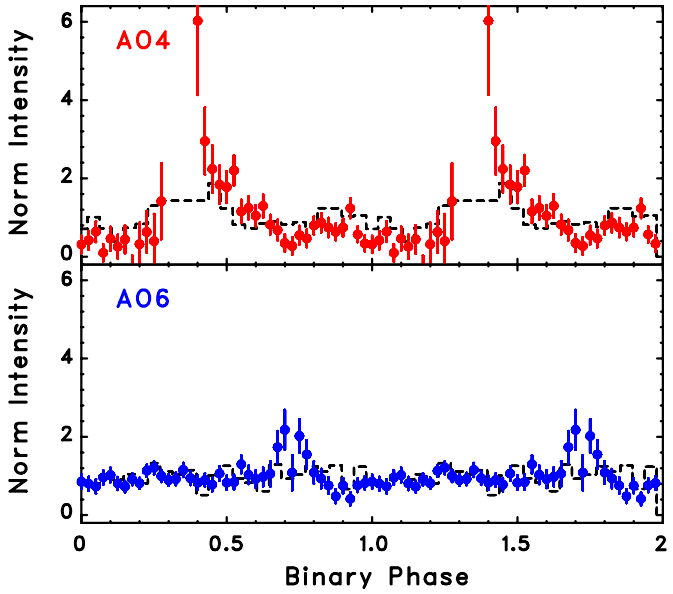

Figure 7. Folded X-ray light curves of 1FGL J1311.7-3429 reconstructed from the XIS data taken in *Suzaku* AO4 (top; red) and AO6 (bottom) observations. All the XIS0, 1, and 3 data are summed in the energy range of 0.4–10 keV. The phase zero is defined as MJD 56010.76808. The vertical axis represents the source counts divided by the average source intensity in the frame. The dashed line represents the folded X-ray light curves of a nearby field source (src B in Maeda et al. 2011) to confirm that observed excess is not due to artifacts caused by orbital gaps in the *Suzaku* data.

(A color version of this figure is available in the online journal.)

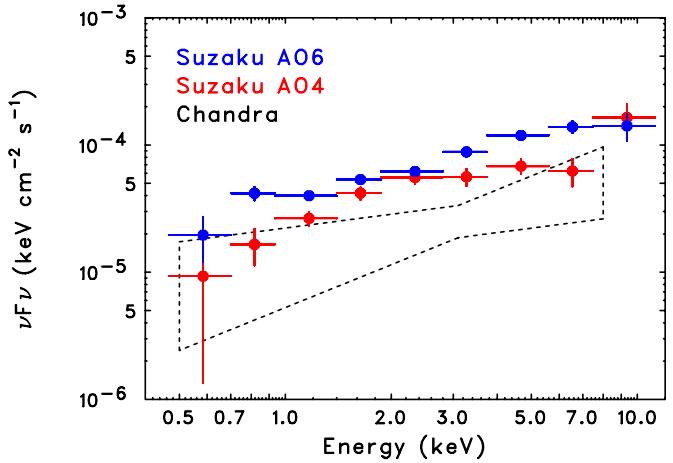

Figure 8. Comparison of the average X-ray spectra of 1FGL J1311.7-3429 observed in 2009 (AO4; red) and 2011 (AO6; blue) *Suzaku* observations. The X-ray data points represent the weighted mean of XIS0, 1, and 3. In addition, a bow-tie shows the best-fit parameters of the corresponding *Chandra* source, CXOU J131145.7-343030, observed in 2010 (Cheung et al. 2012).

(A color version of this figure is available in the online journal.)

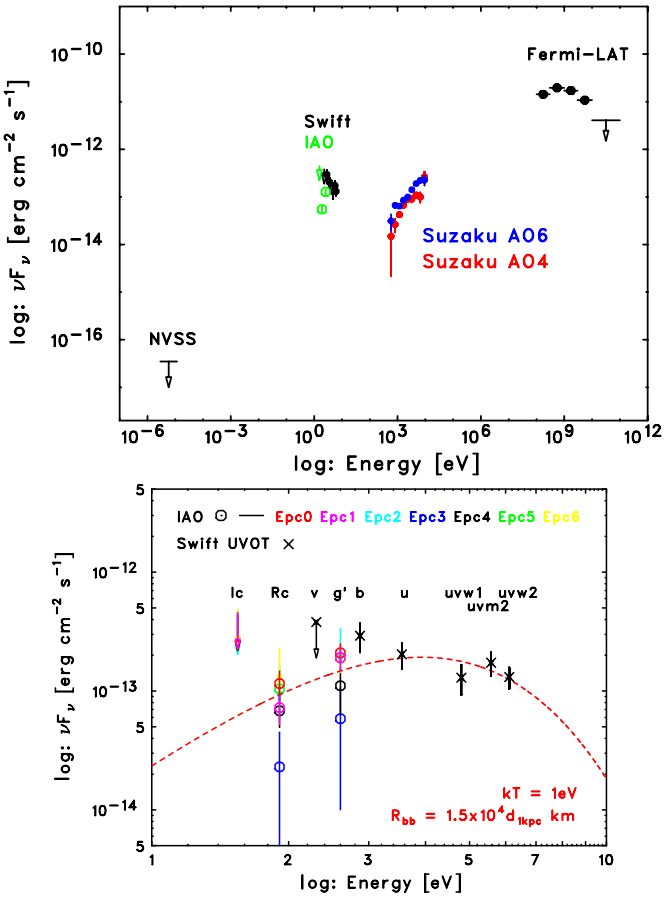

Figure 9. (Top) Broadband spectrum of 1FGL J1311.703429. The X-ray data are as presented in Figure 8. The gamma-ray data points are taken from the 2FGL catalog (Nolan et al. 2012). The radio upper limit of 2.5 mJy at 1.4 GHz is taken from the NVSS catalog (Condon et al. 1998). The optical and UV data represents *Swift* UVOT data (see Maeda et al. 2011 and Cheung et al. 2012). (Bottom) Close-up of the broadband spectrum in the optical–UV range. Epochs 0–6 (1200 s each) correspond to time ranges defined in Figure 2. Note that the optical–UV spectrum is well fitted by a blackbody model of $kT \sim 1$ eV with a radius of the emission volume of $R_{\rm bb} \simeq 1.5 \times 10^4\ d_{\rm kpc}$ km, where $d_{\rm kpc}$ is distance to the source in unit of 1 kpc.

(A color version of this figure is available in the online journal.)

also detected from 1FGL J2339.7-0531 (Kong et al. 2012, in prep), which is again steady despite the large flux modulation associated with binary motion being observed above 2 keV. Therefore, the fact that X-ray variability is not clearly seen below 1 keV may suggest that there could be some contribution from the surface of the NS, although from the spectral fitting it is not statistically significant. Then the variable, hard X-ray emission could arise from the intrabinary shock rather than the nebula because variability as short as $\simeq$10 ks is unlikely to originate from the extended pulsar wind nebula.[11] Such a shock could readily produce gamma-ray emission (Arons & Tavani 1993). If localized, it could easily account for the orbital modulation as seen in the X-ray emission from 1FGL J2339.7-0531. But if material leaving the companion star, either through Roche lobe overflow or a stellar wind is non-uniform or patchy, we might expect random flaring activity as we see in the X-ray data of 1FGL J1311.7-3429.

We can also speculate on the nature of 1FGL J1311.7-3429 based solely on the gamma-ray properties, an approach already applied to the 1FGL unIDs in Ackermann et al. (2012). Figure 10 (top) presents a comparison of the 2FGL associated (either AGNs (blue) or PSRs (green)) and unassociated sources (red) in the Variability_index and Signif_curve plane. Apparently, 1FGL J1311.7-3429 is situated in the typical PSR regions of this diagnostic plane. Similarly, Figure 10 (bottom) plots the distribution of PSRs and AGNs in the Photon index versus $F_{0.1-100\,\rm GeV}$ plane. In this case, 1FGL J1311.7-3429 is at

[11] Variability has been observed in some pulsar wind nebula in X-rays and gamma-rays, but with typical timescales of a week to months (e.g., Pavlov et al. 2001; Abdo et al. 2011).

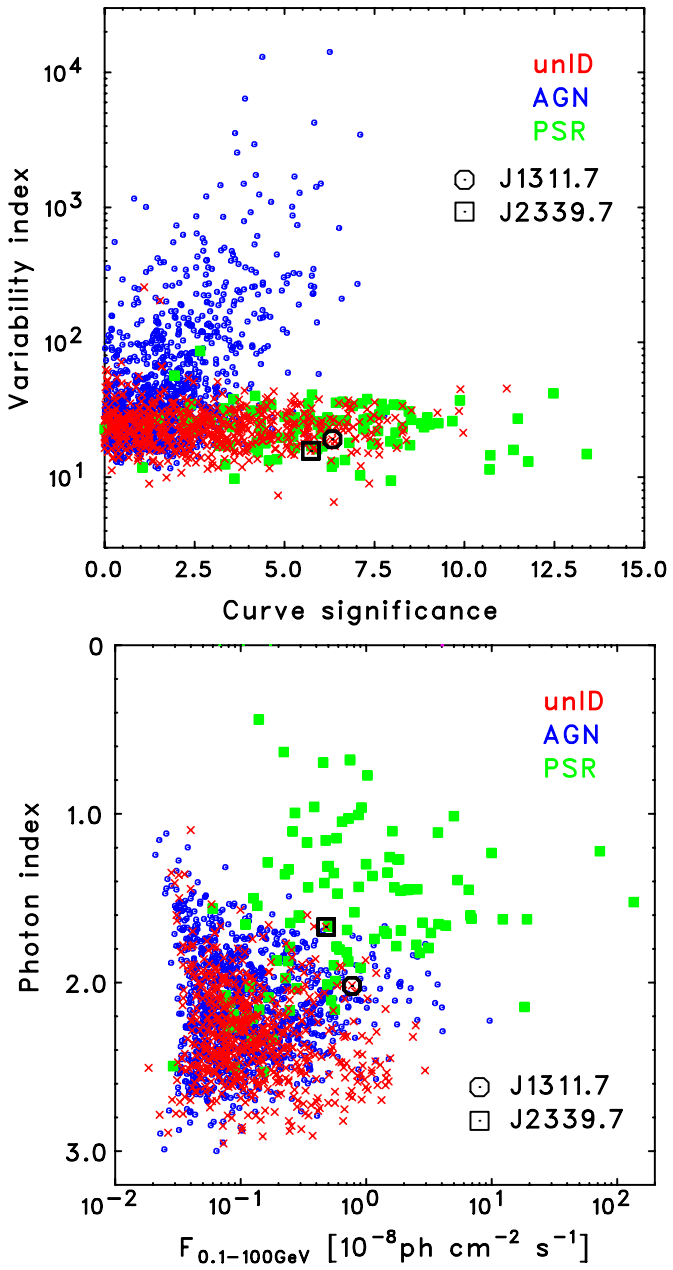

Figure 10. (Top) Comparison of the 2FGL Variability Index vs. Curvature Significance for associated sources (AGN: blue, PSR: green) and unassociated sources (red). (Bottom) Comparison of the 2FGL Photon Index vs. 0.1–100 GeV Flux for the associated sources and unassociated sources. In both panels, a separation between the AGN and PSR populations is evident. Note that 1FGL J1311.7-3429 is situated in the typical PSR region in the top panel, whilst at the boundary of AGN/PSR sources in the bottom panel.

(A color version of this figure is available in the online journal.)

the boundary of AGN and PSR sources, so is still consistent with a PSR association. For comparison, we also plot the gamma-ray parameters for 1FGL J2339.7-0531. In both panels, the gamma-ray properties of 1FGL J1311.7-3429 and 1FGL J2339.7-0531 are quite similar. Again, this supports the idea that 1FGL J1311.7-3429 is a black-widow system and may be a second example of a "radio-quiet" MSP after 1FGL J2339.7-0531.

Finally, if the rapid X-ray flaring variability observed with *Suzaku* may be due to inhomogeneity of shock material and/or rapid changes in the beaming factor, this could be expected to occur also in gamma-rays, as suggested by a smooth connection of the spectrum between X-ray and gamma-ray energies. Moreover, we may see correlated variability also in the optical, which may be related to the change of modulation profile in the r'-band magnitudes that we see in Figure 3. Unfortunately, such fast variability is difficult to observe in gamma-rays as we mentioned for the one-month binned light curve in Section 1, despite the excellent sensitivity of *Fermi*-LAT. The low gamma-ray statistics also make it difficult to run a cross-correlation in order to measure any possible correlated optical, X-ray and gamma-ray variability. Further continuous investigation is necessary to confirm the origin of "variable" X-ray emission observed in the 1FGL J1311.7-3429 system.

This work is partially supported by the Japanese Society for the Promotion of Science (JSPS) KAKENHI 19047002. Work by C.C.C. at NRL is supported in part by NASA DPR S-15633-Y. We thank the anonymous referee for his/her helpful comments that improved the manuscript.

REFERENCES

Abdo, A. A., Ackermann, M., Ajello, M., et al. 2009a, Science, 325, 848
Abdo, A. A., Ackermann, M., Ajello, M., et al. 2009b, ApJ, 706, L1
Abdo, A. A., Ackermann, M., Ajello, M., et al. 2009c, ApJ, 706, L56
Abdo, A. A., Ackermann, M., Ajello, M., et al. 2009d, ApJ, 701, L123
Abdo, A. A., Ackermann, M., Ajello, M., et al. 2009e, Science, 326, 1512
Abdo, A. A., Ackermann, M., Ajello, M., et al. 2009f, ApJS, 183, 46
Abdo, A. A., Ackermann, M., Ajello, M., et al. 2010a, ApJ, 710, L92
Abdo, A. A., Ackermann, M., Ajello, M., et al. 2010b, Science, 327, 1103
Abdo, A. A., Ackermann, M., Ajello, M., et al. 2010c, ApJ, 712, 459
Abdo, A. A., Ackermann, M., Ajello, M., et al. 2010d, ApJ, 713, 154
Abdo, A. A., Ackermann, M., Ajello, M., et al. 2010e, ApJ, 714, 927
Abdo, A. A., Ackermann, M., Ajello, M., et al. 2010f, Science, 329, 817
Abdo, A. A., Ackermann, M., Ajello, M., et al. 2010g, A&A, 512, 7
Abdo, A. A., Ackermann, M., Ajello, M., et al. 2010h, ApJ, 709, L152
Abdo, A. A., Ackermann, M., Ajello, M., et al. 2010i, Science, 328, 725
Abdo, A. A., Ackermann, M., Ajello, M., et al. 2010j, ApJS, 188, 405
Abdo, A. A., Ackermann, M., Ajello, M., et al. 2011, Science, 331, 739
Ackermann, M., Ajello, M., Allafort, A., et al. 2012, ApJ, 753, 83
Archibald, A. M., Kaspi, V. M., Bogdanov, S., et al. 2010, ApJ, 722, 88
Arons, J., & Tavani, M. 1993, ApJ, 403, 249
Atwood, W. B., Abdo, A. A., Ackermann, M., et al. 2009, ApJ, 697, 1071
Casandjian, J.-M., & Grenier, I. A. 2008, A&A, 489, 849
Cheung, C. C., Donato, D., Gehrels., N., et al. 2012, ApJ, 756, 33
Condon, J. J., Cotton, W. D., Greisen, E. W., et al. 1998, AJ, 115, 1693
Fukugita, M., Shimasaku, K., & Ichikawa, T. 1995, PASP, 107, 945
Hartman, R. C., Bertsch, D. L., Bloom, S. D., et al. 1999, ApJS, 123, 79
Hayashida, K., Miyamoto, S., Negoro, H., et al. 1998, ApJ, 500, 642
Huang, K. Y., Urata, Y., Filippenko, A. V., et al. 2005, ApJ, 628, L93
Kataoka, J., Reeves, J. N., Iwasawa, K., et al. 2007, PASJ, 59, 279
Kataoka, J., Takahashi, T., Wagner, S. J., et al. 2001, ApJ, 560, 659
Kong, A. K. H., Huang, R. H. H., Cheng, K. S., et al. 2012, ApJ, 747, L3
Maeda, K., Kataoka, J., Nakamori, T., et al. 2011, ApJ, 729, 103
Marelli, M., De Luca, A., & Caraveo, P. A. 2011, ApJ, 733, 82
Meekins, J. F., Wood, K. S., Hedler, R. L., et al. 1984, ApJ, 278, 288
Monet, D. G., Levine, S. E., Canzian, B., et al. 2003, AJ, 125, 948
Muslimov, A. G., & Harding, A. K. 2003, ApJ, 588, 430
Nolan, P. L., Abdo, A. A., Ackermann, M., et al. 2012, ApJS, 199, 31
Pavlov, G. G., Kargaltsev, O. Y., Sanwal, D., et al. 2001, ApJ, 554, L189
Ransom, S. M., Ray, P. S., Camilo, F., et al. 2011, ApJ, 772, L16
Romani, R. W. 2012, ApJ, 754, L25
Romani, R. W., & Shaw, M. S. 2011, ApJ, 743, L26
Sesar, B., Svilkovic, D., Ivezić, Ž., et al. 2006, AJ, 131, 2801
Takahashi, Y., Kataoka, J., Nakamori, T., et al. 2012, ApJ, 747, 64
Vaughan, S., Edelson, R., Warwick, R. S., & Uttley, P. 2003, MNRAS, 345, 1271
Zavlin, V. E. 2007, Ap&SS, 308, 297

The Astrophysical Journal, 751:159 (20pp), 2012 June 1 doi:10.1088/0004-637X/751/2/159

MULTI-WAVELENGTH OBSERVATIONS OF BLAZAR AO 0235+164 IN THE 2008–2009 FLARING STATE

M. Ackermann[1], M. Ajello[2], J. Ballet[3], G. Barbiellini[4,5], D. Bastieri[6,7], R. Bellazzini[8], R. D. Blandford[2], E. D. Bloom[2], E. Bonamente[9,10], A. W. Borgland[2], E. Bottacini[2], J. Bregeon[8], M. Brigida[11,12], P. Bruel[13], R. Buehler[2], S. Buson[6,7], G. A. Caliandro[14], R. A. Cameron[2], P. A. Caraveo[15], J. M. Casandjian[3], E. Cavazzuti[16], C. Cecchi[9,10], E. Charles[2], A. Chekhtman[17,89], J. Chiang[2], S. Ciprini[18,10], R. Claus[2], J. Cohen-Tanugi[19], S. Cutini[16], F. D'Ammando[20,21], F. de Palma[12], C. D. Dermer[22], E. do Couto e Silva[2], P. S. Drell[2], A. Drlica-Wagner[2], R. Dubois[2], C. Favuzzi[11,12], S. J. Fegan[13], E. C. Ferrara[23], W. B. Focke[2], P. Fortin[13], L. Fuhrmann[24], Y. Fukazawa[25], P. Fusco[11,12], F. Gargano[12], D. Gasparrini[16], N. Gehrels[23], S. Germani[9,10], N. Giglietto[11,12], P. Giommi[16], F. Giordano[11,12], M. Giroletti[26], T. Glanzman[2], G. Godfrey[2], I. A. Grenier[3], S. Guiriec[27], D. Hadasch[14], M. Hayashida[2,28], R. E. Hughes[29], R. Itoh[25], G. Jóhannesson[30], A. S. Johnson[2], H. Katagiri[31], J. Kataoka[32], J. Knödlseder[33,34], M. Kuss[8], J. Lande[2], S. Larsson[35,36,37], S.-H. Lee[38], F. Longo[4,5], F. Loparco[11,12], B. Lott[39], M. N. Lovellette[22], P. Lubrano[9,10], G. M. Madejski[2], M. N. Mazziotta[12], J. E. McEnery[23,40], J. Mehault[19], P. F. Michelson[2], W. Mitthumsiri[2], T. Mizuno[25], C. Monte[12], M. E. Monzani[2], A. Morselli[41], I. V. Moskalenko[2], S. Murgia[2], M. Naumann-Godo[3], S. Nishino[25], J. P. Norris[42], E. Nuss[19], T. Ohsugi[43], A. Okumura[2,44], N. Omodei[2], E. Orlando[2,45], M. Ozaki[44], D. Paneque[46,2], J. H. Panetta[2], V. Pelassa[27], M. Pesce-Rollins[8], M. Pierbattista[3], F. Piron[19], G. Pivato[7], T. A. Porter[2], S. Rainò[12], R. Rando[6,7], D. Rastawicki[2], M. Razzano[8,47], A. Readhead[48], A. Reimer[49,2], O. Reimer[49,2], L. C. Reyes[50], J. L. Richards[48], C. Sbarra[6], C. Sgrò[8], E. J. Siskind[51], G. Spandre[8], P. Spinelli[11,12], A. Szostek[2], H. Takahashi[43], T. Tanaka[2], J. G. Thayer[2], J. B. Thayer[2], D. J. Thompson[23], M. Tinivella[8], D. F. Torres[14,52], G. Tosti[9,10], E. Troja[23,90], T. L. Usher[2], J. Vandenbroucke[2], V. Vasileiou[19], G. Vianello[2,53], V. Vitale[41,54], A. P. Waite[2], B. L. Winer[29], K. S. Wood[22], Z. Yang[35,36], S. Zimmer[35,36]

(the *Fermi*-LAT Collaboration)

R. Moderski[55], K. Nalewajko[55,56], M. Sikora[55]

and

M. Villata[57], C. M. Raiteri[57], H. D. Aller[58], M. F. Aller[58], A. A. Arkharov[59], E. Benítez[60], A. Berdyugin[61], D. A. Blinov[59], M. Boettcher[62], O. J. A. Bravo Calle[63], C. S. Buemi[64], D. Carosati[65,66], W. P. Chen[67], C. Diltz[62], A. Di Paola[68], M. Dolci[69], N. V. Efimova[59,63], E. Forné[70], M. A. Gurwell[71], J. Heidt[72], D. Hiriart[73], B. Jordan[74], G. Kimeridze[75], T. S. Konstantinova[63], E. N. Kopatskaya[63], E. Koptelova[67,76], O. M. Kurtanidze[75], A. Lähteenmäki[77], E. G. Larionova[63], L. V. Larionova[63], V. M. Larionov[78,59,63], P. Leto[64], E. Lindfors[61], H. C. Lin[67], D. A. Morozova[63], M. G. Nikolashvili[75], K. Nilsson[79], M. Oksman[77], P. Roustazadeh[62], A. Sievers[80], L. A. Sigua[75], A. Sillanpää[61], T. Takahashi[44], L. O. Takalo[61], M. Tornikoski[77], C. Trigilio[64], I. S. Troitsky[63], G. Umana[64]

(the GASP-WEBT consortium)

and

E. Angelakis[24], T. P. Krichbaum[24], I. Nestoras[24], D. Riquelme[80]

(F-GAMMA)

and

M. Krips[81], S. Trippe[82]

(IRAM-PdBI)

and

A. Arai[83], K. S. Kawabata[43], K. Sakimoto[25], M. Sasada[25], S. Sato[84], M. Uemura[43], M. Yamanaka[25], M. Yoshida[43]

(Kanata)

and

T. Belloni[85], G. Tagliaferri[85]

(RXTE)

and

E. W. Bonning[86], J. Isler[86], C. M. Urry[86]

(SMARTS)

and

E. Hoversten[87], A. Falcone[87], C. Pagani[88], M. Stroh[87]

(*Swift*-XRT)

[1] Deutsches Elektronen Synchrotron DESY, D-15738 Zeuthen, Germany

[2] W. W. Hansen Experimental Physics Laboratory, Kavli Institute for Particle Astrophysics and Cosmology, Department of Physics and SLAC National Accelerator Laboratory, Stanford University, Stanford, CA 94305, USA; eduardo@slac.stanford.edu, madejski@slac.stanford.edu

[3] Laboratoire AIM, CEA-IRFU/CNRS/Université Paris Diderot, Service d'Astrophysique, CEA Saclay, 91191 Gif sur Yvette, France

[4] Istituto Nazionale di Fisica Nucleare, Sezione di Trieste, I-34127 Trieste, Italy

[5] Dipartimento di Fisica, Università di Trieste, I-34127 Trieste, Italy

[6] Istituto Nazionale di Fisica Nucleare, Sezione di Padova, I-35131 Padova, Italy

[7] Dipartimento di Fisica "G. Galilei," Università di Padova, I-35131 Padova, Italy

[8] Istituto Nazionale di Fisica Nucleare, Sezione di Pisa, I-56127 Pisa, Italy

[9] Istituto Nazionale di Fisica Nucleare, Sezione di Perugia, I-06123 Perugia, Italy
[10] Dipartimento di Fisica, Università degli Studi di Perugia, I-06123 Perugia, Italy
[11] Dipartimento di Fisica "M. Merlin" dell'Università e del Politecnico di Bari, I-70126 Bari, Italy
[12] Istituto Nazionale di Fisica Nucleare, Sezione di Bari, 70126 Bari, Italy; fabio.gargano@ba.infn.it, silvia.raino@ba.infn.it
[13] Laboratoire Leprince-Ringuet, École polytechnique, CNRS/IN2P3, Palaiseau, France
[14] Institut de Ciències de l'Espai (IEEE-CSIC), Campus UAB, 08193 Barcelona, Spain
[15] INAF-Istituto di Astrofisica Spaziale e Fisica Cosmica, I-20133 Milano, Italy
[16] Agenzia Spaziale Italiana (ASI) Science Data Center, I-00044 Frascati (Roma), Italy
[17] Artep Inc., 2922 Excelsior Springs Court, Ellicott City, MD 21042, USA
[18] ASI Science Data Center, I-00044 Frascati (Roma), Italy
[19] Laboratoire Univers et Particules de Montpellier, Université Montpellier 2, CNRS/IN2P3, Montpellier, France
[20] IASF Palermo, 90146 Palermo, Italy
[21] INAF-Istituto di Astrofisica Spaziale e Fisica Cosmica, I-00133 Roma, Italy
[22] Space Science Division, Naval Research Laboratory, Washington, DC 20375-5352, USA
[23] NASA Goddard Space Flight Center, Greenbelt, MD 20771, USA
[24] Max-Planck-Institut für Radioastronomie, Auf dem Hügel 69, 53121 Bonn, Germany
[25] Department of Physical Sciences, Hiroshima University, Higashi-Hiroshima, Hiroshima 739-8526, Japan
[26] INAF Istituto di Radioastronomia, 40129 Bologna, Italy
[27] Center for Space Plasma and Aeronomic Research (CSPAR), University of Alabama in Huntsville, Huntsville, AL 35899, USA
[28] Department of Astronomy, Graduate School of Science, Kyoto University, Sakyo-ku, Kyoto 606-8502, Japan
[29] Department of Physics, Center for Cosmology and Astro-Particle Physics, The Ohio State University, Columbus, OH 43210, USA
[30] Science Institute, University of Iceland, IS-107 Reykjavik, Iceland
[31] College of Science, Ibaraki University, 2-1-1 Bunkyo, Mito 310-8512, Japan
[32] Research Institute for Science and Engineering, Waseda University, 3-4-1, Okubo, Shinjuku, Tokyo 169-8555, Japan
[33] CNRS, IRAP, F-31028 Toulouse cedex 4, France
[34] GAHEC, Université de Toulouse, UPS-OMP, IRAP, Toulouse, France
[35] Department of Physics, Stockholm University, AlbaNova, SE-106 91 Stockholm, Sweden
[36] The Oskar Klein Centre for Cosmoparticle Physics, AlbaNova, SE-106 91 Stockholm, Sweden
[37] Department of Astronomy, Stockholm University, SE-106 91 Stockholm, Sweden
[38] Yukawa Institute for Theoretical Physics, Kyoto University, Kitashirakawa Oiwake-cho, Sakyo-ku, Kyoto 606-8502, Japan
[39] CNRS/IN2p3, Centre d'Études Nucléaires de Bordeaux Gradignan, Université Bordeaux 1, 33175 Gradignan, France
[40] Department of Physics and Department of Astronomy, University of Maryland, College Park, MD 20742, USA
[41] Istituto Nazionale di Fisica Nucleare, Sezione di Roma "Tor Vergata," I-00133 Roma, Italy
[42] Department of Physics, Boise State University, Boise, ID 83725, USA
[43] Hiroshima Astrophysical Science Center, Hiroshima University, Higashi-Hiroshima, Hiroshima 739-8526, Japan
[44] Institute of Space and Astronautical Science, JAXA, 3-1-1 Yoshinodai, Chuo-ku, Sagamihara, Kanagawa 252-5210, Japan
[45] Max-Planck Institut für extraterrestrische Physik, 85748 Garching, Germany
[46] Max-Planck-Institut für Physik, D-80805 München, Germany
[47] Santa Cruz Institute for Particle Physics, Department of Physics and Department of Astronomy and Astrophysics, University of California at Santa Cruz, Santa Cruz, CA 95064, USA
[48] Cahill Center for Astronomy and Astrophysics, California Institute of Technology, Pasadena, CA 91125, USA
[49] Institut für Astro- und Teilchenphysik and Institut für Theoretische Physik, Leopold-Franzens-Universität Innsbruck, A-6020 Innsbruck, Austria
[50] Department of Physics, California Polytechnic State University, San Luis Obispo, CA 93401, USA; lreyes04@calpoly.edu
[51] NYCB Real-Time Computing Inc., Lattingtown, NY 11560-1025, USA
[52] Institució Catalana de Recerca i Estudis Avançats (ICREA), Barcelona, Spain
[53] Consorzio Interuniversitario per la Fisica Spaziale (CIFS), I-10133 Torino, Italy
[54] Dipartimento di Fisica, Università di Roma "Tor Vergata," I-00133 Roma, Italy
[55] Nicolaus Copernicus Astronomical Center, 00-716 Warsaw, Poland; knalew@colorado.edu, sikora@camk.edu.pl
[56] University of Colorado, 440 UCB, Boulder, CO 80309, USA
[57] INAF, Osservatorio Astronomico di Torino, I-10025 Pino Torinese (TO), Italy
[58] Department of Astronomy, University of Michigan, Ann Arbor, MI 48109-1042, USA
[59] Pulkovo Observatory, 196140 St. Petersburg, Russia
[60] Instituto de Astronomía, Universidad Nacional Autónoma de México, México, D. F., Mexico
[61] Tuorla Observatory, University of Turku, FI-21500 Piikkiö, Finland
[62] Department of Physics and Astronomy, Ohio University, Athens, OH 45701, USA
[63] Astronomical Institute, St. Petersburg State University, St. Petersburg, Russia
[64] Osservatorio Astrofisico di Catania, 95123 Catania, Italy
[65] EPT Observatories, Tijarafe, La Palma, Spain
[66] INAF, TNG Fundacion Galileo Galilei, La Palma, Spain
[67] Graduate Institute of Astronomy, National Central University, Jhongli 32054, Taiwan
[68] Osservatorio Astronomico di Roma, I-00040 Monte Porzio Catone (Roma), Italy
[69] Osservatorio Astronomico di Collurania "Vincenzo Cerruli," 64100 Teramo, Italy
[70] Agrupació Astronòmica de Sabadell, 08206 Sabadell, Spain
[71] Harvard-Smithsonian Center for Astrophysics, Cambridge, MA 02138, USA
[72] Landessternwarte, Universität Heidelberg, Königstuhl, D 69117 Heidelberg, Germany
[73] Instituto de Astronomía, Universidad Nacional Autónoma de México, Ensenada, B. C., Mexico
[74] School of Cosmic Physics, Dublin Institute for Advanced Studies, Dublin, 2, Ireland
[75] Abastumani Observatory, Mt. Kanobili, 0301 Abastumani, Georgia
[76] Department of Physics, National Taiwan University, 106 Taipei, Taiwan
[77] Metsähovi Radio Observatory, Aalto University, FIN-02540 Kylmala, Finland
[78] Isaac Newton Institute of Chile, St. Petersburg Branch, St. Petersburg, Russia
[79] Finnish Centre for Astronomy with ESO (FINCA), University of Turku, FI-21500 Piikiiö, Finland
[80] Institut de Radio Astronomie Millimètrique, Avenida, Divina Pastora 7, Local 20, 18012 Granada, Spain
[81] Institut de Radioastronomie Millimétrique, Domaine Universitaire, 38406 Saint Martin d'Hères, France
[82] Department of Physics and Astronomy, Seoul National University, Seoul, 151-742, Korea

[83] Department of Physics, Graduate School of Science, Kyoto University, Kyoto, Japan
[84] Department of Physics and Astrophysics, Nagoya University, Chikusa-ku Nagoya 464-8602, Japan
[85] INAF Osservatorio Astronomico di Brera, I-23807 Merate, Italy
[86] Department of Astronomy, Department of Physics and Yale Center for Astronomy and Astrophysics, Yale University, New Haven, CT 06520-8120, USA
[87] Department of Astronomy and Astrophysics, Pennsylvania State University, University Park, PA 16802, USA
[88] Department of Physics and Astronomy, University of Leicester, Leicester LE1 7RH, UK
Received 2011 October 20; accepted 2012 March 23; published 2012 May 17

ABSTRACT

The blazar AO 0235+164 ($z = 0.94$) has been one of the most active objects observed by *Fermi* Large Area Telescope (LAT) since its launch in Summer 2008. In addition to the continuous coverage by *Fermi*, contemporaneous observations were carried out from the radio to γ-ray bands between 2008 September and 2009 February. In this paper, we summarize the rich multi-wavelength data collected during the campaign (including F-GAMMA, GASP-WEBT, Kanata, OVRO, *RXTE*, SMARTS, *Swift*, and other instruments), examine the cross-correlation between the light curves measured in the different energy bands, and interpret the resulting spectral energy distributions in the context of well-known blazar emission models. We find that the γ-ray activity is well correlated with a series of near-IR/optical flares, accompanied by an increase in the optical polarization degree. On the other hand, the X-ray light curve shows a distinct 20 day high state of unusually soft spectrum, which does not match the extrapolation of the optical/UV synchrotron spectrum. We tentatively interpret this feature as the bulk Compton emission by cold electrons contained in the jet, which requires an accretion disk corona with an effective covering factor of 19% at a distance of 100 R_g. We model the broadband spectra with a leptonic model with external radiation dominated by the infrared emission from the dusty torus.

Key words: BL Lacertae objects: individual (AO 0235+164) – galaxies: active – galaxies: jets – gamma rays: galaxies – radiation mechanisms: non-thermal

Online-only material: color figures

1. INTRODUCTION

Blazars are a class of active galactic nuclei (AGNs) characterized by high flux variability at all wavelengths and compact (milliarcsecond scale) radio emission of extreme brightness temperatures, often exceeding the Compton limit (Urry 1999). Their radio spectra are generally well described by a power-law shape, with a "flat" spectral index $\alpha < 0.5$ (where the flux density $F_\nu \propto \nu^{-\alpha}$). Multi-epoch Very Long Baseline Interferometry (VLBI) observations often show superluminal expansion, and the radio and optical emission is usually highly polarized. These general properties are well described as arising in a relativistic jet pointing close to our line of sight (Blandford & Rees 1978). The jet, presumably deriving its power from accretion onto a supermassive, rotating black hole (BH) surrounded by an accretion disk, contains ultrarelativistic electrons (with particle Lorentz factors γ_{el} reaching 10^3–10^5, depending on the object). These relativistic electrons produce soft photons from radio up to UV (or in some cases, soft X-rays) through synchrotron emission, and high-energy photons up to TeV energies, via the inverse Compton process which involves scattering of synchrotron photons (the SSC scenario), as well as scattering of externally produced soft photons (the External Radiation Compton, ERC, scenario). A contribution to the high-energy radiation can also be provided by synchrotron radiation of pair cascades powered by hadronic processes and by synchrotron emission of ultra-high-energy protons and muons (see reviews of radiative models of blazars by Sikora & Madejski 2001; Levinson 2006; Böttcher 2007). Noting difficulties of hadronic models to explain the spectra of luminous blazars (Sikora et al. 2009; Sikora 2011), we investigate in this paper only leptonic models, i.e., the models which involve production of radiation by directly accelerated electrons. Densely sampled, simultaneous monitoring observations throughout the entire electromagnetic spectrum from the radio to γ-ray bands can provide important constraints on such models.

When emission lines are absent or weak, with an equivalent width (EW) less than 5 Å in the rest frame (see, e.g., Stickel et al. 1991), a blazar is classified as a BL Lac object; otherwise, it belongs to the class of flat-spectrum radio quasars (FSRQs). While in a majority of BL Lac objects—especially in those with the νF_ν spectral energy distribution (SED) peaking in the far UV-to-X-ray range (the so-called HSP or high-synchrotron-peaked BL Lac objects)—detection of emission lines is rare, and if detected, the lines are extremely weak (for recent measurements, see, e.g., Stocke et al. 2011), in the objects where the SED peaks in the infrared or optical range (the so-called LSP or low-synchrotron-peaked BL Lac objects), easily discernible emission lines have been detected often. When detected, such lines provide a measurement of redshift, but also yield crucial information about the details of accretion in the central source. In some cases such as AO 0235+164 (Raiteri et al. 2007), discussed in this paper, and even BL Lacertae (Vermeulen et al. 1995; Corbett et al. 2000), the prototype of the BL Lac class, the EW of emission lines can vary from one observational epoch to another. This is primarily due to the large-amplitude variability of the nonthermal continuum, which becomes brighter or fainter with respect to the presumably less-variable emission lines. Regardless, the detailed properties of the emission lines are crucial in establishing the radiative environment encountered by the jet emerging from the nucleus, and thus are indispensable in establishing the most likely source of seed-photon population for inverse Compton scattering. While the most compelling scenario has the internal jet photons dominating this population in the HSP sub-class, and the external photons (from emission-line region, or disk photons rescattered by the medium confining the lines) in FSRQs, the situation with LSP BL Lac objects is unclear.

[89] Resident at Naval Research Laboratory, Washington, DC 20375, USA.
[90] NASA Postdoctoral Program Fellow, USA.

Studies of an LSP blazar AO 0235+164 provide an exceptional opportunity to answer this question. It is one of the original BL Lac objects in the Stein et al. (1976) compilation, discovered via optical identification of a variable radio source by Spinrad & Smith (1975). Early observations—as well as the inspection of historical plates—revealed that optical variability can range over 5 mag (Rieke et al. 1976), motivating monitoring observations over a wide range of frequencies since its discovery. The redshift $z_{\rm em} = 0.94$ has been inferred from weak optical emission lines by Cohen et al. (1987), but even earlier optical spectroscopy revealed two absorption line systems, one at $z_{\rm ab1} = 0.524$, and another, weaker one at $z_{\rm ab2} = 0.852$ discovered by Burbidge et al. (1976) and by Rieke et al. (1976). The intervening $z_{\rm ab1} = 0.524$ system has also been detected in absorption in the radio, via the redshifted hydrogen 21 cm line by Wolfe & Wills (1977) and Roberts (1976), but also as an Lyα absorber, revealing damped Lyα properties (Snijders 1982) and implying *a considerable absorption in other bands*. Detailed studies of that absorbing system by Junkkarinen et al. (2004) allow accurate corrections to be applied to the observed optical spectra in order to determine reliably the intrinsic spectrum of the blazar. Likewise, since the environment in the field of AO 0235+164 is complex and includes several possibly interacting foreground galaxies at $z_{\rm ab1} = 0.524$ as well as the system at $z_{\rm ab2} = 0.852$, the *emission* in the optical–UV band (and to a much lesser degree, in the soft X-ray band) may be contaminated. One galaxy, probably a normal spiral, is 1.3 arcsec east, while another object, about 2 arcsec to the south, is known to be an AGN and could affect the flux of AO 0235+164 when it is very faint, especially in the bluer part of the spectrum (Raiteri et al. 2005).

Historical data for this source are abundant. Radio observations were performed by many instruments, starting from about 100 MHz up to 300 GHz, and including multi-epoch VLBI studies (Jorstad et al. 2001). Space and ground-based infrared data are available from submillimeter (sub-mm; far-IR) down to micron wavelengths (near-IR); optical bands, UBVRI, have been extensively monitored by many telescopes around the world. AO 0235+164 has also been detected in the high-energy band by essentially all soft X-ray observatories including *Einstein* (Worral & Wilkes 1990), *EXOSAT* (Ghosh & Soundararajaperumal 1995), *ROSAT* (Madejski et al. 1996; Comastri et al. 1997), *ASCA* (Madejski et al. 1996; Junkkarinen et al. 2004), *Beppo-SAX* (Padovani et al. 2004), *RXTE* (Webb et al. 2000), and *XMM-Newton* (Raiteri et al. 2008). This source has also been identified as a powerful and strongly variable γ-ray emitter via observations by *EGRET* on board the *Compton Gamma-Ray Observatory* (*CGRO*) in the high γ-ray energy range from 30 MeV to 20 GeV, with six pointings between 1992 and 1997 providing two detections (Hunter et al. 1993; Madejski et al. 1996) and four upper limits. The mid-energy γ-ray emission was probed by *COMPTEL* during *CGRO* Cycle 4 (1994–1995), yielding only upper limits for the flux in the interval of 0.75–30 MeV. These numerous multi-wavelength observations show that AO 0235+164 is characterized by extreme variability on long (month–years) and short (intraday) timescales over a wide range of the electromagnetic spectrum.

The study of blazars, of their broadband spectra and of their complex variability, has been greatly enriched since the start of scientific observations with the *Fermi* Large Area Telescope (LAT) in 2008 August (Atwood et al. 2009) thanks to its high sensitivity and essentially uninterrupted observations afforded by the survey mode. Such new and sensitive γ-ray observations motivated many multi-band campaigns, often conducted with dedicated facilities, and AO 0235+164 was (and continues to be) one of the well-sampled targets. This paper presents the results of the LAT monitoring of AO 0235+164, as reported in Section 2. The description of multi-wavelength observations conducted between 2008 August and 2009 February when the source showed strong activity in γ-rays as well as in radio through optical and X-ray bands (Corbel & Reyes 2008; Foschini et al. 2008) follows in Section 3. The analysis of those data, including the discussion of the temporal profiles measured in various bands and the connection to the γ-ray activity, is reported in Section 4. A significant part of these data have been independently analyzed by Agudo et al. (2011b). In Section 5, we present the overall SED and its temporal behavior, and discuss the implications of the data on the modeling of emission processes and the structure of the jet in AO 0235+164: there, we argue that while the EW of emission lines in this object might suggest a classification as a BL Lac object, the isotropic luminosity inferred from the data indicates it is a quasar. In Section 6, we show models of the broadband emission in the context of synchrotron + Compton models. Our consideration of the broadband SED suggests that the most likely mechanism for γ-ray emission is the Comptonization of circumnuclear IR radiation from dust, commonly present in quasars. This is a different scenario from the one proposed by Agudo et al. (2011b), who argued for the synchrotron self-Compton process. We discuss these two approaches in Section 7. We conclude with a summary of our results in Section 8.

2. *FERMI*-LAT OBSERVATIONS AND DATA ANALYSIS

The LAT, the primary instrument on board the *Fermi* γ-ray observatory, is an electron–positron pair conversion telescope sensitive to γ-rays of energies from 20 MeV to >300 GeV. The LAT consists of a high-resolution silicon microstrip tracker, a CsI hodoscopic electromagnetic calorimeter, and an anticoincidence detector for the identification of charged particles' background. The full description of the instrument and its performance can be found in Atwood et al. (2009). The large field of view (~2.4 sr) allows the LAT to observe the full sky in survey mode every 3 hr. The LAT point-spread function (PSF) strongly depends on both the energy and the conversion point in the tracker, but less so on the incidence angle. For 1 GeV normal-incidence conversions in the upper section of the tracker, the PSF 68% containment radius is $0\overset{\circ}{.}8$.

The *Fermi*-LAT data of AO 0235+164 presented here were obtained in the time period between 2008 August and 2009 February when AO 0235+164 entered a bright high γ-ray state, and immediately after, dropped to lower states. The data have been analyzed by using the standard *Fermi*-LAT software package.[91] The Pass 6 Diffuse event class and `P6_V3_DIFFUSE` instrument response functions (Atwood et al. 2009) were used in our analysis. We selected events within a 15° region of interest centered on the source position, having energy greater than 100 MeV. The data have been analyzed using the Science Tools software package (version v9r16). In order to avoid background contamination from the bright Earth limb, time intervals when the Earth entered the LAT Field of View were excluded from the data set. In addition, events with zenith angles larger than 105° with respect to the Earth reference frame (Abdo et al. 2009) were excluded from the analysis. The data were analyzed with an

[91] http://fermi.gsfc.nasa.gov/ssc/data/analysis/documentation/Cicerone/

unbinned maximum likelihood technique described by Mattox et al. (1996) using the analysis software (gtlike) developed by the LAT team.[92]

Accurate spectral and flux measurements require a reliable accounting for the diffuse foreground due to the Galactic interstellar emission, as well as the extragalactic diffuse γ-ray emission, the residual cosmic-ray background, and contamination from nearby sources. The fitting procedure simultaneously fits for the parameters of the source of interest as well as of nearby γ-ray sources and the diffuse backgrounds, which in turn have been modeled using gll_iem_v02 for the Galactic diffuse emission and isotropic_iem_v02 for the extragalactic isotropic emission models.[93]

The sources surrounding AO 0235+164 were modeled using a power-law function:

$$\frac{dN}{dE} = \frac{N(1-\Gamma)E^{-\Gamma}}{E_{\rm max}^{1-\Gamma} - E_{\rm min}^{1-\Gamma}}, \quad (1)$$

where N is the normalization factor and Γ the photon index. In the fitting procedure, all sources within 10° were included in the model with the normalization factor N free, while the sources located between 10° and 20° had all the model parameters fixed to the 1FGL catalog values (Abdo et al. 2010a).

The plots in subsequent sections show only statistical errors for the fit parameters. Systematic errors arise mainly from uncertainties on the LAT effective area, which is derived from the on-orbit estimations. These errors could be as large as 10% below 0.1 GeV, <5% near 1 GeV, and 20% above 10 GeV.

2.1. γ-Ray Light Curve

The light curve of AO 0235+164 in the *Fermi*-LAT energy range has been assembled using three day long time bins and covers the first six months of data taken from 2008 August 4 to 2009 February 4, when the source was in a high state and a large set of multi-wavelength observations were available. The light curve is obtained by applying the gtlike fit across the overall energy range considered, from 100 MeV to 100 GeV, in each of the selected time bins. For each time interval, the flux and the photon index of AO 0235+164 are determined using the maximum likelihood algorithm implemented in gtlike, following the procedure outlined in the previous section. The data are modeled with a power-law function with both the normalization factor and photon index left free in the likelihood fit.

The six month γ-ray light curve is reported in Figure 1 together with the photon index resulting from the likelihood fit in each time bin. The trend in the entire energy range from 100 MeV to 100 GeV shows a clear high-state period followed by a final, narrow, high-flux peak.

The temporal behavior of the source in γ-rays was also studied in two separate energy ranges, from 100 MeV to 1 GeV and from 1 GeV to 100 GeV, and the hardness ratio among the two bands has been determined. The analysis follows the same procedure described above to determine the overall light curve and the results are shown in the three bottom panels of Figure 1.

The arrows in the light curves represent 95% upper limits, which are calculated for data points with a test statistic (TS)[94] lower than 10 (which corresponds to a significance somewhat higher than 3σ) or with a value of the ratio between flux error and flux ($F_{\rm err}(E)/F(E)$) $\geqslant 0.5$ in order to obtain meaningful data points.

The results show that both the low- and high-energy profiles follow the same trend. Nevertheless, it is interesting to underline that the narrow peak at the end of the high-state period is mainly due to an enhanced low-energy flux. The ratio among the two fluxes also shows a value higher than the average in the same time interval.

2.2. γ-Ray Spectral Analysis

The unbinned gtlike analysis has been applied to produce the γ-ray energy spectra shown in Figure 2. There, we divided the full energy range from 100 MeV to 100 GeV into two equal logarithmically spaced bins per decade. In each energy bin, a TS value greater than 10 and a ratio between flux error and flux lower than 0.5 was required to quote a flux in that band, otherwise a 95% upper limit was given.

The standard gtlike tool was applied in each energy bin, modeling all the point sources in the region with a simple power-law spectrum with photon index fixed to two. The normalization parameters of all point-like sources within 10° were left as free parameters in the fitting procedure, while the diffuse background components were modeled as described above in Section 2.1. Two time intervals were selected for the γ-ray spectral analysis: the first corresponding to the X-ray flare interval (MJD 54750–54770), the second associated with the subsequent low γ-ray state (MJD 54780–54840). In those time intervals, both power-law and broken-power-law functions provide a good fit of the spectral data. In Table 1, we show the results of the broken-power-law fit, since it provides a better fit to the high-energy spectrum of the source, from 100 MeV to 100 GeV, than a simple power law on the larger time intervals, as already studied in detail by Abdo et al. (2010b):

$$\frac{dN}{dE} = N_0 \times \begin{cases} (E/E_b)^{-\Gamma_1}; & \text{if } E < E_b \\ (E/E_b)^{-\Gamma_2}; & \text{other wise.} \end{cases} \quad (2)$$

In both time intervals, the Γ_1 index remains stable, while Γ_2 increases showing a softening of the high-energy part of the spectrum when the source is in a fainter state, when also an increase in the break energy is observed. As also can be seen in Figure 1, the high γ-ray state around MJD 54760 is essentially due to the low-energy photons (<1 GeV) and the spectra in Figure 2 show that the relative difference between the E^2Flux values above 1 GeV and below 1 GeV is higher in the time interval around the flare than during the low γ-ray state.

3. MULTI-WAVELENGTH OBSERVATIONS AND DATA ANALYSIS

The multi-wavelength campaign conducted on AO 0235+164 in 2008–2009 saw a wide international participation. Table 2 reports the list of participating observatories, the energy bands, the period of observation, and the number of collected data points.

3.1. Effect of Intervening Material in the Line of Sight on the Optical, UV and X-Ray Data

Conversion of the observed optical magnitudes into the intrinsic flux densities requires a special care, because the source emission is absorbed not only in our Galaxy, but

[92] http://fermi.gsfc.nasa.gov/ssc/data/analysis/documentation/Cicerone/Cicerone_Likelihood

[93] http://fermi.gsfc.nasa.gov/ssc/data/access/lat/BackgroundModels.html

[94] The test statistics is defined as TS = $-2\times$(log(L_1)–log(L_0)) with L_0 the likelihood of the Null-hypothesis model as compared to the likelihood of a competitive model, L_1; see Mattox et al. (1996).

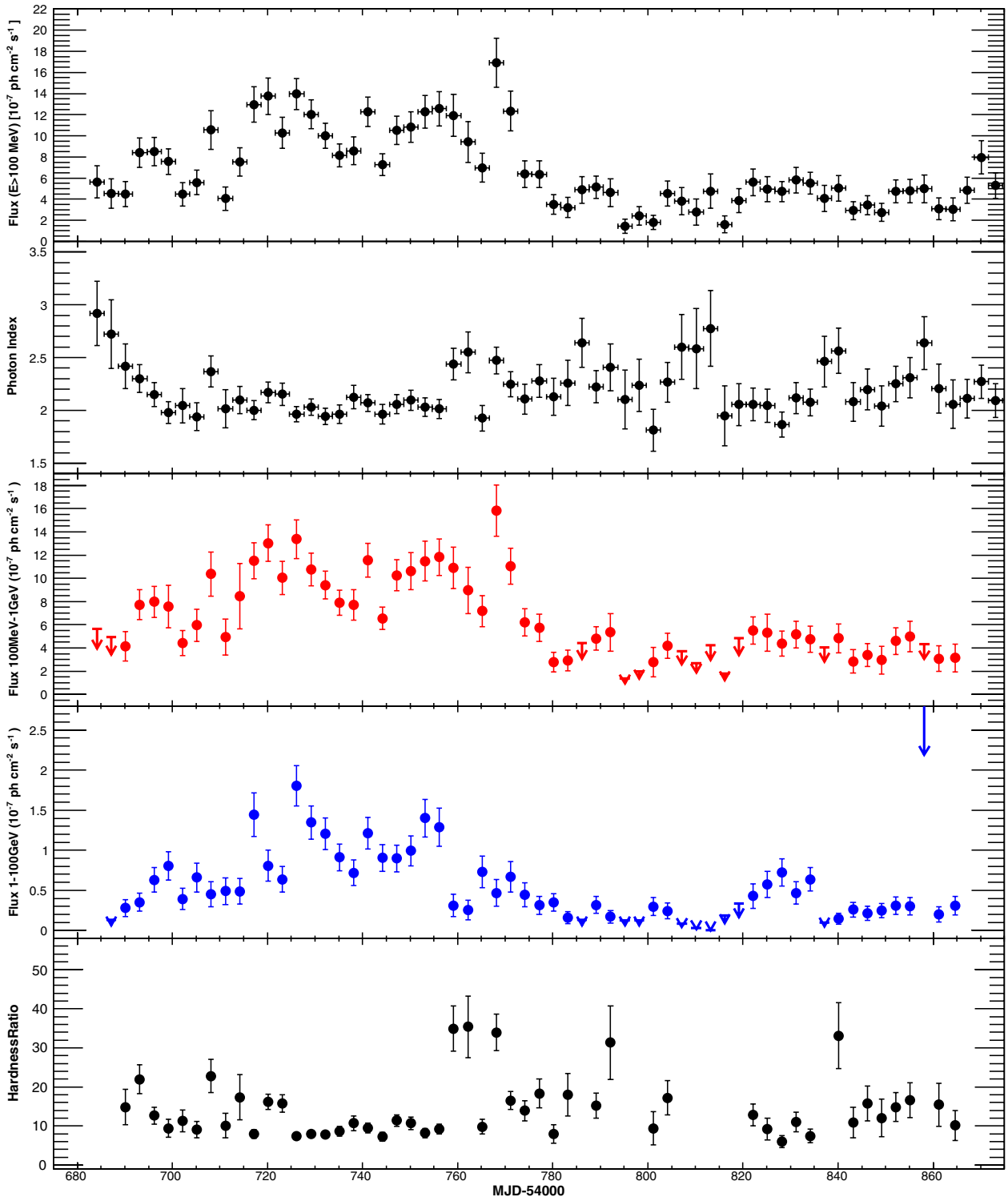

Figure 1. *Fermi*-LAT light curve from 2008 August 4 to 2009 February 4 in three day time intervals. The first panel from the top shows the flux, in the energy range from 100 MeV to 100 GeV, derived from the `gtlike` fit in the three day time intervals, assuming a simple power-law spectrum. The second panel shows the photon index Γ in the same energy range from 100 MeV to 100 GeV. The third panel shows the light curve evaluated in the energy range from 100 MeV to 1 GeV. The fourth panel shows the light curve in the energy range from 1 GeV to 100 GeV. The last panel shows the hardness ratio defined as $(F_{100\ \mathrm{MeV-1\ GeV}})/(F_{1\ \mathrm{GeV-100\ GeV}})$ for the data points having a TS > 10 and $F_{\mathrm{err}}(E)/F(E) > 0.5$ in both energy ranges. The hardness ratio is not evaluated if either of the two fluxes is an upper limit.

(A color version of this figure is available in the online journal.)

Table 1

Results of the `gtlike` Fit of the γ-ray Spectrum During the High and Low States

Time Interval MJD	Flux (10^{-7} photons cm^{-2} s^{-1})	Γ_1	Γ_2	Break Energy (GeV)
54750–54770	11.05 ± 1.48	2.12 ± 0.16	2.37 ± 0.32	2.6 ± 0.8
54780–54840	3.42 ± 0.65	2.07 ± 0.17	2.77 ± 0.32	3.8 ± 1.2

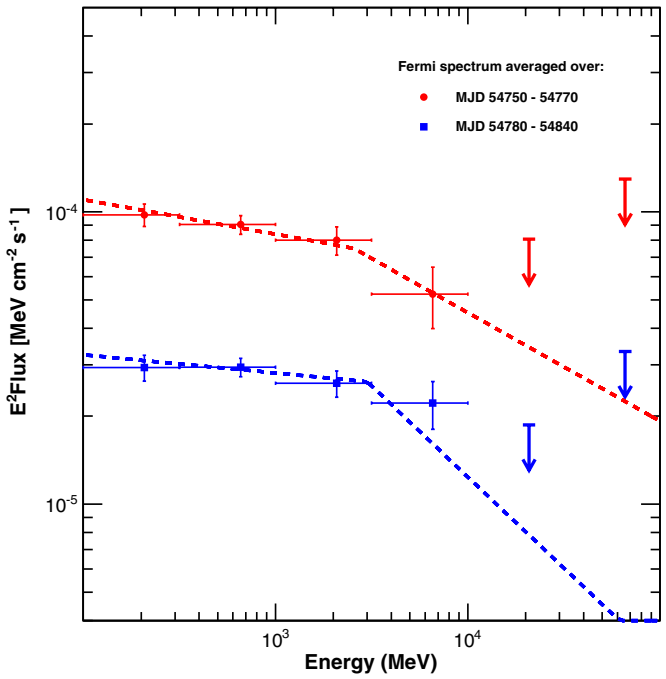

Figure 2. *Fermi*-LAT energy spectrum evaluated in different time intervals corresponding to the X-ray flare (red circles) from MJD 54750–54770 and γ-ray low state (blue squares) from MJD 54780–54840.

(A color version of this figure is available in the online journal.)

also by the elliptical galaxy in the line of sight at redshift $z = 0.524$, as outlined in the Introduction. Junkkarinen et al. (2004) tried several different extinction models for AO 0235+164, concluding that the best fit to their *Hubble Space Telescope*/STIS data is obtained by using models of Cardelli et al. (1989) with $R_V = 3.1$ and $E_{B-V} = 0.154$ for the Galaxy, and $R_V = 2.51$ and $E_{B-V} = 0.227$ for the $z = 0.524$ system. This model accurately reproduces the 2175 Å absorption feature produced by the $z = 0.524$ galaxy, but the far-UV end of their spectrum indicated a sharp hardening. Raiteri et al. (2005) proposed that this far-UV hardening is real and that it marks the onset of a new spectral component. However, the fact that the shape of this feature does not change with the overall optical/UV luminosity indicates that the whole optical/UV spectrum is produced by a single synchrotron component, the intrinsic shape of which must be close to a power law. The far-UV hardening is most likely an artifact of overestimated extinction from the dust in the $z = 0.524$ galaxy. We modify the best-fit extinction model of Junkkarinen et al. (2004) by replacing the Cardelli et al. (1989) model for the $z = 0.524$ galaxy with an analytical model of Pei (1992). In the first step, we modify the "Milky Way" model with parameters listed in Table 4 of Pei (1992) to match the Cardelli et al. (1989) model for $R_V = 2.51$ and $E_{B-V} = 0.227$. In particular, we adopt $\lambda_{2175A} = 2170$ Å and $n_{FUV} = 5.5$, and we multiply the normalization parameters a_i by additional factors f_i: $f_{FUV} = 1.5$, $f_{2175A} = 1.33$, and $f_{BKG} = 1.05$. In the second step, we turn off the "FUV" component of the Pei (1992) model for the $z = 0.524$ galaxy by setting $f_{FUV} = 0$. This modification affects only the observed wavelengths shorter than ~3300 Å, the location of the 2175 Å feature redshifted by $z = 0.524$, and is necessary to align the FUV spectra with the optical–NIR spectra (see Figure 7). We stress that extinction at longer wavelengths is very well constrained by the clear detection of a redshifted 2175 Å feature by Junkkarinen et al. (2004), and thus cannot be increased. The resulting total extinction values A_λ for the *Swift*/UVOT filters are—W2: 2.87; M2: 2.94; W1: 2.52; U: 2.71; B: 1.84; V: 1.46. For the remaining optical and near-IR filters, we use the values from Table 5 of Raiteri et al. (2005)—R: 1.26; I: 0.90; J: 0.46; H: 0.28; K: 0.17. We calculate the incident flux $F_{inc,\lambda}$ in the band corresponding to λ from the observed (absorbed) flux $F_{abs,\lambda}$ via $F_{abs,\lambda}/F_{inc,\lambda} = 10^{A_\lambda/2.5}$. The same corrections are applied to the ground-based optical data.

In addition, the source photometry is contaminated by the emission of a nearby AGN (named ELISA by Raiteri et al. 2005). Hence, we subtracted the ELISA contribution from the observed flux densities and then corrected for the combined extinction of both galaxies, following the prescriptions given by Raiteri et al. (2005) and Raiteri et al. (2008).

Likewise, the X-ray data need to be corrected for the effect of absorption. Here, the absorption effects of *both* our own Galaxy and the intervening $z = 0.524$ system are considerable. Madejski et al. (1996) and Junkkarinen et al. (2004) argue that the absorption in the intervening system originates in material with abundances different from Galactic and, in reality, correct modeling of such absorption should take this into effect. However, as discussed by Madejski et al. (1996), the combined *ROSAT* and *ASCA* spectral fitting suggests that this effect is relatively modest, the joint *ROSAT–PSPC* and *ASCA* data are adequately fitted by an absorbing column of $(2.8 \pm 0.4) \times 10^{21}$ cm^{-2} located at $z = 0$. Since the *Swift* X-Ray Telescope (XRT) data have a somewhat lower signal-to-noise ratio (S/N) than the *ASCA* observations, we simply adopt such a "local" model for absorption, since the main objective of our observations was to determine the underlying continuum of the AO 0235+164 rather than the detailed spectral properties of the absorber. We note that this value is in fact consistent with the spectral fit to the *Swift* XRT data.

3.2. GASP-WEBT

The GLAST-AGILE Support Program (GASP) of the Whole Earth Blazar Telescope (WEBT) was initiated in 2007 with the aim of performing a long-term multi-wavelength monitoring of bright, γ-loud blazars (Villata et al. 2008b, 2009; D'Ammando et al. 2009; Raiteri et al. 2010). The GASP optical (*R* band), near-IR, and radio data are intended to complement the high-energy observations by the *AGILE* and *Fermi* (formerly *GLAST*) satellites.

AO 0235+164 has been the target of several WEBT campaigns in the past (Raiteri et al. 2001, 2005, 2006, 2008) and it is now one of the GASP sources of highest observing priority. During the high γ-ray state observed in the second half of 2008, the source underwent an exceptional optical-to-radio outburst closely monitored by the GASP (Villata et al. 2008a, 2008c; Bach et al. 2008). The GASP optical data presented here were taken at the following observatories: Abastumani, Armenzano, Calar Alto, Crimean, Kitt Peak (MDM), L'Ampolla, Lulin, Roque de los Muchachos (KVA), San Pedro Martir, St. Petersburg, Talmassons, and Tuorla. Near-IR data in the *J*, *H*, and *K* bands are all from Campo Imperatore. Millimeter (mm) and centimeter (cm) radio observations were performed at the SMA (230 and 345 GHz), Noto (43 GHz), Metsähovi (37 GHz), Medicina (5, 8, and 22 GHz), and UMRAO (4.8, 8.0, and 14.5 GHz) observatories. All IR, optical, and UV data are corrected for the effects of the intervening absorber (both due to the Milky Way and the intervening galaxy) as outlined above.

Table 2
Observatories Participating in the Work, Periods of Observations, and Number of Data Points used in this Analysis

Observatory		Bands	Period of Observation	Data Points
		Radio		
GASP-WEBT	Mauna Kea (SMA), USA	345 GHz	54664-54840	10
		230 GHz	54645-54842	23
	Medicina, Italy	5 GHz	54724	1
		8 GHz	54606-54777	7
		22 GHz	54604-54779	7
	Metsähovi (KURP-GIX),Finland	37 GHz	54633-54839	54
	Noto, Italy	43 GHz	54642-54841	8
	UMRAO, USA	5 GHz	54677-54840	16
		8 GHz	54621-54851	20
		14.5 GHz	54633-54848	41
F-GAMMA	Effelsberg 100-m	2.64	54414-55227	23
		4.85 GHz	54414-55227	24
		8.35 GHz	54414-55227	24
		10.45 GHz	54414-55227	25
		14.6 GHz	54422-55227	22
		23.05 GHz	54422-55227	17
		32 GHz	54616-55227	11
		42 GHz	54546-55227	8
	IRAM 30-m	86.2 GHz	54382-55228	17
		142.3 GHz	54382-55228	15
		228.4 GHz	54440-54806	5
IRAM PdBI		88.9 GHz	54700	1
		169 GHz	54883	1
OVRO		15 GHz	54661-54848	49
		Near-infrared		
GASP-WEBT	Campo Imperatore	*J*	54645-54794	87
		H	54645-54794	82
		K	54645-54794	83
Kanata		*J*	54690-54753	21
		V	54690-54753	21
		Ks	54690-54753	21
SMARTS		*J*	54662-54847	69
		K	54662-54842	39
		Optical		
GASP-WEBT	Abastumani 70 cm	R	54687-54780	287
	Armenzano, 40 cm	*R*	54699-54727	16
	Calar Alto	*R*	54712-54887	5
	Crimean 70cm; ST-7	*R*	54691-54805	218
	Kitt Peak (MDM 130 cm)	*R*	54745-54801	50
	L'Ampolla	*R*	54778-54784	2
	Lulin (SLT)	*R*	54688-54862	120
	Roque (KVA 35 cm)	*R*	54748-54862	29
	San Pedro Martir 84 cm	*R*	54709-54773	15
	St. Petersburg	*R*	54698-54865	41
	Talmassons	*R*	54728-54843	11
	Tuorla	*R*	54722-54732	3
SMARTS		*R*	54662-54868	71
		B	54662-54871	69
		V	54662-54859	68
Steward		*R*	54743-54832	39
		V	54743-54863	44
SWIFT-UVOT		*U*	54711-54818	16
		B	54711-54818	16
		V	54711-54818	16
		Ultraviolet		
SWIFT-UVOT		UVW1	54711-54818	16
		UVM2	54711-54818	15
		UVW2	54711-54818	16

3.3. F-GAMMA

During the 2008–2009 flaring period, quasi-simultaneous multi-frequency cm/mm band (from 2.64 GHz to 230 GHz) observations of AO 0235+164 were obtained using the Effelsberg 100 m and IRAM 30 m telescopes, within the framework of a *Fermi* related monitoring program of γ-ray blazars

(F-GAMMA program;[95] Fuhrmann et al. 2007; Angelakis et al. 2008).

The Effelsberg measurements were conducted with the secondary focus heterodyne receivers at 2.64, 4.85, 8.35, 10.45, 14.60, 23.05, 32.00, and 43.00 GHz. The observations were performed quasi-simultaneously with cross-scans, by slewing over the source position in the azimuth and elevation directions with an adaptive number of sub-scans chosen to reach the desired sensitivity (for details, see Fuhrmann et al. 2008; Angelakis et al. 2008). Consequently, pointing offset correction, gain correction, atmospheric opacity correction, and sensitivity correction have been applied to the data.

The IRAM 30 m observations were carried out with calibrated cross-scans using the single pixel heterodyne receivers B100, C150, B230 operating at 86.2, 142.3, and 228.4 GHz. The opacity-corrected intensities were converted into the standard temperature scale and finally corrected for small remaining pointing offsets and systematic gain-elevation effects. The conversion to the standard flux density scale was done using the instantaneous conversion factors derived from frequently observed primary (Mars, Uranus) and secondary (W3(OH), K3-50A, NGC 7027) calibrators.

3.4. OVRO

Observations of AO 0235+164 at 15 GHz with the Owens Valley Radio Observatory (OVRO) 40 m telescope were made as part of an ongoing blazar monitoring program (Richards et al. 2011). The 40 m telescope is equipped with a cooled receiver at the prime focus, with a 3.0 GHz bandwidth centered on 15.0 GHz and 2.5 GHz noise-equivalent reception bandwidth. The receiver noise temperature is about 30 K, and the total system noise temperature including CMB, atmospheric, and ground contributions is about 55 K. A dual off-axis corrugated horn feed projects to approximately Gaussian beams (157 arcsec full width at half-maximum, FWHM) on the sky, separated in azimuth by 12.95 arcmin. Dicke switching between the two beams is performed using the cold sky in the off-source beam as a reference, and a second level of switching is performed by alternating the source between the two beams to cancel atmospheric and ground noise. Calibration is achieved using a stable diode noise source for relative calibration and is referred to observations of 3C 286, for which we assume a flux density of 3.44 Jy (Baars et al. 1977) with about 5% absolute scale error. OVRO flux density measurements have a minimum uncertainty of 4 mJy in 32 s of on-source integration, and a typical rms relative error of 3%.

3.5. IRAM Plateau de Bure Interferometer (PdBI)

The Plateau de Bure Interferometer (PdBI; Winters & Neri 2010) is able to observe in three atmospheric windows located around wavelengths of 1.3 mm, 2 mm, and 3 mm. Each of these bands covers a continuous range of frequencies that are available for observations; these ranges are 201–267 GHz for the 1.3 mm band, 129–174 GHz for the 2 mm band, and 80–116 GHz for the 3 mm band.

Systematic monitoring of AGN is a by-product of regular observatory operations. The PdBI uses AGNs as phase and amplitude calibrators. Usually, one or two calibrators are measured every ∼20 minutes for ∼2 minutes (per source) throughout an observation. Antenna temperatures are converted into physical flux densities using empirical antenna efficiencies as conversion factors. These factors are functions of frequencies and are located in the range from ∼22 Jy K^{-1} (for the 3 mm band) to ∼37 Jy K^{-1} (for the 1.3 mm band).

The PdBI is equipped with dual linear polarization Cassegrain focus receivers. This makes it possible to observe both orthogonal polarizations—"horizontal" (H) and "vertical" (V) with respect to the antenna frame—simultaneously. Due to the hardware layout of the correlators, it is not yet possible to observe all Stokes parameters. We collect linear polarization data on point sources via the Earth rotation polarimetry, i.e., we monitor the fluxes in the H and V channels as functions of parallactic angle ψ. The source polarization is derived from the parameterization

$$q(\psi) = \frac{V - H}{V + H}(\psi) \equiv m_L \cos[2(\psi - \chi)]. \quad (3)$$

Here, m_L is the fraction of linear polarization (ranging from 0 to 1) and χ is the polarization angle (ranging from 0° to 180° and counted from north to east). For details, please refer to Trippe et al. (2010).

3.6. Kanata

We performed the *V*-, *J*-, and *Ks*-band photometry and polarimetry of AO 0235+164 from 2008 August to 2008 October, using the TRISPEC instrument (Watanabe et al. 2005) installed at the 1.5 m Kanata telescope located at the Higashi–Hiroshima Observatory. TRISPEC has a CCD and two InSb arrays, enabling photo-polarimetric observations in one optical and two NIR bands simultaneously. We obtained 21 photometric data points in the *V, J, Ks* bands. A unit of the polarimetric observing sequence consisted of successive exposures at four position angles of the half-wave plates: 0°, 45°, 22.°5, 67.°5. The data were reduced according to the standard procedure of CCD photometry. We measured the magnitudes of objects with the aperture photometry technique. We performed differential photometry with a comparison star taken in the same frame of AO 0235+164. Its position is R.A. = 02:38:32.31, decl. = +16:35:59.7 (J2000) and its magnitudes are $V = 12.720$, $J = 11.248$, and $Ks = 10.711$ (Gonzalez-Perez et al. 2001; Cutri et al. 2003). The photometric data have been corrected for the Galactic extinction of $A(V) = 1.473$, $A(J) = 0.458$, and $A(Ks) = 0.171$, as explained in Section 3.1.

We confirmed that the instrumental polarization was smaller than 0.1% in the *V* band using observations of unpolarized standard stars, and hence we applied no correction for it. The zero point of the polarization angle is corrected as standard system (measured from north to east) by observing the polarized stars, HD19820 and HD25443 (Wolff et al. 1996).

3.7. SMARTS

AO 0235+164 was observed at the Cerro Tololo Inter-American Observatory (CTIO) as part of a photometric monitoring campaign of bright blazars with the Small and Moderate Aperture Research Telescope System (SMARTS). The source was observed with the SMARTS 1.3 m telescope and ANDICAM instrument (DePoy et al. 2003). ANDICAM is a dual-channel imager with a dichroic linked to an optical CCD and an IR imager, from which it is possible to obtain simultaneous data from 0.4 to 2.2 μm. Optical and near-infrared observations were taken in the *B*, *V*, *R*, *J*, and *K* bands.

[95] http://www.mpifr-bonn.mpg.de/div/vlbi/fgamma/fgamma.html

Optical data were bias-subtracted, overscan-subtracted, and flat-fielded using the CCDPROC task in IRAF. Infrared data were sky-subtracted, flat-fielded, and dithered images were combined using in-house IRAF scripts. The raw photometry of comparison stars in the field of the blazar were calibrated using photometric zero points that were measured from 2008 to 2009 observations with ANDICAM of optical (Landolt 1992) and near-infrared (Persson et al. 1998) primary standards for each filter, correcting for atmospheric extinction derived from all the standards taken together. The averages of the comparison stars were used as a basis of differential photometry with respect to the blazar for all observations. Errors were determined by calculating the 1σ variation in the magnitude of the comparison stars.

Fluxes were computed using values for Galactic extinction from Schlegel et al. (1998) and subtracting the nearby AGN "ELISA" as described in Raiteri et al. (2005). In addition, we accounted for the absorption of the $z = 0.524$ system as outlined in Junkkarinen et al. (2004).

3.8. Steward Observatory

Optical spectropolarimetry and spectrophotometry of AO 0235+164 during fall 2008 were provided by the monitoring program being conducted at Steward Observatory (Smith et al. 2009). This program utilizes the Steward Observatory CCD Spectropolarimeter (SPOL; Schmidt et al. 1992b) at either the 2.3 m Bok telescope located on Kitt Peak, AZ or the 1.54 m Kuiper telescope on Mt. Bigelow, AZ. The publicly available data[96] include linear polarization and flux spectra (in first order) spanning 4000–7550 Å. General data taking and reduction procedures used for this project are described in detail in Smith et al. (2003) and Smith et al. (2009). For the monitoring of AO 0235+164, a $3''$ or $4''$ wide slit was used for spectropolarimetry, depending on the observing conditions, yielding a spectral resolution of 20–25 Å. An L-38 blocking filter was inserted into the collimated beam for all observations to prevent significant contamination from second-order light until well past 7600 Å. Total exposure times of between 24 and 80 minutes were used depending on the brightness of AO 0235+164 and the sky/seeing conditions. Usually, a high signal-to-noise ratio measurement (S/N $>$ 100) of the degree of polarization (P) is determined from each observation by taking the median linear, normalized Stokes parameters (q and u) in a 2000 Åwide bin centered at 6000 Å. The reported values of P have been corrected for statistical bias as in Wardle & Kronberg (1974), but this correction is typically not significant because of the high S/N of the binned data. The position angle (theta) of the optical linear polarization is calibrated by observing interstellar polarization standard stars (Schmidt et al. 1992a). Likewise, the flux spectra resulting from the spectropolarimetry are calibrated using observations of spectrophotometric standard stars (Massey et al. 1988). The flux spectra are corrected for atmospheric extinction using the standard extinction curves given in Baldwin & Stone (1984) and Stone & Baldwin (1983). Flux information for AO 0235+164 was obtained through differential spectrophotometry of the blazar and a nearby field star ("Star 4"; Gonzalez-Perez et al. 2001). The spectrophotometry employed slits with widths of $7\farcs6$ or $12\farcs7$ to minimize seeing- and color-dependent slit losses since the SPOL slit is left fixed in an east–west orientation on the sky and is not aligned with the parallactic angle. The wide-slit spectra of AO 0235+164 and the comparison star were convolved with standard filter transmission curves to determine differential magnitudes and derive the apparent magnitude of the blazar in the V and R bandpasses. The spectrophotometric observations were much shorter in duration (typically <5 minutes) than the spectropolarimetry, but of sufficient S/N to be used to correct the much higher S/N flux spectra of AO 0235+164 resulting from the spectropolarimetry for any slit losses associated with the narrower slits used for those measurements.

[96] http://james.as.arizona.edu/~psmith/Fermi

Table 3
The log of *Swift* Observations Yielding Good XRT Data

Date (MJD−54000)	Exposure (s)	Photon Index	$F_{2-10\ \mathrm{keV}}$ (10^{-12} erg cm^{-2} s^{-1})
711.4976	6876	1.91 ± 0.09	3.1 ± 0.3
719.8695	1257	2 (assumed)	3.2 ± 0.4
737.9059	1448	2 (assumed)	3.7 ± 0.3
747.7476	2123	2 (assumed)	4.3 ± 0.3
758.7420	1133	$2.44^{+0.07}_{-0.08}$	17.3 ± 1.4
761.7541	1181	2.60 ± 0.08	15.0 ± 1.2
781.0545	1144	2 (assumed)	2.8 ± 0.3
789.5603	1087	2 (assumed)	4.1 ± 0.4
803.7109	1175	2 (assumed)	4.5 ± 0.5
818.5249	1210	2 (assumed)	4.8 ± 0.4

Notes. In all cases, the spectrum was fitted with a power-law model absorbed by gas with Galactic abundances with a column of 2.8×10^{21} cm^{-2} placed at $z = 0$: such an absorption form is only approximate, but it adequately fits *ROSAT* and *ASCA* data, which in turn possess better signal to noise than individual *Swift* pointings (see the text). Since the quality of the data at MJD 54719, 54737, 54747, 54781, 54789, 54803, and 54818 have too low an S/N for reliable determination of spectrum, we assumed a photon index of two for those pointings.

3.9. Swift XRT and UVOT

AO 0235+164 was monitored as a result of an approved target of opportunity request by the *Swift* satellite (Gehrels et al. 2004), with weekly observations of ≈1–2 ks performed from 2008 September 2 to 2008 December 18 (Table 3) with the XRT (Burrows et al. 2005) and with the Ultraviolet/Optical Telescope (UVOT; Roming et al. 2005).

The XRT data were reduced with the standard software (`xrtpipeline v0.12.4`) applying the default filtering and screening criteria (HEADAS package, v6.9[97]). We extracted the XRT light curve in the 0.3–10 keV energy band using the software tool `xrtgrblc`. The source events were extracted from circular regions centered on the source position. During the outburst we excluded the inner two pixels of the source to avoid pileup. Exposure maps were used to account for the effects of vignetting, PSF losses, and the presence of hot pixels and hot columns.

Since the source X-ray flux and spectrum are known to vary strongly, co-adding individual XRT observations could be misleading. We thus extracted the XRT data from each individual pointing separately, and fitted individual spectra using `XSPEC`. We rebinned the XRT data, requiring at least 25 counts in each new energy bin. As discussed in Section 3.1, we assumed that the combined Galactic and $z = 0.524$ absorption is adequately described by a column of 2.8×10^{21} cm^{-2} at $z = 0$: this is in fact consistent with the spectral fit to the *Swift* XRT data. We determined the unabsorbed X-ray flux by performing the spectral fit with fixed absorption, and then determining the

[97] http://heasarc.gsfc.nasa.gov/lheasoft/

Table 4
Results of *Swift* UVOT Observations of AO 0235+164

Date	*M* (v)	*F* (v)	*M* (b)	*F* (b)	*M* (u)	*F* (u)	*M* (w1)	*F* (w1)	*M* (m2)	*F* (m2)	*M* (w2)	*F* (w2)
711.50	16.95 ± 0.05	2.32	17.93 ± 0.04	1.49	18.07 ± 0.06	1.04	18.16 ± 0.06	0.49	18.57 ± 0.07	0.43	18.93 ± 0.06	0.28
719.87	16.79 ± 0.09	2.69	17.81 ± 0.08	1.65	17.75 ± 0.11	1.39	17.99 ± 0.11	0.57	18.23 ± 0.16	0.59	18.47 ± 0.10	0.42
729.65	16.17 ± 0.07	4.76	17.03 ± 0.06	3.41	17.13 ± 0.08	2.46	17.18 ± 0.08	1.21	17.46 ± 0.11	1.20	17.85 ± 0.08	0.75
737.91	16.29 ± 0.06	4.26	17.11 ± 0.05	3.17	17.11 ± 0.07	2.51	17.47 ± 0.08	0.93	17.62 ± 0.11	1.03	18.04 ± 0.08	0.63
740.65	15.89 ± 0.06	6.18	16.80 ± 0.05	4.20	17.00 ± 0.08	2.77	17.17 ± 0.08	1.22	17.37 ± 0.10	1.30	17.78 ± 0.08	0.80
747.75	16.17 ± 0.05	4.76	17.01 ± 0.04	3.46	17.14 ± 0.06	2.45	17.36 ± 0.06	1.03	17.43 ± 0.07	1.23	17.94 ± 0.06	0.69
758.74	15.93 ± 0.06	5.95	16.86 ± 0.05	3.96	16.85 ± 0.07	3.18	16.83 ± 0.07	1.67	17.10 ± 0.09	1.66	17.61 ± 0.07	0.93
761.75	16.05 ± 0.06	5.33	16.92 ± 0.05	3.76	16.99 ± 0.07	2.79	17.09 ± 0.08	1.31	17.29 ± 0.09	1.40	17.55 ± 0.07	0.99
768.80	...	...	17.06 ± 0.07	3.30	17.08 ± 0.10	2.58	16.96 ± 0.07	1.47	...	...	17.45 ± 0.12	1.08
780.31	17.07 ± 0.16	2.07	17.99 ± 0.15	1.40	17.91 ± 0.19	1.2	18.14 ± 0.17	0.50	18.17 ± 0.28	0.62	18.46 ± 0.15	0.43
781.06	17.31 ± 0.13	1.66	17.85 ± 0.09	1.59	17.97 ± 0.14	1.13	18.08 ± 0.13	0.53	18.39 ± 0.17	0.51	18.63 ± 0.11	0.37
789.56	16.63 ± 0.08	3.11	17.50 ± 0.07	2.21	17.46 ± 0.10	1.81	17.81 ± 0.11	0.68	17.98 ± 0.16	0.74	18.25 ± 0.09	0.52
790.83	16.60 ± 0.11	3.20	17.40 ± 0.09	2.41	17.80 ± 0.16	1.32	17.73 ± 0.14	0.73	18.04 ± 0.18	0.70	18.34 ± 0.13	0.48
803.71	17.66 ± 0.16	1.21	18.77 ± 0.18	0.69	18.63 ± 0.21	0.62	18.79 ± 0.20	0.27	18.51 ± 0.17	0.46	19.19 ± 0.16	0.22
813.64	18.10 ± 0.24	0.81	18.87 ± 0.21	0.63	18.97 ± 0.31	0.45	18.96 ± 0.24	0.23	19.00 ± 0.28	0.29	19.00 ± 0.16	0.26
818.52	17.43 ± 0.15	1.49	18.34 ± 0.15	1.01	18.87 ± 0.32	0.50	18.63 ± 0.20	0.32	19.07 ± 0.23	0.27	19.17 ± 0.17	0.22

Notes. The data are listed for six *Swift* UVOT filters. Each pair of columns corresponds to the observed, uncorrected magnitude *M* (left entry) and corrected flux density *F*, in units of milliJansky (right entry). To correct for absorption in the Milky Way plus that at $z = 0.524$, we used the following values of absorption A_λ for the respective UVOT filters—W2: 2.87; M2: 2.94; W1: 2.52; U: 2.71; B: 1.84; V: 1.46. We calculate the incident flux $F_{\rm inc,\lambda}$ in the band corresponding to λ from the observed (absorbed) flux $F_{\rm abs,\lambda}$ via $F_{\rm abs,\lambda}/F_{\rm inc,\lambda} = 10^{A_\lambda/2.5}$. The same corrections are applied to ground-based optical data.

incident flux by forcing the absorption to be zero. We include those fluxes in the 2–10 keV band in the last column of Table 3. We note that the source was detected at a sufficiently good S/N to determine the spectrum unambiguously only in the observations on MJD54711, MJD54758, and MJD54761. In other observations, we assumed a photon index of $\Gamma = 2$, consistent with previous X-ray observations of this source in the low state, and note that the error resulting from such assumption on the inferred flux is comparable to the statistical error quoted in the last column of Table 3.

The UVOT photometry was done using the publicly available UVOT FTOOLS data reduction suite and is based on the UVOT photometric system described in Poole et al. (2008), but see also Breeveld et al. (2011) for an updated calibration. As discussed above, we adopted the corrections to the observed flux due to the absorption by the Milky Way plus the intervening galaxy at $z = 0.524$ as outlined in Section 3.1. The results of *Swift* UVOT observations are presented in the Table 4.

3.10. RXTE

As part of our campaign, 30 observations of AO 0235+164 were obtained with *Rossi X-ray Timing Explorer* (*RXTE*) between 2008 October 18 and 2008 December 27. We analyzed the data from the Proportional Counter Array (PCA) following standard procedures. We selected only data from PCU2, the best-calibrated module and the only one which is always turned on. The data were screened in the following way: with a source elevation above the horizon $>10^\circ$, a pointing offset smaller than $0.^\circ02$, at least 30 minutes away from a South Atlantic Anomaly passage, and an electron contamination smaller than 0.1. This resulted in a total exposure of 192.3 ks. Single net PCA exposures range from 2.1 ks to 14.1 ks. Background was estimated with standard procedures and the detector response matrices extracted with the *RXTE* tools (command PCARSO v. 10.1).

For the spectral analysis, the fitting procedure was done with the XSPEC software package. The spectra from the channels corresponding to nominal energies of 2.6 to 10.5 keV are adequately fitted by a single power-law model, absorbed by a fixed column of 2.8×10^{21} cm^{-2} at $z = 0$ as determined by the *ROSAT* and *ASCA*—in an analogous manner to the spectral fitting performed to the *Swift* XRT data above. The parameters of the fits are reported in Table 5; again, the last column reports the unabsorbed X-ray flux.

4. VARIABILITY OF THE SOURCE

4.1. Multi-wavelength Light Curve

In this section, we present the results of the multi-wavelength observations conducted on AO 0235+164 from 2008 August to 2009 January. Figure 3 shows the multi-wavelength data available. From the top to the bottom are: radio, near-infrared, optical, polarization degree (%), polarization angle (deg), and UV, X-ray, and γ-ray from 100 MeV to 100 GeV data are grouped together.

The optical behavior is the best sampled among all. Two main flare peaks are visible in the period around 2008 October (MJD 54730–54750), and they are surrounded by other smaller peaks. The radio data show that the flux started to increase smoothly starting around the middle of 2007 (MJD 54500, which is apparent in Figure 4), reaching its maximum during the optical flare activity, and slowly decreasing when the source returned to a low-flux state in near-IR, optical, X-ray, and γ-ray bands. The near-infrared data show the same temporal trend as the optical bands. The UV data from *Swift* UVOT do not show the level of activity seen in the optical band. The X-ray data from *Swift* XRT and *RXTE* present a very pronounced peak clearly delayed with respect to the optical activity.

The *Fermi* light curve, as already discussed in Section 2.1, shows a broad high-state period followed by a final narrow peak succeeding the X-ray peak before getting to the low-flux state. Since then (up to the time of submitting this paper in autumn 2011), the source has been in a very quiet state.

Figure 4 shows the light curves constructed from the radio, mm and sub-mm data in an extended time interval, from 2007 to 2010 June (MJD 54400–55230). In the lowest energy band, the increasing trend of the flux started months before the

Table 5
Best-fit Parameters for the PCA Data of each *RXTE* Observation with the Absorption Fixed at the Value Measured by ROSAT + ASCA, with the Column of $N_{\rm H} = 28 \times 10^{20}$ cm^{-2} with Galactic Abundances

Date	MJD−54000	Exposure (s)	Photon Index Γ	χ^2_r/dof	F_{2-10}
2008 Oct 18 18:56	757.805	2688	2.46 ± 0.13	0.60/9	2.00 ± 0.08
2008 Oct 19 13:35	758.684	12416	2.55 ± 0.06	0.41/9	2.09 ± 0.04
2008 Oct 20 13:09	759.566	3024	2.73 ± 0.14	0.62/9	1.79 ± 0.07
2008 Oct 21 14:16	760.647	6384	2.56 ± 0.10	0.38/9	1.70 ± 0.05
2008 Oct 22 13:53	761.597	3104	2.34 ± 0.12	0.56/9	1.87 ± 0.07
2008 Oct 23 18:08	762.773	2976	2.47 ± 0.12	0.58/9	2.03 ± 0.07
2008 Oct 25 14:08	764.704	12656	2.57 ± 0.07	0.43/9	1.77 ± 0.04
2008 Oct 26 15:13	765.653	3136	2.71 ± 0.14	0.57/9	1.68 ± 0.08
2008 Oct 27 13:09	766.567	3200	2.35 ± 0.16	0.83/9	1.41 ± 0.07
2008 Oct 28 19:01	767.806	2320	2.71 ± 0.21	0.34/9	1.26 ± 0.08
2008 Oct 31 14:32	770.624	3152	2.24 ± 0.27	0.44/9	0.71 ± 0.06
2008 Nov 2 17:03	772.850	14448	2.26 ± 0.18	0.29/9	0.53 ± 0.03
2008 Nov 3 13:07	773.566	3200	2.46 ± 0.40	0.55/9	0.54 ± 0.07
2008 Nov 4 19:11	774.880	9072	2.72 ± 0.36	0.34/9	0.37 ± 0.04
2008 Nov 5 18:34	775.858	9680	2.12 ± 0.31	0.48/9	0.35 ± 0.04
2008 Nov 6 18:07	776.774	3200	1.91 ± 0.55	0.59/9	0.32 ± 0.06
2008 Nov 7 14:32	777.723	12992	2.50 ± 0.38	0.45/9	0.28 ± 0.03
2008 Nov 10 16:07	780.696	2880	3.53 ± 0.79	0.79/9	0.38 ± 0.09
2008 Nov 11 11:11	781.486	3264	2.37 ± 0.61	1.40/9	0.27 ± 0.06
2008 Nov 13 11:53	783.613	13168	2.37 ± 0.38	0.39/9	0.25 ± 0.03
2008 Nov 14 12:56	784.625	9888	2.39 ± 0.36	0.59/9	0.30 ± 0.04
2008 Nov 15 11:00	785.543	9904	2.37 ± 0.36	0.63/9	0.31 ± 0.04
2008 Nov 17 10:09	787.474	6336	2.50 ± 0.59	0.46/9	0.24 ± 0.05
2008 Nov 19 09:10	789.429	5568	2.94 ± 0.44	0.81/9	0.39 ± 0.05
2008 Nov 20 07:10	790.411	12192	1.99 ± 0.36	0.34/9	0.26 ± 0.03
2008 Nov 21 16:48	791.366	9744	2.92 ± 0.63	0.39/9	0.23 ± 0.04
2008 Nov 23 10:33	793.492	6432	2.08 ± 0.68	0.42/9	0.21 ± 0.04
2008 Dec 27 14:06	827.672	9664	2.69 ± 0.50	0.40/9	0.25 ± 0.04

Notes. Description of columns: (1) and (2) Observing date, (3) Exposure (s), (4) photon index and error, (5) reduced χ^2 and No. of degrees of freedom, and (6) Flux in the 2–10 keV band, in units of 10^{-11} erg cm^{-2} s^{-1}.

increased level of activity seen in the optical and higher energy bands. After the period of the increased radio/mm flux associated with the optical flaring activity, the source enters a period of gradually declining flux.

4.2. Cross-correlation Studies and Time Delays

We searched for correlations of variability between different bands, with the goal to understand the relationship between the fluxes of AO 0235+164 at different energies. The cross-correlation studies between the optical *R* band and γ-ray fluxes are illustrated in the top panel of Figure 5. Those data have a Spearman correlation coefficient[98] of 0.75 (Spearman 1904). The relations between the γ-ray and 230 GHz and 345 GHz fluxes have also been evaluated and the results are shown in Figure 5 in the bottom panel: the Spearman correlation coefficient between γ-ray fluxes and 230 GHz data is 0.70, showing that there exists a correlation between the two data sets. On the other hand, the sampling at 345 GHz is poor, with only a few data points at that frequency and the evaluation of a correlation has not been performed. In all cases, no correlation is found at 90% confidence level. We note here that Agudo et al. (2011b), using data collected for this object over a longer time span than that covered by our observations, performed a light-curve correlation analysis following the method described by Agudo et al. (2011a). They found that these bands are correlated at a 99.7% confidence level. In our case, no correlation is found at 90% confidence level: it is very likely that the stronger correlation of signals derived by Agudo et al. (2011b) is caused by their use of a significantly longer time span, amounting to roughly eight years. All this suggests that the variability of the source in the γ-ray and radio-to-mm regimes on long timescales is correlated, but the situation on shorter timescales is less clear.

Since the time series in the optical *R* band and γ-ray are the best sampled in this study, it was possible to calculate lags/leads between those bands. To this end, we calculated the discrete correlation function (DCF; Edelson & Krolik 1988). We binned the data sets in order to smooth the intraday features in the optical light curves and to obtain similar sampling in the γ-ray band. We tried several bin sizes from one to seven days to check how sensitive the results are to this smoothing procedure. The DCF from the optical and γ-ray data do not show significant peaks on short timescales (one day) meaning no optical–γ correlation is detected over the observing period. Figure 6 shows the result of this DCF analysis when the light curves are binned over one day. A peak can be seen at 15 days (with optical lagging γ-rays), however the significance is modest. Agudo et al. (2011b) found that, for a similar period, the optical flux lags the γ-rays by ∼10 days, but their DCF peak is much broader, and could be interpreted as being consistent with no lag.

4.3. Time Dependence of Optical Polarization

As illustrated in Figure 3, the polarization degree and angle are highly variable; the former correlates with the optical flux

[98] Wessa, P. (2011), Free Statistics Software, Office for Research Development and Education, version 1.1.23-r7, http://www.wessa.net/

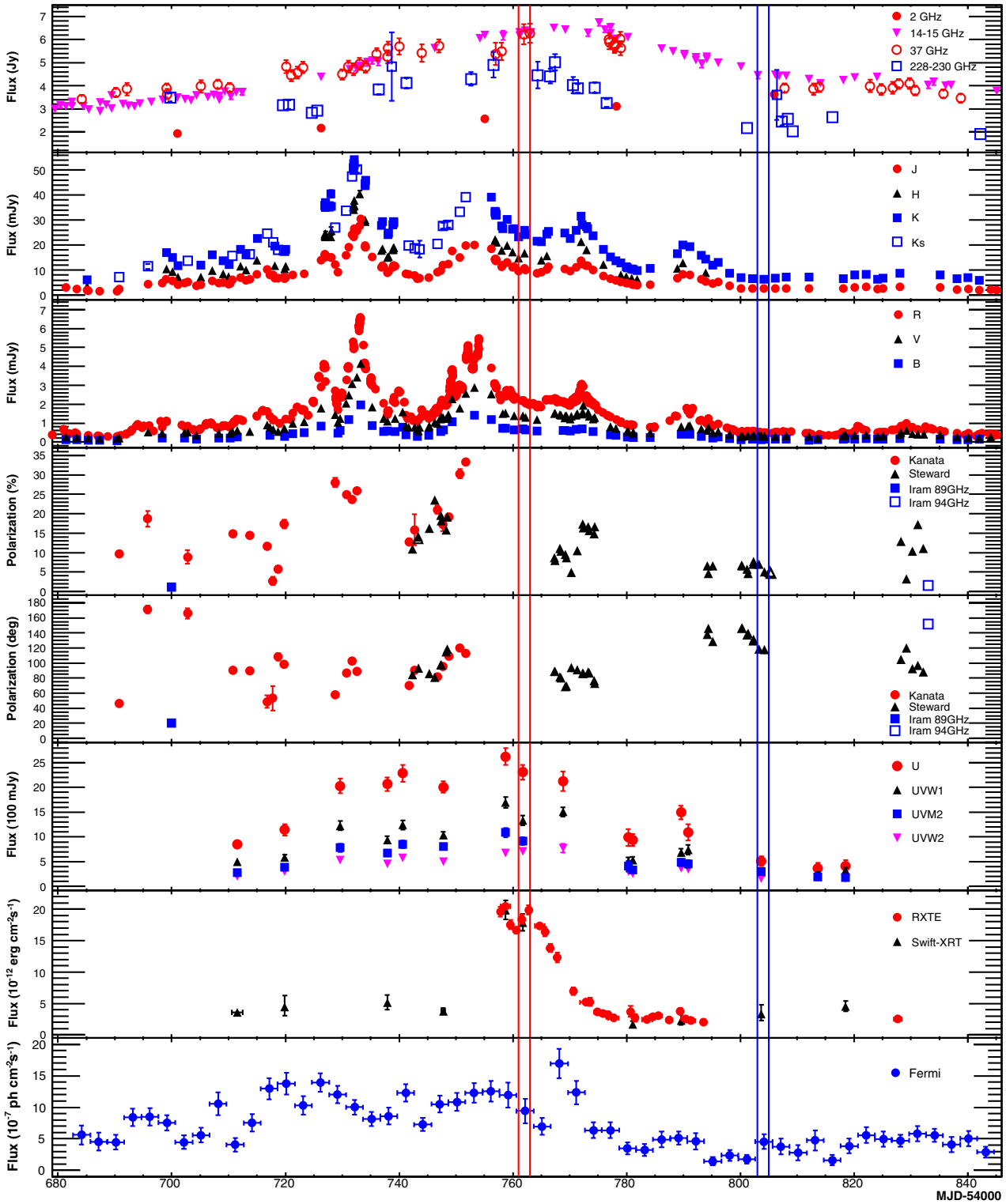

Figure 3. AO 0235+164 light curve from 2008 August 4 to 2009 February 4 in different energy ranges. From the top to the bottom: radio, near IR, optical, UV, X-rays, and γ-rays above 100 MeV. Panels 4 and 5 from the top report the polarization data from the Kanata optical observatory and IRAM radio telescope. Two double vertical lines mark the epochs for which we extracted the SEDs modeled in Section 6.

(A color version of this figure is available in the online journal.)

and at the two largest flux peaks reaches values of 25% and 35%, respectively. This correlation was studied over a longer period of time (from 2008 August 12 to 2009 February 18) by Sasada et al. (2011), and in the past, during the outburst of 2006 December, by Hagen-Thorn et al. (2008). A trend of the stabilization of the polarization angle during flares is seen both in 2006 and 2008, but around different values, with the electric vector polarization angle (EVPA) at $\sim -30^\circ$ and $\sim 100^\circ$, respectively. Comparing EVPA with the position angle of the parsec-scale jets, Hagen-Thorn et al. (2008) found that there is a trend of their alignment during high states. However, since the parsec-scale jet in AO 0235+164 shows large changes of direction with time (Jones

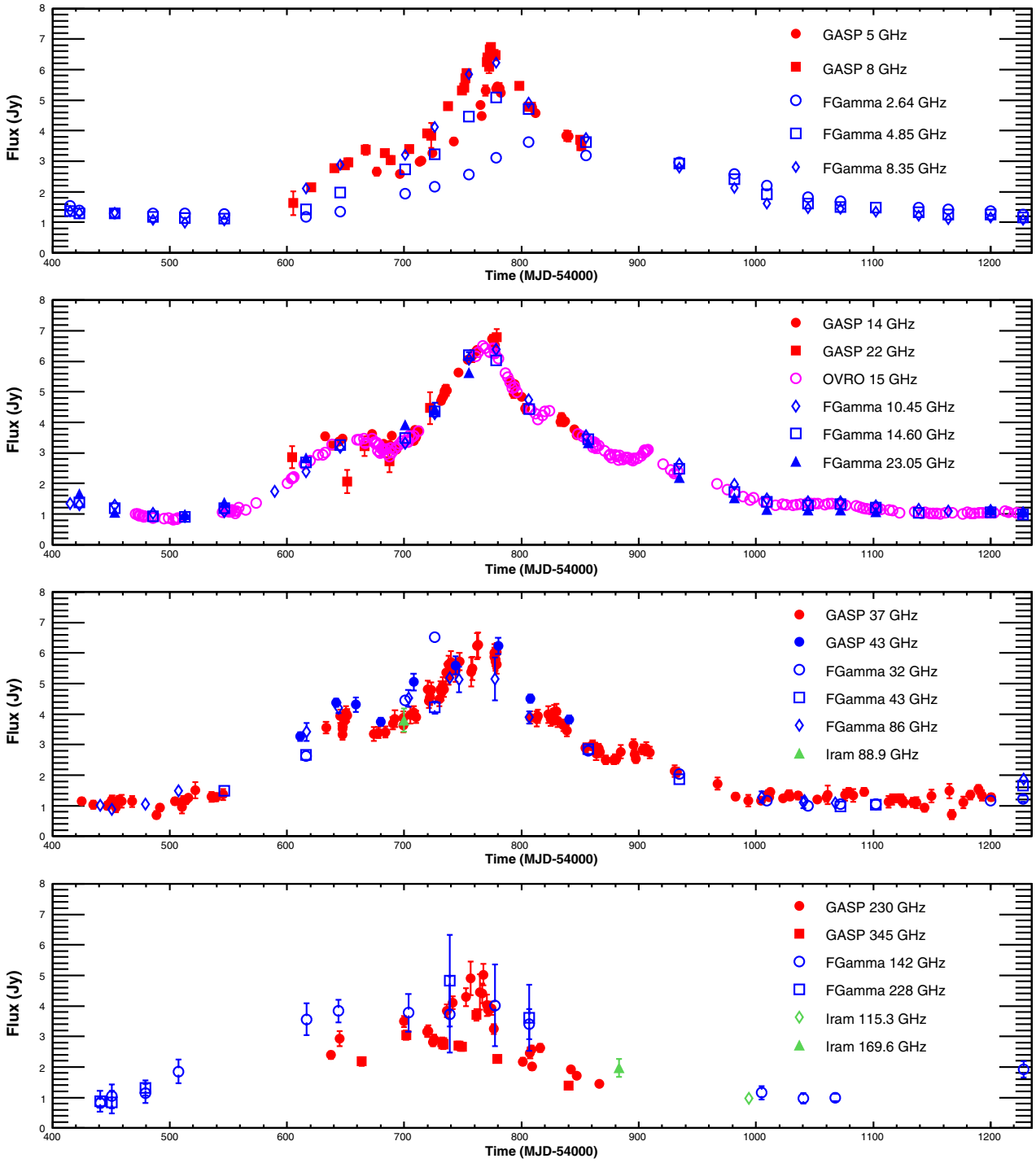

Figure 4. Radio, millimeter, and submillimeter light curves of AO 0235+164 from mid 2007 until 2010 June (MJD 54400–55230). In these energy bands, the flux began to increase around the middle of 2007 (MJD 54500), months before the start of the optical and higher energy activity of the source.

(A color version of this figure is available in the online journal.)

et al. 1984; Chu et al. 1996; Jorstad et al. 2001; Piner et al. 2006) and the jet direction to which EVPA was compared was inferred from the VLBI maps taken in different epochs, the claimed alignment could be accidental. Indeed, comparison of EVPA during flux peaks in 2008 with the direction of the jet determined during the same epoch by VLBI observations does not confirm such an alignment (Agudo et al. 2011b). On the contrary, both angles are oriented perpendicular rather than parallel to each other, albeit with a large scatter, with EVPA at optical flux peaks $\sim 100^\circ$ versus $\chi_{\rm jet} \sim 0^\circ$. This implies a parallel orientation of the magnetic fields to the jet and may indicate production of flares in a reconfinement shock (Nalewajko 2009).

5. BROADBAND SPECTRAL ENERGY DISTRIBUTION

Our unprecedented time sampling of AO 0235+164 in several spectral bands allows us to extract accurate instantaneous SEDs, which are needed to correctly interpret the broadband emission of the source. We reiterate that in order to build the intrinsic SED and correctly convert the observed magnitudes to de-absorbed fluxes, extinction must be taken into account, including both

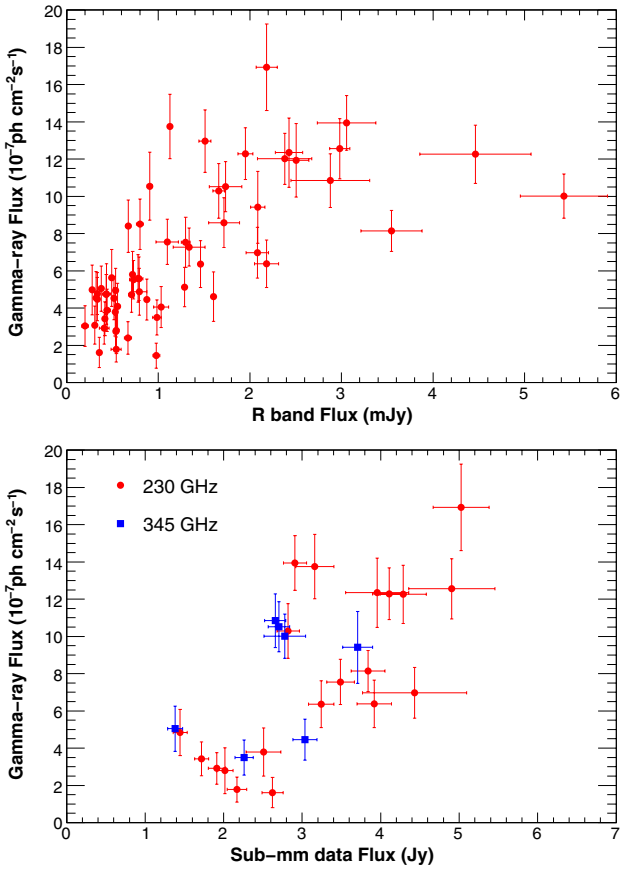

Figure 5. Top: plot of the γ-ray flux vs. *R*-band flux; both fluxes are averaged in three day time intervals. The data suggest that γ-ray and optical fluxes follow each other, but the correlation is small with γ-ray flux reaching a plateau at the level $\sim 1.2 \times 10^{-6}$ when the optical flux reaches $\sim$3 mJy, but not increasing beyond $\sim 1.2 \times 10^{-6}$ when the optical flux increases to $\sim$5 mJy. Bottom: similar plot of γ-ray flux vs. high-frequency radio-band flux; both fluxes are averaged in three day time intervals. Likewise, there is a general trend of increase in both bands, but the correlation is small.

(A color version of this figure is available in the online journal.)

Galactic extinction, and that due to the $z = 0.524$ system. We discussed in Section 3.1 how the IR, optical, UV data, and soft X-rays are affected by the absorption due to both systems. Following the prescriptions from Junkkarinen et al. (2004), we assume that the soft X-ray absorption is adequately described by a column density of 2.8×10^{21} cm^{-2} at $z = 0$. However, for the far-UV data, we use a modified extinction model based on the work of Pei (1992).

Figure 7 shows the broadband SEDs obtained by plotting simultaneous radio, NIR, optical, UV, X-ray data in the following two 2 day epochs.

1. MJD 54761–54763 (shown in red) corresponding to the maximum of the X-ray flare, coincident with a highly variable near-IR/optical/UV state and a high γ-ray state.
2. MJD 54803–54805 (shown in blue) corresponding to a low state in all bands, following the high-activity period.

The plotted data points were extracted from the larger data sets as follows.

1. *Radio data*. Most of the data points are simultaneous measurements. Although the sampling at some particular wavelengths is poor, the available radio light curves show very smooth and slow trends, thus we have also plotted interpolated values based on the extended data set of about 10 days in length, centered on the main observation period.

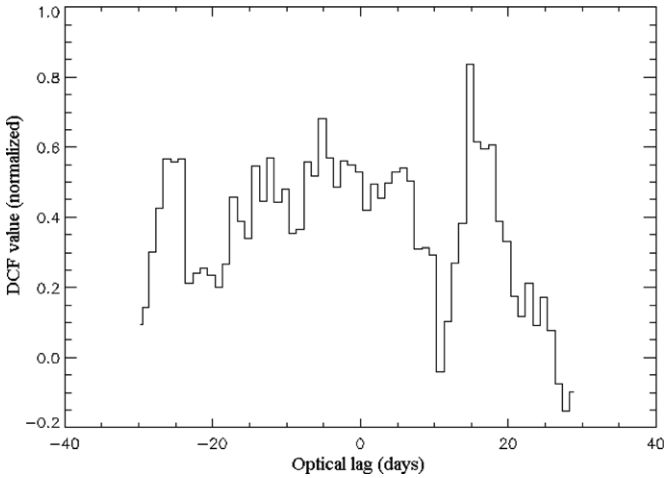

Figure 6. Discrete correlation function (DCF) calculated between optical *R* band and *Fermi*-LAT γ-ray data binned over one day intervals. Positive values correspond to γ-rays leading the optical signal.

2. *Near-IR/optical/UV*. All the data shown are simultaneous measurements made by GASP-WEBT, SMARTS, and *Swift* UVOT telescopes.
3. *X-ray data*. In the first epoch (MJD 54761–54763), we present the *Swift* XRT observation with a butterfly plot. In the second epoch (MJD 54803–54805), the S/N for the *Swift* XRT measurement is too low to allow a good spectral representation and only the flux upper limit is reported.
4. *γ-ray data*. The γ-ray spectra have been built following the analysis procedure described in Section 2.2. Since the time intervals chosen to build the broadband SED are too short to allow a good reconstruction of the γ-ray spectrum, longer periods have been used. The first time interval, MJD 54750–54770, corresponds to a period of high γ-ray emission, which includes the X-ray flare period. The high state is followed by a lower emission state whose spectrum is averaged in the interval MJD 54780–54840.

The overall SED, plotted in Figure 7, appears quite similar to that measured for other blazars. There is one marked difference: at least for the first period, the X-ray spectrum is soft, yet it is not located on the extrapolation of the optical/UV spectrum. For this to be the case, extinction would have to be significantly greater, with the error at the level of at least 50%, which we consider unlikely. Assuming that we adopted the correct extinction, the broadband SED does show a distinct feature in the soft X-ray band, separate from the two broad peaks forming the SED in most blazars, and we discuss its origin below.

6. MODELING OF THE BROADBAND SPECTRUM

AO 0235+164, like many other luminous, low-frequency-peaked BL Lac objects, shows broad emission lines (BELs; Cohen et al. 1987; Nilsson et al. 1996; Raiteri et al. 2007). Using the emission-line spectrum reported in Raiteri et al. (2007), correcting the line flux for extinction, and assuming that the contribution of the lines measured by them to the total luminosity of BELs is the same as in the composite spectrum of quasars (Francis et al. 1991), we find $L_{\rm BEL} \sim 4 \times 10^{44}$ erg s^{-1}. For the typical covering factor of the broad-line region (BLR) $\xi_{\rm BEL} \sim 0.1$, this implies a luminosity of the accretion disk of $L_d \sim 4 \times 10^{45}$ erg s^{-1}. With such a high accretion luminosity, if observed directly, i.e., without being overshone by the jet nonthermal radiation, AO 0235+164 would satisfy a formal

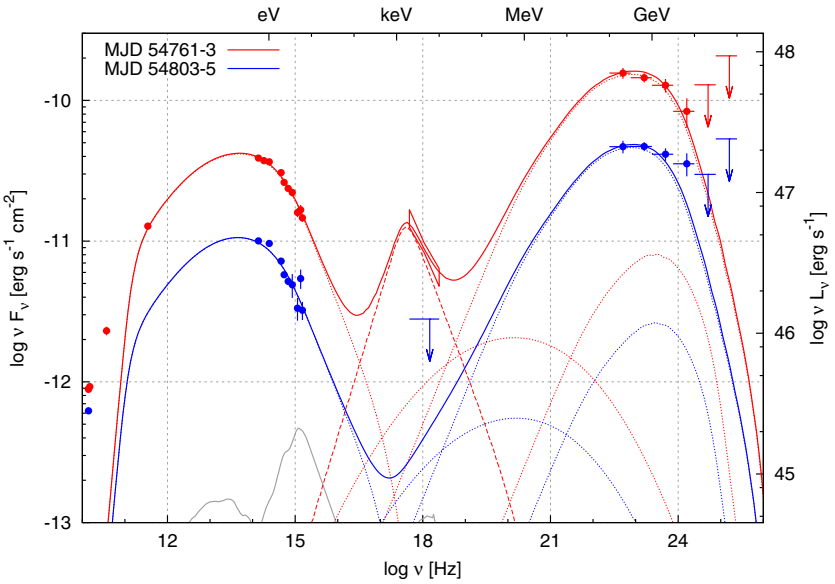

Figure 7. Numerical models fitted to observed spectral states of AO 0235+164, dominated energetically by the Comptonization of the infrared radiation from the dusty torus (ERCIR). Red lines show a fit to the high state (MJD 54761-3), including the bulk-Compton feature (dashed line). Blue lines show a fit to the low state (MJD 54803-5). Dotted lines indicate individual spectral components, in order of increasing peak frequencies: synchrotron, SSC, ERCIR, ERCBEL. Solid lines show the sums of all individual components. Note that presented models do not cover the radio production which at $\nu < 100$ GHz is strongly synchrotron-self-absorbed for our source parameters and must originate at much larger distances from the BH than a few parsecs. The gray line shows the quasar composite SED adopted from Elvis et al. (1994) and normalized to the accretion disk luminosity $L_d = 4 \times 10^{45}$ erg s^{-1}.

(A color version of this figure is available in the online journal.)

criterion to be classified as a quasar (see also Murphy et al. 1993). This means that, according to the AGN unification models, it should possess a typical dusty torus, a strong source of thermal infrared radiation (IR) with a typical covering factor of $\xi_{\rm IR} \sim 0.1$ (e.g., Haas et al. 2004). Recent mid-IR interferometric observations for a sample of nearby AGNs show that such tori can extend beyond 10 pc from the central BH (Tristram & Schartmann 2011). The mass of the BH in this object is likely to be in the range $M_{\rm BH} \sim 2$–$6 \times 10^8\, M_\odot$ (Liu et al. 2006; Raiteri et al. 2007; Wu et al. 2011), which implies the Eddington ratio $L_d/L_{\rm EDD} \geqslant 0.1$.

In order to determine which process dominates the high-energy emission, whether it is ERC or SSC, one can estimate their luminosity ratio as $L_{\rm ERC}/L_{\rm SSC} \simeq u'_{\rm ext}/u'_{\rm syn}$, where $u'_{\rm ext}$ is the comoving energy density of the external radiation, which, depending on the source location, could be dominated either by $u'_{\rm BEL}$ or $u'_{\rm IR}$, and $u'_{\rm syn}$ is the comoving energy density of the synchrotron radiation. These energy densities scale like $u'_{\rm BEL(IR)} \simeq \Gamma_{\rm j}^2 u_{\rm BEL(IR)} \simeq \Gamma_{\rm j}^2 \xi_{\rm BEL(IR)} L_{\rm d}/(4\pi r_{\rm BEL(IR)}^2 c)$ for $r \leqslant r_{\rm BEL(IR)}$, respectively, and $u'_{\rm syn} \simeq L_{\rm syn}/(4\pi R^2 \mathcal{D}^4 c)$, where $r_{\rm BEL} \sim 0.1 (L_{\rm d,46})^{1/2}$ pc is the characteristic radius of the BLR, $r_{\rm IR} \sim 2.5 (L_{\rm d,46})^{1/2}$ pc is the inner radius of the dusty torus, R is the emitting zone radius related to its distance by $r = R\Gamma_{\rm j}$, $\Gamma_{\rm j} = (1-\beta_{\rm j}^2)^{-1/2}$ is the jet Lorentz factor, and $\beta_{\rm j}$ is the jet velocity in units of c (Sikora et al. 2009). Considering the emitting zone located at either characteristic radius, i.e., $r \simeq r_{\rm BEL(IR)}$, and neglecting the distinction between the Doppler factor $\mathcal{D}$ and the Lorentz factor $\Gamma_{\rm j}$, we obtain $L_{\rm ERC}/L_{\rm SSC} \simeq \xi_{\rm BEL(IR)} \Gamma_{\rm j}^4 (L_{\rm d}/L_{\rm syn})$. In the case of AO 0235+164, we observe $L_{\rm d}/L_{\rm syn} \sim 0.01$ and thus $L_{\rm ERC}/L_{\rm SSC} \simeq 160 (\xi_{\rm BEL(IR)}/0.1)(\Gamma_{\rm j}/20)^4$. Hence, even for a moderate bulk Lorentz factor, in order for the SSC component to dominate the ERC component, one requires covering factors two orders of magnitude lower than typically assumed in quasars.

In this section, we verify the ERC scenario by fitting the observed SEDs with one-zone leptonic models (Moderski et al. 2003). We follow the evolution of relativistic electrons injected into a thin spherical shell propagating conically with a constant Lorentz factor $\Gamma_{\rm j}$ undergoing adiabatic and radiative losses due to the synchrotron and inverse Compton emission. The external radiation includes BELs of characteristic photon energy $E_{\rm BEL} \sim 10$ eV and infrared dust radiation of characteristic energy $E_{\rm IR} \sim 0.3$ eV. We attempted to fit the high state of MJD 54761-3 with a "blazar zone" located either within (ERCBEL model) or outside the BLR (ERCIR model). In the ERCBEL model, the electron break inferred from the synchrotron spectrum is too low to reproduce the γ-ray spectrum above ~1 GeV. This problem is absent in the ERCIR model (red lines in Figure 7). This is because Comptonization of IR photons is subject to much weaker Klein–Nishina suppression in the GeV band than Comptonization of optical/UV emission-line photons. The parameters of the ERCIR model are: location $r = r_{\rm IR}$, Lorentz factor $\Gamma_{\rm j} = 20$, opening angle $\theta_{\rm j} = 1/\Gamma_{\rm j} = 2.^\circ9$ (hence the Doppler factor $\mathcal{D}_{\rm j} = \Gamma_{\rm j}$), magnetic field strength $B' = 0.22$ G, and viewing angle $\theta_{\rm obs} = 2.^\circ3$. Electrons are injected with a doubly broken energy distribution with $\gamma_{\rm br,1} = 100$, $\gamma_{\rm br,2} = 5800$, $p_1 = 1.5$, $p_2 = 2.03$, and $p_3 = 3.9$.

The rate of electron energy injection is $\dot{E}'_{\rm e,inj} \sim 4.8 \times 10^{43}$ erg s^{-1}. Over comoving time $\Delta t' \sim r_{\rm IR}/(2\Gamma_{\rm j}\beta_{\rm j} c) \sim 4 \times 10^6$ s, the total injected electron energy is $E'_{\rm e,inj} \sim \dot{E}'_{\rm e,inj} \Delta t' \sim 1.9 \times 10^{50}$ erg. At the end of the injection, the total number of electrons is $N_{\rm e} = 6.6 \times 10^{54}$ and their total energy in the comoving frame is $E'_{\rm e} \sim 1.1 \times 10^{50}$ erg. The average efficiency of electron energy losses is $\eta_{\rm e,loss} = 1 - (E'_{\rm e}/E'_{\rm e,inj}) \sim 0.42$. The electron flux is $\dot{N}_{\rm e} \sim \pi \Gamma_{\rm j} R^2 c N_{\rm e}/V' \sim 1.2 \times 10^{49}$ s^{-1}, where $V' \sim 4\pi R^3/3$ is the volume of the emitting region in the comoving frame and $R \sim \theta_{\rm j} r$ is the jet radius. The electron energy flux is $L_{\rm e} \sim \pi \Gamma_{\rm j}^2 R^2 c E'_{\rm e}/V' \sim 4.1 \times 10^{45}$ erg s^{-1}

and the proton energy flux is $L_{\rm p} \sim \pi\Gamma_{\rm j}^2 R^2 c N_{\rm p} m_p c^2/V' \sim 3.6\times10^{47}\,(n_p/n_e)$ erg s^{-1}, where $N_{\rm p} \sim N_{\rm e}(n_p/n_e)$ is the total number of protons and (n_e/n_p) is the lepton-to-proton number ratio. The magnetic energy flux is $L_{\rm B} = \pi\Gamma_{\rm j}^2 R^2 c u'_{\rm B} \sim 4.4\times10^{45}$ erg s^{-1}. The resulting jet magnetization parameter is $\sigma_{\rm B} \sim L_{\rm B}/L_{\rm p} \sim 0.012(n_e/n_p)$, and the radiative efficiency is $\eta_{\rm rad,j} \sim L_{\rm obs}/(2\Gamma_{\rm j}^2 L_{\rm p}) \sim 0.022(n_e/n_p)$, where $L_{\rm obs} \sim 6.4\times10^{48}$ erg s^{-1} is the observed bolometric luminosity of the source. The relation between the jet power and accretion disk luminosity is $L_{\rm p}/L_{\rm d} \sim 91(n_p/n_e)$. Parameterizing the jet production efficiency by $L_{\rm p} \sim \eta_{\rm j}\dot{M}_{\rm acc}c^2$ and the radiative efficiency of the accretion disk $L_{\rm d} \sim \eta_{\rm rad,d}\dot{M}_{\rm acc}c^2$, where $\dot{M}_{\rm acc}$ is the accretion rate, we obtain $n_e/n_p \sim 91(\eta_{\rm rad,d}/\eta_{\rm j})$. For $\eta_{\rm rad,d} \sim 0.1$ and $\eta_{\rm j} \sim 1$, we have $n_e/n_p \sim 9.1$ and hence $\sigma_{\rm B} \sim 0.11$ and $\eta_{\rm rad,j} \sim 0.2$. We are thus able to match the jet power with the accretion power onto the central BH, adopting a reasonably low jet magnetization, which allows formation of strong shock waves. The ratio of electrons to protons is consistent with the results of Sikora & Madejski (2000). This model predicts the observed variability timescale of $t_v \simeq (1+z)R/(c\Gamma_{\rm j}) \sim 8$ days, consistent with the timescale of the significant variations of the optical and γ-ray flux.

As we noted above, the X-ray spectrum, at least during the first of the two epochs considered here, is too soft to be interpreted as an SSC component and cannot be the high-energy tail of the synchrotron component since it does not lie on the extrapolation of the optical–UV spectrum (but see the caveats above, related to the corrections for extinction). Instead, it can be explained by Comptonization of external radiation by a population of relatively cold electrons (Begelman & Sikora 1987; Ravasio et al. 2003). Such bulk Compton radiation is expected to be produced in a jet much closer to the BH than the nonthermal blazar radiation, at distances at which cooling of even mildly relativistic electrons is very efficient. There, the jet is still in the acceleration phase and, therefore, its bulk Lorentz factor is expected to be smaller than in the blazar zone. But noting that according to magnetohydrodynamical models the acceleration process is very smooth (see, e.g., Komissarov et al. 2007) and that the bulk Compton radiation must be significantly Doppler boosted to be visible in the blazar spectra, the dominant contribution to bulk-Compton radiation is expected to be produced at distances which are already well separated from the base of the jet (Sikora et al. 2005; Celotti et al. 2007). We consider a stationary emitting region at a characteristic radius of $r_{\rm b} \sim 100R_{\rm g} \sim 6\times10^{15}$ cm, where $R_{\rm g} = GM_{\rm BH}/c^2$ is the gravitational radius of the central BH of mass $M_{\rm BH} \sim 4\times10^8\,M_\odot$. The bulk Lorentz factor is $\Gamma_{\rm b} \sim 10$ and the Doppler factor is $\mathcal{D}_{\rm b} = 1/[\Gamma_{\rm b}(1-\beta_{\rm b}\cos\theta_{\rm obs})] \sim 16$. Bulk-Compton luminosity is given by the approximate formula

$$L_{\rm b} \simeq N_{\rm e,b}|\dot{E}_{\rm e,IC}|_{\rm b}\frac{\mathcal{D}_{\rm b}^3}{\Gamma_b}\,, \quad (4)$$

where $N_{\rm e,b}$ is the number of electrons enclosed in the $\Delta r \sim r_{\rm b}$ portion of a jet, $|\dot{E}_{\rm e,IC}|_{\rm b} = (4/3)c\sigma_T u_{\rm ext,b}\Gamma_{\rm b}^2$ is the rate of production of Compton radiation by a single electron, and $u_{\rm ext,b} = \xi_{\rm b}L_{\rm d}/(4\pi r_{\rm b}^2 c)$ is the energy density of the external radiation field, which at distances $\leqslant 100R_{\rm g}$ is very likely to be dominated by rescattering of disk radiation by electrons in the accretion disk corona of covering factor $\xi_{\rm b}$. The energy spectrum of the external radiation is approximated by a broken power-law distribution $u_{\rm ext,b}(E) \propto E^{-\alpha_i}$ with $\alpha_1 = 0, \alpha_2 = 1.8$, and $E_{\rm br} = 10$ eV (Richards et al. 2006; Shang et al. 2011). The electron flux is $\dot{N}_{\rm e,b} \sim N_{\rm e,b}c/r_{\rm b}$. Assuming that it matches the electron flux in the blazar zone ($\dot{N}_{\rm e,b} \sim \dot{N}_{\rm e}$), we calculate the total number of electrons producing the bulk-Compton component to be $N_{\rm e,b} \sim 2.4\times10^{54}$. We find that the X-ray spectrum of luminosity $L_{\rm b} \sim 8.7\times10^{46}$ erg s^{-1} can be reproduced with cold electrons for $\xi_{\rm b} \simeq 0.19\,(r_{\rm b}/6\times10^{15}$ cm).

Multi-wavelength light curves show that X-rays do not correlate with radiation in other spectral bands. This suggests that the X-ray variability of the bulk-Compton radiation can be caused by local wiggling of the jet, e.g., caused by variations of the average direction of non-axisymmetric outflows generated near the BH. Jet wiggling can also explain independent variability in the blazar zone. We have fitted the low state (MJD 54803-5) with an ERCIR model (blue lines in Figure 7) very similar to the one for the high state, changing only the viewing angle, from $\theta_{\rm obs} = 2.^\circ3$ to $\theta_{\rm obs} = 3.^\circ7$, and the magnetic field strength, from $B' = 0.22$ G to $B' = 0.20$ G. With the new viewing angle, the observer is placed outside the jet opening cone and the observed luminosity decreases due to a lower effective Doppler factor. The change in the magnetic field strength reduces the synchrotron luminosity by ∼30% relative to the ERC luminosity. The overall spectral shape is matched without any adjustment in the electron energy distribution.

7. DISCUSSION

Multi-wavelength observations of blazars, including AO 0235+164, show that events associated with periods of greater activity occur over the entire electromagnetic spectrum, from radio to γ-rays. Light curves taken in different spectral bands correlate on timescales longer than a month, while on shorter timescales correlations are weaker and some lags are claimed. In particular, monthly lags of the radio signals following the γ-rays are observed (Pushkarev et al. 2010). This is interpreted in terms of the synchrotron opacity at radio frequencies and indicates that γ-rays are produced at distances from the BH that are several parsecs smaller than the position of the radio cores. Whether γ-ray emission is smoothly distributed over several decades of distance (Blandford & Levinson 1995), or is associated with specific locations of energy dissipation in a jet, is still debated. The localized dissipation zones could be related to: reconnection of magnetic fields which may operate efficiently at distances of <0.01 pc, where the magnetization parameter σ is expected to be large (Nalewajko et al. 2011); internal shocks resulting from collisions between the jet portions moving with different velocities (Spada et al. 2001), which become efficient at distances at which σ drops below 0.1; oblique/reconfinement shocks which are formed at distances at which interactions of supersonic jets start to feel the influence of the external medium (Hughes et al. 2011; Daly & Marscher 1988; Komissarov & Falle 1997; Nalewajko & Sikora 2009).

Using the SED of AO 0235+164, we showed in Section 6 that the spectrum of this object can be reproduced using a model where the dissipation takes place at a distance of $r \sim 1.7$ pc from the BH and production of γ-rays is dominated by the Comptonization of NIR radiation of hot dust. The activity of AO 0235+164 during the same epoch was analyzed independently by Agudo et al. (2011b). They included the VLBI imaging data, and concluded that the γ-ray emission zone is associated with the 7 mm radio core (i.e., at ∼12 pc from the BH) and propose that production of γ-rays is dominated by a turbulent multi-zone SSC process. We comment on these differences below, noting

that we perform detailed modeling of the broadband spectrum of the object.

As the long term radio light curves of AO 0235+164 indicate, the active season in 2008 started about 200 days before reaching the maximum. During this period of time, any portion of the jet propagates over a distance of $\Delta r \sim c\Gamma^2 t_{\rm obs}/(1+z) \geqslant$ tens of parsecs, i.e., much larger than the length of a "blazar zone" inferred from the timescales of the short term flares. Such flares are very likely to be produced by inhomogeneities of the flow, radiating when passing through the region where energy dissipation is intensified. Particularly prominent flares are seen in the optical light curves. Their ∼10 day timescales imply that the extension of the dissipative zone is

$$\Delta r \sim \frac{c t_{\rm fl}}{(1+z)(1-\beta\cos\theta_{\rm obs})} \sim 1.7\ {\rm pc}\left(\frac{t_{\rm fl}}{10\ {\rm days}}\right)\left(\frac{\Gamma}{20}\right)^2 (\mathcal{D}/\Gamma)\,, \quad (5)$$

which nicely corresponds with the location of the blazar zone derived from our model. In order to form such flares at a distance of 12 pc, a Lorentz factor of $\Gamma \sim 50$ is required. Interestingly, a similarly large Lorentz factor is required in the Agudo et al. (2011b) model to explain the observed $t < 20$ day timescale of the flux decay at $\lambda = 1$ mm. This can be inferred by taking into account that radiative cooling of electrons emitting at 1 mm is inefficient and that the timescale of the flux decrease, as determined by the adiabatic losses, is $t_{\rm ad} \simeq (R/c)(1+z)/(\theta_j \Gamma \mathcal{D})$. VLBI observations of AO 0235+164 do not exclude such a large value of the bulk Lorentz factor (Jorstad et al. 2001; Piner et al. 2006).

Finally, we comment about the objections made by Agudo et al. (2011b) regarding the application of ERC models for the production of γ-rays in AO 0235+164. They pointed out that in this model it is impossible to explain the lack of correlation between short-term variations of the γ-ray and optical fluxes because of a lack of variations of the external radiation field. However, in the fast cooling regime, variations of the inverse Compton flux are determined not by variations of the seed radiation field, but by variations of the electron injection function. It does not matter whether the seed radiation is external or internal, so this criticism may also be applied to the SSC models. Hence, the lack of a clear correspondence between variations in these two spectral bands must have a different origin than fluctuations in the background radiation. They can be related to variations of the Doppler factor and magnetic fields in the kinematically and geometrically complex dissipative zone. In particular, this can be the case if such a zone is associated with the oblique and/or reconfinement shocks, which in AO 0235+164 is indicated by the roughly perpendicular orientation of the optical EVPA with respect to the jet axis (see Section 4.3).

8. CONCLUSIONS

Fermi-LAT detected enhanced activity in the high-redshift BL Lac object AO 0235+164 during the first six months of operations. We present the results of an intensive multi-wavelength campaign covering radio, mm, near-IR, optical, UV, and X-ray bands, as well as optical polarimetry. Extinction in the optical/UV/X-ray band, complicated by the existence of an additional absorbing system at intermediate redshift, has been carefully taken into account. We proposed a modification to the extinction model introduced by Junkkarinen et al. (2004) and used by Raiteri et al. (2005) that corrects a spurious spectral feature in the FUV band.

The γ-ray spectrum is consistent with a broken power law. Hints of spectral variability can be seen in episodic increases of the (1–100 GeV)/(0.1–1 GeV) hardness ratio. The brightest γ-ray flare is much more pronounced in the 0.1–1 GeV energy band.

The γ-ray activity is roughly correlated with the activity in the optical/near-IR band. There is a possible delay of 15 days of the R-band flux with respect to the γ-ray flux. The optical flux is also correlated with the optical polarization degree, which reaches values up to 35%. At the same time, the optical polarization angle is close to 100° with moderate scatter. As is typical for blazars, the activity in the radio band is smoother and begins months before the optical/γ-ray activity, while the radio-flux peaks are delayed by several weeks with respect to the higher energy bands.

The behavior of the source in the X-ray band is distinct from other bands, as it shows a 20 day high state delayed by a month from the main optical/γ-ray flare. The X-ray spectrum during the high state is unusually soft, $\Gamma \sim 2.6$, and is inconsistent with the extrapolation of the optical/UV spectrum, unless we assume a much stronger extinction. We interpret this X-ray component as the bulk-Compton emission, i.e., Comptonization of the accretion-disk radiation reprocessed at the distance of ∼100 $R_{\rm g}$, in the region of ongoing jet acceleration and collimation. Such a feature has been tentatively reported before in a few sources, however the present case is still not definitive. The short duration of the high X-ray state can be explained by a rapid "wiggling" of the inner jet.

The broadband SEDs extracted for two different activity states are, with the exception of the X-ray feature, typical for luminous blazars. We interpret the broadband SEDs in the standard leptonic scenario, with the low-energy bump due to synchrotron radiation and the high-energy bump due to Comptonization of the external infrared radiation from the dusty torus (ERCIR). The energetic constraints are very tight, because, if the jet power is comparable to the Eddington luminosity of the central BH, the required radiative efficiency of the jet is ∼20%, the magnetization is $\sigma_{\rm B} \sim 11\%$, and the pair-to-proton ratio is $n_{\rm e}/n_{\rm p} \sim 9$. The bulk Compton feature in the high X-ray state requires, if the electron number flux is to be matched to the model of the flaring state, a covering factor of the accretion disk corona $\xi_{\rm b} \sim 19\%$. An alternative interpretation of the high-energy bump with the SSC emission requires a very low covering factor for the dusty torus, in conflict with the observations of quasars.

The *Fermi* LAT Collaboration acknowledges generous ongoing support from a number of agencies and institutes that have supported both the development and the operation of the LAT as well as scientific data analysis. These include the National Aeronautics and Space Administration and the Department of Energy in the United States, the Commissariat à l'Energie Atomique and the Centre National de la Recherche Scientifique/Institut National de Physique Nucléaire et de Physique des Particules in France, the Agenzia Spaziale Italiana and the Istituto Nazionale di Fisica Nucleare in Italy, the Ministry of Education, Culture, Sports, Science and Technology (MEXT), High Energy Accelerator Research Organization (KEK) and Japan Aerospace Exploration Agency (JAXA) in Japan, and the K. A. Wallenberg Foundation, the Swedish Research Council and the Swedish National Space Board in Sweden.

Additional support for science analysis during the operations phase is gratefully acknowledged from the Istituto Nazionale di Astrofisica in Italy and the Centre National d'Etudes Spatiales in France.

We acknowledge the support by the Polish MNiSW grant N N203 301635.

L. C. Reyes acknowledges support from NASA through *Swift* Guest Investigator Grant NNX10AJ70G; as well as support by the Kavli Institute for Cosmological Physics at the University of Chicago through grants NSF PHY-0114422 and NSF PHY-0551142 and an endowment from the Kavli Foundation and its founder Fred Kavli.

This research is partly based on observations with the 100 m telescope of the MPIfR (Max-Planck-Institut für Radioastronomie) at Effelsberg. This work has made use of observations with the IRAM 30 m telescope.

This paper is partly based on observations carried out at the German–Spanish Calar Alto Observatory, which is jointly operated by the MPIA and the IAA-CSIC.

The Abastumani team acknowledges financial support by the Georgian National Science Foundation through grant GNSF/ST08/4-404.

The Metsähovi team acknowledges the support from the Academy of Finland to our observing projects (numbers 212656, 210338, 121148, and others).

The Submillimeter Array is a joint project between the Smithsonian Astrophysical Observatory and the Academia Sinica Institute of Astronomy and Astrophysics and is funded by the Smithsonian Institution and the Academia Sinica.

The acquisition and analysis of the SMARTS data are supported by Fermi GI grants 011283 and 31155 (PI: C. Bailyn).

Data from the Steward Observatory spectropolarimetric monitoring project were used. This program is supported by Fermi Guest Investigator grants NNX08AW56G and NNX09AU10G.

UMRAO research is supported by a series of grants from the NSF and NASA, most recently AST-0607523 and Fermi GI grants NNX10AP16G and NNX11AO13G, respectively; funds for telescope operation are provided by the University of Michigan.

REFERENCES

Abdo, A. A., Ackermann, M., Ajello, M., et al. 2009, ApJS, 183, 46
Abdo, A. A., Ackermann, M., Ajello, M., et al. 2010a, ApJS, 188, 405
Abdo, A. A., Ackermann, M., Ajello, M., et al. 2010b, ApJ, 710, 1271
Agudo, I., Jorstad, S. G., Marscher, A. P., et al. 2011a, ApJ, 726, L13
Agudo, I., Marscher, A. P., Jorstad, S. G., et al. 2011b, ApJ, 735, L10
Angelakis, E., Fuhrmann, L., Marchili, N., Krichbaum, T. P., & Zensus, J. A. 2008, Mem. Soc. Astronom. Ital., 75, 282
Atwood, W. B., Abdo, A. A., Ackermann, M., et al. 2009, ApJ, 697, 1071
Baars, J. W. M., Genzel, R., Pauliny-Toth, I. I. K., & Witzel, A. 1977, A&A, 61, 99
Bach, U., Gurwell, M. A., Leto, P., et al. 2008, ATel, 1849
Baldwin, J. A., & Stone, R. P. S. 1984, MNRAS, 206, 241
Begelman, M. C., & Sikora, M. 1987, ApJ, 322, 650
Blandford, R. D., & Leninson, A. 1995, ApJ, 441, 79
Blandford, R. D., & Rees, M. J. 1978, in Pittsburgh Conference on BL Lac Objects, ed. A. M. Wolfe (Pittsburgh: Univ. Pittsburgh Press), 328
Böttcher, M. 2007, Ap&SS, 309, 95
Breeveld, A. A. 2011, in Proc. of AIP Conf. Ser. Vol. 1358, An Updated Ultraviolet Calibration for the Swift/UVOT (New York: AIP) 1358, 373
Burbidge, E. M., Caldwell, R. D., Smith, H. E., Liebert, J., & Spinrad, H. 1976, ApJ, 205, L117
Burrows, D. N., Hill, J. E., Nousek, J. A., et al. 2005, Space Sci. Rev., 120, 165
Cardelli, J. A., Clayton, G. C., & Mathis, J. S. 1989, ApJ, 345, 245
Celotti, A., Ghisellini, G., & Fabian, A. C. 2007, MNRAS, 375, 417
Chu, H. S., Baath, L. B., Rantakyro, F. T., et al. 1996, A&A, 307, 15
Cohen, R. D., Smith, H. E., Junkkarinen, V. T., et al. 1987, ApJ, 318, 577
Comastri, A., Fossati, G., Ghisellini, G., & Molendi, S. 1997, ApJ, 480, 534
Corbel, S., & Reyes, L. C. 2008, ATel, 1744
Corbett, E. A., Robinson, A., Axon, D. J., & Hough, J. H. 2000, MNRAS, 311, 485
Cutri, R. M., Skrutskie, M. F., van Dyk, S., et al. 2003, VizieR On-line Data Catalog, http://adsabs.harvard.edu/abs/2003yCat.2246....0C
Daly, R. A., & Marscher, A. P. 1988, ApJ, 334, 539
DePoy, D. L., Atwood, B., Belville, S. R., et al. 2003, Proc. SPIE, 4841, 827
D'Ammando, F., Pucella, G., Raiteri, C. M., et al. 2009, A&A, 508, 181
Edelson, R. A., & Krolik, J. H. 1988, ApJ, 333, 646
Elvis, M., Wilkes, B. J., McDowell, J. C., et al. 1994, ApJS, 95, 1
Foschini, L., Iafrate, G., & Longo, F. 2008, ATel, 1784
Francis, P. J., Hewett, P. C., Foltz, C. B., et al. 1991, ApJ, 373, 465
Fuhrmann, L., Krichbaum, T. P., Witzel, A., et al. 2008, A&A, 490, 1019
Fuhrmann, L., Zensus, J. A., Krichbaum, T. P., Angelakis, E., & Readhead, A. C. S. 2007, in AIP Conf. Proc. 921, The First GLAST Symposium (Melville, NY: AIP), 249
Gehrels, N., Chincarini, G., Giommi, P., et al. 2004, ApJ, 611, 1005
Ghosh, K. K., & Soundararajaperumal, S. 1995, ApJS, 100, 37
Gonzalez-Perez, J. N., Kidger, M. R., & Martin-Luis, F. 2001, AJ, 122, 2055
Haas, M., Müller, S. A. H., Bertoldi, F., et al. 2004, A&A, 424, 531
Hagen-Thorn, V. A., Larionov, V. M., Jorstad, S. G., et al. 2008, ApJ, 672, 40
Hughes, P. A., Aller, M. F., & Aller, H. D. 2011, ApJ, 735, 81
Hunter, S. D., Bertsch, D. L., Dingus, B. L., et al. 1993, ApJ, 409, 134
Jones, D. L., Unwin, S. C., Baath, L. B., & Davis, M. M. 1984, ApJ, 284, 60
Jorstad, S. G., Marscher, A. P., Mattox, J. R., et al. 2001, ApJS, 134, 181
Junkkarinen, V. T., Cohen, R. D., Beaver, E. A., et al. 2004, ApJ, 614, 658
Komissarov, S. S., Barkov, M. V., Vlahakis, N., & Königl, A. 2007, MNRAS, 380, 51
Komissarov, S. S., & Falle, S. A. E. G. 1997, MNRAS, 288, 833
Landolt, A. U. 1992, ApJ, 104, 340
Levinson, A. 2006, Int. J. Mod. Phys. A, 21, 6015
Liu, F. K., Zhao, G., & Wu, X.-B. 2006, ApJ, 650, 749
Madejski, G., Takahashi, T., Tashiro, M., et al. 1996, ApJ, 459, 156
Massey, P., Strobel, K., Barnes, J. V., & Anderson, E. 1988, ApJ, 328, 315
Mattox, J. L., et al. 1996, ApJ, 461, 396
Moderski, R., Sikora, M., & Błażejowski, M. 2003, A&A, 406, 855
Murphy, D. W., Browne, I. W. A., & Perley, R. A. 1993, MNRAS, 264, 298
Nalewajko, K. 2009, MNRAS, 395, 524
Nalewajko, K., Giannios, D., Begelman, M. C., et al. 2011, MNRAS, 413, 333
Nalewajko, K., & Sikora, M. 2009, MNRAS, 392, 1205
Nilsson, K., Charles, P. A., Pursimo, T., et al. 1996, A&A, 314, 754
Padovani, P., Costamante, L., Giommi, P., et al. 2004, MNRAS, 347, 1282
Pei, Y. C. 1992, ApJ, 395, 130
Persson, S. E., Murphy, D. C., Krzeminski, W., Roth, M., & Rieke, M. J. 1998, AJ, 116, 2475
Piner, B. D., Bhattarai, D., Edwards, P. G., & Jones, D. L. 2006, ApJ, 640, 196
Poole, T. S., Breeveld, A. A., Page, M. J., et al. 2008, MNRAS, 383, 627
Pushkarev, A. B., Kovalev, Y. Y., & Lister, M. L. 2010, ApJ, 722, L7
Raiteri, C. M., Villata, M., Aller, H. D., et al. 2001, A&A, 377, 396
Raiteri, C. M., Villata, M., Bruschini, L., et al. 2010, A&A, 524, A43
Raiteri, C. M., Villata, M., Capetti, A., et al. 2007, A&A, 464, 871
Raiteri, C. M., Villata, M., Ibrahimov, M. A., et al. 2005, A&A, 438, 39
Raiteri, C. M., Villata, M., Kadler, M., et al. 2006, A&A, 459, 731
Raiteri, C. M., Villata, M., Larionov, V. M., et al. 2008, A&A, 480, 339
Ravasio, M., Tagliaferri, G., Ghisellini, G., et al. 2003, A&A, 408, 479
Richards, G. T., Lacy, M., Storrie-Lombardi, L. J., et al. 2006, ApJS, 166, 470
Richards, J., Max-Moerbeck, W., Pavlidou, V., et al. 2011, ApJS, 194, 29
Rieke, G. H., Grasdalen, G. L., Kinman, T. D., et al. 1976, Nature, 260, 754
Roberts, M. S., Brown, R. L., Brundage, W. D., et al. 1976, AJ, 81, 293
Roming, P. W. A., Kennedy, T. E., Mason, K. O., et al. 2005, Space Sci. Rev., 120, 95
Sasada, M., Uemura, M., Fukazawa, Y., et al. 2011, PASJ, 63, 489
Schlegel, D. J., Finkbeiner, D. P., & Davis, M. 1998, ApJS, 500, 525
Schmidt, G. D., Elston, R., & Lupie, O. L. 1992a, AJ, 104, 1563
Schmidt, G. D., Stockman, H. S., & Smith, P. S. 1992b, ApJ, 398, L57
Shang, Z., Brotherton, M. S., Wills, B. J., et al. 2011, ApJS, 196, 2
Sikora, M. 2011, in IAU Symp. 275, Jets at All Scales, ed. G. E. Romero, R. A. Sunyaev, & T. Belloni (Cambridge: Cambridge Univ. Press), 59
Sikora, M., Begelman, M. C., Madejski, G. M., & Lasota, J.-P. 2005, ApJ, 625, 72
Sikora, M., & Madejski, G. 2000, ApJ, 534, 109
Sikora, M., & Madejski, G. 2001, Am. Inst. Phys. Conf. Ser., 558, 275
Sikora, M., Stawarz, Ł., Moderski, R., et al. 2009, ApJ, 704, 38
Snijders, M. A. J., Bocksenberg, A., Penston, M. V., & Sargent, W. L. W. 1982, MNRAS, 201, 801

Smith, P. S., Montiel, E., Rightley, S., et al. 2009, Fermi Symposium, eConf Proceedings C091122 (arXiv:0912.3621)
Smith, P. S., Schmidt, G. D., Hines, D. C., & Foltz, C. B. 2003, ApJ, 593, 676
Spada, M., Ghisellini, G., Lazzati, D., & Celotti, A. 2001, MNRAS, 325, 1559
Spearman, C. 1904, Am. J. Psychol., 15, 72101
Spinrad, H., & Smith, H. 1975, ApJ, 201, 275
Stein, W. A., O'Dell, S. L., & Strittmatter, P. A. 1976, ARA&A, 14, 173
Stickel, M., Padovani, P., Urry, C. M., Fried, J. W., & Kuehr, H. 1991, ApJ, 374, 431
Stocke, J. T., Danforth, C. W., & Perlman, E. S. 2011, ApJ, 732, 1312
Stone, R. P. S., & Baldwin, J. A. 1983, MNRAS, 204, 347
Trippe, S., Neri, R., Krips, M., et al. 2010, A&A, 515, A40
Tristram, K. R. W., & Schartmann, M. 2011, A&A, 531, A99
Urry, C. M. 1999, in ASP Conf. Ser. 159, BL Lac Phenomenon, ed. L. O. Takalo & A. Sillanpää (San Francisco, CA: ASP), 3
Vermeulen, R. C., & Taylor, G. B. 1995, AJ, 109, 1983
Villata, M., Raiteri, C. M., Carosati, D., et al. 2008a, ATel, 1724
Villata, M., Raiteri, C. M., Gurwell, M. A., et al. 2009, A&A, 504, L9
Villata, M., Raiteri, C. M., Larionov, V. M., et al. 2008b, A&A, 481, L79
Villata, M., Raiteri, C. M., Larionov, V. M., et al. 2008c, ATel, 1785
Wardle, J. F. C., & Kronberg, P. P. 1974, ApJ, 194, 249
Watanabe, M., Nakaya, H., Yamamuro, T., et al. 2005, PASP, 117, 870
Webb, J. R., Howard, E., Benítez, E., et al. 2000, AJ, 120, 41
Winters, J. M., & Neri, R. 2010, An Introduction to the IRAM Plateau de Bure Interferometer, Public IRAM Document, Version 4.1-01
Wolfe, A. M., & Wills, B. 1977, ApJ, 218, 39
Wolff, M. J., Nordsieck, K. H., & Nook, M. A. 1996, AJ, 111, 856
Worral, D. M., & Wilkes, B. J. 1990, ApJ, 360, 396
Wu, X.-B., Liu, F. K., Kong, M. Z., et al. 2011, J. Astrophys. Astron., 32, 209

The Astrophysical Journal Letters, 747:L3 (5pp), 2012 March 1 doi:10.1088/2041-8205/747/1/L3

DISCOVERY OF AN UNIDENTIFIED *FERMI* OBJECT AS A BLACK WIDOW-LIKE MILLISECOND PULSAR

A. K. H. Kong[1,10], R. H. H. Huang[1], K. S. Cheng[2], J. Takata[2], Y. Yatsu[3], C. C. Cheung[4,11], D. Donato[5,6], L. C. C. Lin[7], J. Kataoka[8], Y. Takahashi[8], K. Maeda[8], C. Y. Hui[9], and P. H. T. Tam[1]
[1] Institute of Astronomy and Department of Physics, National Tsing Hua University, Hsinchu 30013, Taiwan; akong@phys.nthu.edu.tw
[2] Department of Physics, The University of Hong Kong, Hong Kong
[3] Department of Physics, Tokyo Institute of Technology 2-12-1, Ookayama, Meguro, Tokyo, 152-8551, Japan
[4] National Research Council Research Associate, National Academy of Sciences, Washington, DC 20001, USA
[5] CRESST and Astroparticle Physics Laboratory NASA/GSFC, Greenbelt, MD 20771, USA
[6] Department of Astronomy, University of Maryland, College Park, MD 20742, USA
[7] General Education Center, China Medical University, Taichung 40402, Taiwan
[8] Research Institute for Science and Engineering, Waseda University, 3-4-1 Okubo, Shinjuku, Tokyo 169-8555, Japan
[9] Department of Astronomy and Space Science, Chungnam National University, Daejeon, Republic of Korea
Received 2011 November 7; accepted 2012 January 17; published 2012 February 7

ABSTRACT

The *Fermi* γ-*ray Space Telescope* has revolutionized our knowledge of the γ-ray pulsar population, leading to the discovery of almost 100 γ-ray pulsars and dozens of γ-ray millisecond pulsars (MSPs). Although the outer-gap model predicts different sites of emission for the radio and γ-ray pulsars, until now all of the known γ-ray MSPs have been visible in the radio. Here we report the discovery of a "radio-quiet" γ-ray-emitting MSP candidate by using *Fermi*, *Chandra*, *Swift*, and optical observations. The X-ray and γ-ray properties of the source are consistent with known γ-ray pulsars. We also found a 4.63 hr orbital period in optical and X-ray data. We suggest that the source is a black widow-like MSP with a $\sim$0.1 $M_{\odot}$ late-type companion star. Based on the profile of the optical and X-ray light curves, the companion star is believed to be heated by the pulsar while the X-ray emissions originate from pulsar magnetosphere and/or from intrabinary shock. No radio detection of the source has been reported yet, and although no γ-ray/radio pulsation has been found we estimate that the spin period of the MSP is $\sim$3–5 ms based on the inferred γ-ray luminosity.

Key words: binaries: close – gamma rays: stars – pulsars: general – stars: individual (1FGL J2339.7-0531, SDSS J233938.74-053305.2) – X-rays: stars

Online-only material: color figure

1. INTRODUCTION

The *Fermi* Large Area Telescope (LAT) has detected 1873 γ-ray point sources during its first 24 months of operation (Abdo et al. 2011). The majority of the extragalactic sources have been identified as active galactic nuclei (AGNs; Abdo et al. 2010a), while many of the Galactic sources have been identified as γ-ray-emitting pulsars (Abdo et al. 2010b). γ-ray pulsars are typically either young and energetic, such as the Crab and Vela pulsars, or very short period millisecond pulsars (MSPs). Throughout this Letter we will refer to these two classes as the energetic and millisecond pulsars. In this second source catalog (2FGL), there are more than 100 identified energetic and millisecond pulsars. About half of them with γ-ray pulsations were discovered previously by using radio pulsation search (e.g., Ransom et al. 2011; Keith et al. 2012; Cognard et al. 2011; Caraveo 2010). In addition, although there were 35 γ-ray pulsars identified from the energetic class using a blind Fourier search of the LAT data (see Pletsch et al. 2012 and references therein), only four were subsequently identified as radio pulsars by folding the radio data with the pulsar ephemerides (Camilo et al. 2009; Saz Parkinson et al. 2010; Pletsch et al. 2012). This indicates that there is a population of "radio-quiet" energetic pulsars as seen from the Earth. However, all 21 γ-ray-emitting MSPs are "radio-loud." Based on current observations, we can classify the current population of γ-ray-emitting pulsars into "radio-loud" energetic pulsars, "radio-quiet" pulsars and "radio-loud" MSPs. However, it is unclear if there is a class of "radio-quiet" γ-ray-emitting MSPs.

It is well known that the radio emissions of pulsars are associated with the activity of a polar cap accelerator. On the other hand, the high-energy emissions from the pulsar magnetosphere have been studied with a polar cap model (Ruderman & Sutherland 1975), a slot gap model (Muslimov & Harding 2003) and an outer gap model (Takata et al. 2010b). The polar cap model assumes that the emission region is close to the stellar surface and above the polar cap, and therefore the model implies that radio-loud γ-ray pulsars are much more common than radio-quiet γ-ray pulsars. The outer gap and slot gap models assume an acceleration region extending to the outer magnetosphere and indicate that radio-quiet γ-ray pulsars are the major population of γ-ray pulsars. Based on the spectral shape in the GeV bands and the population of radio-quiet γ-ray pulsars found with *Fermi* (Abdo et al. 2010b), the outer gap or slot gap region is more favorable as the origin of the γ-rays from energetic pulsars (Takata et al. 2010b).

For MSPs, "radio-quiet" millisecond γ-ray pulsars have not been identified so far. This may be due to following reasons: (1) the present sensitivity of blind frequency search prevents a detection of millisecond pulsation in *Fermi* data; (2) most known radio MSPs are in binaries that γ-ray searches would be insensitive to, and (3) γ-ray emissions from MSPs always accompany radio emissions. On the other hand, Venter et al. (2009) found that the pulse profiles of six MSPs detected by *Fermi* can be fitted by the geometries with outer gap or the slot models. This implies that the emission regions of the γ-rays are different from the radio emission site for some of the MSPs

[10] Golden Jade Fellow of Kenda Foundation, Taiwan.
[11] Resident at Naval Research Laboratory, Washington, DC 20375, USA.

and thus we expect that there are "radio-quiet" γ-ray MSPs for which the radio beam is outside the line of sight. It is worth noting that "radio-quiet" here does not mean no intrinsic radio emission, just none beamed in our direction.

In this Letter, we report a multiwavelength identification of a "radio-quiet" γ-ray MSP candidate. In a separate paper, Romani & Shaw (2011) arrived at similar conclusions via optical spectroscopy.

2. UNIDENTIFIED *FERMI* SOURCE AS A "RADIO-QUIET" γ-RAY-EMITTING MILLISECOND PULSAR

To identify suitable targets of "radio-quiet" γ-ray MSPs, we first selected candidates from the *Fermi*-LAT first source catalog (1FGL; Abdo et al. 2010c) based on four criteria: (1) no known association at other wavelengths, (2) source variability, (3) Galactic latitude, and (4) γ-ray spectral shape.

We used the variability index in the 1FGL catalog to characterize source variability. γ-ray pulsars have always been found to be steady sources of γ-ray emission (Abdo et al. 2010c, 2011). This property can therefore be used to help identify which of the unidentified sources are probably pulsars. The 1FGL catalog defines a variability index, for which a value greater than 23.21 means that there is less than a 1% probability of it being a steady source. We therefore selected sources with a variability index less than 23.

MSPs are in general older than energetic γ-ray pulsars. Young objects like energetic γ-ray pulsars ($\tau < 1$ Myr) are likely located in the Galactic plane, while a fraction of MSPs should be at higher Galactic latitudes. We thus selected *Fermi* sources with high Galactic latitudes ($|b| > 40^\circ$). The choice of this value is based on Monte-Carlo simulations for the Galactic population of MSPs, which show that no energetic γ-ray pulsar exists above $|b| = 40^\circ$ (Takata et al. 2011).

Finally, we identified potential candidates from the γ-ray spectra. Although only a power-law spectrum is listed in the first-year catalog, it also has a curvature index to indicate how good is the power-law fit. For γ-ray pulsars, their γ-ray spectra are usually described by a power-law plus an exponential cutoff model (Abdo et al. 2010b). According to the 1FGL catalog, the curvature index, for which a value greater than $C = 11.34$ indicates less than 1% chance that the power-law spectrum is a good fit. Hence we chose objects with a curvature index larger than 12.

If a 1FGL source satisfied all four criteria, we shortlisted it as a potential candidate. From the short list, we further searched for X-ray imaging data (*Chandra*, *XMM-Newton*, and *Swift*) from public archives and looked for X-ray sources within the error circles of *Fermi* as the first step for multiwavelength investigation. In this Letter, we focus on one of our targets, 1FGL J2339.7–0531.[12]

3. MULTIWAVELENGTH IDENTIFICATION

1FGL J2339.7–0531 is one of the 205 bright γ-ray sources detected with *Fermi*-LAT during its first three months of operation (Abdo et al. 2009). It remains an unidentified source in the second *Fermi*-LAT source (2FGL) catalog. In the 1FGL catalog (Abdo et al. 2010c), 1FGL J2339.7–0531 has a variability index of 9.2 and a curvature index of 22.7. By comparing the 1FGL and 2FGL catalogs (Abdo et al. 2011), the γ-ray flux of 1FGL J2339.7–0531 is constant and near 3×10^{-11} erg s^{-1} cm^{-2}. With better statistics, the second source catalog shows that a log parabola spectrum can provide a better spectral fit compared to a power-law model (Abdo et al. 2011). With its high Galactic latitude (-62°) and unidentified nature in all *Fermi* catalogs, 1FGL J2339.7–0531 is therefore one of the best targets to search for "radio-quiet" γ-ray MSPs.

1FGL J2339.7–0531 was observed with *Chandra* and *Swift*/XRT for 21 ks on 2009 October 13 (PI: Cheung), and for 3.2 ks on 2009 November 4, respectively. The *Chandra* imaging was operated with ACIS-I while the XRT was in the photon counting imaging mode. We reprocessed with updated calibration files. HEASOFT version 6 and CIAO version 4.2 were used for data reduction and analysis. Within the 95% error circle of *Fermi* (based on the refined position in the 2FGL catalog), there is only one relatively bright X-ray source in both observations. The brightest X-ray source (CXOU J233938.7–053305) near the center of the error circle has an X-ray flux of 3×10^{-13} erg s^{-1} cm^{-2} (0.3–10 keV) based on a spectral fitting using an absorbed power law with a best-fit photon index of 1.1 (based on the *Chandra* observation). This indicates that the ratio between the X-ray and γ-ray (>100 MeV) flux ($F_\gamma \sim 3 \times 10^{-11}$ erg s^{-1} cm^{-2}) as measured by *Fermi* (Abdo et al. 2011) becomes $F_X/F_\gamma \sim 0.01$, which is consistent with typical observed values for γ-ray pulsars. It is worth noting that there are nine much fainter *Chandra* sources in the error circle and their X-ray-to-γ-ray flux ratios are less than 0.1%. Although we cannot totally rule out their association with the γ-ray source, such a low flux ratio is not typical. We therefore identified CXOU J233938.7–053305 as the potential X-ray counterpart to 1FGL J2339.7–0531.

Within the *Chandra* error circle (0.6 arcsec at 90% level) of CXOU J233938.7–053305, there is a $R \sim 19$ star from the USNO catalog (Monet et al. 2003). The same optical source is also seen in the Sloan Digital Sky Survey (SDSS) Data Release 8 images as SDSS J233938.74-053305.2 with $u' = 20.85$, $g' = 19.0$, $r' = 18.61$, $i' = 18.25$, and $z' = 18.23$, as well as in the *Galaxy Evolution Explorer* (*GALEX*) images with NUV=22.88 (177–283 nm). *Swift*/UVOT observations taken simultaneously with the X-ray observations detected the source with $U = 19.58$, $B = 19.53$, and $V = 18.88$. The X-ray-to-optical flux ratio (390) is much too high for a foreground star and an AGN (e.g., Green et al. 2004; Laird et al. 2009). Moreover, the spectral energy distribution from UV to optical indicates that it is unlikely to be an AGN (e.g., Richards et al. 2002). Instead, it looks like an F- or G-type star. In a separate paper, Romani & Shaw (2011) show via optical spectroscopy that the stellar object is consistent with a late-type star. We also had a long-term optical monitoring program with the MITSuME 50 cm telescope (Kotani et al. 2005) located at Akeno Observatory in Japan from 2010 September to 2010 November. MITSuME is equipped with a tricolor camera that can perform simultaneous imaging in the g', R, and I bands. It is clear from Table 1 that all three bands show noticeable variability. Based on the above observations, we believe that the γ-ray/X-ray source is likely a binary system with optical emission from the irradiation of the companion star, while the central compact object is responsible for the X-ray and γ-ray emission.

Because 1FGL J2339.7–0531/CXOU J233938.7–053305 may be a new class of interesting objects, we carried out an intensive optical monitoring campaign using the 1 m telescope at Lulin Observatory in Taiwan and the 0.8 m Tenagra Telescope in Arizona (see Table 1 for the observation log).

[12] We will use the 1FGL naming conversion throughout the Letter, and the source is called 0FGL J2339.8–0530 and 2FGL J2339.6–0532 in the bright source catalog and 2FGL catalog, respectively.

Table 1
Optical Observation Log of 1FGL J2339.7–0531

Date and Time (UT)	Telescope	Filter	Exposure[a]
2010-10-25 14:44–15:57	Lulin 1 m	V	2 min
2010-10-26 13:33–15:59	Lulin 1 m	V	2 min
2010-10-31 10:23–15:53	Lulin 1 m	White	2 min
2010-11-01 11:33–16:27	Lulin 1 m	White	2 min
2010-11-11 01:45–06:20	Tenagra 0.8 m	White	5 min
2007-09-13 22:32:08	*GALEX*	NUV=22.88	1642 s
2008-11-20 05:25–05:29	SDSS	$u' = 20.85$, $g' = 19.0$, $r' = 18.61$, $i' = 18.25$, $z' = 18.23$	54 s
2009-11-04 07:56–16:07	UVOT	$U = 19.58$, $B = 19.53$, $V = 18.88$	1144, 838, 1144 s
2010-09-13 14:52:26	MITSuME 0.5 m	$g' = 18.51$, $R = 18.04$, $I = 17.53$	60 s[b]
2010-09-17 14:46:37	MITSuME 0.5 m	$g' = 18.54$, $R = 17.98$, $I = 17.63$	
2010-09-20 13:17:30	MITSuME 0.5 m	$g' = 18.15$, $R = 17.33$, $I = 17.38$	
2010-10-04 15:55:20	MITSuME 0.5 m	$g' = 18.51$, $R = 17.93$, $I = 17.53$	
2010-10-10 14:28:06	MITSeME 0.5 m	$g' = 19.12$, $R = 18.53$, $I = 17.94$	
2010-11-09 13:21:22	MITSeME 0.5 m	$g' = 18.43$, $R = 17.82$, $I = 17.21$	
2010-11-10 13:22:43	MITSeME 0.5 m	$g' = 18.98$, $R = 18.12$, $I = 17.51$	
2010-11-11 13:19:40	MITSeME 0.5 m	$g' > 20.19$, $R = 19.44$, $I = 19.04$	
2010-11-12 11:22:28	MITSeME 0.5 m	$g' = 18.43$, $R = 17.70$, $I = 17.44$	
2010-11-14 12:39:55	MITSeME 0.5 m	$g' = 19.00$, $R = 18.16$, $I = 17.84$	
2010-11-15 12:40:11	MITSeME 0.5 m	$g' = 18.07$, $R = 17.91$, $I = 17.51$	
2010-11-18 12:53:05	MITSeME 0.5 m	$g' > 20.02$, $R = 21.77$, $I = 19.16$	
2010-11-21 12:46:57	MITSeME 0.5 m	$g' = 18.70$, $R = 17.61$, $I = 17.49$	

Notes.
[a] Exposure time for each frame.
[b] Some frames were combined to increase the signal-to-noise ratio.

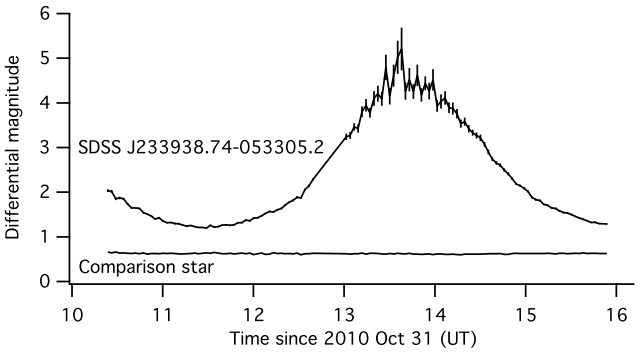

Figure 1. Representative optical (white light) light curve of the optical counterpart to 1FGL J2339.7–0531, as observed by the Lulin 1 m telescope in Taiwan. The differential magnitudes are derived by comparison with several comparison stars in the field. Periodicity on a timescale of 4–5 hr is clearly seen. Also shown is the light curve of a comparison star (with an average error of 0.01–0.02 mag). The timing resolution is 2 minutes.

All images are flat-fielded and bias corrected and we performed relative photometry by comparing with several comparison stars in the field. On all five nights, the light curves clearly show variability on a timescale of 4–5 hr (see Figures 1 and 2). We then performed a timing analysis by using the Lomb–Scargle periodogram on the combined optical data and found a period of 4.6342(9) hr. Figure 2 shows the folded light curves of all the optical data (upper panel) and *Chandra* data (lower panel) at a period of 4.6342 hr. The phase zero is chosen at MJD 55500. In addition, we folded the optical colors ($g' - I$) obtained with MITSuME and X-ray hardness ratio (1.5–8 keV/0.3–1.5 keV) at the same period (Figure 2).

4. DISCUSSION

Using multiwavelength data, we found an X-ray/optical counterpart to 1FGL J2339.7–0531. The X-ray-to-γ-ray flux ratio is consistent with a γ-ray pulsar while the γ-ray spectrum deviates from a power law which is commonly seen in MSPs. The X-ray spectrum is very hard with a power-law photon index of 1.1. Such a hard spectrum is not typical for an X-ray binary, an AGN, or a foreground star. However, some MSPs show similar spectral characteristics (e.g., Archibald et al. 2010; Tam et al. 2010) and such a hard spectrum could be from a pulsar wind nebula. We propose that 1FGL J2339.7–0531 is a γ-ray-emitting MSP in a binary system and the optical emission is from a late-type companion star with contribution from the heating on the stellar surface.

The optical light curve shows clear modulation at a period of 4.6342 hr (Figure 2). It is beyond any doubt that the periodicity is associated with the orbital period of the system. Given the large variation (about 3–4 mag) in the optical light curve, the inclination must be high. Better photometric data in the near-infrared and light-curve modeling will be able to constrain the inclination in the future. Assuming the companion has filled its the Roche lobe, the mass limit of the companion star can be estimated from the orbital period. For a 4.6 hr orbital period, the mass for a normal main-sequence star is $<0.5\,M_{\odot}$ (Wilson et al. 1999).

The large optical variability and hints of color variation (Figure 2) suggest that the companion is being heated by the pulsar. The irradiation of pulsar γ-ray emissions onto the companion star can produce the orbital modulation of the optical emission from the binary system (e.g., Takata et al. 2010a, 2012). In this model, the optical maximum occurs at the inferior conjunction, where the pulsar is located between the companion star and the Earth. Furthermore, during the optical maximum, the color of the star tends to be bluer because of the heating effect. There is some indication from the MITSuME data that the color of the star has become bluer during the optical maximum (Figure 2). The maximum luminosity of the optical emission can be estimated as $\delta L_{\rm opt} \sim (\pi\theta^2/\delta\Omega)L_{\gamma} \sim$

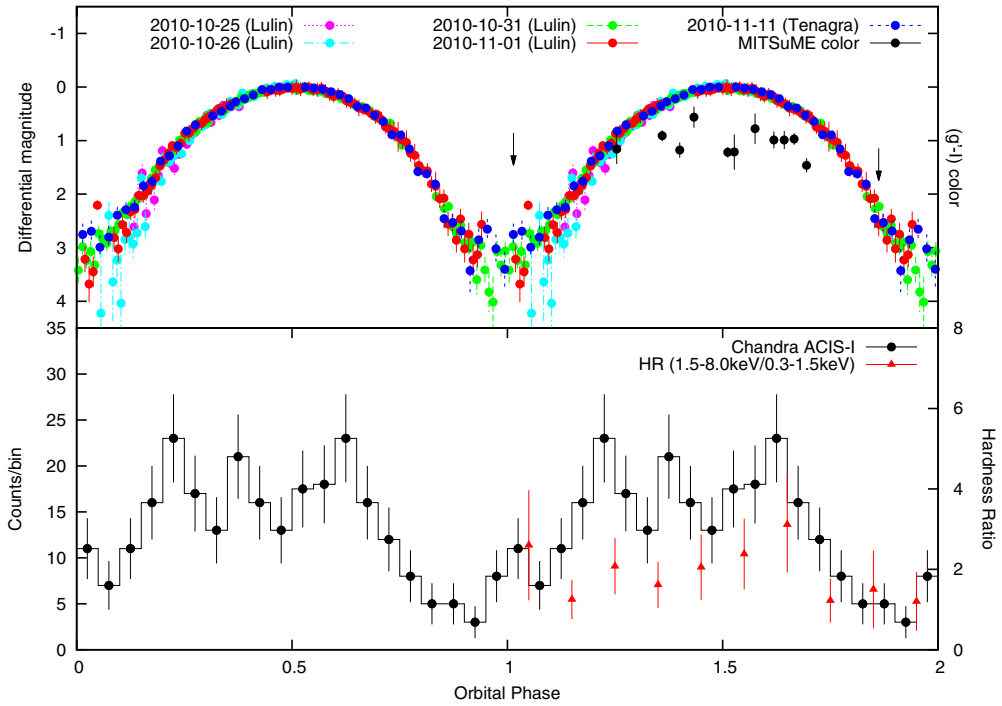

Figure 2. Folded light curve of optical and *Chandra* observations of 1FGL J2339.7–0531 with a best-fit period of 4.6342 hr. Optical colors ($g' - I$) obtained with MITSuME are also plotted. The phase zero is defined as 2010 October 31 (MJD 55500). Also plotted with the X-ray light curve is the X-ray hardness ratio (1.5–8 keV/0.3–1.5 keV) with triangles. It is evident that both optical and X-ray light curves show similar modulation. The X-ray hardness ratio exhibits some variability when the X-ray light curve is at its minimum. Note that the *Chandra* data only cover about one orbital period.

(A color version of this figure is available in the online journal.)

$10^{31}(\theta/0.1\,\mathrm{rad})^2(\delta\Omega/3\,\mathrm{rad})^{-1}(L_\gamma/10^{33}\ \mathrm{erg\ s^{-1}})\ \mathrm{erg\ s^{-1}}$, where θ is the angular size of the companion star measured from the pulsar and $\delta\Omega$ is the solid angle of the γ-ray beam. The observed maximum R-band magnitude of 1FGL J2339.7–0531 is about 18 (see Table 1), which is consistent with the above estimation.

It has been suggested that X-ray emission from black widow systems originate from the pulsar magnetosphere and/or from an intrabinary shock due to the interaction between the pulsar wind and the injected material from the low-mass star (e.g., Kulkarni et al. 1992; Stappers et al. 2003). If the X-rays are produced in the magnetosphere, the orbital modulation will be produced due to the physical eclipse of the pulsar by the companion star. In this case, the minima of the X-ray and optical light curves should be at the same phase, and we indeed observed that (see Figure 2). Alternatively, if the X-rays originate from the intrabinary shock region, an effect of the Doppler boosting relating with the post-shock flow can produce the orbital modulation (Arons & Tavani 1993). It has been suggested for the pulsar and massive stellar system (e.g., PSR B1259-63/LS 2883 system, Bogovalov et al. 2008), the post-shock flow can be accelerated into the relativistic regime because of an explosion in the downstream region (see also Tam et al. 2011). The Doppler boosting increases the intensity as $I_\nu \propto D^{3+\alpha} I_\nu^{'}$, where $I_\nu^{'}$ is the intensity in the comoving frame, D is Doppler factor and α is the spectral index in the comoving frame. An orbital modulation by a factor of five may suggest that the Doppler factor $D \sim 1.6$ with $\alpha \sim 0.5$.

The X-ray hardness ratio roughly correlates with the X-ray light curve (Figure 2). It may suggest that the pulsar (which has a very hard X-ray spectrum) is physically eclipsed by the companion and that the soft emission is an extra source of light (e.g., a wind shock). There is some support for this in the asymmetry of the optical light curve. Much better X-ray and optical photometric data are required for serious modeling.

The source has a very low absorption (3×10^{20} cm^{-2}) along the line of sight in comparison with Geminga with $N_{\rm H} = 1.5 \times 10^{20}$ cm^{-2} and a distance of 150–250 pc, and SAX J1808.4–3658 with $N_{\rm H} = 4 \times 10^{20}$ cm^{-2} and a distance of 1.3 kpc. The distance of 1FGL J2339.7–0531 is therefore likely to be between 300 and 1000 pc. If the companion star is a late-type main sequence (e.g., a M5 dwarf), and has $V \sim 21$ during optical minimum when the heating effect is at minimum, the implied distance is about 700 pc.

If we assume a distance of 700 pc, then the γ-ray power is $L_\gamma \sim 10^{33}$ erg s^{-1}. Most MSPs have an efficiency of about 10%, which gives a spin-down luminosity $L_{sd} \sim 10^{34}$ erg s^{-1}. According to Takata et al. (2012), the spin period of the MSP can be derived from the spin-down power. Using the estimated spin-down power, the spin period will be ~4 ms. We note that the distance to the source is uncertain; for instance, Romani & Shaw (2011) estimated a distance of 1.1 ± 0.3 kpc. If we assume a distance error of a factor of two (i.e., 350–1400 pc), the spin period will be 3–5 ms.

The bright *Fermi* source 1FGL J2339.7–0531 is an intriguing object that is potentially the first "radio-quiet" γ-ray-emitting MSP in a binary system. Despite 1FGL J2339.7–0531 being one of the brightest unidentified pulsar-like *Fermi* sources located at high Galactic latitude, no radio detection has been reported. Based on a recent pulsation search with the Green Bank Telescope, 1FGL J2339.7–0531 was not detected (Ransom et al. 2011). It may indicate that 1FGL J2339.7–0531 is "radio-quiet," or the radio emission must be very weak.

The system resembles black widow MSP for which the MSP has a very low-mass ($\ll 0.1\ M_\odot$) companion in an orbit less than

a day. The optical light curve of black widow systems usually shows large orbital variation because the irradiation produces strong heating on the companion facing the pulsar. It is therefore suggestive that the companion (usually a white dwarf) is being evaporated by the high-energy radiation from the pulsar. On the other hand, there is a class of black widow MSPs with high mass ($\gtrsim$0.1 $M_\odot$) non-degenerate companions. One classic example is PSR J1023+0038 that has a 0.2 $M_\odot$ companion (Archibald et al. 2009). The X-ray/γ-ray properties of 1FGL J2339.7–0531 are similar to that of PSR J1023+0038, but no radio emission from the former has been detected yet.

Hence, we suggest that 1FGL J2339.7–0531 is a new class of a black widow-like MSP system, with no or very faint radio emission along the line-of-sight. The high-mass non-degenerate companion indicates that 1FGL J2339.7–0531 is in the late stages of recycling. The absence of radio emission is the result of different emission regions for radio and γ-rays. For instance, the radio emission is from the polar cap with the radio beam out of the line of sight. On the other hand, the γ-ray emission is from the outer magnetosphere, which is predicted by the outer gap model.

An intensive search for radio emission and pulsation from 1FGL J2339.7–0531 in the future can confirm the above scenario. At the same time, a search for γ-ray/X-ray pulsation from the MSP will reveal the true nature of the system.

We thank the supporting staff at the Lulin Observatory for arranging the service observations. The Lulin Observatory is operated by the Graduate Institute of Astronomy in National Central University, Taiwan. We also thank Roger Romani for providing insights and useful comments as well as his quick-look optical spectroscopic results. This project is supported by the National Science Council of the Republic of China (Taiwan) through grants NSC100-2628-M-007-002-MY3 and NSC100-2923-M-007-001-MY3. A.K.H.K. gratefully acknowledges support from a Kenda Foundation Golden Jade Fellowship. C.C.C. and D.D. were supported in part by Chandra award GO0-11022A. C.Y.H. is supported by the National Research Foundation of Korea through grant 2011-0023383. K.S.C. and J.T. are supported by the GRF grant HKU 700911P.

REFERENCES

Abdo, A. A., Ackermann, M., Ajello, M., et al. 2009, ApJS, 183, 46
Abdo, A. A., Ackermann, M., Ajello, M., et al. 2010a, ApJ, 715, 429
Abdo, A. A., Ackermann, M., Ajello, M., et al. 2010b, ApJS, 187, 460
Abdo, A. A., Ackermann, M., Ajello, M., et al. 2010c, ApJS, 188, 405
Abdo, A. A., Ackermann, M., Ajello, M., et al. 2011, ApJS, submitted (arXiv:1108.1435)
Archibald, A. M., Kaspi, V. M., Bogdanov, S., et al. 2010, ApJ, 722, 88
Archibald, A. M., Stairs, I. H., Ransom, S. M., et al. 2009, Science, 324, 1411
Arons, J., & Tavani, M. 1993, ApJ, 403, 249
Bogovalov, S. V., Khangulyan, D. V., Koldoba, A. V., Ustyugova, G. V., & Aharonian, F. A. 2008, MNRAS, 387, 63
Camilo, F., Ray, P. S., Ransom, S. M., et al. 2009, ApJ, 705, 1
Caraveo, P. A. 2010, arXiv:1009.2421
Cognard, I., Guillemot, L., Johnson, T. J., et al. 2011, ApJ, 732, 47
Green, P. J., Silverman, J. D., Cameron, R. A., et al. 2004, ApJS, 150, 43
Keith, M. J., Johnston, S., Bailes, M., et al. 2012, MNRAS, 419, 1752
Kotani, T., Kawai, N., Yanagisawa, K., et al. 2005, Nuovo Cimento C, 28, 755
Kulkarni, S. R., Phinney, E. S., Evans, C. R., & Hasinger, G. 1992, Nature, 359, 300
Laird, E. S., Nandra, K., Georgakakis, A., et al. 2009, ApJS, 180, 102
Monet, D. G., Levine, S. E., Canzian, B., et al. 2003, AJ, 125, 984
Muslimov, A. G., & Harding, A. K. 2003, ApJ, 588, 430
Pletsch, H. J., Guillemot, L., Allen, B., et al. 2012, ApJ, 744, 105
Ransom, S. M., Ray, P. S., Camilo, F., et al. 2011, ApJ, 727, L16
Richards, G. T., Fan, X., Newberg, H. J., et al. 2002, AJ, 123, 2945
Romani, R. W., & Shaw, M. S. 2011, ApJ, 743, L26
Ruderman, M. A., & Sutherland, P. G. 1975, ApJ, 196, 51
Saz Parkinson, P. M., Dormody, M., Ziegler, M., et al. 2010, ApJ, 725, 571
Stappers, B. W., Gaensler, B. M., Kaspi, V. M., van der Klis, M., & Lewin, W. H. G. 2003, Science, 299, 1372
Takata, J., Cheng, K. S., & Taam, R. E. 2010a, ApJ, 723, L68
Takata, J., Cheng, K. S., & Taam, R. E. 2012, ApJ, 745, 100
Takata, J., Wang, Y., & Cheng, K. S. 2010b, ApJ, 715, 1318
Takata, J., Wang, Y., & Cheng, K. S. 2011, ApJ, 726, 44
Tam, P. H. T., Hui, C. Y., Huang, R. H. H., et al. 2010, ApJ, 724, L207
Tam, P. H. T., Huang, R. H. H., Takata, J., et al. 2011, ApJ, 736, L10
Venter, C., Harding, A. K., & Guillemot, L. 2009, ApJ, 707, 800
Wilson, C. A., Dieters, S., Finger, M. H., Scott, D. M., & van Paradijs, J. 1999, ApJ, 513, 464

The Astrophysical Journal Letters, 760:L27 (4pp), 2012 December 1 doi:10.1088/2041-8205/760/2/L27

OPTICAL EMISSION OF THE BLACK HOLE X-RAY TRANSIENT MAXI J1659−152 DURING QUIESCENCE

Albert K. H. Kong[1]
Institute of Astronomy and Department of Physics, National Tsing Hua University, Hsinchu 30013, Taiwan; akong@phys.nthu.edu.tw
Received 2012 August 24; accepted 2012 October 24; published 2012 November 7

ABSTRACT

We report on the optical detection of the black hole X-ray transient MAXI J1659−152 during its quiescent state. By using the Canada–France–Hawaii Telescope, we observed MAXI J1659−152 about seven months after the end of an X-ray outburst. The optical counterpart of MAXI J1659−152 is clearly detected with an r'-band magnitude of 23.6–23.8. The detection confirms that the optical emission of MAXI J1659−152 during quiescence is relatively bright compared to other black hole X-ray transients. This implies that the distance to MAXI J1659−152 is 4.6–7.5 kpc for an M2 dwarf companion star or 2.3–3.8 kpc for an M5 dwarf companion star. By comparing with other measurements, an M2 dwarf companion is more likely.

Key words: binaries: close – stars: individual (MAXI J1659−152) – X-rays: binaries

1. INTRODUCTION

Galactic black hole X-ray binary systems manifest themselves as X-ray novae and most of them are discovered via their sudden dramatic increase in X-ray brightness. Such an X-ray outburst is due to a change of the amount of material accreted from the companion star by the central compact object. In addition to X-ray follow-up observations following the evolution of the outburst, multi-wavelength observations play an important role in understanding the physics of these systems. In particular, reprocessing in the accretion disk and the companion star will also generate optical emission. We therefore expect to see a dramatic change in optical brightness when an X-ray nova is in outburst.

Optical observations provide the data necessary to determine the orbital period, the evolutionary state of the secondary, the binary mass function, and mass of the compact object itself. In combination with X-ray spectral and timing studies, these provide a detailed picture of the accretion process and the nature of the compact object. Although the optical counterpart of an X-ray nova is usually discovered during an outburst, observations when the source returns to quiescence are also extremely important. While the optical emission of an X-ray nova is very faint in quiescence, it is the best time to study the nature of the companion star and the geometry of the binary system, and to measure the mass function via radial velocity measurements.

The X-ray transient MAXI J1659−152 was first discovered with the *Swift* Burst Alert Telescope (BAT) on 2010 September 25 as a gamma-ray burst (GRB 100925A; Mangano et al. 2010). Independent discovery made with the Gas Slit Camera (GSC; Mihara et al. 2011) on board the *Monitor of All-sky X-ray Image* (*MAXI*; Matsuoka et al. 2009) suggested that it is a previously unknown Galactic X-ray transient. The optical counterpart of MAXI J1659−152 was discovered with the *Swift* UltraViolet/Optical Telescope (UVOT) immediately after the BAT trigger (Marshall 2010). Subsequent multi-wavelength observations from radio to hard X-ray showed that MAXI J1659−152 is a black hole binary candidate. In particular, frequent X-ray dips with a recurrent time of 2.4 hr were found in *RXTE*, *Swift*, and *XMM-Newton* observations (Kennea et al. 2011; Kuulkers et al. 2012). This strongly suggests that MAXI J1659−152 is a highly inclined system with an orbital period of 2.4 hr, the shortest among all the black hole X-ray binaries.

MAXI J1659−152 returned to quiescence as observed with *Chandra* on 2011 May 3 (Jonker et al. 2012), but it underwent a mini-outburst from 2011 May 6 (Yang & Wijnands 2011a, 2011b; Jonker et al. 2012). The source has finally settled down in the quiescent state from 2011 mid-August based on a *Chandra* monitoring program (Jonker et al. 2012).

The optical counterpart of MAXI J1659−152 has been monitored regularly with *Swift* UVOT and ground-based telescopes during the outburst (Russell et al. 2010; Yang et al. 2011; Yang & Wijnands 2011a, 2011b). In general, the optical activity tracked the X-ray outburst (Russell et al. 2010, 2011; Kong et al. 2011). The optical counterpart of MAXI J1659−152 is not detected in the Digitized Sky Survey indicating that the quiescent magnitude is >21. A tentative quiescent counterpart was reported by Kong et al. (2010) using the Pan-STARRS 1 (PS1) data. The source was only marginally seen in the image with an r'-band magnitude of ∼22.4. This was challenged by Kennea et al. (2011) and Kuulkers et al. (2012) noting that it is too bright for MAXI J1659−152.

In this Letter, we report our new deep optical imaging observation of MAXI J1659−152 in quiescence using the Canada–France–Hawaii Telescope (CFHT) aimed at measuring an accurate quiescent optical magnitude. We also re-analyzed the PS1 data for comparison.

2. OBSERVATIONS AND DATA ANALYSIS

2.1. CFHT

MAXI J1659−152 was observed with the MegaPrime/MegaCam at the CFHT on 2012 March 23. We checked the *MAXI* GSC daily data and the source was not detected in soft X-ray, indicating that it was likely in quiescence. However, we caution that if there is an X-ray mini-outburst, MAXI J1659−152 will not be detected with *MAXI* due to its low sensitivity. The MegaCam has an array of 36 CCDs, giving a total of $1^\circ \times 1^\circ$ field of view. We obtained two r'-band images under a seeing condition of ∼0.″8 with an exposure time of 980 s each. The two images were separated by about 30 minutes.

[1] Golden Jade Fellow of Kenda Foundation, Taiwan.

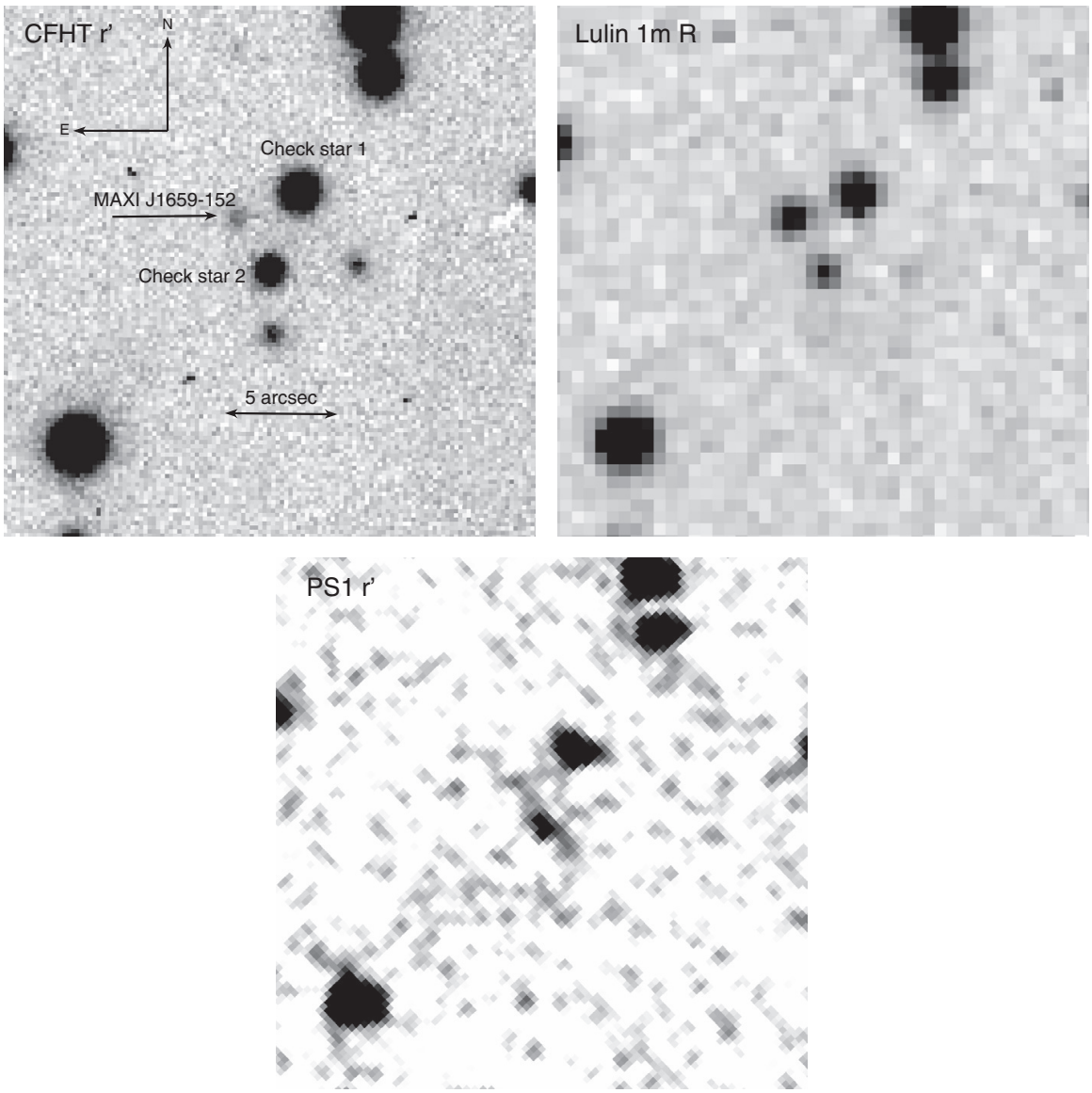

Figure 1. CFHT/MegaCam r'-band (top left), Lulin 1 m R-band (top right), and PS1 r'-band (bottom) images of MAXI J1659−152. The CFHT image was taken on 2012 March 23, about seven months after the end of an X-ray outburst. MAXI J1659−152 is clearly seen. The Lulin 1 m image was taken with the 1 m telescope at the Lulin Observatory in Taiwan; the image was taken near the end of an X-ray outburst on 2011 July 30 and the source has an R magnitude of ∼21 (see also Kong et al. 2011). Comparing with the CFHT image, MAXI J1659−152 is much brighter in the Lulin image. The PS1 image was taken as part of the 3π sky survey on 2010 June 19, three months before the discovery of an X-ray outburst (Kong et al. 2010).

The raw images were processed with Elixir[2] for bias, flat field, overscan, bad pixel mask, and zero point.

We next corrected the CFHT images for the astrometry. By using 10 stars surrounding MAXI J1659−152, we used the IRAF task *ccmap* to compare with the USNO point source catalog. The resulting registration errors are 0.″21 in R.A. and 0.″226 in declination.

By examining the CFHT image together with images taken during the outburst (Russell et al. 2010; Kong et al. 2011; see also Figure 1), the optical counterpart of MAXI J1659−152 is clearly a variable (see Figure 1). We further compared the CFHT position of MAXI J1659−152 with the European very long baseline interferometry Network position (Paragi et al. 2010); the offset between the two positions is 0.″043, indicating that it is the true optical counterpart. We then performed aperture photometry using the task *phot* in IRAF. In addition to our target, we also measured the optical magnitude for a few nearby stars for checking (see Figure 1).

2.2. PS1

We also re-analyzed the PS1 image taken before the outburst of MAXI J1659−152 (Kong et al. 2010) by using the same method for the CFHT data. We obtained postage stamp images from the Postage Stamp Server maintained by the PS1 Image Processing Pipeline team at the University of Hawaii. As part of the 3π survey, the field of MAXI J1659−152 was observed with various filters several times each, but the source was only marginally seen with the r'-band filter taken on 2010 June 19

[2] http://www.cfht.hawaii.edu/Instruments/Elixir

Table 1
Optical (r'-band) Magnitudes of MAXI J1659−152 and Check Stars

Source	CFHT		PS1
	Epoch 1	Epoch 2	
MAXI J1659−152	23.81 ± 0.06	23.62 ± 0.06	22.8 ± 0.3
Check star 1	20.738 ± 0.004	20.731 ± 0.005	20.65 ± 0.05
Check star 2	21.85 ± 0.01	21.86 ± 0.01	21.7 ± 0.1

with an exposure time of 40 s. Since it is a few months before the first discovery of the outburst, the source should be in quiescence. As a check, the *MAXI* GSC light curve did not show any enhancement in the X-ray flux. Since MAXI J1659−152 is not in the 3π survey catalog, we determined its magnitude by comparing with several cataloged stars. Like the CFHT data, we performed an aperture photometry for MAXI J1659−152 as well as the comparison and check stars. The magnitudes of the check stars measured by us are entirely consistent with the 3π survey catalog.

3. RESULTS

In Table 1, we list the r'-band magnitudes of MAXI J1659−152 and a couple of check stars of the CFHT and PS1 observations. Given that our new CFHT observations were taken more than seven months after the end of an X-ray outburst confirmed by *Chandra* (Jonker et al. 2012) and there is no unusual X-ray activity shown in the *MAXI* GSC data, MAXI J1659−152 is likely in the quiescent state although we cannot totally rule out a mini-outburst or a very long optical decay. The r'-band magnitude of MAXI J1659−152 varied between 23.62 ± 0.06 and 23.81 ± 0.06 in 30 minutes. The two check stars near MAXI J1659−152 did not show any variability, indicating that MAXI J1659−152 is likely a variable star.

For the PS1 data, MAXI J1659−152 is marginally visible with an r'-band magnitude of 22.8 ± 0.3 (see Figure 1). This is roughly consistent with the quick-look analysis reported by Kong et al. (2010). We examined all the PS1 images in this field and the observation reported here has the best seeing and image quality among all the images. This may explain why MAXI J1659−152 was only detected in this observation. Furthermore, the CFHT images indicate that MAXI J1659−152 can be fainter than the PS1 measurement. It could happen that the PS1 observation was taken during a relatively bright state in the quiescence.

4. DISCUSSION

From both the CFHT and PS1 observations, we can conclude that the optical counterpart of MAXI J1659−152 shows variability during or near quiescence. In Figure 1, we also show an R-band image taken near the end of an outburst with the 1 m telescope at the Lulin Observatory in Taiwan (Kong et al. 2011). MAXI J1659−152 is clearly much fainter during our CFHT observations. Optical variability is quite common for black hole X-ray transients in quiescence. For example, GRS 1124−684, A0620-00, J0422+32, GS 2000+25, and V404 Cyg show flarings on timescales of a few minutes to 60 minutes with a typical amplitude of 0.1–0.6 mag (Zurita et al. 2003; Shahbaz et al. 2003, 2010). BW Cir (= GS 1354−64) is another quiescent black hole that exhibits large (0.5–1 mag) optical variability (Casares et al. 2009). The origin of optical flaring during quiescence is not well understood. Possible mechanisms include X-ray irradiation of the accretion disk (Hynes et al. 2004), magnetic reconnection events (Zurita et al. 2003), and direct synchrotron emission from an advective-dominated flow (Shahbaz et al. 2003). Simultaneous X-ray and optical observations are required to understand their nature (e.g., Hynes et al. 2004).

In addition to optical flaring activity, the orbital variation can contribute to the observed variability. MAXI J1659−152 is shown to have a 2.4 hr orbital period based on the dip-like events in the X-ray light curves (Kuulkers et al. 2012). In particular, the two CFHT observations are separated by about 30 minutes, equivalent to about 0.2 orbital phase. Variability is therefore not unexpected. The 0.2 mag difference is also consistent with other black hole X-ray transients with measured optical orbital modulation (e.g., see Figure 1 of Zurita et al. 2003). Future optical monitoring observations will be crucial to reveal the optical orbital modulation.

Our new CFHT observations strongly suggest that the proposed optical counterpart of MAXI J1659−152 is real and it shows noticeable variability that could be from flaring or orbital modulation. Even though we adopt the faintest measurement from our CFHT observations ($r' = 23.8$), it is in contrast to the suggestion that the quiescent magnitude is >27 (Kuulkers et al. 2012). We note that the orbital modulation cannot produce such a huge optical variability (>3 mag) unless the compact object has strong radiation to evaporate the companion like black-widow-type pulsars (e.g., Kong et al. 2012). The suggested quiescent optical magnitude is based on a relationship between the optical outburst amplitude of an X-ray transient and the orbital period found by Shahbaz & Kuulkers (1998; hereafter SK98). With an orbital period of 2.4 hr, the V-band magnitude difference between the outburst and quiescence should be as large as 11 mag, yielding $V > 27$ in the quiescence. Taking the inclination effect into account, the quiescent V magnitude is >26.2 (Kuulkers et al. 2012). By using previous PS1 measurement in the r' band (Kong et al. 2010) and the limiting magnitudes of the PS1 3π survey, Kuulkers et al. (2012) derived an expected V-band magnitude of $V \gtrsim 22.8$; although it cannot rule out a much fainter object, a difference of at least 3 mag indicates that MAXI J1659−152 unlikely follows the SK98 relation. However, we caution that the SK98 relation is an empirical relation based on a sample of 11 black hole transients and there are many factors (e.g., the stellar type of the companion star, the inclination effect on the disk emission, and the peak mass transfer rate) affecting the correlation. Hence, scatter on the correlation is not unexpected.

To estimate the V-band magnitude, we first assume the spectrum of the companion. Given that MAXI J1659−152 is likely an M2 or M5 dwarf (Kuulkers et al. 2012; Jonker et al. 2012), the colors will become $B - V = 1.52$ (M2 dwarf) or $B - V = 1.61$ (M5 dwarf). We then correct the colors for the reddening assuming the Galactic values provided by Schlafly & Finkbeiner (2011). Using the transformation of Tonry et al. (2012), we get a reddened $r' - R$ color of 0.3 for both cases. The reddened V−R is 1.9 and 2.2 for an M2 dwarf and an M5 dwarf, respectively. This implies that $V - r'$ is 1.6 (1.9) for an M2 dwarf (M5 dwarf). Using the observed r'-band magnitude (23.8) from our CFHT observation, we have $V = 25.4$ for an M2 dwarf and $V = 25.7$ for an M5 dwarf. These are consistent with the above limits derived by Kuulkers et al. (2012). In any case, the estimated quiescent V-band magnitude is within 1 mag difference for a high-inclination (80°) system although the difference could be as large as 2 mag for a lower inclination (65°) system.

Based on our new CFHT measurement, although the estimated V-band magnitude is still brighter, it is not a large offset as proposed by Kuulkers et al. (2012). As we mentioned above, there are other factors causing scatter on the SK98 correlation. For instance, the black hole X-ray binary XTE J1118+480 has an orbital period of 4.08 hr and the outburst amplitude is about 6–7 mag. According to SK98, the amplitude is at least 9.4 mag. However, XTE J1118+480 is underluminous in outbursts; the outburst X-ray spectra are hard in contrast to typical high/soft state of X-ray transients in outbursts, and the X-ray-to-optical flux ratio is low (∼5; see Zurita et al. 2006 for a discussion). Unlike XTE J1118+480, the X-ray spectral behaviors and X-ray-to-optical flux ratio of MAXI J1659−152 are similar to a typical X-ray transient in outburst (Kennea et al. 2011). Follow-up photometric and spectroscopic observations of MAXI J1659−152 in the future will be able to provide better constraints. On the other hand, the quiescent X-ray luminosity of MAXI J1659−152 as measured with *Chandra* is an order of magnitude higher than that derived from the orbital period–X-ray luminosity correlation (Jonker et al. 2012). Given that both optical and X-ray brightnesses are higher than expected, one simple explanation is that MAXI J1659−152 is not in a true quiescent state. It is worth noting that some short orbital period black hole systems have a long decay time. For example, GRO J0422+32 reached its optical quiescent state 760 days after an outburst (Garcia et al. 1996). Further optical and X-ray observations will confirm this.

We can now use the absolute magnitude of the companion to estimate the distance to the source. The absolute V-band magnitude of an M2 dwarf and an M5 dwarf is 10 and 11.8, respectively. Since $V-R$ is 1.5 (1.8) for an M2 (M5) dwarf, this implies that M_R is 8.5 (10). By using the transformation of Tonry et al. (2012), M_r becomes 8.77 (10.27). Comparing with the reddening ($A_r = 1.4$; Schlafly & Finkbeiner 2011) corrected r'-band magnitude, the distance is 5.3 kpc (M2 dwarf) or 2.7 kpc (M5 dwarf). If we further assume the accretion disk contributes 50% of the visible light (see Jonker et al. 2012), then the distance would be between 7.5 kpc (M2 dwarf) and 3.8 kpc (M5 dwarf). If A_r is as large as 1.7 (Schlegel et al. 1998), then the distance to MAXI J1659−152 will be 4.6–6.5 kpc and 2.3–3.3 kpc for an M2 dwarf and an M5 dwarf, respectively. Comparing with previous estimations (e.g., Kennea et al. 2011; Kaur et al. 2012; Kuulkers et al. 2012; Jonker et al. 2012), an M2 dwarf companion star is more likely. This is also consistent with the conclusion made by Jonker et al. (2012). On the other hand, if MAXI J1659−152 has an M5 dwarf companion star and a distance of ∼2 kpc, the observed X-ray luminosity will be consistent with the orbital period–X-ray luminosity correlation (Jonker et al. 2012). Future optical spectroscopy during quiescence will be crucial to determine the stellar type of the companion star and hence the distance to the system. In addition, an ellipsoidal light curve modeling during quiescence will allow us to derive the inclination angle of the system. These observations will also test if the SK98 correlation holds for MAXI J1659−152. Combining with a deep X-ray observation during the quiescent state, we could constrain the orbital period–X-ray luminosity correlation.

We thank an anonymous referee for comments that have improved this paper. Ground-based observations were obtained with MegaPrime/MegaCam, a joint project of CFHT and CEA/DAPNIA, at the Canada–France–Hawaii Telescope (CFHT), which is operated by the National Research Council (NRC) of Canada, the Institut National des Science de l'Univers of the Centre National de la Recherche Scientifique (CNRS) of France, and the University of Hawaii. Access to the CFHT was made possible by the Institute of Astronomy and Astrophysics, Academia Sinica, National Tsing Hua University, and National Science Council, Taiwan.

The Pan-STARRS1 Surveys (PS1) have been made possible through contributions of the Institute for Astronomy, the University of Hawaii, the Pan-STARRS Project Office, the Max-Planck Society and its participating institutes, the Max Planck Institute for Astronomy, Heidelberg, and the Max Planck Institute for Extraterrestrial Physics, Garching, The Johns Hopkins University, Durham University, the University of Edinburgh, Queen's University Belfast, the Harvard-Smithsonian Center for Astrophysics, the Las Cumbres Observatory Global Telescope Network Incorporated, the National Central University of Taiwan, the Space Telescope Science Institute, and the National Aeronautics and Space Administration under Grant No. NNX08AR22G issued through the Planetary Science Division of the NASA Science Mission Directorate. We thank the PS1 Builders and PS1 operations staff for construction and operation of the PS1 system and access to the data products provided.

This project is supported by the National Science Council of the Republic of China (Taiwan) through grant NSC100-2628-M-007-002-MY3 and NSC100-2923-M-007-001-MY3. A.K.H.K. gratefully acknowledges support from a Kenda Foundation Golden Jade Fellowship.

Facilities: CFHT, PS1

REFERENCES

Casares, J., Orosz, J. A., Zurita, C., et al. 2009, ApJS, 181, 238
Garcia, M. R., Callanan, P. J., McClintock, J. E., & Zhao, P. 1996, ApJ, 460, 932
Hynes, R. I., Charles, P. A., Garcia, M. R., et al. 2004, ApJ, 611, L125
Jonker, P. G., Miller-Jones, J. C. A., Homan, J., et al. 2012, MNRAS, 423, 3308
Kaur, R., Kaper, L., Ellerbroek, L. E., et al. 2012, ApJ, 746, L23
Kennea, J. A., Romano, P., Mangano, V., et al. 2011, ApJ, 736, 22
Kong, A. K. H., Huang, R. H. H., Cheng, K. S., et al. 2012, ApJ, 747, L3
Kong, A. K. H., Lin, C.-C., Chen, Y.-T., et al. 2010, ATel, 2976
Kong, A. K. H., Yang, Y. J., & Wijnands, R. 2011, ATel, 3524
Kuulkers, E., Kouveliotou, C., Belloni, T., et al. 2012, A&A, submitted (arXiv:1204.5840)
Mangano, V., Hoversten, E. A., Markwardt, C. B., et al. 2010, GCN Circ., 11296
Marshall, F. E. 2010, GCN Circ., 11298
Matsuoka, M., Kawasaki, K., Ueno, S., et al. 2009, PASJ, 61, 999
Mihara, T., Nakajima, M., Sugizaki, M., et al. 2011, PASJ, 63, S623
Paragi, Z., van der Horst, A. J., Granot, J., et al. 2010, ATel, 2906
Russell, D. M., Lewis, F., Bersier, D., et al. 2010, ATel, 2884
Russell, D. M., Lewis, F., Schreuder, L., et al. 2011, ATel, 3517
Schlafly, E. F., & Finkbeiner, D. P. 2011, ApJ, 737, 103
Schlegel, D. J., Finkbeiner, D. P., & Davis, M. 1998, ApJ, 500, 525
Shahbaz, T., Dhillon, V. S., Marsh, T. R., et al. 2003, MNRAS, 346, 1116
Shahbaz, T., Dhillon, V. S., Marsh, T. R., et al. 2010, MNRAS, 403, 2167
Shahbaz, T., & Kuulkers, E. 1998, MNRAS, 295, L1
Tonry, J. L., Stubbs, C. W., Lykke, K. R., et al. 2012, ApJ, 750, 99
Yang, Y. J., & Wijnands, R. 2011a, ATel, 3339
Yang, Y. J., & Wijnands, R. 2011b, ATel, 3379
Yang, Y. J., Wijnands, R., & Russell, D. M. 2011, ATel, 3249
Zurita, C., Casares, J., & Shahbaz, T. 2003, ApJ, 582, 369
Zurita, C., Torres, M. A. P., Steeghs, D., et al. 2006, ApJ, 644, 432

Monthly Notices
of the
ROYAL ASTRONOMICAL SOCIETY

Mon. Not. R. Astron. Soc. **421,** 181–189 (2012) doi:10.1111/j.1365-2966.2011.20289.x

Multiyear and multisite photometric campaigns on the bright high-amplitude pulsating subdwarf B star EC 01541–1409

M. D. Reed,[1⋆] D. Kilkenny,[2] S. O'Toole,[3] R. H. Østensen,[4] C. Honer,[1] J. T. Gilker,[1] A. C. Quint,[1] A. M. Doennig,[1] L. H. Hicks,[1] M. A. Thompson,[1] P. A. McCart II,[1] E. Zietsman,[5] W.-P. Chen,[6] C.-W. Chen,[6] C.-C. Lin,[6] P. Beck,[4] P. Degroote,[4] B. N. Barlow,[7,8] D. E. Reichart,[7] M. C. Nysewander,[7] A. P. LaCluyze,[7] K. M. Ivarsen,[7] J. B. Haislip,[7] A. Baran,[9] M. Winiarski[9] and M. Drozdz[9]

[1]*Baker Observatory and Department of Physics, Astronomy and Materials Science, Missouri State University, 901 S. National, Springfield, MO 65897, USA*
[2]*Department of Physics, University of the Western Cape, South Africa*
[3]*Australian Astronomical Observatory, PO Box 296, Epping, NSW 1710, Australia*
[4]*Instituut voor Sterrenkunde, Katholieke Universiteit Leuven, Celestijnenlaan 200 D, 3001 Leuven, Belgium*
[5]*South African Astronomical Observatory, PO Box 9, Observatory 7935, South Africa*
[6]*Graduate Institute of Astronomy, National Central University, Chung-Li, Taiwan*
[7]*Department of Physics and Astronomy, University of North Carolina, Chapel Hill, NC 27599-3255, USA*
[8]*Department of Astronomy & Astrophysics, Pennsylvania State University, University Park, PA 6802, USA*
[9]*Kraków Pedagogical University, ul. Podchorążych 2, 30-084 Kraków, Poland*

Accepted 2011 November 29. Received 2011 November 25; in original form 2011 October 4

ABSTRACT

We present follow-up observations of the pulsating subdwarf B (sdB) star EC 01541–1409 as part of our efforts to resolve pulsation spectra for use in asteroseismological analyses. This paper reports on data obtained from a single-site campaign, during 2008, and a multisite campaign, during 2009. From limited 2008 data, we were able to clearly resolve and pre-whiten 24 periods. A subsequent multisite campaign spanning nearly 2 months found over 30 individual periodicities most of which were unstable in amplitude and/or phase. Pulsation amplitudes were found to the detection limit, meaning that further observations would likely reveal more periodicities.

EC 01541–1409 reveals itself to be one of two sdB pulsators with many pulsation frequencies covering a large frequency range. Unlike the other star of this type (PG 0048+091), it has one high-amplitude periodicity which appears phase stable, making EC 01541–1409 an excellent candidate for exoplanet studies via pulsation phases. No multiplets were detected leaving EC 01541–1409 as yet another rich p-mode sdB pulsator without these features, limiting observational constraints on pulsation modes.

Key words: stars: individual: EC 01541–1409 – stars: oscillations – subdwarfs – stars: variables: general.

1 INTRODUCTION

Subdwarf B (sdB) stars are horizontal branch stars with masses $\approx 0.5\,M_{\odot}$, thin ($<10^{-2}\,M_{\odot}$) hydrogen shells, and temperatures from 22 000 to 40 000 K (for a review see Heber 2009). There are two known types of pulsating sdB stars (for a review, see Østensen 2010): short period (90–600 s) and long period (45 min to 2 h). This work concentrates on the short-period pulsators, which are designated as V361 Hya variables, but often referred to as sdBV stars, which we will do. They typically have pulsation amplitudes near 1 per cent, and detailed studies reveal a few to dozens of frequencies. The longer period pulsators are designated as V1093 Her variables and typically have amplitudes less than 0.1 per cent. They are also cooler than the V361 Hya type pulsators, though there is some overlap, and they are most likely g-mode pulsators.

Asteroseismology of pulsating sdB stars can potentially probe the interior structure and provide estimates of total mass, shell mass, luminosity, helium fusion cross-sections, and coefficients for radiative levitation and gravitational diffusion. To apply the tools of asteroseismology, however, it is necessary to resolve the pulsation frequencies and associate pulsation modes with periodicities. Recent

⋆E-mail: MikeReed@missouristate.edu

observations from the *Kepler* spacecraft have allowed mode identification for the g-mode pulsators via period spacings and shown them to be low-degree ($\ell = 1$ and 2) pulsators (Reed et al. 2011a). However, only one p-mode pulsator is being observed by *Kepler* which means that ground-based observations will remain the main tool for their study in the foreseeable future. Typical observations use extensive photometric campaigns, preferably at several sites spaced in longitude to reduce day/night aliasing.

We have been engaged in a long-term programme to resolve poorly studied sdB pulsators, principally from single-site data, but using multisite campaigns as often as possible. This method has proved useful for several sdBV stars (Reed et al. 2004, 2006, 2007a,b, 2009, 2011a; Zhou et al. 2006). Here, we report the results of our observations of EC 01541–1409 (hereafter EC 01541), a bright, high-amplitude sdBV star. EC 01541 ($B = 12.1$) was discovered to be a member of the V361 Hya class by Kilkenny et al. (2009). Their observations covered five nights with the longest duration being 3.7 h. They also obtained a low-dispersion spectrum from which, using He I lines, they roughly estimated an effective temperature 'significantly hotter' than PG 1219+534, and Østensen et al. (2010a) obtained $T_{\rm eff} = 33\,500$ K and $\log g = 5.71$. There are no indications that EC 01541 is a binary from the spectroscopic observations.

2 OBSERVATIONS

Data were obtained from six different observatories, each with a somewhat different CCD setup. South African Astronomical Observatory's (SAAO's) 1.0-m telescope observed during both 2008 and 2009. These observations were made using the University of Cape Town CCD which is a Wright Instruments system utilizing a thinned, back-illuminated EEV P86321/T chip. It was used in frame-transfer mode so that there is essentially a continuous sequence of observations with no 'dead' time. Observations at the Baker Observatory (0.4 m) and Lulin Observatory (1.0 m) were obtained with Princeton Instruments RS1340 CCD cameras. Data from the Baker Observatory were binned 2 × 2 with an average dead time of 1 s, while observations from the Lulin Observatory used the full frame with an average dead time of 3 s. Mt. Suhora Astronomical Observatory (0.6 m) data were obtained with an SBIG ST-10XME CCD camera with a dead time of 3 s. At the Mercator 1.2-m telescope, we used the Merope CCD camera, which was recently upgraded with a new E2V frame-transfer CCD with 2048 × 3074 illuminated pixels (Østensen 2010). This instrument also had near-zero dead time. All observations used a red cut-off filter (BG38 or BG40), so the effective bandpass covers the *B* and *V* filters and is essentially that of a blue-sensitive photomultiplier tube. Such a setup allows us to maximize light throughput while maintaining compatibility with observations obtained with photomultipliers. We also obtained two-colour data using the Panchromatic Robotic Optical Monitoring and Polarimetry Telescopes (PROMPT; Reichart et al. 2005). Over five consecutive nights, we obtained Johnson *U* and *V* data from the PROMPT 0.4-m telescopes equipped with Apogee U47 CCDs. The dead time was about 5 s and there is a small gap each night while the telescopes switched sides of the German equatorial mount. In this paper, we only report on the *V* data. A follow-up paper will report on multicolour and time-resolved spectroscopic observations. Table 1 provides the details of our observations including date, start time, run length and integration time. The observations total over 210 h of data for the 2009 multisite campaign which spanned 37 d with a 10-d gap near the middle. Accurate time was kept using NTP (Baker and PROMPT observatories) or GPS receivers (Lulin, Mercator, SAAO and Suhora observatories) and corrected to barycentric time during data reductions.

Table 1. Observations of EC 01541.

Telescope	Date (UT)	Start (h:min:s)	Length (h)	Int. (s)
	2008 data			
SAAO 1.0 m	October 25	18:26:06	8.2	12
SAAO 1.0 m	October 26	18:16:40	7.3	10
SAAO 1.0 m	October 27	18:12:20	7.7	12
	2009 campaign, part 1			
SAAO 1.0 m	October 21	19:56:00	1.3	12
SAAO 1.0 m	October 22	19:10:20	6.9	12
Mercator 1.2 m	October 22	23:46:56	4.2	20
SAAO 1.0 m	October 23	19:05:55	3.9	12
Mercator 1.2 m	October 24	00:38:30	2.9	20
Baker 0.4 m	October 24	06:05:45	3.5	15
SAAO 1.0 m	October 24	20:09:40	5.4	12
Mercator 1.2 m	October 24	23:21:07	5.0	20
Suhora 0.6 m	November 25	19:20:25	6.1	15
Mercator 1.2 m	October 25	23:16:27	3.7	10
SAAO 1.0 m	October 26	18:43:15	7.1	12
Mercator 1.2 m	October 27	01:24:31	0.5	20
SAAO 1.0 m	October 27	20:29:20	2.7	12
Baker 0.4 m	October 29	03:33:40	1.1	15
Baker 0.4 m	October 31	04:21:45	5.3	15
Baker 0.4 m	November 1	02:39:23	7.0	15
Baker 0.4 m	November 2	02:47:30	8.6	15
Baker 0.4 m	November 3	02:55:00	1.0	15
Suhora 0.6 m	November 3	18:30:20	5.0	15
PROMPT5 0.4 m	November 4	00:46:13	6.8	20
Baker 0.4 m	November 4	02:51:30	6.0	15
PROMPT5 0.4 m	November 5	00:46:11	6.4	20
Baker 0.4 m	November 5	02:50:45	5.1	15
Suhora 0.6 m	November 5	20:55:06	4.9	15
PROMPT5 0.4 m	November 6	02:05:44	5.2	20
Baker 0.4 m	November 6	02:36:40	6.6	15
Baker 0.4 m	November 7	03:00:01	5.0	15
PROMPT5 0.4 m	November 7	04:17:27	5.2	20
PROMPT5 0.4 m	November 8	00:40:03	6.2	20
	2009 campaign, part 2			
Lulin 1.0 m	November 18	17:11:14	0.9	10
Lulin 1.0 m	November 19	10:46:14	7.2	10
SAAO 1.0 m	November 19	18:03:10	6.1	15
Baker 0.4 m	November 20	01:36:30	3.1	15
Lulin 1.0 m	November 20	10:04:34	7.8	15
SAAO 1.0 m	November 20	18:05:27	5.6	20
Lulin 1.0 m	November 21	15:56:14	1.9	20
SAAO 1.0 m	November 21	18:09:47	5.9	20
Lulin 1.0 m	November 22	15:56:10	1.9	15
SAAO 1.0 m	November 22	17:59:44	5.0	20
Lulin 1.0 m	November 23	11:48:25	5.9	15
Lulin 1.0 m	November 24	10:51:01	6.8	15
Lulin 1.0 m	November 25	11:37:00	6.0	15
Mercator 1.2 m	November 25	22:39:50	3.6	20
Baker 0.4 m	November 26	02:07:40	5.6	15
Lulin 1.0 m	November 26	12:23:21	5.2	15

Standard image reduction procedures, including bias subtraction, dark current and flat-field corrections, were followed using IRAF packages. Differential magnitudes were extracted from the calibrated images using MOMF (Kjeldsen & Frandsen 1992) or occasionally they were extracted using IRAF aperture photometry with

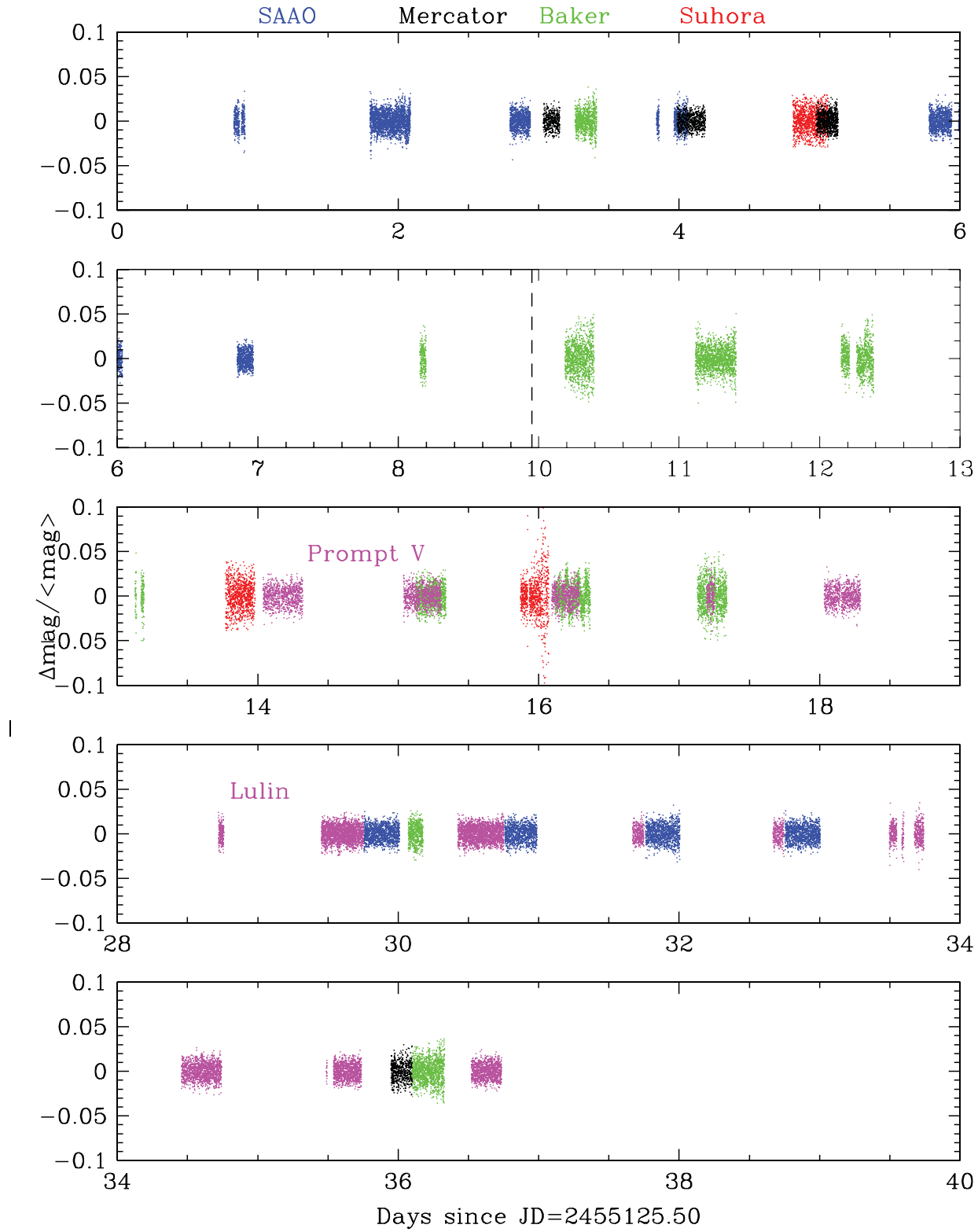

Figure 1. Light curves showing the 2009 data coverage. Each panel covers 6 d and the dashed vertical line indicates that day 9 was skipped as no data were collected. The top three panels are part 1 and the bottom two panels are part 2 of the campaign. Colour coded by observatory in the online version with the Prompt Observatory and Lulin Observatory sharing the same colour.

extinction and cloud corrections using the normalized intensities of several field stars, depending on conditions. As sdB stars are substantially hotter, and thus bluer, than typical field stars, differential light curves using an ensemble of comparison stars are not flat due to differential colour extinctions. A low-order polynomial was fitted to remove these trends from the data on a night-by-night basis. Light curves are shown in Fig. 1 (colour coded by observatory in the online version).

3 PULSATION ANALYSIS

2008 observations. During 2008, EC 01541 was observed during three consecutive nights collecting 23.2 h of data. These data have a $1/T$ resolution of 5.0 μHz and a 4σ detection limit of 0.37 mmag, where σ is the average value of the temporal spectrum outside regions containing pulsations. The temporal spectrum (or Fourier transform) is shown in Fig. 2 as well as the pre-whitening sequence. Frequencies, amplitudes and phases were determined by simultaneously fitting a non-linear least-squares solution to the data. We were easily able to pre-whiten 24 frequencies with residuals below the detection limit. The only peak remaining is the well-known SAAO telescope drive period near 8333 μHz. The frequencies, corresponding periods and amplitudes are provided in Table 2. Since pre-whitening effectively removed the pulsation peaks and corresponding aliases, we can deduce that over this 3-d span the amplitudes and phases were constant to within the detection limit. While the frequencies span more than 8 700 μHz, there are no combination frequencies.

2009 multisite campaign. During our 2009 multisite campaign, telescope time was assigned during two blocks separated by about 10 d. Thus, we examined the campaign as a whole and also by parts. The data have a $1/T$ resolution of 0.67, 1.44 and 0.32 μHz for part 1, part 2 and the combined data, and detection limits of 0.48, 0.32 and 0.33 mmag, respectively. The temporal spectra of the entire campaign and parts 1 and 2 are shown in Fig. 3.

For these data, pre-whitening was not as successful as during 2008. Even the high-amplitude peak, which pre-whitened nicely during 2008, left a residual just above 4σ in the combined 2009 data. This is most likely caused by amplitude variations across the duration of the campaign, which will be addressed in Section 4.2. Frequencies and amplitudes for the entire campaign and parts 1 and 2 are provided in Table 2. Note that in the table we have attempted to associate common pulsation frequencies from the different reductions. This includes those frequencies a daily alias away (e.g. f8 for which 2009 P2's frequency is nearly a daily alias smaller), and where crowded frequencies occur, matching by amplitude (e.g. f13 whereas 2009 P1's f12 is slightly closer in frequency). Data from part 2 with the worst temporal resolution but the lowest detection limit have the highest number of periodicities. We were able to fit and pre-whiten double the number of frequencies from part 2 compared to part 1, with the entire campaign having a number in between, as would be expected. 19 of the detections from part 2 have amplitudes lower than the part 1 detection limit, though four of these frequencies were detected in part 1 also. Since we detected the most frequencies with the lowest detection limit rather than the highest resolution, this suggests that unresolved frequencies are not a problem. Frequencies that are only detected once during 2009 are listed as *suggested* in Table 2 (s35–s45).

We also note that f31 is near to $2\times$f2 and f32 is near to $2\times$f3. This is most likely a chance occurrence as harmonic frequencies are normally caused by deviations from sinusoidal pulsations due to high amplitudes. Neither f2 nor f3 is sufficiently high and since f4 is an order of magnitude larger in amplitude and does not produce any combination of harmonic frequencies, f2 and f3 should not. Additionally, f31 and f32 are not at precisely

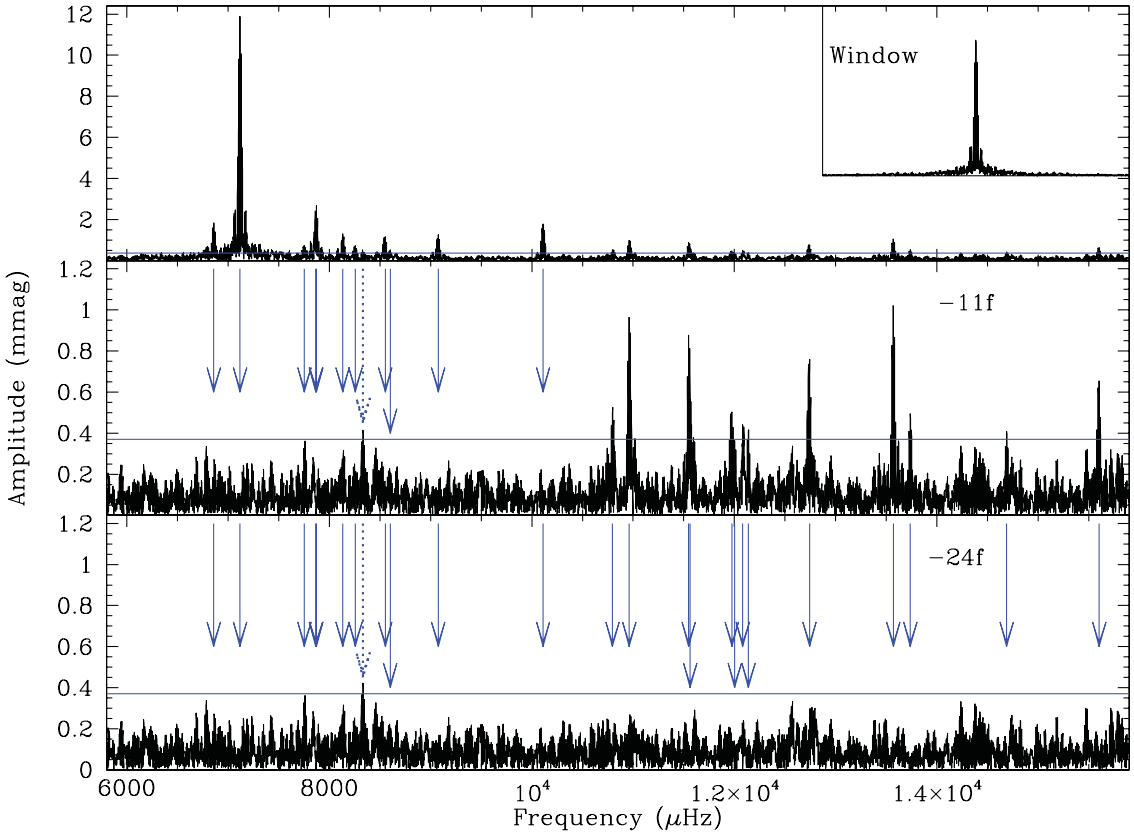

Figure 2. Temporal spectrum and pre-whitening sequence for the 2008 data set. The horizontal line indicates the 4σ detection limit of 0.37 mmag and the dotted arrow indicates the telescope drive period. The top panel shows a temporal spectrum for the original data (with a data window inset) and the next two panels show the spectrum pre-whitened by 11 and 24 frequencies, indicated by the arrows. The top panel has an amplitude scale 10 times that of the bottom two panels.

Table 2. Frequencies and amplitudes for EC 01541 from the 2008 single-site and 2009 multisite campaigns. (The entire campaign is noted as 2009 A, part 1 as P1 and part 2 as P2.) Formal least-squares errors are in parentheses.

ID	Frequency (μHz)				Amplitude (mmag)			
	2008	2009 A	2009 P1	2009 P2	2008	2009 A	2009 P1	2009 P2
f1	–	6098.892 (03)	6098.72 (08)	6098.83 (21)	–	0.34 (7)	0.43[a] (11)	0.37 (11)
f2	–	6785.089 (03)	6783.95 (06)	6787.06 (19)	–	0.39 (7)	0.57 (11)	0.41 (11)
f3	6859.47 (25)	6859.559 (11)	6859.27 (03)	6859.58 (06)	1.56 (18)	1.22 (9)	1.46 (12)	1.44 (11)
f4	7117.75 (03)	7117.487 (01)	7117.45 (01)	7117.51 (01)	11.90 (18)	8.91 (9)	8.62 (12)	9.45 (11)
f5	7753.07 (74)	7751.445 (24)	7750.59 (05)	7751.50 (12)	0.54 (18)	0.55 (9)	0.75 (12)	0.65 (11)
f6	7867.65 (39)	7865.937 (23)	–	7866.24 (20)	1.17 (18)	0.57 (9)	–	0.87 (11)
f7	7872.50 (17)	7872.860 (38)	–	7873.13 (21)	2.59 (18)	0.35 (9)	–	0.39 (11)
s35	–	–	8129.44 (05)	–	–	–	0.81 (13)	–
f8	8131.78 (32)	8130.198 (16)	8130.29 (05)	8121.62 (20)	1.25 (18)	0.83 (9)	0.91 (13)	0.41 (11)
s36	–	–	–	8241.85 (17)	–	–	–	0.48 (11)
f9	–	8249.048 (27)	–	8248.98 (20)	–	0.48 (9)	–	0.44 (11)
f10	8257.19 (49)	8255.486 (24)	8255.28 (05)	8255.93 (18)	0.81 (18)	0.56 (9)	0.74 (12)	0.48 (11)
f11	–	8313.775 (31)	–	8314.83 (09)	–	0.42 (9)	–	0.96 (11)
s37	–	–	–	8319.70 (17)	–	–	–	0.53 (12)
s38	–	–	–	8456.75 (13)	–	–	–	0.42 (07)
f12	–	8541.136 (22)	8549.88 (07)	–	–	0.60 (9)	0.59 (12)	-
f13	8552.55 (32)	8551.396 (15)	8552.50 (04)	8551.49 (07)	1.25 (18)	0.87 (9)	0.99 (12)	0.73 (07)
s39	–	–	8573.89 (06)	8583.03 (06)	–	–	0.71 (12)	0.94 (07)
f14	8602.16 (80)	–	–	–	0.51 (18)	–	–	–
f15	9075.81 (31)	–	–	–	1.25 (18)	–	–	–
f16	–	9249.812 (08)	9249.77 (02)	9249.73 (07)	–	1.34 (7)	1.90 (12)	0.72 (07)
s40	–	–	–	10 097.92 (14)	–	–	–	0.42 (08)
f17	10 111.69 (21)	10 109.903 (17)	10 110.23 (06)	10 109.33 (11)	1.82 (18)	0.64 (7)	0.69 (12)	0.54 (08)
f18	10 797.54 (33)	10 795.814 (30)	–	10 796.75 (15)	0.57 (08)	0.36 (7)	–	0.36 (07)
f19	–	10 951.287 (20)	10 951.16 (06)	10 951.39 (08)	–	0.55 (7)	0.55 (10)	0.69 (07)
f20	10 960.90 (19)	–	10 957.48 (06)	10 959.27 (12)	0.99 (08)	–	0.55 (10)	0.45 (07)
f21	–	11 016.662 (22)	11 015.69 (06)	11 016.31 (10)	–	0.49 (7)	0.63 (10)	0.56 (07)
f22	11 548.77 (27)	11 551.631 (18)	11 550.57 (06)	11 548.65 (09)	0.96 (12)	0.63 (7)	0.55 (10)	0.70 (08)
f23	–	11 558.130 (23)	–	11 552.03 (06)	–	0.47 (7)	–	1.06 (08)
f24	11 563.37 (42)	11 565.505 (25)	11 565.62 (05)	–	0.62 (12)	0.43 (7)	0.74 (10)	–
s41	–	–	–	11 580.28 (12)	–	–	–	0.49 (08)
s42	–	–	–	11 581.97 (13)	–	–	–	0.47 (08)
s43	–	–	–	11 962.29 (14)	–	–	–	0.39 (07)
f25	11 974.62 (35)	11 968.253 (26)	–	11 968.23 (12)	0.54 (08)	0.41 (7)	–	0.47 (07)
f26	12 002.55 (49)	–	–	–	0.40 (09)	–	–	–
f27	12 083.01 (49)	–	–	12 071.12 (14)	0.39 (09)	–	–	0.36 (07)
f28	12 139.38 (45)	–	–	12 141.08 (11)	0.43 (09)	–	–	0.46 (07)
s44	–	–	–	12 719.77 (18)	–	–	–	0.31 (07)
f29	12 730.79 (26)	12 734.196 (24)	–	12 734.10 (07)	0.73 (08)	0.46 (7)	–	0.72 (07)
f30	–	12 742.236 (29)	–	12 743.97 (09)	–	0.38 (7)	–	0.59 (07)
s45	–	12 749.315 (30)	–	–	–	0.37 (7)	–	–
f31[b]	13 568.75 (18)	13 568.065 (09)	13 568.10 (04)	13 568.15 (04)	1.02 (08)	1.14 (7)	0.99 (10)	1.22 (07)
f32[c]	13 737.52 (39)	13 736.871 (22)	–	13 736.95 (15)	0.49 (08)	0.48 (7)	–	0.34 (07)
f33	14689.44 (46)	–	–	–	0.42 (08)	–	–	–
f34	15 602.83 (29)	15 602.668 (25)	15 602.60 (05)	15 601.88 (13)	0.66 (08)	0.43 (7)	0.64 (10)	0.38 (07)
Limits	5.0	0.32	0.67	1.44	0.37	0.33	0.48	0.32

[a]This amplitude is below the formal 4σ detection limit, [b]is 2f2, and [c]is 2f3, though they are not likely overtones, based on amplitudes.

the harmonic frequencies, which they should be if that were the cause.

4 DISCUSSION

4.1 Comparison with the discovery data

The goal of our observational programme is to resolve the pulsation frequencies and characterize their amplitudes and phases for asteroseismic analysis. The discovery observations, of which only two runs were combined, have a temporal resolution of 10 μHz[1] and a detection limit of ∼2.0 mmag (Kilkenny et al. 2009). Our 2008 observations which seemed to resolve all the pulsations have twice the resolution with a detection limit over five times better. The 2009 observations obtained a temporal resolution 31 times better than the discovery observations with a detection limit slightly better than in 2008.

[1] Calculated as 1/T rather than the 1.5/T used in Kilkenny et al. (2009).

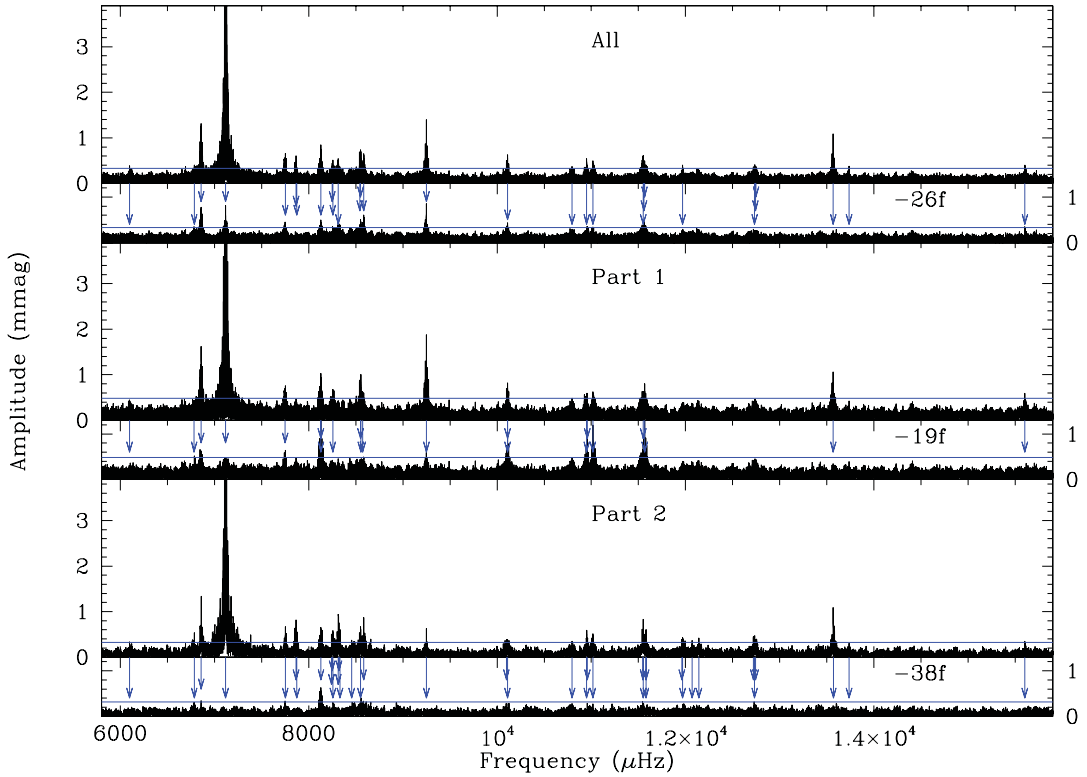

Figure 3. Temporal spectrum and residuals for the 2009 multisite campaign. The top two panels show the entire campaign, the next two part 1 and the bottom two part 2 of the campaign. The arrows indicate pre-whitened frequencies (26, 19 and 37 for the entire campaign, parts 1 and 2, respectively) and the horizontal lines indicate the 4σ detection limit. The vertical axis is truncated in the original spectra so the lower amplitude peaks may be seen.

The best measure of the success of follow-up observations is the number of additional frequencies detected. The discovery observations only revealed six frequencies, while the 2008 data contained 24 frequencies and the 2009 campaign detected 31 frequencies with 11 more listed as *suggested*.

4.2 Amplitude and phase variations

The majority of sdBV stars do *not* have stable amplitudes and/or phases (Reed et al. 2007b; Kilkenny 2010) and EC 01541 is no exception. The 2008 data pre-whiten below the detection limit, indicating that the amplitudes and phases were relatively stable during those three days, yet even in these data there are some signs of residuals, just below the detection limit. As the 2009 campaign covered significantly more time, it is no surprise that the temporal spectrum contains many residuals above the detection limit. Figs 4 and 5 show the amplitudes and phases of the four well-separated frequencies with average amplitudes greater than 1 mmag for the individual runs. The phases are fractional so that a change of 0.1 indicates a change of 10 per cent and normalized to zero phase.

In combining data from several different telescopes, most with different CCDs which may themselves have differing colour responses, it is possible to introduce systematic amplitude variations. There is no obvious evidence for this, as the amplitudes and/or phases do not appear to have any systematic trends which correlate with observatory. However, as the main periodicity (f4) is easily detected and can be measured with the highest accuracy, we used it to conduct an experiment. For this experiment, we assumed that the amplitude of f4 is constant across our multisite campaign and multiplied the individual light curves by a constant to bring them to an average value (9.0 mma). Amplitudes and phases were refitted (keeping the frequencies fixed) for the well-separated frequencies and pre-whitening was repeated for the modified light curve. The amplitudes (other than f4) remained variable and pre-whitening did not improve residuals. As such, we conclude that the amplitude variability is intrinsic to the star and not induced by detector efficiency.

For EC 01541, the main cause for the residuals appears to be amplitude variations. Only f3 shows sizeable phase variations, while f4 remains constant, except for one possible outlier. The amplitudes for f4 also change very little, though sufficient to cause the small residual in Fig. 3. The other three frequencies have significant amplitude variations, particularly during the first week of the campaign. At no time during 2009 were the pulsations stable over a 3 d period such as they were during 2008. While sufficient to subvert effective pre-whitening, the phases are too stable to indicate stochastically excited pulsations (Pereira & Lopes 2005; Reed et al. 2007b).

4.3 Constraints on the pulsation modes

In addition to detecting new frequencies, we wish to observationally correlate pulsation frequencies with modes. Pulsation modes are mathematically described by spherical harmonics with three quantum numbers, n (or k), ℓ and m. When present, rotation breaks the m degeneracy by separating each degree ℓ into a multiplet of $2\ell + 1$ components, so multiplet structure is a very useful tool to

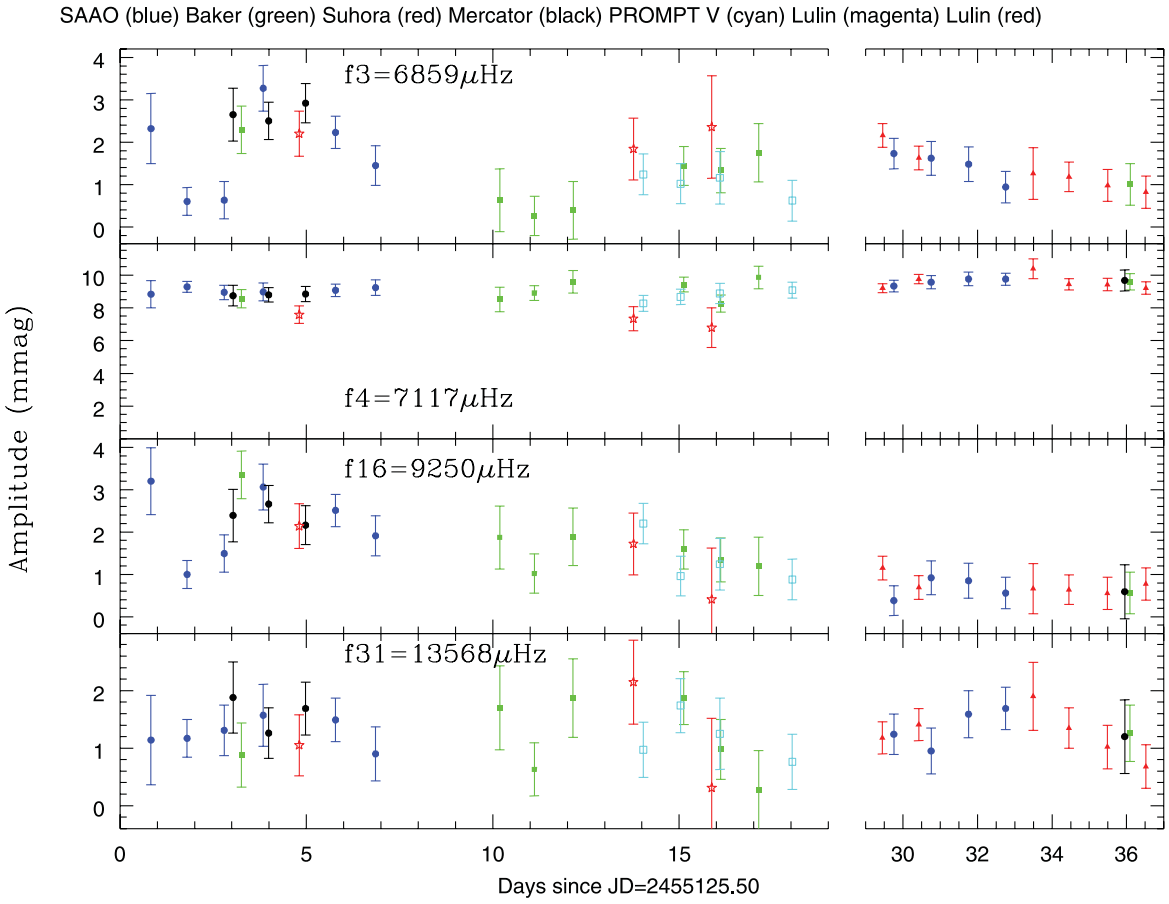

Figure 4. Amplitudes for well-separated frequencies with average amplitudes above 1.0 mmag.

correlate frequencies with modes (see Winget et al. 1991; Baran et al. 2009).

For slow rotators, as most sdB stars are thought to be (Heber, Reid & Werner 2000; Geier et al. 2010), rotationally split multiplets should be nearly equally spaced in frequency. Thus far only low-resolution spectra have been obtained for EC 01541 (Østensen et al. 2010a), which are not appropriate for measuring line broadening due to rotation. While these spectra are not optimal for discerning whether multiplets should be distorted by rapid rotation, the Balmer and helium lines are consistent with other sdB stars and can rule out rotation velocities $>75\,\mathrm{km\,s^{-1}}$, which means it is likely spinning slower than PG 1336−018 (with $v \sin i$ of $74.2\,\mathrm{km\,s^{-1}}$, Vučković et al. 2009), which does appear to have evenly spaced multiplets (Kilkenny et al. 2003). So while EC 01541 appears to have 45 frequencies, there are no indications of multiplets evenly spaced in frequency, which is consistent with most pulsating sdB stars. Rather, the separations between frequencies are smoothly distributed.

Mode density can also be used to infer high-degree ($\ell \geq 3$) modes (see Reed et al. 2007b). A general rule is one n order per ℓ degree per 1000 μHz, producing three frequencies per 1000 μHz or nine frequencies if all possible m values are used. As we observe no indication of rotational multiplets, we infer that all $m \neq 0$ modes are degenerate, leaving some regions overdense for solely low-degree modes. For these regions, a few of the frequencies must either be $m \neq 0$ or $\ell \geq 3$ modes. If $m \neq 0$ modes are present, then even the densest frequency regions can be accommodated with $\ell \leq 2$ modes. As such, EC 01541 is not particularly dense.

5 CONCLUSIONS

From follow-up data acquired during 2008 and a multisite campaign in 2009, we have detected 34 frequencies, including the six from the discovery paper (Kilkenny et al. 2009). During three nights in 2008, EC 01541 appeared to have been amplitude and phase stable, but was not during 2009. We examined amplitude and phase stability, which has been used to infer stochastically excited oscillations in the sdBV star PG 0048 (Reed et al. 2007a) and possibly KPD 1930 (Reed et al. 2011b). While during 2009 the amplitudes varied, they were insufficient to be stochastically driven and the phases were reasonably stable. As EC 01541 is relatively bright with one high-amplitude phase-stable frequency, it is an excellent candidate for follow-up photometric studies to examine phase variations. Such variations have been used to detect planets (Silvotti et al. 2007).

Similar to other sdBV stars, EC 01541 is a rich pulsator yet has no indications of multiplets, which could be used to observationally constrain the modes. The mode density marginally indicates high-degree ($\ell \geq 3$) modes are present but while there are many pulsation frequencies, they are spread across ∼9000 μHz, which is rare for an sdBV star.

As in the discovery data, EC 01541 was dominated by a single high-amplitude periodicity with the remaining 33 having low

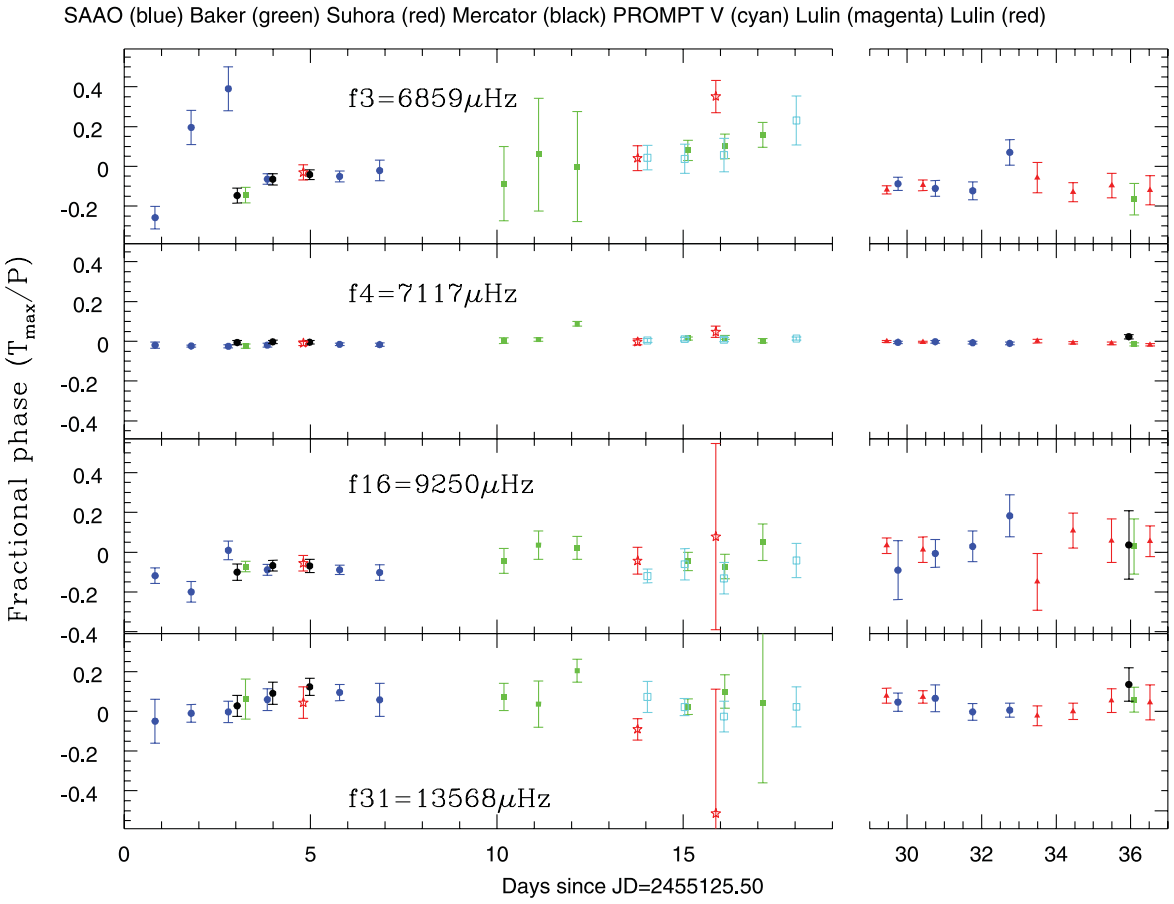

Figure 5. Phases for well-separated frequencies with average amplitudes above 1.0 mmag.

amplitudes right down to the detection limit. It is likely that data with an even lower limit would detect more frequencies, perhaps even including multiplets which would provide welcome constraints on modes. In addition to our photometric campaign, we also obtained some time-resolved spectroscopy which we will report on in a future paper, together with the PROMPT two-colour observations.

ACKNOWLEDGMENTS

We would like to thank the participating observatories' time allocation committees for generous time allocations, without which this work would not have been possible. CH, JTG, ACQ, AMD, LHH, MAT and PAM were supported by the Missouri Space Grant which is funded by NASA. MDR received funding from an American Astronomical Society Small Research Grant, partially funded by the National Science Foundation and by a Faculty Research Grant from Missouri State University. Any opinions, findings and conclusions or recommendations expressed in this material are those of the author(s) and do not necessarily reflect the views of the National Science Foundation or NASA. DK was partially funded by the South African National Research Foundation. RHØ has received funding from the European Research Council under the European Community's Seventh Framework Programme (FP7/2007–2013)/ERC grant agreement No. 227224 (PROSPERITY) and from the Research Council of K.U.Leuven (GOA/2008/04). AB gratefully acknowledges support from the Polish Ministry under grant No. 554/MOB/2009/0. PROMPT observations were made possible by the Robert Martin Ayers Science Fund.

REFERENCES

Baran A. et al., 2009, MNRAS, 392, 1092
Geier S., Heber U., Podsiadlowski P., Edelmann H., Napiwotzki R., Kupfer T., Müller S., 2010, A&A, 519, 25
Heber U., 2009, ARA&A, 47, 211
Heber U., Reid I. N., Werner K., 2000, A&A, 363, 198
Kilkenny D., 2010, Ap&SS, 329, 175
Kilkenny D. (The Whole Earth Telescope collaboration) et al., 2003, MNRAS, 345, 834
Kilkenny D., O'Donoghue D., Crause L., Engelbrecht C., Hambly N., MacGillivray H., 2009, MNRAS, 397, 453
Kjeldsen H., Frandsen S., 1992, PASP, 104, 413
Østensen R. H., 2010, Astron. Nachr., 331, 1029
Østensen R. et al., 2010, A&A, 513, A6
Pereira T. M. D., Lopes I. P., 2005, ApJ, 622, 1068
Reed M. D. (The Whole Earth Telescope Collaboration) et al., 2004, MNRAS, 348, 1164
Reed M. D., Eggen J. R., Zhou A.-Y., Terndrup D. M., Harms S. L., An D., Hashier M. A., 2006, MNRAS, 369, 1529
Reed M. D. et al., 2007a, ApJ, 664, 518
Reed M. D., Terndrup D. M., Zhou A.-Y., Unterborn C. T., An D., Eggen J. R., 2007b, MNRAS, 378, 1049
Reed M. D. et al., 2009, A&A, 493, 175
Reed M. D. et al., 2011a, MNRAS, 414, 2885

Reed M. D. (The Whole Earth Telescope Collaboration) et al., 2011b, MNRAS, 412, 371
Reichart D. et al., 2005, Il Nuovo Cimento C, 28, 767
Silvotti R. et al., 2007, Nat, 449, 189
Vučković M., Østensen R. H., Aerts C., Telting J. H., Heber U., Oreiro R., 2009, A&A, 505, 239
Winget D. E. (The Whole Earth Telescope Collaboration) et al., 1991, ApJ, 378, 326
Zhou A.-Y. et al., 2006, MNRAS, 367, 179

This paper has been typeset from a TEX/LATEX file prepared by the author.

Monthly Notices
of the
ROYAL ASTRONOMICAL SOCIETY

Mon. Not. R. Astron. Soc. **424,** 649–665 (2012) doi:10.1111/j.1365-2966.2012.21244.x

The complex case of V445 Lyr observed with *Kepler*: two Blazhko modulations, a non-radial mode, possible triple mode RR Lyrae pulsation, and more

E. Guggenberger,[1⋆] K. Kolenberg,[2,3] J. M. Nemec,[4] R. Smolec,[1,5] J. M. Benkő,[6] C.-C. Ngeow,[7] J. G. Cohen,[8] B. Sesar,[8] R. Szabó,[6] M. Catelan,[9] P. Moskalik,[5] K. Kinemuchi,[10] S. E. Seader,[11] J. C. Smith,[11] P. Tenenbaum[11] and H. Kjeldsen[12]

[1]*Institut für Astronomie, Universität Wien, Türkenschanzstrasse 17, A-1180 Vienna, Austria*
[2]*Harvard–Smithsonian Center for Astrophysics, 60 Garden Street, Cambridge, MA 02138, USA*
[3]*Instituut voor Sterrenkunde, Celestijnenlaan 200D, B-3001 Leuven, Belgium*
[4]*Department of Physics & Astronomy, Camosun College, Victoria, British Columbia V8P 5J2, Canada*
[5]*Copernicus Astronomical Center, Polish Academy of Sciences, ul. Bartycka 18, 00-716 Warszawa, Poland*
[6]*Konkoly Observatory, Research Center for Astronomy and Earth Sciences, PO Box 67, H-1525 Budapest, Hungary*
[7]*Graduate Institute of Astronomy, National Central University, Jhongli City, Taoyuan County 32001, Taiwan*
[8]*California Institute of Technology, Mail Stop 249-17, 1200 East California Boulevard, Pasadena, CA 91125, USA*
[9]*Departamento de Astronomía y Astrofísica, Facultad de Física, Pontificia Universidad Católica de Chile, Av. Vicuña Mackenna 4860, 782-0436 Macul, Santiago, Chile*
[10]*NASA Ames Research Center/Bay Area Environmental Research Institute, Mail Stop 244-30, Moffett Field, CA 94035, USA*
[11]*SETI Institute/NASA Ames Research Center, Moffett Field, CA 94035, USA*
[12]*Department of Physics and Astronomy, Aarhus University, DK-8000 Aarhus C, Denmark*

Accepted 2012 May 4. Received 2012 April 30; in original form 2012 February 23

ABSTRACT

Rapid and strong changes in the Blazhko modulation of RR Lyrae stars, as have recently been detected in high-precision satellite data, have become a crucial topic in finding an explanation of the long-standing mystery of the Blazhko effect. We present here an analysis of the most extreme case detected so far, the RRab star V445 Lyr (KIC 6186029) which was observed with the *Kepler* space mission. V445 Lyr shows very strong cycle-to-cycle changes in its Blazhko modulation, which are caused by both a secondary long-term modulation period and irregular variations. In addition to the complex Blazhko modulation, V445 Lyr also shows a rich spectrum of additional peaks in the frequency range between the fundamental pulsation and the first harmonic. Among those peaks, the second radial overtone could be identified, which, combined with a metallicity estimate of [Fe/H] = −2.0 dex from spectroscopy, allowed us to constrain the mass (0.55–0.65 $M_{\odot}$) and luminosity (40–50 $L_{\odot}$) of V445 Lyr through theoretical Petersen diagrams. A non-radial mode and possibly the first overtone are also excited. Furthermore, V445 Lyr shows signs of the period-doubling phenomenon and a long-term period change. A detailed Fourier analysis along with a study of the O − C variation of V445 Lyr is presented, and the origin of the additional peaks and possible causes of the changes in the Blazhko modulation are discussed. The results are then put into context with those of the only other star with a variable Blazhko effect for which a long enough set of high-precision continuous satellite data has been published so far, the *CoRoT* star 105288363.

Key words: asteroseismology – methods: data analysis – techniques: photometric – stars: individual: KIC 6186029 (V445 Lyr) – stars: individual: CoRoT 105288363 – stars: variables: RR Lyrae.

1 INTRODUCTION

RR Lyrae stars, which are low-mass helium-burning stars on the horizontal branch, were long thought to be rather simple radial pulsators. They follow a period–luminosity–colour relation which makes them valuable distance indicators, and because of their age

⋆E-mail: elisabeth.guggenberger@univie.ac.at

and evolutionary status, they are also used to study the formation and evolution of the Galaxy (Catelan 2009). They can oscillate in the fundamental radial mode (type RRab), the first overtone (type RRc) or both modes simultaneously (type RRd), and their high amplitudes of up to 1.5 mag in V for RRab type stars made their variability easy to discover, so they have been known since the end of the 19th century.

Already more than a hundred years ago, however, it turned out that there is an aspect to RR Lyrae stars which is not understood at all: Blazhko (1907) found a 'periodic change in the period' of RW Dra, which he could not explain, and which still remains unexplained today. Shapley (1916) later found in his observations of RR Lyrae that the brightness of the maxima and the light-curve shape also show periodic changes. With increasing data quality in the recent past, the unsolved problem got even more severe, as it turned out that not just a rather small fraction of exceptional RR Lyrae stars were affected, but probably around 40–50 per cent of all RRab stars (Jurcsik et al. 2009; Benkő et al. 2010; Kolenberg et al. 2010). Also among RRc type stars, amplitude and phase modulation was found to be surprisingly widespread (Arellano Ferro et al. 2012).

This so-called Blazhko effect was long thought to be a periodic/regular phenomenon. Traditionally, only one Blazhko period was assigned to each modulated star, and the phenomenon was expected to repeat in every Blazhko cycle, agreeing with the widely used definition that 'the Blazhko effect is a periodic amplitude and/or phase modulation with a period of several tens to hundreds of pulsation periods'. There were several reports about changes in the Blazhko modulation of various stars (see section 5 of Guggenberger et al. 2011 for a recent summary), but those reports usually had to rely on sparse data with large gaps, so that it was impossible to say when exactly a change took place and whether it happened continuously or abruptly. The Blazhko effect was therefore still considered to be a strictly repetitive phenomenon with only some rare exceptions showing secondary modulation periods (e.g. CZ Lac; Sódor et al. 2011) or changes on very long time-scales. It was not until the availability of ultraprecise data from space missions like *CoRoT* that strong and irregular cycle-to-cycle changes of a Blazhko star were documented and that it became obvious that seemingly chaotic phenomena need to be accounted for when modelling the Blazhko effect.

While the detection of cycle-to-cycle changes in the Blazhko modulation posed a significant challenge for all classical models that required a clock-work-like behaviour, some new ideas were published. Stothers (2006) suggested that transient small-scale magnetic fields modulate the turbulent convection inside the helium and hydrogen ionization zones, a mechanism which certainly could explain subsequent Blazhko cycles of different strengths. This scenario, however, was recently tested on the basis of hydrodynamical models by Smolec et al. (2011) who found that it was not possible to reproduce all observed properties of the light curve, even when allowing a huge modulation of the mixing length. On the other hand, Buchler & Kolláth (2011) successfully modelled both regular and irregular modulations by using the amplitude equation formalism. In their models, a strange attractor in the dynamics causes chaotic behaviour. The 9:2 resonance between the fundamental mode and the ninth overtone that was found by Kolláth, Molnár & Szabó (2011) to be the reason for the recently discovered phenomenon of period doubling (Szabó et al. 2010) seems to play an important role in causing a Blazhko modulation.

We present here a study of the most extreme case detected so far: V445 Lyr (KIC 6186029). This RRab star not only shows the strongest cycle-to-cycle change found up to now, but also shows a rich spectrum of additional modes in the region between 2 and 4 d^{-1}. Both Fourier and O − C analyses are used to investigate the variability of the pulsation and the modulation (Section 4), and the results are compared to the case of CoRoT 105288363 in Section 6. Spectroscopy and theoretical Petersen diagrams are used to determine the fundamental parameters such as metallicity, luminosity and mass (Section 5). Additionally, the new *analytic modulation approach* for data analysis recently proposed by Benkő, Szabó & Paparó (2011) is applied to the data in Section 4.4.

2 BACKGROUND INFORMATION ON V445 LYR

V445 Lyr, with the coordinates RA $18^h58^m26^s$ and Dec. $41°35'49''$ (J2000), is also known as KIC 6186029, or GR244, and has a *Kepler* magnitude of $Kp = 17.4$. Two publications from the pre-*Kepler* era exist for this target: Romano (1972) found it to be variable and classified it as an RR Lyrae, and Kukarkin et al. (1973) included it into his name list of variable stars. Romano (1972) also lists the photographic brightnesses of maximum and minimum to be 15.3 and 17.3 mag, respectively, indicating a surprisingly large amplitude of 2 mag, which is much higher than the amplitude observed even during extreme Blazhko maxima in the modern data. This might at least partly be explained, however, by the difference between the observed bandpasses. Unfortunately, no details of the observations and no light curves are given, and the forthcoming paper that was announced by the author could not be found. We therefore cannot know if the observed amplitude of 2 mag is real or it is possibly due to some observational errors. No error estimations of the observations were given by Romano (1972).

Since *Kepler* data have become available, two more publications have dealt with V445 Lyr, both presenting the *Kepler* data up to Q2: Szabó et al. (2010) listed V445 Lyr as a possible candidate for the period-doubling phenomenon, and Benkő et al. (2010) already noted changes in the Blazhko modulation of V445 Lyr and reported the presence of radial overtones.

3 *KEPLER* PHOTOMETRY

The *Kepler* space mission was launched on 2009 March 6 into an Earth-trailing heliocentric orbit (Koch et al. 2010). Its primary purpose is the detection of Earth-sized planets in the habitable zone of solar-like stars through the transit method, which requires continuous and ultraprecise photometry of over 150 000 stars for at least 3.5 years. This is also the duration of the primary mission. *Kepler* therefore not only provides the longest continuous data sets ever observed for RR Lyrae stars, but also does so with the highest photometric precision ever obtained, as a consequence greatly improving our knowledge about stellar pulsations.

The *Kepler* spacecraft carries a Schmidt telescope with an aperture of 0.95 m and 42 science CCDs which cover a field of view of about 115 deg^2 (Jenkins et al. 2010). The photometric bandpass ranges from 423 to 897 nm, thus avoiding the Ca II H&K lines in the blue, and fringing due to internal reflection in the red. The *Kepler* band is therefore slightly broader than a combination of Johnson V and R, and *Kepler* magnitudes are usually about 0.1 mag from R for most of the stars (Koch et al. 2010).

Every quarter orbit, the spacecraft is rotated in order to keep the solar panels oriented towards the Sun, and the radiator that cools the focal plane towards deep space (Haas et al. 2010). Data from different quarters are denominated Q1, Q2, etc. Each of the quarters which is used here has a time base of about 90 d, except Q1 which covers about 33 d.

Each measurement is based on a 6.02 s exposure plus a 0.52 s readout time. To obtain long cadence (LC) data (29.4 min), 270 measurements are co-added; for short cadence (SC) data (1 min) nine exposures are co-added (Christiansen et al. 2011).

The time of each measurement is given in truncated Barycentric Julian Date (HJD − 240 0000), and refers to the mid-point of the measurement.

3.1 The V445 Lyr data set

Fig. 1 illustrates the data obtained for V445 Lyr. In this paper, we present LC data obtained in quarters 1–7, with a total time base of 588 d. Because of the loss of module 3, which happened in 2010 January, there are no data available for this target in Q5. Some smaller gaps are also present in the data as can be seen in Fig. 1. Some of them are due to unplanned safe mode events or loss of fine point control, others are caused by the regular downlinks where the spacecraft's antenna is pointed towards Earth for data transmission, and science data collection is interrupted.

Kepler provides light curves in two different formats: raw flux or corrected flux. The latter has been processed for planet transit search by the Pre-search Data Conditioning (PDC) pipeline which is sometimes known to remove astrophysical features and which does not preserve all stellar variability. Hence here, and for the study of variable stars in general, we make use only of the raw time series.

As the spacecraft is rotated every quarter orbit, the target falls on different CCDs after each 'roll', resulting in differences in average flux due to different sensitivity levels. Additionally, trends might occur due to image motion on the CCD or sensitivity changes. The scaling and detrending which has to be performed before starting the analysis is a delicate task especially for targets like RR Lyrae stars which have high amplitudes, long periods and changes in the amplitudes [see Celik et al. (2012) for a detailed discussion]. Here, we removed linear trends which were determined from a running average separately for every quarter, and scaled every quarter to the same mean brightness. The continuity of the upper and lower envelope of the light curve was a good indicator of correct scaling. Note that due to the gap during Q5, the continuity could not be checked there. For this reason, the scaling of the data obtained after the gap might not exactly be consistent with the scaling applied before Q5.

The scaled and detrended data that were used in this analysis are available as online material in the format displayed in Table 1 (see Supporting Information).

Fig. 1(a) shows the complete combined data set of V445 Lyr. A total of 5.5 and 3.5 Blazhko cycles were observed before and after the large gap, respectively, and 900 pulsation cycles were observed. From panel (a) it is obvious that the Blazhko effect shows strong and fast changes, with almost all observed cycles having a different appearance. Panel (b) compares in a phase diagram directly a light curve from a Blazhko maximum with one obtained during the subsequent Blazhko minimum, illustrating the extremely low pulsation amplitude that occurs during some, but not all, modulation minima. Note that due to the very small amplitude and the distorted light curve showing a double maximum (see also Fig. 1d) it would not be possible to recognize the RR Lyrae nature of this star when

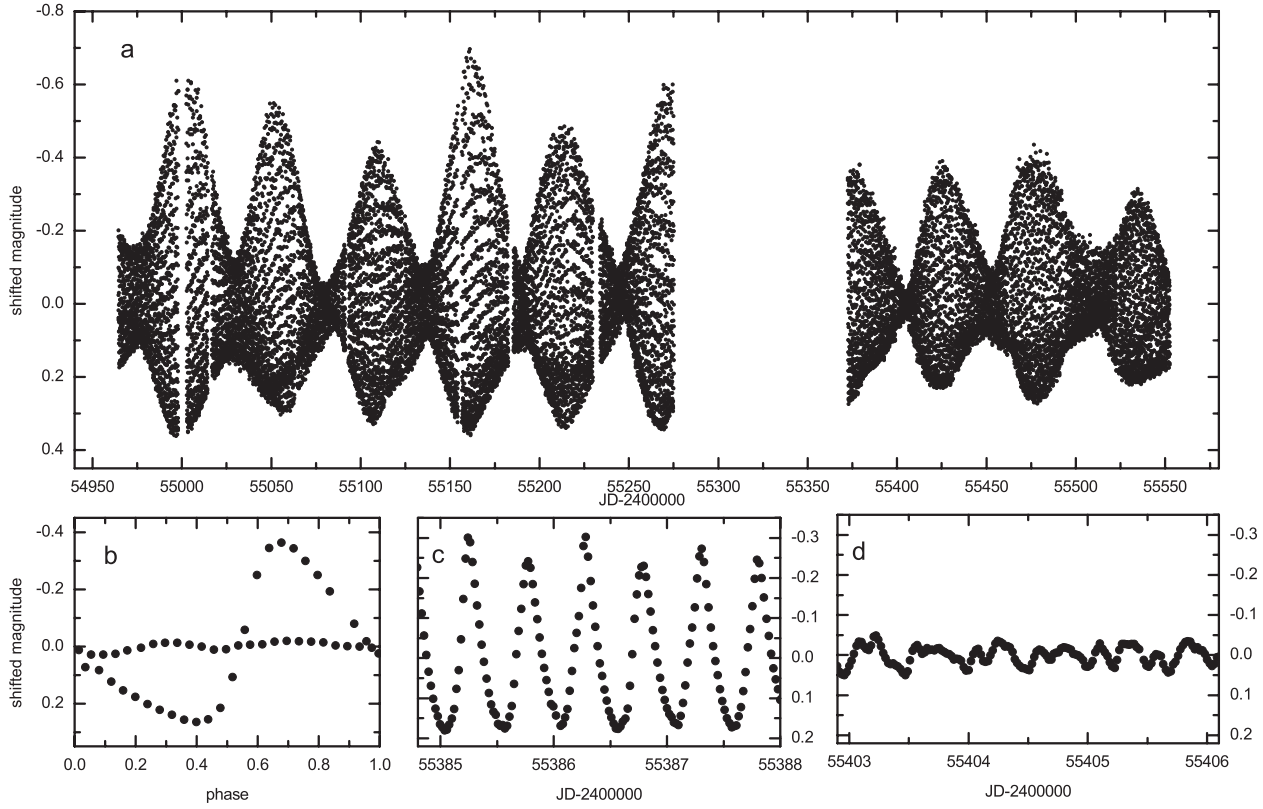

Figure 1. Panel (a) shows the complete light curve of V445 Lyr presented in this paper, including quarters Q1–Q7. Due to failure of a module, there are no data from Q5, resulting in the gap from MJD 55273 to 55372. Panel (b) illustrates the extreme Blazhko modulation by comparing a pulsation cycle at Blazhko maximum to one at Blazhko minimum. The light variation has an extremely low amplitude during this Blazhko minimum and shows a double maximum. In panel (c), a zoom into a region with period doubling is shown as an example and panel (d) emphasizes the distorted light-curve shape that occurs during some Blazhko minima.

Table 1. The scaled and detrended data set of V445 Lyr that was used for the analysis in this paper. Column 1 gives the truncated Barycentric Julian Date, column 2 gives the magnitude with the average shifted to zero and column 3 gives the quarter in which data were obtained. The full table is available as Supporting Information with the online version of the paper.

HJD − 240 0000	Magnitude	Quarter
54964.512 11	0.044 188 798	Q1
54964.532 54	0.038 912 686	Q1
54964.552 98	0.017 979 982	Q1
54964.573 41	−0.023 960 246	Q1
54964.593 85	−0.099 222 117	Q1
...	...	...

observing it only during Blazhko minimum where the peak-to-peak amplitude can be as low as 70 mmag. Extremely low pulsation amplitudes during Blazhko minima were recently also reported by Sódor et al. (2012) for two of the RRab type stars, and the occurrence of a strong bump during Blazhko minimum was noted in RZ Lyr (Jurcsik et al. 2012). In Fig. 1(c), a small part of the light curve around JD 245 5386 is shown, illustrating the phenomenon of period doubling (alternating higher and lower light maxima) which was recently discovered in *Kepler* Blazhko stars (Szabó et al. 2010) and which is also present in V445 Lyr.

4 ANALYSIS AND RESULTS

Due to the quasi-continuous coverage and the high photometric precision, the conditions for a Fourier analysis are more than favourable. The spectral window function (see Fig. 2) is almost perfect, without any alias peaks visible at first glance. Because of the Earth-trailing orbit, no orbital frequencies like the ones that cause trouble in the data from many other space missions are present here.

A well-known feature in the *Kepler* data is the momentum desaturation of the reaction wheel, which happens every 2.98 d. During the thruster firings which are necessary to release the angular momentum that has built up in the reaction wheels, the spacecraft momentarily loses the fine point control (Van Cleve & Caldwell 2009). This results in a missing data point during every desaturation in the otherwise regularly spaced data, leading to a comb-like structure in the Fourier transform with a spacing of 0.335 d^{-1}. In the spectral window, those peaks have a very low normalized amplitude of only 0.004 mag. A zoom into the spectral window (see lower panel of Fig. 2) reveals this comb of tiny peaks. When carefully removing all high-amplitude peaks from the Fourier spectrum before turning to interpreting features with amplitudes which are orders of magnitude smaller as discussed in Section 4.1.5, those alias peaks are not expected to cause any trouble.

Other features in the spectral window function are two harmonics of the monthly data downlink frequency, at 0.065 and 0.13 d^{-1}, with normalized amplitudes of 0.05 and 0.03 mag, respectively.

Due to the time base of 588 d, the Rayleigh frequency resolution is 0.0017 d^{-1}.

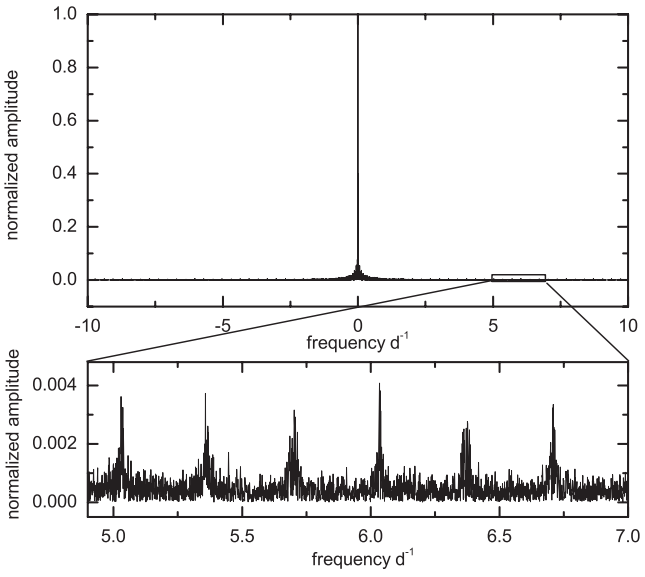

Figure 2. Spectral window function of the complete V445 Lyr data set. Lower panel: magnification of the region between 5 and 7 d^{-1}, showing some examples of the low-amplitude features caused by the reaction wheel.

4.1 Fourier analysis of the full data set

As a first step, a Fourier analysis of the complete data set was performed, keeping in mind that changes in the fundamental period might occur during the time of the observations and that the changes of the Blazhko modulation cause a large number of peaks close to the classical pulsation and modulation components. The Fourier analysis of the full data set, however, is necessary to obtain an overall picture of the pulsation and modulation properties of V445 Lyr to find the mean values of the pulsation and modulation periods and to detect possible long-term periodicities which can be resolved with a long time base only.

The Fourier analysis of the complete data set was performed with PERIOD04 (Lenz & Breger 2005) and then checked with SIGSPEC (Reegen 2007). The results agreed within the errors. The Fourier analysis revealed a mean pulsation period of 0.513 075 ± 0.000 005 d and a mean Blazhko period of 53.1 ± 1 d with the ephemeris

$$\mathrm{HJD}(T_{\mathrm{max,pulsation}}) = 245\,5550.514 + 0.513\,075 E_{\mathrm{pulsation}},$$

$$\mathrm{HJD}(T_{\mathrm{max,Blazhko}}) = 245\,5534.2 + 53.1 E_{\mathrm{Blazhko}}.$$

Note that the presence of close peaks has a great influence on the fitting and frequency optimization procedure, and the errors are therefore larger than would normally be expected for a Fourier fit to data of the given quality.

4.1.1 Multiplet components

The Blazhko multiplets (i.e. the pattern of peaks which is typical for Blazhko stars with peaks at the positions $kf_0 \pm nf_B$, with k and n being integers denoting the harmonic order and the multiplet order, respectively, and with f_0 and f_B denoting the fundamental and the Blazhko frequency) were found to be very asymmetric in amplitude. Much higher amplitudes appeared on the right-hand (higher frequency) side than on the left. This is the more common case, which is observed in three-fourths of all Blazhko RRab stars (Alcock et al. 2003). Components were detected up to quintuplet order on the right-hand side, while on the left-hand side of the main pulsation component only one side peak (i.e. a triplet component, $n = 1$) could be found. In some orders, peaks were found near the positions that would be expected for septuplets, but the deviations

from the exact frequency values were considered too big to identify the peaks safely as septuplet components.

In addition to the classical Blazhko multiplets around the fundamental mode and its harmonics, a secondary modulation component, f_S, could also be identified. It manifests itself as a series of additional peaks next to the classical modulation side peaks of the Fourier spectrum, appearing in every order with a spacing of $0.006\,98 \pm 0.000\,27\,d^{-1}$, indicating a secondary modulation period of 143.3 ± 5.8 d. The secondary peaks appearing on the right-hand side of the classical peaks show surprisingly high amplitudes, while the secondary peaks to the left of the classical multiplet have small amplitudes and could only be detected after pre-whitening a large number of higher amplitude peaks. Interestingly, the peaks belonging to this additional series could also be detected at higher multiplet orders ($n = 3$) than the classical multiplet, making it difficult to explain the peaks as combination frequencies. Their amplitudes seem to decrease less quickly with increasing harmonic order k (see also Section 4.1.3), making them easier to spot at high orders.

Fig. 3 shows the Fourier transform of the data, providing also zooms into the regions around the third, fourth and fifth harmonic order where both the classical multiplet and the additional components can be seen. The highest peaks among the multiplet components, which can be seen even before pre-whitening the original data, are marked with arrows.

Fig. 4 illustrates the pattern of detected frequencies in the vicinity of the fundamental pulsation and its harmonics in the style of an 'echelle' diagram. In this diagram, which is similar to the diagrams used to unveil equally spaced peaks in helioseismology, the frequency of each peak is plotted against (f modulo f_0), i.e. $f/f_0 - \mathrm{INT}(f/f_0)$ or $f/f_0 - \mathrm{INT}(f/f_0) - 1$ for peaks to the left of the harmonic, therefore clearly revealing patterns which repeat in every harmonic order. Peaks belonging to the same group of combinations align in vertical ridges. We stress that unlike in the helioseismic application, where the ridges denote different radial orders of same degree, in this case the echelle diagram only serves the purpose of displaying in a very practical and easy way the repeating patterns in different harmonic orders of non-sinusoidal fundamental radial pulsation.

4.1.2 Deviation of the harmonics

Due to the non-sinusoidal light-curve shape typical for RR Lyrae stars, harmonics of the fundamental mode are expected to appear at frequencies kf_0, where k is an integer denoting the harmonic order. The classical Blazhko multiplets in the modulated stars are spaced equidistantly, implying frequency values of $kf_0 \pm nf_B$ with n denoting the multiplet order. Long-term period changes and close peaks caused by irregular phenomena, however, can distort this frequency pattern. When analysing time series of Blazhko RR Lyrae stars, there are two options for fitting the data: one is to fix the frequencies of the harmonics and Blazhko multiplets to their expected values of $kf_0 + nf_B$, thereby reducing the number of free parameters in the fit. The other option is to let all parameters, including the frequency values, free. When the latter option was applied to this data set, the harmonics were observed to deviate systematically and significantly from their expected values, which can also be noticed as a slight rightwards tilt of the ridges in the echelle diagrams (Fig. 4). Normally, one would expect that this is simply caused by a wrong value of f_0, but in this case, no value of f_0 could be found which could solve the issue, i.e. every detected harmonic, when divided by its order, required a different f_0. We therefore decided in favour of

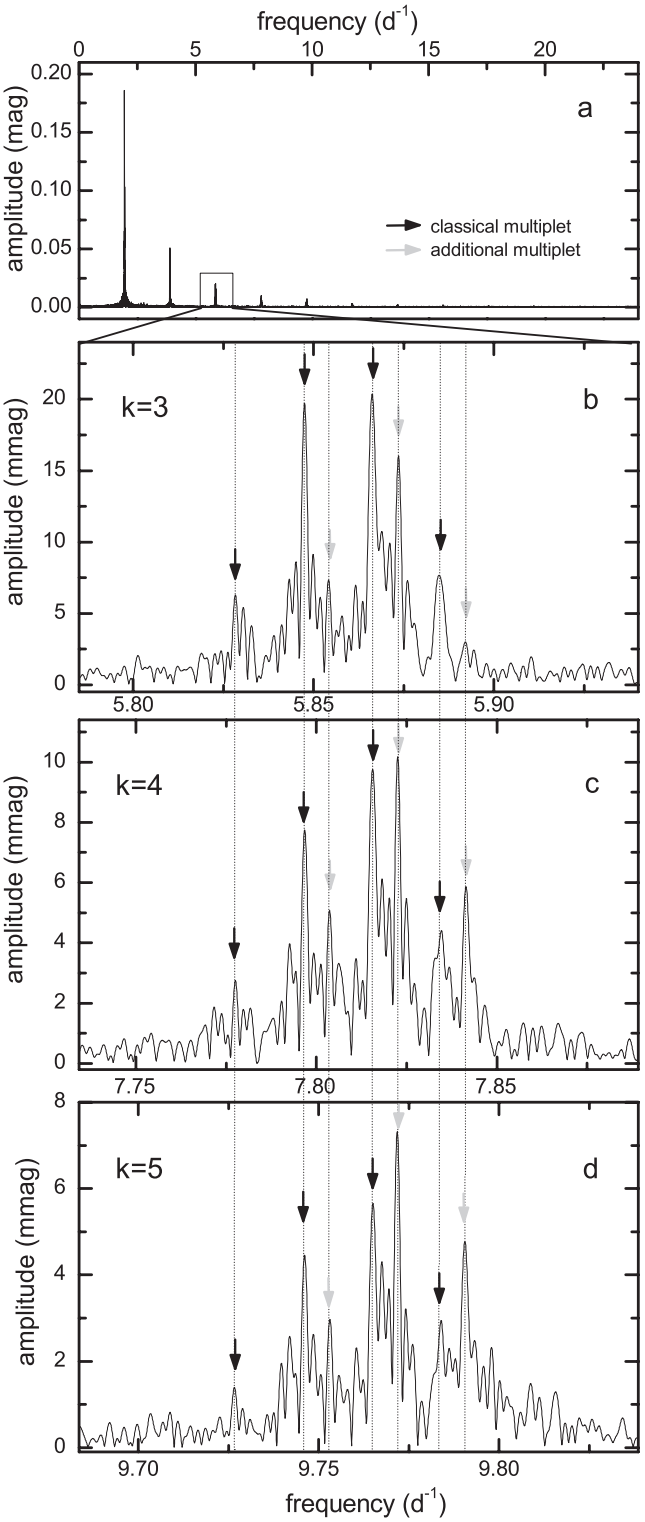

Figure 3. Fourier transform of the complete V445 Lyr data set (upper panel). In the lower panels (b, c and d), the regions around the harmonics kf_0 with $k = 3$, 4 and 5 are shown in detail. Black arrows indicate the peaks belonging to the classical Blazhko multiplet with $kf_0 - f_B$, kf_0, $kf_0 + f_B$ and $kf_0 + 2f_B$, while grey arrows indicate some of the peaks belonging to the secondary multiplet which within itself has a spacing equal to the Blazhko frequency, but is shifted with respect to the classical multiplet by $0.006\,98\,d^{-1}$. Note that from order $k = 4$ onwards, the highest amplitude peak in this order is a peak belonging to the secondary multiplet.

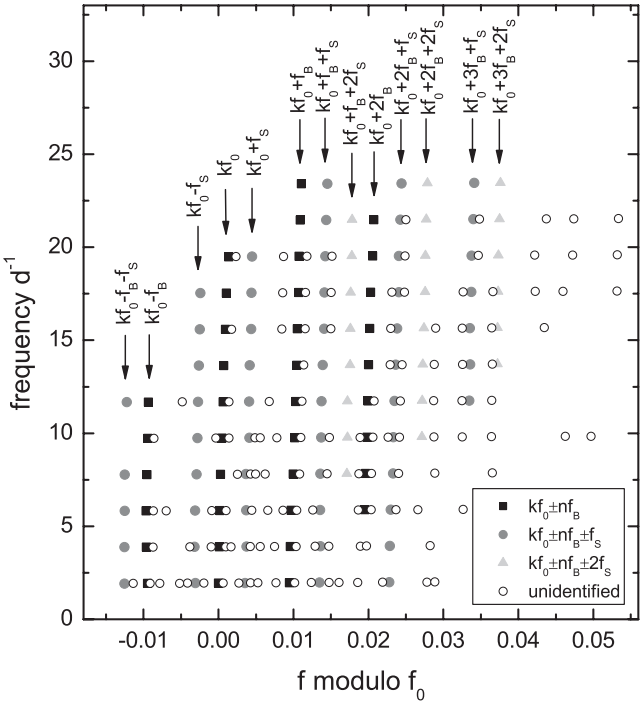

Figure 4. 'Echelle' diagram of the peaks detected in the vicinity of the fundamental pulsation mode and its harmonics. Frequency is plotted versus f modulo f_0, so that regularly spaced peaks which appear in every order align in vertical patterns, making it easy to identify combinations with f_0. Peaks belonging to the category $kf_0 \pm nf_B$ are shown as black squares, peaks of the group $kf_0 \pm nf_B + f_S$ are shown as grey circles and components of $kf_0 + nf_B + 2f_S$ are plotted with light-grey triangles. Open circles denote unidentified and/or unresolved peaks, some of which originate from the non-repetitive nature of the modulation and long-period changes.

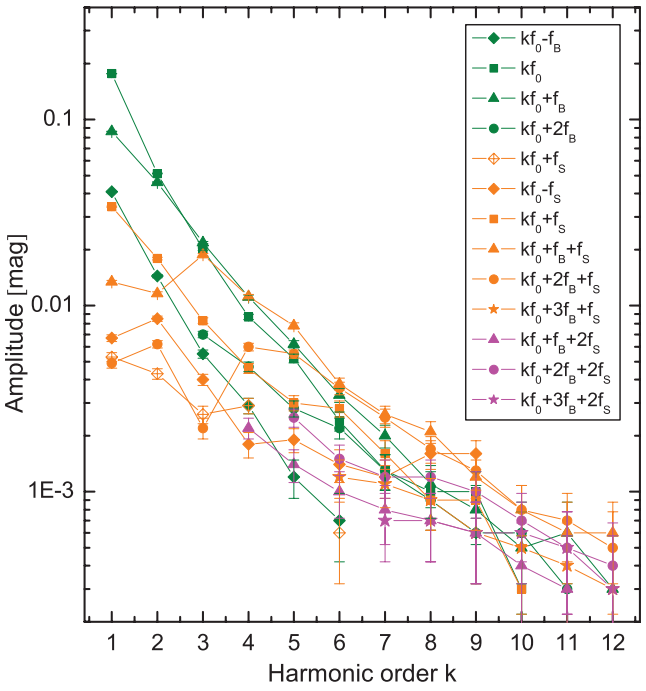

Figure 5. Amplitudes of all components versus harmonic order. Components belonging to the classical Blazhko multiplet are shown with green symbols, peaks which are combinations with f_S are shown in orange, and components with a $2f_S$ term are shown in magenta. It can be seen that the amplitude of the f_S multiplets decrease less steeply than those of the classical Blazhko multiplet, reaching the same amplitude in the fourth order and dominating the frequency spectrum for higher orders.

the more pure approach and did not fix the frequency values to the expected positions, but left all parameters free in the fit of the complete data set. The problem disappeared, however, when analysing different subsets of data separately (see Section 4.2), and we therefore suspect it to be either the result of period changes which take place during certain seasons (see also Section 4.3) and/or close unresolved peaks which are known to strongly influence the results of both the Fourier analysis and the multisine fitting procedure.

4.1.3 Amplitudes versus harmonic order

It is a well-known fact that in Blazhko RRab stars the amplitudes of the multiplet side peaks decrease less rapidly with harmonic order than that of the main component. This was first described by Jurcsik et al. (2005), and then confirmed for other well-studied stars such as SS For (Kolenberg et al. 2009), RR Lyr (Kolenberg et al. 2011) and CoRoT 105288363 (Guggenberger et al. 2011). As expected, the result is the same for V445 Lyr (see Fig. 5), but in an extreme way with the amplitude of the right-hand side peak exceeding that of the main component as early as in the third order. Additionally, the amplitudes of the secondary modulation multiplet, i.e. combinations with the secondary modulation f_S, could be studied in this case. It turned out that the amplitudes of the secondary multiplet components decrease even less steeply, therefore dominating the Fourier spectrum from the fourth order onwards. The strongest signal then comes from the combination $f_0 + f_B + f_S$, i.e. the peak on the right-hand side of the right triplet component. Also, combinations with the term $2f_S$ could be detected, and their amplitudes are plotted in Fig. 5. They also show a very slow amplitude decrease.

4.1.4 Number of relevant frequencies

Due to the dense spectrum of peaks which is caused by the cycle-to-cycle changes of the Blazhko effect, an analysis in the classical sense, i.e. taking into account all frequencies down to a certain signal-to-noise ratio level or a certain significance criterion, might not be optimal in a case like V445 Lyrae, as it does not yield meaningful results. A large number of the detected peaks is likely to be the result of 'stellar noise' caused by irregular and/or long-periodic phenomena, and many of them are not resolved with the available time span. Tests revealed that as many as 771 frequencies can be found when performing an analysis until the generally adopted criteria of significance are reached. Many of them were not resolved, and many could not be attributed to any combination of other modes, and did not show repeating patterns in the echelle diagrams. Therefore, instead of choosing the classical approach, the analysis was stopped after a certain number of the highest peaks in every harmonic order were found and pre-whitened, usually around 20 peaks per order. It turned out that after subtracting approximately 20 peaks in a given harmonic order, no meaningful combinations could be identified among the following peaks, and many unresolved peaks appeared. In Fig. 4 only the highest peaks of every order are shown, already including some unresolved peaks which could not be avoided due to their high amplitudes. As the Nyquist frequency of LC data is 24.4 d^{-1}, 12 harmonic orders could be observed, and 239 frequencies were subtracted around the main pulsation components until the attention was turned towards the additional peaks which are

present in the region between the harmonics of the fundamental mode (see the next section).

Altogether, 239 frequencies were included, of which one is the fundamental mode, nine are harmonics of the fundamental mode, 104 are combinations of f_0 or its harmonics with the Blazhko frequency f_B and/or the secondary modulation f_S and 125 are unidentified.

4.1.5 Additional frequencies: radial overtone and non-radial pulsation

It was already noted by Benkő et al. (2010) that V445 Lyr shows a rich spectrum of frequencies in the region between the harmonics of the fundamental mode. Those frequencies are not at all typical for ab-type RR Lyrae stars and have never been detected in such a large number in an RR Lyrae star. Some peaks were suspected to be radial overtones by Benkő et al. (2010), and also frequencies which are half-integer multiples of the fundamental mode are expected to appear in this region as a consequence of the period-doubling phenomenon as described by Szabó et al. (2010). However, there is more than this in the case of V445 Lyr.

Fig. 6 shows the frequency spectrum after subtraction of the relevant peaks around the multiples of the fundamental pulsation as discussed in the previous section (their former positions are marked with arrows). The additional frequencies can clearly be seen to be the dominant signal with an amplitude of 3.7 mmag for the highest peak. The region between the fundamental mode and its first harmonic is indicated with a grey box and enlarged in the insert (panel b). Four frequency regions with enhanced signal can be noted in the enlargement: around 2.65, 2.8, 2.9 and 3.33 d^{-1}. This pattern repeats in every harmonic order, indicating combinations of the frequencies with the fundamental mode and its surrounding peaks. The presence of combinations is a strong evidence that the additional signal is not introduced by a possible background star.

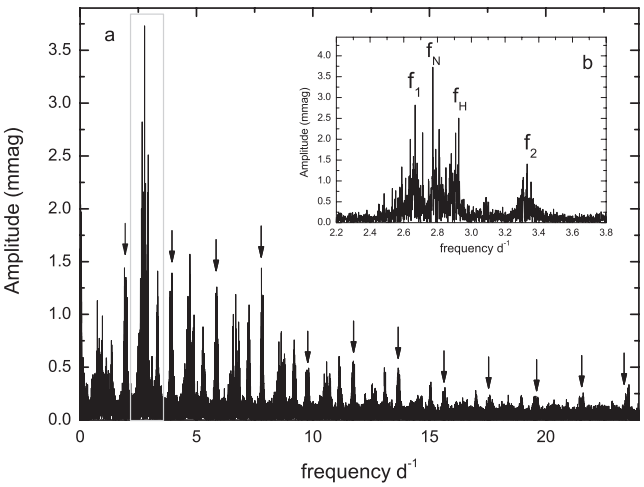

Figure 6. Fourier spectrum after pre-whitening 239 frequencies in the vicinity of the fundamental mode and its harmonics. Very clearly, additional frequencies can be seen between the harmonic orders and their combinations with f_0 which are present up to high harmonic orders. Arrows mark the places where the harmonics and the Blazhko as well as the secondary multiplets were located before pre-whitening. Some signal remains around their positions, as discussed in Section 4.1.4. The insert (panel b) shows a zoom into the region between the fundamental mode and the first harmonic (2–4 d^{-1}), indicated as a grey square.

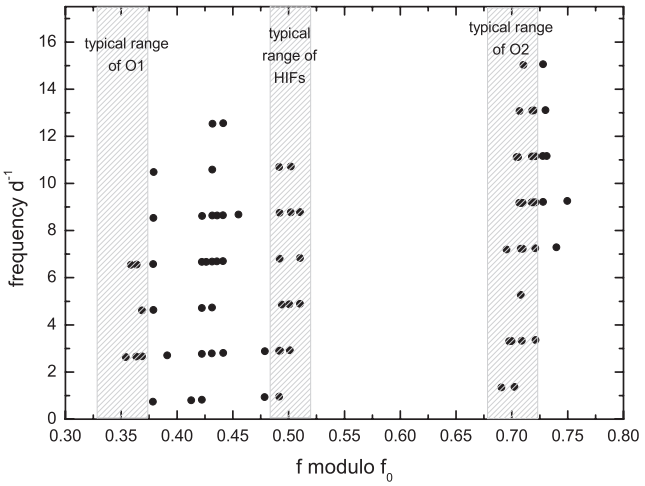

Figure 7. Echelle diagram of the additional frequencies, showing how the patterns repeat in every harmonic order. Shaded boxes indicate the ranges which would be typical for the first and second overtones (O1 and O2, respectively), as well as for the HIFs.

In a Fourier analysis of the relevant frequency regions, 80 peaks (including combinations) were considered significant and were subtracted. A closer inspection of the result revealed that the dominant peaks formed combinations not only with the fundamental mode but also with the Blazhko multiplet peaks (including quintuplets!) and in some cases also with the peaks belonging to the secondary multiplet. Negative combinations such as $f_N - f_0 - f_B$ also occur. Significant combination peaks can be traced up to the fifth harmonic order, but an excess in signal is visible in the Fourier spectrum even at much higher orders (see Fig. 6). In Fig. 7, an echelle diagram is plotted for the additional peaks, clearly showing the combinations with the fundamental mode aligned in vertical patterns. Shaded boxes indicate the typical regions in which overtone modes and half-integer combination frequencies would be expected to be situated. Please note that it was shown by Szabó et al. (2010) that due to the onset and offset of the period-doubling phenomenon, the half-integer frequency (HIF) peaks are not necessarily located at the exact positions of the half-integer multiples, but might deviate by several per cent. Therefore, the shaded box at (f modulo f_0) = 0.5 in Fig. 7 has a distinct width.

In V445 Lyr, the frequency at 2.9256 d^{-1} deviates by only 0.0021 d^{-1} (i.e. 0.07 per cent) from the exact value of $3f_0/2$. Given the fact that clear signs of period doubling are indeed visible in the light curve (see Fig. 1c), and considering the above-mentioned findings of Szabó et al. (2010), it is quite safe to interpret this frequency as an HIF caused by period doubling. We hereafter refer to it as f_H. Four significant HIFs (which can also be interpreted as combinations of f_H with f_0) were found in the Fourier spectrum: $3f_0/2$, $5f_0/2$, $9f_0/2$ and $11f_0/2$. Combinations with the Blazhko frequency, both positive and negative, could also be identified (see Table 2 for a complete list).

Another interesting feature is the peak at 3.3307 d^{-1} which shows a frequency ratio of $f_0/f_2 = 0.585$ with the fundamental mode, and which we hereafter refer to as f_2. Its period ratio is typical for the second overtone. Peaks with similar period ratios have already been reported for several RR Lyrae stars. Poretti et al. (2010) were the first to find them in the star CoRoT 101128793. The frequency ratio in their study was 0.584 with the fundamental mode at $f_0 = 2.11895\,d^{-1}$. They interpreted the peak as the second radial overtone. The same authors also re-analysed the data of V1127

Table 2. List of the highest peaks in every one of the four regions of excess signal, and their combinations.

	Frequency (d^{-1})	Amplitude (mmag)
f_N	2.7719	3.67
$f_N + f_0$	4.7211	1.58
$f_N + 2f_0$	6.6778	0.74
$f_N + 3f_0$	8.6196	0.51
$f_N - f_0$	0.8228	0.75
$f_N + f_B$	2.7895	1.64
$f_N + f_0 + f_B$	4.7389	1.43
$f_N + 2f_0 + f_B$	6.6880	1.22
$f_N + 3f_0 + f_B$	8.6372	0.83
$f_N + 4f_0 + f_B$	10.5864	0.54
$f_N + 5f_0 + f_B$	12.5359	0.33
$f_N - f_0 - f_B$	0.8044	0.69
$f_N + 2f_B$	2.8091	2.24
$f_N + 2f_0 + 2f_B$	6.7067	0.87
$f_N + 3f_0 + 2f_B$	8.6559	0.57
$f_N + 5f_0 + f2f_B$	12.5543	0.34
$f_N + 2f_0 + f_S$	6.6778	0.74
$f_N + 2f_0 + f_B + f_S$	6.6964	0.76
$f_N + 3f_0 + f_B + f_S$	8.6456	0.81
$f_N + 3f_0 + 3f_B + f_S$	8.6828	0.53
f_1	2.6676	2.80
$f_1 + f_0$	4.6166	1.08
$f_1 + f_0 + f_B$	4.6362	1.16
$f_1 + 2f_0 + f_B$	6.5851	1.02
$f_1 + 3f_0 + f_B$	8.5343	0.77
$f_1 + 4f_0 + f_B$	10.4838	0.45
$f_1 - f_0 + f_B$	0.7374	1.16
f_H	2.9256	2.55
$f_H + f_0$	4.8736	0.87
$f_H + 3f_0$	8.7743	0.60
$f_H + 4f_0$	10.7234	0.43
$f_H - f_B$	2.9070	2.29
$f_H + f_0 - f_B$	4.8607	0.89
$f_H + 2f_0 - f_B$	6.8060	0.95
$f_H + 3f_0 - f_B$	8.7549	0.57
$f_H + 4f_0 - f_B$	10.7029	0.40
$f_H - f_0 - f_B$	0.9579	1.01
$f_H + f_0 + f_B$	4.8924	1.00
$f_H + 2f_0 + f_B$	6.8413	0.71
$f_H + 3f_0 + f_B$	8.7905	0.58
f_2	3.3307	1.43
$f_2 + f_0$	5.2781	0.85
$f_2 + 2f_0$	7.2268	0.79
$f_2 + 3f_0$	9.1760	1.04

Aql (Chadid et al. 2010) and MW Lyr (Jurcsik et al. 2008) and found frequency ratios of 0.582 ($f_0 = 2.8090 d^{-1}$) and 0.588 ($f_0 = 2.5146 d^{-1}$), respectively. In the sample of *Kepler* RRab stars, Benkő et al. (2010) reported the presence of the second overtone in four different stars: V354 Lyr (a Blazhko star with $f_0 = 1.780\,37 d^{-1}$), V2178 Cyg (a Blazhko star with $f_0 = 2.054\,23$), V445 Lyr (the subject of this paper) and the non-modulated RRab star V350 Lyr ($f_0 = 1.682\,82$) which was the first example of a non-Blazhko double-mode RR Lyrae star with the fundamental (F) and the second overtone (O2) excited. Guggenberger et al. (2011) found evidence for the second overtone in CoRoT 105288363, a Blazhko star with rapid changes in the Blazhko effect, and Nemec et al. (2011) found the second overtone in KIC 7021124, therefore providing another example of a non-modulated RRab star pulsating in both F and O2 ($f_0 = 1.606\,445 d^{-1}, f_0/f_2 = 0.593$).

It is interesting to note how different the stars are for which the second overtone has been documented so far: their fundamental frequencies range from about 1.6 to 2.8 d^{-1}, covering almost the full bandwidth of RRab pulsation, and with respect to stability they range from non-modulated stars with almost perfectly regular RRab pulsation (V350 Lyr, KIC 7021124) to Blazhko stars with a rather regular Blazhko effect (CoRoT 101128793 and V1127 Aql) and finally to modulated stars that show dramatic changes of their Blazhko modulation (CoRoT 105288363 and V445 Lyr). Moreover, they cover a significant range of Blazhko periods, from 16.6 d to more than 200 d, as estimated for V2178 Cyg.

The combinations of f_2 in V445 Lyr deserve some special attention. While as many as 32 peaks are detected near the positions of $f_2 + kf_0$, and clearly an excess of signal is visible in every harmonic order (see Figs 6 and 7), it was not possible to identify most of the detected peaks as exact combinations with the known frequencies. For f_H (which was discussed in the previous paragraph), 12 out of 16 peaks could be attributed to combinations while for f_2, only three combinations with f_0 were found at their exact positions. All the other peaks in the vicinity of the combinations deviated too much from the calculated values to be safely matched with the combinations. This is especially remarkable as the amplitudes of those peaks are surprisingly large in higher harmonic orders compared to the combinations of the other additional frequencies. From Fig. 6 it is obvious that in the first harmonic order, f_2 has a small amplitude compared to the other additional frequencies, while at the orders 4–5 they become equal, and at higher orders, the peaks in the area around $f_2 + kf_0$ are the dominant features. This is also illustrated in Fig. 8, where the amplitudes of the safely identified peaks versus frequency are shown. The large number of unidentified peaks around f_2 might indicate that the amplitude of f_2 is variable, either irregularly or on a time-scale other than the Blazhko frequency. This will be discussed in more detail in Section 4.2.1.

The highest amplitude peak among the additional frequencies (3.7 mmag) is the one at 2.7719 d^{-1}. This peak was interpreted as the first overtone by Benkő et al. (2010), but its ratio with the

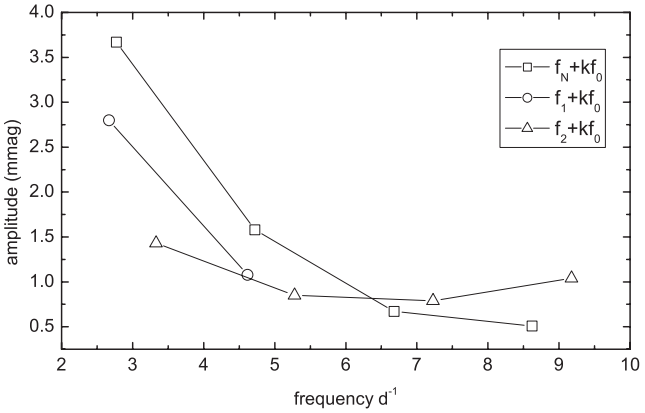

Figure 8. Amplitudes of the additional frequencies and their combinations with f_0 versus frequency. While the amplitudes of f_N and f_1 decrease exponentially with harmonic order, the amplitude of f_2 remains almost stable. Amplitude errors are smaller than the symbols.

fundamental ($f_0/f_N = 0.703$) is very low compared to the canonical value of 0.74–0.75. Note that the OGLE III RR Lyrae stars in the Galactic bulge have f_0/f_1 values going down to about 0.726 only (see Soszynski et al. 2011). Extremely high metallicity values would be necessary according to models (Popielski, Dziembowski & Cassisi 2000; Szabó, Kolláth & Buchler 2004; Smolec & Moskalik 2008) to fit this frequency ratio with the first overtone. New spectroscopic results revealed, however, that the metallicity of V445 Lyr is [Fe/H] $= -2.0 \pm 0.3$ (see Section 5), rendering it impossible to explain this frequency with a radial overtone mode. f_N is therefore most likely to be a non-radial mode. We note that Van Hoolst, Dziembowski & Kawaler (1998) found in their non-adiabatic and non-radial calculations the excitation of non-radial modes in the vicinity of the radial mode in RR Lyrae stars to be very likely, and Dziembowski & Cassisi (1999) noted in their model survey the presence of strongly trapped non-radial modes with very high growth rates near the first overtone.

Among the additional modes in V445 Lyr, f_N is the one that shows the clearest pattern of combination frequencies: of 20 peaks which were found significant in relation to f_N, all 20 could be unambiguously identified as exact combinations with f_0, the Blazhko frequency and the secondary modulation frequency (see also Table 2 and Fig. 9, which illustrate the regular pattern of combination peaks). We note that the possible non-radial mode, which was found by Chadid et al. (2010) in V1127 Aql, has a very similar frequency ratio (0.696), may be hinting at a possible systematic preference in non-radial mode excitation in RR Lyrae stars.

There remains, however, the fourth region of increased signal with a main peak at 2.6676 d^{-1}, which, with a frequency ratio of $f_0/f_1 = 0.731$ is in principle in the possible range of the first overtone pulsation. One has to note that double-mode RR Lyrae stars usually follow a well-defined empirical sequence in the Petersen diagram; in other words, there is a relation between f_0 and f_0/f_1 (see Popielski et al. 2000; Soszynski et al. 2009). If the peak at 2.6676 d^{-1} is indeed the first overtone, V445 Lyr would be an exception to this relation, which is very unlikely. On the other hand, outliers from the sequence similar to V445 Lyr have recently been reported by Soszynski et al. (2011) in the OGLE III survey of the Galactic bulge.

The metallicity needed to reproduce a frequency ratio of $f_0/f_1 = 0.730$ with models ($Z = 0.004$, see Fig. 10) is much larger than the spectroscopic value ($Z = 0.0002$, see also Section 5). Moreover, the average frequency values are quite far ($2f_1 - f_0 - f_2 = 0.055$) from the resonance condition that could explain the presence of the second overtone by resonant excitation, and which would also have the power to shift the frequency away from the expected value in the Petersen diagram. We note, however, that the frequency values of f_1 and f_2 are not strictly constant during the observed time span, but undergo irregular fluctuations. We performed a time-dependent Fourier analysis (see also Section 4.2.1) and found the resonance criterion to be fulfilled occasionally. For f_1, one combination with f_0 and five combination frequencies with f_0 and f_B were found, leaving the other six significant peaks unidentified. One of them, a peak at 2.639 d^{-1} (with a frequency ratio of 0.739 with the fundamental mode), would fulfill the resonance criterion, but its amplitude is only 1.9 mmag, compared to 2.8 mmag of f_1. We therefore conclude that the identities of the peaks at 2.6676 and 2.639 d^{-1} cannot be unambiguously assessed.

The highest peaks in every region and their combinations are listed in Table 2. Altogether, 80 frequencies were found to be significant in the vicinity of the additional peaks: four of these were independent frequencies, 40 were combinations of these independent terms with f_0, f_B and/or f_S, and 36 were peaks which could not be identified as combinations. Together with the 239 frequencies found in the vicinity of the fundamental mode and its harmonics (see Section 4.1.4), this results in a total of 319 frequencies included in the analysis.

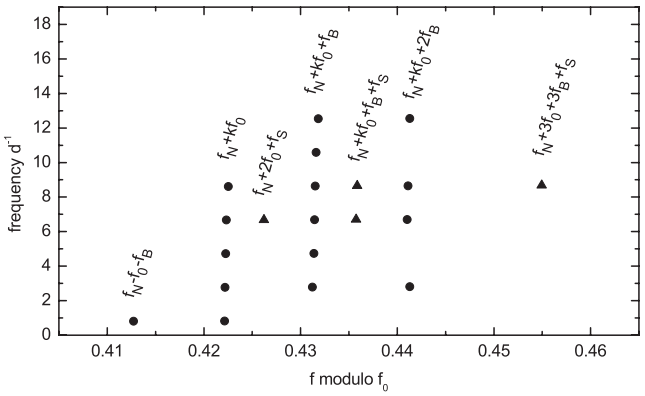

Figure 9. Details of the echelle diagram, showing only the vicinity of the mode f_N. All detected peaks could clearly be identified as combinations of f_N with either the classical Blazhko multiplet or the secondary multiplet. The fact that no unidentifiable peaks are among the highest ones points towards a very stable amplitude of this mode, compared to the other additional peaks that were found in this star.

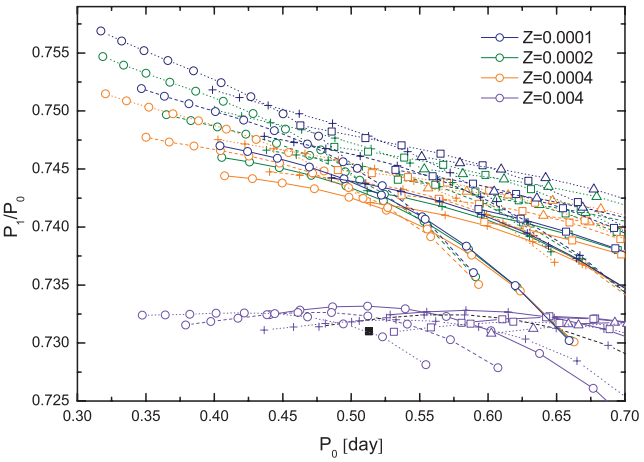

Figure 10. Petersen diagram for the peak at 2.6676 d^{-1} illustrating that a metallicity of $Z = 0.004$ would be necessary to identify this peak as the first radial overtone mode. Models around the spectroscopically derived value of $Z = 0.0003$ (see Section 5) are also shown for comparison. Different symbols indicate different luminosities and different line styles indicate different masses (see also Section 5). Models were calculated with the Warsaw codes (Smolec & Moskalik 2008).

4.2 Separate analysis of subsets

To study the time-dependent behaviour of the frequency pattern, we used both PERIOD04 and the *time-resolved* feature of SIGSPEC (Reegen 2007), which makes it possible to analyse large numbers of data subsets in an automated way. The top panel of Fig. 11 illustrates the variation of f_0 with time as calculated with SIGSPEC for overlapping subsets of 15 d. With PERIOD04, we analysed larger subsets of data, consisting of one or more quarters each. During this process we note that in the subset containing Q1 to Q4 (Blazhko period 53.9 d), no

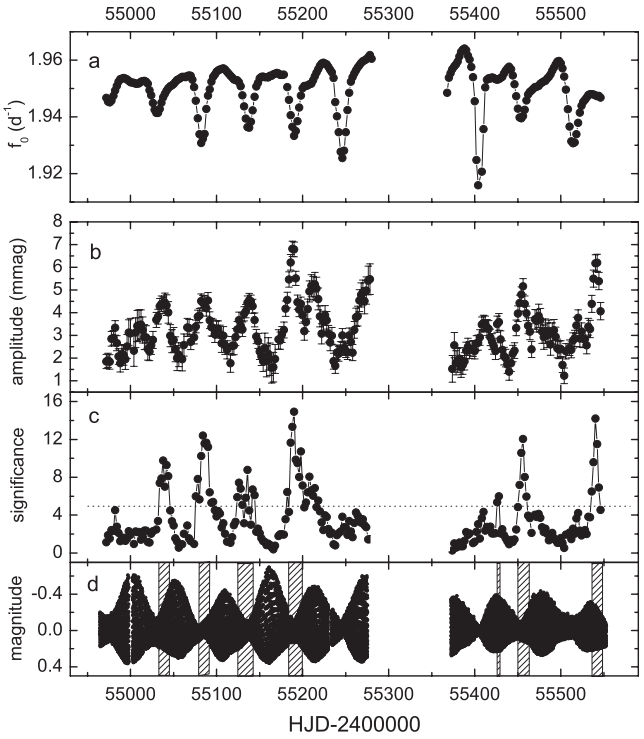

Figure 11. Variation of f_0 over the complete data set (panel a). Middle panels show the variation of the amplitude (panel b) and the significance (panel c) of the second overtone f_2, calculated for bins of 15 d duration with a step width of 2 d. The bottom panel (d) shows the light curve for orientation. The times of significant f_2 amplitude are marked with shaded boxes.

deviation of the harmonics as described in Section 4.1.2 is observed. This phenomenon seems to occur only in quarters Q6 and Q7 where the Blazhko periods found in separate analyses of the quarters were 79.8 and 80.4 d, respectively.

4.2.1 *Stability of the additional frequencies*

The results discussed in Section 4.1.5 hint towards a variability of the amplitude of f_2, and we therefore studied the temporal evolution of this peak in detail. Using the time-resolved mode of SigSpec, we performed a Fourier analysis of overlapping bins with a duration of 15 d in steps of 2 d, limiting the frequency range to the region around f_2. The resulting amplitudes are plotted in Fig. 11(b). While there is a clear variation of the amplitude ranging from 2 to ∼7 mmag, no clear periodicity is discernible. We also performed a Fourier analysis on the resulting amplitude curve and found no significant frequency of variability. We note that in Fig. 11, all values of $A(f_2)$ were included, regardless of the significance of the frequency. Only bins with an insufficient number of data points and/or bad frequency resolution were discarded. Therefore we provide as a supporting plot the time-dependent significance of the peaks in panel (c), where the most commonly used significance criterion of sig ≥ 5 is indicated with a dashed line.

For better orientation, the bottom panel shows the full data set (light curve) of V445 Lyr, and shaded boxes indicate the regions of enhanced f_2 amplitude. There seems to be a preference for phases close to Blazhko minima, which are also the phases where the minima of the fundamental frequency f_0 occur, but there is no strict rule that can predict a high f_2 amplitude. This irregular amplitude variability can explain the numerous peaks around f_2 and its combinations which can be seen in the echelle diagram (Fig. 7) and which are discussed in Section 4.1.5.

We also check the temporal variations of the frequency values of all the additional frequencies and find, in addition to the variation of f_0 which is plotted in Fig. 11(a), slight irregular variations of f_1 and f_2, which lead to an exact parametric resonance during some time intervals in the observed data. This might result in the momentary and transient excitation of f_2 which is seen in Fig. 11. We note that from the theoretical point of view, a resonance is necessary to excite the second overtone in this parameter range, because otherwise this overtone would not become unstable.

4.2.2 *Variation of the Blazhko modulation parameters*

The modulation parameters are normally used to describe the properties of the Blazhko modulation of a given star. The traditional parameters are $R_k = A_+/A_-$ where A_+ and A_- are the amplitudes of the peak on the higher frequency and the lower frequency sides of the triplet, respectively, and the phase difference $\Delta\varphi_k = \varphi_+ - \varphi_-$. The parameter k denotes the harmonic order. Moreover, the asymmetry parameter $Q = (A_+ - A_-)/(A_+ + A_-)$, which was introduced by Alcock et al. (2003), is widely used, as is the power difference $\Delta A^2 = A_+^2 - A_-^2$. This parameter was recently shown by Szeidl & Jurcsik (2009) to be the physically most meaningful one, as it is directly correlated to the phase difference between the amplitude and the phase modulation components in their model of modulated oscillation.

As the main aspect of V445 Lyr is the variability of the Blazhko cycles, we show here not only the average Fourier parameters for every order (which are listed in Table 3) but also their time-dependent behaviour in Fig. 12. To calculate the modulation parameters for every cycle, the data set was divided into bins, starting and ending around Blazhko minimum. The length of the bins was about 60 d, with the exception of the last bin which was only 50 d. Some overlap was allowed to guarantee frequency resolution of the Blazhko multiplet.

It was an important result for the star CoRoT 105288363 that the phasing between the two types of modulation was found to change (see section 5.3 of Guggenberger et al. 2011). Such a phase change is also indicated by the variation of ΔA^2 of V445 Lyr (bottom panel of Fig. 12).

4.2.3 *Fourier parameters*

As the so-called Fourier parameters R_{k1} (amplitude ratio) and φ_{k1} (epoch-independent phase difference) are considered useful tools to

Table 3. Overall modulation parameters of V445 Lyr found from the fit to the complete data set for the first six harmonic orders.

k	R_k	$\Delta\varphi_k$	Q_k	A_k^2
1	2.112	−0.87	0.357	0.005 779
2	3.179	0.27	0.521	0.001 900
3	3.991	−0.24	0.599	0.000 445
4	3.806	−0.08	0.584	0.000 114
5	5.382	−0.30	0.687	0.000 037
6	4.715	−0.39	0.650	0.000 011

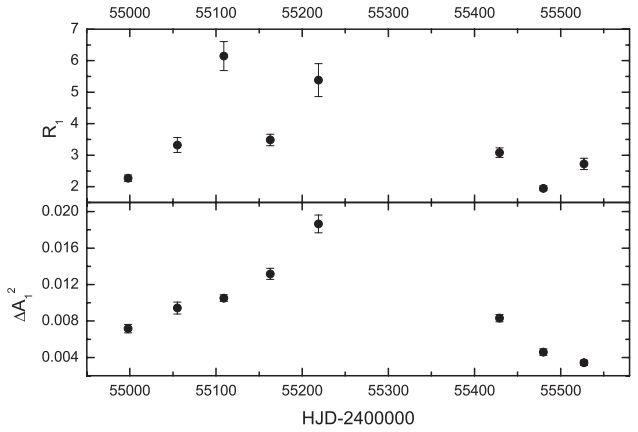

Figure 12. Modulation parameters of V445 Lyr versus time. The top panel shows the variation of R_1, which is defined as the amplitude ratio between the right and the left modulation side peak, and the bottom panel displays the variation of the power difference ΔA_1^2. The variation of ΔA_1^2 points towards a shift in the phasing between the two types of modulation.

study and compare the properties of RR Lyrae stars, we calculated their time variability for V445 Lyr. In contrast to the modulation parameters discussed in the previous section, they describe the pulsation rather than the modulation properties. The Fourier parameters are defined as $R_{k1} = A_k/A_1$ and $\varphi_{k1} = \varphi_k - k\varphi_1$. The data were subdivided into 239 bins of 2 d duration, therefore containing about four pulsation periods. On such short time-scales, the Blazhko effect is expected to play only a minor role. The effect of period doubling, however, causes a large error in some bins which are more affected by this effect than others. A fit including the fundamental pulsation and 10 harmonics is calculated for each bin, and the results are displayed in Fig. 13 (amplitude ratios are shown in the left-hand panels and phase differences in the right-hand panels). The average values of the parameters (derived from the complete data set) are given in Table 4.

Some interesting details are immediately obvious: while the amplitude A_1 of 0.18 mag is quite small compared to other RR Lyrae stars, but still in the normal range, the amplitude ratios R_{k1} are significantly smaller than those of the non-modulated stars (for comparison, see fig. 6 in Nemec et al. 2011). The sharp upward spikes are an intriguing feature in the R_{21} variation, which occur only during some of the observed Blazhko minima. When looking at the phases one notes that, while φ_1 has a smooth periodic variation, the phases φ_2, φ_3 and φ_4 show a more or less continuous progression (with exceptions in some cycles), leading to apparent phase jumps in the φ_{k1} parameters.

The stability of the results was tested by also using other binnings, and the size of the bins was found to play only a minor role.

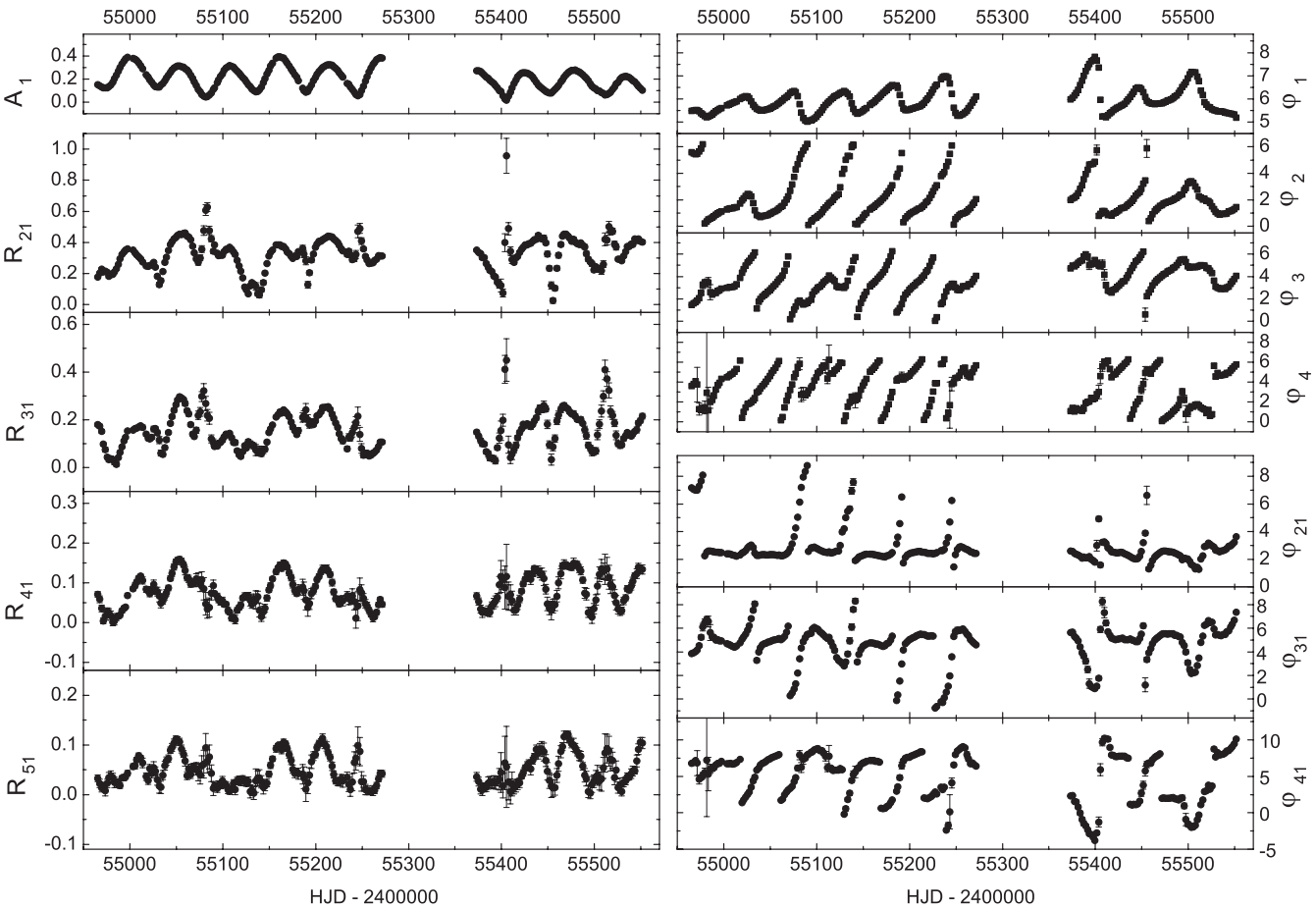

Figure 13. Variation of the Fourier parameters during the observed time span, calculated for subsets of 2 d duration each. Left-hand panels: at the top, the amplitude A_1 is displayed to indicate where Blazhko maxima and minima are located, while lower panels show the amplitude ratios R_{21}, R_{31}, R_{41} and R_{51}. Right-hand panels: at the top, the phases φ_1, φ_2, φ_3 and φ_4 are plotted, while the lower panels show the phase differences φ_{21}, φ_{31} and φ_{41} in the sine frame. Where error bars are not visible, they are smaller than the symbols.

Table 4. Average Fourier parameters of V445 Lyr.

Parameter	Value	Parameter	Value
A_1	0.184	φ_1	5.84
R_{21}	0.268	φ_{21}	2.34
R_{31}	0.096	φ_{31}	4.95
R_{41}	0.033	φ_{41}	1.08
R_{51}	0.013	φ_{51}	3.69

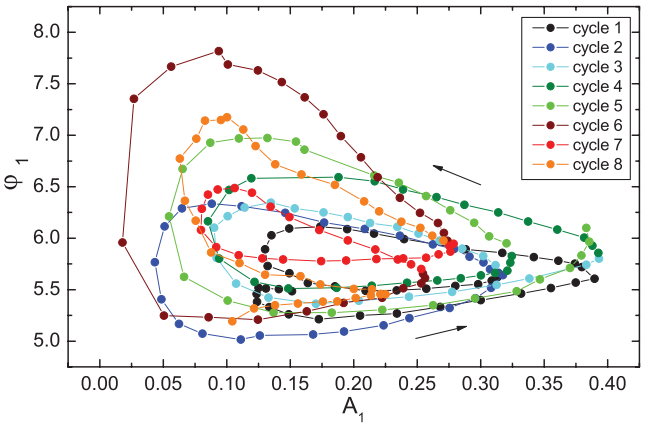

Figure 14. φ_1 versus A_1 diagram of V445 Lyr. In this plot it can be seen how various observed cycles differ from each other. Both the phase modulation component and the amplitude modulation component change over the observed time span. Moreover, their relative phasing changes from cycle to cycle.

4.2.4 Loop diagrams

A good indicator for the relative contributions of phase modulation and amplitude modulation, and for the phasing between those two types of modulation, is the A_1 versus φ_1 diagram. The resulting loops for V445 Lyr are plotted in Fig. 14. The direction of motion is indicated with arrows. Cycles are defined for this purpose as from one maximum of A_1 to the next, except for the beginning and the end of the data set where additional points are added to the adjacent cycles. Cycles 1 to 5 correspond to data obtained before the gap in the observations, and cycles 6 to 8 correspond to data after the gap. Even though the contents of Fig. 14 are partly redundant with the upper panels of Fig. 13, the representation as a loop diagram allows us to better compare the observed Blazhko cycles. All observed Blazhko cycles have a different appearance in this diagram, and the contributions of amplitude and phase modulation change without notable correlation between each other.

4.3 O − C diagrams and long-term period change

In addition to the Fourier analysis which reveals the average Blazhko period, and the time-dependent analysis which shows the fundamental mode as a function of time, we also constructed an O − C diagram, as it can reveal additional details, especially when it comes to long-term period changes. The O − C diagram obtained from all maxima in the *Kepler* V445 Lyr light curve is shown in the top panel of Fig. 15. An intriguing feature is the non-sinusoidal variation of the O − C values with a few points at very low O − C values in some of the cycles. A closer inspection of the phase diagrams at the affected times reveals that these drops in O − C are happening at the epochs with the very unusual distorted light-curve shape showing double maxima (the double maxima are illustrated in Figs 1b and d). The determination of the time of the light maximum becomes ambiguous here, depending on the maximum that is chosen. The original maximum seems to move 'to the left' (causing negative O − C values) while a bump on the descending branch gets stronger and takes the role of the maximum for the next Blazhko cycle. This also explains the rather abrupt transition from very low to high O − C values.

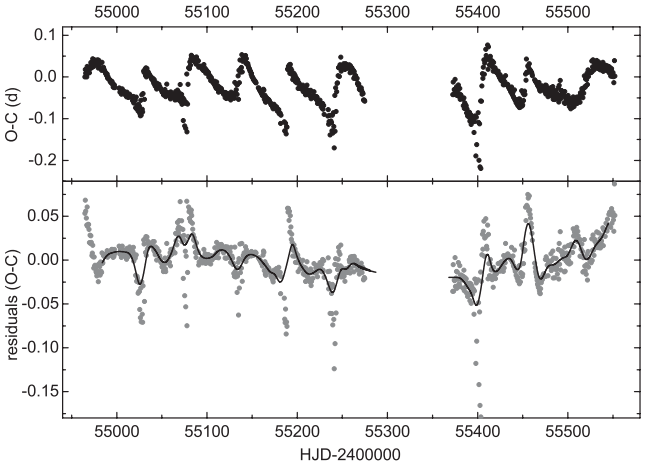

Figure 15. O − C diagram of the complete data set of V445 Lyr (top panel), and residuals after subtracting a fit with the Blazhko frequency, its harmonics and the secondary modulation frequency (bottom panel). To guide the eye, a line through the means of the residuals in bins of 10 maxima has been plotted.

We also performed a Fourier analysis on the O − C data to check whether the secondary modulation is also present in the phase variation. We clearly found the Blazhko frequency f_B, in this case 0.0184 d^{-1}, as well as the harmonics $2f_B$ and $3f_B$ in the O − C curve, which are introduced by the non-sinusoidal variation of the O − C curve. The secondary modulation, with a value of $f_S = 0.0064$ d^{-1}, as well as the combination peak $f_B + f_S$, was also directly detected in the Fourier spectrum. We note that slight differences in the frequency values obtained from the O − C diagram compared to those obtained from the magnitudes do not come unexpectedly, as the phase and AMs are not strictly correlated.

As the quasi-periodic Blazhko modulation is the dominant signal in the O − C curve, it is necessary to subtract a fit including the above-mentioned frequencies from the O − C curve to be able to identify long-term changes. The residuals of this fit are shown in the bottom panel of Fig. 15 and reveal quite clearly a long-term period change. It remains unclear, however, whether it is a periodic or a continuous linear period change.

4.4 The analytic modulation approach

Due to the limitations of the classical Fourier analysis discussed in Section 4, we applied a new method of analysis to the *Kepler* data of V445 Lyr, which was recently described by Benkő et al. (2011, hereafter B11). In this approach, the amplitude and frequency modulations are treated similarly to the theory of electronic signal transmission, reducing dramatically the necessary number of free parameters. This would be especially useful for stars like V445 Lyr where a classical Fourier analysis yields several hundreds of combination peaks.

As a first step of such an analysis we have to select the fitting formula, using table 1 in B11. The AM with the frequency of f_B is

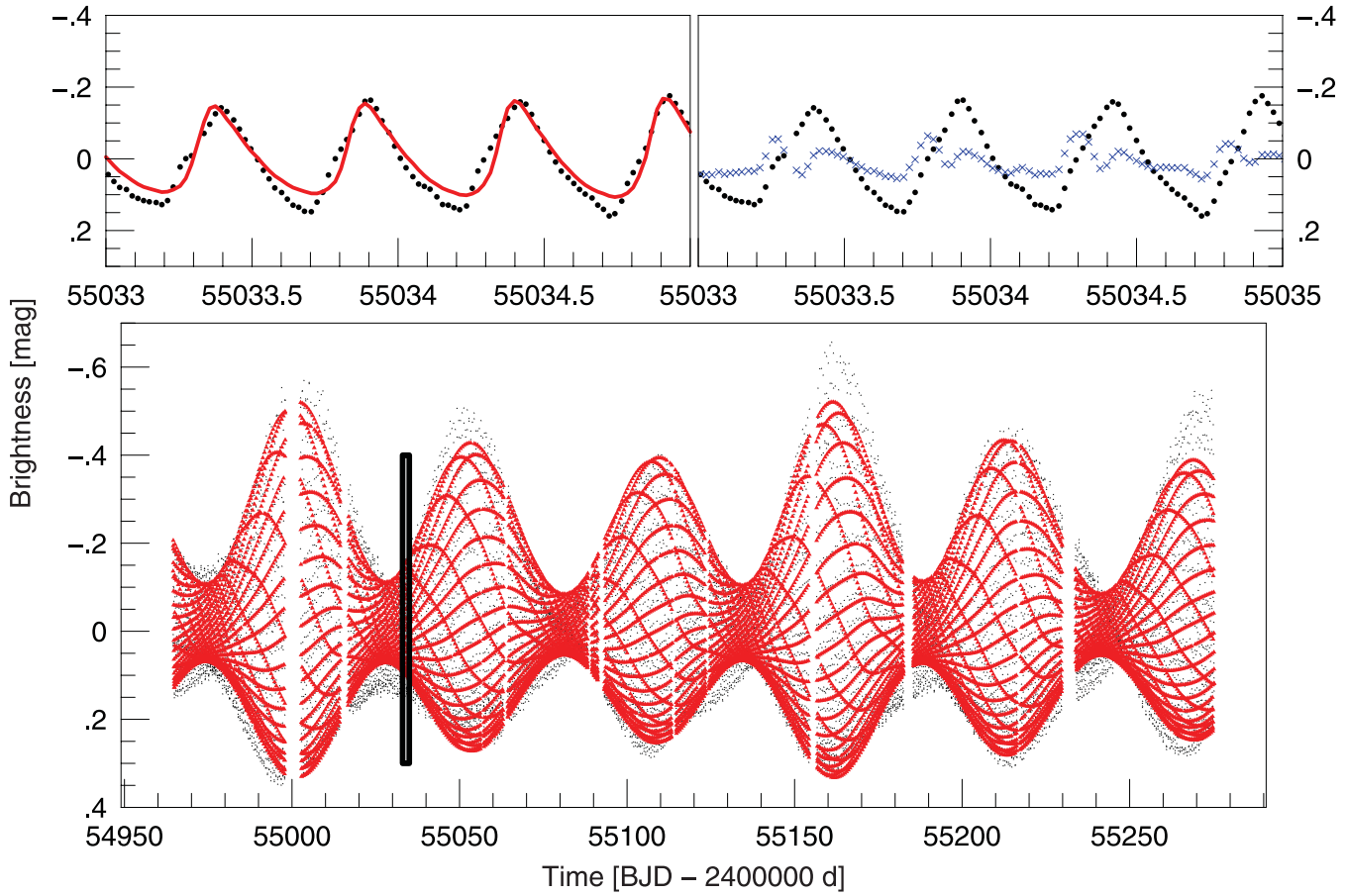

Figure 16. The light-curve fit of V445 Lyr during Q1–Q4 using the modulated signal approach. The bottom panel shows the global 32-parameter fit (red continuous line) with the original data (black dots). The upper panels show a local fit (left) and residual light curves (blue crosses) in the interval indicated by the rectangle in the bottom panel.

evident already from the shape of the light curve in Fig. 1. Since the envelope curve is nearly horizontally symmetric for all Blazhko cycles, the AM of f_B can be approximated by a simple sinusoidal function (see formulae 20 and 21 in B11).

The high asymmetry of the multiplet peaks' amplitudes suggests a frequency modulation (FM) as well. Its non-sinusoidal nature is clear from both the frequency variation function (Fig. 11a) and the O−C diagram (Fig. 15). The combined sinusoidal AM and non-sinusoidal FM modulation of f_B can be described by formula (49) in B11, where $q' = 1$.

As mentioned above V445 Lyr shows a secondary modulation f_S as well, which is included in the form of an AM because of the changing amplitudes of the Blazhko cycles. As a first approximation we also assumed this modulation as sinusoidal. The linear combination of f_B and f_S shows interaction between the two modulations; therefore, we have to apply the formula of modulated modulation (AM cascade – equation 27 in B11).

The situation of the FM in f_S is a bit controversial. The existence of an FM seems to be well established, based upon the detection of f_S in the Fourier analysis of the O − C diagram; however, a combined AM with FM in f_S does not improve the significance of our numerical Levenberg–Marquardt fit. This may be explained on the basis of the long cycle length of this modulation and/or its weak FM.

The used best-fitting model contains a sinusoidal AM and a non-sinusoidal FM represented by a three-term Fourier sum for the Blazhko modulation and a sinusoidal AM for the second modulation. The two modulations are assumed to be modulating each other. The free parameters are the pulsation frequency f_0 and its harmonics' amplitude and phase up to the ninth order (A_1, A_2, ..., A_9, φ_1, φ_2, ..., φ_9), the modulation frequency f_B, the amplitudes and phases of its AM (a^A_{B1}, φ^A_{B1}) and FM (a^F_{Bi}, φ^F_{Bi}, $i = 1, 2, 3$), the secondary modulation frequency f_S and its AM modulation parameters (a^A_{S1}, φ^A_{S1}). They represent 32 parameters (with the zero-point a_{00}). The model light curve shows the global properties of the observed one (see Fig. 16); however, the variance of the residual (observed minus fitted) is surprisingly high (0.0025 mag).

There may be various reasons for this large variance. Some of them are method specific, others are object specific. An important limit of the method is (as mentioned by B11) that it does not describe the migration of the humps and bumps caused by the Blazhko effect, a phenomenon which is exceptionally strong in V445 Lyr. The situation is demonstrated well in the upper panels of Fig. 16. The other problem is that our method assumes regular signals. The light curve of V445 Lyr shows, however, irregular behaviour. The loop diagram in Fig. 14 illustrates the cycle-to-cycle variations of the relative strengths of the AM and FM components of the modulation. Any static (regular) models including the Fourier method face similar troubles when using them for such a time-dependent (irregular) phenomenon. Therefore, we conclude that even though applying the method leads to a success in obtaining a reasonable fit with a comparably small number of parameters, it is

nevertheless not optimal for a complicated data set like the one on V445 Lyr.

5 SPECTROSCOPY, COLOUR PHOTOMETRY AND FUNDAMENTAL PARAMETERS

In the framework of ground-based follow-up observations, three spectra were obtained with the HIRES spectrograph at the Keck 10-m telescope in 2011 August (Nemec, Cohen & Sesar, in preparation). Exposure times were 1200 s, and according to the ephemerides given in Section 4.1 the spectra were obtained shortly after maximum light. Due to its faintness ($Kp = 17.4$ mag), V445 Lyr is not an easy target to observe. From a preliminary analysis, heliocentric radial velocities of -392, -390 and -388 km s^{-1}, and a metallicity of [Fe/H] $= -2.0 \pm 0.3$ dex on the Carretta et al. (2009) scale, corresponding to $Z = 0.0003$, were obtained.

Based on the metallicity value derived from spectroscopy and with the frequency value of the second overtone mode, we were able to constrain the mass and luminosity of V445 Lyr with the help of a theoretical Petersen diagram which is shown in Fig. 17. Linear pulsation models (Smolec & Moskalik 2008) were calculated for a set of masses (0.55, 0.65 and 0.75 $M_\odot$, which are plotted as solid, dashed and dotted lines, respectively) and different luminosities (40, 50, 60 and 70 $L_\odot$, plotted as circles, pluses, squares and triangles, respectively). The metallicity values necessary to theoretically fit the observed frequencies agree very well with the measured metallicity, and the luminosity and mass of V445 Lyr found from Fig. 17 are 40–50 $L_\odot$ and 0.55–0.65 $M_\odot$, respectively.

As the model period ratios depend on the opacity tables and the abundance mixture used in the computations, we tested the stability of our results. The effects of different opacities and mixtures (Grevesse & Noels 1993; Asplund et al. 2009), however, were checked and found to play only a minor role. In Fig. 17, the models based on OPAL opacities and the mixture of Asplund et al. (2004) are shown. V445 Lyr is plotted as a black square in the diagram, while the other RRab stars for which the presence of the second overtone has been reported are shown as open squares. From the wide spread which the stars show in Fig. 17 it is obvious that very different parameters are needed to model different stars that show the second overtone. Larger masses are necessary to fit the period ratios of the stars with longer periods, while higher metallicities are needed to obtain a model for the shorter periods. Models for V350 Lyr and V354 Lyr have already been shown by Benkő et al. (2010) in their fig. 6 and by Nemec et al. (2011) in their fig. A2. It is already noted in Section 4.1.5 that the stars in which the second overtone is excited form a very diverse sample, therefore it is not surprising that they also cover a wide range in mass and metallicity.

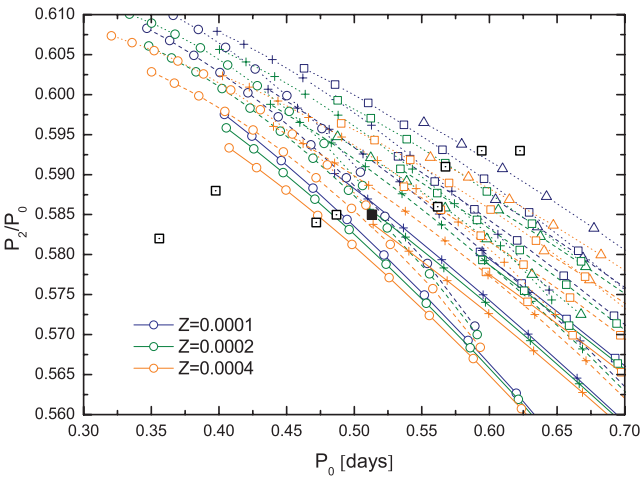

Figure 17. Petersen diagram for V445 Lyr (shown as black square) for the second overtone, based on models computed with the Warsaw code (Smolec & Moskalik 2008). Other RRab Lyr stars with possible second overtones (as discussed in Section 4.1.5) are plotted as open squares.

5.1 Ground-based colour photometry

To complement the *Kepler* data with colour information on our target, V445 Lyr was observed from the ground in *BVRI* (of which the *RI* bands are in Cousins system) using telescopes at the Lulin Observatory, including the Lulin One-metre Telescope (LOT), Lulin 0.4 m SLT and the Tenagra II Observatory (TNG, with a 0.8-m telescope). The imaging data were reduced with IRAF in a standard manner, including bias and dark subtraction, and flat-fielding. Photometry was obtained from the images using SExtractor (Bertin & Arnouts 1996), and calibrated to the standard magnitudes using standard star observation from Landolt (2009). Further details about the telescopes, the CCDs and the reduction of the imaging data can be found in Szabó et al. (2011) and Ngeow (2012), who used the same instrumentation for monitoring the Cepheid V1154 Cyg located within the *Kepler* field of view (Szabó et al. 2011).

The observations were performed between 2011 March 29 and July 24 (i.e. during the course of two Blazhko cycles) and they comprised about 70 measurements per filter with typical uncertainties of about 0.06 mag. As the data cover the pulsation cycle well, they allow the determination of an average brightness in each colour. The following average magnitudes in the standard system were obtained for V445 Lyr on the basis of the magnitudes of the single measurements: $B = 17.80$ mag, $V = 17.38$ mag, $R = 17.09$ mag and $I = 16.81$ mag.

6 COMPARISON WITH COROT 105288363

With the tools developed for the analysis of V445 Lyr, we revisited CoRoT 105288363 to apply the same techniques in a consistent way. Unlike in previous studies, the frequencies were kept as free parameters during the pre-whitening and fitting procedure, in spite of the increase of computing time. This has the advantage that the Blazhko period can be determined not only from one measured distance between two peaks, but also from a large number of independently detected peaks. The standard deviation of that set of measured values also gives a good error estimate. The Blazhko period found by this method is 34.6 ± 1.1 d and our solution agrees within the error of the previous published value of 35.6 d (Guggenberger et al. 2011).

When the echelle diagram diagnostic was applied to CoRoT 105288363, some previously undiscovered features could be unveiled. The first and most important finding is a well-resolved secondary modulation which is very similar to the one in V445 Lyr, in the sense that it has a ratio of $f_B/f_S = 2.5 \pm 0.27$ with the primary modulation, which is close to the value of $f_B/f_S = 2.7 \pm 0.12$ in V445 Lyr. Moreover, its combination peaks appear in similar positions: they are clearly found in the higher frequency side of the harmonics, and also preferentially on the higher frequency side of the classical Blazhko multiplets. The echelle diagram for CoRoT 105288363 is shown in Fig. 18. One has to note that, unlike in V445 Lyr, no systematic deviation of the harmonics from their expected positions (see Section 4.1.2) is found in CoRoT 105288363. Therefore, no tilt of the orders in the echelle diagram can be seen.

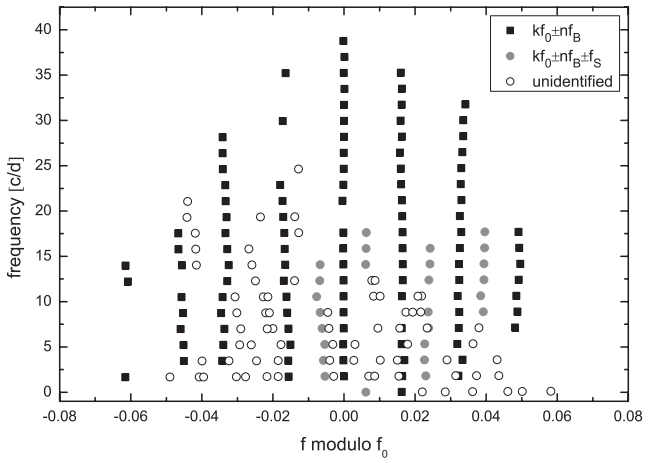

Figure 18. Same as Fig. 4 but for CoRoT 105288363. Note that the multiplet structure is more symmetrical than in V445 Lyr, in the sense that approximately the same number of multiplet components appear on both sides of the fundamental mode. The peaks belonging to the secondary modulation are in similar positions as in V445 Lyr. Again, several additional peaks occur which cannot be identified as combination peaks of either one of the modulations. This is most likely due to either the irregular or the yet unresolved changes of the Blazhko effect. Unlike in V445 Lyr, no combinations including a $2f_S$ term could be found.

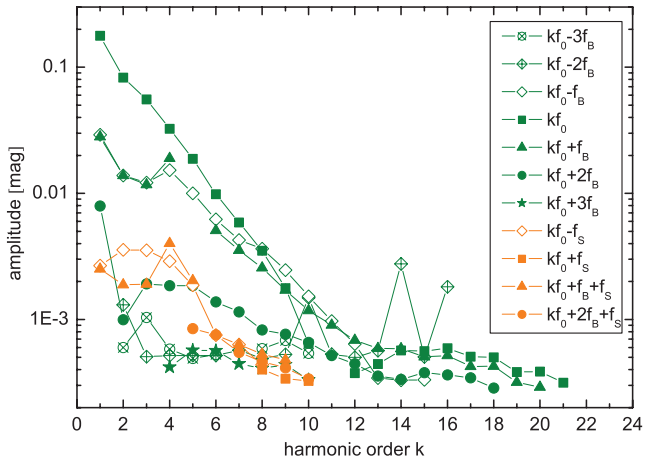

Figure 19. Same as Fig. 5 but for CoRoT 105288363. Here, in contrast to V445 Lyr, the components belonging to the secondary modulation never reach amplitudes higher than that of the classical multiplet, which might be connected to the fact that the changes in the Blazhko effect of CoRoT 10528836 are not so dramatic as they are in V445 Lyr. Their amplitude decrease is almost as rapid as for the classical components.

There are, however, some irregularities in the pattern with some peaks showing deviations from the exact position, though not in a systematic manner. The decrease of amplitudes of the secondary modulation components with increasing harmonic order is shown in Fig. 19. These figures should be compared to the corresponding ones for V445 Lyr (Figs 4 and 5, respectively).

The data of CoRoT 105288363 were then inspected carefully for signal outside the vicinity of the Blazhko multiplets to find evidence for overtones and other possible additional modes. The pre-whitening of not only the classical Blazhko multiplet but also the secondary modulation and the additional peaks (which also leads to the disappearance of all aliases) significantly reduced the noise level of the residuals in the frequency region of interest. The

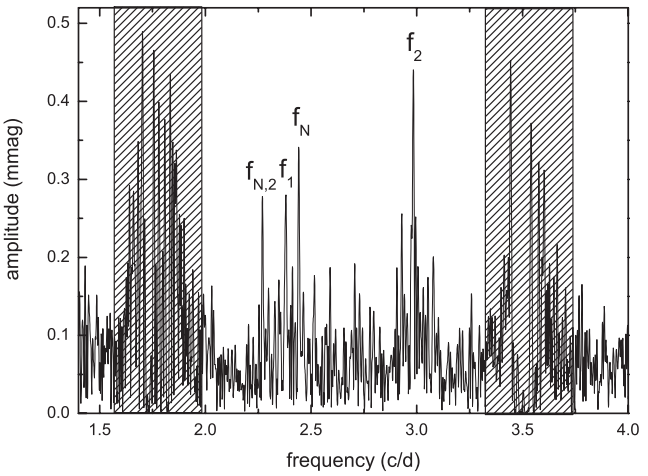

Figure 20. Fourier spectrum of CoRoT 105288363 after subtraction of 135 frequencies around the fundamental mode and its harmonics. A zoom into the region between f_0 and $2f_0$ is shown, clearly revealing the four additional peaks discussed in the text. The former positions of the multiplets around f_0 and $2f_0$ are marked with shaded boxes.

second overtone that was reported by Guggenberger et al. (2011) was also found in the new analysis (see Fig. 20, where it is labelled f_2). Due to the reduced noise, combinations of f_2 with kf_0 up to $k = 5$ could also be detected, clearly indicating that the frequency is not due to noise and is not caused by a background star. Moreover, three additional frequencies could be found (see also Fig. 20). A peak at 2.3793 d^{-1} with an amplitude of 0.3 mmag is found to be most likely the first overtone due to its ratio of $f_0/f_1 = 0.741$ with the fundamental mode. Moreover, a resonance with f_0 and f_2 is possible in this case, because $2f_1 - f_2 - f_0$ is only 0.01. Another peak appears at $f_N = 2.4422$ d^{-1} with an amplitude of 0.35 mmag. It cannot be attributed to any overtone. This and the fact that it appears between the positions of the first and the second overtones makes it quite similar to the observations in V445 Lyr (see Section 4.1.5). Furthermore, its amplitude is slightly higher than that of the suspected first overtone, as is the case for V445 Lyr. The third frequency found in this range is at $f_{N,2} = 2.2699$ d^{-1} and has an amplitude of 0.3 mmag. It cannot be identified as a radial overtone, and it has no counterpart in V445 Lyr.

Table 5 compares the main characteristics of the two stars, including the ratios of the Blazhko modulation, while Table 6 compares the additional (overtone) modes.

Table 5. Comparison of the main characteristics of the two stars. The fundamental mode frequencies, the Blazhko periods and the periods of the secondary modulation are very different. Interestingly, however, the ratios between the primary and the secondary modulations are very similar.

	CoRoT 105288363	V445 Lyr
f_0 (d^{-1})	1.762 31	1.949 03
P_0 (d)	0.5674	0.5131
P_B (d)	34.6	53.1
f_B (d^{-1})	0.0289	0.0188
f_S (d^{-1})	0.0115	0.0069
P_S (d)	86.5 ± 9	143.3 ± 5.8
P_B/P_S	2.5 ± 0.27	2.7 ± 0.12
P_B/P_0	60.9	103.5

Table 6. Comparison of the overtone modes and the additional frequency of the two stars.

	CoRoT 105288363	V445 Lyr
f_2 (d^{-1})	2.9856	3.3307
$A(f_2)$ (mmag)	0.5	1.4
f_0/f_2	0.590	0.585
f_1 (d^{-1})	2.3793	2.6676
$A(f_1)$ (mmag)	0.3	2.7
f_0/f_1	0.741	0.731
f_N (d^{-1})	2.442	2.7719
$A(f_N)$ (mmag)	0.4	3.6
f_0/f_N	0.722	0.703

In CoRoT 105288363, there is no sign of period doubling, and no frequencies could be detected at or near the positions of the characteristic HIFs ($3f_0/2$, $5f_0/2$, etc.).

7 SUMMARY AND CONCLUSIONS

7.1 An unusual star with unusual phenomena

V445 Lyr is an RRab star with such a strong Blazhko modulation that at Blazhko minimum the peak-to-peak amplitude decreases down to 0.07 mag compared to approximately 1 mag during Blazhko maximum (a difference by a factor of 14), leading to the rather low overall amplitude A_1 of 0.18 mag.

The light curve around Blazhko minimum shows a strong distortion with a secondary maximum, making it impossible to even identify V445 Lyr as an RRab pulsator when observed only during Blazhko minimum.

In V445 Lyr the full variety of all the recently discovered new features in RR Lyrae stars – period doubling, strong irregular changes in the Blazhko effect, a secondary modulation, radial overtone pulsation and a non-radial mode – are combined in one single star. Therefore, it serves as an example of how ultraprecise and uninterrupted space photometry can change our view on seemingly well-known types of stars. The Fourier phases show an unusual behaviour which has not been detected before in an RR Lyrae star. Moreover, the distinct spikes in the temporal variation of the Fourier amplitude ratios are a previously unknown feature which is most likely caused by the pronounced double maximum at those phases.

7.2 Secondary modulation, irregular behaviour and long-term period change

In V445 Lyr, we find the most extreme variations of the Blazhko modulation known so far. This is partly, but not fully, explained by the secondary modulation of 143 d which we find in the *Kepler* data. Irregular/chaotic changes of the Blazhko modulation and/or even longer modulation periods also seem to be present, leading to a dense spectrum of peaks around the harmonics of the fundamental mode, in which with classical methods up to 771 frequencies would be found.

The amplitudes of the peaks connected to the secondary modulation were found to decrease less steeply with harmonic order than the components of the classical Blazhko multiplets. This interesting feature still awaits a physical explanation.

A long-term period change is also present, but it could not yet unambiguously be determined whether it is a periodic or a linear change (or neither). Future *Kepler* observations in the upcoming quarters will certainly reveal more about this long-term change.

7.3 Additional frequencies

We find at least four additional frequencies not connected to the fundamental mode, its harmonics and the Blazhko peaks. One of these peaks was interpreted as the second radial overtone, the second one could possibly be the first radial overtone, the third one was found to be due to period doubling and the fourth one was attributed to a non-radial frequency.

The second overtone is not always present during the observations. A strict dependence of the f_2 amplitude on the Blazhko phase could not be found. Instead, it seems to vary rather irregularly.

Amplitudes and frequencies of all additional peaks change notably during the time span of the data. It is possible that fluctuations in the frequency values of f_1 lead to transient resonances which temporarily excite the second overtone.

The additional peaks form numerous combinations with f_0 and the Blazhko multiplets (including quintuplet peaks) and also with the peaks belonging to the secondary modulation, indicating that they are all intrinsic to the target. Altogether, 80 peaks were found above the significance level at or near the combinations of those four frequencies with the other intrinsic frequencies of the target.

7.4 Spectroscopy, Petersen diagrams and an alternative method of light-curve analysis

Spectroscopy with the Keck telescope revealed a metallicity of [Fe/H] $= -2.0 \pm 0.3$, and Petersen diagrams based on linear pulsation models point towards a mass of 0.55–0.65 $M_\odot$ and a luminosity of 40–50 $L_\odot$.

We also applied the new analytic modulation technique to the light curve, and found that the best model contains a sinusoidal AM, a non-sinusoidal FM and a sinusoidal AM for the secondary modulation. Due to the migration of a strong bump feature and due to the irregular/stochastic changes, however, the method faces troubles similar to that of Fourier analysis.

7.5 Comparison with another peculiar star

A revisit of the data on CoRoT 105288363 revealed a secondary modulation period with a similar period ratio (2.5) with the primary modulation period as V445 Lyr (2.7).

The new analysis of the CoRoT 105288363 data also points towards the excitation of more additional modes than the previously published second overtone. A non-radial mode as well as the first overtone might also be excited.

V445 Lyr also shows a change in the phasing of the two types of modulation (amplitude and phase modulation), similar to what was observed in CoRoT 105288363.

ACKNOWLEDGMENTS

Funding for this discovery mission is provided by NASA's Science Mission Directorate. EG acknowledges support from the Austrian Science Fund (FWF), project number P19962-N16. KK is presently a Marie Curie Fellow (IOF-255267). The research leading to these results has received funding from the European Commission's Seventh Framework Programme (FP7/2007-2013) under grant agreement no. 269194 (IRSES/ASK). RSz and JMB are supported by the Lendület programme of the Hungarian Academy of Sciences

and the Hungarian OTKA grants K83790 and MB08C 81013. RSz was supported by the János Bolyai Research Scholarship of the Hungarian Academy of Sciences. C-CN thanks the funding from the National Science Council (of Taiwan) under the contract NSC 98-2112-M-008-013-MY3. We acknowledge the assistance of the queue observers, Chi-Sheng Lin and Hsiang-Yao Hsiao from the Lulin Observatory, and we thank Jhen-kuei Guo and Neelam Panwar for coordinating observations at the Tenagra II Observatory. JGC and BS are grateful to NSF grant AST-0908139 for partial support. Support for MC is provided by the Ministry for the Economy, Development, and Tourism's Programa Inicativa Científica Milenio through grant P07-021-F, awarded to The Milky Way Millennium Nucleus; by Proyecto Basal PFB-06/2007; by FONDAP Centro de Astrofísica 15010003; by Proyecto FONDECYT Regular #1110326; and by Proyecto Anillo ACT-86. The authors gratefully acknowledge the entire *Kepler* team, whose outstanding efforts have made these results possible.

REFERENCES

Alcock C. et al., 2003, ApJ, 598, 597
Arellano Ferro A., Bramich D. M., Figuera Jaimes R., Giridhar S., Kuppuswamy K., 2012, MNRAS, 420, 1333
Asplund M., Grevesse N., Sauval A. J., Allende Prieto C., Kiselman D., 2004, A&A, 417, 751
Asplund M., Grevesse N., Sauval A. J., Scott P., 2009, ARA&A, 47, 481
Benkő J. M. et al., 2010, MNRAS, 409, 1585
Benkő J. M., Szabó R., Paparó M., 2011, MNRAS, 417, 974 (B11)
Bertin E., Arnouts S., 1996, A&AS, 117, 393
Blazhko S. N., 1907, Astron. Nachr., 175, 325
Buchler R., Kolláth Z., 2011, ApJ, 731, 24
Carretta E., Bragaglia A., Gratton R., D'Orazi V., Lucatello S., 2009, A&A, 508, 695
Catelan M., 2009, Ap&SS, 320, 261
Çelik L. et al., 2012, preprint (arXiv:1202.3607)
Chadid M. et al., 2010, A&A, 510, 39
Christiansen J. L. et al., 2011, Kepler Data Characteristics Handbook (KSCI-19040-002). NASA Ames Research Center, Moffett Field, CA
Dziembowski W., Cassisi S., 1999, Acta Astron., 49, 371
Grevesse N., Noels A., 1993, in Prantzos N., Vangioni-Flam E., Casse M., eds, Origin and Evolution of the Elements. Cambridge Univ. Press, Cambridge, p. 15
Guggenberger E., Kolenberg K., Chapellier E., Poretti E., Szabó R., Benkő J. M., Paparó M., 2011, MNRAS, 415, 1577
Haas M. et al., 2010, ApJ, 713, L115
Jenkins J. M. et al., 2010, ApJ, 713, L87
Jurcsik J. et al., 2005, A&A, 430, 1049
Jurcsik J. et al., 2008, MNRAS, 391, 164
Jurcsik J. et al., 2009, MNRAS, 400, 1006
Jurcsik J. et al., 2012, MNRAS, 423, 993
Koch D. G. et al., 2010, ApJ, 713, L79
Kolenberg K. et al., 2009, MNRAS, 396, 263
Kolenberg K. et al., 2010, ApJ, 713, 198
Kolenberg K. et al., 2011, MNRAS, 411, 878
Kolláth Z., Molnár L., Szabó R., 2011, MNRAS, 414, 1111
Kukarkin B. V., Kholopov P. N., Kukarkina N. F., Perova N. B., 1973, Inf. Bull. Var. Stars, 834, 1
Landolt A. U., 2009, AJ, 137, 4186
Lenz P., Breger M., 2005, Commun. Asteroseismol., 146, 53
Nemec J. M. et al., 2011, MNRAS, 417, 1022
Ngeow C.-C., 2012, in Qian S., Leung K.-C., Zhu L., Kwok S., eds, ASP Conf. Ser. Vol. 451, The 9th Pacific Rim Conf. on Stellar Astrophysics, Astron. Soc. Pac., San Francisco, p. 103
Popielski B. L., Dziembowski W. A., Cassisi S., 2000, Acta Astron., 50, 491
Poretti E. et al., 2010, A&A, 520, A108
Reegen P., 2007, A&A, 467, 1353
Romano G., 1972, Inf. Bull. Var. Stars, 645, 1
Shapley H., 1916, ApJ, 43, 217
Smolec R., Moskalik P., 2008, Acta Astron., 58, 193
Smolec R., Moskalik P., Kolenberg K., Bryson S., Cote M. T., Morris R. L., 2011, MNRAS, 414, 2950
Sódor A. et al., 2011, MNRAS, 411, 1585
Sódor A. et al., 2012, preprint (arXiv:1201.5474v1)
Soszynski I. et al., 2009, Acta Astron., 59, 1
Soszynski I. et al., 2011, Acta Astron., 61, 1
Stothers R., 2006, ApJ, 652, 643
Szabó R., Kolláth Z., Buchler J. R., 2004, A&A, 425, 627
Szabó R. et al., 2010, MNRAS, 409, 1244
Szabó R. et al., 2011, MNRAS, 413, 2709
Szeidl B., Jurcsik J., 2009, Commun. Asteroseismol. 160, 17
Van Cleve J., Caldwell D. A., 2009, Kepler Instrument Handbook (KSCI 19033). NASA Ames Research Center, Moffett Field, CA
Van Hoolst T, Dziembowski W. A., Kawaler S. D., 1998, MNRAS, 297, 536

SUPPORTING INFORMATION

Additional Supporting Information may be found in the online version of this article:

Table 1. The scaled and detrended data set of V445 Lyr that was used for the analysis in this paper.

Please note: Wiley-Blackwell are not responsible for the content or functionality of any supporting materials supplied by the authors. Any queries (other than missing material) should be directed to the corresponding author for the article.

This paper has been typeset from a TEX/LATEX file prepared by the author.

共食いする「毒蜘蛛」中性子星

― 新種のパルサー発見に、日本の総力を結集 ―

日本天文学会2012年春季年会 記者発表資料

2012年3月19日、京都大学で行われた天文学会記者発表において、**東工大・早稲田大・国立清華大（台湾）による共同研究「共食いする毒蜘蛛中性子星」**を発表しました。

発表内容を簡単にまとめた事前配付資料: PDF (9.3MB)

発表のためのスライド: PDF (17.1MB)

研究の背景

フェルミガンマ線天文衛星が発見した正体不明の天体

日米欧が開発し、2008年に打ち上げられた「フェルミ」ガンマ線天文衛星（図1)は、非常にエネルギーが高く透過力の強い電磁波の一種「 ガンマ線 」を使って全天をくまなく探査しています。我々の目に見える「可視光」も電磁波の一種ですが、フェルミ衛星の観測するガンマ線は、それより100億倍以上高いエネルギーを持つ電磁波です。

このようなガンマ線を放射する天体では、電子や陽子などが非常に高いエネルギーにまで加速され「宇宙線」が作られていると考えられ、このメカニズムを解明することが現代の天体物理学における最も重要なトピックの一つになっています。この様な天体現象は、近年ヒッグス場(粒子)の解明に向け注目を集める大型加速器LHC/CERNを用いても到底実現することのできない、超高エネルギー・巨大かつ極限の物理現象です。

図1. フェルミガンマ線天文衛星(想像図/NASA)

フェルミ衛星の主検出器には日本の浜松ホトニクス社製の高性能半導体センサが使われており、そのガンマ線検出感度は過去の衛星に比べて圧倒的に高く、精細な画像を撮ることが出来ます(図2―左)。このおかげで、今まで知られていなかった「ガンマ線で明るく輝く」正体不明の天体が数多く発見されています。実際、フェルミの見つけたガンマ線天体の約3割が、未だなぞのまま残されているのです(図2―右)。これらの正体を解明すべく、私たちの研究グループは2009年からX線天文衛星「すざく」や地上望遠鏡を使ってガンマ線天体の詳細なフォローアップ観測を行ってきました。今回紹介する「毒蜘蛛中性子星」2FGL2339.6-0532も、その観測の一環で発見されました。

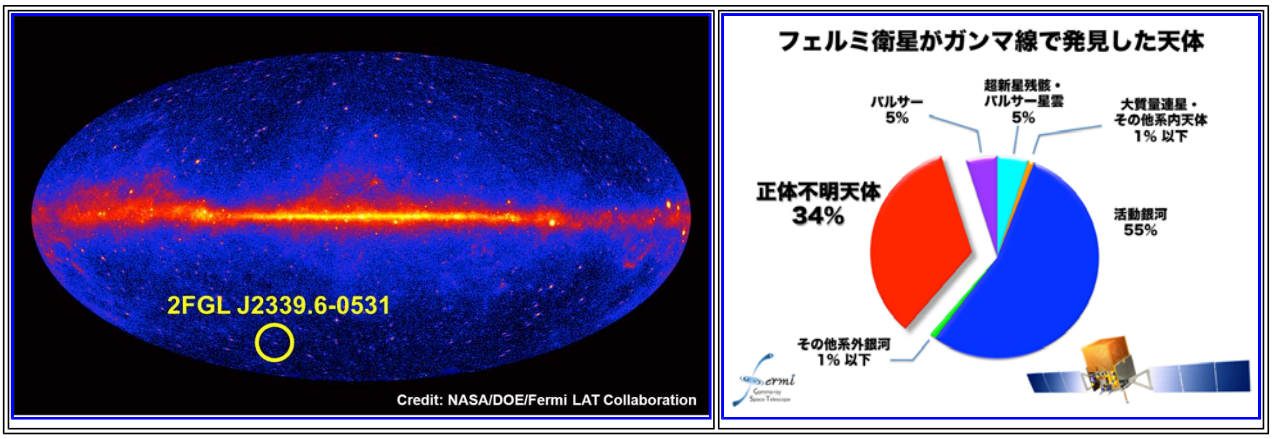

図2. (左)フェルミ衛星が観測したガンマ線による全天画像。黄色丸印が本研究の対応天体の位置を示す。(画像をクリックすると高解像度版を見られます。)

毒蜘蛛中性子星の発見前夜

正体不明の天体 2FGL2339.6-0532

今回ご報告するガンマ線天体 2FGL2339.6-0532 は、私たちの天の川銀河面から離れた位置にある明るいガンマ線源です(図2 黄色丸)。これは星座でいうと「みずがめ座」の方角にあたり、肉眼でみると星の少ない秋の天域に対応します。この天体への最初のアプローチは、米国のX線天文衛星「チャンドラ」を用いた正 確な位置決めから始まりました。チャンドラは1秒角(0.0003 度)という大変優れた解像度を持っており、フェルミの予想した天体位置の誤差円の中から、対応すると思われる 点光源を発見しました。この正確な座標情報を元に、国立清華大(台湾)・東工大・早稲田大を中心とする研究チームが可視光での追観測を行い、可視光対応天体の明るさが激しく変動していることを発見しました。さらに、国立清華大のKong教授らは鹿林(Lulin)天文台の1m望遠鏡を使い、その光度変動が4.63 時間の周期性を持つことを初めて捉え、この天体が二つの星がペアになって公転する「連星系」であることを明らかにしました。また、これらの可視光観測で我々が見たものは、この連星系を成している「伴星」の方であり、太陽の1/10 程度の小さな恒星らしいことがスタンフォード大学(米)のグループから報告されています。

日本の総力を結集して「相方」の正体を暴く

残る問題はこの連星系の主星の正体です。通常、太陽の 1/10 しかない小さな恒星がガンマ線でこれほど明るく輝くことはなく、ガンマ線は主星から放射されていると考えられます。これまでに観測されたガンマ線連星の多くは、中性子星もしくはブラックホールを主星としていましたが、チャンドラのX線データはどちらかと言えば 中性子星の特徴を備えています。しかしながら、高速で回転する中性子星(パルサー)に特有の「パルス放射」が電波で全く見られないことから、その正体は謎のままでした。そこで我々は日本の総力を結集してこの天体の謎に挑みました。

Limiting Magnitude and Sky Background Brightness Measurements at Lulin Observatory

Lin, Chien-Cheng, Yang, Ting-Chang, Daisuke Kinoshita, Chow-Choong Ngeow

Institute of Astronomy, NCU, Taiwan

ABSTRACT

The Lulin One-meter Telescope at Lulin Observatory in Taiwan is going to be used for the follow-up observations for the Pan-STARRS sky surveys. In order to evaluate the performance of the CCD photometric system and the characteristics and quality of the site, we have obtained the data of photometric standards as well as calibration data on 01 August, 2009. We report the results of our analysis, including sky background brightnesses and limiting magnitudes for $BVRI$ bands.

1. Introduction

Institute of Astronomy at National Central University (IANCU) is participating the Pan-STARRS[1](PS1) Science Consortium, and will be able to access the data of PS1 sky surveys. In order to achieve our scientific goals, immediate and intensive follow-up observations are necessary. The Lulin Observatory (Longitude = $120°52'25''E$, Latitude = $23°28'7''N$ and at a height of 2862 m above sea level) is one of the best sites for following up the PS1 sky survey. Because of its location, there is no other observatory join PS1 project between Hawaii and Europe. Besides, the latitude of Lulin observatory is also comparable with Hawaii. On the other hand, we can propose as much time as we need since Lulin One-meter Telescope (LOT) is operated by IANCU.

Before scientific follow-up observations begin, it is extremely important to evaluate and calibrate the instrument of the observatory. The performance and characteristics of the imaging camera, which currently installed at LOT now, was done by Kinoshita et al. (2005); however, we have replaced a set of broadband filters in 2007. Moreover, a new set of SDSS like filters[2], g'-, r'-, i'-, z'-band, will be installed soon. Thus, we need to characterize the new photometric system , and measure the limiting magnitude of the imaging system as well as the sky background brightness of the site for the future follow-up observations.

[1]http://pan-starrs.ifa.hawaii.edu/public/

[2]http://www.sdss.org/dr7/instruments/imager/index.html#filters

2. Observation and Data Reduction

Photometric standard star field PG2213-006 (RA= $22^h16^m24^s$, Dec. = $-00°21'27''$) was observed at Lulin observatory with 1-m telescope using Bessell system B-, V-, R-, and I-band filters (Yang & Lin 2006) on 01 August, 2009. PI1300B CCD camera was used(1300 × 1340 pixels, $\sim 11'.0 \times 11'.0$ field of view). The CCD has a readout noise of 4.6 ± 0.5 e^- and a gain of 1.95 ± 0.02 e^-/ADU(Huang et al. 2008), and the plate scale is $0''.516$ pixel^{-1}. Flat-field exposures were obtained on the twilight sky. The seeing condition within this run of observation varied between $1''.8$ and $2''.3$, because of thin clouds sometimes appeared during observation, as compared to the average seeing at Lulin Observatory is $1''.59$ (Lin 2007).

There were 16 exposures of PG2213-006 in total. Pairs of two consecutive exposures were taken for B, V, R, I bands. Our observational strategy is suitable for calculating limiting magnitudes. The journal of observations is summarized in Table 1. The standard data reduction routines including bias and dark current subtraction and flat-field correction using an image-analysis software package IRAF(Image Reduction and Analysis Facility, provided and maintained by NOAO)(Tody 1986, 1993).

3. Photometric Calibration

We detected the point sources using "`source extractor`[3]"(Bertin & Arnout 1996) and measured positions and instrumental magnitudes. Then, we used the "`imwcs`" task of WCSTools[4] together with the USNO-B1.0 catalog (Monet et al. 2003) to convert the image coordinate system into world coordinate system. In order to compare our results of photometry with other instruments, we need to calibrate the magnitudes from instrumental system into the standard system. According to our observation schedule, half an hours interval and only one field observation, we could not have enough airmass information of different zenith distances to estimate the extinction

[3]http://sextractor.sourceforge.net/

[4]http://tdc-www.harvard.edu/software/wcstools/

Table 1. Journal of Photometric Observations of PG2311+006 FOV,

Observation Date	Filter	Airmass	Exposure Times [sec]	Seeing[arcsec]
2009 August 1	B	1.259/1.297	40×2/320×2	2.3/2.0
2009 August 1	V	1.267/1.338	20×2/160×2	2.1/1.9
2009 August 1	R	1.274/1.364	10×2/80×2	2.0/1.8
2009 August 1	I	1.280/1.386	20×2/160×2	1.8/2.0

coefficients. We, therefore, ignored the extinction coefficient term and color term of the transformation equations. We defined simple transformation equations for the conversions,

$$B_{\rm std} = B_{\rm inst} + \triangle_B, \quad (1)$$
$$V_{\rm std} = V_{\rm inst} + \triangle_V, \quad (2)$$
$$R_{\rm std} = R_{\rm inst} + \triangle_R, \quad (3)$$
$$I_{\rm std} = I_{\rm inst} + \triangle_I, \quad (4)$$

where $B_{\rm std}, V_{\rm std}, R_{\rm std}, I_{\rm std}$ are the standard magnitude, $B_{\rm inst}, V_{\rm inst}, R_{\rm inst}, I_{\rm inst}$ are the instrumental magnitudes, and $\triangle_B \sim 22.78, \triangle_V \sim 22.48, \triangle_R \sim 22.59, \triangle_I \sim 21.83$ are relative zero point magnitudes. 7 standard stars provided by Landolt (2009) were used to calibrate magnitudes.

4. Sky Background Brightness

We used the data taken on 01 August, 2009 to measure the sky background brightness. The moon phase was 10.1. During the observation, the moon was below the horizon, and the angular separations between the moon and our target field was 72 degrees. `Source extractor` were used to obtain the mean background values in each bands. Using the equations 1 to 4, we derived the magnitudes of sky background brightness in the standard system. The sky background brightness in BVRI bands are $B = 21.38 \pm 0.41$, $V = 20.14 \pm 0.26$, $R = 20.06 \pm 0.24$, and $I = 18.92 \pm 0.20$ mag arcsec^{-2}, respectively. Our results are slight different from Kinoshita et al. (2005) with, $B = 22.0, V = 21.3, R = 20.9$, and $I = 19.5$. Since we had narrow range of airmass ~ 1.30 in each bands, we ignored the airmass coefficients and color terms while we evaluated the transformation equations. Therefore, we believe the results are consistent with Kinoshita et al. (2005).

5. Limiting Magnitudes

The detection limit of the images can be estimated and/or measured in several ways: (1)Number of stars count with histogram (Gwyn 2008), (2)Magnitudes versus error of magnitudes (Gwyn 2008), (3)Differential magnitudes of two images (Ito 1998). The first method is very simple. The peak value of the histogram, where the star counts start to turn over, is a rough measure of the detection limit of the image. Figure 1 shows the number of stars count with histogram. Figure 2 shows estimated magnitude against magnitude errors using second method, a 10-sigma detection corresponds to a signal-to-noise ratio (S/N) of 10 and equal to a magnitude error of 0.1 magnitudes.

However, we used third method to evaluate the limiting magnitude. We identified the matching detection point sources with 2 consecutive exposure time images using "`match_2d`" package of

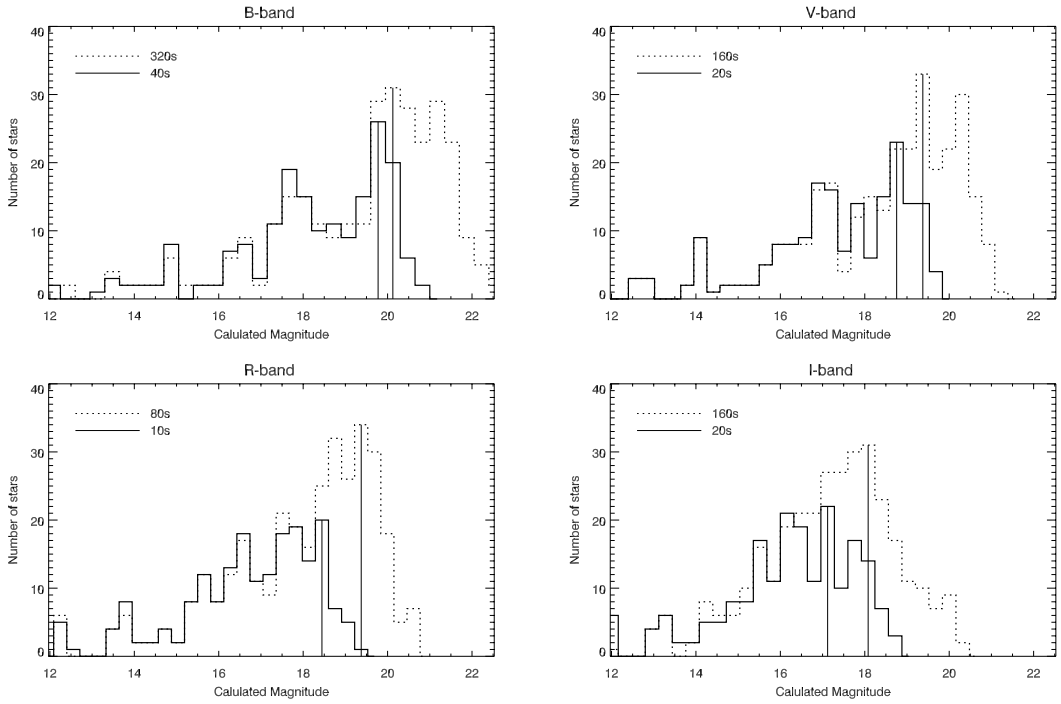

Fig. 1.—: Number of stars count with histogram for $BVRI$ bands. The dash lines show long exposure time, while the solid lines show short exposure time. Vertical solid straight lines indicate the maximum star count related the limiting magnitude.

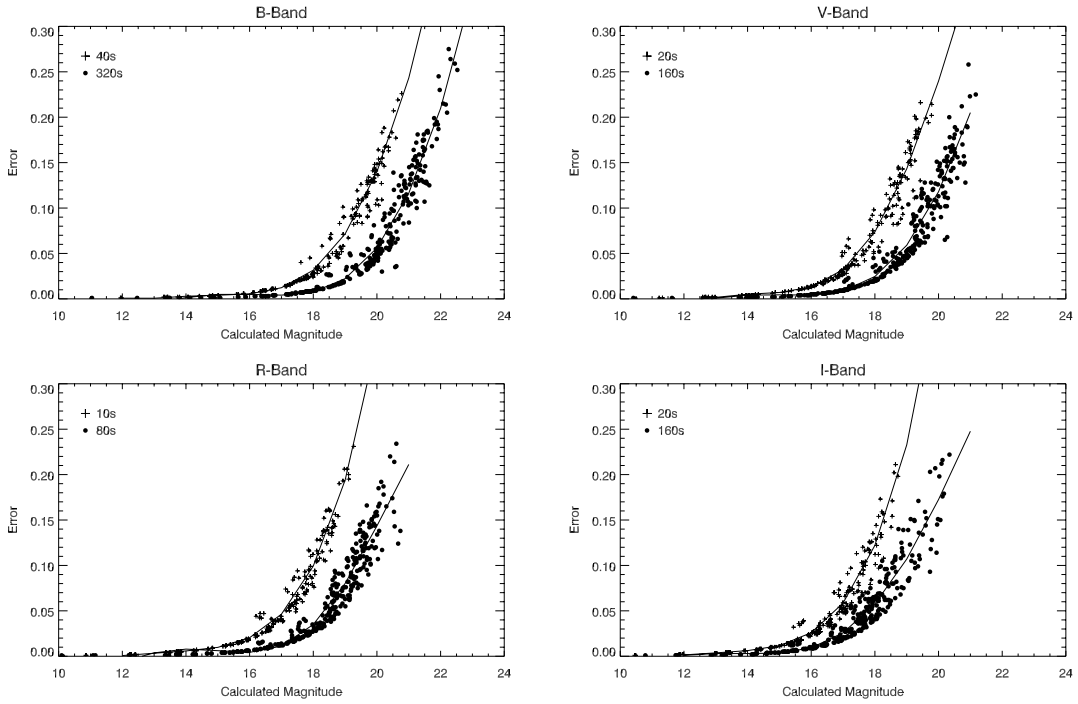

Fig. 2.—: Calculated magnitude using transformation equations versus magnitude errors for $BVRI$ bands. Crosses are short exposure time with 40, 20, 10, 20 seconds for BVRI band, respectively, while fill circles are long exposure time with 320, 160, 80, 160 seconds, respectively. The solid curves are fitted results to these data.

IDL 7.0[5] (Interactive Data Language). Since we observed two images within very short time intervals, we can ignore the systematic changes of observing conditions during the acquisitions of pairs of images. Considering the standard deviation of measured magnitudes are expressed as,

$$(m_1 - m_2)_{stddev} = \sqrt{\sigma_1^2 + \sigma_2^2} \sim \sqrt{2}\sigma, \tag{5}$$

where σ is the standard deviation of the measurement. Figure 3 to Figure 6 demonstrate calculated magnitudes against differential magnitudes. We estimated the limiting magnitude for S/N=10 or, equivalently, a differential magnitude error of 0.1 magnitudes. The results for $BVRI$ filters of different methods are shown in Table 2. Compare with the result of Kinoshita et al. (2005), their derived limiting magnitudes for slow readout mode are, $B = 21.4, V = 21.2, R = 21.1$, and $I = 19.9$ mag for the signal-to-noise ratio of 10 under the integration time of 300 sec and the aperture size of 3 arcsec.

We also used the CCD Equation (Massey 1990) as follow form,

$$\frac{\mathrm{S}}{\mathrm{N}} = \frac{N_{star}t}{\sqrt{N_{star}t + n_{pix}(N_{sky}t + N_{dark}t + N_{readout}^2)}}, \tag{6}$$

where S/N is signal-to-noise ratio, $N_{star}, N_{sky}, N_{dark}$, and $N_{readout}$ is the count rate per second, n_{pix} is pixel number within an aperture area, and t is the CCD integration time. Our results are $B = 21.2, V = 20.5, R = 20.4$, and $I = 19.6$ mag which are consistent with previous study.

6. Conclusion

One night observation data, 01, August 2009, was used to perform the analysis in sky brightness and limiting magnitudes. We derived simple transformation equations without considering the extinction coefficient and the relation of instrumental and standard colors. The sky background brightness seems consistent with five years ago. Three limiting magnitude evaluation methods are demonstrated, the differential magnitude method can be used to estimate the limiting magnitudes.

REFERENCES

Bertin, E. & Arnouts, S. 1996, A&A Supplement 317, 393

Gwyn S. D. J. 2008, PASP, 120, 212

Huang, H.F. , Kinoshita, D., and Shih, C.Y. 2008, JTAM Vol. 6, p. 18.

[5]http:// www.ittvis.com/

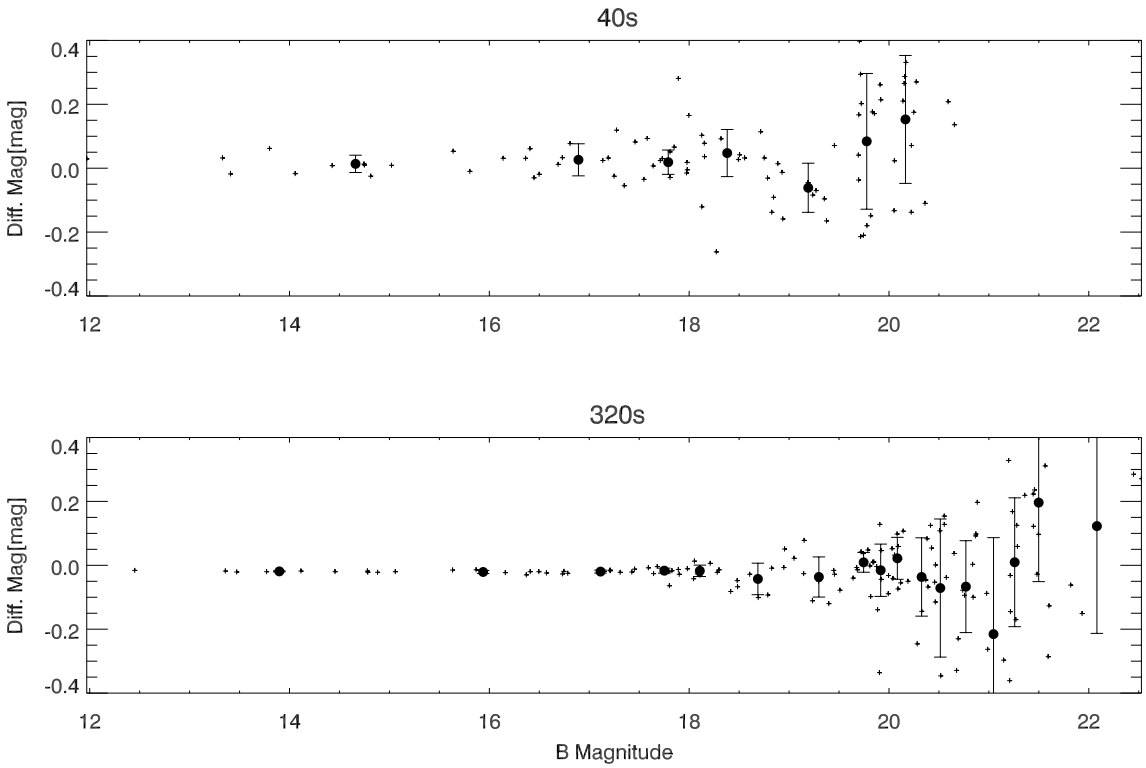

Fig. 3.—: Calculated B-band magnitude against differential magnitude with 2 images. The figure on the top is short exposure, and bottom one is long exposure. Solid circles are averages for each bin and with error bars.

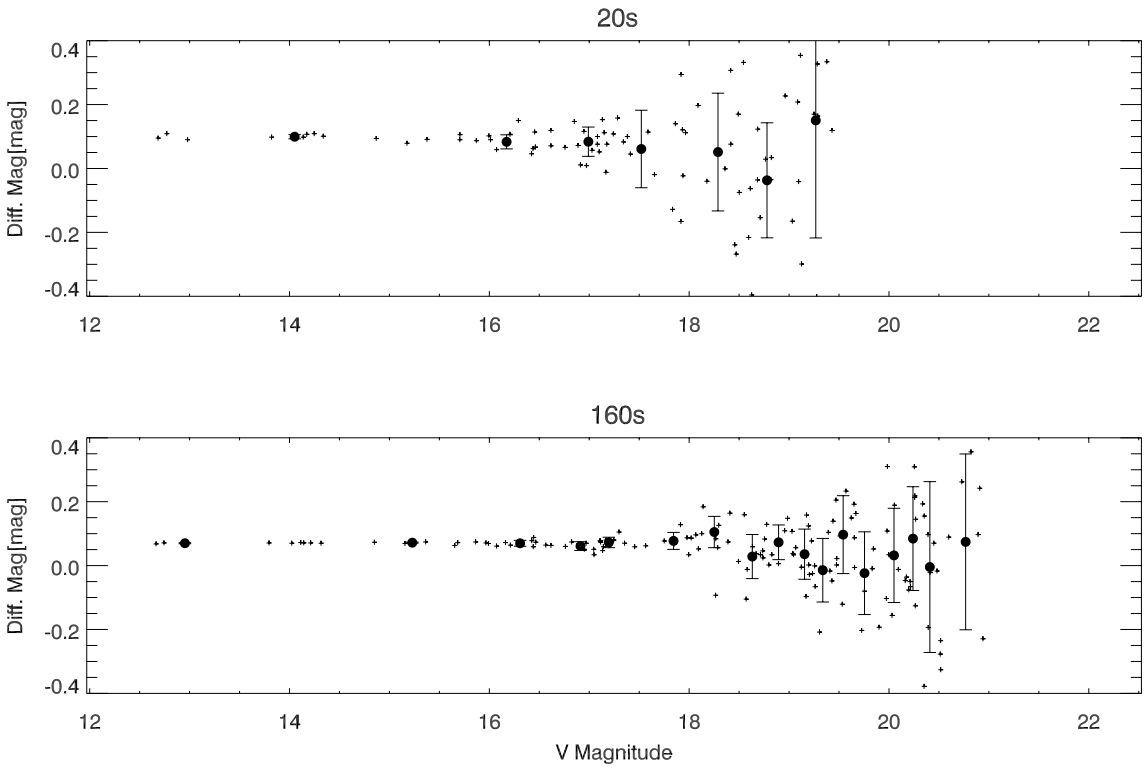

Fig. 4.—: Sampe as Figure 3, but for V-Band.

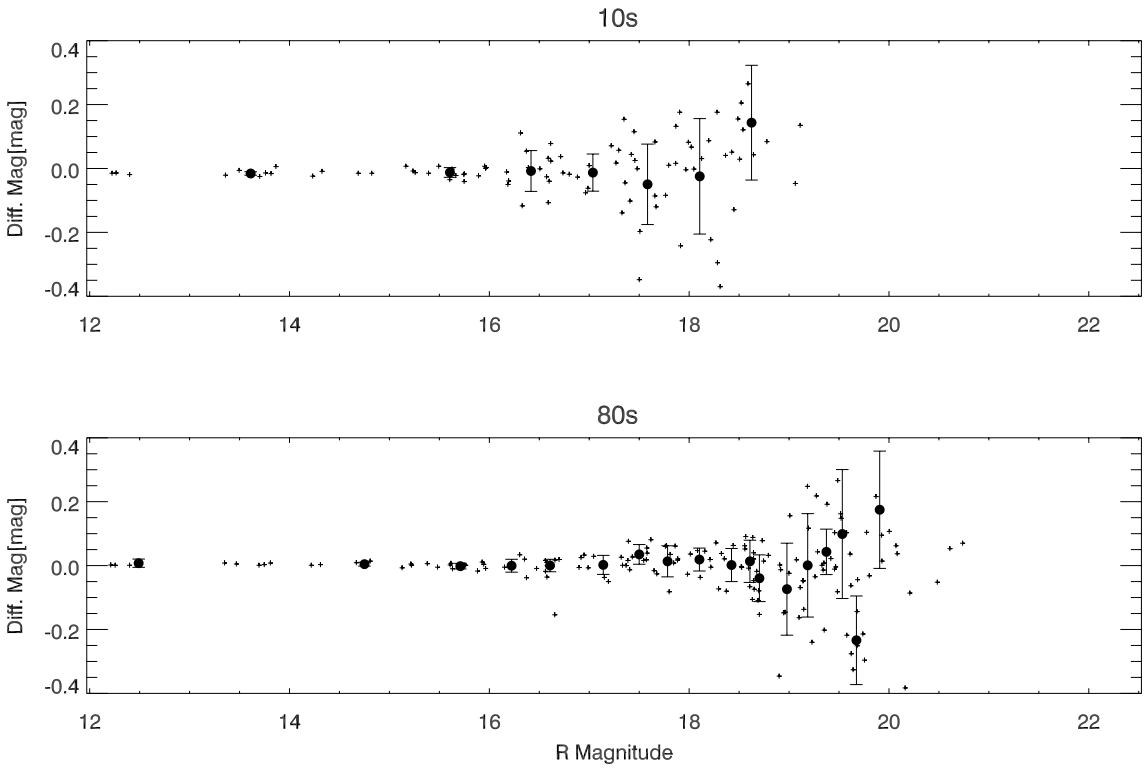

Fig. 5.—: Sampe as Figure 3, but for R-Band.

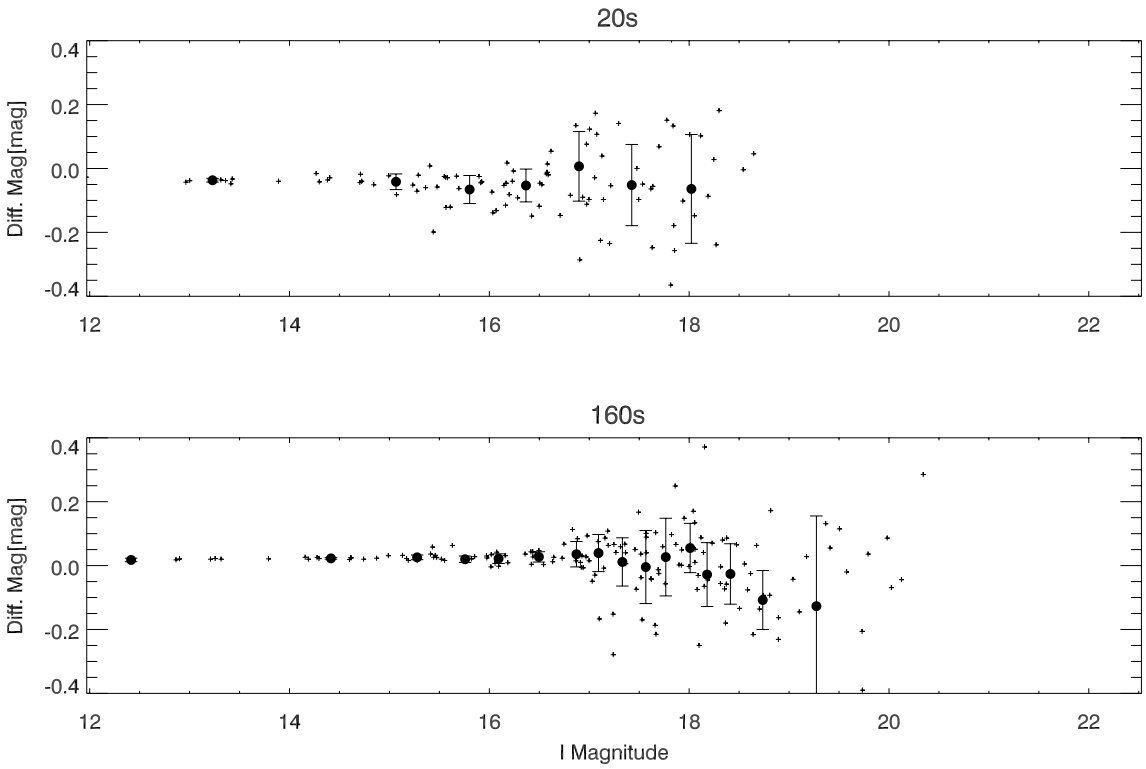

Fig. 6.—: Sampe as Figure 3, but for I-Band.

Ito Nobunari, 1998, Report of Kiso Observatory,
http://www.ioa.s.u-tokyo.ac.jp/kisohp/INSTRUMENTS/2kccd/reports/981126.ps

Kinoshita, D., Chen, C. W., Lin, H. C., Lin, Z. Y., Huang, K. Y., Chang, Y., & Chen, W. P. 2005, Chin. J. Astron. Astrophys., 5, L315

Landolt, A. U. 2009, AJ, 137, 4186

Lin, H.C. 2007, Annual Report of Lulin Observatory, edited by Chang, M.S., p. 72.

Massey, P. 1990, NOAO Newsletter, March, p. 16.

Monet, D., et al. 2003, AJ, 125, 984

Tody, D. 1986, "The IRAF Data Reduction and Analysis System" in Proc. SPIE Instrumentation in Astronomy VI, ed. D.L. Crawford, 627, 733

Tody, D. 1993, "IRAF in the Nineties" in Astronomical Data Analysis Software and Systems II, A.S.P. Conference Ser., Vol 52, eds. R.J. Hanisch, R.J.V. Brissenden, & J. Barnes, 173.

Yang, T.C., Lin, H.C. 2006, In: Chang M.S. ed., Annual Report of Lulin Observatory, (in Chinese), p. 67.

Table 2. Comparison of limiting magnitudes from the three methods mentioned in text.

Filter	Exposure Times [sec]	Number of Stars	Method 1[a] S/N=10	Method 2[b] S/N=10	Method 3[c] S/N=10
B	20	111	19.1mag	18.3mag	18.5mag
B	160	187	20.3mag	19.5mag	19.4mag
V	20	109	19.0mag	18.2mag	18.2mag
V	160	194	20.0mag	19.5mag	19.8mag
R	20	126	19.5mag	18.9mag	18.8mag
R	160	239	20.7mag	20.2mag	19.9mag
I	20	167	18.2mag	17.6mag	17.9mag
I	160	295	19.0mag	18.9mag	18.5mag

[a]Number of stars count with histogram

[b]Magnitudes versus error of magnitudes

[c]Differential magnitudes.

Reveal the magnetic structure in the filamentary cloud

Jia-Wei Wang and Shih-Ping Lai
Institute of Astronomy, NTHU

Recent Spitzer and Herschel survey discovered numerous filamentary clouds in the star forming regions throughout the Galaxy (Churchwell et al. 2009; Molinari et al. 2010). Stretching many parsecs in the sky, these filaments often encompass dense clumps that are fertile ground of massive star or cluster.

Filaments may form from compression of large scale convergent flows (Mac Low & Klessen 2004). However, strong magnetic fields could also modulate filament formation by allowing gas to collapse along the field lines (Ostriker et al. 2001). The newly released Herschel data have revealed the complex network of filaments within a cloud which favors the scenario that the filaments network are generated by large scale MHD turbulence and the filaments fragment in to prestellar cores by gravitational instability (Andre et al. 2010, Arzoumanian et al. 2011). On the other hand, recent magnetic field measurements with infrared and optical polarization show that the magnetic field are well perpendicular to the direction of filaments, which implies the magnetic field energy is larger than or at least comparable to the gravitational energy (Chapman et al. 2011, Sugitani et al. 2011), suggesting the magnetic field should play an important role in the formation of the filaments. Since only a few of the filamentary clouds have magnetic measurements, the question of how the filaments form still cannot be answered.

In order to reveal how magnetic field interacts with filamentary cloud, we have measured the morphology of magnetic field in the filamentary clouds Aquila Rift, IC5146 and L1455 on July 25-29, July 27, and Dec 12-16, 2012, respectively. The observations for Aquila Rift are weathered out, and the observations for L1455 also suffer weather problem. Here we show the results of the IC5146 filamentary cloud we observed in July, 2012 in Figure 1.

Figure 1 shows the polarization map we measured with TRIPOL of Lulin Observatory as well as the previous observations we obtained with ARIES Image Polarimeter (AIMPOL) in India toward the largest “sub-filament” (a branch extended from the main-filament) of IC5146. The large scale structure of magnetic field measured by TRIPOL is consistent with AIMPOL, which suggest the result is reliable. The results show that the magnetic field in the cloud is well paralleled to the filament, which is different from the B213 (Chapman et al. 2011), Serpens South cluster (Sugitani et al. 2011) and our own observation of IC5146 main-filament (Wang and Lai, in prep), where the magnetic field is perpendicular to filament. Since Herschel only finds a few starless core and no YSO in the sub-filament (Arzoumanian et al. 2011), the sub-filament should be relatively quiescent in IC5146.

Therefore, it is possible that this sub-filament is not gravitationally bounded and mass is still accreting along the magnetic field. Further observations in gas kinematics are necessary to prove this scenario.

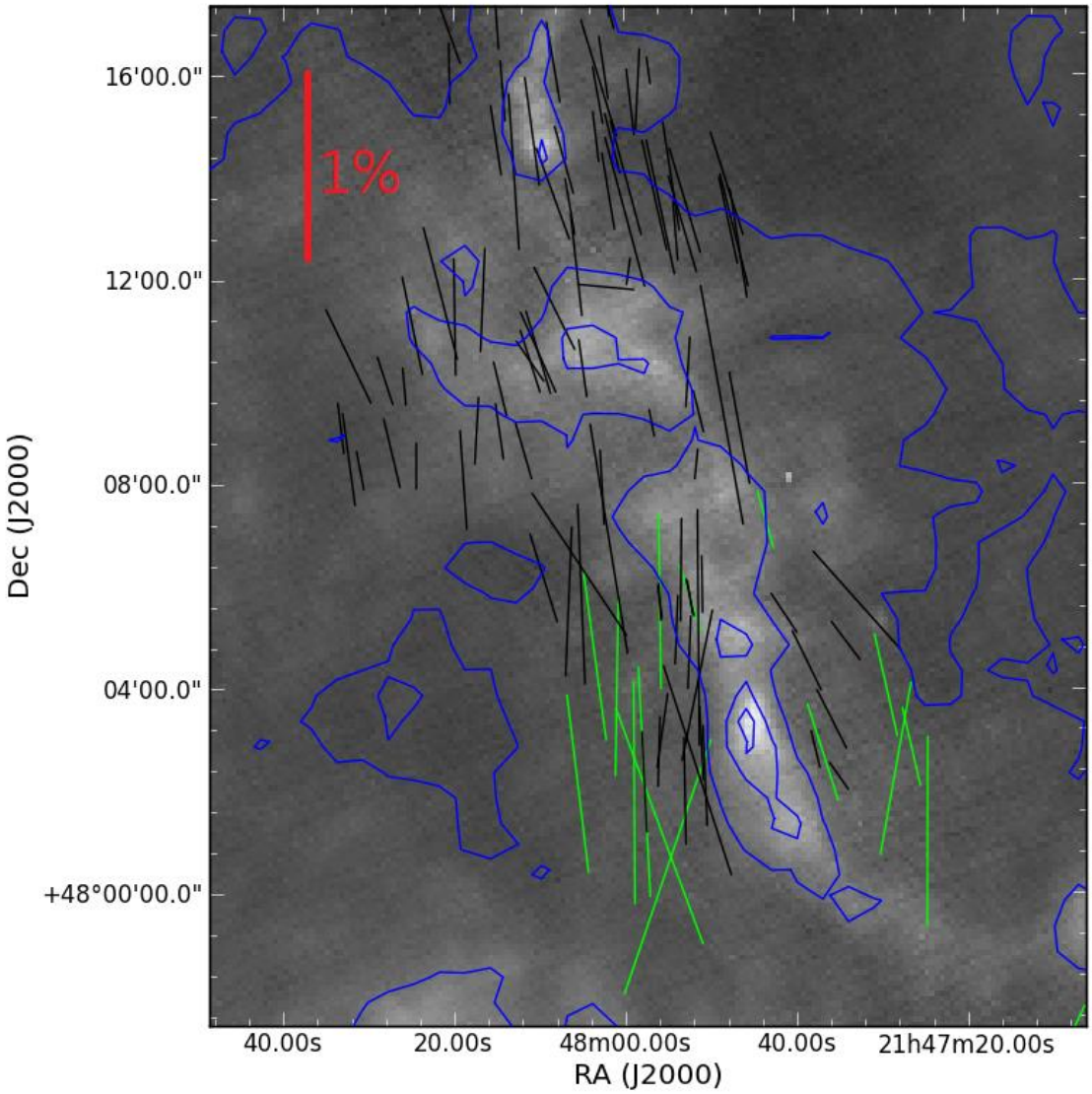

Figure 1 The polarization vectors in northern stream of IC5146 overlapped on Herschel 250 micron image. The black vectors are measured by TRIPOL in Lulin, and the green vectors are by AIMPOL in ARIES.

Reference

Arzoumanian et al. 2011

Andre et al. 2010

Chapman et al. 2011

Churchwell et al. 2009

Mac Low & Klessen 2004

Molinari et al. 2010

Ostriker et al. 2001

Sugitani et al. 2011

NEA Photometry Observations of Lulin

Lin, Chien-Hsien[1]; Lin, Zhong-Yi[2]; Ip, Wing-Huen[1, 2]

1. Space Science Institute, Macau University of Science and Technology
2. Graduate Institute of Astronomy, National Central University

Due to the lack of physical information of Near-Earth Asteroids (NEAs), we focus on the photometry observations of them both by LOT and SLT. The goal is to derive the rotation periods of some notable targets and the color survey for recent observable NEAs. Below we just display part of our results and the publication of two to three papers for the lightcurves and color measurement of the NEAs is in progress.

A. Differential Photometry of clear filter by SLT

Figure 1 shows the fitted rotation phase lightcurves of two NEAs, 2011 YV15 and 2006 VY13 by the method of Lomb-Scargle algorithm. The rotation period of 2011 YV15 is estimated to be 2.858 hrs from our result. It is only about 0.3% different between the value derived by Skiff, B.A., 2012 which is 2.848 hrs. This rotation rate indicates that 2011 YV15 is a fast rotator, close to the cutoff of about 2 hours. The rotation period of 2006 VY13 is estimated to be 17.375 hrs. It is obvious this asteroid has a large magnitude variance of about 1.2 value. We infer that it might be a binary asteroid. However we still need more observations to verify.

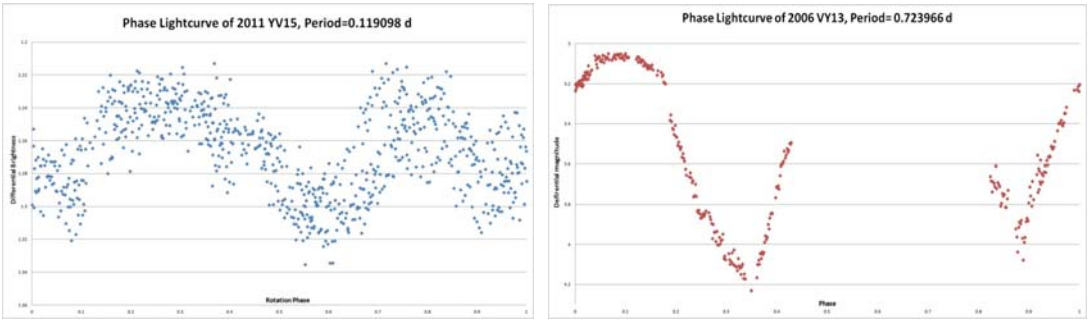

Figure 1: The left is folded phase lightcurve of NEA 2011 YV15 observed on Mar. 17, 18 and the right is the one of 2006 VY13 observed on Mar. 18, 19, 21, 23.

B. BVRI photometry of the NEAs by LOT

Figure 2 shows the color measurements of the NEA 297274 in three different time on May 22. We can see that there's an apparent color variance especially in B-V index. The mean value of is 0.743 for B-V, 0.486 for V-R, and 0.331 for R-I. Figure 3 shows the rotation phase lightcurve of 297274 based on the data on May 22 and 23. The rotation period is estimated to be 4.656 hrs. The amplitude of magnitude is about 0.44 which indicates the ratio of the long axis to short axis (a/b) is about 1.50.

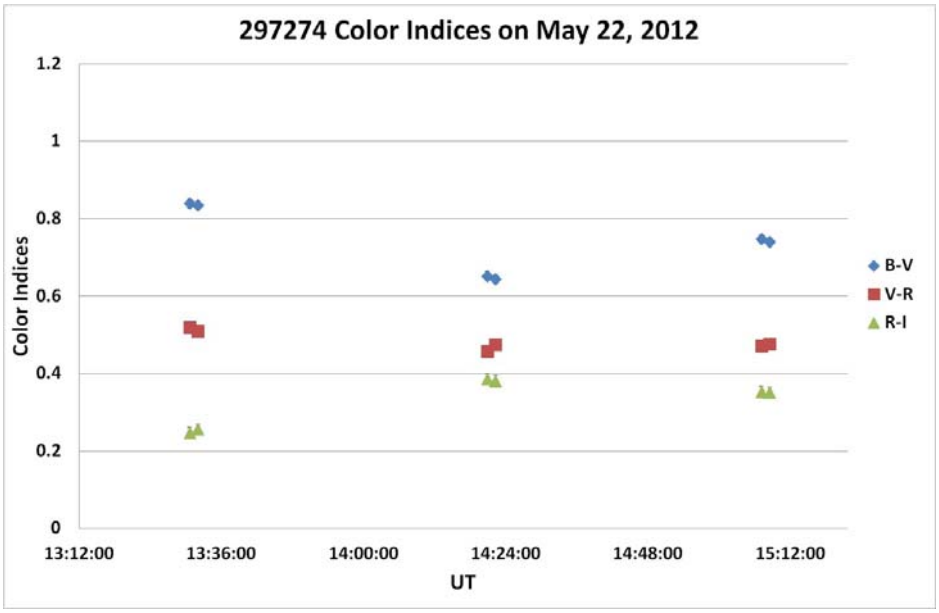

Figure 2: The diagram of three color indices of NEA 297274 measured in different time on May 22. The biggest variance in B-V is about 0.2.

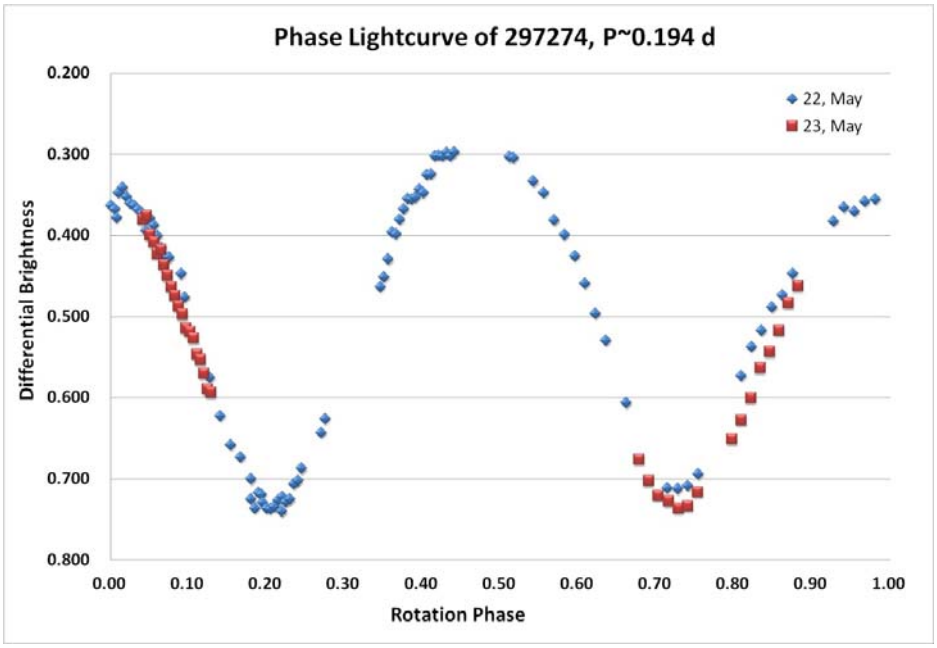

Figure 3: The folded phase lightcurve of 297274 from the data on May 22 and 23.

木曽KWFC超新星探査プロジェクトKISS プレスリリース 2012/06/27

最終更新日 2012/06/26

「木曽シュミット望遠鏡超広視野CCDカメラKWFCでの超新星発見」

- 会見日時: 2012年6月27日(水) 11:00 - 12:00
- 会見場所: 長野県木曽合同庁舎内
  長野県木曽郡木曽町福島2757-1
  http://www.pref.nagano.lg.jp/xtihou/kiso/index.htm
- 出席者:

諸隈 智貴 (東京大学大学院理学系研究科天文学専攻　助教)
酒向 重行 (東京大学大学院理学系研究科天文学専攻　助教)
三戸 洋之 (東京大学大学院理学系研究科天文学専攻　特任研究員)

発表概要

非常に重い星や、連星の一部は、その一生の最期に超新星爆発と呼ばれる大爆発を起こします。宇宙に存在する元素の多くは、超新星爆発の際に生成されたと考えられており、宇宙全体の進化を担ってきた重要な現象であるため、近年、世界中の多くの研究機関で、超新星をターゲットとした観測が行われています。

しかし、これまで可視光で爆発の「瞬間」であるショックブレイクアウト現象を捉えた観測例はなく、爆発の詳細なメカニズムや、爆発直前の星の姿は未解明のままです。

東京大学大学院理学系研究科附属天文学教育研究センター木曽観測所を中心とする、甲南大学、国立天文台、ロチェスター工科大学、広島大学、台湾国立中央大学らの研究者からなるグループでは、同観測所が新しく開発した超広視野CCDカメラKiso Wide Field Camera (KWFC)を用いた大規模な超新星探査プロジェクトKiso Supernova Survey (KISS)を2012年4月より開始しました。KISSプロジェクトの目的は、空の広い領域を一晩に複数回、頻繁に監視するという、他の超新星探査とは違う手法で、極めて稀な現象である超新星爆発の瞬間をとらえることです。既に3つの超新星爆発の発見に成功し、国際天文学連合(IAU)によりSN 2012cm、SN 2012cq、SN 2012ctと命名されました。今後予定している3年間の観測により、計100個以上の超新星を発見し、その中の数個の超新星に対しては、その爆発の瞬間をとらえることができる見通しです。また、KISSプロジェクトは、天文学に興味のある一般の方々との協力体制を組み、共同で研究を進めるという世界的にも珍しい試みを始めようとしている点も特徴です。

本発表では、KISSプロジェクトを開始したことをお知らせするとともに、最新の成果と期待される展開についてご報告いたします。

超新星とは

太陽の8倍以上の重さの星や、二つの星がお互いのまわりを回っている星(連星)の一部は、その一生の最期に超新星爆発と呼ばれる大爆発を起こし、太陽約5億個分もの明るさで数十日間輝きます。宇宙に存在する水素とヘリウム以外の元素の多くは、超新星爆発の際に生成されたと考えられており、宇宙全体の進化を担ってきた重要な現象です。

超新星研究の意義

超新星爆発は、そこに星が存在していたことを示す直接の証拠です。私たちの住む天の川銀河やお隣のアンドロメダ銀河のような一部の銀河を除くと、個々の星は暗いため、一つ一つ調べることは難しく、明るく輝く超新星爆発の観測が重要になります。しかし、これまで可視光で爆発の「瞬間」であるショックブレイクアウト現象を捉えた観測例はなく、爆発の詳細なメカニズムや、爆発直前の星の姿は未解明のままです。ショックブレイクアウト現象とは、超新星爆発の瞬間に星内部で発生した衝撃波が、星の表面を通過する際に、急激に、わずか数時間の間、明るく青く(高温)輝く現象です(図1、図2)。爆発の瞬間の超新星の光は、多くの情報を私たちに与えてくれます。例えば、通常は測定することが難しい、爆発前の星の大きさをより正確に求めることができるようになり、星の一生のより正確な理解が可能となります。また、2011年のノーベル物理学賞の受賞理由となった、宇宙の加速膨張の発見に使われた種類の超新星(Ia型; いちえーがた)の爆発の瞬間の光は、いまだ不明な爆発前の連星の正体を知る手がかりになります。

超新星探査KISSプロジェクト

東京大学大学院理学系研究科附属天文学教育研究センター木曽観測所(以下、東京大学木曽観測所)を中心とする、甲南大学、国立天文台、ロチェスター工科大学、広島大学、台湾国立中央大学らの研究者からなるグループでは、この超広視野CCDカメラKiso Wide Field Camera (KWFC、図3)を用いた大規模な超新星探査プロジェクトKISSを2012年4月より開始しました。KISSプロジェクトの目的は、空の広い領域を一晩に複数回、頻繁に監視することで、極めて稀な現象である超新星爆発の、その爆発の瞬間であるショックブレイクアウト現象をとらえることです。

そこで、研究グループは、他の超新星探査とは手法を変え、一晩の間に1時間おきに空の同じ領域を監視する手法をとることにしました。超新星爆発は、普通の銀河では約100年に1度の頻度でしか起こらない稀な現象であるため、効率良く発見するためには、一度に大量の銀河を観測する必要があります。東京大学木曽観測所の開発したKWFCは、2度角四方の領域(満月16個分)を一度に観測することができる超広視野カメラであり、珍しい現象をとらえるのに最適なカメラです。

KISSプロジェクトの初期成果と今後の展望

2012年5月13日、諸隈 智貴 (東京大学)、冨永 望 (甲南大学)、田中 雅臣 (国立天文台)、森 健彰 (甲南大学)らがKISSプロジェクトにおける最初の超新星をかに座の方向に発見しました(図3)。木曽シュミット望遠鏡KWFC、および広島大学東広島天文台かなた望遠鏡での追加観測により、この天体は約4億光年先の超新星であることが判明し、国際天文学連合(IAU)へ報告し、2012年5月27日にSN 2012cmと命名されました(図4、図7)。この超新星は、発見時、爆発後約10日経過したものであることがわかりました。その後、報告したSN 2012cq (図5、図7、かに座の方向、約3億光年先、爆発約5日後の発見、かなた望遠鏡、台湾国立中央大学鹿林天文台1m望遠鏡、ガリレオ3.6m望遠鏡で追加観測)、SN 2012ct (図6、図8、ヘルクレス座の方向、約5億光年先、爆発約3日後の発見、台湾国立中央大学鹿林天文台1m望遠鏡、ガリレオ3.6m望遠鏡で追加観測)を含め、計3個の超新星の発見に成功しています。2012年秋の探査本格開始後、予定している3年間の観測により、合計100個以上の超新星を発見し、その中の数個の超新星に対しては、その爆発の瞬間をとらえることができる見通しです。また、木曽観測所におけるもう一つの大規模観測プロジェクトである天の川銀河面変光星探査でも、順調に未知の変光星が発見されつつあります。

また、KISSプロジェクトでは、天文学に興味のある一般の方々との協力体制を組み、共同で研究を進めるという世界的にも珍しい試みを始めようとしています。超新星発見までの過程において、研究グループでは、画像同士の引き算を行い、引き算画像上にうつっている天体、すなわち明るさの変化している天体を超新星候補とします。しかし、この引き算画像には、本物の超新星以外に、宇宙線や引き算のミス等の偽物が、本物の超新星よりも多く存在します。これらを人間の目でチェックし、本物だけを選び出す作業を、アマチュアチームによって行い、その結果を受けて、早急な追加観測を行うことを予定しています。

---> ページTopへ

画像

| 画像の使用について | お問い合わせ |

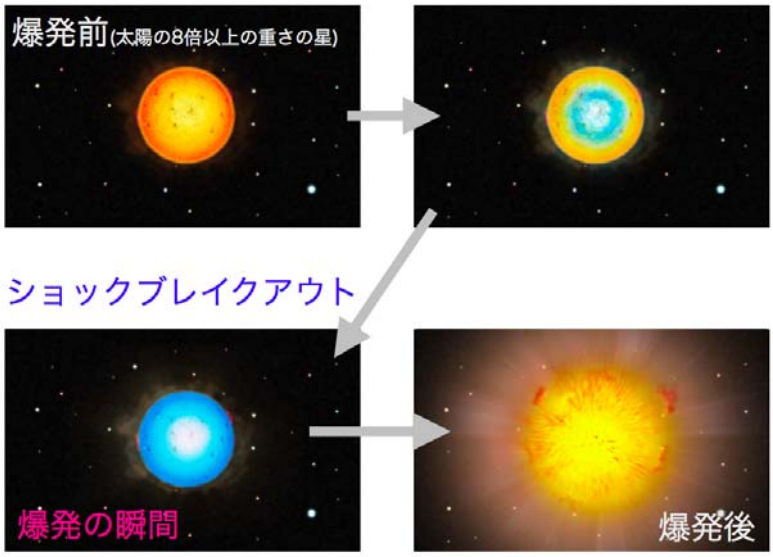

図1: 超新星ショックブレイクアウトの想像図 (高画質画像: 全体、左上[爆発前]、右上、左下[ショックブレイクアウト]、右下[爆発後])
爆発の瞬間は、爆発前の赤い星が急激に青く(高温に)明るく輝き、爆発後、徐々に赤く(温度が下がって)行きます。画像制作: 学術コミュニケーション支援機構。

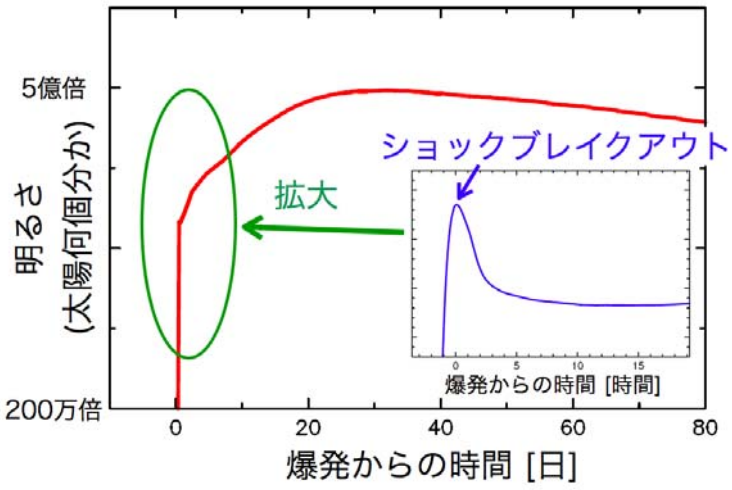

図2: 超新星ショックブレイクアウトの予想される明るさの変化(光度曲線) (画像)
赤い線は、これまでによく観測されている超新星の光度曲線。爆発の瞬間、ショックブレイクアウト現象により、わずか数時間明るく輝く時期(拡大図の青線)があると理論的に予想されています。

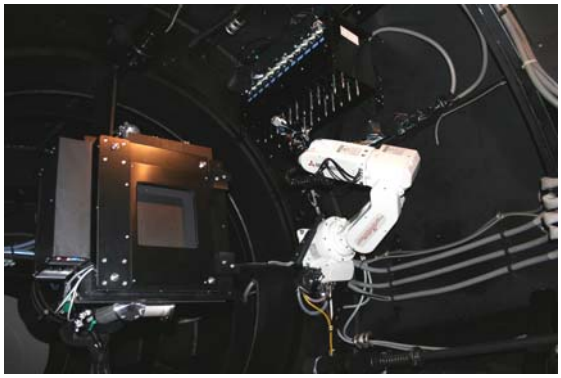

図3: KWFCの写真 (高画質画像)

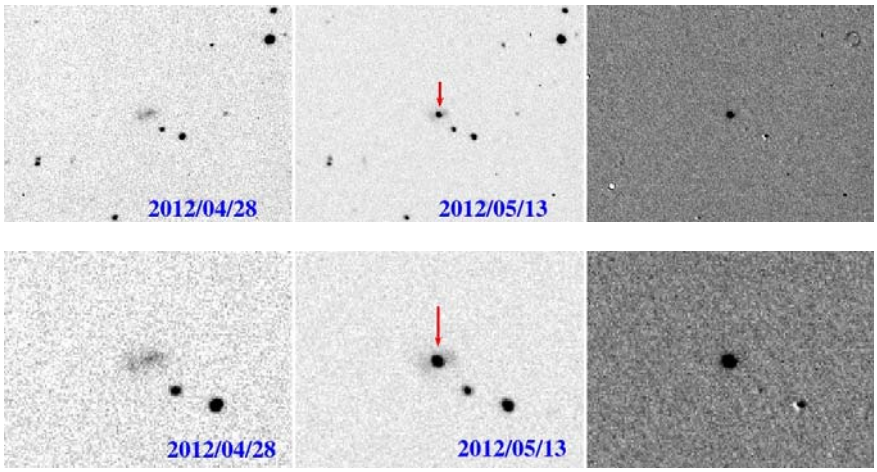

(拡大図)

図4: SN 2012cmの発見。左から順に2012年4月28日の画像、2012年5月13日の画像、これらを引き算した画像となっています。新しく明るく輝く天体が2012年5月13日の画像にはうつっており、引き算の画像にも残っていることがわかります。(高画質画像)

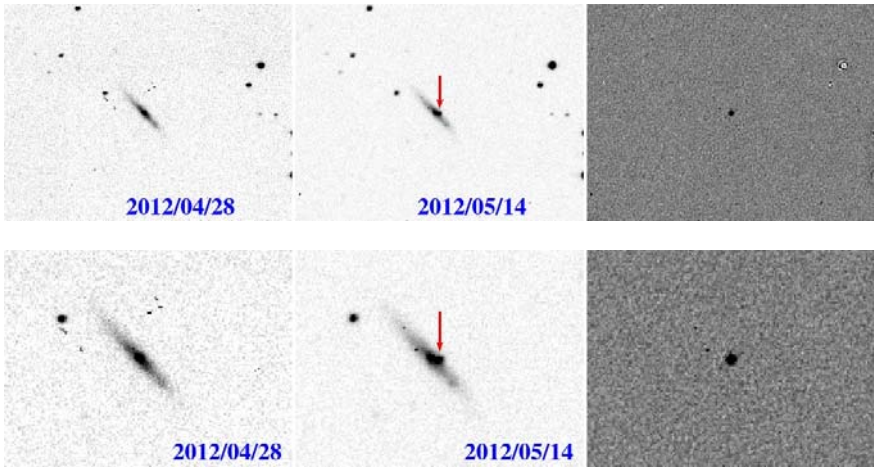

(拡大図)

図5: SN 2012cqの発見。左から順に2012年4月28日の画像、2012年5月14日の画像、これらを引き算した画像となっています。新しく明るく輝く天体が2012年5月14日の画像にはうつっており、引き算の画像にも残っていることがわかります。(高画質画像)

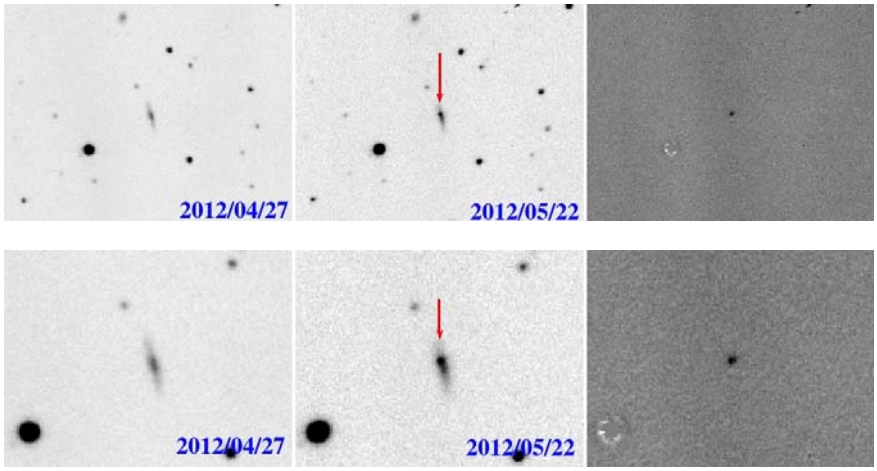

(拡大図)

図6: SN 2012ctの発見。左から順に2012年4月27日の画像、2012年5月22日の画像、これらを引き算した画像となっています。新しく明るく輝く天体が2012年5月22日の画像にはうつっており、引き算の画像にも残っていることがわかります。(高画質画像)

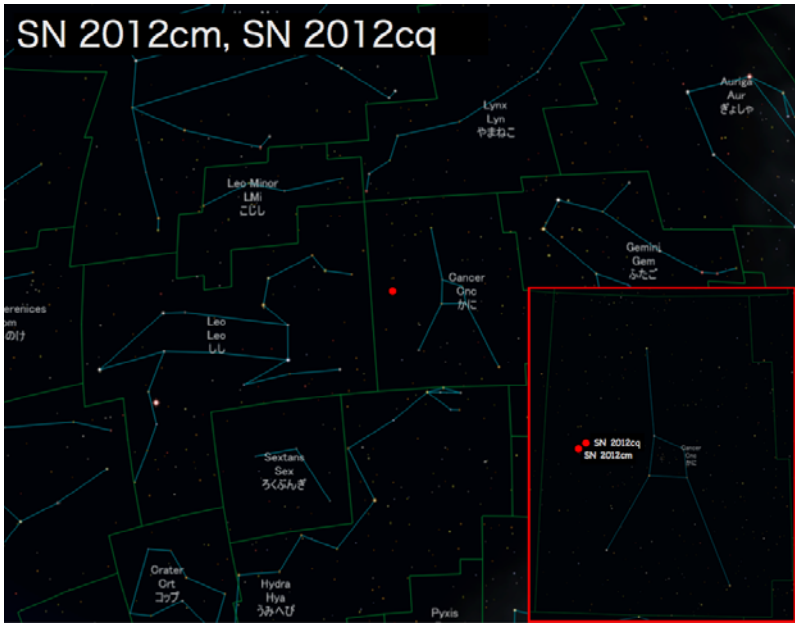

図7: SN 2012cm、SN 2012cqの位置。かに座の領域。(高画質画像)

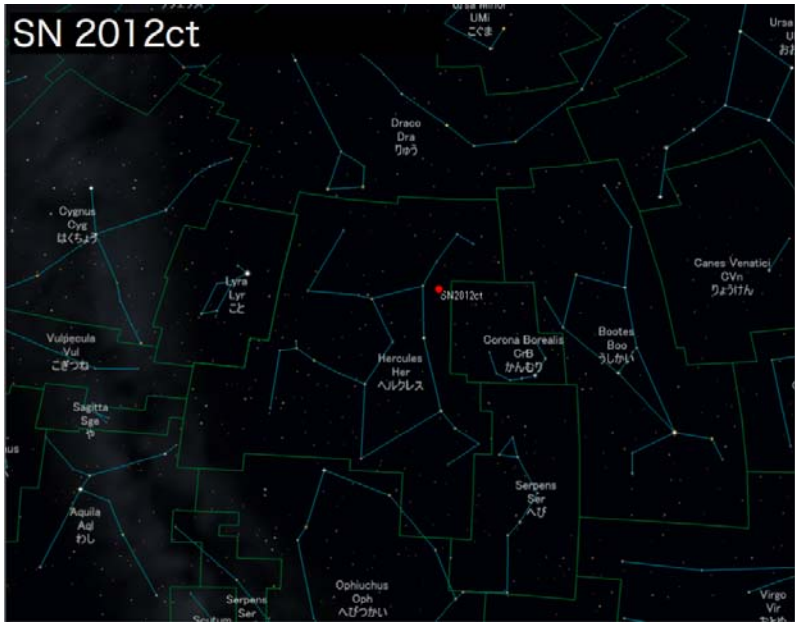

図8: SN 2012ctの位置。ヘルクレス座の領域。(高画質画像)

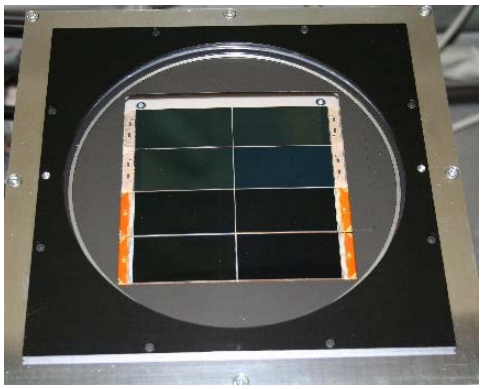

図9: KWFCに8個のCCDがモザイク状に並んでいる様子。(高画質画像, 約3MB)

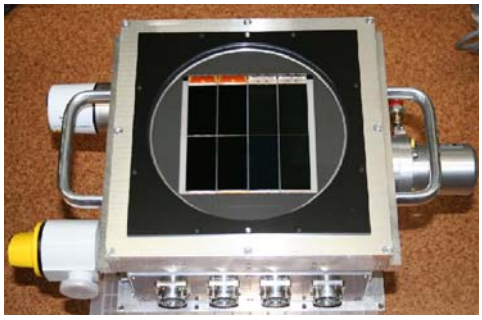

図10: KWFCの外観。(高画質画像, 約3MB)

---> ページTopへ

雑誌発表

International Astronomical Union Circular (国際天文学連合)

「Supernova 2012ct」, CBET 3145

発表日: 2012年6月19日

web:
http://www.cbat.eps.harvard.edu/iau/cbet/003100/CBET003145.txt
著者: 諸隈 智貴 (東京大学), 冨永 望, 森 健彰 (甲南大学), 田中 雅臣, 浮田 信治 (国立天文台), 酒向 重行, 松永 典之, 土居 守, 小林 尚人, 宮田 隆志, 家中 信幸, 中田 好一, 青木 勉, 征矢野 隆夫, 樽澤 賢一, 三戸 洋之 (東京大学), Michael W. Richmond (ロチェスター工科大学), 浦田 裕次 (台湾国立中央大学)

- 「Supernova 2012cq IN UGC 4792」, CBET 3139

発表日: 2012年6月13日
web:
http://www.cbat.eps.harvard.edu/iau/cbet/003100/CBET003139.txt
著者: 諸隈 智貴 (東京大学), 冨永 望, 森 健彰 (甲南大学), 田中 雅臣, 浮田 信治 (国立天文台), 酒向 重行, 松永 典之, 土居 守, 小林 尚人, 宮田 隆志, 家中 信幸, 中田 好一, 青木 勉, 征矢野 隆夫, 樽澤 賢一, 三戸 洋之 (東京大学), Michael W. Richmond (ロチェスター工科大学), 浦田 裕次 (台湾国立中央大学), 伊藤 亮介, 川端 弘治, 高木 勝俊, 上野 一誠, 秋田谷 洋 (広島大学)

- 「Supernova 2012cm」, CBET 3126

発表日: 2012年5月27日
web:
http://www.cbat.eps.harvard.edu/iau/cbet/003100/CBET003126.txt
著者: 諸隈 智貴 (東京大学), 冨永 望, 森 健彰 (甲南大学), 田中 雅臣, 浮田 信治 (国立天文台), 酒向 重行, 松永 典之, 土居 守, 小林 尚人, 宮田 隆志, 家中 信幸, 中田 好一, 青木 勉, 征矢野 隆夫, 樽澤 賢一, 三戸 洋之 (東京大学), Michael W. Richmond (ロチェスター工科大学), 伊藤 亮介, 川端 弘治, 高木 勝俊, 上野 一誠, 秋田谷 洋 (広島大学)

画像の使用について

クレジット: 東京大学
星図(図7、図8)は株式会社アストロアーツのステラナビゲータを使用しました。

問い合わせ先

東京大学大学院理学系研究科天文学専攻 助教
諸隈 智貴
e-mail: tmorokuma_atmark_ioa.s.u-tokyo.ac.jp ("_atmark_"を"@"で置き換えてください)
TEL: 0422-34-5049
FAX: 0422-34-5041

用語解説

- 超新星爆発:
英語ではsupernova(スーパーノヴァ)。太陽の8倍以上の重さの星や、二つの星がお

互いのまわりを回っている星 (連星)の一部がその一生の最期に起こす爆発現象。太陽約5億個分もの明るさで数十日間輝きます。

- KWFC:
東京大学木曽観測所の持つ105cmシュミット望遠鏡に取り付けられる超広視野CCDカメラ。Kiso Wide Field Cameraの略。2度角四方の領域(満月を縦横4個ずつ並べた広さ) を一度に観測することができます。
- 超新星の名前:
国際天文学連合(IAU)へ登録された超新星は、順番にSN 2012A、SN 2012B、…、SN 2012Z、SN 2012aa、…、SN 2012az、SN 2012ba、…と名前が付けられ、国際天文学連合電報中央局(CBET)により全世界へ周知されます。

関連リンク

- 木曽観測所
- KWFC
- International Astronomical Union Circulars (国際天文学連合回報)

---> ページTopへ

Development of Visible 4-color Simultaneous Imager "Dogioya" for Medium-sized Telescopes

Kinoshita Daisuke and Chen Tse-Chuan

March 2013

Abstract

In order to carry out immediate follow-up observations for new discoveries by large scale astronomical surveys, a visible 4-color simultaneous imager "Dogioya" has been developed. Three dichroic mirrors are used to split the beam from the telescope, and images at four different pass bands are recorded simultaneously by four CCD cameras. The main scope of this instrument is to conduct efficient and reliable color measurements of moving and transient celestial objects, such as asteroids and supernovae, even under relatively poor condition nights. Optical multi-band color information of an astronomical object right after its discovery is a clue for understanding the origin, physical properties, and chemical composition of the body. Visible 4-color simultaneous imager also improves the observing efficiency due to the fact that we are able to obtain the imaging data at different pass bands at the same time. We have successfully developed key components of the instrument, including a fully depleted CCD imager "NCUcam-1", and assembled the system in the laboratory. Four unit cameras, including "NCUcam-1" has been tested using existing 1-m telescope at Lulin observatory, and unit cameras have been characterized using the data both from the observatory and laboratory. The whole system of "Dogioya" is now ready to be tested with a telescope, and the shipping to Hawaii is planed this year for the test observation using 2.2-m telescope at the summit of Mauna Kea under the collaboration with University of Hawaii. We report the scientific objectives, design, development strategy, current status of the instrument, status of the instrumentation laboratory, testing and characterization of the instrument, and near-future plan for the first-light observation of the whole Dogioya system.

Key Words: Methods: observational – Instrumentation – Techniques: photometric

1 Introduction

Panoramic Survey Telescope and Rapid Response System (hereafter, Pan-STARRS) is an innovative and unique cyclical wide-field astronomical survey project (Kaiser 2004). A prototype telescope, PS1, is installed and being operated at the summit of Haleakala on Maui island of Hawaii (Fig. 1). It is a telescope with the aperture of 1.8-m. Thanks to three sets of corrector lenses, a wide field-of-view of three degrees in diameter is achieved. A dedicated imaging instrument, named Giga Pixel Camera (hereafter, GPC) is attached to the telescope (Fig. 2). GPC is an wide-field imager with 1.4 giga pixels which covers the entire region of the focal plane of PS1 telescope. CCD chips used for this instrument are orthogonal transfer CCDs. Orthogonal transfer CCDs are capable of moving electrical charges to neighbouring pixels in both vertical and horizontal directions during the exposure, and hence offer the on-chip guiding to improve the image quality. PS1 system is one of the most powerful observing facilities in the world to perform astronomical wide-field surveys. The official surveys of PS1 has started in May 2011, and this telescope is now being used to carry out a sky survey for 75% of the sky which is observable from Hawaii. It is the first trial to image such a wide area of the sky repeatedly in a sysmatic way. PS1 provides unique data sets for time-domain astronomy, and it opens new opportunities for knowing variable universe. Intensive studies on moving objects in solar system, such as asteroids and trans-Neptunian objects, and transient objects, such as supernovae, and gamma-ray bursts, are expected.

In order to maximize scientific outputs of PS1 sky surveys, quick follow-up observations are essential to investigate physical properties, chemi-

Figure 1: A photo of PS1 dome at the summit of Haleakala taken by Kinoshita Daisuke in November 2007.

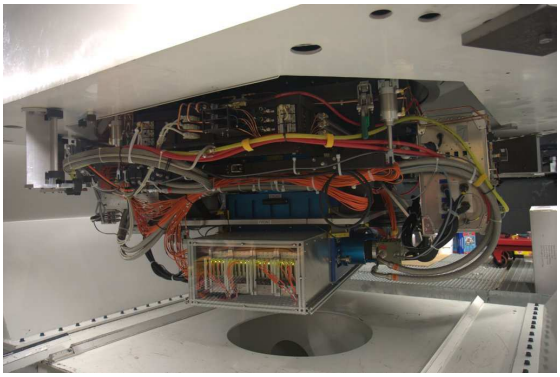

Figure 2: Giga Pixel Camera installed at PS1 telescope. This photo was taken by Kinoshita Daisuke in November 2007.

cal compositions, and origin of newly discovered objects and mechanisms of observed phenomena. Note that PS1 keeps observing wide area of the sky, and cannot focus on small number of celestial objects to monitor. Telescopes exclusively used for follow-up observations are highly needed. For our case, a new 2-m telescope is being constructed at Lulin observatory in Taiwan. The primary mirror has an effective aperture of 2.0-m. The diameter of 2.0-m is chosen to make us possible to observe majority of PS1 discovered objects in imaging mode. The mirrors are made of low thermal expansion glass of Astro-Sitall, and the protective layer of SiO is coated on the surface after the aluminizing of the mirrors. The optical system is a Ritchey-Chrétien, and the focal length of the system is 16.0-m for Cassegrain focus. This results in F/8, and it allows us to share some instruments with existing 1-m telescope at the same site. The mount of the telescope is alt-az mount. The expected image quality is 0.35 arcsec, and it is reasonably good considering a typical seeing condition of $\sim$ 1.5 arcsec at Lulin observatory. The pointing accuracy of 2 arcsec in RMS and tracking accuracy of 0.3 arcsec per 10 min are expected. The telescope is designed to have a maximum slew speed of 4 deg per second to enable efficient observations and quick response of sudden change of the observing plan. The telescope sometimes needs to do quick pointings right after the triggers of transient alert.

We have decided to build a visible 4-color simultaneous imager "Dogioya" for the 2-m telescope to carry out sophisticated follow-up observations for PS1 sky surveys. This report describes scientific objectives, design, development strategy, current status of the instrument, status of the instrumentation laboratory, testing and characterization of the instrument, and near-future plan for the first-light observation of the whole Dogioya system in following sections.

2 Visible 4-Color Simultaneous Imager "Dogioya"

A visible 4-color simultaneous imager "Dogioya" was selected to be the first generation instrument for the 2-m telescope. There are two reasons for this decision. First, the most important task of the 2-m telescope is to perform follow-up observations for celestial objects discovered by PS1 sky surveys. Then, majority of targets are (1) moving objects, such as asteroids, comets, and trans-Neptunian objects, and (2) transient objects, such as variable stars, supernovae, and gamma-ray bursts. Moving objects in solar system are irregularly shaped and are spinning in general. This fact suggests that these bodies change their cross-section and exhibit brightness variation. Color change may also be attributed to the rotation of the body and heterogeneity on the surface. Needless to say, transient objects change the brightness and/or colors by their nature. It means that we need to complete the brightness measurements at two or more pass bands for accurate color determination before those objects change their brightness in order to avoid false colors. Simultaneous measurements of brightness at two or more pass bands dramatically improve the quality of color measurements of variable targets. Second, Lulin observatory is not the world's best observing site, like Mauna Kea in Hawaii and high altitude desert in northern Chile. The sky condition at Lulin is often unstable and is variable within a night. We see occasional cloud passing, and only have limited number of photometric nights. The utilization of poor condition nights has to be well-considered, otherwise significant fraction of observing time may be wasted. Again, simultaneous imaging at multiple pass band provide us the data taken under exactly the same atmospheric transparency, and

make the photometric calibration easier. To summarize, target objects intrinsically change their brightness and the transparency of the sky changes within a night under the typical condition. We need to measure colors of a target accurately in this situation.

Reliable and efficient color measurements of celestial objects are achieved by simultaneous imaging using a set of dichroic mirrors. The beam from the telescope is split into two or more, and images at different wavelength regions are recorded exactly at the same time. In this way, derived colors are less affected by intrinsic variability of targets and change of atmospheric conditions. It also makes the calibration and data analysis easier under the assumption that the transmittance of the cirrus is neutral over the wavelength coverage of the instrument, and the use of the simultaneous imager increases the number of observable nights. Furthermore, the simultaneous imaging improves the observing efficiency of the telescope. In conventional method of multi-color photometry by exchanging filters, the total amount of observing time needed T_c is given by

$$T_c = (t_{exp} + t_{ro}) \times N_{band}, \quad (1)$$

where t_{exp} is the integration time necessary for each band, t_{ro} is the readout time, and N_{band} is the number of filters used. On the other hand, the total amount of observing time needed for simultaneous imaging T_s is shown by

$$T_s = \frac{t_{exp}}{E_{throughput}} + t_{ro}, \quad (2)$$

where $E_{throughput}$ is the throughput of the additional optics in the instrument. Substituting values of $t_{exp} = 60$ sec, $t_{ro} = 8$ sec, $N_{band} = 4$, then we obtain $T_c/T_s \sim 3.3$, and the simultaneous imaging is suggested to be about three times more efficient than the conventional observations. These advantages are critically important for the operation and scientific productivity of Lulin observatory.

2.1 Scientific Objectives

In astronomy, color measurements are often used to obtain the first look of the physical conditions and chemical composition of celestial objects. An example of scientific objectives of this instrument is the color measurements of asteroids. Some asteroids are known to be rocky composition and classfied as S-type asteroids. Some other asteroids are known to be carbonaceous composition and classified as C-type asteroids. The reflectance spectra for different types of asteroids differ due to the compositional differences of the surface (Fig. 3). Color measurements are a technique to do the taxonomic classification. It gives us a clue to understand the chemical composition, origin, and evolution of the body. It is essential to know the taxonomic type of the object to infer the origin and nature, when an asteroid with peculiar orbital properties is discovered. In addition, dozens of pairs and clusters of asteroids with extremely similar orbits have been identified recently. Color determination of pairs / clusters asteroids is useful to support (or deny) the common origin hypothesis (Kinoshita et al. 2007). Color measurements and successive classification are equally important for other classes of astronomical objects.

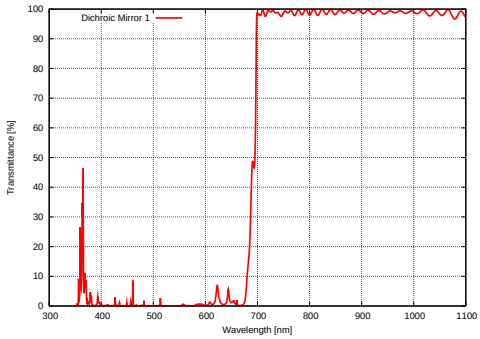

Figure 4: An example of transmittance curve of dichroic mirror. For this case, the light bluer than 700 nm is reflected on the surface of the dichroic mirror, and the light redder than 700 nm is transmitted. Hence, the beam from the telescope can be split into two components, and it allows us to have images of bluer band and redder band are recorded at the same time.

2.2 Conceptual Design

In a conventional method of color measurements, we image the target using a filter, then later reimage the same object using another filter. In this way, there is a time lag between two measurements at different wavelength. Our targets, transient objects and moving objects, change their brightness with time, and the conventional color measurements may produce false colors due to the time lag between exposures.

A different and new approach is proposed here. That is, accurate measurements can be achieved by observing the target at two or more different wavelength regions simultaneously. This is realized by beam splitting using dichroic mirrors. The dichroic mirror is an optical device that reflects the light shorter than the characteristic wavelength and transmits the light longer than the characteristic wavelength (Fig. 4). By using three dichroic mirrors and four bandpass filters and detectors,

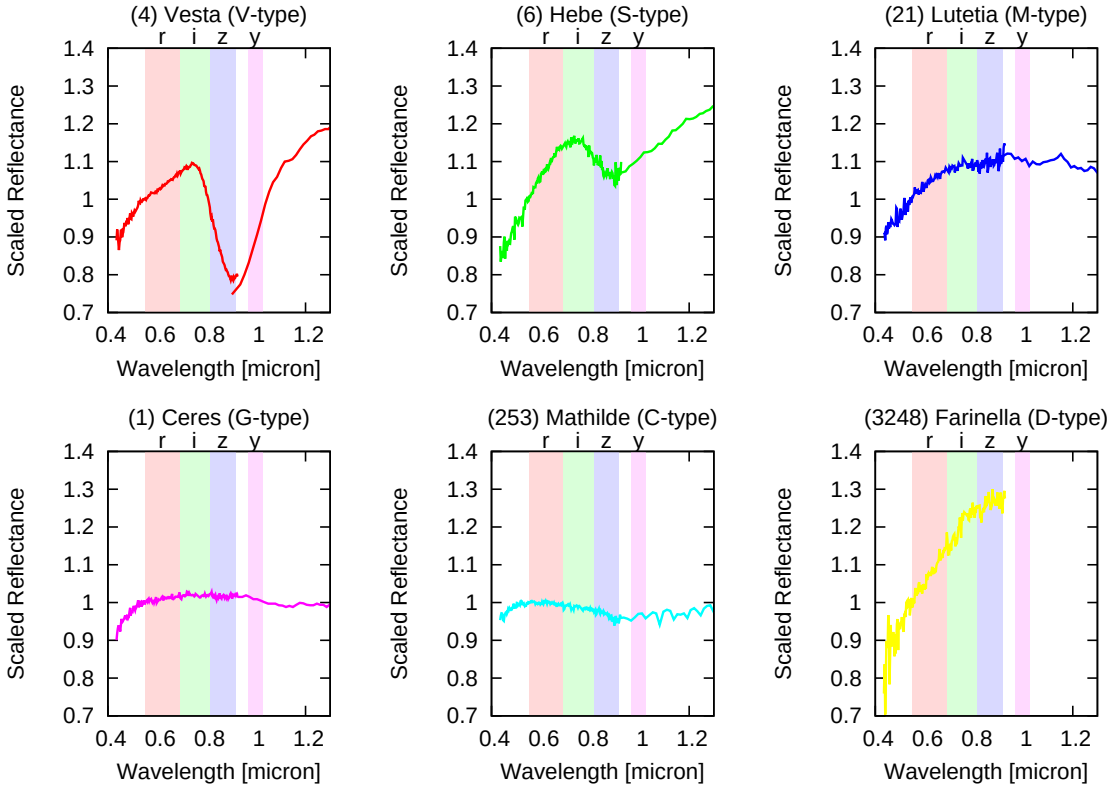

Figure 3: Typical spectra of major subclasses of asteroids. Rocky asteroids exhibit deep absorption band around 0.9-1.0 micron, while carbonanceous asteroids show rather flat reflectance spectra.

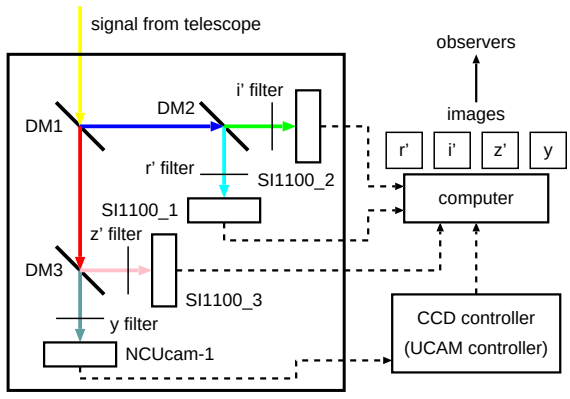

Figure 5: The conceptual design of the visible four-color simultaneous imager. Three dichroic mirrors, shown as DM1, DM2, and DM3, split the signal from the telescope into four, and four detectors acquire images at different wavelength regions at the same time.

one is able to measure the target flux at four different wavelength regions at the same time.

The conceptual design of the visible 4-color simultaneous imager is shown in Fig. 5. Three dichroic mirrors on the optical path split the light from the telescope into four components. These four beams pass through the bandpass filters (PS1 r', i', z', and y filters), and the signals are received by four detectors at the same time. In order to combine data both from PS1 in Hawaii and the 2-m telescope in Taiwan, the filter system of our visible 4-color simultaneous imager "Dogioya" is designed to be compatible with those of PS1 filter system. The transmittance properties of PS1 r', i', z', and y filters are shown in Fig. 6. Four unit CCD cameras are used as detectors. Each camera is equipped with 4096 $\times$ 2048 pixels CCD chip. The pixel size is 15 μm, and resultant pixel scale with the 2-m telescope is 0.19 arcsec per pixel. 2 $\times$ 2 binning is planned for usual operation. These unit cameras provide a field-of-view of 13.2 arcmin $\times$ 6.6 arcmin. In order to reduce the noise, the CCD chips are cooled down to -100°C.

2.3 Development Strategy

When we discussed the development strategy, we have focused on following two aspects. First, it is important to deliver the instrument in timely fashion. If the project has a delay and the instrument is delivered after the PS1 mission, then there will be less scientific impact and we have less scientific outputs from this instrument. Also, early scientific results are very appealing to the scientific community. Significant delay of the project may affect

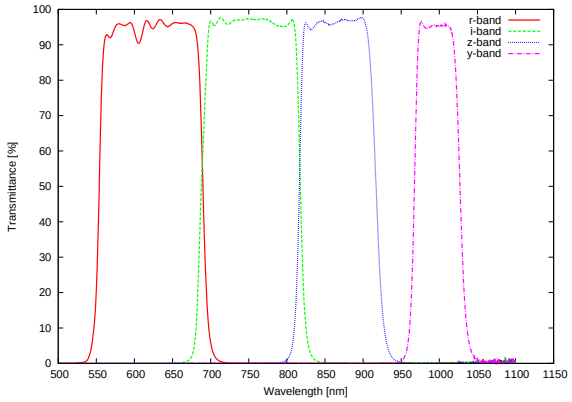

Figure 6: The measured transmittance properties of PS1 r', i', z', and y-band filters for our instrument. The filter system of visible four-color simultaneous imager will be compatible with those of PS1 filter system. These filters were manufactured by Asahi Spectra, Inc., and the transmittance data was obtained using Cary 60 spectrometer at NCU main campus.

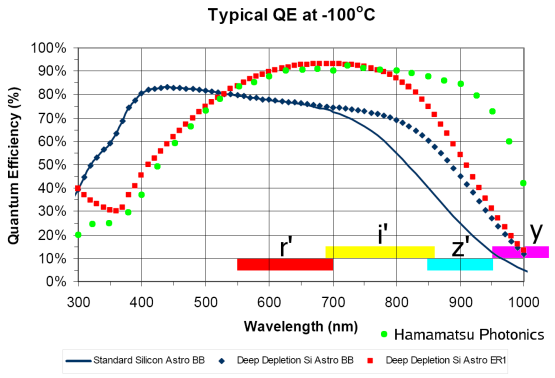

Figure 7: The comparison of quantum efficiencies of conventional thinned back-illuminated CCD and fully depleted CCD. The data shown by red squares are quantum efficiency of 44-82-1-D23 chip manufactured by E2V, and the data shown by green circles are quantum efficiency of fully depleted CCD manufactured by Hamamatsu Photonics. Thicker depletion layer for fully depleted CCD dramatically increases the sensitivity at Y-band.

to successive projects. Second, it is equally important to do in-house developments of some key components and accumulate experiences. If one uses commercially available products only for the research activities, then the uniqueless of the data is not easily emphasized. With the data obtained commercially available instruments, the competition with other facilities is tough. Meanwhile, in-house development may add unique functions to the instrument and/or achieve advantages in sensitivity / data quality, and one may be able to obtain a set of data that nobody else has. Unique and high quality data sets produce publications more easily.

CCD cameras are key components of our instrument, and we have reached to following conclusion for the development strategy. We have decided to purchase three commercially available CCD cameras to secure the delivery of the instrument by the telescope first-light, while fourth camera is developed by ourselves to let us accumulate experiences from the development processes. This strategy fulfills both two aspects mentioned above. Even in the situation of the delay of fourth camera, the instrument is able to start the early-science observations as 3-color simultaneous imager, and it will not be a fatal problem for the project. Three CCD cameras for r', i', and z' bands, we have purchased SI1100 series cameras of Spectral Instruments, Inc. in USA. A reason that we have chosen this product is that the manufacturer allows us to select a CCD chip to install in the camera. The CCD chips we selected are CCD 44-82-1-D23 of E2V, Inc. It is a scientific grade (grade 1) CCD chip with 4K × 2K format. The pixel size of this CCD is 15 μm. The fringe suppression process is given to the chip, so that significant degradation of photometric accuracy due to the fringing on the image in z'-band is significantly reduced. There are two amplifiers and A/D convertors for this CCD chip, and the readout time is shortened by a factor of two using both two readout ports. Fourth camera, namely "NCUcam-1", is developed by ourselves. NCUcam-1 will be used for imaging at y-band ($\lambda \sim 1\,\mu m$). We have decided to utilize a recently developed fully depleted CCD chip (Kamata et al. 2008). Majority of CCD chips used for astronomical observation at this moment are thinned back-illuminated CCDs. Because of thin depletion layer compared to the absorption depth of silicon, the sensitivity of thineed back-illuminated CCDs are very low at longer wavelength. Typical quantum efficiency of thinned back-illuminated CCDs at $\lambda \sim 1\,\mu m$ is about 10% or less. The low sensitivity of CCD at this wavelength region is critical problem for small aperture telescopes, and in fact we had difficulty to carry out observations at z and Y bands using small aperture telescopes due to poor sensitivity. To overcome the difficulty, we have decided to use a fully depleted CCD for NCUcam-1. The quantum efficiency of fully depleted CCD with 200 μm thickness reaches 40% at $\lambda \sim 1\,\mu m$, and it dramatically improves the sensitivity of y-band imaging (Fig. 7).

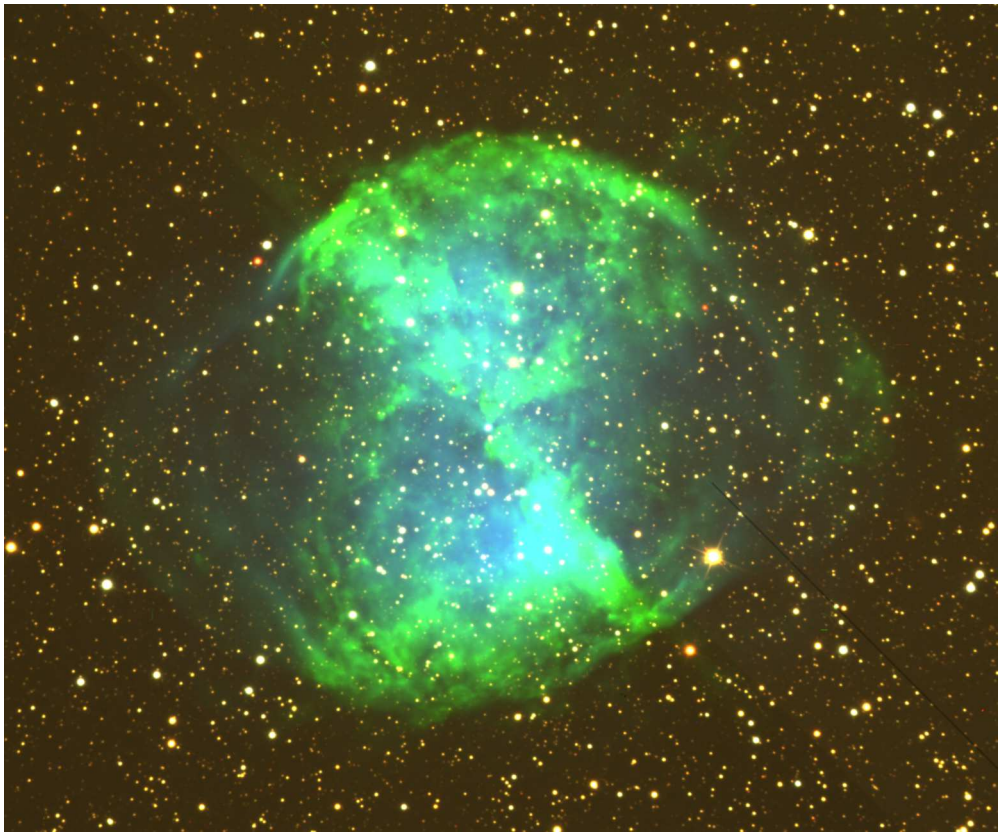

Figure 8: The first light image of the CCD camera SI1100-156. M27 was imaged using 1-m telescope at Lulin observatory at 17:10-17:54 on 20 July 2010. SDSS g', r', and i' filters were used for this observation. The integration time was 10 min for each band. The image shown here has the field-of-view of 10.0 arcmin $\times$ 8.3 arcmin.

2.4 Development

2.4.1 Instrumentation Laboratory

We first established a laboratory for the instrumentation at the Institute of Astronomy, National Central University. The Institute provided the room 1001 of the Science Building 4 for the laboratory space. We have arranged dark room with an optical table, clean room, and mechanical assembly and testing area in the laboratory space. The dark room is used for the tests and experiments of unit cameras. The clean room is used for the installation of CCD chip into the camera body of NCUcam-1 and assembly of the camera system. The mechanical assembly and testing area is used for the soldering, development of electric boards, assembly and testing of mechanical parts, and software development. The power supply with UPS (Uninterruptible Power Supply) was arranged, and the wired and wireless network was settled in the laboratory. A set of tools was purchased. We also pay attention to the operation and maintenance of the laboratory, and regularly check the availability and condition of tools and equipments in the laboratory. We have been developing the instrument in this laboratory space since 2008.

2.4.2 SI-1100 Series Cameras

As described in previous section, we purchased three SI-1100 series CCD cameras from Spectral Instruments, Inc. in Arizona, USA, as three unit cameras for our instrument. For the CCD chip inside the camera, we specified CCD 44-82-1-D23 manufactured by E2V, Inc. of UK/France. This is 2K $\times$ 4K CCD chip with the pixel size of 15 μm. It gives 13.2 arcmin $\times$ 6.6 arcmin field-of-view when attached to the 2-m telescope of F/8. This field-of-view is reasonably large for our observations even for relatively fast moving objects. In order to reduce the dark current, we have chosen a model with the cryocooler. The CCD can be cooled down to -100°C. Under the operation temperature of -100°C, we do not need to take dark exposures, and it simplify the observations. The CCD controller allows us to have overscan region along with the imaging data, and the overscan region can be used to estimate the bias level. Three SI-1100 series cameras were delivered to us in sum-

mer 2010. We have developed a filter wheel for test observations of SI-1100 series cameras, and those cameras were tested using 1-m telescope at Lulin observatory. The first-light of SI-1100 series cameras was achieved in July 2010 (Fig. 8). Through the experiences of test observations at Lulin, we learned a lot on the installation and operation of the instrument. For CCD camera which is cooled by a cryocooler, a good consideration for the arrangement of the cryocooler lines and compressor is needed. An attention to the cable lengths for various signal cables, such as RS-232C, USB, and fibre optic cables, is always required.

2.4.3 NCUcam-1

Fourth unit camera "NCUcam-1" has been designed, developed, and being tested by ourselves at Institute of Astronomy, National Central University. Fig. 9 shows the schematic design of NCUcam-1. The main body of the camera head is a vacuum dewar made of aluminum. The vacuum environment is required to keep stable low temperature of the CCD chip. The vacuum pump is connected to the camera dewar, and the vacuum level of $\sim 10^{-6}$ torr is achieved before the observation. During night time observation, the vacuum pump is disconnected from the camera head to prevent the vibration.

At the top of the vacuum dewar, a glass window made of fused silica is attached. The fused silica has excellent transparent properties at visible wavelength which is suitable for optical astronomical observations. Properties of fused silica is summarized in Table 1. The size of the CCD is 30.7-mm × 61.4-mm, and we decided to have ϕ = 90-mm fused silica window for our camera. We have estimated required thickness for the fused silica window. A set of equations for the calculation is given by

$$\sigma_{max} = \frac{3P(3+\nu)}{32}\left(\frac{D}{t}\right)^2 < \frac{F_a}{S} \quad (3)$$

$$l = \frac{3P(1-\nu)(5+\nu)}{256E}\frac{D^4}{t^3} \quad (4)$$

$$R = \frac{l^2 + \left(\frac{D}{2}\right)^2}{2l} \quad (5)$$

Here, D is the diameter of the circular window, t is the thickness of the window, σ_{max} is the stress to the window surface at the window center, P is the pressure difference between the inside and outside of the dewar, ν is the Possion ratio, F_a is the breaking strength, S is the safety factor, l is the displacement of the window surface at the window center, E is the Young's modulus, and R is the curvature radius of the deformed window. According to Okamura et al. (1996) and Miyazaki et al. (2002), it is recommended to have safety factor of 4 or larger. Under the condition of the safety factor of 3 or smaller a small impact may break the window. The window thickness, window displacement at the center, and curvature radius of the deformed window are calculated for $S = 3, 4, 5, 6, 7, 8, 9$, and summarized in Table 2. The thickness of the window for the safety factor of 4 is calculated as 4.5-mm. We conclude to use a 5-mm thickness fused silica for the dewar window. The fused silica window must be anti-reflection coated before the installation. The broad-band anti-reflection coating was designed by our partner, Photocoding Inc., and our fused silica windows were coated when a set of corrector lenses was AR coated. The reflectance property of AR coating on fused silica is shown in Fig. 10.

Breaking strength	$F_a = 4.892 \times 10^7$ Pa
Young's modulus	$E = 6.966 \times 10^{10}$ Pa
Poisson ratio	$\nu = 0.17$

Table 1: The properties of fused silica. The data are from Okamura et al. (1996) and Miyazaki et al. (2002).

S	t [mm]	l [μm]	R [m]
3	3.9	83	12.2
4	4.5	53	18.8
5	5.0	38	26.2
6	5.5	29	34.5
7	5.9	23	43.4
8	6.3	19	53.1
9	6.7	15	63.3

Table 2: Calculated window thickness, window displacement at the center, and curvature radius of the deformed window for given $S = 3, 4, 5, 6, 7, 8, 9$.

Cryocooler is used to achieve the CCD operation temperature of -100°C. For the choice of the cryocooler, we have carried out the calculations for the thermal design of the dewar. The nominal CCD operation temperature is set to -100°C mainly because dark current is negligible at this temperature. In order to estimate the required cooling power of the cryocooler, the calculations of inflow heat flux into the dewar are needed. Here, we assume a cylindrical shaped dewar with the diameter of 150-mm and the height of 100-mm. The size of a circular window of the dewar is set to be ϕ = 90-mm. The total inflow heat flux into the dewar was calculated as follows. Four heat sources were considered. Those are the radiation from the dewar window, the radiation from the dewar wall, the conduction through the supporting structure

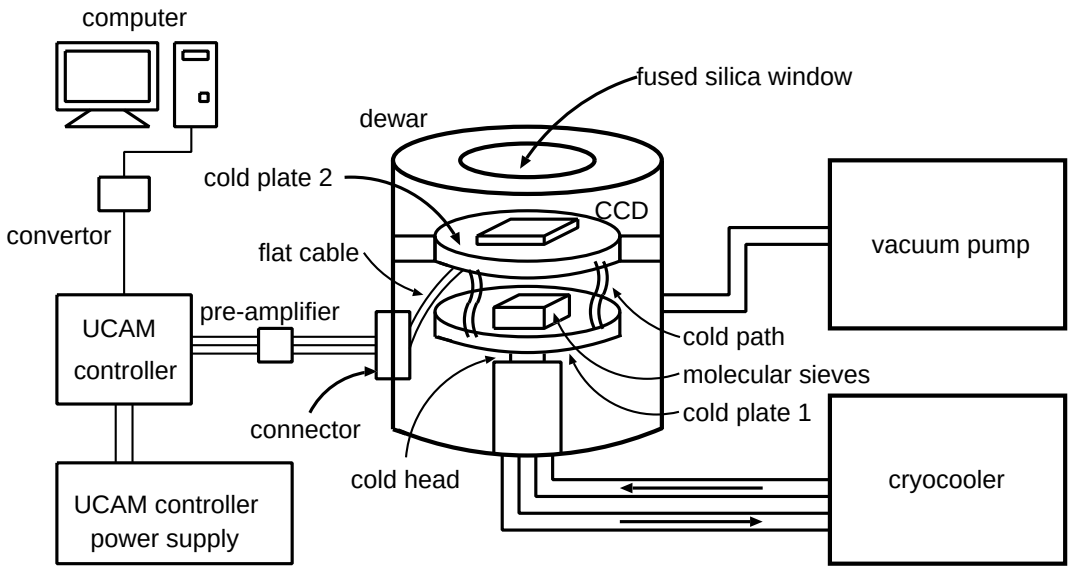

Figure 9: The schematic drawing of NCUcam-1. The CCD chip is installed in the dewar, and a vacuum pump and a cryocooler are connected to the dewar. The temperature control electronics and heaters are used to make the CCD temperature stable. UCAM CCD controller is used to acquire images.

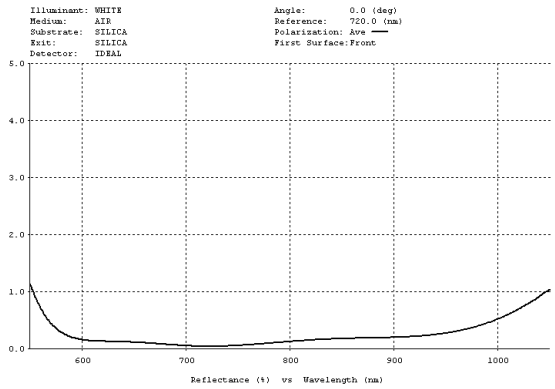

Figure 10: The design of broad-band anti-reflection coating on fused silica. It was designed by our partner, Photocoding, Inc.

of the CCD chip, and the conduction through signal lines. The incoming heat flux by the thermal transfer due to the radiation from the dewar window is expressed as

$$\dot{Q}_{win} = \sigma \left(T_{ambient}^4 - T_{CCD}^4\right) A_{win} \times \frac{\epsilon_{win}\epsilon_{CCD}}{\epsilon_{win} + \epsilon_{CCD} - \epsilon_{win}\epsilon_{CCD}}. \quad (6)$$

Here, $\dot{Q}_{win}$ is the inflow heat flux by the radiation from the window, σ is the Stephan-Boltzmann constant ($\sigma = 5.67 \times 10^{-8}$ Wm^{-2}K^{-4}), A_{win} is the area of the dewar window, $T_{ambient}$ is the ambient temperature near the dewar window, T_{CCD} is the CCD operation temperature, ϵ_{win} is the emissivity of the fused silica window, ϵ_{CCD} is the emissivity of the CCD. The area of the dewar window is $A_{win} = \pi \left(\frac{D_{win}}{2}\right)^2 = 6.36 \times 10^{-3}\,\mathrm{m}^2$. The ambient temperature near the window and CCD temperature are chosen to be $T_{amb} = 283\,\mathrm{K}$ and $T_{CCD} = 173\,\mathrm{K}$, respectively. The emissivities of the window and CCD are assumed as $\epsilon_{win} = 1.0$ and $\epsilon_{CCD} = 0.5$, respectively. Then, the heat inflow by the radiation from the dewar window is estimated as $\dot{Q}_{win} = 1.0$ W. The incoming heat flux by the thermal transfer due to the radiation from the dewar wall is expressed as

$$\dot{Q}_{wall} = \sigma \left(T_{ambient}^4 - T_{CCD}^4\right) A_{wall} \times \frac{\epsilon_{Al}\epsilon_{CCD}}{\epsilon_{Al} + \epsilon_{CCD} - \epsilon_{Al}\epsilon_{CCD}}. \quad (7)$$

Here, $\dot{Q}_{wall}$ is the inflow heat flux by the radiation from the wall, A_{wall} is the area of the dewar wall, ϵ_{Al} is the emissivity of the dewar wall which is made of the aluminum. The area of the dewar wall is $A_{wall} = \pi \left(\frac{D_{win}}{2}\right)^2 = 5.84 \times 10^{-2}\,\mathrm{m}^2$. The emissivity of the aluminum are assumed as $\epsilon_{Al} = 0.06$. Then, the heat inflow by the radiation from the dewar wall is estimated as $\dot{Q}_{wall} = 1.0$ W. The incoming heat flux by the thermal transfer due to the conduction through the supporting structure of the CCD chip is expressed as

$$\dot{Q}_{post} = \frac{A_{post}}{L_{post}} \int_{T_{amb}}^{T_{CCD}} \kappa_{post}(T) dT \sim \frac{A_{post}}{L_{post}} \bar{\kappa}_{post} \left(T_{amb} - T_{CCD}\right). \quad (8)$$

Here, $\dot{Q}_{post}$ is the inflow heat flux by the conduction through a polycarbonate post, A_{post} is the

cross-section of the polycarbonate post, L_{post} is the length of the polycarbonate post, κ_{post} is the thermal conductivity of the polycarbonate post, $\bar{\kappa}_{post}$ is the mean thermal conductivity of the polycarbonate post. The cross-section and length of the polycarbonate post are assumed to be $A_{post} = 20 \times 20\,\mathrm{mm}^2$ and $L_{post} = 40$ mm, respectively. The mean thermal conductivity of the polycarbonate is assumed as $\bar{\kappa}_{post} = 0.2$ W m^{-1} K^{-1}. The number of polycarbonate posts is 4. Then, the heat inflow by the conduction through the polycarbonate posts is extimated as $\dot{Q}_{posts} = 0.9$ W. The incoming heat flux by the thermal transfer due to the conduction through the copper line is expressed as

$$\begin{aligned} \dot{Q}_{line} &= \frac{A_{line}}{L_{line}} \int_{T_{amb}}^{T_{CCD}} \kappa_{Cu}(T) dT \\ &\sim \frac{A_{line}}{L_{line}} \bar{\kappa}_{Cu} \left(T_{amb} - T_{CCD} \right). \end{aligned} \quad (9)$$

Here, $\dot{Q}_{line}$ is the inflow heat flux by the conduction through a copper line, A_{line} is the cross-section of a copper line, L_{line} is the length of a copper line, $\bar{\kappa}_{Cu}$ is the mean thermal conductivity of the copper. The cross-section and length of the copper line are assumed to be $A_{line} = 75 \times 18$ μm^2 and $L_{line} = 150$ mm, respectively. The mean thermal conductivity of the copper is assumed as $\bar{\kappa}_{post} = 420$ W m^{-1} K^{-1}. The number of copper lines is 50. Then, the heat inflow by the conduction through the copper lines is extimated as $\dot{Q}_{lines} = 0.02$ W. Therefore, the total inflow heat flux is estimated to be $\sim$ 3W under the ideal situation. The cryocooler PT-30 manufactured by Polycold, Inc., has the cooling power of 22W at 173K, and it is confirmed to be powerful enough for our camera. The cold-end of the cryocooler is installed in the camera head. The cold-end and the CCD chip is connected using copper lines, and the heater is placed in between to achieve stable temperature. The analog feedback circuit developed by us starts heating when the CCD needs to be warmed up, and stops heating CCD temperature is higher than the setting temperature. Near the cold-end, molecular sieves are installed to absorb remaining gas particles. This is critically important to keep vacuum level because the vacuum pump is switched off and disconnected during the observation. Remaining gas particles are sticked on the surface of molecular sieves under low temperature, and hence good vacuum environment is kept in the dewar as long as the cryocooler is working.

The military-grade hermetic connector is used to have signals from the CCD while keeping the vacuum condition. The pins on the back-side of the CCD package and the hermetic connector is connected via flat cable. Lines from the temperature sensors are also connected to the hermetic connector. Signals from the CCD are transfered to the CCD controller through the hermetic connector.

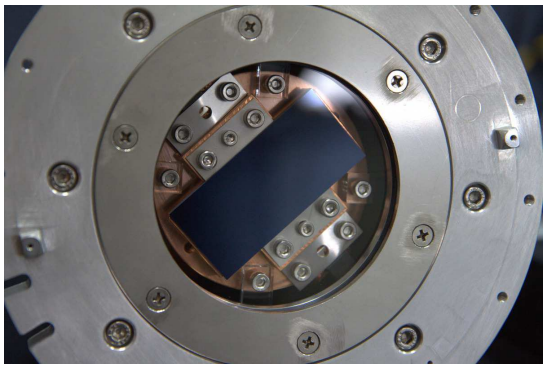

Figure 11: The engineering grade CCD chip installed in the dewar. The chip is supported by the copper plate. The window in front of the CCD is fused silica.

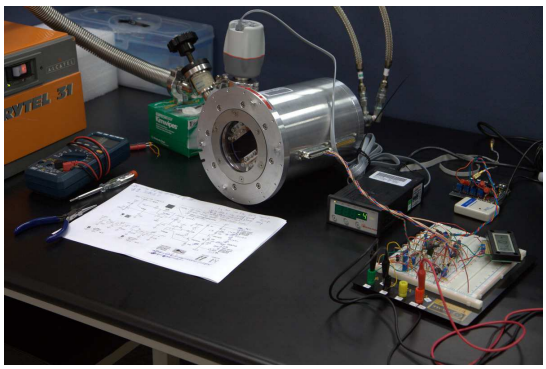

Figure 12: Assembled NCUcam-1 under testing in the laboratory. NCUcam-1 consists of the camera head, vacuum pump, cryocooler, temperature control electronics, and CCD readout electronics.

Outside the dewar, the electric circuit board is attached to the hermetic connector. This circuit board has functions to communicate with the CCD chip and control the heaters in the dewar. The signal lines from the circuit board are feeded into the pre-amplifier, and amplified signals are sent to the CCD controller. The CCD controller we use is Universal Camera Controller (hereafter, UCAM) developed by AET (Astronomical Electronics Technology). UCAM is operated by a Linux PC.

An engineering grade CCD chip was installed in the camera dewar (Fig. 11), Assembly of NCUcam-1 was done with an engineering grade CCD chip in autumn 2010. Fig. 12 shows the assembled NCUcam-1 in the laboratory. At first, we found a problem for keeping reasonably good vacuum level,

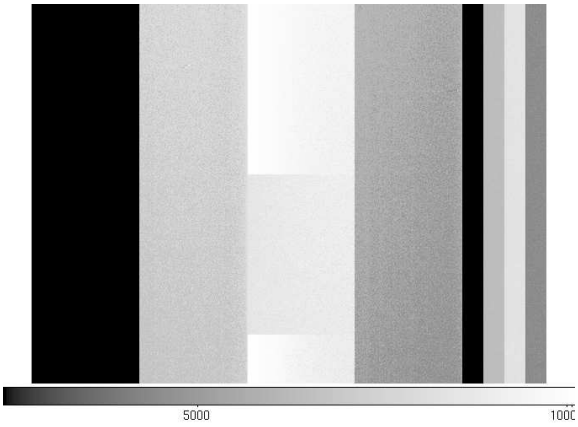

Figure 13: The bias frame obtained by NCUcam-1 with an engineering grade chip of the fully depleted CCD manufactured by Hamamatsu Photonics. The CCD was drived by UCAM controller. The CCD has four readout ports, and the mean levels of the bias for each region are slightly different. The most left side of the CCD was not working properly. Four narrow stripes on the right hand side are overscan regions.

and the aluminum surface near the hermetic connector was polished again and the problem was fixed. In December 2010, NCUcam-1 was drived successfully using UCAM and the bias frame was acquired (Fig. 13). Later on, scientific grade CCD chip was installed in the camera dewar, and the first data from the scientific grade chip were read from the camera in May 2011. Fig. 14 is the dark frame with the exposure time of 3600 sec. Due to thicker depletion layer, cosmic rays do not appear as points, but trailed patterns are seen. The dark current generation rate was measured to be $\sim$ 4 e^- under the cooling temperature of -100°C, and it fulfills the specifications. The readout noise was also estimated, and it was $\sim$ 4 e^- per read when the sampling speed of 125 kHz was selected. This is good enough for most of our application, because the sky background noise dominates for exposures of 20-30 sec or longer.

After the tests and ajustments in the laboratory, we brought the whole system of NCUcam-1 to Lulin observatory, and NCUcam-1 was tested using existing 1-m telescoep there as a stand-alone CCD imager. Although we have struggled with the setting and adjustment of UCAM controller, shutter controller, and control software for a while, NCUcam-1 successfully received the star light from the sky and acquired astronomical images for the first time in July 2011 (Fig. 15). We believed it was a big achievement for our project and also for our institute that our "hand-made" CCD imager finally worked. Before NCUcam-1, only commercially available CCD cameras were used at Lulin observatory. With those cameras, it is not easy to obtain unique data sets for our research. We often need to accumulate data for longer time span to complete with other researchers. Now, our institute has an ability to design, develop, test, and characterize astronomical instruments. NCUcam-1 exhibits superb sensitivity even around wavelength of 1 micron, and there are only a few such CCD imager in the world at this moment. This is a great advantage for our institute. It is also worth to note that NCUcam-1 is the first CCD imager cooled by cryocooler at Lulin observatory and it achieves the cooling temperature of -100°C. Previous CCD cameras at Lulin were all cooled by thermoelectric cooler and we had to take dark frames and deal with dark current subtraction.

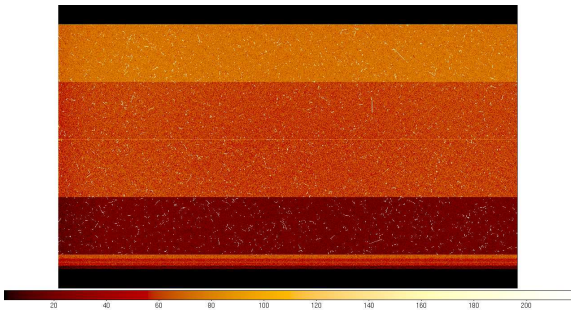

Figure 14: 3600 sec dark exposure of NCUcam-1. Four regions on the CCD image is recognized, and this is because the CCD chip is equipped with four amplifiers. Four narrow stripes are also found at the bottom of the image, and those are overscan regions for each amplifier.

The detection limits of NCUcam-1 with Lulin 1-m telescope were estimated. Here, the definition of the detection limit is given by the magnitude of an astronomical object detected with signal-to-noise ratio of 10 for specified integration time. The aperture radius is set to be 1.5 times of FWHM of stellar point-spread function. We took two consecutive images of standard star fields for PS1-compatible r', i', z', and Y filters. These data sets provide two independent photometric measurements of field stars under the same instrumental and atmospheric conditions. By comparing two measurements, and statistical analysis of errors enables us to estimate detection limits. Note that there are not information for calibrated magnitudes for field stars, but photometric standard star can be used to calibrate field stars. The data were taken on 11 December 2012 using NCUcam-1 and Lulin 1-m telescope. The standard field of Ru149 was selected, and photometric standard star Ru149F was used for the analysis of r', i', and z' band images, while Ru149 on UKIRT IR bright

Figure 15: The first-light image of NCUcam-1 with Lulin 1-m telescope. Lagoon Nebula M8 was imaged using PS1 r', i', and z' filters on 6 July 2011. The exposure times for r', i', and z' bands are 60 sec × 8, 60 sec × 8, 90 sec × 8, respectively. The field-of-view of this image is 26.4 arcmin × 13.2 arcmin.

	r'	i'	z'	Y
Lim. Mag.	20.0	19.5	19.0	17.1
PSF	1.5"	1.4"	1.4"	1.3"

Table 3: The estimated detection limit of NCUcam-1.

standard catalog was used for the analysis of Y band images. The integration time of each exposure is set to 90 sec. The airmass of Ru149 field at the time of the observation was ∼ 1.1-1.2. We used astronomical image analysis software package IRAF (Image Reduction and Analysis Facility), developed by NOAO (National Optical Astronomy Observatory) of USA, for our data processing. The flow chart of the analysis is shown in Fig. 16. For the estimation of the detection limit, we divided field stars into 0.1 mag bins according to their brightness. Fig. 17 shows the magnitude differences of photometric measurements from 1st and 2nd images of r'-band. The data shows wider scattering toward fainter sources. Fig. 18 is a figure of RMS error vs. magnitude. Roughly speaking, signal-to-noise ratio of 10 corresponds to RMS error of 0.1 mag. According to our definition, magnitude which corresponds to 0.1 mag RMS error is the detection limit. The resultn of the anaysis is summarized in Table 3. The detection limit of single 90-sec integration is 20.0 mag for r'-band while it is 17.1 mag for Y-band.

Currently, a series of experiments with NCUcam-1 in the laboratory in NCU main campus is being carried out. These experiments utilizes an integrating sphere, and the goals of the experiments are the measurements of (1) full well capacity, (2) linearity of the response, (3) gain and readout noise. The ingrating sphere was developed by ourselves. Two half-sphere foamed styrol were used to make a main body of the integrating sphere, and the interior of the sphere was painted and eight LEDs were installed (Fig. 19). We also developed a circuit board using current regulative diode (CRD) to provide stable electric current. Note that the brightness of LED depends on the current provide. We measured the stability of the brightness of inner wall of integrating sphere. Fig. 20. The standard deviation of the brightness variation in the integration sphere is found to be 0.16% of the mean brightness over 1.5 hours. This is good enough for our purpose. We plan to compete the experiments by the end of April 2013.

2.4.4 Beam Splitter and Corrector Lens

The optics part of visible 4-color simultaneous imager "Dogioya" has been outsourced to Photocoding, Inc. in Japan. This is mainly because we needed to concentrate on the development of NCUcam-1 considering the amount of available human resources. The optics part is composed of the beam splitter to separate the beam from the telescope into four components, and corrector lens system to improve the image quality over the entire field-of-view of the instrument. The optical layout of the beam splitter and corrector lens is shown in

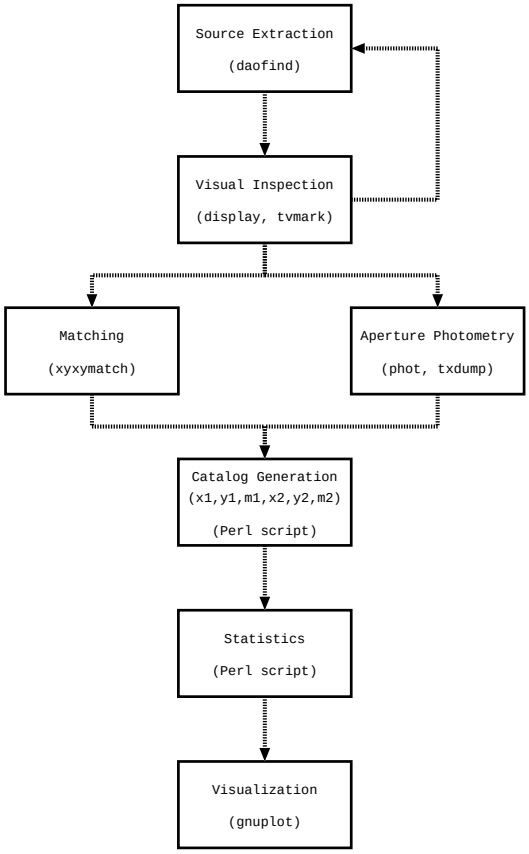

Figure 16: The flow chart of detection limit analysis. First, all the sources in the image are identified and extracted. After the visual inspection of the result of source extraction, the source lists of 1st and 2nd images are compared and matching is tried. At the same time, precise aperture photometry is applied to each source in the image. Then, a complete catalogue with object ID and photometric measurements is generated. After the statistical analysis, the detection limit is calculated.

Fig. 21. Three dichroic mirrors are placed on the optical path, and the light from the telescope are divided into four components which correspond to r', i', z', and Y band images. The beam splitter "BS A" split the beam into (r'+i') and (z'+Y). The transmittance property of "BS A" is shown in Fig. 22. All the three beam splitters are confirmed to satisfy the specifications. We did not find any problem on the anti-reflection coating on the corrector lenses and surface irregularity on the surface of beam splitters and band-pass filters. To examine the expected image quality, diameters of 80% encircled energy were checked. The results are shown in Table 4. Optics part of the instrument was delivered to us in summer 2011. We have assembled the optics and four unit cameras in our laboratory, and the system was successfully

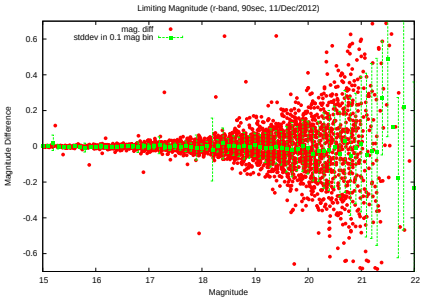

Figure 17: The magnitude differences of 1st and 2nd images vs. field star magnitude for r'-band. The data are binned for each 0.1 mag, and standard deviation is calculated for distribution of data points in each bin.

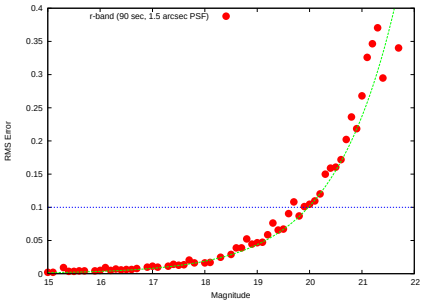

Figure 18: RMS error vs. magnitude for r'-band. The magnitude which corredsponds to RMS error of 0.1 mag is the detection limit.

integrated (Fig. 23).

2.4.5 Software

The basic commands to acquire the image from NCUcam-1 was written by ourselves. A set of command-line interface tools offers a way to conduct observations. Spectral Instruments provided a CCD camera control software and SDK (Software Development Kit) for SI-1100 series camera. In order to achieve the simultaneous imaging by all the four unit cameras, we have decided to develop a server / client model software. The main control PC sends commands to camera control PCs, and then four camera control PCs start exposures. After the completion of the data acquisition, camera control PCs send the data back to the main control PC. Nick Enterprise, Inc. in Taipei supported us to develop TCP/IP server / client software platform for our instrument. The system now works fine, and is able to control four cameras and acquire four images by typing a single command on the main control PC.

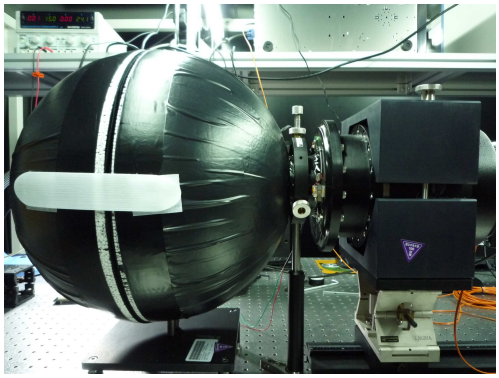

Figure 19: The low-cost integrating sphere developed by us. Foamed styrol is used for the body of the sphere, and LEDs are used as light sources.

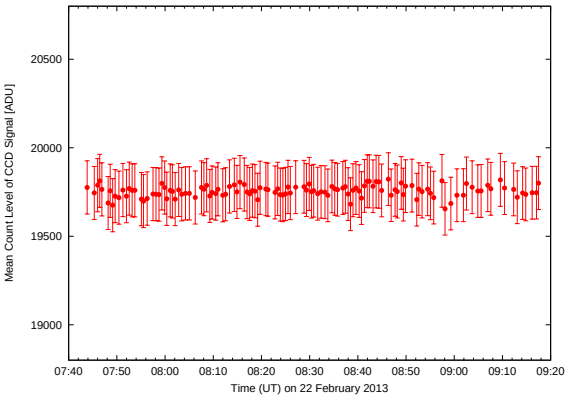

Figure 20: The stability of brightness in the integrating sphere. The brightness of LEDs is controlled by current regulative diode. The standard deviation of the brightness variation is 0.16% of mean signal level.

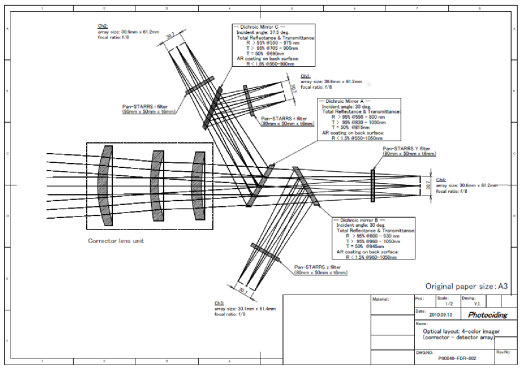

Figure 21: The optical layout of the beam splitter and corrector lens. The corrector lens improves the image quality, and the beam splitter split the beam from the telescope and feed them to CCD imagers.

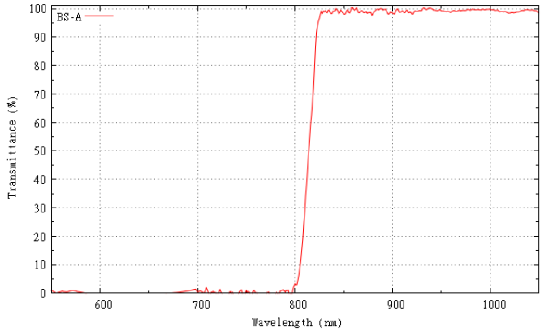

Figure 22: The transmittance property of the beam splitter "BS A". This dichroic mirror splits the beam from the telescope. The light of wavelength shorter than 815 nm is reflected on the surface and the light of wavelength longer than 815 nm is transmitted.

2.5 Current Status

We had worked on the development of visible 4-color simultaneous imager "Dogioya" for years, and now all the components, including unit cameras, optics, electronics, mechanics, and software, are ready. Unfortunately, Lulin 2-m telescope is not yet installed at Lulin observatory due to the delay caused by the environmental assessment study. Dogioya is tightly linked with large-scale astronomical surveys, such as Pan-STARRS and PTF (Palomar Transient Factory), and immediate start of the operation is highly expected. To start the observation by Dogioya, we have established a collaboration with Institute for Astronomy, University of Hawaii. University of Hawaii (UH) provides 2.2-m telescope at the summit of Mauna Kea, and NCU provides Dogioya. UH will have a right to use Dogioya with 2.2-m telescope, and NCU will have telescope time of 2.2-m telescope. It gives mutual benefits to both sides of the collaboration. Note that both NCU and UH joins Pan-STARRS project. Both side of the collaboration agree to operate the instrument for four years in Hawaii. We were planning to send all the components of the instrument to Hawaii in April 2013. However, the telescope and dome of UH 2.2-m telescope was damaged at the beginning of February 2013, and UH-side now requests us to postpone the instrument test using the telescope by half a year. With our current plan, we will ship our instrument to Hawaii in autumn this year, and will assemble all the components in Hawaii, and attach Dogioya to bent-Cassegrain focus of 2.2-m telescope. We expect to have a first-light of Dogioya using UH 2.2-m telescope by the end of this year.

	r'	i'	z'	Y
80EE Dia. (arcsec)	0.14	0.29	0.22	0.19

Table 4: The diameter of 80% encircled energy for r', i', z', and Y bands are summarized. The specifications is 0.60 arcsec, and we have satisfactory results for all the four bands.

Figure 23: Assembled 4-color imager in the laboratory. All the four unit cameras were attached to the system.

3 Summary

For quick and efficient follow-up observations for large-scale astronomical surveys, visible 4-color simultaneous imager "Dogioya" is proposed. We have designed and developed Dogioya, and the instrument is ready to be used. We have established a collaboration with University of Hawaii, and Dogioya will be shipped to Hawaii later this year. Dogioya will be operated using UH 2.2-m telescope for four years. The advantages Dogioya includes, but not limited to, (1) reliable color measurements by simlutaneous imaging, (2) high sensitivity of fully depleted CCD imager "NCUcam-1" which has been developed by ourselves, and (3) PS1-compatible band-pass filters which allow us to combine the data from Pan-STARRS and Dogioya in easier way. More importantly, we have gained through the development of astronomical instrument. The astronomical instrumentation project requires wide range of knowledge and experiences, such as mechanics, electronics, optics, software, and project management. Those are usually new to astronomers. Here, at NCU, this project, the development of Dogioya, was the very first trial to design and develop an instrument. We believe that the trial was successful, and we have a working instrument and have accumulated experiences. The instrumentation is a key activity in astronomical research, and it is a way to produce unique, useful, and valuable scientific data. The project is close to the end, and we are now ready to go even further.

References

[1] Jia, L., Wei, M., Zou, S., Luo, Y., "The UCAM CCD system of LAMOST", 2010, Proceedings of the SPIE, Volume 7733, pp. 77335E-77335E-11.

[2] Kaiser, N., "Pan-STARRS: a wide-field optical survey telescope array", 2004, Proceedings of the SPIE, vol. 5489, pp. 11-22.

[3] Kamata, Y., Miyazaki, S., Nakaya, H., Tsuru, T. G., Tsunemi, H., Miyata, E., Muramatsu, M., Suzuki, H., Miyaguchi, K., "Evaluation of the fully-depleted back-illuminated CCD for Subaru Suprime-Cam", 2008, Proceedings of the SPIE, vol. 7021, pp. 70211S-70211S-9.

[4] Kinoshita, D., Ohtsuka, K., Sekiguchi, T., Watanabe, J., Ito, T., Arakida, H., Kasuga, T., Miyasaka, S., Nakamura, R., Lin, H.-C., "Surface heterogeneity of 2005 UD from photometric observations", 2007, A&A, 466, 1153-1158.

[5] Miyazaki et al., 2002, PASJ, 54, 833-853.

[6] Okamura et al., 1996, "Suprime-Cam Final Design Review".

工作報告

國立中央大學鹿林天文台申請使用辦法

101 年 6 月 26 日鹿林天文台管理委員會會議訂定
101 年 11 月 16 日總務會議場地管理委員會會議暨 101 年 12 月 13 日總務會議通過

第一條　為使鹿林天文台發揮最大效能並有週全之管理維護，依本校『鹿林天文台管理辦法』第 11 條訂定本申請使用辦法（以下簡稱本辦法）。

第二條　本辦法所指『場地』為本校鹿林天文台基地及其附屬基礎設施、空間。（不含望遠鏡觀測申請，觀測申請及審核由時間分配小組辦理）

第三條　凡本校各單位及依法成立之機關、學校、團體以研究、教學或推廣教育為目的之計畫均可提出申請使用。

第四條　本場地使用以天文所之正式計畫優先使用，本校其他單位之研究計畫居次，其他單位申請借用再次之。

第五條　本場地使用需核准後方得申請入山，依申請使用時間分為下列申請案：
1. 臨時使用：一個月以內之使用申請，全年不得超過三個月。
2. 短期使用：三個月以內之使用申請，全年不得超過六個月。
3. 長期使用：三個月以上之申請案。

第六條　本場地使用申請之申請時間、審核程序如下：
1. 臨時使用申請應於至少 7 天前填具申請表、簡易設備資料至天文所，經天文台台長核准後使用。
2. 短期使用申請應於至少 15 天前填具申請表、計畫內容摘要、設備說明等資料至天文所，經天文台台長核准後使用。
3. 長期使用申請案應於至少 1 個月前填具申請表、使用計畫內容、設備所需資源及空間、需支援事項等書面說明資料，由天文台台長提交天文台管理委員會(以下簡稱管委會)審核同意後方得使用。

第七條　長期使用申請應訂立使用合約，計畫申請使用期間內，管委會得每年檢討、終止使用計畫合約。

第八條　各申請使用計畫之設備應由使用單位自行負責運送、操作、管理、維護；使用場地內設施應經天文台專責人員指導及同意後方得使用；使用完畢後使用人應負責場地之回復。

第九條　各申請使用計畫所使用之設備，應提供天文台相關安維資訊，如有涉及各項管制規定者，應自行向相關主管機關申請、核備。

第十條　使用本場地應依『鹿林天文台場地使用收費標準』，依計畫申請使用之空間、期間與基礎設施使用量繳交使用費，場地收入全數納入校務基金，並提撥百分之五十由鹿林天文台運用，但有特殊情形經專案簽准者除外。

第十一條　場地收入支用依本校相關規定辦理，優先支用用途如下:

1、場地設施所需之維護修繕、更新費用及相關勞務費。

2、日常營運需要之經常性支出費用、公務車維修、相關稅捐。

3、教學、研究、推廣教育相關活動、研討會、宣導教材之經費。

4、儀器設備費用。

5、其他經專案簽奉同意支用之項目。

第十二條　使用本場地，如造成設施、其他儀器損壞或公物遺失，使用人應負賠償之全部責任。

第十三條　本辦法由鹿林天文台管理委員會通過，報請本校場地管理委員會及總務會議核定後公布實施，修正時亦同。

鹿林天文台場地使用收費標準

101 年 6 月 26 日鹿林天文台管理委員會會議訂定
101 年 11 月 16 日總務會議場地管理委員會會議暨 101 年 12 月 13 日總務會議通過

一、鹿林天文台場地之使用收費，按申請使用單位收費分級如下:

一級(按核計使用費全額收費)：非本校之申請單位。

二級(按核計使用費五折收費)：本校其他單位或社團。

三級(免全部費用)：天文所之正式計畫。

二、本收費標準之數額為每月使用費總額，單位以元計，元以下採四捨五入計算，未滿一個月者以一個月計。

三、本場地使用費依使用面積為使用費核計基準，使用面積於 10 平方公尺以內(含)者，其使用費為 5,000 元；超過 10 平方公尺者，以 10 平方公尺為單位，每單位累進 5,000 元計算應繳使用費。唯計畫設備若有高耗電、高資料傳輸需求等特殊情況者，其使用費應另依實際狀況，由使用單位或駐站主任提報台長核計其加成費用。

四、以點或線狀使用鹿林天文台相關基礎設施或資源，無法以面積計算使用費者，應依使用實際狀況，以千元為單位，由使用單位或駐站主任提報台長核計其使用費。

五、本場地所收使用費含電（電信）費及管理費，衍生之相關稅捐由使用單位負擔，依使用費之應稅總額外加計收。

六、使用單位應於申請使用計畫核准後，於實際使用前繳納使用費；唯雙方合約另有約定者，從其約定。

七、本標準由鹿林天文台管理委員會通過，報請本校場地管理委員會及總務會議核定後公布實施，修正時亦同。

鹿林天文台觀測時數統計(2003-2012)

林宏欽、蕭翔耀、林啓生

鹿林天文台自 2002 年 9 月開始有人員常駐，2003 年 LOT 一米望遠鏡上線，開始有正式觀測時數紀錄，可供瞭解鹿林長期的觀測條件。依 10 年來(2003-2012)的統計資料，鹿林天文台每年觀測時數約爲 1450 小時。以月份來說，

- 10-12 月爲最佳觀測季。
- 1-3 月爲次佳觀測季。
- 4 月雨季開始，5-6 月受梅雨影響，天氣最差。
- 7-9 月受颱風及午後對流雲系影響，天氣好壞差別很大。

詳細統計資料及統計圖如下(扣除最高及最低值後取平均)，

表 1 每月觀測時數統計 (2003-2012)

Month	2003	2004	2005	2006	2007	2008	2009	2010	2011	2012	Average
1	78.75	125	163.25	129	127.32	179	234.52	206.9	90.8	113.42	141.84
2	142.5	145.98	94.75	149	128.55	118.25	165.7	100.6	123.8	64.88	125.43
3	147.5	163	143	126.05	116.4	138.5	146.75	181.3	75.9	168.23	143.68
4	126.5	110.5	144.75	86.8	53.75	85.25	71.8	75.8	151.45	32.75	94.39
5	129.75	106.25	136.25	59.5	106.6	98.25	167.4	86.05	56.6	74.3	99.62
6	24	133	45	39.3	54	37	81.75	26.5	61.5	35.15	47.53
7	222.5	48	167.75	91.57	128.88	88.4	76.6	99.85	81.75	106.4	105.15
8	137.75	142	76	111.65	56.6	118.95	6.8	98.3	97.9	35.7	91.61
9	142	116	129.25	60.05	69.55	59.8	0	109.95	90.1	117.35	94.01
10	149.25	219.75	210.25	150.6	172.63	191.38	175.6	139.8	136.95	214.51	175.50
11	166.5	214.5	216.25	71.75	160.55	152.55	175.8	163.65	87.2	93.81	151.82
12	271.5	232.45	129	132	261.09	211.17	169.8	169.65	115.25	132.21	179.67
Total	1738.5	1756.43	1655.5	1207.27	1435.92	1478.5	1472.52	1458.35	1169.2	1188.71	1454.41

* 2009 年因受 88 風災影響，自八月八日起至十月初約 2 個月期間，受停電影響以至於無法觀測。

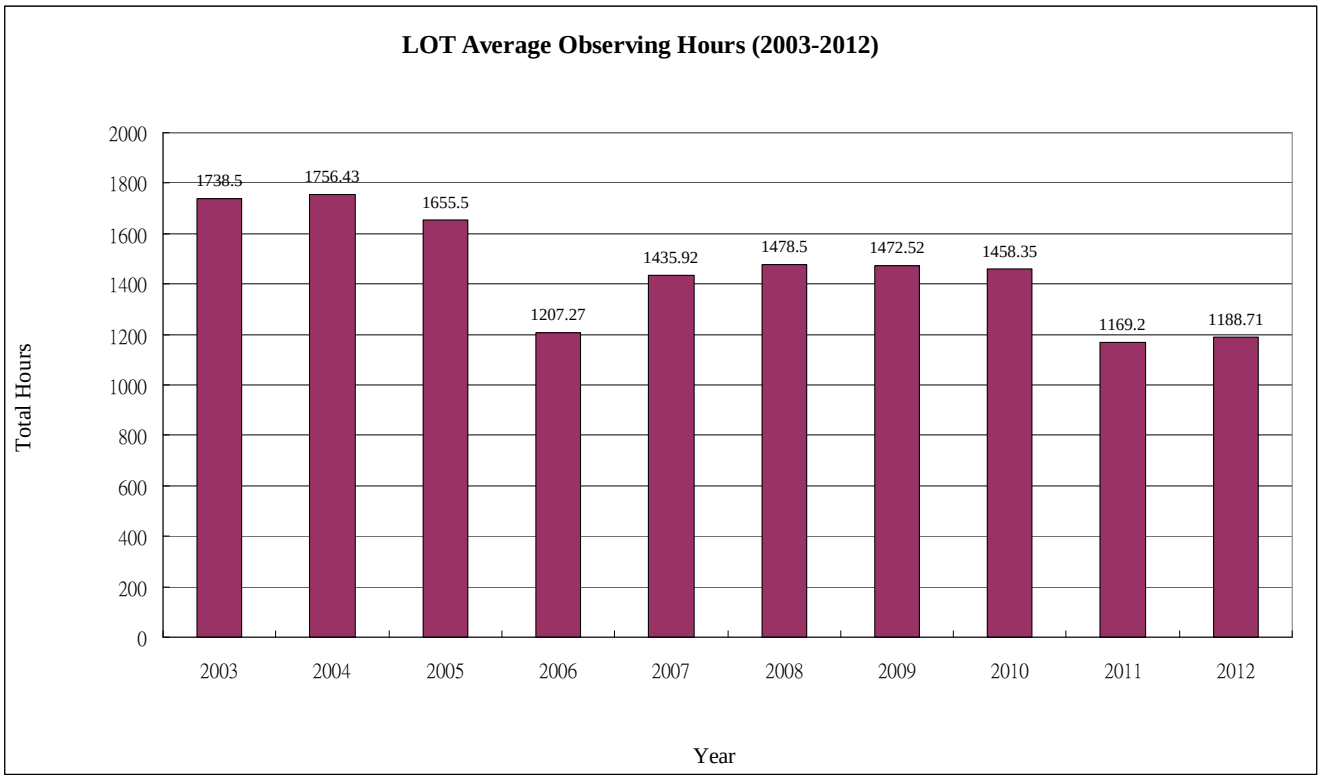

圖 1　鹿林天文台歷年觀測時數統計圖 (2003-2012)

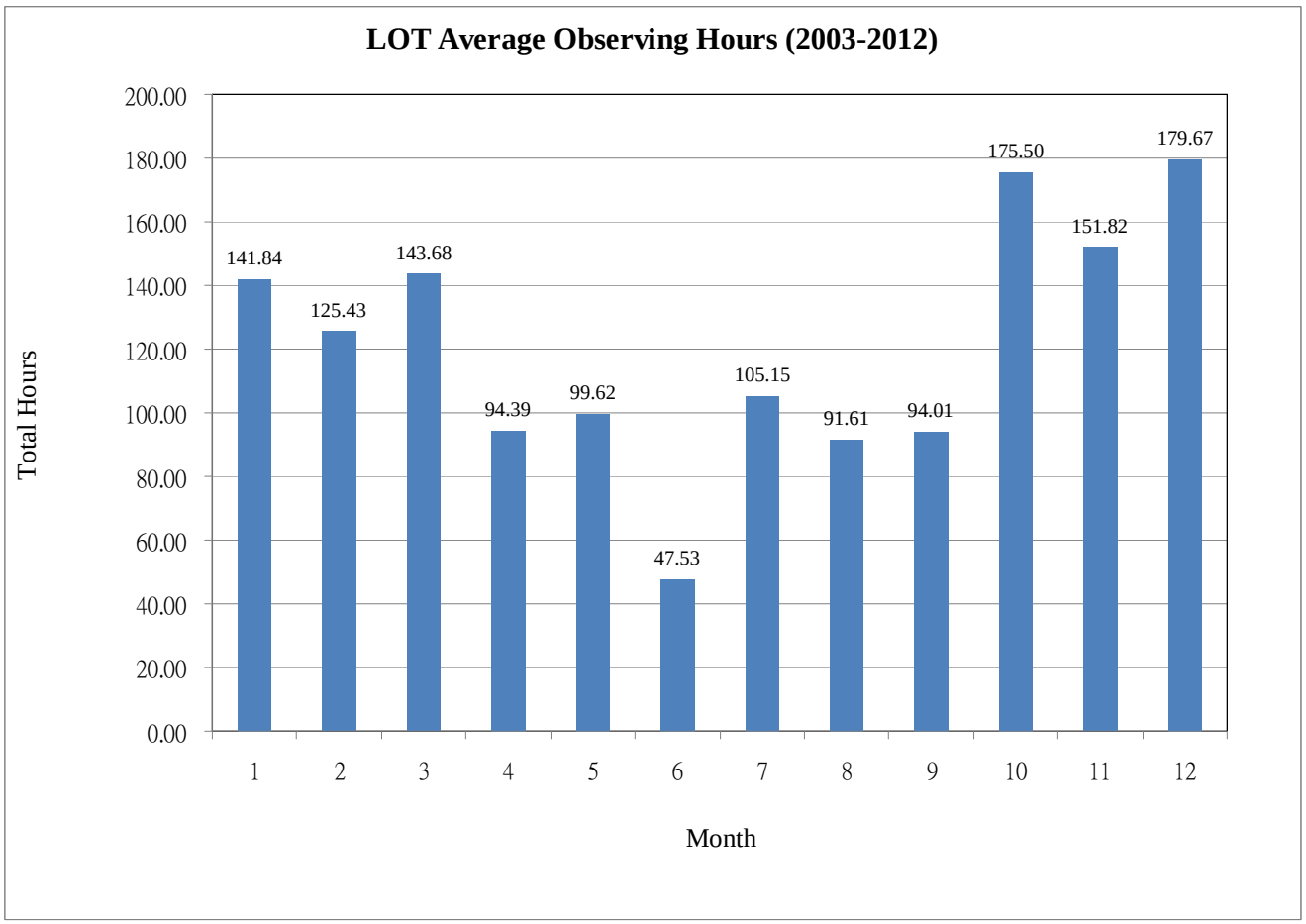

圖 2　鹿林天文台月平均觀測時數統計圖 (2003-2012)

鹿林天文台參訪團體統計(2010-2012)

2012 年

日期	單位	人數
1 月 19 日	成功高中天文社	15
2 月 14 日	逢甲/交大天文社	12
3 月 24 日	塔塔加警察隊	4
4 月 4 日	台北教育大學自然科學教育學系	15
4 月 18 日	中大學務長帶隊參訪	14
4 月 21 日	前環保署張署長參觀	20
5 月 17 日	經濟部標準局	23
5 月 22 日	馬來西亞 521 日環食觀測隊	9
5 月 23 日	阿里山國中小	12
6 月 20 日	香港大學學生會天文學會	
7 月 15 日	林青處長	25
8 月 10 日	高雄市廢棄物處理公會	20
9 月 15 日	黃郁翔	4
10 月 5 日	荒野保護協會-台中分會	17
10 月 6 日	高雄醫學大學登山社	30
10 月 8 日	環境督察總隊南區督察大隊	3
10 月 13 日	士林社大	27
10 月 14 日	屏東萬年溪保育協會	
10 月 20 日	中國醫藥大學通識中心	25
11 月 3 日	台南大學附屬小學+環宇蒙特梭利實驗小學	50
11 月 13 日	達邦國小	40
12 月 8 日	國家文官學院 100 年度簡任官訓練班	
12 月 9 日	高師大地理系	25
12 月 15 日	彰中天文社	19
12 月 22 日	成功大學天文社	

2011 年

日期	單位	人數
1 月 15 日	JIMO 小大讀書會	
1 月 28 日	清大天文社	22
1 月 29 日	成功天文社	20
2 月 10 日	中大天文社	
3 月 12 日	寶國社區親子團	28
3 月 12 日	凱基證券	18
4 月 4 日	政大天文社+台大天文社	26
4 月 16 日	香港電視台錄製節目	4
4 月 24 日	經濟部標準檢驗局	27
4 月 27 日	警察小隊長官視察參訪	4
5 月 1 日	成大天文社+高醫天文社	20
6 月 13 日	警察小隊參觀	12
6 月 22 日	國科會	20
6 月 27 日	年第二屆海峽兩岸天文科學教育論壇	
7 月 1 日	經濟部中部辦公室	
7 月 2 日	台中市文山社大	26
7 月 5 日	台中市立大里高中	20
7 月 9 日	彰化高商科創社	25
8 月 12 日	立法委員參訪	20
8 月 19 日	中大理學院邱秘書等	9
8 月 20 日	親子觀星會	50
8 月 25 日	營管所與營繕組等參訪	7
9 月 7 日	林務局東勢林區管理處(處長、鞍馬山莊主任等)	6
9 月 11 日	長興化工	20
11 月 11 日	西湖國小	
11 月 20 日	jimo 讀書會	
11 月 18 日	大型醫療緊急救護協會暨內政部前部長葉金鳳	13
12 月 2 日	達邦國小	35
12 月 23 日	玉管處生態健行訓練	

2010 年

日期	單位	人數
1 月 14 日	林務局	6
2 月 8 日	師大附中	47
2 月 10 日	成功高中	15
3 月 13 日	逢甲天文社	21
3 月 14 日	大田精密工業	30
4 月 2 日	交大天文社	7
4 月 10 日	日本系魚川市訪問團(玉管處日語翻譯)	7
4 月 17 日	國際扶輪社青少年交換委員會	40
5 月 1 日	國際扶輪社青少年交換委員會	41
5 月 8 日	士林與文山社大	30
5 月 29 日	瑞祺電通	
6 月 12 日	台南縣仁德國中教師會	
6 月 12 日	彰化高中	
6 月 13 日	古坑華南國小	30
7 月 10 日	知識探索協會	30
8 月 14 日	中大校友會	
8 月 21 日	大里高中	15
8 月 22 日	高醫大生物系	3
8 月 28 日	高雄中學	50
9 月 11 日	寶國社區發展協會	
9 月 17 日	交大張俊彥教授	4
9 月 24 日	國家公園義工活動	
9 月 25 日	塔塔加警察小隊與警政署長官	
10 月 9 日	彰化地方法院（警察小隊）	26
10 月 21-22 日	台視熱線追蹤採訪	
10 月 22-24 日	攝輯手拍攝國科會天文影片	7
10 月 28 日	達邦國小	45
10 月 29 日	國家公園全國義工活動	
11 月 6 日	屏縣環境教育輔導團	20
12 月 19 日	嘉義縣警察局	13

2008-11-23 廣達基金會參訪鹿林天文台

2010-05-08 士林與文山社大參訪鹿林天文台

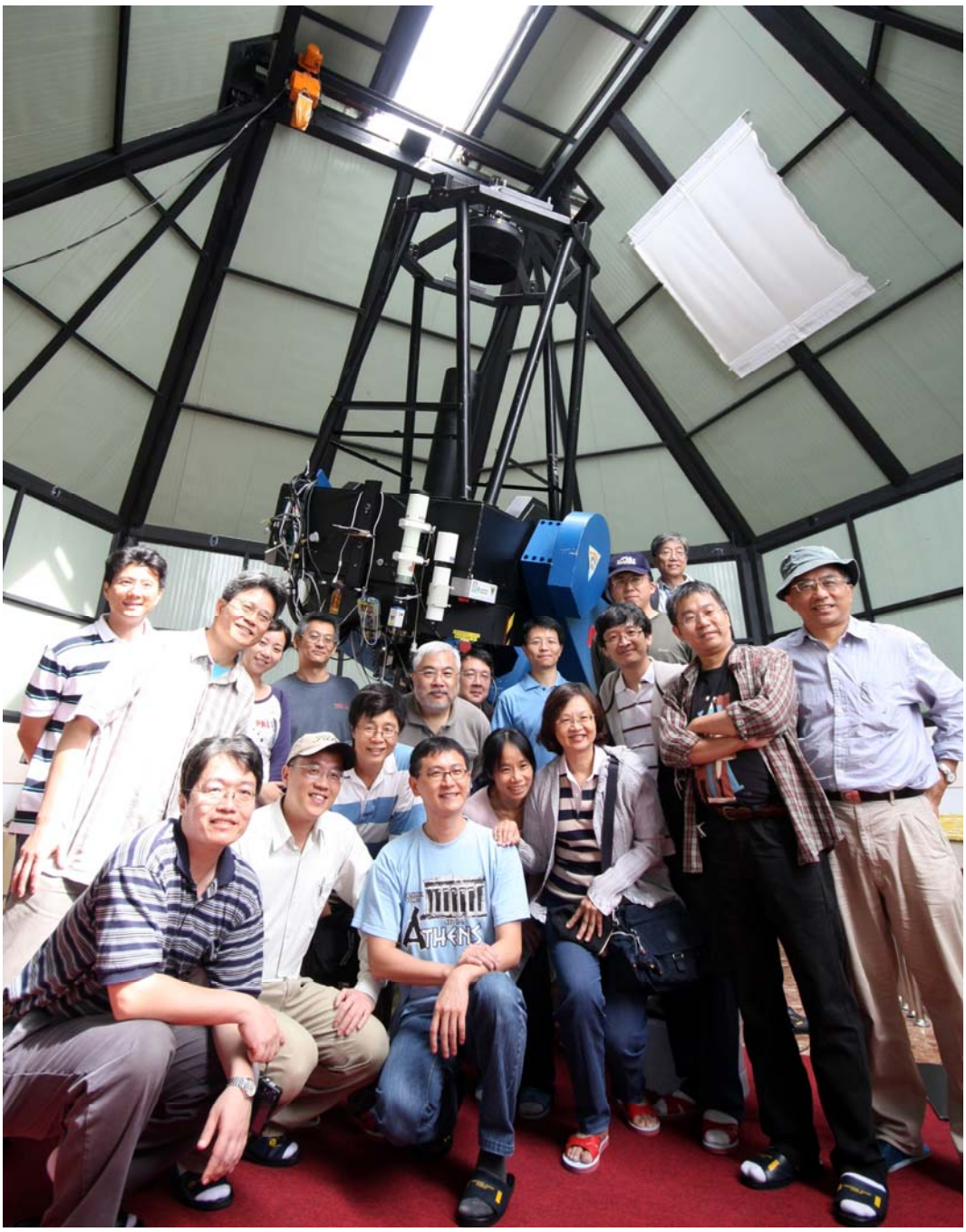

2011-06-22 國科會委員參訪鹿林天文台

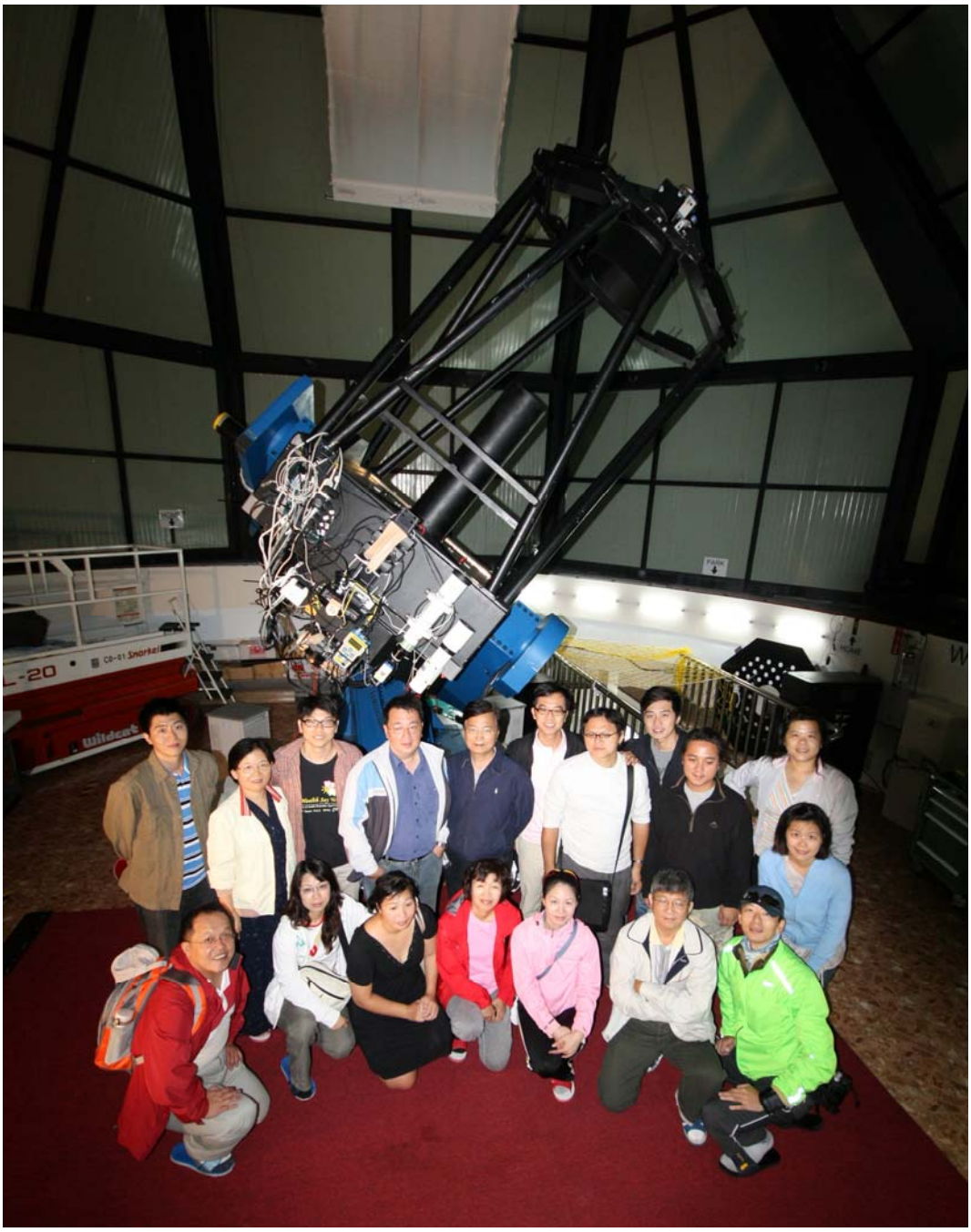

2011-08-12 立法院參訪鹿林天文台

2012-05-22 馬來西亞日環食觀測團參訪鹿林天文台

LOT 2012A Project List (2012/2-2012/7)

#	Title
1	Student Training for NTHU's "Fundamentals of Observational Astronomy" Course
2	Monitoring the activity of the retorgrade comet C/2009 P1 (Garradd)
3	Measurement of the Speed of Light from Extraterrestrial Sources
4	The Follow-Up Photometric Observations of Young Planetary Nebula M 1-11
5	Shakedown of the Imaging Polarimeter TRIPOL
6	Tests of New LOT Control Software
7	Dust production in young core-collapse type supernovae
8	PS1 follow-up: Jovian Trojan and Outer Solar System Objects
9	Determine the Rotational Curves of C-type Asteroids
10	Lulin CCD Imaging School with NCUcam-1
11	Deep survey of the coma structure on the asteroids in cometary orbits
12	Monitoring and Spectroscopic Observations of C/2011 F1(LINEAR) and 596(Schelia)
13	Reveal the magnetic structure in the _lamentary cloud, Aquila rift
14	Gamma-Ray Burst Follow-up Observations
15	Color Measurements and Pair Identi_cation of Possible Common Origin Asteroids
16	Core-collapse Supernova and Optical Transients
17	OPTICAL IDENTIFICATION OF NON-BLAZAR GAMMA RAY SOURCES
18	Rotationally Resolved Spectroscopic Observations of Asteroids
19	Simultaneous Observations of Be Stars with Strong Near Infrared Excess
20	A Test Program of Hiyayo High-Dispresion Grism
21	Monitoring the activity of comet C/2011 L4 (PANSTARRS)

LOT 2012B Project List (2012/8-2013/1)

#	Title
1	LOT Observation Training for NCU’s Observational Astronomy Course
2	LOT Experience for Summer Undergraduate Students
3	Optical Observations of Near-Earth Asteroids for Physical Properties
4	Measurement of the Speed of Light from Extraterrestrial Sources
5	Polarimetric Observations of Themis Asteroid Family
6	Searching for Transiting Young Exoplanets in Galactic Open Clusters
7	Magnetic Field Structure in Molecular Cloud Probed by Optical Polarization
8	Practical Class of “Observational Astronomy"
9	Optical Spectroscopy for Star Membership of An embedded Open Cluster
10	Simultaneous Observations of Be Stars with Strong Near Infrared Excess
11	The nature of an unidentified Fermi object
12	Light-curves of Jovian Trojans with long rotational periods
13	Revealing the importance of magnetic field in filaments and sub-filaments structure
14	The hosts of episodic radio galaxies
15	Variability of Color for Intra-Night Optical Variable AGNs
16	Rotationally Resolved Spectroscopic Observations of Asteroids
17	Optical Identification of the Unidentified Fermi Objects
18	Color Measurements of Extremely Young Asteroid Pairs
19	Cooling Temperature Optimization of Newly Developed NCUcam-1
20	Gamma-Ray Burst Optical Afterglows
21	Core-collapse Supernova and Optical Transients
22	Follow-up Observation of MAXI flare M-dwarfs
23	Deep survey of the coma structure on the asteroids in cometary orbits
24	Search for Large Magnitude Variation in Jovian Trojans.

相關報導

7 天文學者挺「聲」　破除末日傳說

「如撲克牌伎倆」學者駁末日傳言
科學方式破除末日說 七學者闢謠　張寧 報導

末日說傳的沸沸揚揚，中央大學天文所，有專家看不下去了!七位天文專家，一起拍攝影片，駁斥 2012 世界末日傳說。而針對世界會因爲黑洞而毀滅，還有外星人會毀滅地球等傳言，他們也透過科學方式破解，有學者形容 末日說就像是「撲克牌伎倆」。

天搖地動，山崩地裂，離馬雅預言的 2012 世界末日越來越近，不少人心驚驚，甚至有人打造挪亞方舟、避難艙等設備，但是 12 月 21 號這天地球真的會毀滅 嗎？中央大學天文所，有 7 位天文專家拍攝影片，駁斥末日說。 學者認爲，馬雅曆法是從西元前 3114 年 8 月 13 日開始計算，到 2012 年 12 月 21 號爲止，剛好是一個完整循環，卻被大家誤會是世界末日，不過傳言中 2012 年冬至，黑洞、太陽、地球連成一線時，將會造成地球滅亡，到底是真是假？　　透過科學方式破除末日傳言，學者們針對外星人是否毀滅地球、世界是否會因爲黑洞而毀滅等等說法，一一破解，就怕大家相信錯誤說法，自己嚇自己。

原文轉載自【2012-12-18/台視新聞】

【影】中央大學七教授　拍七短片破末日迷思

生活中心／綜合報導

12 月 21 日是傳聞的「世界末日」，選在這一天，中央大學和校友總會共同舉辦「末日？重生？」晚會，以觀星、學者座談等方式，迎接 22 日的「重生」，來破 除迷信。事實上，中大天文所長高仲明等七位教授，今年 2 月起就陸續在 YouTube 上傳七段短片，分別從七種天文科學角度，破除世界末日的各種迷思。

這七位天文學者分別是：高仲明、葉永烜、陳文屏、周翊、黃崇源、饒兆聰，和中研院博士黃麗錦(見上圖，取自 YouTube)。第一段影片是陳文屏駁斥 2012 世界末日傳說，他指出，今年的末日潮來自馬雅的曆法的一個周期結束，其中最常聽到的說法是，「2012 年冬至時，銀河中心黑洞、太陽黑洞、地球形 成一直線，其合併重力會造成地球毀滅或是磁場的變化。」但事實上，太陽繞銀河一周的周期約二億多年，過去數十萬年來，每年年底左右時，銀河中心、太陽、地 球都會處在相同的相對位置。但地球並沒毀滅，每年大家都一樣快樂的過著聖誕節。而引力也不會造成磁場的改變。

高仲明談的是最受一般民眾 好奇的「2012 外星人毀滅地球」的話題，他指出，「退一步來說，我們害怕外星人，其實是害怕會破壞我們家園的『壞星人』。如果是『好星人』我們應該會張 開雙手歡迎他們。假如銀河系真的有一群『壞星人』四處搗亂，除非他們很珍惜這個行星，要不然只要幾百年、一千年就可以把這個行星消耗殆盡，再找另外的獵物 了。」

高仲明要大家想想，「到目前地球都沒有被『壞星人』消耗掉的機率有多少呢？『壞星人』剛好在人類有文明的時候來搞破壞的機率有多 少？人類有文明出現到現在大約一萬年。一千年、一萬年在天文來說真的是一眨眼的功夫，兩個眨眼相遇的機會是否會比人類在未來一萬年內毀在自己的手裡的機會 來得小呢？」

原文轉載自【2012-12-18/ETtoday 新聞雲　　ETtoday 生活新聞 】

破除末日謬論！ 中大 7 教授製短片反駁

【記者劉愛生／桃園縣報導】

二〇一二年十二月廿一日末日說甚囂塵上，中央大學天文所長高仲明等七位教授，除罕見自製系列影片上傳 YouTube 反駁，昨並透過中央大學發布新聞，希望從天文科學的角度，破除社會大眾對末日說的迷思。

中央大學天文所教授陳文屏認為，末日說影響人心，「是撲克牌伎倆！」「世界末日」等電影在虛構的情節中，穿插了部分科學知識以及一些似是而非的謬論，「就像洗牌一樣夾雜在一起，讓人虛實難判」，讓不少人誤信為真。

為破除迷思，中央大學和校友總會也決定，廿一日傳聞世界末日來臨的這天，將共同舉辦「末日！重生？」晚會，以觀星、學者座談和牽手祈福等方式，陪伴民眾直到凌晨十二時，迎接希望的明天。

「我們學天文科學的，怎會相信一個已經消失的文明，如何能夠預測數千年之後整個世界的命運？」高仲明表示，幾部災難電影加上一些傳說，就把全世界的人搞的人心惶惶，「我們有責任反駁，七名學者因而製作七部短片，化解疑慮」。

高仲明與葉永烜、陳文屏、黃崇源、周翊、饒兆聰教授及中研院博士黃麗錦等七位天文學家，今年二月間就挺身而出，透過 YouTube 影像，以科學知識解說末日說不可信。

陳文屏強調，「馬雅曆法」並沒有「預測未來世界」；曆法循環是生活一部分，每年過年、過生日都是例子。「世界末日說，有部分看似科學，卻無科學根據的立 論」，陳文屏表示，例如地球磁場逆轉，大約幾十萬年會發生一次；太陽風暴的發生，約每十一年一周期，去年剛經過太陽活動最低峰，但磁場逆轉、太陽風暴從沒 有嚴重到全球會滅絕。

主張末日說的人士還指出，銀河系中心的黑洞，會在這天與太陽、地球連成一線，對地球造成毀滅性影響。天文所教授周翊說，事實上黑洞離地球非常遙遠，是地球與太陽距離的十七億倍，對地球造成的重力影響，只有太陽對重力影響的一兆分之一。

原文轉載自【2012-12-18/聯合報/A1 版/要聞】

「會滅亡嗎？」 校長被問急 教授拍片駁末日

當時的中大代理校長 提議學者各定主題破解迷思 上傳 9 個月、點閱 4 千次 冷門「有

心理準備 」

【記者劉愛生／桃園縣報導】

中央大學天文研究所長高仲明等七位教授，爲破解末日說迷思，七人各拍一段影片，促成七人「聯手出擊」，是因當時的代理校長劉振榮在多次聚會中，老是被與會人士追問「地球真的會突然毀滅嗎？」

電影「二〇一二、明天過後」年初上演後，引起一些好奇民眾議論，加上國家地理頻道、Discovery 節目不斷播放馬雅曆法與消失的古文明文化，末日疑懼隨之而起。

當時的中央大學代理校長劉振榮常被友人問及末日議題，「馬雅曆法真有世界末日之說？」劉振榮於是校內會議提議，太多人好奇、質疑世界末日，「我們學科學的，是否該替社會做些事，破除世界末日之說。」

高仲明表示，他們接受代理校長劉振榮的建議，七名學者各選定一個末日說的主題，製作三到五分鐘的影片。拍攝以教授直接口述內容爲主，或是請助教幫忙繪畫解說，兩周就拍攝且後製完稿。

今年二月完成後上傳 YouTube，至今九個多月，約四千多人瀏覽，高仲明說，點閱率不高有心理準備，因爲天文學原本就是一門冷門的科學。

他認同台中科博館館長孫維新的看法，人們擔心地球被外星人或其他天象毀滅，還不如擔心人類自己惡整地球，破壞生態，人類自己毀滅自己的速度恐比地球以外的不確定因素更可怕。

原文轉載自【2012-12-18/聯合報/A5 版/話題】

7 天文學者挺「聲」YouTube 破除末日說

末日傳言如「撲克牌伎倆」

〔記 者湯佳玲、賴筱桐／綜合報導〕馬雅曆法傳言今年十二月二十一日（本週五）爲世界末日，爲破除末日說，中央大學天文所七位天文專家一同挺身而出，透過 YouTube 影像，破除社會大眾對末日的迷思。學者形容末日傳言就像是「撲克牌伎倆」，事實與謬論夾雜，所以迷惑了不少人。

影片 2 月上傳 點閱率夯

中大天文所所長高仲明、教授葉永烜、陳文屏、黃崇源、周翊、老師饒兆聰與中研院黃麗錦博士等七位天文專家分別錄製影像上傳至 YouTube，內容包括「駁 斥 2012 世界末日傳說」、「2012 世界是否會因黑洞而毀滅？」「2012 外星人是否毀滅地球？」等，希望透過科學對話方式，破除馬雅曆法世界末日傳 言；影片自二月上傳以來，獲得極高的回響和點閱率。

陳文屏認爲，末日傳聞之所以甚囂塵上，除了電影的推波助瀾外，關鍵在於傳言內容穿插了部分科學事實，他形容這是「撲克牌伎倆」，部分事實與一些似是而非的謬論像

洗牌一樣夾雜在一起，讓人虛實難判。

另外，淡江大學美洲研究所所長陳小雀說，馬雅文化同時使用太陽曆、祭祀曆（卓爾金曆）及長紀曆三種曆法，馬雅人有「敬天惜地」觀念，也相信「周而復始」。

陳小雀分析，馬雅人採二十進位法，太陽曆以二十天爲一個月，十八個月便是三百六十天，馬雅人知道一年有三百六十五天，因此剩下五天由第十九個月補齊，這五 天被馬雅人視爲不祥的禁忌日。另外，祭祀曆同樣以二十天爲一個月，但只有十三個月，太陽曆每走五十二年，會與祭祀曆重疊，在馬雅人眼中，每五十二年是一個 新的循環。馬雅曆法指末日是循環

長紀曆的計算單位分別是「金」（kin，一天）、「烏依納」（uinal，二十天）、「敦」（tun，三百六十天）、「卡敦」（katun，七千兩百天）及「巴克敦」（baktun，十四萬零四千天），其中又以十三巴克敦爲分界點，約五千 兩百年；自西元前三一一四年八月十三日開始計算，至二〇一二年十二月二十一日止，恰好是一個完整循環，卻被大家誤會是世界末日。

陳小雀強調，馬雅文化不可能有末日預言，據文獻記載，過去馬雅也曾遭遇洪水、豪雨及火山爆發等天災，但馬雅人相信，災難過後，必定有新生開始。

原文轉載自【2012-12-18/自由時報/A12 版/生活新聞】

校長被問急　教授拍片駁末日

2012/12/18 10:00 記者劉愛生／桃園縣報導

中央大學天文研究所長高仲明等七位教授，爲破解末日說迷思，七人各拍一段影片，促成七人「聯手出擊」，是因當時的代理校長劉振榮在多次聚會中，老是被與會人士追問「地球真的會突然毀滅嗎？」

電影「二〇一二、明天過後」年初上演後，引起一些好奇民眾議論，加上國家地理頻道、Discovery 節目不斷播放馬雅曆法與消失的古文明文化，末日疑懼隨之而起。

當時的中央大學代理校長劉振榮常被友人問及末日議題，「馬雅曆法真有世界末日之說？」劉振榮於是校內會議提議，太多人好奇、質疑世界末日，「我們學科學的，是否該替社會做些事，破除世界末日之說。」

高仲明表示，他們接受代理校長劉振榮的建議，七名學者各選定一個末日說的主題，製作三到五分鐘的影片。拍攝以教授直接口述內容爲主，或是請助教幫忙繪畫解說，兩周就拍攝且後製完稿。

今年二月完成後上傳 YouTube，至今九個多月，約四千多人瀏覽，高仲明說，點閱率不高有心理準備，因爲天文學原本就是一門冷門的科學。

他認同台中科博館館長孫維新的看法，人們擔心地球被外星人或其他天象毀滅，還不如擔心人類自己惡整地球，破壞生態，人類自己毀滅自己的速度恐比地球以外的不確定因素更可怕。

原文轉載自【2012-12-18/華視新聞網】

「末日！重生？」在中大 觀星、聽講、守末日

【大 紀元 2012 年 12 月 16 日訊】(大紀元記者徐乃義台灣桃園報導)今年 12 月 21 日爲世界末日？當晚你想怎麼過？千萬別錯過國立中央大學舉辦的「末日！重 生？」晚會活動，一同守夜跨入下個長紀元！ 中大校友總會將於 21 日下午五點半開始至隔日凌晨，舉行一連串精彩活動，包括「末日電影院」、「觀末日星空」、「末日預言秘密大公開：人文、科學與宗教的 對話」講座，並舉辦「末日宣言」才藝競賽，最後於午夜 12 點進行「千人牽手祈福會」。

「末日預言」是當前備受矚目的熱門話題，眾多傳聞的 末日情節，像是超級大颱風、地震、太陽風暴、天體撞擊等地球環境課題，正是中央大學系所專長的領域，爲解開大眾對於 2012 末日的關注與迷思，特別舉辦 「末日重生」系列活動。晚會活動將於 12 月 21 日下午五點半開始，由末日電影院《2012》與《明天過後》揭開序幕。

該校教授以及各領域 專家學者進行對談，帶領深入探索末日傳言的來龍去脈，中場並穿插「末日宣言」才藝競賽，展現年輕活力。另外活動會場草皮上還會有本校天文所架設望遠鏡，觀 察天體，包括月球、木星、星雲等，讓您一窺末日星空的變化。會後繞行中大校門圓環，於星空下進行「千人牽手祈福活動」，共同點亮心中燈火，爲新的開始獻上 祝福。

歡迎大家共度充滿知性與感性的夜晚，「末日重生」歲末活動 21 日下午五點半開始，至隔日凌晨。（責任編輯：呂美琪）

原文轉載自【2012-12-16/大紀元時報首頁 > 新聞 > 台灣地方新聞 > 文教工商 > 正文】

12/21 世界末日 天文學者認爲不會發生

編輯／謝俊峰

最近外界對於馬雅曆法預言 2012 年 12 月 21 號是世界末日的傳言甚囂塵上，不過，中央大學天文所所長高仲明和陳文屏教授等 7 位天文專家，卻強調這個末日預言不會發生，並且他們還透過 YouTube 影像，以科普來做機會教育，希望可以破除社會大眾對末日的迷思。

受到電影和馬雅曆法傳言的影響，今年 12 月 21 號究竟是不是世界末日，引發外界熱烈的討論，不論是馬雅曆法大循環結束的預言說，或者是地球磁場倒轉，還有 黑洞會和太陽與地球連成一線，對地球造成毀滅性影響的說法，都讓民眾擔心世界末日的來臨，但是中央大學多位天文所專家卻駁斥這些末日說的說法，認爲 12 月 21 號並不會出現世界末日。

中央大學天文所教授陳文屏表示，2012 的末日傳聞主要是受到電影賣座的影響，再加上它把部分科學事實放進劇 情裡，使得部份民眾深信不疑，可是這些劇情包括像是天體撞地球、太陽風暴和地球失去磁場等等，短期都不會在地球發生，並且他還強調，其實馬雅曆法並沒有 12 月 21 號是末日的意思，因爲循環有長有短，當這個大循環結束之後，下個循環才正要開始。

陳文屏教授也指出，行星連成一線在歷史上已經發生很多次，不過，事實上，這些行星離地球很遠，它們對地球產生的萬有引力，比地球上汽車的萬有引力還要小，所以行星連成一線，對地球造成毀滅性影響的說法並不存在。

中央大學也將在 12 月 21 號當天共同舉辦「末日！重生？」晚會，並以觀星、專家學者座談和牽手祈福等方式，陪伴大家共同迎接充滿希望的下一個明天。

原文轉載自【2012-12-18/中國網路電子報】

世界末日說純屬無稽教授拍片打破迷思

【記者游婉琪】

馬雅曆法傳言 21 日是世界末日，加上電影推波助瀾，讓不少人擔心。爲破除末日傳言，中央大學天文所所長高仲明率所內教授挺身而出，錄製 YouTube 科普 教學影片，解除社會大眾對於末日的迷思，同時也將在 21 日當天舉辦「末日！重生？」晚會，陪民眾觀星、座談、牽手祈福直到午夜 12 時。

中央大學天文所教授陳文屏以「撲克牌伎倆」形容末日傳聞。他指出，之所以有越來越多民眾相信末日傳聞，除了電影與媒體的渲染，關鍵在於內容穿插了部分的科學，讓事實與謬論像洗牌般夾雜在一起，讓人虛實難判。

「一個已經消失的文明，如何預測數千年後整個世界的命運？」陳文屏強調，其實馬雅曆法並非要預言世界末日，曆法代表的是循環，就像日常生活中過年、過生日 一樣，完全不需要擔心。他坦承，世界末日說法中有部分科學根據，例如地球磁場的逆轉，大約幾十萬年會發生一次；太陽風暴也是每 11 年產生一次周期，但對地 球的影響都是微乎其微。

原文轉載自【2012-12-18/Upaper/3 版/焦點】

2012 世界末日？中央大學天文學教授：災難片的撲克牌伎倆

生活中心／綜合報導

馬雅傳說中的 12 月 21 日世界末日即將到來，相關討論也不斷在網路上發酵。中央大學天文所教授陳文屏特別拍攝影片，表示世界末日只是一種撲克牌伎倆，將各種似是而非的論點攪和在一起，混淆虛實。

陳文屏認爲，電影與電視將末日傳言炒作太過火。他認爲這一天不過是馬雅曆法循環

結束的一日，就像一個月或一年的結束，但會展開新的循環，所以大家還是要記得繳房貸跟考學測。

電影與名嘴們的推波助瀾，則是一種撲克牌伎倆。在 2011 年中時出現大量的傳言，當時對此傳言相當熱絡，但在災難片下片後的今日，相關討論反而相當冷清。電影將這些傳言混淆，專業知識不夠者，就會被騙過。

陳文屏舉過去的傳言爲例，電影中提到的太陽風暴與地球磁場等狀況，都不可能造成地球全面毀滅。

原文轉載自【2012-12-18/NOWnews 今日新聞網 新奇新聞 】

末日傳聞　中央大學天文所破迷思齊發聲

中廣新聞網－ 2012 年 12 月 18 日 下午 1:20 末日傳聞話題不斷，引起廣泛討論，中央大學天文所高仲明所長等七位天文專家一起挺身而出，YouTube 影像破除末日的預言及大眾迷思，十二 月二十一日當天共同舉辦「末日！重生？」晚會，以觀星、專家學者座談和牽手祈福方式，迎接希望的明天。（李明朝報導）

末日傳聞一直引起話題，中央大學天文所高仲明所長認爲這只是傳聞，大家不用在意，民眾還是要安心過生活；高仲明教授認爲以天文的角度來看，不太可能在一天發生。

高仲明教授表示，他們把相關看法透過網路來機會教育，破除社會大眾對末日的迷思。

中央大學和中大校友總會也將在十二月二十一日當天共同舉辦「末日！重生？」晚會，以觀星、專家學者座談和牽手祈福方式，陪伴大家直到凌晨十二點，迎接希望的明天，邁向下個紀元。

原文轉載自【2012-12-18/中廣新聞網】

天文學者拍科普影片　破除末日迷思

記者黃朝琴／臺北報導

受到電影和馬雅曆法預言的影響，今年 12 月 21 日是世界末日的傳言甚囂塵上，中央大學天文所高仲明和陳文屏等 7 位天文學者，共同拍攝科普影片，並上傳至 YouTube，內容包括「駁斥 2012 世界末日傳說」、「2012 世界是否會因黑洞而毀滅？」、「2012 外星人是否毀滅地球？」等單元，希望破除社會 大眾對末日的迷思。

中央大學 12 月 21 日將舉辦「末日！重生？」晚會，並以觀星、專家學者座談和牽手祈福等方式，陪伴大家迎接充滿希望的下一個明天。

陳文屏表示，受到賣座電影推波助瀾，加上內容穿插部分科學事實，導致部份民眾對 2012 的末日傳聞深信不疑，但天體撞地球、太陽風暴和地球失去磁場等劇情，短期都不會在地球發生，就像是「撲克牌伎倆」，部分事實和似是而非的言論夾雜在一起，讓

人虛實難辨。

陳文屏表示，馬雅曆法並沒有 12 月 21 日是末日的意思，因爲循環有長有短，當這個大循環結束之後，下個循環才正要開始。陳文屏也指出，行星連成一線在歷史 發生很多次，這些行星離地球很遠，對地球產生萬有引力，比地球上汽車的萬有引力還要小，行星連成一線對地球毀滅性影響的說法並不存在。

中央大學天文研究所副教授周翊表示，黑洞離我們非常遙遠，大約是地球到太陽距離的 17 億倍，黑洞對地球造成的重力影響只有太陽對重力影響的一兆分之一，因此黑洞是否跟太陽連成一線，對地球的影響微乎其微，這個預言根本不成立。

原文轉載自【2012-12-18/青年日報/11 版/教育藝文】

破末日迷思　中大自製科普影片

（中央社記者許秩維台北 17 日電）中央大學的天文學者自行製播影片，用科普作機會教育，希望破除大家的世界末日迷思。

鑒於民眾對世界末日預言的迷思，中央大學天文研究所教授陳文屏號召天文所的學者，共同製播科普影片，並上傳到 YouTube，內容包括「駁斥 2012 世界 末日傳說」、「2012 世界是否會因黑洞而毀滅？」、「2012 外星人是否毀滅地球？」等，希望透過科普教育，幫大家破除迷思。

陳文屏表示，電影推波助瀾，加上內容穿插部分科學事實，導致末日傳聞廣爲流傳，這就像是「撲克牌伎倆」，部分事實和似是而非的言論夾雜在一起，讓人虛實難辨。

「一個消失的文明，如何預測數千年後整個世界的命運呢？」陳文屏指出，循環有長有短，這個大循環結束後，就代表下個循環要開始，就像每年過年和生日一樣；而地球磁場的逆轉，幾十萬年會發生一次，大小地震的發生，大家也都習以爲常，但從來沒有嚴重到全球會滅絕。

中央大學天文研究所副教授周翊也表示，黑洞離我們非常遙遠，大約是地球到太陽距離的 17 億倍，因此黑洞對地球造成的重力影響只有太陽對重力影響的一兆分之一，因此黑洞是否跟太陽連成一線，對地球的影響微乎其微，這個預言根本不成立。1011217

原文轉載自【2012-12-17/中央社首頁 > 教育文化】

國際年輕天文學者講座

【聯合晚報／記者林進修／即時報導】 2012.10.30 01:50 pm

國立中央大學與台達電子文教基金會發起的「國際年輕天文學者講座」，今年秋季獲獎者爲英國的司馬特教授，他今天來台受獎，11 月 2 日下午 2 時將在中央大學 天文所進行學術演講，11 月 3 日上午 9 時在台中一中進行科普演講。演講均以英文進行，第

二場有中文解說，講題與超新星有關，歡迎有興趣的民眾參與。
【2012/10/30 聯合晚報】@ http://udn.com/

原文轉載自【2012-11-02/聯合新聞網/生活 即時新聞 】

國際天文講座　英學者獲獎

中央社 － 2012 年 10 月 30 日 下午 2:22（中央社記者許秩維台北 30 日電）中央大學今天表示，英國學者史瑪特獲頒國際年輕天文學者講座，史瑪特除了來台領獎，也受邀舉行兩場演講。

中央大學與台達電子文教基金會發起國際年輕天文學者講座，表彰 45 歲以下、在研究領域有卓越表現的國際天文學者；講座活動由中央大學執行，經費由台達電子文教基金會提供，得獎者除來台機票補助，還會獲頒講座獎金。

中央大學表示，每年預計頒發兩位講座，獲頒講座者除了和中央大學天文所進行交流，也會在台達電子指定的高中進行科普演講；今年秋季獲獎者爲英國學者史瑪特(Stephen J. Smartt)，他今天上午也到中大接受頒獎，接下來將在中大和台中一中演講。

中央大學表示，史瑪特專長爲超新星，這是恆星演化到晚期所產生的劇烈爆發現象，剛爆發的超新星非常明亮，即使在遙遠星系中的超新星也觀測得到。史瑪特也是國際泛星計畫成員，利用位於夏威夷的望遠鏡觀測剛爆發的超新星，以了解超新星的形成和變化。

原文轉載自【2012-10-30/中央社】

中大天文所廿週年慶　星光閃耀

慶祝中央大學天文研究所成立二十週年，中大廿日邀請了歷屆頒贈的小行星回娘家，見證亞洲這塊發現小行星最活躍之地。同時頒贈「蔡文祥小行星」，感念這位台 灣天文研究的開路先鋒。中大校友總會也舉辦一場科普演講，由天文所 陳文屏 教授主講「說盡一夜星空」，分享精彩的天文知識饗宴。

談起 台灣本土天文研究的肇始、全國最高鹿林天文台的籌建，就一定要提起「蔡文祥」這個名字。中央大學特別將 2006 年 8 月 12 日發現經國際天文學聯合會(IAU/CSBN)通過的 175410 號小行星，命名爲「蔡文祥」(Tsayweanshun)，感念這位 台灣可見光天文學研究的先驅。

此外，也邀請了歷屆頒贈的小行星一同回娘家，包括中大、鹿林、嘉義、溫世仁、鄭崇華、鄒族、南投、 沈 君山、玉山、雲門、慈濟、小林村、中壢、李國鼎、桃園、吳大猷、苗栗、鄧雨賢、鍾理和、陳其寬、馮元楨等。從歷屆小行星命名之中，尋找其深度意涵，跨科學 探索、人文藝術、普世關懷之美。

蔡文祥教授　鹿林天文台的推手

蔡文祥教授 1981 年畢業於中央大學物理與天文研究所，爲台灣本土培養的第一位天文碩士。他在擔任研究生與助教期間，全程參與中大科學一館天文台建設，於 1981 年啓用的 61 公分望遠鏡，爲當時臺灣最大的天文望遠鏡。

1989 年學成歸國，返回母校物理系任教，引進天文研究用的 CCD（Charge Coupled Device, 電荷耦合元件）相機，是國內第一個專攻天文觀測的學者。臺灣天文界許多人都是他的門生，像是鹿林天文台站長林宏欽，正是他指導的第一屆天文所畢業生。

他回憶當年帶著首屆天文研究所學生，到玉山國家公園進行天文觀測教學，在燦爛星空下，幾位不曾見過「銀河」的都市小孩，忙於感受宇宙浩瀚，忽然有人迸出一句「爲什麼天上那一大片白雲都不動？」他定睛一看，原來那亮麗耀眼的「銀河」，被誤認爲「白雲」，才發覺需要創造更多機會，讓學生接近大自然與浩瀚宇宙。

當時因中壢市區急遽發展，校內外建設大幅增加，光害污染日趨嚴重。蔡文祥說，中壢校區天文台已不適合從事天文觀測與研究，必須另覓理想的觀測地點。 1990 年，在國科會支持下，他開始進行臺灣天文選址計畫，歷經三年的視相、氣候、大氣穩定度等條件調查研究後，確定玉山國家公園的鹿林前山爲優良的天文 台址。

蔡文祥說，蓋天文台，要考慮的因素很多，過程中曾評估恆春半島、阿里山、合歡山等地，鹿林前山特殊之處是它在環山之間，並非在最 高峰處，晴天率高。但空口無憑，要證明這個地點的好壞，必須由長期累積的觀測資料做科學性說明。他一手包辦選址探勘的鹿林天文台，終於在 1999 年設置完 成，自製 76 公分望遠鏡也正式啓用。

現居美國的他，仍親自動手於自家後院蓋的天文臺，進行變星觀測，同時進行天文科普的推廣工作。

鹿林天文台　一個劃時代的開始

中央大學天文研究所所長高仲明表示，中大的天文研究能在世界舞台發光發熱，有賴於 蔡文祥教授當年的高瞻遠矚，以及華路藍縷的籌設過程。海拔 2,862 公尺 的鹿林前山，沒水、沒電，更沒有路，山青一步一腳印將鐵皮、建材等揹上山，從一只鐵皮屋（觀測站），到現在亞洲最重要的天文觀測據點， 蔡文祥 教授一手參與選址探勘工作，功不可沒。

因鹿林天文台籌建，讓中大得以參與多項國際大型計畫，包括中美掩星計畫(TAOS)、與 美國夏威夷大學天文所合作的泛星計劃(Pan-STARRS)、與加州理工學院帕羅馬天文台合作的臺灣新世代可見光紅外光學研究-探高計畫(Tango) 以及目前最大的地面望遠鏡-阿塔卡瑪大型毫米波及次毫米波陣列（ALMA）計畫。同時發現許多新天體，從 2002 年發現台灣第一顆小行星，迄今累計發現約 800 顆小行星，成爲亞洲發現小行星最活躍的地方之一。2007 年更發現台灣第一顆彗星「鹿林彗星」和台灣第一顆近地小行星，成果十分豐碩。

原文轉載自【2012-10-20/楊梅新聞網 - udn 部落格】

中央大學天文研究所 20 週年　校友共聚話星空

【大紀元 2012 年 10 月 20 日訊】(大紀元記者徐乃義台灣桃園報導)慶祝中央大學天文研究所成立二十週年，中大廿日邀請了歷屆頒贈的小行星回娘家，見證亞洲 這塊發現小行星最活躍之地。頒贈「蔡文祥小行星」，感念台灣天文研究的開路先鋒。中大校友總會也舉辦一場科普演講，由天文所陳文屏教授主講「說盡一夜星 空」，分享精彩的天文知識饗宴。

全國最高鹿林天文台的籌建，一定要提起「蔡文祥」這個名字。中央大學將 2006 年 8 月 12 日發現經國際天 文學聯合會(IAU/CSBN)通過的 175410 號小行星，命名爲「蔡文祥」（Tsayweanshun），感念這位台灣可見光天文學研究的先驅。 20 日邀請了歷屆頒贈的小行星一同回娘家，包括中大、鹿林、嘉義、溫世仁、鄭崇華、鄒族、南投、沈君山、玉山、雲門、慈濟、小林村、中壢、李國鼎、桃園、 吳大猷、苗栗、鄧雨賢、鍾理和、陳其寬、馮元楨等。從歷屆小行星命名之中，尋找其深度意涵，跨科學探索、人文藝術、普世關懷之美。

蔡文祥教授 1981 年畢業於中央大學物理與天文研究所，爲台灣本土培養的第一位天文碩士。他在擔任研究生與助教期間，全程參與中大科學一館天文台建設，於 1981 年啓用的 61 公分望遠鏡，爲當時臺灣最大的天文望遠鏡。

1989 年學成歸國，返回母校物理系任教，引進天文研究用的 CCD（Charge Coupled Device, 電荷耦合元件）相機，是國內第一個專攻天文觀測的學者。臺灣天文界許多人都是他的門生，像是鹿林天文台站長林宏欽，正是他指導的第一屆天文所畢業生。

他回憶當年帶著首屆天文研究所學生，到玉山國家公園進行天文觀測教學，在燦爛星空下，幾位不曾見過「銀河」的都市小孩，忙於感受宇宙浩瀚，忽然有人迸出一 句「爲什麼天上那一大片白雲都不動？」他定睛一看，原來那亮麗耀眼的「銀河」，被誤認爲「白雲」，才發覺需要創造更多機會，讓學生接近大自然與浩瀚宇宙。

蔡文祥說，蓋天文台，要考慮的因素很多，過程中曾評估恆春半島、阿里山、合歡山等地，鹿林前山特殊之處是它在環山之間，並非在最高峰處，晴天率高。但空口 無憑，要證明這個地點的好壞，必須由長期累積的觀測資料做科學性說明。他一手包辦選址探勘的鹿林天文台，終於在 1999 年設置完成，自製 76 公分望遠鏡也 正式啓用。

現居美國的他，仍親自動手於自家後院蓋的天文臺，進行變星觀測，同時進行天文科普的推廣工作。（責任編輯：呂美琪）

原文轉載自【2012-10-20/大紀元時報首頁 > 新聞 > 台灣新聞 > 正文】

中大小行星命名者回娘家

國立中央大學慶祝天文研究所成立 20 週年，是亞洲發現小行星最活躍之地，研究所昨天邀請歷年發現小行星且命名者回娘家，包括「中大」、「鹿林」、「嘉 義」、「中壢」、「沈君山」等 21 名發現者。台灣本土培養的首位天文碩士蔡文祥，也獲中大頒贈「蔡文祥小行星」，他是台灣首位發現小行星且命名者，堪稱是 台灣天文研究的開路先鋒。（記者沈繼昌）

原文轉載自【2012-10-21/自由時報/A8 版/生活新聞】

中央大學今辦天文活動與講座

【聯合晚報／記者劉愛生／即時報導】 2012.10.20 09:20 am

爲慶祝桃園縣中央大學天文研究所成立 20 周年，中央大學今天上午 10 時在學校科學四館舉行系列慶祝活動，頒贈「蔡文祥小行星」，感念台灣天文研究的開路先鋒，廣邀歷屆頒贈的小行星回娘家，見證亞洲這塊發現小行星最活躍之地。

中央大學校友總會舉辦普通科學演講，由陳文屏教授主講「說盡一夜星空」，分享精彩的天文知識饗宴。

原文轉載自【2012-10-20/聯合新聞網　地方　即時新聞】

北市天文館教你認識火星

【聯合晚報／記者嚴文廷／即時報導】
2012.08.31 10:55 am

「好奇號」成功登入火星，這次任務要解答的問題包含火星是否適合生命居住？火星是否曾經有生命生存？爲了讓民眾對火星有更深入的瞭解，天文館將於 9 月 8 日 下午 2 時，舉辦火星季專家演講活動，主題爲「百年熒惑說分明—認識火星」，邀請中央大學天文研究所教授陳文屏主講，爲民眾揭開火星神秘的面紗。欲知詳情請 洽詢：02-28314551 轉分機 703 。

原文轉載自【2012-08-31/聯合新聞網 生活　即時新聞 】

《新聞中的科學》 傳遠距訊號…靠深空網路、人造衛星

距地球遠　電磁波延遲 14 分鐘 傳遠距訊號…靠深空網路、人造衛星

【劉盈慧】

好奇號成功登陸火星，開啓人類對這顆紅色星球的各種想像。但火星距離地球約六千萬公里，電磁波在傳遞的過程中，會發生訊號衰竭。中研院士研究員管一政說，要達成這趟長距離的遙控技術，「還要透過深空網路，與火星軌道上人造衛星的幫忙才行」。

管一政說，爲了在宇宙間以無線電傳遞訊號，美國太空總署分別在美國內華達州莫哈維沙漠中、西班牙馬德里附近與澳大利亞坎培拉近郊，各建置一個直徑 65 公尺 大的碟形無線電天線，構成深空網路（Deep Space Network，DSN）。他還說，透過每跨越經

度 120 度處，就設立一個接受器，等分地球三處的配置安排，「讓地球就算怎麼轉，都接收得到訊號」。並且 這些無線電都設置在半山腰，以避開射頻干擾。

「但火星並不像月亮一樣，永遠都是用同一面朝向地球」，管一政說。因此當火星轉到背對地球時，或是好奇號移動到火星上背對地球的區域時，就無法通訊。

「就像光線一樣，電磁波也是走直線」。這時便要仰賴「運行在火星軌道上的人造衛星、太空船，把訊號轉送出去」，達成長距離的訊號傳送。

管一政也說，光是從地球這端發出電磁波，到好奇號接受為止，地球與火星的距離，就會讓電磁波訊號，產生 14 分鐘的延遲。

中央大學天文研究所教授陳文屏說，好奇號具備兩種天線，一種天線能與火星上的太空船、人造衛星通訊。就像我們打手機是透過基地台傳送訊號，好奇號是藉由火 星上的太空船、人造衛星與地球通訊；另一種是高增益天線，能放大訊號，但因為瓦數大、高耗電，通常只在緊急情況下使用，像是軌道上沒有太空船時。但如果通 訊時遇上了太陽風暴的干擾，「這時也只能先等它結束，再傳送指令了」。

原文轉載自【2012-09-03/聯合報/AA3 版/新聞中的科學】

好奇號登火星　盼找到生命跡象

◎專題報導／記者羅智華

很多人好奇，在宇宙中有那麼多星體，為什麼目前科學家都認為只有火星比較有可能出現生命跡象，甚至寄望未來人類有朝一日能移民至火星上當「太空新住民」。 對此，葉永烜解釋在眾多行星中，水星、金星、地球、與火星因為距離太陽比較近，因此又稱為太陽系的內行星。其中，金星與地球的質量大小因為很接近，所以金 星又被稱為是地球的「孿生兄弟」。

但質量接近不等於金星就擁有和地球一樣適合生物繁衍的星體環境，葉永烜表示，海洋為孕育各種生物的大地之母，要有水的存在，才能衍生出生命。以金星來說，由於其表面非常炙熱，溫度可達攝氏四百多度，在這樣環境下很難發現有水的蹤影，更何況是生物足跡。

反觀火星，則恰好與金星相反，火星表面溫度低，約為零下四十度。加上火星表面有發現宛如大峽谷般的地質構造，同時科學家也發現火星過去有水的證據存在，因此推估火星之前的氣候環境可能與地球相近不遠，因而讓火星成了眾多星體中，最可能存有生命跡象的一顆星球。

為了讓對探索太空有興趣的天文迷可以更了解此次登陸火星任務的來龍去脈，台北市立天文館也將八月及九月訂為「火星季」，推出一系列活動。林琦峰表示，此次 天文館特別與師範大學科教中心及美國在台協會合作，共同推出「2012 火星最前線」展覽，內容除展出火星探測器的發展與演進外、還結合多媒體球投影、親身 體驗漫遊火星的互動模型。八月十九日當天下午二時則有「星期天談星」活動，九月底前的每周日下午

三時會舉行「假日探星趣-前進火星」活動，由解說員帶領民 眾動手做好奇號模型，讓民眾對好奇號有深入了解。

表面充滿氧化鐵火星成爲紅色星球

專題報導／記者羅智華

眾所矚目的美國國家航空暨太空總署（NASA）火星探測器「好奇號」，於八月六日成功登陸火星，並順利從火星拍下第一張彩色照片傳回地球，讓全球太空迷與天文學家爲之振奮，這也是 NASA 團隊首次使用以火箭作爲動力的空中起重機，幫助好奇號可以順利登上火星。

西元 1969 年，成功登陸月球的阿姆斯壯用雙腳，踏出人類探索太空的一大步，到了 2012 年，火星探測器「好奇號」則用六個輪胎，邁向人類探索天體星球的另一個大步，對許多天文迷來說，這不僅是天文科學研究上的里程碑，也見證了歷史的重要一刻。

台北市立天文科學教育館解說員林琦峰表示，造價約 25 億美元的好奇號是一台擁有六個輪子、宛若汽車大小般的火星探測器，相較於 2004 年登陸火星的探測車「機會號」及「精神號」，重量約達 900 公斤的「好奇號」，不但比它們重五倍以上，長度也增加兩倍。有別於之前的探測器，「好奇號」除了體積變大外，更是 第一輛由 NASA 研發採用核動力驅動的火星探測器。

爲何要改採核動力來驅動探測器呢？國內知名太空權威、現任中央大學天文研究所教授葉 永烜表示，以往登陸火星的探測器都是運用太陽能來當作動力來源，一旦探測器無法照射到太陽光時，就無法產生動能運作，導致探測工作因此中斷，但如果改用核 動力來製造動能則可避免這樣的問題，無論是白天或夜晚，好奇號都可以全天候進行探測任務，從探測技術上來說，這不但是美國首次將核能技術結合行星探測器， 也是太空科技的一大突破，因此格外引發國際關注。

因爲體積變大，也讓「好奇號」可以搭載更多探測儀器，除了用來拍攝影像的照相機外，還包括光譜儀、化學攝影機、火星樣本分析儀器等。

葉永烜表示，不同於 2008 年登陸火星的「鳳凰號」只能在原地，此次「好奇號」將以火星赤道附近的蓋爾隕坑爲主要探測地點，從中找尋火星是否曾經有生命存 在的蛛絲馬跡，好奇號預計將在火星上探測一個火星年的時間，接近於地球上的兩年，由於探測區域比之前登陸火星的探測器都來得廣大，因此科學家也預估將帶來 更多令人期待的探測資料。

葉永烜表示，火星是八大行星中的一個星體，其誕生年齡與我們所居住的地球相近，大約是在四十五點六億年前形成。火星表面含有許多氧化鐵，因此讓星體顏色偏橘紅，因此火星又有「紅色星球」之稱。

原文轉載自【2012-08-10/人間福報/遇見科學】

全球第一顆台灣當代文學家命名小行星 「鍾理和小行星」正式命名通過

(中央社訊息服務 20120806 17:25:00) 全球第一顆以台灣當代文學家命名的「鍾理和」小行星，8 月 4 日於國立台灣文學館舉辦命名通過慶祝儀式，發現行星的中央大學製作小行星銘版及模型，頒贈台灣 文學館及鍾理和文教基金會；當天是鍾理和逝世 52 週年紀念日，鍾理和家屬及親友從全台各地趕來參與盛會，氣氛溫馨感人。

台灣發現的小行星以「鍾理和」爲名，鍾家家屬感到無比的榮耀，孫女鍾怡彥帶著媽媽、妹妹、伯伯、叔叔和姑姑前來參加活動，包括鍾理和八十歲的姪子鍾佐鵬，鍾理和第四代的五歲外曾孫女彭筠雅，全家族一起分享這份榮耀。

鍾理和小行星，在 2008 年 10 月 23 日由中央大學天文所蕭翔耀與廣州中山大學葉泉志共同發現，外型像一顆馬鈴薯，經國際天文學聯合會(IAU/CSBN)通過， 號 237187，正式命名爲「鍾理和」(Zhonglihe)。發現時，位於金牛座位置，現在則在寶瓶座。

主辦單位精心規劃，請來鋼琴家現場彈奏〈原鄉人〉，有關鍾理和的故事及文學成就，又浮現在眾人心中；鍾怡彥說，從獲知命名到現在她依然感到興奮，尤其想到天空有一顆祖父的星星，她一直有不可置信的驚喜。

國立中央大學代理校長李誠，恭賀鍾家、鍾理和文教基金會，小行星能以鍾理和爲名是令台灣人引以爲傲的事。他說，小行星以「鍾理和」爲名，主要是因鍾理和當年探尋原鄉的過程，精神就像天文家致力追尋新的天文知識，探尋太陽系的起源一般。

台灣文學館館長李瑞騰表示，鍾理和小行星的命名，代表人文與科技的結合，做爲以研究、典 藏、推廣台灣文學爲目標的台灣文學館，能參與辦理這項活動，他有一種撿到寶的感覺，非常高興。包括鍾理和文教基金會董事長曾貴海、高雄市副市長李永得等人 都上台致詞，對於小行星以台灣文學家命名感動不已。台灣聯合大學系統副校長葉永烜教授更直言，鍾理和當年前往大陸再返回故鄉，追尋原鄉，他的原鄉就是台灣 文學。

鍾 理和，高雄美濃人，自小熱愛文學，貧困中成長，仍堅持文學志業，至死不渝，被譽爲「倒在血泊中的筆耕者」，他的作品記錄農村生活 樣貌，流露悲天憫人的情懷，是台灣當代重要文學家。另外於活動中現場播放十七分鐘的記錄片《鍾理和文學路》，片中專訪作家鍾肇政，以及鍾理和已故夫人鍾台 妹、長子鍾鐵民，暢談他們對鍾理和的點滴回憶，珍貴的畫面，令在場觀眾動容，該片由彭啓原導演費時十年拍成。

原文轉載自【2012-08-06/中央社】

台灣/「鍾理和小行星」命名通過暨頒贈儀式

蔡清欽/報導

全球第一顆以台灣當代文學家命名的「鍾理和」小行星，8 月 4 日於國立台灣文學館舉辦命名通過慶祝儀式，發現行星的中央大學製作小行星銘版及模型，頒贈台灣 文學館及鍾理和文教基金會；當天是鍾理和逝世 52 週年紀念日，鍾理和家屬及親友從全

台各地趕來參與盛會，氣氛溫馨。

台灣發現的小行星以「鍾理和」爲名，鍾家家屬感到無比的榮耀，孫女鍾怡彥帶著媽媽、妹妹、伯伯、叔叔和姑姑前來參加活動，包括鍾理和八十歲的姪子鍾佐鵬，鍾理和第四代的五歲外曾孫女彭筠雅，全家族一起分享這份榮耀。

主辦單位精心策劃，請來鋼琴家現場彈奏〈原鄉人〉，有關鍾理和的故事及文學成就，又浮現在眾人心中；鍾怡彥說，從獲知命名到現在她依然感到興奮，尤其想到天空有一顆祖父的星星，她一直有不可置信的驚喜。

國立中央大學代理校長李誠恭喜鍾家、鍾理和文教基金會，小行星以鍾理和爲名是令台灣人引以爲傲的事。他說，小行星以「鍾理和」爲名，主要是因鍾理和當年探尋原鄉的過程，精神就像天文家致力追尋新的天文知識，探尋太陽系的起源一般。

台灣文學館館長李瑞騰表示，鍾理和小行星的命名，代表人文與科技的結合，做爲以研究、典藏、推廣台灣文學爲目標的台灣文學館，能參與辦理這項活動，他有一種撿到寶的感覺，真是太高興了。

包括鍾理和文教基金會董事長曾貴海、高雄市副市長李永得等人都上台致詞，對於小行星以台灣文學家命名感動不已。台灣聯合大學系統副校長葉永烜教授更直言，鍾理和當年前往大陸再返回故鄉，追尋原鄉，他的原鄉就是台灣文學。

鍾理和，高雄美濃人，自小熱愛文學，貧困中成長，仍堅持文學志業，至死不渝，被譽爲「倒在血泊中的筆耕者」，他的作品記錄農村生活樣貌，流露悲天憫人的情懷，是台灣當代重要文學家。

另外活動中並播放十七分鐘的記錄片《鍾理和文學路》，片中專訪作家鍾肇政，以及鍾理和已故夫人鍾台妹、長子鍾鐵民，暢談他們對鍾理和的點滴回憶，珍貴的畫面，令在場觀眾動容。該片由彭啓原導演費時十年拍成。

鍾理和小行星，在 2008 年 10 月 23 日由中央大學天文所蕭翔耀與廣州中山大學葉泉志共同發現，外型像一顆馬鈴薯，經國際天文學聯合會 (IAU/CSBN)通過，編號 237187，正式命名爲「鍾理和」(Zhonglihe)。發現時，位於金牛座位置，現在則在寶瓶座。

台灣文學館曾於 2004 年策劃「鍾理和文學展」，展出鍾理和的作品、手稿及文物，2011 出版《台灣現當代作家研究資料彙編 11 鍾理和》，彙集其生平、作 品、創作年表及評論文集；目前，館內並典藏鍾理和相關圖書及手稿約 30 餘件。另外，鍾理和生前使用最久、最鍾愛的寫字檯，因年久失修缺損，文學館專業修護 人員曾協助修復，館內目前則保存其複製品。

原文轉載自【2012-08-06/中央日報網路報-教育藝文】

鍾理和小行星　台首顆依文學家命名

【大紀元 2012 年 08 月 07 日訊】(大紀元記者賴友容台南報導)全球第一顆以台灣當代文學家命名的「鍾理和」小行星，4 日於國立台灣文學館舉辦命名通過慶祝 儀式，發現行星的中央大學製作小行星銘版及模型，頒贈台文館及鍾理和文教基金會，4 日是鍾

理和逝世 52 周年紀念日，鍾理和家屬及親友趕來參與盛會，氣氛溫 馨。 台灣發現的小行星以鍾理和爲名，鍾家家屬感到無比的榮耀，孫女鍾怡彥帶著家族成員前來參加活動，一起分享這份榮耀。從獲知命名到現在依然感到興奮的鍾怡彥 說，尤其想到天空有一顆祖父的星星，一直有不可置信的驚喜。

國立中央大學代理校長李誠表示，小行星以鍾理和爲名是令台灣人引以爲傲的事。他說，主要是因鍾理和當年探尋原鄉的過程、精神，就像天文家致力追尋新的天文知識一般。鍾理和文教基金會董事長曾貴海、高雄市副市長李永得等人都上台致詞，對於小行星以台灣文學家命名感動不已。

鍾理和，高雄美濃人，自小熱愛文學，貧困中成長，仍堅持文學志業，至死不渝，被譽爲「倒在血泊中的筆耕者」，他的作品記錄農村生活樣貌，流露悲天憫人的情懷，是台灣當代重要文學家。

鍾理和小行星，在 2008 年 10 月 23 日由中央大學天文所蕭翔耀與廣州中山大學共同發現，外型像一顆馬鈴薯，經國際天文學聯合會通過，編號 237187，正式命名爲「鍾理和」（Zhonglihe）。◇

原文轉載自【2012-08-07/大紀元時報首頁 > 新聞 > 台灣地方新聞 > 南部綜合 > 正文】

火星探測邁大步 尋找生物圈證據 若大氣中存在甲烷 就能證明生命確曾存在

【李宗祐／台北報導】

「好奇號跨出的一小步，不但使火星探測計畫邁進一大步，更把人類追尋其他有生命存在的星球的夢想，帶進全新且無限可能的境界！」中央大學天文研究所教授葉永烜指出，「好奇號」主要任務是探測火星是否有生物圈存在或曾經存在的證據。

葉永烜說，這次如果真的能偵測到甲烷氣體，火星就成爲太陽系除了地球之外，第一個被發現有生物圈存在證據的星球。

葉永烜表示，過去登陸火星的探測登陸器，都是被包裹在「安全氣囊」裡面，以降落方式著登，受限於「安全氣囊」裝載體積，探測登陸器都是以小型爲主。「好 奇號」則是以「天空起重機」吊掛降落，有了這次成功登陸的經驗，以後各種行星探測登陸器就能突破大小限制，可以任意搭載科學儀器，所能發揮的功能就有無限 可能。

此外，「好奇號」也捨棄過去慣用的太陽能動力系統，改採小型核反應器，可以跑得更快、更高、更遠；葉永烜認爲，「好奇號」對太空探測科技而言，整體上向 前邁進一大步。尤其是探測登陸器突破大小限制後，搭載的科學儀器跟過去完全不一樣，例如用雷射光照射並融化岩石後，再以望遠鏡結合光譜儀分析岩石釋出的氣 體成分；也搭載有儀器蒐集把火星大氣濃縮後再分析成分，部分設備已應用到核武技術。

葉永烜強調，火星大氣到底有沒有甲烷存在，是「好奇號」這次任務最主要的探測目的，因爲甲烷是生物「運作」後的產物，例如微生物「吃水」或吸收二氧化碳 後，

就會排放甲烷；白蟻啃食木頭以後，也會釋放出甲烷；牛羊經消化作用打嗝出來的氣體，也是甲烷。「好奇號」如果能探測證實火星大氣有甲烷，就證實火星有 生物圈存在。

葉永烜表示，火星上面都是陸地、沒有海洋，陸地面積跟地球差不多，被科學家認爲最有可能變成可被人類利用的星球，甚至比地球更適合生物發展。科學家推 論，火星生物圈在四十億年前雖因氣候變遷而消失，但也深信生命的堅韌性，只要給予一點點機會就會重燃生機，這也是各國科學家熱中火星探險的主因。

原文轉載自【2012-08-07/中國時報/A10 版/話題】

台灣學者／好奇號一小步　太空史一大步

〔記 者陳怡靜／台北報導〕全球都關注的「好奇號」昨天順利登陸火星，國內太空與天文學者也相當振奮，認爲此次太空任務意義非凡，自然科學博物館館長孫維新笑 說：「好奇號登陸的一小步，是未來人類能否踏上火星的一大步。」若能找到微生物，將可能重重影響人類的哲學思考與宇宙觀。

天文學者孫維新強調：「這是非常非常好的里程碑！」火箭專家、太空中心資深研究員陳彥升也直說：「這對人類很有意義，也是史上最困難的太空任務之一。」全程觀看直播的中央大學天文所教授陳文屏更是興奮：「看到好奇號回傳的第一張照片，感動又開心！」

孫維新指出，「好奇號」已是ＮＡＳＡ第三代火星探測車，好奇號前有隔熱罩抵擋，衝破大氣層時，能承受六萬五千磅拉力的降落傘從後方彈出，加上逆向火箭底部 噴氣造成的反作用力，雙雙減緩降落速度。不同於前兩代火星任務，好奇號儼然是個小型實驗室，隨身攜帶十幾台相機、化學與生命科學儀器，可走到哪、拍到哪， 還能用鏟子採集樣本或用雷射槍氣化岩石，將樣本直接放進儀器中分析成分，再將數據傳回地球，讓科學家得以了解火星的狀況。好奇號先人類一步上火星，就是希 望觀察火星是否適合生命發展，成爲另一個可能的地球。

孫維新也指出，過去兩代任務多在尋找「水」的痕跡，也確實觀測到類似乾涸的湖底或河 床，但好奇號的任務更重要，它得試著偵測有無細菌、微生物等，「若真的找到有生命存在的形式，對人類來說，是很巨大的震撼，人類就會知道生命是如何在宇宙 產生的，將可能重重影響人類的哲學思考與宇宙觀」。

原文轉載自【2012-08-07/自由時報/A3 版/焦點新聞】

台北直播　天文迷激動相擁

【記者陳瑄喻／台北報導】

美國火星探測器「好奇號」，昨天登陸火星。成功的訊號一傳回地球，讓台北市立天

文館觀看直播的天文迷開心互相擁抱，直呼「太值得了」。

爲了這場天文盛會，台北市立天文館邀請中央大學天文所教授陳文屏、葉永烜到場，並與美國太空總署華裔科學家劉登凱連線，講解火星相關資料。

「耶！我們登陸火星了，我們成功了」，當好奇號順利登陸的消息傳回地球，位於天文館的三百多名天文迷也激動不已，有人開心地流下眼淚，大聲疾呼說「火星，我們來了！」

昨天天文館進行直播的宇宙劇場內座無虛席，連走道都坐滿人。甚至有人早上六點就去排隊。一早特地從台中北上的許姓學生，找了五個同學同行。許同學表示，這次能親眼看到好奇號登陸的相關影片，真的「永生難忘」。

負責現場解說的陳文屏表示，登陸火星就能仔細調查，火星上曾存在水及氧氣，爲何會變成不適合生物生存的環境。這也是好奇號此行最重要的目的，了解火星環境的演變歷史，探討地球是否會走上相同命運。

「人類演變至今，探索的範圍遲早會擴及外太空」，葉永烜也指出，探索火星，跟跟歐洲十五到十七世紀發現新大陸一樣，藉由這項任務，能拓展人類對於宇宙的知識。

原文轉載自【2012-08-07/聯合報/A3 版/話題】

史上高難度任務　好奇號成功登陸火星

劉偉瑩／綜合報導

火星探測器「好奇號」昨天成功在火星著陸，完成史上最精密高超的登陸火星計畫。美國太空總署的噴射推進實驗室任務控制中心人員，接收到好奇號傳回的第一個訊號後，興奮擁抱、擊掌歡呼。

斥資二十五億美元打造的好奇號，昨天在臺灣時間下午一點三十一分，降落在火星表面的蓋爾隕石坑。數分鐘後，好奇號傳回火星表面三張影像，分別顯示如同一輛房車大小的好奇號，搭載著精密儀器抵達火星，以及好奇號在火星上投射出的倒影。

同一時間，臺北市立天文館內也有三百多名民眾緊盯著銀幕，觀看火星登陸實況轉播。「哇！成功登陸了！」好奇號登陸那一刻，小朋友興奮鼓掌，也對這項火星任務充滿好奇。

臺北市立天文館展示組組長陳俊良表示，好奇號登陸成功，象徵兩個意義：一是意味著人類未來也有登陸火星的可能；二是隨著好奇號登陸，人們對於火星上生命跡象的探究又前進一步。

負責現場解說的中央大學天文所教授陳文屏表示，假設火星上曾經存在水和氧氣，爲何現在會變成不適合人類生存的環境，從火星環境的演變歷史，可以探討地球在未來是不是也會走上相同命運。

原文轉載自【2012-08-07/國語日報】

好奇號登火星　天文館連線看

【中央社台北六日電】 2012/08/0

台北市立天文科學教育館，今天與美國同步直播火星探測器好奇號（Curiosity）登陸火星。學者表示，這代表人們始終想知道地球的後院有沒有生物。

美國太空總署 NASA 的火星探測器好奇號約於台灣時間六日下午二時著陸火星，隨即回傳火星表面的三張影像。好奇號將展開兩年任務，爲火星上是否曾存在生物尋求解答。

台北市立天文館今天在宇宙劇場與美國 NASA 連線直播，並安排專家解說，讓數百名台灣民眾也能親身感受這場太空饗宴。花了二個多小時排隊、差點無法進場的何姓學生看完直播大呼值得，認爲探索宇宙有無生命的議題確實值得人類深思。

負責天文館現場解說的中央大學天文所教授陳文屏表示，假設火星上曾經存在水及氧氣，爲何現在會形成不適合人類生存的環境，這也是好奇號這次的火星任務，最主要就是去了解火星環境的演變歷史，探討地球在未來是不是也會走上相同命運。

中央大學天文所教授葉永烜則說，歐美探索火星，除代表人類始終想知道「我們的後院有沒有生物」，其實也跟歐洲十五到十七世紀發現新大陸一樣，藉由向外拓展帶動成長與創造力，「不去探索（火星）才奇怪」。

葉永烜表示，透過研究與地球生成年代相近、環境曾與地球相似的火星，有助於人類因應目前遇到的氣候危機。

【中央社加州巴沙迪納五日綜合外電報導】火星探測器好奇號（Curiosity）今天成功在火星著陸，完成史上最精密高超的登陸火星計畫。

美國太空總署（NASA）的噴射推進實驗室（Jet Propulsion Laboratory）任務控制成員表示：「好奇號確認登陸火星。我們著陸火星了！我的天啊。」

美國有線電視新聞網（CNN）直播畫面顯示，控制中心人員接收到好奇號回傳的首個訊號後，彼此擁抱、擊掌歡呼，爲歷史性時刻慶祝。

原文轉載自【2012-08-07/台灣新生報/1 版/今日焦點】

登火星下一步　送樣本回地球

【台灣醒報記者陳珮瑜台北報導】美國「好奇號」終於接觸火星表面！針對此劃時代的太空進展，國內多位天文學者均認爲，太空技術的一日千里，已可確保精密偵測儀 器登陸火星，並分析火星上是否有生命存在的證據，包括尋找碳基化合物、甲烷等等。中央大學天文所教授陳文屏特別指出，NASA 下一步將會研究如何將火星的 樣本帶回地球，甚至思考登陸火星的可能性。

經過 8 個多月的飛行，美國太空總署「好奇號」終於在昨天下午成功登陸火星，這個造價 25 億元 的火星探測器能運轉 10 年，攜帶的儀器和探測技術都較過去先進，主要

任務是尋找有沒有構成生命的碳基化合物，及可能曾經適合生命存活的生物聚集處，並不是 外界所認爲，只爲偵測火星有無生命。

「從小學時代的阿姆斯壯登陸月球，到好奇號登陸火星，太空技術進步一日千里。」中央大學天文所教授 陳文屏想起過去美國登陸月球、太空梭爆炸，到現今的登陸火星，情緒仍激動萬分。他說，尤其美國爲了快速傳回影像，還特別調度某些衛星，使得好奇號所拍攝的 照片在 1、2 分鐘之內即傳回地球，更令人感動。

好奇號是 NASA 第三代的火星探測車，不同於過去「逗留者號」、「精神號」和「機會號」，陳文屏說，好奇號這次的降落過程非常縝密，首先是借力大氣煞車，接著使用降落傘和逆向火箭噴射，減緩降落速度，還特別使用繩索吊掛的方式，防止沙塵揚起。

談到「好奇號」的特性，自然科學博物館館長孫維新指出，如房車般大小的好奇號功能齊備，隨身攜帶十幾台相機、化學和生命科學儀器，還能以鑱子採集樣本或以 雷射槍氣化岩石，將樣本放入儀器中分析，再將數據傳回地球。孫維新說，這次的好奇號並未裝備回地球的火箭，因此只能以電腦傳輸的方式揭密。

「過去的任務多是尋找水，這次則是嘗試偵測有無細菌存在的環境。」孫維新表示，前幾代火星探測車裝備較陽春，因此以「尋水」爲主要任務，也的確找到類似乾涸的湖底或河床；但好奇號會尋覓有無生命存在的證據，一旦成功發現，人類的宇宙觀將有劃時代的變革。

中央大學天文所葉永烜則提到，火星有生命存在的機率很高，過去就曾有火星的大氣層含有甲烷的證據，而這也是好奇號最重要的探測工作之一。他進一步說明，甲烷是生物運作過後的產物，例如微生物吸收二氧化碳、動物經消化作用之後，都會產生甲烷。

至於美國的下一步，陳文屏指出，這次的降落非常成功，代表以後發送至火星的探測器車可以更重，亦即裝備可以更齊備。他說，NASA 下一步應該會研究如何將火星的樣本帶回地球，更甚者，也不排除太空人登陸火星的可能性。

延伸閱讀：好奇號登陸火星火星現場直播紀錄（美國總統歐巴馬發表聲明說，好奇號的成功「代表一項空前的科技壯舉，是未來多年美國引以爲傲的成就」。）（中天新聞台）

原文轉載自【2012-08-07/台灣醒報】

下一步　人類上火星 好奇號登陸　傳回 3 張照

【綜合報導】「好奇號確定著陸，喔天啊！我們抵達火星了!」美國航太總署（NASA）科學家昨在加州透過電腦設備監測，證實好奇號成功降落火星，欣喜若狂。我 國中央大學天文所陳文屏教授比喻，過去火星任務送上去的探測器是玩具車，這次登陸的是休旅車，體積和重量都大很多，裡面也裝載很多先進儀器，可直接在火星 上實驗，他直呼：「這比看奧運轉播還興奮！」

好奇號（Curiosity）於台灣時間昨下午 1 時 32 分登陸火星，加州噴射推進實驗室（Jet Propulsion Laboratory）爆出如雷般歡呼與掌聲。探測計劃主任麥奎遜表示，釐清宇宙是

否只有地球人、火星如何從有水的狀態變成乾燥的星球，以及人類未來能否 踏上火星的科學任務至關重要，「若能成功，將成爲行星探索史上最偉大成就。」探測器登陸小組副主管華裔科學家陳艾倫（譯音，Allen Chen）也說：「這實在令人難以置信。」

從土壤探生命蹤跡

好奇號任務預計 26 個月，NASA 強調不是要找外星人或生物，是希望藉由分析土壤及岩石，尋找生命基本構成元素的蹤跡，另一目的是研究火星環境，爲人類未來登陸火星做準備。

好奇號成功著陸，對近來預算頻頻遭砍的美國太空計劃，無疑是一大勝利和重要里程碑。美國總統歐巴馬說：「這是科技上的空前成就。」

好奇號著陸火星赤道附近蓋爾隕石坑的數分鐘後，立即透過「火星奧德賽號」人造衛星傳回 3 張影像。首張照片是由好奇號的後置相機，照出輪子停在火星表面，數秒再傳回它在火星上的倒影。它下月開始移動，月底首度採集樣本。

太空旅行 5.7 億公里

太陽系中火星是除了金星外最靠近地球的行星，運行特點和表面環境跟地球有諸多近似處，成爲太空探測的熱門目標，俄羅斯、歐洲、日本與中國，嘗試過 30 多次 把人工衛星或探測器送住火星，但逾半失敗。這次 NASA 花了逾 8 年研發，去年 11 月 26 日把好奇號送上太空，經 5.7 億公里太空旅行，終於登陸火星。

可以直接分析實驗

這次最棘手部分是驚險的降落過程，NASA 直言是「恐怖 7 分鐘」。好奇號重約 900 公斤，比以往探測器重上 5 倍，體型大逾 2 倍，無法循先前用氣囊爲彈性著陸的緩衝降落方式，改採新式一連串煞車抑速的著陸模式。

好奇號是至今最先進火星探測器，正式名稱「火星科學實驗室」，配備 10 項先進儀器，其中的化學相機具雷射槍功能，能擊碎 7 公尺外的岩塊，再由特殊望遠鏡透 過揚起的粉末影像，分析其成分。中央大學天文所陳文屏教授指出，以核熱能爲動力的好奇號無法把火星樣本送回地球，因此在火星上直接分析實驗格外重要。

爲讓國內民眾目睹好奇號登陸過程，北市天文教育館昨開放宇宙劇場，300 名民眾透過大銀幕一同觀看 NASA 最新畫面。因好奇號登陸前有「恐怖 7 分鐘」，在場民眾屏息以待，直到出現 NASA 人員開心相擁，才爆出掌聲。

看登陸「像上火星」

NASA 台裔科學家劉登凱是這次火星探險計劃副總工程師，天文館昨和他視訊連線，劉登凱分析，好奇號可這麼快傳回照片，顯示電腦、相機等儀器都未受損，推估其他儀器也可正常運作。對於登陸成功，他興奮地說：「晚上要和同事開派對！」

民眾鄭凱文說，「看到第一時間回傳照片覺得很興奮，好像自己上火星。」

從數字看好奇號任務

7 次 NASA 第 7 次成功登陸火星

2.1 萬公里 進入火星大氣層的時速
2.4 公尺 好奇號在火星每分鐘的行進距離
5.7 億公里 從地球到火星的航程
8 個多月 飛到火星的時間
8 年 任務籌備時間
10 種 好奇號上的科學儀器數量
75 公斤 好奇號上的裝備重量
2011.11.26 發射升空日期

網友吆喝：火星人出來
pw080325043 美國領土擴展到火星了!!!!!!!!!!!!
shwkz 真的跟電影一樣，哈哈！
JOHNJJ 看到一堆天才在慶祝的感覺真奇妙。
ChiChiGo 火星人快出來打招呼啊！
king622 史上最強大的遙控車團隊。
資料來源：PTT 實業坊（telnet://ptt.cc）

好奇號登陸火星 Q&A
Q 這次計劃花多少錢？準備多久？
A 耗費 25 億美元（約 750 億元台幣），2004 年開始準備，去年 11 月 26 日升空，飛行 8 個多月後昨天抵火星。
Q 爲何選擇登陸火星？
A 太陽系中火星是除金星外離我們最近的行星，且可能曾有生命。
Q 這次任務目的？
A 尋找火星是否存在過生命、研究當地氣候與地質特性，進一步替未來人類登陸火星作準備。
Q 好奇號要在火星待多久？
A 預計在火星執行 1 年任務，等於地球的 26 個月。
Q 爲何選在蓋爾隕石坑登陸？
A 登陸火星赤道附近的蓋爾隕石坑，因當年火星若有大量流水，會流經赤道附近。
Q 如果遇上火星人或外星人該怎麼辦？
A 不能怎麼辦。好奇號配備有一管可擊碎石頭的雷射槍，但功率很小，不能當武器使用，因此好奇號並無自衛能力。

原文轉載自【2012-08-07/蘋果日報/A2 版/要聞】

好奇號登火星　天文館同步連線

（中央社記者游凱翔、陳亦偉台北 6 日電）台北市立天文科學教育館，今天與美國同步直播火星探測器好奇號（Curiosity）登陸火星。學者表示，這代表人們始終想知道地球的後院有沒有生物。

美國太空總署 NASA 的火星探測器好奇號約於台灣時間 6 日下午 2 時著陸火星，隨即回傳火星表面的 3 張影像。好奇號將展開兩年任務，爲火星上是否曾存在生物尋求解答。

台北市立天文館今天在宇宙劇場與美國 NASA 連線直播，並安排專家解說，讓數百名台灣民眾也能親身感受這場太空饗宴。花了 2 個多小時排隊、差點無法進場的何姓學生看完直播大呼值得，認爲探索宇宙有無生命的議題確實值得人類深思。

負責天文館現場解說的中央大學天文所教授陳文屏表示，假設火星上曾經存在水及氧氣，爲何現在會形成不適合人類生存的環境，這也是好奇號這次的火星任務，最主要就是去了解火星環境的演變歷史，探討地球在未來是不是也會走上相同命運。

中央大學天文所教授葉永烜則說，歐美探索火星，除代表人類始終想知道「我們的後院有沒有生物」，其實也跟歐洲 15 到 17 世紀發現新大陸一樣，藉由向外拓展帶動成長與創造力，「不去探索（火星）才奇怪」。

葉永烜表示，透過研究與地球生成年代相近、環境曾與地球相似的火星，有助於人類因應目前遇到的氣候危機。1010806

原文轉載自【2012-08-06/中央社】

小行星以台灣文學家「鍾理和」命名　孫女大呼奇妙　「仰望星空　祖父正在注視我」

【洪榮志／台南報導】

科學不忘人文！中央大學兩年多前發現一顆未被命名的小行星，決定獻給「台灣現代文學之父」鍾理和，經向國際天文學聯合會申請最近通過命名，四日在台灣文學館舉行頒贈儀式；鍾理和孫女鍾怡彥說，「抬頭仰望星空，發現祖父正在注視我，這種感覺太奇妙了！」

中央大學天文所所長高仲明指出，小行星是目前唯一可以被發現單位命名的天體，以古代文學家李白、杜甫、蘇東坡命名的小行星都已經出爐，當代華人文學家金庸小行星也有了，全球第一顆以台灣文學家命名的小行星則是「鍾理和」。

鍾理和小行星於民國九十七年十月廿三日被中大天文所觀測員蕭翔耀先以鹿林天文台望遠鏡側錄，再由廣州中山大學葉泉志以電腦軟體初步證實是新發現的太陽系 小行星，直徑約二千公尺，外型像一顆馬鈴薯，經國際天文學聯合會通過，編號二三七一八七，並命名爲「鍾理和」。發現時，位於金牛座位置，現在則在寶瓶座。

高仲明說，小行星的命名及確認過程十分慎重，被觀測到的小行星，必須要在不同的夜晚也被觀察到，並報告國際小行星中心，經確認爲新 發現的小行星後，即可擁有一個國際統一格式的暫定編號；同時，還必須等到這顆小行星至少四次在回歸中心被被

觀測到，並精確測定出其運行軌道參數後，才能得 到國際小行星中心給予的永久編號。

中大代理校長李誠強調，這顆小行星以「鍾理和」命名，主要是因鍾理和當年懷抱理想，從台灣遠赴大陸，又再返回故鄉美濃，探尋人生價值、原鄉意義的過程，就像天文家致力追尋新的天文知識，探尋太陽系的起源一般。

另外，鍾理和的孫女鍾怡彥在中大攻讀中文研究所博士班，她的指導教授則是台灣文學館館長李瑞騰。諸多因緣促成中大以「鍾理和」命名小行星，因此於昨天鍾 理和逝世五十二周年紀念日，移師台文館舉辦小行星命名通過慶祝儀式，並製作小行星銘板及模型分別頒贈給台文館及鍾理和文教基金會收藏，讓李瑞騰直呼「台文 館賺到了！」

中大說，目前該校鹿林天文台發現的新小行星共有廿二顆，已公布命名的有十八顆。其中，有六顆是人名，依命名先後分別是：溫世仁、鄭崇華、沈君山、李國鼎、吳大猷及鍾理和。

原文轉載自【2012-08-05/中國時報/A14 版/文化新聞】

鍾理和小行星　中大送給台文館

第 1 顆用台灣當代文學家命名的小行星 中大送銘版與模型 象徵鍾理和守護熱愛的台灣文學

【記者莊宗勳／台南報導】

中央大學昨天將「鍾理和」小行星銘版與模型致贈給台灣文學館，作家鍾理和已不只是「倒在血泊中的筆耕者」，而是回到原鄉，化身爲全球第 1 顆用台灣當代文學家命名的小行星，高掛天際，默默守護著台灣文學。

中央大學所屬的鹿林天文台於民國 97 年 10 月 23 日，在火星與木星間的小行星群中，發現 1 顆直徑約 2000 公尺，形狀像馬鈴薯的小行星。經過國際天文學聯合會小行星命名委員會審查，命名爲「鍾理和」。

中大天文研究所技士張光祥說，國際間曾用蘇東坡、李白、杜甫與金庸等作家命名小行星，但用台灣當代文學家命名則是全球首例。因鍾理和曾在小說「原鄉人」 中，反覆探討原鄉的概念，名句「原鄉人的血，必須流返原鄉，才會停止沸騰！」就像天文學家研究小行星，探索太陽系起源一樣，具有指標性意義。

鍾理和畢生致力於台灣文學，中大天文研究所教授葉永烜認爲，「鍾理和的原鄉就是台灣文學」。

昨天是鍾理和逝世 52 周年紀念日，中央大學選在台灣文學館慶祝「鍾理和」小行星的誕生。鍾理和的媳婦（鍾鐵民妻子）郭明琴與孫女鍾怡彥、鍾舜文等家屬都到場觀禮，追念鍾理和充滿辛酸血淚的一生。

鍾怡彥說，去年接到中大通知，表示要將小行星命名爲「鍾理和」時，還以爲是詐騙

集團，沒想到竟是真的。雖然沒有親眼見過祖父，但現在只要抬頭仰望星空，彷彿就能看見祖父的模樣，「心情真的很激動！」

中大代理校長李誠將小行星銘版與模型交給台灣文學館長李瑞騰時，現場響起「原鄉人」的音樂，就像歌詞中敘述的，「我張開一雙翅膀，背馱著一個希望，飛過那陌生的城池，去到我嚮往的地方」，彷彿鍾理和已飛到天際，守護著他最熱愛的台灣文學。

原文轉載自【2012-08-05/聯合報/B1 版/大台南・運動】

鍾理和小行星　遺族慶命名

〔記者洪瑞琴／台南報導〕全球第一顆以台灣本土當代文學家命名的行星「鍾理和」，昨天在國立台灣文學館舉辦命名通過慶祝儀式，發現行星的中央大學製作小行星銘版及模型致贈台灣文學館及鍾理和文教基金會，這天正逢鍾理和逝世五十二週年紀念日，別具意義。

鍾理和小行星，二〇〇八年十月廿三日由中央大學天文所蕭翔耀與廣州中山大學葉泉志共同發現，外型像一顆馬鈴薯，經國際天文學聯合會（IAU/CSBN）通過，編號二三七一八七，正式命名爲「鍾理和」（Zhonglihe）。發現時，位於金牛座位置，現在則在寶瓶座。

鍾理和家屬及各地親友參與盛會，包括鍾理和八十歲的姪子鍾佐鵬，鍾理和第四代的五歲外曾孫女彭筠雅，全家族一起分享榮耀。

中央大學代理校長李誠表示，小行星以鍾理和爲名是台灣人引以爲傲的事，以「鍾理和」爲名，主要是因他當年探尋原鄉過程，精神就像天文學家致力追尋新的天文知識，探尋太陽系的起源一般。

中央大學天文所表示，小行星是目前唯一可被發現單位命名的天體，過去中國曾以當代文學家金庸、古代文學家蘇東坡、李白等命名，鍾理和小行星則是台灣本土第一位當代文學家爲名。

鍾理和孫女鍾怡彥目前在中央大學攻讀中文研究所博士，指導老師正是台文館長李瑞騰；鍾怡彥說，從獲知命名到現在，依然驚喜興奮，「偶爾抬頭仰望星空，有顆祖父星星正凝視著我，實在太奇妙了。」

鍾理和，高雄美濃人，自小熱愛文學，貧困中成長，仍堅持文學志業，至死不渝，被譽爲「倒在血泊中的筆耕者」，他的作品記錄農村生活樣貌，流露悲天憫人的情懷，是台灣當代重要文學家。

昨日播放十七分鐘紀錄片《鍾理和文學路》，片中專訪作家鍾肇政，以及鍾理和已故夫人鍾台妹、長子鍾鐵民，暢談對鍾理和的點滴回憶，該片由彭啓原導演費時十年拍成。

原文轉載自【2012-08-05/自由時報首頁 > 南部新聞】

兩岸共同發現小行星　以台作家鍾理和命名

中評社台南 8 月 4 日電（記者　趙家麟）由兩岸共同發現、全球第一顆以華人當代文學家命名的行星“鍾理和”，訂 8 月 4 日在台灣客籍作家鍾理和逝世 52 週年紀念日的當天，於台南的台灣文學館將舉辦慶祝儀式。

“鍾理和”小行星，在 2008 年 10 月 23 日由台灣中央大學天文研究所觀測助理蕭翔耀與廣州中山大學學生葉泉志共同發現，外型像一顆馬鈴薯，經國際天文學聯合會（IAU/CSBN）通過，編號 237187，正式命名爲“鍾理和”(Zhonglihe)。

已故台灣文學家鍾理和（1915～1960 年），高雄美濃人，自小熱愛文學，貧困中成長，仍堅持文學志業，至死不渝，這位客籍作家被譽爲“倒在血泊中的筆耕者”。其作品記錄農村生活樣貌，流露悲天憫人的情懷，是台灣當代重要文學家。

以“鍾理和”爲名，主要是因鍾理和當年懷抱著理想，從台灣遠赴大陸，最後又再返回故鄉美濃，探尋人生價值、原鄉意義的過程，就像天文家致力追尋新的天文知識，探尋太陽系的起源一般。

小行星是目前唯一可以被發現單位命名的天體，而以現代文學家命名，鍾理和爲第一人，過去曾以文學家爲名的僅有古代文學家蘇東坡。台灣文學館館長李瑞騰對於小行星以台灣作家命名，成功聯結天文與人文，認爲是台灣文學受到肯定的一種展現。

4 日在台灣文學館的慶祝活動，將播放鍾理和小行星的簡介影片，以及鍾理和人物記錄片，讓世人加深入鍾理和的文學生命。

原文轉載自【2012-08-04/中國評論新聞】

華人文學家命名　「鍾理和」星天上對孫女微笑

【動新聞/台南報導】全球第一顆以華人當代文學家命名的行星「鍾理和」，昨天下午將在國立台灣文學館舉辦慶祝儀式，發現行星的中央大學特別製作小行星銘版及模型，頒贈台灣文學館及鍾理和文教基金會收藏；昨天也是鍾理和逝世 52 週年紀念日，別具意義。

中央大學天文所所長高仲明表示，鍾理和小行星，在 2008 年 10 月 23 日由中央大學天文所蕭翔耀與廣州中山大學葉泉志共同發現，外型像一顆馬鈴薯，經國際 天文學聯合會(IAU/CSBN)通過，編號 237187，正式命名爲「鍾理和」(Zhonglihe)。發現時，位於金牛座位置，現在則在寶瓶座。

小行星以鍾理和爲名，背後很多巧合。鍾理和的孫女鍾怡彥目前在發現行星的中央大學攻讀中文研究所博士班，她的指導老師正是國立台灣文學館館長李瑞騰；鍾理 和家人對於小行星以鍾理和命名感到激動又驕傲，孫女鍾怡彥難掩興奮的表示，「偶爾抬頭仰望星空，發現祖父正在注視著我，這種感覺真是太奇妙了！」。

原文轉載自【2012-08-05/蘋果日報】

小行星命名鍾理和　紀念華人當代文學家

〔本報訊〕全球第一顆以華人當代文學家命名的行星「鍾理和」，下午於國立台灣文學館舉辦慶祝儀式，今天剛好也是鍾理和逝世 52 週年紀念日，別具意義。

國立台灣文學館下午舉辦「鍾理和」小行星命名通過慶祝儀式，鍾家數十人到場分享榮耀，鍾理和的孫子鍾怡彥表示：「想到天空有一顆祖父的星星，我一直有不可置信的驚喜。」

「鍾理和」小行星，2008 年 10 月 23 日由國立中央大學天文台觀測員蕭翔耀和中國大陸廣州中山大學學生葉泉志共同發現。中央大學特別製作小行星銘版及模型，送給台灣文學館和鍾理和文教基金會。

中央大學代理校長李誠說，小行星以「鍾理和」爲名，主因是鍾理和當年探尋原鄉過程的精神，就像天文家追尋新的天文知識，探尋太陽系的起源。國際天文學聯合 會 2011 年 10 月通過命名編號 237187 號「鍾理和」（Zhonglihe）小行星，這顆小行星外型就像顆馬鈴薯。

鍾理和是高雄美濃人，出生於 1915 年，去世於 1960 年，自小熱愛文學，在貧困中成長。因病中修改小說《雨》時，喀血而死，血濺書稿，被譽爲「倒在血泊中的筆耕者」，作品記錄農村生活樣貌，是台灣當代重要文學家。代表作品爲《笠山農場》、《貧賤夫妻》、《原鄉人》。

原文轉載自【2012-08-04/自由電子報 即時新聞】

小行星「鍾理和」　首顆以華人文學家命名

2012 年 08 月 04 日 14:34 全球首顆以華人當代文學家命名的行星「鍾理和」，今天下午 2 時在國立台灣文學館辦慶祝儀式，發現行星的中央大學特別製作小行星銘版及模型，頒贈台灣文學館及鍾理和文教基金會收藏；今天也是鍾理和逝世 52 週年紀念日。

中央大學天文所所長高仲明說，鍾理和小行星 2008 年 10 月 23 日由中央大學天文所蕭翔耀與廣州中山大學葉泉志發現，外型像 1 顆馬鈴薯，經國際天文學聯合會通過，編號 237187，命名爲「鍾理和」(Zhonglihe)。

小行星以鍾理和爲名，背後很多巧合，鍾理和孫女鍾怡彥在中央大學攻讀中文研究所博士班，她指導老師正是國立台灣文學館館長李瑞騰，鍾怡彥難掩興奮說，「偶爾抬頭仰望星空，發現祖父正在注視著我，這種感覺真是太奇妙了!」

原文轉載自【2012-08-04/蘋果日報　即時新聞】

鐘理和小行星慶祝典禮

【聯合報／記者莊宗勳／即時報導】 2012.08.04 08:40 pm

全球第一顆以台灣當代文學家命名的「鍾理和」小行星，今天在台灣文學館舉辦命名通過慶祝儀式。發現小行星的中央大學製作小行星銘版及模型，致贈給台灣文學館。鍾理和媳婦與孫女等家屬都到場觀禮，場面溫馨。
【2012/08/04 聯合報】@ http://udn.com/

原文轉載自【2012-08-04/聯合新聞網 生活　即時新聞】

鍾理和小行星命名　台文館同慶

記者黃微芬報導

慶祝全球第一顆以台灣當代文學家爲名的「鍾理和小行星」命名通過，國立台灣文學館四日在該館舉辦慶祝儀式，並由發現此星的中央大學校長將小行星銘版及模型，分別頒贈給台文館及鍾理和文教基金會。昨天適逢鍾理和逝世五十二週年紀念日，讓活動格外具有意義。

頒贈儀式昨天下午二時三十分舉行，鍾理和的孫女鍾怡彥帶著媽媽、妹妹、伯伯、叔叔和姑姑，包括鍾理和八十歲的姪子鍾佐鵬、第四代的五歲外曾孫女彭筠雅等，全家族一起分享這份榮耀。

鍾怡彥說，從獲知命名到現在，她依然感到興奮，尤其想到天空有一顆祖父的星星，她一直有不可置信的驚喜。

中央大學代理校長李誠表示，小行星以「鍾理和」爲名，主要是因鍾理和當年探尋原鄉的過程，精神就像天文家致力追尋新的天文知識，探尋太陽系的起源一般。

台文館長李瑞騰表示，「鍾理和小行星」代表人文與科技的結合，台文館以研究、典藏、推廣台灣文學爲目標，能舉辦這項活動讓他有撿到寶的感覺。

活動中播放導演彭啓原費時十年完成的十七分鐘的記錄片《鍾理和文學路》，片中專訪作家鍾肇政及鍾理和已故夫人鍾台妹、長子鍾鐵民，暢談他們對鍾理和的點滴回憶。珍貴的畫面，令在場觀眾動容。

「鍾理和小行星」小檔案

鍾理和小行星是二〇〇八年十月廿三日由中央大學天文所蕭翔耀與廣州中山大學葉泉志共同發現，外型像一顆馬鈴薯，經國際天文學聯合會（ IAU/CSBN）通過，編號二三七一八七，命名爲「鍾理和」（ Zhonglihe）。發現時，位於金牛座位置，現在位在寶瓶座。

原文轉載自【2012-08-05/中華日報】

小行星鍾理和　紀念台灣文學家

（中央社記者張榮祥台南 4 日電）「想到天空有一顆祖父的星星，我一直有不可置信的驚喜。」鍾怡彥今天在以祖父鍾理和爲名的小行星命名慶祝儀式上如此表示。

國立台灣文學館下午舉辦「鍾理和」小行星命名通過慶祝儀式，鍾家數十人到場分享榮耀，包括鍾理和 80 歲的姪子鍾佐鵬，及第四代的 5 歲外曾孫女彭筠雅。

台灣文學館表示，這是首顆以台灣當代文學家名字命名的小行星，在 8 月 4 日鍾理和去世這天舉行慶祝儀式，別具意義。

「鍾理和」小行星，2008 年 10 月 23 日由國立中央大學天文台觀測員蕭翔耀和中國大陸廣州中山大學學生葉泉志共同發現。中央大學特別製作小行星銘版及模型，送給台灣文學館及鍾理和文教基金會。

中央大學代理校長李誠說，小行星以「鍾理和」爲名，主因是鍾理和當年探尋原鄉過程的精神，就像天文家追尋新的天文知識，探尋太陽系的起源。

鍾理和是高雄美濃人，出生於 1915 年，去世於 1960 年，自小熱愛文學，在貧困中成長，被譽爲「倒在血泊中的筆耕者」，作品記錄農村生活樣貌，是台灣當代重要文學家。

國際天文學聯合會 2011 年 10 月通過命名編號 237187 號「鍾理和」（Zhonglihe）小行星，這顆小行星外型就像顆馬鈴薯。1010804

原文轉載自【2012-08-04/中央社即時新聞 CNA NEWS/教育文化 】

臺北天文館與 NASA 連線　現場直播

◎記者洪永成／臺北報導

登陸火星倒數計時，今日美國火星科學實驗室「好奇號」即將登上火星。這是有史以來最大規模的火星登陸，好奇號上攜帶了先進的科學儀器，有助於人類對火星有 更深一層的認識。如果您想參與這次登陸火星的重要時刻，千萬別錯過這次機會。臺北天文館與 TVBS、科學人、中央大學天文所、國立師範大學科教中心、美國 在台協會、台達電子文教基金會及 momo 親子台合作，於今日中午十二點三十分在天文館宇宙劇場辦理「登陸火星現場直播」，當天將與美國 NASA 連線，讓您 感受登陸火星第一現場的氣氛，並邀請中央大學天文所教授陳文屏現場講解，及 NASA 華裔科學家爲大家解惑火星相關問題，精彩的天文盛會歡迎您的參與。因爲 活動場地有限，當日開放八十位現場民眾排隊入場。

活動結束後，天文館邀請最受小朋友歡迎的 Momo 牛奶哥哥，將與您共遊天文館，帶領您參觀「前進火星」及「二〇一二珍稀地球」特展，並與小朋友同歡及拍照，期待帶給大家一趟兼具趣味及知性的天文之旅，爲親子間留下特別的暑假回憶。

原文轉載自【2012-08-06/青年日報首頁 > 搜奇 】

好奇號 10 儀器　探火星生命 雷射槍碎石化驗　登陸秀今直播

「好奇號」10 項儀器構造圖

【張 翠蘭／綜合報導】人類在宇宙中是孤單的嗎？火星上有生命嗎？美國航太總署（NASA）重金打造的「好奇號」火星探測器，預計台灣時間今天下午 1 時 31 分登 陸火星，朝找出解答邁出第一步。中央大學天文所陳文屏教授昨指出，好奇號配備最先進儀器，包括有如在科幻電影中的雷射槍，可擊碎岩塊以利分析其成份，找出 火星何時曾存在生命的證據。

好奇號（Curiosity）經過 8 個多月太空旅行，即將抵達有「紅色星球」之稱的火星，預計台灣時間今午著陸。NASA 稱「好奇號狀況良好，所有系統正常運作」。

全球天文迷企盼

除了降落過程 7 分鐘極爲艱險，天候也是成功其一因素，NASA 噴射推進實驗室科學家瓦沙瓦達指，火星目前天候不錯，一旦降落成功，NASA 很快會收到好奇號傳回黑白影像。

全球各地天文迷期盼這項太空任務，NASA 將在紐約地標時報廣場實況轉播，台北市立天文科學教育館今也在宇宙劇場舉辦「登陸火星現場直播」免費活動，中午 12 時 15 分開放 80 位民眾排隊進場，由中央大學天文所陳文屏教授講解，並與 NASA 華裔科學家劉登凱連線，解答問題。

好奇號配備 10 項科學儀器，體型與重量特別大，因此須首創採空吊方式降落火星。陳文屏昨接受《蘋果》電訪時表示，好奇號「配備彩色相機，拍攝出來就是實際顏色」，還 有很特殊雷射光束功能，「很像科幻電影裡的雷射槍，可擊碎前方岩塊」，由於好奇號無法把火星上的樣本送回地球，須當場化驗，它以機械臂的勺子挖起岩塊或土 壤，放進探測器車體裡的實驗分析儀，「加溫 1000 多度氣化後，分析其成分。」

選擇近赤道石坑

以往太空任務多爲探測地形或描繪磁場等科學研究，此次最特別是探索生命環境。陳文屏說：「火星南半球地勢高於北半球，早年若有大量流水，會流經赤道，因此特地首度選在火星赤道附近的蓋爾隕石坑」。另一重要目標，是找出將來人類登陸火星的適合環境。

好奇號 小檔案

★尺寸：長 3 公尺、寬 2.7 公尺、高 2.1 公尺；約莫休旅車大小

★重量：900 公斤

★最高時速：每秒 4 公分

★零組件：

・機械臂：可延長至 2.3 公尺

・共 6 組機輪：直徑 50 公分，各有其驅動馬達

★動力來源：配備 4.8 公斤的二氧化鈽，經由輻射衰變的熱氣產生電力。最低壽命 14

年。

原文轉載自【2012-08-06/蘋果日報/A15 版/國際焦點】

天文館直播　教授講解

〔記者邱紹雯／台北報導〕「火星上有生命嗎？」「火星人長得跟海綿寶寶一樣嗎？」「人類也有機會登上火星嗎？」這些有關火星的疑問，有機會在火星探險車「好奇號」登陸火星後，一一解開。

登陸火星倒數計時中，美國航太總署發射火星探測車「好奇號」，預計今天登陸火星。台北市立天文館與科學人、中央大學天文所、國立師範大學科教中心、美國在 台協會、台達電子文教基金會、TVBS 及 momo 親子台合作，今天中午 12 點將在天文館宇宙劇場辦理「登陸火星現場直播」，現場邀請中央大學天文所教授陳 文屏全程講解，另由 NASA 華裔科學家連線替民眾解開火星之謎。

天文館表示，這是有史以來最大規模的火星登陸，好奇號攜帶先進的科學儀器，有助於人類對火星有更深一層的認識。因活動場地有限，僅開放 80 位民眾排隊入場，參與這場天文盛會。

此外，活動結束後，天文館也將帶領民眾參觀「前進火星」及「2012 珍稀地球」特展，天文館 8、9 月也推出「火星季」活動，相關訊息可上天文館網站查詢 http://www.tam.gov.tw/）。

原文轉載自【2012-08-06/自由時報/A10 版/國際萬象】

火星登陸「恐怖 7 分鐘」空吊探測器難度高 台天文館明直播

【張 翠蘭、許敏溶／綜合報導】神祕的「紅色星球」火星又成焦點。飛行 8 個多月後，美國航太總署（NASA）的火星探測器「好奇號」明天就要登陸火星，首度挑戰 以空吊降下探測器，媒體形容其難度有如軍方直升機在戰區降下吉普車般，NASA 稱這段過程爲「恐怖 7 分鐘」。台北市立天文科學教育館明午 12 時 30 分起將 同步進行登陸的現場直播。

「好奇號」（Curiosity）登陸火星任務於去年 11 月 26 日升空後展開，飛行 5.7 億公里後，預計台灣時間明下午 1 時 30 分進入火星大氣層。由於無線電波從火星傳回地球有 14 分鐘落差，NASA 工程師把降落的指令傳給好奇號後，除了追蹤著陸過程，只能等待結果。

砸 750 億解謎火星

此計劃耗資約 750 億元台幣，將探測 2 年，提供火星地表岩石的詳細資料，有助解開

火星是否曾有生命的謎題。

好奇號是送上太空首部研發最完善的移動式分析實驗室，重 899 公斤，比 2004 年登陸火星的精神號與機會號重上 5 倍，體型也大逾 2 倍，降落方式也不同。此 次太空艙的隔熱罩直徑 4.5 公尺，可抵禦攝氏 1600 度高溫，降落時採歷來最大與最堅固的超音速降落傘，並首創以「空中起重機」空吊降下探測器。太空艙將 以時速 2.1 萬公里進入火星大氣層，減速後隔熱罩脫離，再釋出空中起重機與好奇號，最後由起重機用纜繩懸吊緩降好奇號。過程僅 7 分鐘，每個步驟環環關鍵， 風險極高。

每次火星探測任務總面臨相同問題，最令科學家感興趣的探勘區域，往往是著陸最困難處，探測器須降落在平坦空曠地形。

降落蓋爾隕石坑口

NASA 以往總讓探測器降落平坦處再移往目的地，此次好奇號將降落可採集樣本的蓋爾隕石坑口。

台北市立天文科學教育館明中午 12 時 30 分到下午 2 時將進行好奇號登陸火星直播，當天將依序開放 80 人進場，票價每人 100 元。天文館解說員林琦峰昨說，明直播現場將邀中央大學天文所教授陳文屏與 NASA 華裔科學家劉登凱連線。

火星探測器「好奇號」著陸示意圖
資料來源：GRAPHIC NEWS
好奇號降落火星，將展開 2 年任務，尋找火星上是否存在生命的證據。

原文轉載自【2012-08-05/蘋果日報/A16 版/國際焦點】

美登陸火星　6 日天文館直播

【記者陳瑄喻／台北報導】

本月六日美國火星科學實驗室好奇號將登上火星。北市立天文館表示，這將是有史以來最大規模的火星登陸，當天中午將在宇宙劇場與美國太空總署 NASA 連線直播實況。

「好奇號」共耗資廿四億美元，天文館表示，這是有史以來最昂貴的火星探測任務，去年十一月廿六日出發，預計在六日台灣時間下午一時卅一分降落在火星赤道以南的蓋爾隕石坑（Gale Crater）。

天文館表示，火星車「好奇號」長三公尺、寬二點七公尺、高二點一公尺，重約九百公斤，它能夠跨過七十五公分的障礙物，每小時最高可以前進九十公尺，若考慮地形等因素，每小時平均前進卅公尺。

天文館當天將與 NASA 連線，民眾可感受到登陸火星第一現場的氣氛，並邀請中央大學天文所教授陳文屏講解，及 NASA 華裔科學家為大家解答相關問題。洽詢電話（〇

二）二八三一四五五一。

原文轉載自【2012-08-04/聯合報/A6 版/生活】

6 日來天文館　看好奇號登陸火星　現場直播將與 NASA 連線並邀科學家解惑 開放 80 位民眾現場排隊入場 另 12 日晚可看英仙座流星雨

【石文南／台北報導】

登陸火星倒數計時！六日美國火星科學實驗室（ＭＳＬ）將登上火星，這是有史以來最大規模的火星登陸。台北市立天文科學教育館六日舉辦「登陸火星現場直播」活動。

天文館於六日十二時卅分在宇宙劇場辦理登陸火星現場直播，與美國航空暨太空總署（ＮＡＳＡ）連線，邀中央大學天文所陳文屏教授及ＮＡＳＡ華裔科學家為大家解惑火星問題。場地有限，當日僅開放八十位現場民眾排隊入場。

天文館指出，去年十一月廿六日耗資廿四億美元的「火星科學實驗室」在美國佛羅里達州卡納維拉爾角空軍基地發射升空，預計台灣時間八月六日下午一時卅一分 降落在火星赤道以南的蓋爾隕石坑，最受矚目的是實驗室上的「好奇號」（curiosity）火星車將第三度登上火星表面探勘。

「好奇號」此行研究火星的適居性，將調查至少一個目標區域其環境是否蘊藏生命發展潛力；其次則調查火星地表及地表淺層的化學成分及礦物組成。另也將了解火星的演化和是否可能存在生命。

天文館推出「火星季」活動，詳情可上天文館網站 http://www.ta m.gov.tw/。

天文科學教育館也表示，今年英仙座流星雨極大期預估在十二日晚間八時至十時卅分，每小時約有一〇〇顆的流星雨，可從當晚一直觀察到隔日凌晨，可詳查天文館網站（www.tam.gov.tw/MP_104051.ht ml）。

原文轉載自【2012-08-04/中國時報/C1 版/台北焦點・運動　】

小行星　命名馮元楨星

記者李大明聖地牙哥報導 世界新聞網 北美華人社區新聞

August 02, 2012 09:00 AM

法國巴黎為總部的國際天文學聯合會（International Astronomical Union，即 IAU）日前宣布，離地球 2 億 2500 萬哩的一顆太陽系小行星已被命名為「馮元楨星」，藉以表示對著名華裔科學家、「生物力學之父」馮元楨教授的崇敬。

下月 15 日將屆滿 93 歲的馮元楨是江蘇省武進市橫林鎮余巷村人，1934 年畢業於北

京四中，1937 年考入國立中央大學航空工程系，1943 年獲該校碩士 學位後赴美深造，1948 年獲加州理工學院（Cal Tech）博士學位並留校任教，1966 年轉任聖地牙哥加州大學（UCSD）教授。

1960 年代初，馮元楨的科研興趣從航空工程轉入生物學與生理學，並致力於一個新領域——生物力學的開拓。他將工程學的原理運用於人體機能的研究，取得多 項具有里程碑意義的重要成就。之後，他又爲 UCSD 創辦生物工程系，使之成爲該領域最具規模、最富成果的人才搖籃。馮元楨因此被譽爲「生物力學之父」。

馮元楨畢生建樹甚豐，這使他成爲美國國家科學院院士、國家工程院院士、國家醫學科學院院士，以及北京的中國科學院院士與台北的中央研究院院士。2000 年，他榮獲美國國家科學獎章；2007 年又獲堪與諾貝爾獎媲美的「拉斯獎」（Russ Prize）。雖然年屆耄耋，他仍經常出席各種學術與社交活動。他的毛筆書法與印章篆刻也堪稱一絕。

新近命名的「馮元楨星」編號 210434，位於太陽系內火星與木星軌道之間的「主小行星帶」（Main Asteroid Belt ）。這一區域的小行星估計多達 50 萬顆，每顆直徑平均爲 400 公里左右。其中許多小行星已被冠以中國古今科學家、文學家的名字，如張衡、祖沖之、沈括、一 行和尚、郭守敬、吳健雄、袁隆平、巴金、陳省身、錢學森、陳景潤、錢三強、金庸、周光召、沈君山、朱光亞等。

原文轉載自【2012-08-02/世界新聞網-北美華文新聞、華商資訊】

北市天文館 8/6　登陸火星現場直播　開放網路報名

中廣新聞網－ 2012 年 7 月 26 日 下午 5:30

八月六號，美國火星科學實驗室「好奇號」，即將登上火星，台北市立天文科學教育館表示，這是有史以來，最大規模的火星登陸，「好奇號」上攜帶了先進的科學儀器，有助於人類對火星有更深一層的認識。

而這次台北市立天文館、中央大學天文所、國立師範大學科教中心等單位合作，八月六號中午十二點半在天文館宇宙劇場，辦理「登陸火星現場直播」活動，當天將 與美國 NASA 連線，讓民眾感受登陸火星第一現場氣氛，現場也會邀請中央大學天文所教授陳文屏現場講解，爲大家解惑火星相關問題。天文館表示，這次的「登 陸火星現場直播」活動，採網路報名，民眾只要上網站填寫報名資料，並提出一個火星相關問題，就有機會參加「登陸火星現場直播」活動。前兩百位提問民眾，可 以獲得「好奇號火星車紙模型」材料一份。

原文轉載自【2012-07-26/中廣新聞網】

問題大聲公-火星召集令歡迎你來問

新浪新聞中心-體育新聞

大成報 (2012-07-26 16:48)

【記者黃則華/台北報導】火星上有生命嗎？登陸火星的過程隱含著什麼危機？人類有機會登陸火星嗎？如果您對火星有更多的疑問，千萬別錯過這次機會。天文館與TVBS、科學人、中央大學天文所、國立師範大學科教中心、美國在台協會、台達電子文教基金會及 momo 親子台合作，將於 8 月 6 日中午 12 點 30 分在天文 館宇宙劇場辦理「登陸火星現場直播」，當天將與美國 NASA 連線，讓您感受登陸火星第一現場的氣氛，並邀請中央大學天文所陳文屏教授現場講解，及 NASA 華裔科學家爲大家解惑火星相關問題，精彩的天文盛會歡迎您的參與。

2012 年 8 月 6 日美國火星科學實驗室（MSL，好奇 號，curiosity）即將登上火星。這是有史以來最大規模的火星登陸，好奇號上攜帶了先進的科學儀器，有助於人類對火星有更深一層的認識。本活動將開 放網路報名，民眾只要上網站填寫報名資料，並提出一個火星相關問題，就有機會參加「登陸火星現場直播」活動。前 200 位提問的民眾，可以獲得「好奇號火星 車紙模型」材料一份，並有機會獲得【科學人精采特輯】《發現天文之美》一本，歡迎民眾踴躍報名參加。詳情請洽詢：02-28314551 轉分機 703。

另外，天文館於 7 月至 9 月推出「火星季」活動，活動豐富，欲知詳情請上天文館網站 www.tam.gov.tw 。

原文轉載自【2012-07-26/新浪新聞】

新行星命名通過 「鍾理和」閃耀銀河

【羅安達 桃園】

國際編號 237187 的一顆新發現小行星，被中央大學鹿林天文台發現，這次他們將這顆新行星以客籍作家「鍾理和」爲名，在國際天文學聯合會審查命名通過，成爲華人世界第一次以台灣當代文學家命名的小行星，被譽爲倒在血泊中的筆耕者鍾理和，從此高掛天空、輝映人世。

繞行太陽，位在火星與木星間小行星群中，有一顆直徑約 2 千公尺，形狀像一顆馬鈴薯，國際編號爲 237187 的小行星，被中央大學鹿林天文台在 2008 年 10 月 23 日發現，天文台主任表示，這顆小行星存在宇宙這樣多年，一直沒有被人類發現，當然，對於研究者而言，發現它實在是一件很高興的事情。

中央大學鹿林天文台駐站主任林宏欽：「它是一個它存在在宇宙中這麼多年，一直到，一直到我們發現它之前都不爲人所知，那這個能發現到，當然是一個很特別的事情，尤其是它可以做一個小行星，唯一我們可以做一個命名的天體。」

負責爲小行星命名人員之一的張光祥表示，命名須送國際天文學聯合會，小行星命名委員會審查，這次以客籍文學家來命名，他覺得很光榮，也希望讓世人看見鍾理和對台灣文學的貢獻。

中央大學天文研究員 張光祥：「他當初對客家文學的創作，對農村的介紹，還有台灣

人民生活的情形表達的很完善，所以我們可以用這個活動來發起，對他文學作品的回憶跟溫習，是很適合的一件事情。」

發現行星的中央大學天文所，將於 8 月 4 日在台灣文學館舉行慶祝儀式，並頒贈小行星銘板及模型給台灣文學館及鍾理和文教基金會珍藏，鍾理和小行星位於小行星帶，直徑約 2000 公尺，等於有阿里山的大小，中央大學鹿林天文台說，台灣已爲 20 多顆小行星命名，名稱多數是科學家或是縣市地名，以客籍文學作家命名是 第一次，也是全球首度以近代華人作家命名。 (2012-07-21)

原文轉載自【2012-07-21/客家電視台 CH 17】

以作家之名　小行星鍾理和　照亮宇宙原鄉

【記者修瑞瑩／台南報導】

全球第一顆以近代華人作家命名的小行星「鍾理和」，下個月將在國立台灣文學館舉辦慶祝儀式，紀念這位「倒在血泊中的筆耕者」。

發現這顆小行星的中央大學鹿林天文台表示，台灣已爲廿多顆小行星命名，名稱多數是科學家、縣市地名，以文學作家命名是第一次，也是全球首度以近代華人作家命名，過去大陸曾以古文人「蘇東坡」爲小行星命名。

鍾理和一九六〇年去世，享年四十四歲，一生貢獻文學，染肺疾仍不斷創作，最後咯血在作品上去世。

「有一顆小行星叫鍾理和，真的好奇妙！」鍾理和孫女鍾舜文說，去年十月接獲消息，激動情緒延續至今，「就像祖父在天上默默地凝視親人，默默守護大地」。

「鍾理和」小行星位在火星與木星間小行星群中，直徑約兩千公尺，形狀像一顆馬鈴薯，鹿林天文台於二〇〇八年十月廿三日發現，經過一連串認證才順利命名。

負責命名人員之一張光祥表示，命名須送國際天文學聯合會小行星命名委員會審查，以華人文學家命名，希望讓世人重視華文文學的價值，原本思考過其他同樣重量 級的作家，例如吳濁流等人，但鍾理和與妻子當年從台灣遠赴大陸再返回，在原鄉人一書中對「原鄉」有許多探討，就像是天文學家研究小行星，探尋太陽系起源的 意義。

原文轉載自【2012-07-18/聯合報/A6 版/生活】

新發現小行星　命名鍾理和

國際編號 237187 的一顆新發現的小行星，以台灣本土作家「鍾理和」爲名命名通過，成爲華人世界第一次以台灣當代文學家命名的小行星。被譽爲「倒在血泊中的筆耕者」，從此高掛天空輝映人世。

發現行星的中央大學天文所將於 8 月 4 日在台灣文學館共同舉行慶祝儀式，並頒贈小

行星銘板及模型給台灣文學館及鍾理和文教基金會珍藏。鍾理和小行星位於小行星帶，形狀如不規則的馬鈴薯，直徑約 2000 公尺。

（記者蔡文居）

原文轉載自【2012-07-18/自由時報/A9 版/生活新聞】

小行星「鍾理和」 照亮宇宙「原鄉」

時間：2012/7/18 09:31
新聞引據：聯合報

全球第一顆以近代華人作家命名的小行星「鍾理和」，下個月將在國立台灣文學館舉辦慶祝儀式，紀念這位「倒在血泊中的筆耕者」。

發現這顆小行星的中央大學鹿林天文台表示，台灣已爲 20 多顆小行星命名，名稱多數是科學家、縣市地名，以文學作家命名是第一次，也是全球首度以近代華人作家命名，過去大陸曾以古文人「蘇東坡」爲小行星命名。

鍾理和 1960 年去世，享年 44 歲，一生貢獻文學，染肺疾仍不斷創作，最後咯血在作品上去世。

鍾理和孫女鍾舜文說，有 1 顆小行星叫鍾理和，真的好奇妙！鍾舜文說，去年 10 月接獲消息，激動情緒延續至今，就像祖父在天上默默地凝視親人，默默守護大地。

「鍾理和」小行星位在火星與木星間小行星群中，直徑約 2 千公尺，形狀像 1 顆馬鈴薯，鹿林天文台於 2008 年 10 月 23 日發現，經過一連串認證才順利命名。

負責命名人員之一張光祥表示，命名須送國際天文學聯合會小行星命名委員會審查，以華人文學家命名，希望讓世人重視華文文學的價值，原本思考過其他同樣重 量級的作家，例如吳濁流等人，但鍾理和與妻子當年從台灣遠赴大陸再返回，在原鄉人一書中對「原鄉」有許多探討，就像是天文學家研究小行星，探尋太陽系起源 的意義。
原文轉載自【2012-07-18/中央廣播電臺新聞頻道】

▼搜尋小行星

◎作者：文與圖／張光祥

鄰近阿里山與玉山的鹿林天文台，夜間盡是星海、銀河、動物聲，陪伴觀測員浪漫又寂寞的冷冽時光。鹿林天文台是鹿的原鄉，天文台南方是旗山溪上游的楠梓仙 溪，美濃與荖濃溪會合即是高屏溪，天文台北面是神木溪，往下游匯入陳有蘭溪，再匯入濁水溪，可見鹿林是水、星星、鹿的原鄉。人類在此探索宇宙，觀察星空找 到新發現來滿足好奇心。

觀測員與觀測助理的血液裡流著鄒族傳統勇士精神，不眠、不休在觀察天地宇宙的變化。白天片刻的休息時段，便將來自 星星的訊息，利用四通八達的電腦網路傳送給各

地的天文學家。在科學教育者的眼光下，每個人都在與時間競賽，想爲人類提供宇宙的新發現。每年偶有遇到特殊天 象時，也就是鹿林山最熱鬧的時候，民眾與媒體記者都聚焦於來自鹿林天文台的第一手新訊息。

然而，鍾理和小行星的發現，只是利用我們鹿林天 文台望遠鏡所看到的一顆石頭而已，此發現並不特別，但是經過大家巧思就能發揮科學與文學的創作，引起人們重新欣賞他的文學鉅作，作品中有著北京、瀋陽、台 灣的故事。看到鍾理和與鍾台妹在北京的足跡，就像搜尋到小行星一樣，令人興奮與陶醉，人們的原鄉，隨祖先的遷移可知；而人們想知道宇宙空間的原鄉，可從小 行星的探索開始。鍾理和小行星形如不規則的馬鈴薯，直徑約兩千公尺左右，與阿里山的海拔高度相當。鍾理和小行星是中大鹿林天文台發現八百多顆小行星中的一 顆，經世界天文學聯合會小行星命名委員會命名通過的，在國際小行星中心的永久編號是：237187，鹿林巡天計畫 LUSS 的環境、設備與全球五大巡天計畫 的設備比較有如小舢舨與航空母艦的懸殊差距，只能算是「小蝦米對大鯨魚」，而且鹿林天文台沒有路，重要的是，「在這個世界的舞台上，我們沒有缺席。」根據 國際天文學聯合會小行星中心（IAU: Minor Planet Center）的統計資料，鹿林天文台已成爲亞洲發現小行星最活躍的地方，全球排名第四十八名。

天文台經過環評的流程後，籌畫人員從過程 中理解到，天文台所在的這塊寶地，潛藏著許多從前所未知的故事；如施工過程中爲了不干擾棲息的動植物，所以工程要細心而緩慢，對防火逃生、儀器運送、環境 監測、施工時的安全，更是需要嚴加遵守的事項，而且現有觀測團隊的運作，又不能因施工而停擺，這些要求在平地並不困難，但在海拔近三千公尺，又沒有正式道 路的情況下，兩公尺望遠鏡要能開光使用，甚至比太空探測任務還要艱鉅。一如俗話所說：「比登天還難。」

我們經常從國際新聞聽聞中東情勢的不穩定，以色列與鄰國又有紛爭，可能引發戰爭。如果再從環評報告書仔細端詳，會發覺每次鑑界的過程，爲何如此之冗長與繁 複，參與的單位與人數眾多，把鹿林山頭擠得滿滿，甚至已無立錐之地，這時天文台助理，最頭痛的是如何在沸點只有八十六度 C 的水溫下煮好一大鍋麵條，好讓這 次鑑界的人員能夠在工作之後填飽肚子。在此過程中，由於這個山頭是嘉義、南投縣界，土地管轄的單位爲台大實驗林與嘉義林區管理處，再加上玉山國家管理處， 建管單位是嘉義縣政府、南投縣政府、水土保持局等，周邊單位是環保署，還有將來營運配合的單位如台電、通訊公司、消防局……等單位，眾多部會的意見，使得 每一次的會勘當下都未必會產出結論，可以說鹿林天文台要進行一項申請案，必須從位處土石流區域的道路開始，風雨無阻冒險上山的進行聯合會勘，依各單位表述 後，才可以進行下一個流程……，而每經一個流程都會出現未曾接觸到的陌生的法規。土地界線有很多的不確定性，想起小時候，看見鄰居大吵一架不相往來，其紛 爭原因往往是房子土地鑑界而產生，所以把鹿林山的處境想像成以色列是很貼切的。

天文台每個月都接受三個團體的參觀，有一次一個學童說，中 央大學怎麼那麼小，只有兩棟校舍，因爲他只看到三角點旁立牌上寫的大字國立中央大學，沒繼續往下方較小的字看完，就很大聲的在山頂上笑著說：「中央大學好 小！」助理聽到急忙出來解釋：「這是學校的天文台，校區在北部的中壢，你不相信再好好看清楚立牌下方的字，亦可

上網看，更可以了解。」

我 們好辛苦奮鬥了二十二年才有的小基地，兩棟建物：一棟是嘉義阿里山鄉自忠七十八號，另一棟是南投信義鄉鹿林一號。往下方看到的鹿林山莊是依我們的門牌號， 才申請編定出的鹿林二號。兩公尺口徑望遠鏡天文台完成後的門牌號應該是嘉義縣阿里山鄉中山村六鄰自忠七十六號，與玉山的排雲山莊同樣是中山村。我曾經說過 一段話:「要在台灣的高山上建天文台，要有不怕死、像瘋子的精神，才能安然爲望遠鏡開光。」當然此話是喝了會令人陶醉又能壯膽的飲料後才說的。

二〇一二年八月，我們將在台南的台灣文學館舉行鍾理和小行星頒贈活動，雖然兩公尺望遠鏡在那時尚未建成，希望將來完成時能邀請您的家人前往鹿林天文台，從 兩公尺望遠鏡向您問候（天上的鍾理和小行星）。這裡所言的兩公尺望遠鏡，曾引發一個笑話：我們此計畫有聘一位計畫助理，簡稱兩米助理。有外人聽到兩米助理 的稱呼，即時誤解爲：貴所的助理兩米高嗎？我們笑答：是口徑兩公尺望遠鏡天文台計畫的助理。幾年後，大家如果有機會，申請前往鹿林天文台參觀，將會大吃一 驚，原來兩公尺望遠鏡要進行科學觀察，它需要一棟約二十米高（將近六層樓）的建築物。

鹿林夜空的獵戶星座，像慈祥的父親在高高的天上祝福 著即將遠行的兒女，數百光年之遙的參宿四散發出溫暖的光芒。明亮的月光像母親般的溫暖人間。哲學家康德所言:「兩件人生最美好的事情：一是人們善良的心 靈，另一件就是我們頭頂上美麗的星空。」兩公尺望遠鏡天文台的落成是一件令人引頸期盼的百年大夢。

原文轉載自【2012-07-12/人間福報/副刊 】

恆星亮度奇特　中大團隊意外觀測到行星胚胎

生活中心／台北報導

國立中央大學 1 日表示，利用鹿林天文台 1 米和 40 公分望遠鏡，搭配國際其他望遠鏡數據，天文團隊意外觀測到初誕生恆星周圍形成原始行星證據。成果將刊在最新 1 期「天文物理期刊」。

這項成果爲中央大學天文所研究生胡佳伶以及指導教授陳文屏共同研究，中央大學表示，將有助於對行星的形成，有更進一步認識。

胡佳伶說，中大團隊參加由國際天文台觀測網，監測 Trumpler 37 這個年輕星團，年齡只有約 400 萬年，希望利用「掩星」方式，也就是行星運行到恆星前方所產生的亮度變化，來偵測行星存在。

胡佳伶說，在分析資料時，發現編號爲「仙王座 GM」這顆星球的亮度有奇特的變化方式，它大約相隔 1 年，會變暗長達 1 個月，這是前所未見的現象。陳文屏說，原來想找行星，但沒有找到，卻意外偵測到可能是行星胚胎形成的首要步驟。

國際知名行星科學專家、中央大學天文所教授葉永烜說，行星形成的關鍵，就是恆星周圍的塵埃盤開始變得不均勻。在很多年輕恆星周圍可能也有類似現象，值得繼續發掘。

國外天文學家之前觀測距離地球僅只有 25 光年，並且比太陽更亮 20 倍的恆星「北落師門」，它的名氣有一部分來自於冰環內部的行星 Form b，卻又難以確認它是否存在，在阿塔卡瑪大型毫米波天線陣(ALMA)的新觀測中謎底揭曉，這顆恆星的薄冰環有兩顆行星，而且行星質量遠小於原先認定，不 會比地球大很多倍，而非土星大小。

北落師門(Fomalhaut)是一顆非常年輕的恆星，年齡只有 2 至 3 億歲，本身是個明顯易見的天體。

原文轉載自【2012-06-01/ETtoday 新奇新聞　ETtoday 新聞雲】

行星胚胎形成關鍵　中央大學觀測發現

【台灣醒報記者劉運綜合報導】中央大學主導的國際天文團隊最近利用鹿林天文台的望遠鏡，搭配國際其他望遠鏡數據，觀測到初誕生恆星周圍形成原始行星的證據，將 有助科學家對行星的形成，有更進一步認識。中央大學天文所教授陳文屏笑說，原本想找行星，卻意外探測到行星胚胎形成的步驟，非常有價值。

中央大學天文所研究生胡佳伶以及指導教授陳文屏觀測到行星胚胎形成的關鍵步驟，她說道：「很高興有機會使用臺灣的設備，得到不錯的科學成果。」中大團隊參 加國際天文台觀測網，監測年輕星團 Trumpler 37，其年齡只有約 4 百萬年，利用行星運行到恆星前方所產生的亮度變化，來偵測行星存在。

陳文屏強調，原來想找行星，但卻意外偵測到可能是行星胚胎形成的首要步驟。國際知名行星科學專家、中央大學天文所葉永烜教授說：「行星形成的關鍵，就是恆星周圍的塵埃盤開始變得不均勻。在很多年輕恆星周圍可能也有類似現象，值得繼續發掘。」

研究團隊的資料主要來自鹿林天文台望遠鏡，以及中央大學天文所操作、位於美國亞利桑納州的 Tenagra 望遠鏡。而此成果也將刊載於 6 月出版的《天文物理期刊》（The Astrophysical Journal）。

原文轉載自【2012-05-31/台灣醒報】

金星凌日再見　相約 105 年後

（中央社記者林紳旭台北 6 日電）歷時 6 個多小時的天文奇景「金星凌日」，在今天中午 12 時 48 分結束。中央氣象局說，台灣西部地區受到雲層影響，偶有撥雲見日空檔可觀察，錯過這次機會，下次再等 105 年。

金星凌日再見　相約 105 年後

中央氣象局說，這場罕見的金星凌日在上午 6 時 11 分登場，當時台灣北部多雲，從 6 時 11 分起的「初外切」受到雲層影響不可見，直到約 6 時 29 分時的「初內切」時，太陽透過較稀薄的雲層乍現，接下來，雲層漸少，觀察的時間增加。

台灣中南部今天也是多雲到晴的天氣，恆春半島和台東地區在上午則有下雨，但只要

雨勢歇息、雲層散去，全台灣各地都有機會見到金星凌日。

中央氣象局表示，金星凌日的天文現象每 243 年發生 4 次，發生的年序間隔爲 8 年、105.5 年、8 年、121.5 年，上次金星凌日發生在 2004 年 6 月 8 日，時隔 8 年後，這次發生的時間爲今天上午，下次再出現金星凌日爲 2117 年 12 月 11 日。

包括台北市立天文科學教育館、中央大學天文社、嘉義市天文學會等單位，都在各地舉辦金星凌日的觀測活動與教學，並安排專業志工協助指導，吸引許多國中、國小學生及民眾參與。

前鎮高中天文社員 20 多人總動員，上午在學校請公假，清晨 6 時 11 分就到校就位以天文望遠鏡全程觀測，一早雲層頗多，太陽時而露臉，時而被雲層遮住，但仍不減學生觀測興致，不過，天公不作美，上午 10 時以後太陽就不再露臉。

嘉義市天文學會在僑平國小舉辦戶外教學，透過望遠鏡投影，讓學童一窺金星凌日的過程，也有學童拿出自製的遮光眼鏡保護眼睛後，直接觀察太陽表面。

這場金星凌日，中央氣象局也透過中華電信 HiChannel 和 MOD 平台直播整個過程。（中央社記者董俊志攝 101 年 6 月 6 日）

原文轉載自【2012-06-06/中央社 】

金星凌日奇景　全台都有看見

中央社／台北六日電

歷時六個多小時的天文奇景「金星凌日」，在今天中午十二時四十八分結束。中央氣象局說，台灣西部地區受到雲層影響，偶有撥雲見日空檔可觀察，錯過這次機會，下次再等一〇五年。

中央氣象局說，這場罕見的金星凌日在上午六時十一分登場，當時台灣北部多雲，從六時十一分起的「初外切」受到雲層影響不可見，直到約六時二十九分時的「初內切」時，太陽透過較稀薄的雲層乍現，接下來，雲層漸少，觀察的時間增加。

雲到晴的天氣，恆春半島和台東地區在上午則有下雨，但只要雨勢歇息、雲層散去，全台灣各地都有機會見到金星凌日。

中央氣象局表示，金星凌日的天文現象每二四三年發生四次，發生的年序間隔爲八年、一〇五點五年、八年、一二一點五年，上次金星凌日發生在二〇〇四年六月八日，時隔八年後，這次發生的時間爲今天上午，下次再出現金星凌日爲二一一七年十二月十一日。

包括台北市立天文科學教育館、中央大學天文社、嘉義市天文學會等單位，都在各地舉辦金星凌日的觀測活動與教學，並安排專業志工協助指導，吸引許多國中、國小學生及民眾參與。

前鎮高中天文社員二十多人總動員，上午在學校請公假，清晨六時十一分就到校就位以天文望遠鏡全程觀測，一早雲層頗多，太陽時而露臉，時而被雲層遮住，但仍不減學生觀測興致，不過，天公不作美，上午十時以後太陽就不再露臉。

嘉義市天文學會在僑平國小舉辦戶外教學，透過望遠鏡投影，讓學童一窺金星凌日的過程，也有學童拿出自製的遮光眼鏡保護眼睛後，直接觀察太陽表面。

這場金星凌日，中央氣象局也透過中華電信 HiChannel 和 MOD 平台直播整個過程。

原文轉載自【2012-06-07/中華日報/A3 版/焦點】

原始行星　中央大學團隊發現

【本報台北訊】中央大學天文研究所參與國際「Young Exoplanet Transit Initiative 觀測計畫」，在二〇一〇年至二〇一一年間，觀測到初誕生在恆星周圍的原始行星證據，這項成就刊登在最新一期的《天文物理期刊》。

團隊成員之一的胡佳伶表示，研究團隊原本要觀測行星，在分析資料時，「不小心」發現編號爲「仙王座 GM」這顆星球亮度有奇特變化，它大約相隔一年，會變暗長達一個月，「這是前所未見的現象」，團隊發現環星盤有不均勻現象，這些不均勻團塊，就是行星形成的早期證據。

胡佳伶說，她和指導教授陳文屏利用鹿林天文台的一百公分與四十公分望遠鏡觀測，再搭配國際其他望遠鏡數據，取得重要成果，將對行星形成有更進一步的認識。

原文轉載自【2012-06-02/人間福報/綜合／社區 】

中大天文所　發現原始行星證據

【記者沈育如／台北報導】

中央大學天文研究所參與國際「Young Exoplanet Transit Initiative 觀測計畫」（簡稱 YETI），在 2010 年至 2011 年間，觀測到初誕生在恆星周圍的原始行星證據，這項觀測成就刊登在最新一期的《天文物理期刊》。

團隊成員之一的胡佳伶表示，研究團隊原本要觀測行星，在分析資料時，「不小心」發現編號爲「仙王座 GM」這顆星球亮度有奇特變化，它大約相隔一年，會變暗長達一個月，「這是前所未見的現象」。

胡佳伶表示，團隊在「仙王座 GM」旁，發現環星盤有不均勻現象，這些不均勻團塊，就是行星形成的早期證據。

胡佳伶說，她和指導教授陳文屏，利用鹿林天文台的 100 公分與 40 公分望遠鏡觀測，再搭配國際其他望遠鏡數據，取得重要成果，將對行星形成有更進一步認識。

原文轉載自【2012-06-02/聯合報/AA4 版/教育】

中大：觀測到行星胚胎形成關鍵

（中央社記者林思宇台北 1 日電）國立中央大學今天表示，利用鹿林天文台一米和 40 公分望遠鏡，搭配國際其他望遠鏡數據，天文團隊觀測到初誕生恆星周圍形成原始行星證據，成果將刊在最新 1 期「天文物理期刊」。

這項成果爲中央大學天文所研究生胡佳伶以及指導教授陳文屏共同研究，中央大學表示，將有助於對行星的形成，有更進一步認識。

胡佳伶說，中大團隊參加由國際天文台觀測網，監測 Trumpler 37 這個年輕星團，年齡只有約 400 萬年，希望利用「掩星」方式，也就是行星運行到恆星前方所產生的亮度變化，來偵測行星存在。

胡佳伶說，在分析資料時，發現編號爲「仙王座 GM」這顆星球的亮度有奇特的變化方式，它大約相隔 1 年，會變暗長達 1 個月，這是前所未見的現象。

陳文屏說，原來想找行星，但沒有找到，卻意外偵測到可能是行星胚胎形成的首要步驟。

國際知名行星科學專家、中央大學天文所教授葉永烜說，行星形成的關鍵，就是恆星周圍的塵埃盤開始變得不均勻。在很多年輕恆星周圍可能也有類似現象，值得繼續發掘。

原文轉載自【2012-06-01/中央社首頁 > 教育文化 > 】

中央大學天文團隊觀測行星胚胎形成關鍵步驟

〔新網記者歸鴻亭台北報導〕　由我國學者主導的國際天文團隊，觀測到初誕生恆星周圍形成原始行星的證據，成果將刊載於 6 月 1 日出版之《天文物理期刊》。

中央大學天文所研究生胡佳伶以及指導教授陳文屏，利用鹿林天文台 1 米和 40 公分望遠鏡，搭配國際其他望遠鏡數據，取得重要成果，將有助於讓我們對行星的形成，有更進一步認識。

中央大學天文所指出，太陽、地球以及其他行星、衛星來自太空某團雲氣，由於自身萬有引力收縮，導致旋轉越來越快，成爲扁平形狀。雲氣由氣體與塵埃組成，收縮後溫度升高，最中央部分最終形成太陽，內部進行核子反應，產生光與熱。周圍盤狀雲氣當中的塵埃彼此凝集，逐漸變大成爲小行星、行星。

換句話說，行星是形成恆星的副產品，太空中應該有很多行星。天文學家的確在「嬰兒時期」的恆星周圍，觀測到由塵埃構成的盤狀結構，另方面則在「已經成年」超過數百顆恆星周圍找到具體成形的行星。

胡佳伶任職台北天文教育館，這個研究是她就讀中大天文所的碩士論文內容，中大團隊參加由國際天文台觀測網，監測 Trumpler 37 年輕星團，年齡只有約 400 萬年，希望利用「掩星」方式，也就是行星運行到恆星前方所產生的亮度變化，來偵測行星存在。

但是胡佳伶在分析資料時，發現編號爲「仙王座 GM」這顆星球的亮度有奇特的變化方式，它大約相隔 1 年，會變暗長達 1 個月，這是前所未見的現象。

陳文屏指出，原來想找行星沒有找到，卻意外偵測到可能是行星胚胎形成的首要步驟。

中央大學天文所教授葉永烜表示，行星形成的關鍵，就是恆星周圍的塵埃盤開始變得不均勻。在很多年輕恆星周圍可能也有類似現象，值得繼續發掘。

原文轉載自【2012-05-31/《新網新聞網》新網報導】

伸手摘星　科學人帶你「發現天文之美」

(2012-05-28 21:42)

絢爛的星空裡藏著多少秘密？無垠的宇宙正展現著哪些令人嘆爲觀止的美景？其他的星球是什麼模樣？宇宙中是否有其他生命存在？《科學人》繼去年 4 本大受好評的精采特輯，6 月再接再厲，推出「發現天文之美」精采特輯，集結《科學人》過往 10 年經典天文篇章，一饗廣大天文迷！

「發現天文之美」特輯，內容由近而遠，分爲 4 大單元：「深入星空」幫助讀者輕易推開天文學的厚重大門，參與恆星嘉年華，一窺星系傳奇的奧妙、見證行星創世紀，探索系外超級地球，也好好認識自小熟知的阿姆斯壯腳下的月球，以及太陽系裡的搞怪衛星。

「天文奇景」讓讀者戴上天際的項鍊，遠望太陽發火，領略驚天一爆超新星的神奇，探索太陽系八大奇景，了解星流魅影的來龍去脈。「星際奇航」率領眾讀者前進 水星，看看那貌似地球的衛星，一蹦卻又從月球到火星，才發現火星曾是水世界。「探索之眼」讓喜愛天文學的讀者，在攤開宇宙的藍圖之前，向哈伯致敬，再好好 透視韋伯望遠鏡，最終我們明白星空多麼的希臘，寄望未來的巨無霸望遠鏡能解開宇宙間更多的謎。

「發現天文之美」特輯特地邀請國立自然科學博物館館長孫維新爲讀者進行導讀，另有中研院地球科學研究所所長趙丰、中央大學天文研究所教授陳文屏、台大講座教授陳丕燊、知名天文部落客謝隆欽等多位國內天文學者專家撰寫書評。

孫維新的導讀內文提到，隨著科學發展，今日天文學的研究已經不再受政治和民粹的干擾，而能讓科學工作者單純根據所觀測到的現象探討其背後的道理，也逐漸發展出了「欣賞－探索－認知－珍惜」四階段的心理歷程，讓我們更了解自己的渺小，與面對大自然該有的謙卑。

趙丰則表示，現在越通達天文、地理的學者越不敢述說自己的學問，因爲學得越多，會知道「未知」才是更多，所知卻是相對越少。今年是熱鬧的天文奇景年，從超 級月亮、日環食到金星凌日，台灣掀起一股天文風潮，閱讀「發現天文之美」特輯，有助深入了解這些天文奇景的起源與演變。

廣告大師李奧貝納曾說「伸手摘星，即使徒勞無功，亦不致於滿手污泥」。身爲擁有無窮好奇心的渺小人類，該如何探索如此美麗又神秘的天文學，值得就從這本特輯開始。（整理／唐澄暐）

原文轉載自【2012-05-28/台灣立報 】

天氣放晴　天文迷爭睹上帝指環

- 李宗祐／綜合報導

天賜金戒　她要他求婚

連下一星期的豪大雨，昨日碰到睽違半世紀的日環食奇景，出奇放晴，新竹以北到基隆北海岸及金馬地區幾乎都看到「上帝指環」。尤其金門的天氣好到讓每天拜天公的天文迷直呼，「有拜有差，這裡的天氣好得太誇張了！」

爲了觀測拍攝台灣地區睽違五十四年的日環食奇景，台大資訊網路及多媒體研究所博士生顏易程上周末就跟著高雄市天文學會及高雄市科學教育輔導團五十多位天文迷趕赴金門。顏易程說，金門直到星期天還在下雨，沒有想到昨天凌晨拜拜後，天氣就變好了。

「我們凌晨三點不到，就開始架儀器準備觀測，觀測中，有幾次眼看著天氣好像要變壞，但雲飛來飛去，就是不會遮住太陽。」顏易程興奮地說，「老天爺要讓你看，擋都擋不住！」

清晨六點八分，月亮陰影整個切入太陽表面，全球矚目的日環食「上帝指環」登場。顏易程說，「這時天空完全沒有雲，看起來很漂亮，戴著太陽眼鏡看，覺得太陽中間灰灰的，但外圍很亮，有種神秘感，好像太陽中間的黑洞會把人吸進去一樣。」剎那間，大家都拍手鼓掌。

業餘天文觀測家蔡元生帶著全家人駐守在北海岸翡翠灣，他說，昨天早上翡翠灣附近一直多雲，偶爾從雲縫看到太陽露臉。好在，月亮完全切進太陽的時候，雲剛好散開，「我們看到一分鐘左右的日環食，也算很好運！」

中央大學鹿林天文台觀測助理林啓生星期天傍晚連夜下山，趕到北海岸跳石停車場架起望遠鏡「獵日」。

他說，剛開始太陽躲在雲裡，還好日環食登場時，雲散開幾十秒，辛苦總算有代價！

氣象局天文站技士鄭振豐直接殺到馬祖架設望遠鏡，並透過網路視訊現場轉播。但因網路湧進人數太多，清晨五點多就被塞爆當機，直至日食結束仍未恢復。氣象局稍晚已把精彩畫面公布上網，馬上引起網友爭相點閱。

原文轉載自【2012-05-22/中國時報/A5 版/生活新聞】

找到 16 小行星　我高中生名列第二

【許 敏溶／台北報導】台灣五所高中共三十餘名高一生，參加國際天文搜尋聯盟主辦的搜尋小行星活動，歷經近一個月努力，合計找出十六顆小行星，佔整體成果近三分 之一，在七個參賽國中名列第二，爲參賽三年最佳成績。其中宜蘭羅東高中獲五顆小行星

的暫時編號，數年後可望確認命名，參與學生直呼：「辛苦是值得的！」

分析影像找天體

台灣泛星計劃共同主持人、中央大學天文所教授陳文屏說，國際天文搜尋聯盟上月十五日至本月十九日舉辦搜尋小行星活動，台灣、美國、巴西、保加利亞、德國、 波蘭、葡萄牙七國共四十所高中或大學學生參與；台灣有羅東高中、北一女中、彰化高中、惠文高中、大里高中共三十多名高一生參賽。

陳文屏說，參賽學生透過網路下載尚未經科學家分析的影像，再用軟體找出移動天體，將發現的疑似小行星送回主辦單位就算「初步發現」，台灣初步發現十六顆，經後續觀測並驗證軌道後，即取得暫時編號，得再耗時數年才能將小行星確認命名，命名權歸屬國際天文搜尋聯盟。

「辛苦是值得的」

羅東高中爲首次參賽學校，負責指導的地科老師蘇敬怡說，學生何中楷發現三顆小行星取得暫時編號，是參與學生中最多，何說：「很高興，辛苦是值得的。」

初步發現小行星者並無獎金或獎牌。國立自然科學博物館館長孫維新說，台灣天文基礎設備不是最佳，能拿佳績讓人感動，凸顯台灣學生在天文影像比對與軟體操作上勝過他國。

原文轉載自【2012-04-26/蘋果日報/A8 版/要聞】

我高中生追星　1 個月發現 16 顆

【記者蔡永彬／台北報導】

有群愛「追星」的青少年，不是拿著相機跑去機場、演唱會看偶像；而是利用電腦分析天空影像，希望自己變成某顆小行星的發現者。台灣 5 所高中、30 多位學生花了 1 個多月追星，共發現 16 顆取得暫時編號的星體。

3 月 15 日到 4 月 19 日，「國際天文搜尋聯盟」（International Astronomical Search Collaboration，IASC）主辦尋找小行星活動，共有 7 個國家、40 所學校參加；台灣的羅東、北一女、彰化、惠文、大里 5 所高中的 30 多位學 生也一起參與「追星行動」。

中央大學天文研究所教授陳文屏表示，學生利用電腦軟體比對「泛星計畫」釋出、還沒經過科學家分析的影像，看 看有沒有「不該在這個時間、出現在這個位置的小亮點」。他說，當學生發現某顆亮點值得研究，會先和國際小行星中心的已知天體資料庫比對，若沒有符合的星 體，就算初步發現；初步找到的「疑似小行星」如果通過後續驗證，就能取得暫時編號。

陳文屏說，1 個月來共找到 59 顆暫時編號的小行星，台灣學生貢獻 16 顆，僅次於德

國的 20 顆；羅東高中獲得 5 個暫時編號，在所有學校中排第 3。

學生們都認爲，尋找小行星最難的不是技術問題，而是如何分工合作。各校指導老師除了教導他們科學技術之外，也告訴他們「你們不會因爲這個成名！」希望他們先別想著出名，而是利用這次機會好好學習。

羅東高中指導老師蘇敬怡說，他還記得大家發現第 1 顆移動星體時的激動。

原文轉載自【2012-04-26/聯合報/AA4 版/教育】

中大發現小行星　命名苗栗

(2012/4/25) 張彩鳳/苗栗報導

苗栗縣政府昨天舉行「苗栗小行星」命名通過記者會，正式宣布由中央大學發現的新行星，命名爲「苗栗小行星」。這顆行星位在火星和木星之間的小行星帶，距離 地球最近的距離約一點五億公里，繞太陽一圈約四點四三年。縣長劉政鴻表示，苗栗小行星代表所有的苗栗鄉親子弟在各領域發光發熱，榮耀苗栗，爲山城再寫下一 頁精采的傳奇。

中央大學代理校長劉振榮指出，民國五十一年時，中大在臺復校，學校發源地選在苗栗，當時地方人士捐出將軍山一帶約二十餘 甲土地，作爲復校地點；到了民國五十七年，學校又遷地中壢，如今中央大學已經是一所綜合性研究型大學，爲教育部「邁向頂尖大學計畫」之重點培植大學。爲感 念過往，將在民國九十七年十二月十八日，由學校天文所觀測助理蕭翔耀和廣州中山大學葉泉志同學共同發現的小行星，命名爲「苗栗」。

劉政鴻表示，很高興中央大學能將新發現的小行星命名爲「苗栗」，要在浩瀚的宇宙中發現新天體，除了專業之外，更需要恆心和毅力，這顆「苗栗小行星」不只讓世界看到苗栗，更讓苗栗揚名宇宙。

原文轉載自【2012-04-25/國語日報/2 版/文教新聞】

苗栗小行星　揚名宇宙

【大 紀元 2012 年 04 月 23 日訊】（大紀元記者陳文敏台灣苗栗報導）地靈人傑的苗栗是中央大學在台復校的發源地，中央大學飲水思源，特別將所發現的編號 246643 小行星命名「苗栗」(Miaoli)，23 日上午在苗栗縣府大廳舉行「苗栗小行星」命名通過記者會，讓苗栗躍上國際、揚名宇宙。

中央大學代理校長劉振榮頒贈小行星模型給苗栗縣現長劉政鴻，中大天文研究所所長周翊、苗栗教育界及中大在苗栗復校第 1 個成立的地球物理所畢業校友一起見證。

中大天文研究所所長周翊指出，苗栗小行星是 2008 年 12 月 18 日由中大天文所觀測

助理蕭祥耀與大陸廣州中山大學葉泉志同學共同發現，經國際天文學聯合會(IAU)通過，於 2011 年 10 月 12 日正式命名爲「苗栗」(Miaoli)。

周翊表示，苗栗小行星位於火星和木星之間的小行星帶，距離地球最近的距離約 1.5 億公里，繞太陽一圈約 4.43 年。2008 年發現時位於巨蟹座，目前則在飛馬座附近。

獲頒苗栗小行星，劉政鴻深感榮耀。他表示，中大有台灣最頂尖的科技，讓 「苗栗小行星」獲得國際認可，不只讓世界看到苗栗，更讓苗栗揚名宇宙。 （責任編輯：劉淳義）

原文轉載自【2012-04-23/大紀元時報】

苗栗小行星誕生　苗栗縣長期許揚名宇宙

魏攸芳/ 苗栗縣 報導

苗栗舊稱「貓裏」，位於台灣西部海岸線，境內山多平原少，故有「山城」之雅號。獨特客家美食文化及多采多姿的生態環境，塑造苗栗無限的風光與生命力。地 靈人傑之苗栗，正是中央大學在台復校的發源地，爲此，國內天文研究的搖籃地中央大學特別將所發現之編號 246643 小行星，命名苗栗（Miaoli），有 飲水思源之意涵，也讓「苗栗」能躍上國際、揚名宇宙。

中央大學代理校長劉振榮指出，民國五十一年中央大學在台復校，感謝苗栗縣政府和地 方人士的熱心奔走和大力協助，捐出將軍山一帶約二十餘甲土地，作爲中大復校之始，中大後來選定二平山（聯合大學現址）作爲立足基地，民國五十七年，中央大 學遷校中壢。走過半世紀，中大目前已是一所綜合性研究型大學，爲教育部「邁向頂尖大學計畫」之重點培植大學，並在世界大學評比當中，位居全球前五百大。爲 感念過往，除頒贈苗栗小行星之外，中央大學地科系也將辦理「地物所第一個十年．團聚」活動，邀請苗栗時期的畢業校友一同回到苗栗重溫舊夢。

苗栗小行星的發現，源自中央大學鹿林巡天計畫（Lulin Sky Survey，簡稱 LUSS），中央大學天文所指出，苗栗小行星於 2008 年 12 月 18 日由中央大學天文所觀測助理蕭翔耀和廣州中山大學葉泉志同學共同發現，2011 年 10 月 12 日經國際天文學聯合會(IAU/CSBN)正式通過，命名爲「苗栗」（Miaoli）。苗栗小行星目前位於火星和木星之間的小行星帶，距離地球最近的距離約 1.5 億公里，繞太 陽一圈約 4.43 年。2008 年最早發現時，位於巨蟹座附近，目前則在飛馬座附近。

苗栗縣長劉政鴻表示，很高興這次中央大學能將新發現 的小行星命名爲苗栗，要在浩瀚的宇宙中發現新天體，除了專業之外，更需要恆心和毅力，中央大學有台灣最頂尖的天文研究，這顆「苗栗小行星」不只讓世界看到 苗栗，更讓苗栗揚名宇宙。苗栗縣自從劉縣長上任以來，積極推動各大旗艦計畫，加速苗栗繁榮進步，對於提升縣民光榮感與幸福感，更是不遺餘力，尤其在教育方 面更是著力很深，除了整備縣內中小學各項軟硬體建設之外，對於加強與大專院校的合作更是不遺餘力，希望讓苗栗縣的學子能有更好的教育品質及提升苗栗教育的 競爭力，這顆「苗栗小行星」就代表所有的苗

栗鄉親子弟在各領域發光發熱榮耀苗栗，爲山城再寫下一頁精彩傳奇。（圖／苗栗縣政府提供）

原文轉載自【2012-04-24/ TraNews 台灣：TTNews 大台灣旅遊網】

中大感恩捐校地　小行星命名「苗栗」

2012-04-24 20:36:29

【新唐人亞太台 2012 年 4 月 24 日訊】無垠的星空，有一顆星星，叫做「苗栗」。這顆由國立中央大學鹿林巡天計畫，所發現的編號２４６６４３小行星，在之前被命名爲「苗栗」，而且還經國際天文聯合會通過。帶您一起來瞭解。

送上小行星模型，及由國際天文學聯合會通過命名所頒發的行星登記銘版，讓苗栗縣長劉政鴻相當開心。

苗栗縣長 劉政鴻：「要非常非常感謝我們中央大學，這一次 2008 的時候發現的小行星，竟然能夠把我們苗栗，這個 246643 的號碼釘上去以後，讓我們苗栗躍上國際舞台。」

位於火星和木星之間的這顆小行星，就是「苗栗小行星」，距離地球約 1.5 億公里，中大天文所所長表示，「苗栗小行星」，有著飲水思源的意涵。

中央大學天文研究所所長 周翊：「中央大學在台復校的時候，本來是在苗栗地區，後來才遷到中壢，所以苗栗是相當於，將我們中央大學在台復校這件事情，誕生出來的，所以爲了飲水思 源，我們就把我們發現的一顆小行星，命名給苗栗。」

除了專業之外，天文所的觀測人員可是付出了相當多的時間及努力。

中央大學天文研究所所長 周翊：「如果是碰到天氣好的話，那就是徹夜的觀測，所以說他們的生活跟別人是顛倒的，是一個非常辛苦，很長期日夜顛倒的一個工作。」

中大以苗栗爲小行星命名，讓台灣的天文研究成果，在國際上發光發熱。

新唐人亞太電視 陳彥如 台灣苗栗採訪報導

原文轉載自【2012-04-24/新唐人亞太電視台】

中央大學飲水思源　小行星命名苗栗

【聯合報／記者胡蓬生 ／即時報導】

「246643，你的名字叫苗栗！」國立中央大學在台復校 50 年，爲感念當年苗栗縣捐地設校，中央大學特別將 4 年前發現的小行星以「苗栗」命名，並獲國際天文學聯合會審議通過，從此無盡的蒼穹裡，多了顆名叫「苗栗」的小行星。

中央大學和苗栗縣政府上午向縣民公布這項好消息，小行星命名「苗栗」，不僅讓苗栗縣的名稱躍上國際和宇宙，這次命名也蘊含中央大學飲水思源的寓意；縣長劉政鴻表示很高興中央大學將小行星命名爲苗栗，這顆小行星不只讓世界看見苗栗，且讓苗栗揚

名宇宙。

編號 246643 的「苗栗小行星」，是中央大學鹿林天文台在 2008 年 12 月 18 日，由中央大學天文所觀測助理蕭翔耀和廣州中山大學學生葉泉志共同發現，去年 10 月 12 日經國際天文學聯合會通過命名苗栗 (Miaoli)。

原文轉載自【2012-04-24/聯合新聞網　地方 即時新聞 】

小行星叫苗栗　揚名宇宙

躍上銀河　世界公認　中央大學頒贈模型　劉政鴻感到光榮與驕傲

記者鍾文和苗栗報導

浩瀚無垠的星空，有一顆叫做「苗栗」(Miaoli)的星星，在飛馬座附近閃閃發光！這顆由國立中央大學鹿林巡天計畫所發現的編號２４６６４３小行星，命名為「苗栗」，日前經國際天文聯合會通過，縣長劉政鴻感到光榮與驕傲，並期許「苗栗」能躍上國際、揚名宇宙。

苗栗地靈人傑，擁有獨特的客家人文風貌及生態景觀，苗栗也是中央大學在台復校的發源地，中央大學為飲水思源，將２００８年 12 月 18 日天文所觀測員蕭翔耀及廣州中山大學葉泉志同學共同發現的小行星命名為「苗栗」。

中央大學昨天上午在縣府大廳召開記者會，由代理校長劉振榮頒贈小行星模型給縣長劉政鴻，中大天文研究所所長周翊、苗栗教育界及中大在苗栗復校第 1 個成立的地球物理所畢業校友一起出席見證。

建功國小學童準備大小望遠鏡，生動演出苗栗小行星發現經過；南庄鄉南庄、蓬萊、東河等國小學童分別演奏小提琴古典樂曲，與所有縣民分享苗栗躍上銀河的好消息。

劉振榮表示，中央大學民國 51 年在台復校，感謝苗栗縣政府和地方人士熱心奔走，後來選定二坪山聯合大學現址作為立足基地，民國 57 年才從苗栗遷校中壢，走過半世紀，如今已名列世界五百大，中大對苗栗懷著感恩的心，未來也將與聯大密切合作，帶動地方教育發展。

劉政鴻指出，苗栗這幾年正在銳變中，大型醫院、高鐵苗栗車站等重大建設都將陸續動工興設，相信二年後的苗栗絕對不一樣；此次「苗栗小行星」獲得國際認可，不只讓世界看見苗栗，更期待苗栗能揚名宇宙。

中大天文所所長周翊也表示，苗栗小行星目前位於火星和木星之間的小行星帶，距離地球最近距離約 1.5 億公里，繞太陽一圈約 4.43 年，２００８年剛發現時的位置在巨蟹座附近，目前則在飛馬座和寶瓶座之間。

他說，中大鹿林天文台自２００２年發現台灣第一顆小行星，累計迄今已發現 800 顆，其中有 20 顆已取得永久命名，所有新發現天體命名須報經國際小行星中心和ＩＡＵ小行星命名委員會審議通過，才公諸於世，並為世界各國公認，相當不容易。

原文轉載自【2012-04-24/民眾日報/15 版/北台灣要聞】

中央大學飲水思源　小行星命名苗栗

【記者胡蓬生】

「246643，你的名字叫苗栗！」國立中央大學在台復校 50 年，爲感念當年苗栗縣捐地設校，中央大學特別將 2008 年 12 月間發現的小行星以「苗栗」命名，並獲國際天文學聯合會審議通過，從此無盡的蒼穹裡，多了顆名叫「苗栗」的小行星。

編號 246643 的「苗栗小行星」，是中央大學特鹿林天文台在 2008 年 12 月 18 日，由中央大學特天文所觀測助理蕭翔耀和廣州中山大學學生葉泉志共同發現，去年 10 月 12 日經國際天文學聯合會通過命名苗栗(Miaoli)。

中央大學代理校長劉振榮表示，中央大學特民國 51 年在台復校，當時苗栗縣政府熱心協助，並獲地方人士捐地 20 多甲，中央大學特後來選定在二坪山 (現址爲國立聯合大學)設校，並率先開辦地球物理研究所，苗栗可說是中央大學特在台復校發源地。

民國 57 年中央大學特遷往中壢，走過半世紀，現已成綜合性研究型大學，這次命名也蘊含中央大學特飲水思源的寓意。

原文轉載自【2012-04-24/Upaper/2 版/焦點】

「苗栗」小行星誕生！　劉縣長感到光榮與驕傲

2012 年 4 月 24 日 12:02

記者許素蘭／苗栗報導

浩瀚無垠的星空，有一顆叫做「苗栗」的星星，在飛馬座附近閃閃發光！這顆由國立中央大學鹿林巡天計畫所發現的編號２４６６４３小行星，命名爲「苗栗」，日前經國際天文聯合會通過，縣長劉政鴻感到光榮與驕傲。

苗栗地靈人傑，擁有獨特的客家人文風貌及生態景觀，苗栗也是中央大學在台復校的發源地，中央大學爲飲水思源，將２００８年十二月十八日天文所觀測員蕭翔耀及廣州中山大學葉泉志同學共同發現的小行星命名爲「苗栗」。

22 日上午，中央大學在縣府大廳召開記者會，由代理校長劉振榮頒贈小行星模型給縣長劉政鴻，中大天文研究所所長周翊、苗栗教育界及中大在苗栗復校第一個成立的地球物理所畢業校友一起出席見證。

建功國小學童準備大小望遠鏡，生動演出苗栗小行星發現經過；南庄鄉南庄、蓬萊、

東河等國小學童分別演奏小提琴古典樂曲，與所有縣民分享苗栗躍上銀河的好消息。

劉振榮表示，中央大學民國五十一年在台復校，感謝苗栗縣政府和地方人士熱心奔走，後來選定二坪山聯合大學現址作爲立足基地，民國五十七年才從苗栗遷校中壢，走過半世紀，如今已名列世界五百大，中大對苗栗懷著感恩的心，未來也將與聯大密切合作，帶動地方教育發展。

劉政鴻指出，苗栗這幾年正在銳變中，大型醫院、高鐵苗栗車站等重大建設都將陸續動工興設，相信二年後的苗栗絕對不一樣；此次「苗栗小行星」獲得國際認可，不只讓世界看見苗栗，更期待苗栗能揚名宇宙。

周翊也表示，苗栗小行星目前位於火星和木星之間的小行星帶，距離地球最近距離約一點五億公里，繞太陽一圈約四點四三年，２００８年剛發現時的位置在巨蟹座附近，目前則在飛馬座和寶瓶座之間。

他說，中大鹿林天文台自２００２年發現台灣第一顆小行星，累計迄今已發現八百顆，其中有廿顆已取得永久命名，所有新發現天體命名須報經國際小行星中心和ＩＡＵ小行星命名委員會審議通過，才公諸於世，並爲世界各國公認，相當不容易。

原文轉載自【2012-04-24/NOWnews 今日新聞網】

中大苗栗小行星　獲國際認證

中央大學天文研究所鹿林天文台 97 年底，在火星、木星之間觀測到直徑 2 公里多的小行星，編號 246643，距離地球最近距離約 1.5 億公里，原本在巨蟹座附近，目前已運行到飛馬座附近，去年 10 月經國際天文學聯合會認證通過，命名爲「苗栗」。

中央大學代理校長劉振榮昨天表示，中大民國 51 年在台灣復校，感謝苗栗縣政府和地方人士慨捐苗栗市將軍山約 20 餘甲土地做爲校地；中央大學在民國 57 年遷 移到桃園縣中壢，但感念過往，這顆小行星因此用苗栗命名，代表中大對苗栗縣的飲水思源。用台灣縣市命名的小行星，苗栗是第 5 個，前 4 個爲南投、嘉義、高 雄、桃園。　（圖文：記者李信宏）

原文轉載自【2012-04-24/自由時報/A11 版/生活新聞】

中大發現小行星　命名苗栗

記者葉蒼秀／苗栗報導

一顆由中央大學鹿林巡天計畫所發現的小行星，爲感念苗栗是中大在台復校發源地，命名爲「苗栗」，二十三日上午在縣府大廳召開記者會，由代理校長劉振榮頒贈小行星模型給苗栗縣長劉政鴻。

劉振榮表示，中央大學在台復校，感謝苗栗縣政府和地方人士熱心奔走，中大對苗栗懷著感恩的心，未來也將與聯大密切合作，帶動地方教育發展。

劉政鴻指出，這次「苗栗小行星」獲得國際認可，不只讓世界看見苗栗，更期待苗栗能揚名宇宙。

中大天文所所長周翊表示，中大鹿林天文台自二ＯＯ二年發現台灣第一顆小行星，累計迄今已發現八百顆，其中有二十顆已取得永久命名，所有新發現天體命名須報經國際小行星中心和ＩＡＵ小行星命名委員會審議通過，才公諸於世，並爲世界各國公認，相當不容易。

原文轉載自【2012-04-24/中華日報/A8 版/北部綜合】

中大飲水思源　小行星命名苗栗

記者黃碧霞／苗栗報導

浩瀚無垠的星空，有一顆叫做「苗栗」（Miaoli）的星星，在飛馬座附近閃閃發光！這顆由國立中央大學鹿林巡天計畫所發現的編號 246643 小行星，命名爲「苗栗」，日前經國際天文聯合會通過，縣長劉政鴻感到光榮與驕傲，並期許「苗栗」能躍上國際、揚名宇宙。

苗栗地靈人傑，擁有獨特的客家人文風貌及生態景觀，苗栗也是中央大學在臺復校的發源地，中央大學爲飲水思源，將 2008 年 12 月 18 日天文所觀測員蕭翔耀及廣州中山大學葉泉志同學共同發現的小行星命名爲「苗栗」。

中央大學昨日上午在縣府大廳召開記者會，由代理校長劉振榮頒贈小行星模型給苗栗縣長劉政鴻，中大天文研究所所長周翊、苗栗教育界及中大在苗栗復校第 1 個成立的地球物理所畢業校友一起出席見證。

建功國小學童準備大小望遠鏡，生動演出苗栗小行星發現經過；南庄鄉南庄、蓬萊、東河等國小學童分別演奏小提琴古典樂曲，與所有縣民分享苗栗躍上銀河的好消息。

劉振榮表示，中央大學民國 51 年在臺復校，感謝苗栗縣政府和地方人士熱心奔走，後來選定二坪山聯合大學現址作爲立足基地，民國 57 年才從苗栗遷校中壢，走過半世紀，如今已名列世界五百大，中大對苗栗懷著感恩的心，未來也將與聯大密切合作，帶動地方教育發展。

劉政鴻指出，苗栗這幾年正在銳變中，大型醫院、高鐵苗栗車站等重大建設都將陸續動工興設，2 年後的苗栗絕對不一樣；這次「苗栗小行星」獲得國際認可，不只讓世界看見苗栗，更期待苗栗能揚名宇宙。

周翊則表示，苗栗小行星目前位於火星和木星之間的小行星帶，距離地球最近距離 1.5 億公里，繞太陽一圈約 4.43 年，2008 年剛發現時的位置在巨蟹座附近，目前則在飛馬座和寶瓶座之間。

原文轉載自【2012-04-24/青年日報/13 版/桃竹苗地方通訊】

中央大學小行星　名字叫「苗栗」

【聯合報／記者胡蓬生／苗栗縣報導】

「二四六六四三小行星，你的名字叫苗栗！」國立中央大學二〇〇八年發現一顆小行星，因感念苗栗縣捐地讓中大復校，將小行星命名爲「苗栗」，這項命名獲國際天文學聯合會審議通過，「苗栗」從此揚名宇宙。

編號二四六六四三的「苗栗小行星」，二〇〇八年十二月十八日，由中大天文所觀測助理蕭翔耀和廣州中山大學學生葉泉志，共同在中大鹿林天文台發現。

中央大學天文所所長周翊說，苗栗小行星位在火星和木星間的小行星帶，與地球最近距離約一點五億公里，繞太陽一圈要四點四三年；三年多前發現時，它在巨蟹座附近，今年三月已到了飛馬座和寶瓶座之間。

中大從二〇〇二年發現台灣第一顆小行星，累計發現八百多顆，其中廿顆取得永久命名，是亞洲發現小行星最活躍的地區。

周翊表示，小行星發現者擁有命名權，十年內可隨時行使；但根據國際天文學聯合會規範，小行星命名要排除商業行爲、政治人物等，命名通過後，將成爲這個天體的 永久名字，被世界各國公認。國內已命名的小行星包括嘉義、南投、高雄、桃園、中壢等縣市名稱，還有玉山、慈濟、鄒族、中大等。

中央大學代理校長劉振榮表示，央大一九六二年在台復校，當時在苗栗縣政府和地方人士熱心協調奔走下，獲捐廿多甲土地順利設校，並率先開辦地球物理研究所，苗栗可說是中大在台復校發源地。

他指出，中大後來遷往中壢，如今名列世界大學評比五百大之一，今年中大地球科學系還要辦「地物所第一個十年」團聚活動，邀苗栗時期校友回苗栗重溫舊夢。

原文轉載自【2012-04-24/聯合報/A6 版/生活】

當年來台復校地 中大感恩 將小行星命名「苗栗」

【陳慶居／苗栗報導】

二〇〇八年十二月由中央大學天文所觀測助理蕭翔耀和廣州中山大學學生葉泉志共同發現、目前介於火星與木星間的小行星，已通過國際天文學聯合會命名爲「苗栗」（Miaoli）。

中央大學代理校長劉振榮說，中央大學民國五十一年台灣復校地點就在苗栗，雖因故後來遷校中壢，此行仍以感恩之心授證給苗栗縣長劉政鴻，也象徵飲水思源，並祝福苗栗未來是閃亮之星。

「苗栗」小行星的發現，源自中央大學鹿林巡天計畫。天文所所長周翊表示，二〇〇八年十二月十八日發現這顆行星時，編號爲二四六六四三，確認爲首度發現後，於二 〇一一年十月十二日經國文天文學聯合會命名爲「苗栗」。它目前位置在火星與木星之間，與地球最近距離約一・五億公里，繞太陽一周約四・三年。

周翊表示，這顆小行星最初被發現時位在巨蟹座附近，繞行結果，目前處於飛馬座附近。劉振榮與周翊昨將仿製的小行星和命名認證贈予劉政鴻。劉振榮表示，中大民國五十一年在台復校時，曾受苗縣府及地方支持，捐出將軍山一帶廿多甲土地，後來一度選定二平山即聯合大學現址準備擴建。可惜因交通不便，加上聘請師資不易，校方幾經研究後，五十七年決定遷校中壢。

原文轉載自【2012-04-24/中國時報/A10 版/文化新聞】

中大發現小行星　命名苗栗

（中央社記者管瑞平苗栗縣 23 日電）

國立中央大學鹿林巡天計畫新發現 1 顆小行星，爲感念苗栗是中大在台復校發源地，校方將它命名爲「苗栗」，今天由代理校長劉振榮頒贈小行星模型給苗栗縣長劉政鴻。

中央大學代理校長劉振榮表示，民國 51 年中央大學在台復校，當時地方政府和熱心人士大力奔走協助，捐出 20 餘甲土地作爲復校之始，後因交通不便、師資難覓，民國 57 年遷校中壢。

劉振榮指出，走過半世紀，中大始終沒有忘記苗栗這塊在台復校的發源地，因此是「懷著感恩的心」，以苗栗（Miaoli）爲名，替新發現小行星命名。

中央大學今天在苗栗縣政府召開「苗栗小行星」命名通過記者會，將小行星模型頒贈給苗栗縣長劉政鴻並啓動水晶球，象徵小行星運行長久於天體中；中大天文研究所所長周翊及中大在苗栗復校第 1 個成立的地球物理所畢業校友也一起出席見證。

校方表示，苗栗小行星是公元 2008 年由中央大學天文所觀測助理蕭翔耀和廣州中山大學葉泉志兩名同學共同發現，去年經國際天文學聯合會正式通過，命名爲「苗栗」（Miaoli）。

周翊表示，小行星是目前唯一可由發現者命名並得到世界公認的天體，所有新發現天體命名須報經國際小行星中心和 IAU 小行星命名委員會審議通過，才公諸於世，爲世界各國公認。

他說，中大鹿林天文台自 2002 年發現台灣第一顆小行星，迄今已發現 800 顆，其中有 20 顆已取得永久命名；至於苗栗小行星，目前位於火星和木星之間的小行 星帶，距離地球最近距離約 1.5 億公里，繞太陽一圈約 4.43 年，2008 年剛發現時的位置在巨蟹座附近，目前則在飛馬座和寶瓶座之間。

苗栗縣長劉政鴻則感謝中大，浩瀚宇宙中有顆叫「苗栗」的星星，讓世界看見苗栗；他說苗栗這幾年正努力蛻變，大型醫療園區、高鐵車站等重大建設將陸續動工，未來的苗栗絕對不一樣，期待苗栗能在宇宙中發光揚名。

中大發現小行星　以吳大猷命名

【李宗祐／台北報導】

繼「李國鼎小行星」後，中央大學鹿林天文台在二〇〇八年二月廿七日觀測發現的編號二五六八九二小行星，經國際天文學聯合會審查通過，正式命名爲「吳大猷小行星」，以紀念被喻爲「近代中國物理學之父」的中央研究院已故院長吳大猷在台灣科學發展的卓越貢獻。

曾接受吳大猷指導，於一九五七年獲得諾貝爾物理獎的中研院士楊振寧昨日在香港獲悉「吳大猷小行星」通過命名後，透過友人表達「這個命名很有意義」。中央 大學天文研究所教授葉永烜，在昨日召開的二〇一二中華民國物理年會，致贈「吳大猷小行星」命名證書給「吳大猷學術基金會」，由元智大學校長兼基金會執行長 彭宗平代表接受。

葉永烜表示，吳大猷最爲人津津樂道的是，他在大陸西南聯大指導的兩位得意門生楊振寧和李政道共同在一九五七年獲得諾貝爾物理獎。政府遷台之後，他更呼籲 政府應該制定長期學術發展計畫，促成「國家長期發展科學委員會」成立，並在一九六七年出任國科會主委，可說是台灣科學發展主要奠基者和推動者。

除了國科會主委以外，吳大猷曾在一九八三年到一九九四年接掌中研院，使台灣學術研究逐漸在國際舞台嶄露頭角。直至二〇〇〇年病逝前，吳大猷也對科學教育 和社會文化極爲重視，經常撰文批評時政，不怕得罪當權者。六〇年代，政府計畫研製原子彈，吳大猷在面見先總統蔣公時，犯顏直諫，表達反對立場，展現剛正不 阿的學者風範。

葉永烜表示，隨著時光流逝，許多對台灣科技發展要重要貢獻的人物，近幾年逐漸被國人遺忘，「我們希望透過小行星命名，讓大家重新想起他們所留下的典範。」在此之前，中央大學也曾以「李國鼎小行星」，感念這位科技教父對科技及經濟發展的貢獻。

「吳大猷小行星」由鹿林天文台觀測助理林啓生與廣州中山大學學生葉泉志在二〇〇八年執行「巡天計畫」時共同發現。葉永烜表示，「巡天計畫」自二〇〇六年三月啓動以來，已觀測發現超過八百顆小行星、一顆近地小行星及一顆彗星。

原文轉載自【2012-01-18/中國時報/A11 版/文化新聞】

這顆小行星　叫做「吳大猷」

【記者蔡永彬／台北報導】

2012 中華民國物理年會昨天開幕。開幕式上，台灣聯合大學系統副校長葉永烜將一

塊記載「吳大猷」小行星基本資料的「銘板」，頒贈給吳大猷學術基金會執行長、元智大學校長彭宗平，向吳大猷致意，也表達飲水思源的意涵。

中央大學鹿林天文台觀測助理林啓生、中國大陸廣州中山大學學生葉泉志，2008 年 2 月 27 日共同發現一顆編號 256892 的小行星；去年 6 月 15 日經國際天文學聯合會（IAU）通過後，正式命名爲「吳大猷」（Wutayou）。目前這顆星位於天秤座位置附近。

中大天文研究所所長周翊表示，天文的蓬勃發展源自物理的重要基礎，天文等於是物理的分支。這顆小行星命名「吳大猷」，並有上千位物理學者共同見證頒贈儀式，更有意義。

葉永烜說，「吳大猷」小行星直徑約 3、4 公里，位於火星、木星間的小行星帶，比較靠近火星，距離地球約 2 至 3 個「天文單位」，相當於 3 至 4.5 億公里遠。吳大猷是 1957 年諾貝爾獎物理學獎得主李政道、楊振寧的啓蒙導師，學界尊他爲「近代中國物理學之父」。

原文轉載自【2012-01-18/聯合報/AA4 版/教育】

中大發現新行星　叫它吳大猷

【記者林進修／台北報導】

2008 年 2 月，長駐中央大學鹿林天文台觀測助理林啓生，與廣州中山大學觀測員葉泉志共同發現一顆小行星，編號爲 256892 小行星；去年 6 月經國際天文學聯合會(IAU)通過，命名爲「吳大猷」 (Wutayou)。這顆小行星證書及模型今天正式送給吳大猷基金會。

2012 年物理年會開幕式今天下午在中正大學舉行，台灣聯合大學系統副校長、中央大學天文所葉永烜教授將這顆小行星的證書及模型，頒贈給吳大猷學術基金會執行長、元智大學校長彭宗平，感念「近代中國物理學之父」吳大猷先生對科學發展的卓越貢獻。

中央大學天文研究所所長周翊表示，天文與物理的關係十分密切，天文學能蓬勃發展，來自於物理的重要基礎。這顆小行星命名爲「吳大猷」，不僅向物理大師致意，更有飲水思源的意涵。

葉永烜表示，「吳大猷」小行星位於火星及木星之間的小行星帶，而目前國際天文界發現並確認的十幾萬顆小行星中，中大發現的就占了 800 多顆。國際天文聯合 會小行星中心的統計資料顯示，鹿林天文台爲亞洲發現小行星最活躍的地方之一，發現紀錄數量居全球第 47 名，展現台灣人「以小搏大」的精神。

「吳大猷」小行星是個直徑約幾公里的小型星體，目前位於天秤座附近，距地球約 2 至 4 個天文單位、亦即地球和太陽之間距離的 2 到 4 倍。由於目前尚未從天文望遠鏡看到其光譜，不知明亮度和形狀，只能約略猜測是個不規則形的星體。

葉永烜說，中大發現的小行星，一旦經國際天文學聯合會確認後，就有命名權。這幾年以人物命名的小行星的有「溫世仁」、「李崇華」及「李國鼎」，以團體命名的有「慈

濟」及「雲門」，至於以地域命名的則有「桃園」、「嘉義」、「南投」及「中央大學」等。

原文轉載自【2012-01-17/聯合晚報/A8 版/生活醫藥】

中大發現　小行星命名吳大猷

【中央社）】

中央大學自 2006 年啓動鹿林巡天計畫，至今發現超過 800 顆小行星；爲紀念科學家吳大猷，中央大學經國際天文學聯合會通過，將 2008 年發現的編號 256892 小行星命名爲「吳大猷」。

2012 年物理年會昨天在中正大學舉行，會中由台灣聯合大學系統副校長、中央大學天文研究所教授葉永烜代表頒贈小行星的證書和模型給吳大猷學術基金會執行長、元智大學校長彭宗平，感念「近代中國物理學之父」吳大猷對科學發展的卓越貢獻。

「吳大猷」小行星，是在 2008 年 2 月 27 日由中央大學鹿林天文台觀測助理林啓生與廣州中山大學葉泉志共同發現，該小行星目前位於天秤座附近。

原文轉載自【2012-01-18/Upaper/2 版/焦點】

表揚物理大師　小行星命名吳大猷

楊惠芳/臺北報導

爲感念「近代中國物理學之父」吳大猷先生對科學發展的卓越貢獻，中央大學特別將編號二五六八九二小行星，命名爲「吳大猷」(Wutayou)，並，經國際 天文學聯合會通過。中央大學天文所葉永烜教授昨天在物理年會開幕式中，將這顆小行星證書和模型頒贈給吳大猷學術基金會執行長、元智大學校長彭宗平。

葉永烜教授表示，吳大猷先生爲國際著名之物理大師，曾擔任中央研究院院長。他對物理學界卓越的貢獻和影響，被學界尊爲「近代中國物理學之父」。他的貢獻不僅在物理，更改革台灣的科學教育，爲台灣高科技產業奠定了發展基礎。

中央大學天文研究所所長周翊表示，天文與物理的關係十分密切，今日天文的蓬勃發展，源自物理的重要基礎，早期牛頓發現萬有引力，其實是根據天文的觀測而 來；近代天文的觀測，如暗物質、暗能量等，反而提供物理研究的新課題。小行星命名爲「吳大猷」，不僅向這位物理大師致意，更有飲水思源的意涵。

原文轉載自【2012-01-18/國語日報/2 版/文教新聞】

發現小行星　命名吳大猷

【本報台北訊】中央大學自二〇〇六年啓動鹿林巡天計畫，至今發現超過八百顆小行星。二〇〇八年二月，長駐央大鹿林天文台觀測助理林啓生，與廣州中山大學觀測員 葉泉志共同發現一顆小行星，編號爲二五六八九二小行星；去年六月經國際天文學聯合會通過，命名爲「吳大猷」。這顆小行星證書及模型昨天送給吳大猷基金會。

二〇一二年物理年會開幕式昨天在中正大學舉行，台灣聯合大學系統副校長、中央大學天文所葉永烜教授將這顆小行星的證書及模型，頒贈給吳大猷學術基金會執行長、元智大學校長彭宗平，感念「近代中國物理學之父」吳大猷先生對科學發展的卓越貢獻。

中央大學天文研究所所長周翊表示，天文與物理的關係十分密切，天文學能蓬勃發展，來自於物理的重要基礎。這顆小行星命名爲「吳大猷」，不僅向物理大師致意，更有飲水思源的意涵。

「吳大猷」小行星是個直徑約幾公里的小型星體，位於天秤座附近，距地球約二至四個天文單位、亦即地球和太陽之間距離的二至四倍。由於目前尚未從天文望遠鏡看到其光譜，不知明亮度和形狀，只能約略猜測是個不規則形的星體。

原文轉載自【2012-01-18/人間福報/綜合 】

天秤座附近新行星　命名「吳大猷」

中央大學「鹿林巡天計劃」觀測天文，自 2006 年至今已發現超過 800 顆小行星，其中，長駐鹿林天文台觀測助理林啓生，與廣州中山大學觀測員葉泉志共同發 現、位於天秤座附近的編號 256892 小行星，爲紀念「近代中國物理學之父」吳大猷，去年 6 月經國際天文學聯合會通過，將該行星命名爲「吳大猷」，今將頒 發證書和模型給吳大猷學術基金會。

2012 年物理年會開幕式今天下午在中正大學舉行，台灣聯合大學系統副校長、中央大學天文研究所教授葉永烜，於會中代表將這顆小行的證書和模型，頒贈給吳大猷學術基金會執行長、元智大學校長彭宗平。

原文轉載自【2012-01-17/蘋果即時】

中大發現新行星　取名「吳大猷」

撰稿・編輯：李自立　　新聞引據：聯合晚報

2008 年 2 月，中央大學鹿林天文台觀測助理林啓生，與廣州中山大學觀測員葉泉志共同發現 1 顆小行星，編號爲 256892 小行星；去年 6 月經國際天文學 聯合會(IAU)通過，命名爲「吳大猷」(Wutayou)。這顆小行星證書及模型今天(17 日)正式送給吳大猷基金會。

2012 年物理年會開幕式今天下午在中正大學舉行，台灣聯合大學系統副校長、中

央大學天文所葉永烜教授將這顆小行星的證書及模型，頒贈給吳大猷學術基金會執行長、元智大學校長彭宗平，感念「近代中國物理學之父」吳大猷先生對科學發展的卓越貢獻。

中央大學天文研究所所長周翊表示，天文與物理的關係十分密切，天文學能蓬勃發展，來自於物理的重要基礎。這顆小行星命名爲「吳大猷」，不僅向物理大師致意，更有飲水思源的意涵。

葉永烜表示，「吳大猷」小行星位於火星及木星之間的小行星帶，而目前國際天文界發現並確認的 10 幾萬顆小行星中，中大發現的就占了 800 多顆。國際天文 聯合會小行星中心的統計資料顯示，鹿林天文台爲亞洲發現小行星最活躍的地方之一，發現紀錄數量居全球第 47 名，展現台灣人「以小搏大」的精神。

「吳大猷」小行星是個直徑約幾公里的小型星體，目前位於天秤座附近，距地球約 2 至 4 個天文單位、就是地球和太陽之間距離的 2 到 4 倍。由於目前尚未從天文望遠鏡看到其光譜，不知明亮度和形狀，只能約略猜測是個不規則形的星體。

葉永烜說，中大發現的小行星，一旦經國際天文學聯合會確認後，就有命名權。

原文轉載自【2012-01-17/中央廣播電臺新聞頻道】

教育櫥窗－命名吳大猷

旺報 【（李蜚鴻）】

長駐中央大學鹿林天文台觀測助理林啓生，與廣州中山大學觀測員葉泉志於 2008 年 2 月共同發現一顆小行星，編號爲 256892 小行星；去年 6 月經國際天 文學聯合會（IAU）通過，命名爲「吳大猷」 （Wutayou）。這顆小行星證書及模型日前正式送給吳大猷基金會。

中央大學天文所葉永烜教授說，中大發現的小行星，一旦經國際天文學聯合會確認後，就有命名權。日前台灣聯合大學系統副校長、中央大學天文所葉永烜教授將 這顆小行星的證書及模型，頒贈給吳大猷學術基金會執行長、元智大學校長彭宗平，感念「近代中國物理學之父」吳大猷先生對科學發展的卓越貢獻。

原文轉載自【2012-01-18/旺報】

中大發現新行星　命名吳大猷

爲感念「近代中國物理學之父」、前中研院院長吳大猷先生對科學發展的貢獻，中央大學特別在 2012 年物理年會開幕式中，於物理界 2000 人的見證下，經國際天文學聯合會通過後，將 2008 年所發現的編號 256892 小行星，正式命名爲「吳大猷」。

「吳大猷」小行星是 2008 年 2 月 27 日由中央大學鹿林天文台觀測助理林啓生和與廣

州中山大學葉泉志所共同發現，位於天秤座附近。（圖：中央大學提供/文：記者湯佳玲）

原文轉載自【2012-01-18/自由時報/A12 版/生活新聞】

中大發現小行星　命名吳大猷

（中央社記者許秩維台北 17 日電）中央大學自 2006 年啓動鹿林巡天計畫，至今發現超過 800 顆小行星；爲紀念科學家吳大猷，中央大學經國際天文學聯合會通過，將 2008 年發現的編號 256892 小行星命名爲「吳大猷」。

2012 年物理年會今天下午在中正大學舉行，會中由台灣聯合大學系統副校長、中央大學天文研究所教授葉永烜代表頒贈小行星的證書和模型給吳大猷學術基金會執行長、元智大學校長彭宗平，感念「近代中國物理學之父」吳大猷對科學發展的卓越貢獻。

中央大學天文研究所所長周翊表示，天文與物理的關係十分密切，天文的蓬勃發展源自物理的重要基礎，天文等於是物理的分支；而將小行星命名爲「吳大猷」，不只是向物理大師致意，也有飲水思源的意涵。

「吳大猷」小行星，是在 2008 年 2 月 27 日由中央大學鹿林天文台觀測助理林啓生與廣州中山大學葉泉志共同發現，2011 年 6 月 15 日取得命名通過，目前位於天秤座位置附近。

中央大學表示，中央大學鹿林巡天計畫自 2006 年啓動至今，已發現 800 多顆小行星、1 顆近地小行星和 1 顆彗星，而根據國際天文聯合會小行星中心的資料顯示，鹿林天文台爲亞洲發現小行星最活躍處所之一，發現紀錄居全球第 47 名。

原文轉載自【2012-01-17/中央社】

中大發現小行星　以吳大猷命名

【李宗祐／台北報導】

繼「李國鼎小行星」後，中央大學鹿林天文台在二〇〇八年二月廿七日觀測發現的編號二五六八九二小行星，經國際天文學聯合會審查通過，正式命名爲「吳大猷小行星」，以紀念被喻爲「近代中國物理學之父」的中央研究院已故院長吳大猷在台灣科學發展的卓越貢獻。

曾接受吳大猷指導，於一九五七年獲得諾貝爾物理獎的中研院士楊振寧昨日在香港獲悉「吳大猷小行星」通過命名後，透過友人表達「這個命名很有意義」。中央 大學天文研究所教授葉永烜，在昨日召開的二〇一二中華民國物理年會，致贈「吳大猷小行星」命名證書給「吳大猷學術基金會」，由元智大學校長兼基金會執行長 彭宗平代表接受。

葉永烜表示，吳大猷最爲人津津樂道的是，他在大陸西南聯大指導的兩位得意門生楊振寧和李政道共同在一九五七年獲得諾貝爾物理獎。政府遷台之後，他更呼籲 政

府應該制定長期學術發展計畫，促成「國家長期發展科學委員會」成立，並在一九六七年出任國科會主委，可說是台灣科學發展主要奠基者和推動者。

除了國科會主委以外，吳大猷曾在一九八三年到一九九四年接掌中研院，使台灣學術研究逐漸在國際舞台嶄露頭角。直至二〇〇〇年病逝前，吳大猷也對科學教育 和社會文化極爲重視，經常撰文批評時政，不怕得罪當權者。六〇年代，政府計畫研製原子彈，吳大猷在面見先總統蔣公時，犯顏直諫，表達反對立場，展現剛正不 阿的學者風範。

葉永烜表示，隨著時光流逝，許多對台灣科技發展要重要貢獻的人物，近幾年逐漸被國人遺忘，「我們希望透過小行星命名，讓大家重新想起他們所留下的典範。」在此之前，中央大學也曾以「李國鼎小行星」，感念這位科技教父對科技及經濟發展的貢獻。

「吳大猷小行星」由鹿林天文台觀測助理林啓生與廣州中山大學學生葉泉志在二〇〇八年執行「巡天計畫」時共同發現。葉永烜表示，「巡天計畫」自二〇〇六年三月啓動以來，已觀測發現超過八百顆小行星、一顆近地小行星及一顆彗星。

原文轉載自【2012-01-18/中國時報/A11 版/文化新聞】

這顆小行星　叫做「吳大猷」

【記者蔡永彬／台北報導】

2012 中華民國物理年會昨天開幕。開幕式上，台灣聯合大學系統副校長葉永烜將一塊記載「吳大猷」小行星基本資料的「銘板」，頒贈給吳大猷學術基金會執行長、元智大學校長彭宗平，向吳大猷致意，也表達飲水思源的意涵。

中央大學鹿林天文台觀測助理林啓生、中國大陸廣州中山大學學生葉泉志，2008 年 2 月 27 日共同發現一顆編號 256892 的小行星；去年 6 月 15 日經國際天文學聯合會（IAU）通過後，正式命名爲「吳大猷」（Wutayou）。目前這顆星位於天秤座位置附近。

中大天文研究所所長周翊表示，天文的蓬勃發展源自物理的重要基礎，天文等於是物理的分支。這顆小行星命名「吳大猷」，並有上千位物理學者共同見證頒贈儀式，更有意義。

葉永烜說，「吳大猷」小行星直徑約 3、4 公里，位於火星、木星間的小行星帶，比較靠近火星，距離地球約 2 至 3 個「天文單位」，相當於 3 至 4.5 億公里遠。吳大猷是 1957 年諾貝爾獎物理學獎得主李政道、楊振寧的啓蒙導師，學界尊他爲「近代中國物理學之父」。

原文轉載自【2012-01-18/聯合報/AA4 版/教育】

中大發現新行星　叫它吳大猷

【記者林進修／台北報導】

2008 年 2 月，長駐中央大學鹿林天文台觀測助理林啓生，與廣州中山大學觀測員葉泉志共同發現一顆小行星，編號爲 256892 小行星；去年 6 月經國際天文學聯合會(IAU)通過，命名爲「吳大猷」 (Wutayou)。這顆小行星證書及模型今天正式送給吳大猷基金會。

2012 年物理年會開幕式今天下午在中正大學舉行，台灣聯合大學系統副校長、中央大學天文所葉永烜教授將這顆小行星的證書及模型，頒贈給吳大猷學術基金會執行長、元智大學校長彭宗平，感念「近代中國物理學之父」吳大猷先生對科學發展的卓越貢獻。

中央大學天文研究所所長周翊表示，天文與物理的關係十分密切，天文學能蓬勃發展，來自於物理的重要基礎。這顆小行星命名爲「吳大猷」，不僅向物理大師致意，更有飲水思源的意涵。

葉永烜表示，「吳大猷」小行星位於火星及木星之間的小行星帶，而目前國際天文界發現並確認的十幾萬顆小行星中，中大發現的就占了 800 多顆。國際天文聯合 會小行星中心的統計資料顯示，鹿林天文台爲亞洲發現小行星最活躍的地方之一，發現紀錄數量居全球第 47 名，展現台灣人「以小搏大」的精神。

「吳大猷」小行星是個直徑約幾公里的小型星體，目前位於天秤座附近，距地球約 2 至 4 個天文單位、亦即地球和太陽之間距離的 2 到 4 倍。由於目前尚未從天文望遠鏡看到其光譜，不知明亮度和形狀，只能約略猜測是個不規則形的星體。

葉永烜說，中大發現的小行星，一旦經國際天文學聯合會確認後，就有命名權。這幾年以人物命名的小行星的有「溫世仁」、「李崇華」及「李國鼎」，以團體命名的有「慈濟」及「雲門」，至於以地域命名的則有「桃園」、「嘉義」、「南投」及「中央大學」等。

原文轉載自【2012-01-17/聯合晚報/A8 版/生活醫藥】

中大發現　小行星命名吳大猷

【中央社】

中央大學自 2006 年啓動鹿林巡天計畫，至今發現超過 800 顆小行星；爲紀念科學家吳大猷，中央大學經國際天文學聯合會通過，將 2008 年發現的編號 256892 小行星命名爲「吳大猷」。

2012 年物理年會昨天在中正大學舉行，會中由台灣聯合大學系統副校長、中央大學天文研究所教授葉永烜代表頒贈小行星的證書和模型給吳大猷學術基金會執行長、元智大學校長彭宗平，感念「近代中國物理學之父」吳大猷對科學發展的卓越貢獻。

「吳大猷」小行星，是在 2008 年 2 月 27 日由中央大學鹿林天文台觀測助理林啓生與廣州中山大學葉泉志共同發現，該小行星目前位於天秤座附近。

原文轉載自【2012-01-18/Upaper/2 版/焦點】

表揚物理大師　小行星命名吳大猷

楊惠芳/臺北報導

爲感念「近代中國物理學之父」吳大猷先生對科學發展的卓越貢獻，中央大學特別將編號二五六八九二小行星，命名爲「吳大猷」(Wutayou)，並，經國際 天文學聯合會通過。中央大學天文所葉永烜教授昨天在物理年會開幕式中，將這顆小行星證書和模型頒贈給吳大猷學術基金會執行長、元智大學校長彭宗平。

葉永烜教授表示，吳大猷先生爲國際著名之物理大師，曾擔任中央研究院院長。他對物理學界卓越的貢獻和影響，被學界尊爲「近代中國物理學之父」。他的貢獻不僅在物理，更改革台灣的科學教育，爲台灣高科技產業奠定了發展基礎。

中央大學天文研究所所長周翊表示，天文與物理的關係十分密切，今日天文的蓬勃發展，源自物理的重要基礎，早期牛頓發現萬有引力，其實是根據天文的觀測而 來；近代天文的觀測，如暗物質、暗能量等，反而提供物理研究的新課題。小行星命名爲「吳大猷」，不僅向這位物理大師致意，更有飲水思源的意涵。

原文轉載自【2012-01-18/國語日報/2 版/文教新聞

發現小行星　命名吳大猷

【本 報台北訊】中央大學自二○○六年啓動鹿林巡天計畫，至今發現超過八百顆小行星。二○○八年二月，長駐央大鹿林天文台觀測助理林啓生，與廣州中山大學觀測員 葉泉志共同發現一顆小行星，編號爲二五六八九二小行星；去年六月經國際天文學聯合會通過，命名爲「吳大猷」。這顆小行星證書及模型昨天送給吳大猷基金會。

二○一二年物理年會開幕式昨天在中正大學舉行，台灣聯合大學系統副校長、中央大學天文所葉永烜教授將這顆小行星的證書及模型，頒贈給吳大猷學術基金會執行長、元智大學校長彭宗平，感念「近代中國物理學之父」吳大猷先生對科學發展的卓越貢獻。

中央大學天文研究所所長周翊表示，天文與物理的關係十分密切，天文學能蓬勃發展，來自於物理的重要基礎。這顆小行星命名爲「吳大猷」，不僅向物理大師致意，更有飲水思源的意涵。

「吳大猷」小行星是個直徑約幾公里的小型星體，位於天秤座附近，距地球約二至四個天文單位、亦即地球和太陽之間距離的二至四倍。由於目前尚未從天文望遠鏡看到其光譜，不知明亮度和形狀，只能約略猜測是個不規則形的星體。

原文轉載自【2012-01-18/人間福報/綜合 】

天秤座附近新行星　命名「吳大猷」

中央大學「鹿林巡天計劃」觀測天文，自 2006 年至今已發現超過 800 顆小行星，其中，長駐鹿林天文台觀測助理林啓生，與廣州中山大學觀測員葉泉志共同發 現、位於天秤座附近的編號 256892 小行星，爲紀念「近代中國物理學之父」吳大猷，去年 6 月經國際天文學聯合會通過，將該行星命名爲「吳大猷」，今將頒 發證書和模型給吳大猷學術基金會。

2012 年物理年會開幕式今天下午在中正大學舉行，台灣聯合大學系統副校長、中央大學天文研究所教授葉永烜，於會中代表將這顆小行的證書和模型，頒贈給吳大猷學術基金會執行長、元智大學校長彭宗平。

原文轉載自【2012-01-17/蘋果即時】

中大發現新行星　取名「吳大猷」

撰稿・編輯：李自立　　新聞引據：聯合晚報

2008 年 2 月，中央大學鹿林天文台觀測助理林啓生，與廣州中山大學觀測員葉泉志共同發現 1 顆小行星，編號爲 256892 小行星；去年 6 月經國際天文學 聯合會(IAU)通過，命名爲「吳大猷」(Wutayou)。這顆小行星證書及模型今天(17 日)正式送給吳大猷基金會。

2012 年物理年會開幕式今天下午在中正大學舉行，台灣聯合大學系統副校長、中央大學天文所葉永烜教授將這顆小行星的證書及模型，頒贈給吳大猷學術基金會執行長、元智大學校長彭宗平，感念「近代中國物理學之父」吳大猷先生對科學發展的卓越貢獻。

中央大學天文研究所所長周翊表示，天文與物理的關係十分密切，天文學能蓬勃發展，來自於物理的重要基礎。這顆小行星命名爲「吳大猷」，不僅向物理大師致意，更有飲水思源的意涵。

葉永烜表示，「吳大猷」小行星位於火星及木星之間的小行星帶，而目前國際天文界發現並確認的 10 幾萬顆小行星中，中大發現的就占了 800 多顆。國際天文 聯合會小行星中心的統計資料顯示，鹿林天文台爲亞洲發現小行星最活躍的地方之一，發現紀錄數量居全球第 47 名，展現台灣人「以小搏大」的精神。

「吳大猷」小行星是個直徑約幾公里的小型星體，目前位於天秤座附近，距地球約 2 至 4 個天文單位、就是地球和太陽之間距離的 2 到 4 倍。由於目前尚未從天文望遠鏡看到其光譜，不知明亮度和形狀，只能約略猜測是個不規則形的星體。

葉永烜說，中大發現的小行星，一旦經國際天文學聯合會確認後，就有命名權。

原文轉載自【2012-01-17/中央廣播電臺新聞頻道】

教育櫥窗－命名吳大猷

旺報 【李蜚鴻】

長駐中央大學鹿林天文台觀測助理林啓生，與廣州中山大學觀測員葉泉志於2008年2月共同發現一顆小行星，編號爲256892小行星；去年6月經國際天 文學聯合會（IAU）通過，命名爲「吳大猷」 （Wutayou）。這顆小行星證書及模型日前正式送給吳大猷基金會。

中央大學天文所葉永烜教授說，中大發現的小行星，一旦經國際天文學聯合會確認後，就有命名權。日前台灣聯合大學系統副校長、中央大學天文所葉永烜教授將 這顆小行星的證書及模型，頒贈給吳大猷學術基金會執行長、元智大學校長彭宗平，感念「近代中國物理學之父」吳大猷先生對科學發展的卓越貢獻。

原文轉載自【2012-01-18/旺報】

中大發現新行星　命名吳大猷

爲感念「近代中國物理學之父」、前中研院院長吳大猷先生對科學發展的貢獻，中央大學特別在2012年物理年會開幕式中，於物理界2000人的見證下，經國際天文學聯合會通過後，將2008年所發現的編號256892小行星，正式命名爲「吳大猷」。

「吳大猷」小行星是2008年2月27日由中央大學鹿林天文台觀測助理林啓生和與廣州中山大學葉泉志所共同發現，位於天秤座附近。（圖：中央大學提供/文：記者湯佳玲）

原文轉載自【2012-01-18/自由時報/A12版/生活新聞】

中大發現小行星　命名吳大猷

（中央社記者許秩維台北17日電）中央大學自2006年啓動鹿林巡天計畫，至今發現超過800顆小行星；爲紀念科學家吳大猷，中央大學經國際天文學聯合會通過，將2008年發現的編號256892小行星命名爲「吳大猷」。

2012年物理年會今天下午在中正大學舉行，會中由台灣聯合大學系統副校長、中央大學天文研究所教授葉永烜代表頒贈小行星的證書和模型給吳大猷學術基金會執行長、元智大學校長彭宗平，感念「近代中國物理學之父」吳大猷對科學發展的卓越貢獻。

中央大學天文研究所所長周翊表示，天文與物理的關係十分密切，天文的蓬勃發展源自物理的重要基礎，天文等於是物理的分支；而將小行星命名爲「吳大猷」，不只是向物理大師致意，也有飲水思源的意涵。

「吳大猷」小行星，是在2008年2月27日由中央大學鹿林天文台觀測助理林啓生與

廣州中山大學葉泉志共同發現，2011 年 6 月 15 日取得命名通過，目前位於天秤座位置附近。

中央大學表示，中央大學鹿林巡天計畫自 2006 年啓動至今，已發現 800 多顆小行星、1 顆近地小行星和 1 顆彗星，而根據國際天文聯合會小行星中心的資料顯示，鹿林天文台爲亞洲發現小行星最活躍處所之一，發現紀錄居全球第 47 名。1010117

原文轉載自【2012-01-17/中央社】

每年1,4,7,10月出刊

102年2月5日第11期

中大校友通訊

母校身影

※本欄位長期徵稿，歡迎校友踴躍來稿！

一日如十年，十年如一日： 中大天文所成立20週年誌慶

文 / 張光祥

1992年中央大學成立天文研究所，開創國內天文學研究與教育的第一個機構，至今已20年。好奇號在火星上探索人類未來，中大天文所在培育探索人類未來的科學家。

為了天文觀測的需要，早期中大校園的照明燈都罩上黑色半球的燈罩，目的在於避免光害直接影響星空。現今因光害影響，校內的觀測較少，因此對夜間照明的控制逐漸降低，因而校內的照明燈也就變的五花八門。如果您在中大校園內看到此類型的燈，或許能喚起您對建校初期校園的記憶。中央大學目前是交通最方便的大學。有國際機場、高鐵，未來中壢市將有捷運經過，所以中大天文所可便利地與國內各學術單位交流，並與國際接軌。

黑色半球的照明比較不會影響夜間星空的觀測

光害造成人們的錯覺：浩瀚銀河看成夜間白雲片片

談起中大天文所師生觀測星空與流星雨的有趣故事：本所前所長蔡文祥老師回憶民國八十一年，帶著首屆天文研究所學生，到玉山國家公園進行天文觀測教學，在燦爛星空下，幾位不曾見過「銀河」的都市小孩，陶然自得的感受宇宙浩瀚，忽然有人迸出一句「為什麼天上那一大片白雲都不動？」他定睛一看，原來那亮麗耀眼的「銀河」，被誤認為「白雲」。才發覺需要創造更多機會，讓學生接近大自然與浩瀚宇宙。1998年獅子座流星雨引領大家觀測星空的風潮，曾經流傳一則冷笑話：「請問：看流星雨要用雨衣還是雨傘好？」

中大天文所成立於民國81年，為國內最早成立的天文研究所。20年來積極培育研究天文領域方面的菁英人才，並給予完整而嚴格的科學訓練，畢業校友散佈海內、外，從事研究、教育、儀器或工業研發等相關行業。本所主導規劃的與國際研究接軌所需之前瞻性基礎建設，已分佈在國內，如鹿林山、台南等地，都設立研究與教學使用之天文台，供各地民眾或學生教學觀星使用。

中大天文所師生在鹿林山經過多年謹慎規劃、選址、地形地質勘查、氣象資料蒐集、土木興建、儀器設備架設建構等艱辛歷程，於民國91年設置了一部購自德國，精度高、集光性佳，並配有自動導星系統、高靈敏度電子相機等設備的一公尺口徑望遠鏡，提供該所師生，以及台灣其他大學研究與教學需求。鹿林山天文台另安置了中美掩星計畫的四台50公分口徑超廣角望遠鏡。由於臺灣位於低緯度，佔有可見天區大的優勢，鹿林山天文台已成為國際間小型望遠鏡觀測網的重要成員。鹿林天文台目前為亞洲發現小行星活躍之處，發現記錄居全球第47名。

中央大學鹿林天文台介紹：有「鹿」而沒「路」的天文台

前往鹿林山天台是從臺灣的平原直登上3000公尺左右的大山，生態環境的改變就像從北回歸線到北極圈一樣，可體驗到豐富的生物多樣性。鹿林山，傳說是群鹿如林的地方，目前為台灣最高的天文台，也是國內天文學術的研究重鎮，天文台規模設備雖小，卻有著全世界極佳的觀測優勢。

其得天獨厚的觀測優勢有三，一是台灣高山多，鹿林天文台設於海拔2,862公尺的玉山國家公園旁，光害和塵害很少。其次，接近赤道的低緯度，可以觀測較寬廣的天域，尤其是南天球的天體，這是日本、韓國等高緯度國家所觀測不到的。再者，在經度上位於西太平洋重要觀測據點，沿夏威夷的大天文台群過來，下一次觀測站就是臺灣，國際上扮演著舉足輕重的地位。在國際上沒有一處可以取代它。

披星戴月，篳路藍縷的籌建過程

台灣天文發展最早可追溯至日據時代，但是一九九〇年代，中央大學在鹿林山開始籌備建立一米望遠鏡的天文台，才真正起步。相較於國際知名天文台豐沛的資源，鹿林天文台籌建過程可說是披星戴月，篳路藍縷，建設十餘年了，由於法規的限制，至今尚未有公路通往鹿林天文台，是世上少數幾個沒有路的天文台。車子到不了，即使是諾貝爾獎得主李遠哲前院長也得邊走邊爬上來，建設之困難可以想見。

在鹿林天文台的背後是許多原住民同胞的付出，鹿林海拔二千八百公尺，一般人很難在這麼高的地方工作生活。天文台建設之初，端賴布農族和鄒族原住民披荊斬棘，一磚一瓦揹上山頭。成立迄今，更有四位鄒族同仁全年365天24小時輪班守候，無論颱風來襲或除夕過年，在鹿林前山之巔堅守著崗位。他們是玉山的子民，守護著鹿林。建設鹿林天文台的同時，我們亦同步見證臺灣交通建設多處快速公路的完成，使得師生前往鹿林的時程大大縮短，從一天變半天。在賀伯颱風、921地震、桃芝颱風、88風災等天然災害與環境的巨大變遷（如土石流），重創山區的環境下我們仍一日又一日，滿懷希望。希望在不久的將來，能在對環境衝擊最小的狀況下完成2公尺望遠鏡天文台與道路設施。

參與許多國際大型計畫：第一個十年與第二個十年

透過天文望遠鏡看到的天空面積只有約月亮大小，用這月亮大小的視野逐一搜索整個天空稱為「巡天」，要從浩瀚星空找出會動的目標是一項大海撈針的工作。而且尋找彗星是跟全世界在競爭，每一萬個新發現的移動天體（小行星）裡只有一個彗星，機率只有萬分之一；同時也是跟時間在賽跑，只要晚一秒鐘發現就是別人的，唯有堅持到底才能揚名國際。跟全球幾個大型巡天計畫相比，鹿林巡天的規模只是他們的千百分之一，要想以小博大，就必須策略正確，並持之以恆。

鹿林天文台正是這種策略下的產物，第一個十年：從無到有，完成基礎建設。第二個十年：從一米到二米，佈局全球；有了更大更精良的望遠鏡之後，可以看得更多、看得更遠，培養更多的本土天文人才，在全球的天文學術研究上，讓台灣發光，站上更重要的一席之地。由天文所支撐的鹿林天文台在師生胼手胝足辛苦經營下，已有豐碩成果是國際上罕見的。因為一般研究型天文台的創立與營運，大部分屬國家級的直屬機構。

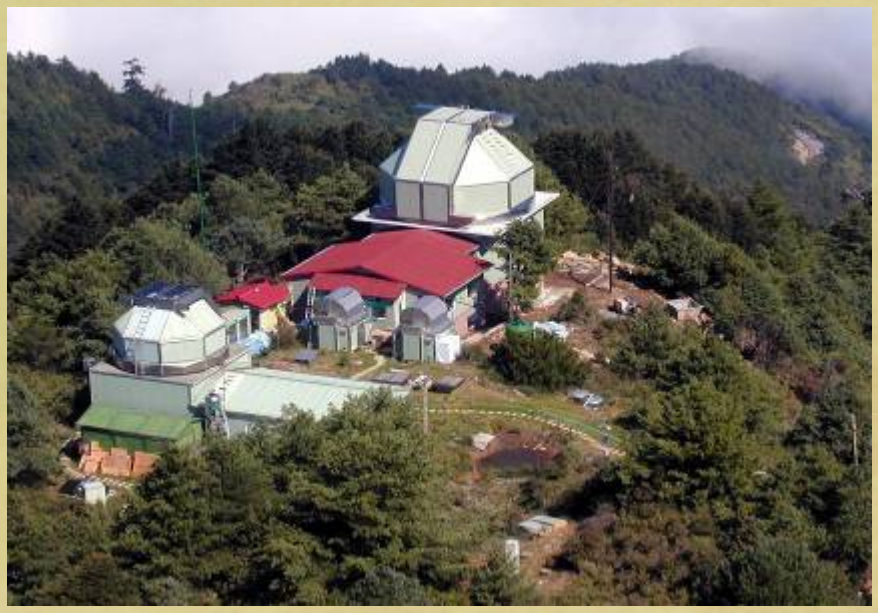

鹿林天文台空拍圖

第一個十年合影（拍攝地點於科學四館天文台）

我們於10月20日邀集百位以上校友來校，並邀請中大已命名的22顆小行星返校共襄盛舉；慶祝中大天文所成立20週年。中大將台灣推向宇宙的創舉，一步一腳印的將小行星名遍佈全台。中大天文所帶領台灣人物、地名、山名及少數民族名神遊宇宙。（22顆小行星：中大、鹿林、嘉義、南投、中壢、桃園、苗栗、玉山、小林村、慈濟、雲門、鄒族、溫世仁、鄭崇華、沈君山、李國鼎、吳大猷、鄧雨賢、鍾理和、蔡文祥、陳其寬、馮元楨）

有位詩人曾說過這樣一名句：
獸類未能完成的，
由人類去完成它。
人類未能完成的，
由渴望去完成它。

中大天文所將持續參與國際型重要天文計劃，共同完成探索宇宙，拓展人類空間領域的夢想。

第二個十年合影：中大天文所20週年慶 （攝影／陳澤銓，2012.10.20）

關於鹿林天文台

● 設立時間：民國88年(1999~迄今)
● 經緯度：東經120度52分，北緯23度28分
● 地點：鹿林前山，海拔2862公尺，位於逆溫層之上

● 參與計畫：
1. 中美掩星合作計畫(TAOS)
2. 低質量雙星系統X射線源
3. 彗星與小行星的觀測
4. 超新星巡天計畫
5. 伽瑪射線爆可見光餘暉認定
6. 參與美國夏威夷大學天文所及美國空軍合作的泛星計劃(Pan-STARRS)
7. 紅色精靈地面觀測與極低頻無線電波(ELF)偵測系統
8. 亞洲大氣污染物之長程輸送與衝擊研究
9. 中大太空所地airglow imager與華衛二號 ISUA之聯合觀測

● 發現新天體：
1. 2002年發現台灣第一顆小行星，迄今累計發現近800多顆。
2.2007年台灣本土望遠鏡發現第一顆彗星，名為「鹿林彗星」。
3. 2007年台灣第一顆近地小行星。

● 國際期刊：
自然《Nature》2篇 科學《Science》6篇

※本文作者為國立中央大學天文研究所專業技術士

>>回前頁

每年1,4,7,10月出刊

102年2月5日第11期

中大校友通訊

母校身影

※本欄位長期徵稿，歡迎校友踴躍來稿！

鍾理和小行星的追尋：科學與人文的創意激盪

文 / 張光祥

鍾理和小行星是一顆以文學家命名的小行星。當年，鍾理和從臺灣遠赴瀋陽，最後再返回故鄉臺灣，其探索原鄉意義的過程，就如同天文學家對宇宙的探索一般。

天文觀察點：鹿林天文台

鄰近阿里山與玉山的鹿林天文台夜間盡是星海、銀河、動物聲，陪伴觀測員浪漫又寂寞的冷冽時光。鹿林天文台是鹿的原鄉，天文台南方是旗山溪上游的楠梓仙溪，在美濃與荖濃溪會合即是高屏溪，天文台北面是神木溪，往下游匯入陳有蘭溪，再匯入濁水溪，可見鹿林是水、星星、鹿的原鄉。人類在此探索宇宙，觀察星空找到新發現來滿足好奇心。

鹿林山、阿里山、玉山環繞出來的雲海像極了一個良好港灣，
說不定在地球激烈的變遷下，會成為可停泊諾亞方舟的鹿港2號

左圖：部落古老的傳說：臺灣曾經歷大洪水
右圖：左為玉山主峰、右為鹿林山

福爾摩沙衛星拍攝下的鹿林山

觀測員與觀測助理的血液裡流著鄒族傳統勇士精神，不眠、不休在觀察天地宇宙的變化。白天片刻的休息時段，便將來自星星的訊息，利用四通八達的電腦網路傳送給各地的天文學家。在科學教育者的眼光下，每個人都在與時間競賽，想為人類提供宇宙的新發現。每年偶有遇到特殊天象時，也就是鹿林山最熱鬧的時候，民眾與媒體記者都聚焦於來自鹿林天文台的第一手新訊息。

左圖：2001年獅子座流星雨採訪
右圖：鹿林山天文台空拍圖

237187：在這個世界的舞台上，我們沒有缺席

然而，鍾理和小行星的發現，只是利用我們鹿林天文台望遠鏡所看到的一顆石頭而已，此發現並不特別，但是經過大家巧思就能發揮科學與文學的創作，引起人們重新欣賞他的文學鉅作，作品中有著北京、瀋陽、臺灣的故事。看到鍾理和與鍾台妹在北京的足跡，就像搜尋到小行星一樣，令人興奮與陶醉，人們的原鄉，隨祖先的遷移可知，當時的原鄉。而人們想知道宇宙空間的原鄉，可從小行星的探索開始；人類宇宙空間原鄉的探索可以憑藉科學與人文的創意發覺宇宙原鄉。

鍾理和小行星形如不規則的馬鈴薯，直徑約2000公尺左右，與阿里山的海拔高度相當。鍾理和小行星是中大鹿林天文台發現800多顆小行星中的一顆，經世界天文學聯合會小行星命名委員會命名通過，在國際小行星中心的永久編號是：237187。鹿林巡天計畫LUSS 的環境、設備與全球五大巡天計畫的設備比較有如小舢舨與航空母艦的懸殊差距，只能算是「小蝦米對大鯨魚」，而且鹿林天文台沒有路，但重要的是，「在這個世界的舞台上，我們沒有缺席」。根據國際天文學聯合會小行星中心 (IAU: Minor Planet Center) 的統計資料，鹿林天文台已成為亞洲發現小行星最活躍的地方，全球排名第48名。此排名公佈於國際天文學聯合會小行星中心的網頁網址如下：
http://www.minorplanetcenter.net/iau/lists/MPDiscSites.html

2010年中大全校運動會開幕式時，將有如馬鈴薯的中壢小行星頒贈給中壢市

鹿林山的鑑界窘境

天文台經過環評的流程後，籌劃人員從過程中理解到，天文台所在的這塊寶地，潛藏著許多從前所未知的故事；如施工過程中為了不干擾棲息的動植物，所以工程要細心而緩慢，對防火逃生、儀器運送、環境監測、施工時的安全，更是需要嚴加遵守的事項，而且現有觀測團隊的運作，又不能因施工而停擺，這些要求在平地並不困難，但在海拔近3000公尺，又沒有正式道路的情況下，2公尺望遠鏡要能開光使用，甚至比太空探測任務還要艱鉅。一如俗話所說：「比登天還難」。

我們經常從國際新聞聽聞中東情勢的不穩定，以色列與鄰國又有紛爭，可能引發戰爭。如果再從環評報告書仔細端詳，會發覺每次鑑界的過程，為何如此之冗長與繁複，參與的單位與人數眾多，把鹿林山頭擠的滿滿，甚至已無立錐之地這時天文台助理，最頭痛的是如何在沸點只有86度C的水溫下煮好一大鍋麵條，好讓這次鑑界的人員能夠在工作之餘飽肚子。在此過程中，由於這個山頭是嘉義、南投縣界，土地管轄的單位為台大實驗林與嘉義林區管理處，再加上玉山國家管理處，建管單位是嘉義縣政

府、南投縣政府、水土保持局等，周邊單位是環保署，還有將來營運配合的單位如台電、通訊公司、消防局...等單位，眾多部會的意見，使得每一次的會勘當下都未必會產出結論，可以說鹿林天文台要進行一項申請案，必須從位處土石流區域的道路開始，風雨無阻冒險上山的進行聯合會勘，依各單位表述後，才可以進行下一個流程...而每經一個流程都會出現未曾接觸到的陌生的法規。土地界線有很多的不確定性，想起小時後，看見鄰居大吵一架不相往來，其紛爭原因往往是房子土地鑑界而產生，所以把鹿林山的處境想像成以色列是很貼切的。

有如已無立錐之地，圖為2011年3月4日申請天文台索道案會勘

期待兩公尺望遠鏡天文台

天文台每個月都接受三個團體的參觀，有一次一個學童說，中央大學怎麼那麼小，只有兩棟校舍，因為他只看到三角點旁立牌上寫的大字「國立中央大學」，沒繼續往下方較小的字看完，就很大聲的在山頂上笑著說：『中央大學好小！』，助理聽到急忙出來解釋：「這是學校的天文台，校區在北部的中壢，你不相信再好好看清楚立牌下方的字，亦可上網看，更可以瞭解。」

我們好辛苦奮鬥了22年才有的小基地，2棟建物：一棟是嘉義阿里山鄉自忠78號，另一棟是南投信義鄉鹿林1號。往下方看到的鹿林山莊是依我們的門牌號，才申請編定出的鹿林2號。兩公尺口徑望遠鏡天文台完成後的門牌號應該是嘉義縣阿里山鄉中山村六鄰自忠76號，與玉山的排雲山莊同樣是中山村。我曾經說過一段話：『要在臺灣的高山上建天文台要有不怕死、像瘋子的精神，才能安然為望遠鏡開光。』當然此話是喝了會令人陶醉又能壯膽的飲料後才說的。

標示牌上有明顯的「國立中央大學」字樣，此圖為2001年李遠哲院長蒞鹿林參訪與觀測獅子座流星雨

幾年後，大家如果有機會，申請前往鹿林天文台參觀，將會大吃一驚，原來兩公尺望遠鏡要進行科學觀察，它需要一棟約20米高（將近六層樓）的建築物。鹿林夜空的獵戶星座，像慈祥的父親在高高的天上祝福著即將遠行的兒女，數百光年之遙的參宿四散發出溫暖的光芒。明亮的月光像母親般的溫暖人

間。哲學家康德所言:兩件人生最美好的事情：「一是人們善良的心靈，另一件就是我們頭頂上美麗的星空。」兩公尺望遠鏡天文台的落成是一件令人引頸期盼的百年大夢。

圖為兩公尺望遠鏡天文台的虛擬圖

圖為獵戶座與參宿四

標題：獅子座流星雨
心得：獅子座流星雨威力強大 震撼人心，
獵戶座像慈祥的父親祝福即將遠行的兒女。
時間：2001年11月19日 02:15 A.M.
地點：麟趾山
相機：Nikon FM2
鏡頭：20 mm
光圈：f 2.8

底片：400
曝光：10分
作者：張光祥

※本文作者為國立中央大學天文研究所專業技術士

>>回前頁

發行單位：國立中央大學秘書室
發行人：周景揚
指導委員：賴景義、陳奇夆
主編：李美儀（第11期開始）
編輯小組：駱季青、邱燕淇
版型設計：謝怡君、戴伯誠
網頁編輯：何庭武
聯絡電話 ：(03)4227151＃57046
E-mail：meiyi@cc.ncu.edu.tw
訂閱本報 | 查詢舊報

出版品
儀科中心年報
儀科中心簡訊
科儀新知雙月刊
奈米檢測技術
光學元件精密製造與檢測
光機電系統整合概論
微機電系統技術與應用
真空技術與應用
儀器總覽
科儀叢書

星光計畫鹿林天文台工作紀要


鹿林天文台

「星光有約」，隨著元旦假期開始，本中心星光研究團隊如同候鳥般前往玉山天文台赴約。於此際寒流伴行，增添此行些許插曲，心中默默祝禱，希望寒流能讓實驗環境濕度降低，能開啓新春研究第一響炮。從新竹出發，由水里入山，沿著彎延曲折的新中橫公路，經和社、台大實驗林，抵達塔塔加鞍部的東埔山莊，展開第一階段星光計畫實驗。

在山櫻花幾乎凋謝的塔塔加鞍部，氣溫還是相當寒冷，自清晨拂曉時刻，到月亮高掛的夜晚，溫度在 6－8℃ 及溼度在 70－80% 之間，這對星光計畫實驗是非常大的挑戰。星光計畫實驗中須在東埔山莊架設一座大口徑平面反射鏡，將天文台傳遞下來的星光折反射回天文台接收，由於天文台到東埔山莊最近的直線距離約 2.3 公里，要將微小光斑聚焦於平面鏡上，再精確地反射回天文台，光路的調校與對準絲毫不能有任何偏差。

在山莊上將所有儀器設備架設完畢後，隨即向玉山下的鹿林天文台前行，當車行至玉管處塔塔加管理站申請入山許可時，才驚覺車外氣溫已相當冷冽，過了塔塔加檢查哨後，再行半小時抵達鹿林前山登山口，即前往鹿林山頂的中大天文台。然而，前往天文台約 0.6 公里的陡峭林道，垂直爬升 120－130 公尺，稀薄又冰冷的空氣是登上天文台最大的挑戰，除簡便行李外，所有儀器設備都勞請原住民朋友協助揹上山，相當辛苦。

由於須整晚進行星光觀測，天文台從傍晚就開始熱鬧起來。夜幕低垂，月亮已升至半空，天文台外一片漆黑，氣溫僅 2－3℃ 左右，此時，追星的戲碼正式登場，星光實驗開始了。首先爲五車二星，它是御夫座中最亮的一顆恆星，是北半球夜空中第 5 顆亮星，僅次於天狼星、大角星、織女星及南河三等星，過了半夜，則由牧夫座大角星上場，直到觀測角度逐漸變小後，才輪到壓軸織女星登場。各個恆星伴著不同天候戲碼，較勁般地訴說各項天文學理的爭辯，直到天亮。

事實上星光實驗是相當辛苦，從架設儀器、調校光路、接收星光，到觀測資料整理，就得忙上一整夜；即使遇到天氣不佳，所有儀器及人員也都要隨時待命，緊盯著天文台即時氣象，只要天氣好轉，就得準備接收星光，記錄觀測數據，整理資料直到天亮。尤其當一個人徹夜未眠，體力精力耗盡時，此時大概僅剩儀器還忠實的記述著夜空星體精靈般難以捉摸的對話。

進行天文台星光實驗多次，每次都有截然不同的體驗，例如綺麗的夕陽爲即席夜空實驗鼓勵，取得星光時的喜悅，撫慰徹夜未眠的疲憊，惹厭的雲霧，不時擊碎如夢似幻的美景。然天文台上的天際星空，總是深湛而透明，2013 玉山初春夜空，因星光計畫有著無限的遐思，於此預祝星光實驗圓滿成功。

遙測光電儀器發展組 林育全

儀科中心簡訊 115 期：中華民國 102 年 02 月 28 日出版

更新日期：2013 年 3 月 15 日

國家實驗研究院儀器科技研究中心 (300 新竹市科學園區研發六路 20 號 地圖)
系統管理人員 (侯琬伊) | 中心服務信箱 | 客戶意見信箱

科技遇上人文 巡天二十年 中大天文觀星記

2013/1/23 | 作者：文／張光祥

文與圖／張光祥

一九九二年中央大學成立天文研究所，開創國內天文學研究與教育的第一個機構，至今已二十年。如今好奇號在火星上探索人類未來，我們在這裡培育探索人類未來的科學家。

夜間白雲與浩瀚銀河

爲了天文觀測的需要，早期校園的照明燈都罩上黑色半球的燈罩，目的在於避免光害直接影響星空。現今因光害影響，校內的觀測較少，因此對夜間照明的控制逐漸降低，校內的照明燈也就五花八門。

當初，半黑半白設計的照明燈只剩校史館前一盞，保留了校園早期原有照明的風味。如果您在中大校園內看到此類型的燈，或許能喚起您對建校初期校園的記憶。

談起天文所師生觀測星空與流星雨的有趣故事：蔡文祥教授回憶民國八十一年，帶著首屆天文研究所學生，到玉山國家公園進行觀測教學，在燦爛星空下，幾位不曾見過「銀河」的都市小孩，陶然自得地感受宇宙浩瀚，忽然有人迸出一句「爲什麼天上那一大片白雲都不動？」他定睛一看，原來那亮麗耀眼的「銀河」，被誤認爲「白雲」。也令人想起，一九九八年獅子座流星雨引領大家觀測星空的風潮，也曾經流傳一則冷笑話：「請問：看流星雨要用雨衣還是雨傘好？」

有「鹿」而沒「路」的天文台

天文所師生在鹿林山經過多年謹慎規畫、選址、地形地質勘查、氣象資料蒐集、土木興建、儀器設備架設等艱辛歷程，於民國九十一年設置了一部購自德國，精度高、集光性佳，並配有自動導星系統、高靈敏度電子相機等設備的一公尺口徑望遠鏡，提供師生，以及台灣其他大學研究與教學。鹿林山天文台另安置了中美掩星計畫的四台五十公分口徑超廣角望遠鏡。由於台灣位於低緯度，占有可見天區大的優勢，鹿林山天文台已成爲國際間小型望遠鏡觀測網的重要成員。

前往鹿林山天台是從台灣的平原直登三千公尺左右的大山，生態環境的改變就像從北回歸線到北極圈一樣，可體驗到豐富的生物多樣性。鹿林山，傳說是群鹿如林的地方，目前爲台灣最高的天文台，也是國內天文學術的研究重鎮，天文台規模設備雖小，卻有著全世界極佳的觀測優勢。

其得天獨厚的觀測優勢不只在於台灣高山多，鹿林天文台設於海拔二八六二公尺的玉山國家公園旁，光害和塵害很少。接近赤道的低緯度，也可以觀測較寬廣的天域，尤其是南天球的天體，這是日本、韓國等高緯度國家所觀測不到的。再者，在經度上位於西太平洋重要觀測據點，沿夏威夷的大天文台群過來，下一次觀測站就是台灣，國際上扮演著舉足輕重的地位。在國際上沒有一處可以取代它。

披星戴月，篳路藍縷

台灣天文發展最早可追溯至日據時代，但是一九九〇年代，中央大學在鹿林山開始籌備建立一米望遠鏡的天文台，才真正起步。相較於國際知名天文台豐沛的資源，鹿林天文台籌建過程可說是披星戴月，篳路藍縷，建設十餘年了，由於法規的限制，至今尚未有公路通往鹿林天文台，是世上少數幾個沒有路的天文台。

在鹿林天文台的背後是許多在地住民的付出，鹿林海拔二千八百公尺，一般人很難在這麼高的地方工作生活。天文台建設之初，端賴布農族和鄒族朋友披荊斬棘，一磚一瓦揹上山頭。成立迄今，更有四位鄒族同仁全年三六五天二十四小時輪班守候，無論颱風來襲或除夕過年，在鹿林前山之巔堅守著崗位。他們是玉山的子民，守護著鹿林。

建設鹿林天文台的同時，我們亦同步見證台灣交通建設多處快速公路的完成，使得師生前往鹿林的時程大大縮短，從一天變半天。在賀伯颱風、九二一地震、桃芝颱風、八八風災等天然災害與環境的巨大變遷，重創山區的環境下我們，仍一日又一日，滿懷希望。希望在不久的將來，能在對環境衝擊最小的狀況下，完成二公尺望遠鏡天文台與道路設施。

兩個十年

透過天文望遠鏡看到的天空面積只有約月亮大小，用這月亮大小的視野逐一搜索整個天空稱爲「巡天」，要從浩瀚星空找出會動的目標是一項大海撈針的工作。而且尋找彗星是跟全世界在競爭，每一萬個新發現的移動天體（小行星）裡只有一個彗星，機率只有萬分之一；同時也是跟時間在賽跑，只要晚一秒鐘發現就是別人的，跟全球幾個大型巡天計畫相比，鹿林巡天的規模只是他們的千百分之一，要想以小博大，就必須策略正確，並持之以恆。

鹿林天文台正是這種策略下的計畫，第一個十年：從無到有，完成基礎建設。第二個十年：從一米到二米，有了更大更精良的望遠鏡之後，可以看得更多、看得更遠，培養更多的本土天文人才，在全球的天文學術研究上，讓台灣發光，站上更重要的一席之地。鹿林天文台在師生胼手胝足辛苦經營下，已有豐碩成果是國際上罕見的。

十月二十日邀集了百位以上校友來校，並邀請中大已命名的二十二顆小行星返校共襄盛舉；慶祝中大天文所成立二十周年，持續地一步一腳印，將小行星名遍布全台，帶領台灣人物、地名、山名及少數民族之名神遊宇宙。

漫天星空的觀察者
鹿林天文台

■黃中

從中央大學天文所葉永烜教授口中的「一個小鐵皮屋」開始，到成爲東南亞地區條件最佳的天文台，鹿林天文台在台灣的天文觀測研究上已有傑出的成績。2005年鹿林天文台參與美國航太總署（NASA）「深撞號」（Deep Impact）觀測計畫，相關地面觀察團隊的論文已刊登在國際知名期刊《科學》（*Science*）上。

葉教授表示，由於到國外租用天文台成本昂貴而且耗時，於是國內開始進行天文台的選址評估。爲了尋找最佳的觀測場地，研究團隊經歷多年的長期視相、氣候、大氣穩定度等條件觀察研究，找到海拔2,862公尺，臨近玉山國家公園的鹿林前山山頂，決定在那裡設立一個天文台，並於民國88年興建完工啓用。

鹿林天文台完工之後，爲了不同的科學觀測任務，陸續設置76公分、50公分、1米等不同口徑的望遠鏡。其中購自德國的1米口徑望遠鏡在「台灣超新星巡天計畫」中有卓越表現，已觀察到十多個超新星爆炸的現象。

葉永烜教授進一步解釋說，觀察超新星可用來測量遠處星系的距離，證明宇宙的膨脹速率仍在增加，並推論出暗物質與暗能量的存在，因此更多的超新星觀測研究對於宇宙學有重要的指標性意義。他指出，利用台灣低緯度的地理優勢，選擇偏南天的星系，能夠發現更多新的超新星。

葉教授表示，世界上的天文台幾乎都集中在西半球，相較之下，東亞地區天文台密度極低。因爲地球自轉的關係，觀察天體的連續變化或短暫出現的天文現象，就要靠位於東半球低緯度的鹿林天文台「接力」進行觀測，因此鹿林天文台的資料有其重要性。葉教授說，國外天文台很多，設備也很好，但他們仍需要鹿林天文台的協助，這是我們占優勢的地方。

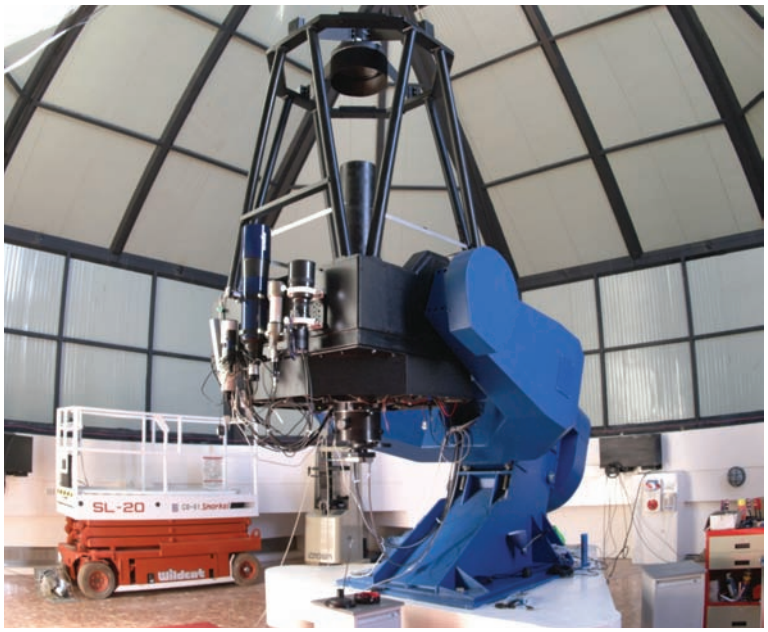

鹿林天文台的1米望遠鏡（又稱LOT）架設於控制中心，2002年開始觀測，執行科學研究及教學任務。

美國NASA「深撞號」在2005年撞向彗星「譚普一號」時，需要全球天文台接力觀測，「當時預估撞擊後最重要的觀測時機，剛好是台灣可以清楚觀測的時刻，於是我們得以參加。」葉教授表示，這就是利用鹿林天文台優勢位置參與國際重要計畫的契機。

「發展天文學研究，就像爬山一樣，要一步一步往上爬。」葉永烜教授表示，接下來他們希望與夏威夷大學合作，共同進行「泛星計畫」（Panoramic Survey Telescope and Rapid Response System, Pan-STARRS），這個計畫的主要任務是偵查可能對地球構成碰撞威脅的近地物體。中央大學研究團隊運用鹿林天文台的經驗，籌劃增設2米口徑望遠鏡，藉此與國際接軌，把國內天文學研究推向新的境界。

黃中
台灣大學新聞研究所

延伸閱讀
1. 鹿林天文台：http://www.lulin.ncu.edu.tw/，3/2/2007
2. 胡瑞華、葉永烜（民94），在疏散星團中尋找系外行星與變星，台北天文館學報，3期，48-56。

【天文學】

台灣鹿林天文台小兵立大功

短爆發型GRB在可見光的首度發現

撰文／邱淑慧

在看似靜謐的星空中，幾乎每天都有劇烈的爆炸發生。其中尤以γ射線爆發（gamma-ray burst, GRB）最為驚人。GRB在極短暫的時間內（0.01~1000秒），會釋放出相當於數百個超新星同時爆炸的能量，而且多集中在γ射線波段。這麼巨大的能量究竟如何產生，目前仍是天文學家亟欲解開的謎題。

台灣的中央大學天文所，自去年7月起與中國大陸的北京天文台、日本東京大學的木曾天文台以及理化學研究所宇宙放射線實驗室合作，進行關於GRB在可見光波段的研究，終於在今年9月24日於台灣的鹿林天文台有重大發現。

GRB觀測上的困難，在於它的γ射線輻射持續的時間很短暫，而且因為大氣的吸收，在地面上無法觀測γ射線，只能仰賴太空望遠鏡。不過令人慶幸的是，經由觀測發現，有些GRB在爆發後，會在其他波段留下持續數小時至數天的餘暉，並且隨時間逐漸變暗。於是，觀察餘暉的變化情形，便成為天文學家推測GRB周遭環境，以及建立相關模型的重要線索。

天文學家利用NASA的「高能暫現事件探索者衛星」（HETE-2）在太空中偵測GRB。當偵測到爆發時，HETE-2會即時通報地面相關天文台，進行可見光的觀測。藉由這樣的方法，對於爆發時間超過兩秒的「長爆發型GRB」已有許多觀測結果。然而，對於爆發時間極短暫的「短爆發型GRB」，則因可見光餘暉從來不曾被觀測到，更令科學家引領而望。

今年9月24日，HETE-2針對編號GRB040924的爆發發出警報，其γ射線僅持續短暫的1.2秒。中央大學天文所鹿林天文台接收到此項訊號後，立即在天候狀況許可時，利用一米望遠鏡（Lulin One Meter Telescope, LOT）在爆發後兩個小時拍到可見光影像。中央大學天文所博士生黃癸雲表示，在對照星圖後確定該位置本來沒有任何星體，經由後續的觀測與資料分析，發現其光度確實隨時間逐漸減弱，因此確認拍攝到GRB040924的

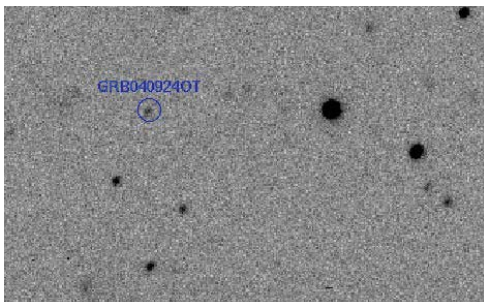

GRB040924爆發後兩小時的可見光影像，圖中標示處原來並沒有星體（觀測者：林宏欽、胡瑞華）

影像來源：黃癸雲（左）、張明新

台灣高山上的眼睛——鹿林天文台

鹿林天文台位於南投縣與嘉義縣交界，鄰近玉山國家公園，海拔高達2862公尺，可大幅減少大氣對觀測的干擾。由於世界天文台幾乎集中在西半球，相較之下，東亞地區天文台密度極低，因地球自轉的關係，當要觀察天體的連續變化或短暫出現的天文現象時，鹿林天文台的資料具有關鍵的重要性。而與東京木曾天文台、北京天文台相較，其可觀測的天區也更廣（除整個北天外，最南可至赤緯-40°）。

更多關於鹿林天文台的資訊可參閱http://www.lulin.ncu.edu.tw/。

可見光餘暉。黃奕雲說：「我們有此重要發現的根本原因，在於鹿林天文台的觀測者都願意在自己的觀測時間，協助自己研究範圍外的即時天象觀測！」

這是首度有短爆發型GRB在可見光被發現，對了解GRB的產生機制具有關鍵性的重要。同時這也是自去年10月起陸續發現六顆超新星之外，台灣的天文台再次展現觀測實力。中央大學天文所負責此計畫的葉永烜教授與其研究團隊，將進一步申請國外更大口徑的望遠鏡，從事光譜與紅外線波段觀測，以期更了解其產生機制。同時也希望繼續藉由鹿林天文台，累積更多關於GRB的觀測資料。

【資訊科技】

RFID新標準上場

射頻識別的技術推廣，邁出了一大步！

撰文／翁千婷

美國零售業大廠威名百貨（Walmart）要求其前100名供應商在2005年1月1日前，必須在所有包裝箱和貨箱架上使用射頻識別標籤（RFID tag），德國連鎖商店麥德龍（Metro）使用RFID貨架的「未來商店」也於今年5月開張，他們都希望藉由RFID技術的導入，提升產品的管理效率。RFID技術已成為科技業者關注的重點之一，然而，缺乏使用頻帶的共識、標籤格式的標準，以及成本高昂等問題，讓有心參與的業者裹足不前。為了解決此一問題，EPCglobal與自動識別實驗室（Auto-ID Lab）合作，為RFID產品供應商提供有關各種無線頻率的硬體和軟體介面的詳盡規格和文件。新的射頻識別標籤標準，將於今年年底出爐。

在10月8日的「EPC射頻識別應用國際高峰論壇」上，EPCglobal技術長巴德爾（Henri Barthel）解釋，RFID根據使用頻帶的不同，分為五個等級，EPCglobal將會制定各等級晶片的規格、在不同頻帶使用的溝通介面與通訊協定等標準。自動識別實驗室主持人之一恩格斯則表示，他們目前正致力於催生第二代標籤的標準。

新一代晶片使用900MHz的第一級晶片，將於2005年開始量產，具有可一次讀取至少200個、多讀取器同時讀取、下密碼自動銷毀等特性，更符合業者的需求，也兼顧到消費者的隱私。RFID標籤生產成本過高的問題也可望解決，降低至每個只要一美分。

過去幾年來，台灣也已經有導入RFID技術的廠商。目前是美國威名百貨亞洲區指定包裝廠商之一的永豐餘公司，將EPCglobal的電子商品條碼系統與既存的企業資源規劃軟體整合，除了可以達到商品資訊透明化，加強與客戶間的信任之外，還可改善庫存管理模式、交易付款模式與交易週期，為公司帶來正面效益。台北醫學大學則將RFID應用於醫療管理，除了追蹤之外，根據讀取器放置的位置，還可達到定位功能，了解病患或醫療藥品所在位置，提供更即時的醫療照護。為了在技術上不落人後，工研院已經成立RFID研發及產業應用聯盟，自行開發出高頻RFID晶片，讓台灣也有能力成為RFID供應商。

RFID技術因其使用無線電波傳輸，可隨時讀取資訊的特性，吸引了人們的眼光。即時追蹤產品流向、管理庫存、自動收費系統等，都是其未來可能的應用（參見2004年2月號〈未來生活的隱形僕人〉）。儘管RFID前景看好，但是仍有許多未知數，標準是否能夠普及、成本能否降低，消費者的接受度等等，都在考驗著它的未來。

射頻識別知多少？

射頻識別（RFID）是一種運用無線電波傳輸訊息的識別技術，一組射頻識別系統由標籤與讀取機組成。標籤上裝有電路，不需要電池。當讀取機從一段距離外間歇發射能量給標籤時，標籤上的電路即可通電，與讀取機交換訊息。標籤基本上是在一塊矽晶片上加裝簡單的天線，然後以玻璃或塑膠組件封裝而成，詳見2004年2月號〈未來生活的隱形僕人〉。

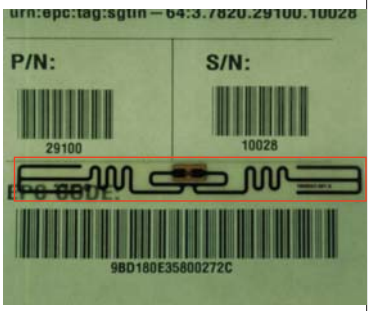

附有條碼的RFID標籤嵌有矽晶片以及感測用的天線（紅框內）。

影像來源：帝商科技

Lulin Observatory, National Central University

Established in 1992, Lulin Observatory administered by National Central University (NCU) is the first graduate program in Taiwan. There are eight full-time faculty members, working in diverse research fields, ranging from merging galaxies, AGNs, GRBs, X-ray binaries, star formation, star clusters, Galactic structure, to solar-system bodies. Currently there are about 20 students in the PhD program and about the same number in the MS program. A diverse curriculum in astronomy and astrophysics is offered by the faculty, both at the graduate level and at the undergraduate level together with the physics and space science majors.

The institute operates the Lulin Observatory, hosting a one-meter, a 40-cm, and a 35-cm telescope. These facilities serve the faculty and students for education and basic research uses. With an elevation of 2862 m above sea level, Lulin is located at the geometric center of the island, amid the central mountain range, with a west


Lulin Observatory

Pacific longitude particularly apt for observing celestial events. The Lulin One-meter Telescope (LOT) is open to the international community, and is equipped with a standard CCD imager, a low-dispersion spectrograph, and an optical tri-color simultaneous imaging polarimeter. A near-infrared imager will be available by the end of 2013. The Lulin Observatory also hosts the Taiwanese-American Occultation Survey (TAOS), which has an array of four telescopes, each with a 50-cm aperture and a field of 2.7 deg in diameter. This array monitors stellar brightness for chance occultation events by Kuiper-belt objects. A two-meter telescope is being planned at Lulin. In addition to competitive access to telescopes such as the CFHT, UKIRT, Subaru, Gemini, VLT, SMA, ALMA and other ground-based facilities, our faculty and students also make use of Fermi, Swift, Suzaku, and Chandra space instruments.

NCU is a member of the international scientific consortium of the Panoramic Survey Telescope And Rapid Response System (Pan-STARRS). Its prototype, PS1, is located in Haleakala, Hawaii. The 1.8 m telescope, equipped with a giga-pixel camera that can render a 7 square degree field, patrols the entire visible sky several times a month at multiple optical wavelengths up to 1 micron. Objects changing brightness (transients, variable stars) or positions (solar-system objects) will be winnowed out, and very deep static sky data are accumulated. Together with several university groups in Taiwan, NCU partners with PS1 institutes, in the USA, Germany, and UK, to pioneer studies on cosmic variability. We are also negotiating to have data access to the Palomar Transient Factory (PTF) project, a time-domain sky survey led by the California Institute of Technology.

The Institute celebrates its 20th anniversary this year, and the international faculty, postdocs and students continue to challenge frontier scientific topics and cutting-edge instrument developments. The institute maintains a vigorous visitor program. Please refer to http://www.astro.ncu.edu.tw for more detailed information about the insitute. ■

Wen-Ping Chen
Professor of Physics at National Central University

Dear President Liu and President Lee:

I was the chairman of the NCU Institute of Physics and Astronomy, 1977-80. This newly established institute was the first graduate astronomy institute of Taiwan. A major mission of mine was establishing the NCU Observatory and this astronomy education program. Ministry of Education had offered an equipment budget NT$ 8,000,000 for the astronomic telescope. Since there was no astronomic telescope and observatory expert in Taiwan, I invited Professor and Mrs. Aden Baker Meinel of the University of Arizona to visit Taiwan and help this project. Professor Meinel had developed several pioneering programs, such as (i) Established the U.S. Kitt Peak National Observatory, (ii) Established the Optical Science Center of the University of Arizona, (iii) Invented and designed the Multi-Mirror Telescope (MMT) for UA Astronomy Observatory. The MMT optics concept was the base of many modern giant telescopes. He had been the presidents of (i) U.S. Astronomy Society and (ii) Optical Society of America. The NCU telescope budget was only good for purchasing a 24 in (60 cm) educational telescope. He was willing to accept my invitation because the NCU observatory project was the pioneer astronomy education program of Taiwan.

At September 23 2002, the University of Arizona held a SPIE symposium celebrating Professor Meinel's 80th birthday. I had offered a paper "Meinel's Taiwan Visits" for this symposium. A copy is attached for your reference. I think that it could provide a part record of NCU's development history at Taiwan.

Professor Meinel passed away, October 2, 2011. A memory biography was published in "Physics Today", May, 2011. A copy is attached for your reference.

Please contact with me if you need more detailed information.

Best regards,

倪祖偉, Tsu-Wei Nee, Ph.D.
CEO and Chief Scientist
Neopola Optical Analysis, Inc.
27 Harbor View Dr.
Richmond, CA 94804-7496
U. S. A.
Tel: 1-510-215-2938 e-mail: tsuw.nee@gmail.com

MEINELS' TAIWAN VISITS

1978-80

SPIE Symposium on A. B. Meinel's 80th Birthday
Univeristy of Arizona, Tucson, AZ
September 23, 2002

Tsu-Wei Nee, NAWCWD, China Lake, CA

- **MEINELS' CONTRIBUTION TO THE ASTRONOMY PROGRAM OF NATIONAL CENTRAL UNIVERSITY**
- **NCU AND ASTRONOMY OBSERVATORY**
- **ROC ASTROMOMY SOCIETY ACTIVITIES, 1978**
- **SIGHTSEEINGS**

MEINELS' CONTRIBUTION TO THE ASTRONOMY PROGRAMS OF TAIWAN 1978 - 80

THE INSTITUTE OF PHYSICS AND ASTRONOMY OF NATIONAL CENTRAL UNIVERSITY WAS ESTABLISHED IN AUGUST 1977. IT IS THE FIRST GRADUATE ASTRONOMY INSTITUTE OF TAIWAN, R.O.C.

Under the support of National Research Council, R.O.C. and National Science Foundation, U.S.A., Dr. and Mrs. A. B. Meinel had participated the following NCU astronomy projects:

- DESIGNED THE NEW NCU OBSERVATORY
- ENGINEERING DESIGN OF THE MAJOR TELESCOPE –
  - 24 INCH CASSEGRAIN AND COUDE OPTICS TELESCOPE
- CONTRACT NEGOTIATION WITH PERKIN-ELMER INC.
- HELPED THE GRADUATE ASTRONOMY PROGRAM
  - DEVELOPMENT OF THE INSTITUTE OF PHYSICS AND ASTRONOMY - BOTH GRADUATE COURESES AND RESEARCH TOPICS

NATIONAL CENTRAL UNIVERISTY

CAMPUS

PRESIDENT S. M. LEE

NATIONAL CENTRAL UNIVERISTY

FACULY PARTY OF THE INSTITUTE OF PHYSICS AND ASTRONOMY

NCU ASTRONOMY OBSERVATORY
CONSTRUCTION 1980

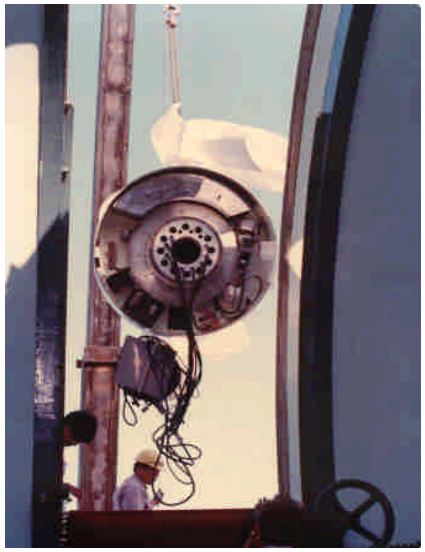

OBSERVATION

GALEXY

HALEY COMET

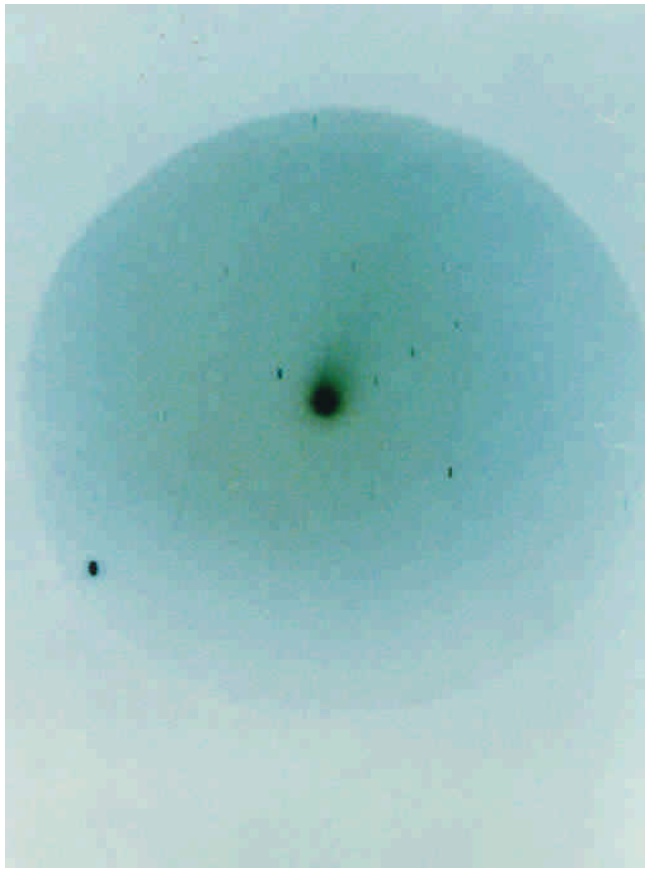

ROC ASTRONOMY SOCIETY ACTIVITIES
10TH ANNUAL MEETING 1978

TAIPEI CITY PUBLIC COLLOQUIUM

VISITED PRESIDENT C. K. YEN

SIGHTSEEING

PALACE MUSIUM

ROADSIDE SHOW

KINMEN ISLAND

YE-LIU BEACH